

GeoPlanet: Earth and Planetary Sciences

Monika B. Kalinowska  
Magdalena M. Mrokowska  
Paweł M. Rowiński *Editors*

# Free Surface Flows and Transport Processes

36th International School of Hydraulics

 Springer

# **GeoPlanet: Earth and Planetary Sciences**

## **Editor-in-chief**

Paweł M. Rowiński

## **Series editors**

Marek Banaszekiewicz, Warsaw, Poland

Janusz Pempkowiak, Sopot, Poland

Marek Lewandowski, Warsaw, Poland

Marek Sarna, Warsaw, Poland

More information about this series at <http://www.springer.com/series/8821>


Monika B. Kalinowska · Magdalena M. Mrokowska  
Paweł M. Rowiński  
Editors


# Free Surface Flows and Transport Processes


36th International School of Hydraulics

 Springer

*Editors*

Monika B. Kalinowska   
Hydrology and Hydrodynamics Department  
Institute of Geophysics, Polish Academy  
of Sciences  
Warsaw  
Poland

Paweł M. Rowiński   
Hydrology and Hydrodynamics Department  
Institute of Geophysics, Polish Academy  
of Sciences  
Warsaw  
Poland

Magdalena M. Mrokowska   
Hydrology and Hydrodynamics Department  
Institute of Geophysics, Polish Academy  
of Sciences  
Warsaw  
Poland

The GeoPlanet: Earth and Planetary Sciences Book Series is in part a continuation of Monographic Volumes of Publications of the Institute of Geophysics, Polish Academy of Sciences, the journal published since 1962 (<http://pub.igf.edu.pl/index.php>).

ISSN 2190-5193

ISSN 2190-5207 (electronic)

GeoPlanet: Earth and Planetary Sciences

ISBN 978-3-319-70913-0

ISBN 978-3-319-70914-7 (eBook)

<https://doi.org/10.1007/978-3-319-70914-7>

Library of Congress Control Number: 2017958606

© Springer International Publishing AG 2018

This work is subject to copyright. All rights are reserved by the Publisher, whether the whole or part of the material is concerned, specifically the rights of translation, reprinting, reuse of illustrations, recitation, broadcasting, reproduction on microfilms or in any other physical way, and transmission or information storage and retrieval, electronic adaptation, computer software, or by similar or dissimilar methodology now known or hereafter developed.

The use of general descriptive names, registered names, trademarks, service marks, etc. in this publication does not imply, even in the absence of a specific statement, that such names are exempt from the relevant protective laws and regulations and therefore free for general use.

The publisher, the authors and the editors are safe to assume that the advice and information in this book are believed to be true and accurate at the date of publication. Neither the publisher nor the authors or the editors give a warranty, express or implied, with respect to the material contained herein or for any errors or omissions that may have been made. The publisher remains neutral with regard to jurisdictional claims in published maps and institutional affiliations.

Printed on acid-free paper

This Springer imprint is published by Springer Nature  
The registered company is Springer International Publishing AG  
The registered company address is: Gewerbestrasse 11, 6330 Cham, Switzerland

## Series Editors

- Geophysics      Paweł M. Rowiński  
*Editor-in-Chief*  
Institute of Geophysics  
Polish Academy of Sciences  
ul. Ks. Janusza 64  
01-452 Warszawa, Poland  
p.rowinski@igf.edu.pl
- Space Sciences    Marek Banaszekiewicz  
Space Research Centre  
Polish Academy of Sciences  
ul. Bartycka 18A  
00-716 Warszawa, Poland
- Oceanology      Janusz Pempkowiak  
Institute of Oceanology  
Polish Academy of Sciences  
Powstańców Warszawy 55  
81-712 Sopot, Poland
- Geology          Marek Lewandowski  
Institute of Geological Sciences  
Polish Academy of Sciences  
ul. Twarda 51/55  
00-818 Warszawa, Poland
- Astronomy        Marek Sarna  
Nicolaus Copernicus Astronomical Centre  
Polish Academy of Sciences  
ul. Bartycka 18  
00-716 Warszawa, Poland  
sarna@camk.edu.pl

# **Managing Editor**

**Anna Dziembowska**

Institute of Geophysics, Polish Academy of Sciences

# Advisory Board

## **Robert Anczkiewicz**

Research Centre in Kraków  
Institute of Geological Sciences  
Kraków, Poland

## **Aleksander Brzeziński**

Space Research Centre  
Polish Academy of Sciences  
Warszawa, Poland

## **Javier Cuadros**

Department of Mineralogy  
Natural History Museum  
London, UK

## **Jerzy Dera**

Institute of Oceanology  
Polish Academy of Sciences  
Sopot, Poland

## **Evgeni Fedorovich**

School of Meteorology  
University of Oklahoma  
Norman, USA

## **Wolfgang Franke**

Geologisch-Paläntologisches Institut  
Johann Wolfgang Goethe-Universität  
Frankfurt/Main, Germany

## **Bertrand Fritz**

Ecole et Observatoire des  
Sciences de la Terre,  
Laboratoire d'Hydrologie  
et de Géochimie de Strasbourg  
Université de Strasbourg et CNRS  
Strasbourg, France

## **Truls Johannessen**

Geophysical Institute  
University of Bergen  
Bergen, Norway

## **Michael A. Kaminski**

Department of Earth Sciences  
University College London  
London, UK

## **Andrzej Kijko**

Aon Benfield  
Natural Hazards Research Centre  
University of Pretoria  
Pretoria, South Africa

## **Francois Leblanc**

Laboratoire Atmospheres, Milieux  
Observations Spatiales, CNRS/IPSL  
Paris, France



**Kon-Kee Liu**

Institute of Hydrological  
and Oceanic Sciences  
National Central University Jhongli  
Jhongli, Taiwan

**Teresa Madeyska**

Research Centre in Warsaw  
Institute of Geological Sciences  
Warszawa, Poland

**Stanisław Massel**

Institute of Oceanology  
Polish Academy of Sciences  
Sopot, Poland

**Antonio Meloni**

Instituto Nazionale di Geofisica  
Rome, Italy

**Evangelos Papathanassiou**

Hellenic Centre for Marine Research  
Anavissos, Greece

**Kaja Pietsch**

AGH University of Science and  
Technology  
Kraków, Poland

**Dušan Plašienka**

Prírodovedecká fakulta, UK  
Univerzita Komenského  
Bratislava, Slovakia

**Barbara Popielawska**

Space Research Centre  
Polish Academy of Sciences  
Warszawa, Poland

**Tilman Spohn**

Deutsches Zentrum für Luftund  
Raumfahrt in der Helmholtz  
Gemeinschaft  
Institut für Planetenforschung  
Berlin, Germany

**Krzysztof Stasiewicz**

Swedish Institute of Space Physics  
Uppsala, Sweden

**Ewa Szuszkiewicz**

Department of Astronomy  
and Astrophysics  
University of Szczecin  
Szczecin, Poland

**Roman Teisseyre**

Department of Theoretical Geophysics  
Institute of Geophysics  
Polish Academy of Sciences  
Warszawa, Poland

**Jacek Tronczynski**

Laboratory of Biogeochemistry  
of Organic Contaminants  
IFREMER DCN\_BE  
Nantes, France

**Steve Wallis**

School of the Built Environment  
Heriot-Watt University  
Riccarton, Edinburgh  
Scotland, UK

**Wacław M. Zuberek**

Department of Applied Geology  
University of Silesia  
Sosnowiec, Poland

**Piotr Źycki**

Nicolaus Copernicus Astronomical  
Centre  
Polish Academy of Sciences  
Warszawa, Poland

# Preface

Water is arguably one of the most significant research challenges of the twenty-first century. There is also growing awareness that addressing water-related problems in an integrated manner can have a range of multiple benefits for society, including synergies with sustainable development goals. Water-related problems do not stop at national borders, and cooperation across countries, including the exchange of experiences and best-practice examples, will become increasingly important in addressing the common challenge that lies ahead. At the same time, developments in hydraulics research, one of key water-related scientific disciplines, have significantly changed the way that people tackle the problems of water resources and their management. Institute of Geophysics of the Polish Academy of Sciences recognized this powerful influence of hydraulics on solving real-life problems, particularly with respect to rivers. This led to the holding of the already 7th International School of Hydraulics in Jachranka, Poland, in May 23–26, 2017. Note that earlier schools had been mostly national events and in total the meeting in Jachranka was 36th in a row. The conference deliberated on a range of hydraulics-related topics. This year School was themed “Free surface flows and transport processes” to provide a platform mostly for academics and young researchers but also for industry practitioners and decision makers to discuss their research projects and other work-in-progress, to promote collaboration for further research as well as to recommend practical measures for water management.

We were honored to have distinguished scholars, namely **Robert Ettema** from Department of Civil and Environmental Engineering, Colorado State University, USA; **John Fenton** from Institute of Hydraulic and Water Resources Engineering, Vienna University of Technology, Austria; **Ana Maria Da Silva** from Department of Civil Engineering, Queen’s University, Canada; and **Silke Wieprecht** from Institute for Modelling Hydraulic and Environmental Systems, University of Stuttgart, Germany, as our keynote speakers. On top of that, invited lectures were given by **Mario Franca** from Swiss Federal Institute of Technology of Lausanne, Laboratory of Hydraulic Constructions, Switzerland; **Artur Magnuszewski** from University of Warsaw, Faculty of Geography and Regional Studies, Poland; and **Wojciech Majewski** from Institute of Meteorology and Water Management—

National Research Institute, Warsaw, Poland. We were also glad to welcome 68 participants from 13 countries from all over the world. In total, 7 lectures, 30 papers, and 7 posters were presented at Jachranka. Submitted proposals were peer reviewed, acceptance being based on quality and relevance of the research. Authors could change their papers after the discussion at the conference so final papers include modifications resulting from that debate. So what appears in the following pages is a series of technical, peer-reviewed papers commonly related to the main subject of the conference. The following proceedings are also an attempt to capture the richness of the presentations and discussions.

Warsaw, Poland

Monika B. Kalinowska  
Paweł M. Rowiński  
School Chairs

# Acknowledgements

The editors are extremely grateful to all people who contributed to the organization of the XXXVI International School of Hydraulics and to the production of this volume.

First of all, we would like to express our sincere thanks to all the authors for their contributions. Next, we would like to thank all the participants and speakers during the XXXVI International School of Hydraulics for sharing their scientific knowledge and passion with others and engagement in all conference events.

The School and this book would not be possible without financial support from Institute of Geophysics statutory funds, Centre for Polar Studies KNOW—Leading National Research Center, and the Committee of Water Resources of the Polish Academy of Sciences. We would like to express our very special thanks also to DHI Poland Company for being with us during the conference and for being a sponsor of the prizes in the competition: “Best Young Researchers Presentation Award.” We were glad to be able to run the conference under the auspices of International Association of Hydro-Environment Engineering and Research. We also wish to thank the IAHR and its representative Maria Galanty for promoting the School and for offering of the IAHR free memberships in 2017 for all “Best Young Researchers Presentation Award” winners.

We would like to express our cordial thanks to all people from the local organizing committee who helped make this conference a success. They are: Anna Łoboda, Marzena Osuch, Łukasz Przyborowski, Agata Szczegielniak-Kwaśniak, and Anna Wielgopolan. Special thanks are due to Anna Wielgopolan who professionally managed the Conference Secretariat with outstanding expertise, commitment, and enthusiasm which have been very important for the successful organization of this School. We should name also Anna Dziembowska responsible for high quality of English of the papers that are in the volume.

Finally, we wish to thank and acknowledge all the reviewers, who have donated their time and expertise to assist in improving the quality of the submitted papers:

- **Jochen Aberle**, Norwegian University of Science and Technology, Norway
- **Robert Bialik**, Institute of Biochemistry and Biophysics, Polish Academy of Sciences, Poland
- **Mário J. Franca**, Swiss Federal Institute of Technology of Lausanne, Switzerland
- **Ian Guymer**, School of Engineering, University of Warwick, UK
- **Monika B. Kalinowska**, Institute of Geophysics, Polish Academy of Sciences, Poland
- **Katinka Koll**, Technical University Braunschweig, Germany
- **J. Russell Manson**, The Richard Stockton College of New Jersey, USA
- **Andrea Marion**, University of Padova, Italy
- **Wojciech Majewski**, Institute of Meteorology and Water Management, Gdynia
- **Marek Mitosek**, Warsaw Technical University, Poland
- **Magdalena M. Mrokowska**, Institute of Geophysics, Polish Academy of Sciences, Poland
- **Jarosław Napiórkowski**, Institute of Geophysics, Polish Academy of Sciences, Poland
- **Marzena Osuch**, Institute of Geophysics, Polish Academy of Sciences, Poland
- **Artur Radecki-Pawlik**, Agricultural University of Cracow, Poland
- **Paweł M. Rowiński**, Institute of Geophysics, Polish Academy of Sciences, Poland
- **Steve Wallis**, School of the Built Environment, Heriot-Watt University, UK

Monika B. Kalinowska  
Magdalena M. Mrokowska  
Paweł M. Rowiński

# Contents

<b>A Study of Large-Scale Horizontal Turbulence in Alluvial Streams, with a View Towards Its Morphological Consequences</b> . . . . .	1
Ana Maria Ferreira da Silva and Arash Kanani	
<b>Ice Concerns for Hydraulic Engineering in Cold, Mountainous Terrain</b> . . . . .	27
Robert Ettema	
<b>Where “Small Is Beautiful”—Mathematical Modelling and Free Surface Flows</b> . . . . .	43
John D. Fenton	
<b>Application of the AISA Hyperspectral Image for Verification of Sediment Transport Results Obtained from CCHE2D Hydrodynamic Model—Zegrze Reservoir Case Study, Poland</b> . . . . .	103
Artur Magnuszewski, Anita Sabat, Anna Jarocińska and Łukasz Sławik	
<b>Natural and Anthropogenic Changes of the Vistula Outlet to the Sea</b> . . . . .	113
Wojciech Majewski	
<b>Numerical Analysis of Steady Gradually Varied Flow in Open Channel Networks with Hydraulic Structures</b> . . . . .	127
Wojciech Artichowicz and Dariusz Gąsiorowski	
<b>Lattice Boltzmann Method for the Numerical Simulations of the Melting and Floating of Ice</b> . . . . .	143
Ayurzana Badarch and Hosoyamada Tokuzo	
<b>Simulation of Flow Characteristics Through Emerged Rigid Vegetation Over a Perturbed Bed</b> . . . . .	155
Paromita Chakraborty and Arindam Sarkar	

<b>Numerical Study of Sedimentation in Uniformly Vegetated Wetlands</b> . . . . .	167
Eleonora Dallan, Andrea Bottacin-Busolin, Nima Sabokrouhiyeh, Matteo Tregnaghi and Andrea Marion	
<b>An Acoustic Technique to Measure the Velocity of Shallow Turbulent Flows Remotely</b> . . . . .	181
Giulio Dolcetti, Anton Krynkina, Kirill V. Horoshenkov and Simon J. Tait	
<b>A CFD Based Comparison of Mixing Due to Regular and Random Cylinder Arrays</b> . . . . .	195
Mahshid Golzar, Fred Sonnenwald, Ian Guymer and Virginia Stovin	
<b>Turbulence Flow Modeling of One-Sharp-Groyne Field</b> . . . . .	207
Oscar Herrera-Granados	
<b>Sensitivity Analysis for the Water-Air Heat Exchange Term</b> . . . . .	219
Monika B. Kalinowska, Magdalena M. Mrokowska and Paweł M. Rowiński	
<b>Time Variation of Scour at Downstream Pier for Two Piers in Tandem Arrangement</b> . . . . .	235
Shivakumar Khaple, Prashanth Reddy Hanmaiahgari and Subhasish Dey	
<b>Geometry Description of Local Scouring Process in Various Laboratory Water Structure Models</b> . . . . .	245
Marta Kiraga and Zbigniew Popek	
<b>An Experimental Investigation of Pressure Wave Celerity During the Transient Slurry Flow</b> . . . . .	259
Apoloniusz Kodura, Michał Kubrak, Paweł Stefanek and Katarzyna Weinerowska-Bords	
<b>Numerical Modeling of Water Flow Conditions with Spatial Distribution of Boulders in Main Channel</b> . . . . .	271
Leszek Książek, Maciej Wyrębek, Mateusz Strutyński and Agnieszka Woś	
<b>Analysis of Pressure Wave Velocity in a Steel Pipeline with Inserted Fiber Optic Cable</b> . . . . .	281
Michał Kubrak, Apoloniusz Kodura and Szymon Imięłowski	
<b>Equilibrium Time of Scour Near Water Engineering Structures on River Floodplains</b> . . . . .	293
Oskars Lauva and Boriss Gjunsburgs	
<b>LDV Measurements of the Flow Induced by an Elongated Bridge Pier: The Fixed Bed Case</b> . . . . .	307
Maria M. C. L. Lima, Elsa Carvalho and Rui Aleixo	

<b>An Experimental Investigation on Porosity in Gravel Beds . . . . .</b>	323
Christy Ushanth Navaratnam, Jochen Aberle and Jana Daxnerová	
<b>Po River Morphodynamics Modelled with the Open-source Code iRIC . . . . .</b>	335
Michael Nones, Alessio Pugliese, Alessio Domeneghetti and Massimo Guerrero	
<b>Characteristics of Flow Around Aquatic Plants in Natural Conditions: Experimental Setup, Challenges and Difficulties . . . . .</b>	347
Łukasz Przyborowski, Anna M. Łoboda, Mikołaj Karpiński and Robert J. Bialik	
<b>Spectral Behavior of Sand Bed Rivers at Small Wavelengths . . . . .</b>	363
Jie Qin and Jochen Aberle	
<b>Spatial Distribution of Dissolved Oxygen at Rapid Hydraulic Structures as an Indicator of Local-Scale Processes . . . . .</b>	377
Agnieszka Rajwa-Kuligiewicz, Karol Plesiński, J. Russell Manson, Artur Radecki-Pawlik and Paweł M. Rowiński	
<b>Characterizing Retention Processes in Streams Using Retention Metrics . . . . .</b>	389
Jevgenijs Savickis, Mattia Zaramella, Andrea Bottacin-Busolin, Matteo Tregnaghi and Andrea Marion	
<b>Higher Order Statistics of Reynolds Shear Stress in Nonuniform Sand Bed Channel . . . . .</b>	401
Anurag Sharma and Bimlesh Kumar	
<b>Analysis of Yellow River Delta Evolution with Flux Variations of Runoff and Sediment . . . . .</b>	415
Hongling Shi, Qin Lu and Zuwen Ji	
<b>Mathematical Modelling of Sand-Gravel Bed Evolution in One Dimension . . . . .</b>	429
Kseniia Snigur and Igor Potapov	
<b>Numerical Modeling of Flow Dynamics on a Gravel Bar During High Discharge in a Mountain River . . . . .</b>	441
Andrzej Strużyński, Dorota Giritat, Ludivine Bouchet, Maciej Wyrębek and Krzysztof Kulesza	
<b>The Impact of Deflectors on Sediment Transport Processes on the Basis of Modelling and Simulations . . . . .</b>	455
Ewelina Szałkiewicz, Tomasz Dysarz, Tomasz Kałuża, Albert Malingier and Artur Radecki-Pawlik	



**Numerical Modeling of Water and Ice Dynamics  
for Analysis of Flow Around the Kiezmark Bridge Piers . . . . . 465**  
Michał Szydłowski and Tomasz Kolarski

**Flow Dependence of the Parameters of the Transient  
Storage Model . . . . . 477**  
Stephen G. Wallis and J. Russell Manson

**Mathematical Modeling of the Impact Range of Sewage  
Discharge on the Vistula Water Quality in the Region  
of Włocławek . . . . . 489**  
Piotr Zima

# A Study of Large-Scale Horizontal Turbulence in Alluvial Streams, with a View Towards Its Morphological Consequences

Ana Maria Ferreira da Silva and Arash Kanani

**Abstract** As is well known, the origin of alternate bars and meandering remains a matter of debate in the literature. This chapter concerns the hypothesis previously raised by a number of authors that large-scale turbulence, and more specifically large-scale horizontal coherent structures (LSHCS's), are the reason for their occurrence, or at least a contributing factor. In order to properly assess the validity of such hypothesis, it is necessary to first develop an understanding of the dynamics of LSHCS's occurring in open-channel and river flows, and establish their characteristic scales. This work is motivated by this need. The work is to be viewed as an extension of recent experimental studies on LSHCS's in shallow flows to the case of deep flows. Accordingly, a laboratory flow having width-to-depth ratio of 7.1, and conveyed in a 1 m wide and 21 m long straight channel, is investigated. The flat channel bed was formed by a coarse silica sand. Flow velocity measurements were carried out with a 2D SonTek™ Micro ADV. Several techniques are used to treat the velocity signals, including continuous wavelet transform and quadrant and spectral density analyses. Special attention is paid to the time and length scales of the LSHCS's, the effect of superimposition of the LSHCS's on the mean flow, and the variation of turbulence structure over the flow depth. To the best knowledge of the writers, this is the first work where LSHCS's have been detected in a deep open-channel flow. The work is used also to shed light on why the initiation of meandering in alluvial streams is not always preceded by the occurrence of alternate bars.

---

A. M. F. da Silva (✉)

Department of Civil Engineering, Queen's University, Kingston, ON K7L 3N6, Canada  
e-mail: anamaria.dasilva@queensu.ca

A. Kanani

MSR Solutions Inc., 125-662 Goldstream Av, Victoria, BC V9B 0N8, Canada

A. Kanani

Queen's University, Kingston, ON K7L 3N6, Canada

© Springer International Publishing AG 2018

M. B. Kalinowska et al. (eds.), *Free Surface Flows and Transport Processes*,

GeoPlanet: Earth and Planetary Sciences,

[https://doi.org/10.1007/978-3-319-70914-7\\_1](https://doi.org/10.1007/978-3-319-70914-7_1)

## 1 Introduction

When sediment is transported, the surface of river beds often becomes covered by sand waves. In the case of tranquil flows, the sand waves commonly are either dunes, ripples, or ripples superimposed on dunes, while in the case of supercritical flows, they (commonly) are antidunes. However, this general rule ceases to be valid if the stream width-to-depth ratio,  $B/h$ , exceeds a certain threshold. In this case, alternate bars, also known as single-row or one-row bars, emerge. These are large-scale, migrating bed forms, characterized by gentle upstream slopes and deep pools at the beginning of their diagonal crests, implying a pattern of alternating holes along the sidewalls (see Fig. 1). The average length of alternate bars is roughly equal to  $6B$  (JSCE 1973; Yalin 1992; da Silva 2006; da Silva and Yalin 2017). The near-bank scour due to alternate bars can reach values of the order of a few channel depths (3–4, say). The occurrence of alternate bars in alluvial streams has several hydraulic, morphological and environmental consequences, well described elsewhere by a number of authors (e.g., Stuart 1953; Ikeda 1984; Chang 1988; Welford 1993; Schweizer et al. 2007). Owing to their practical and scientific significance, alternate bars have become a prominent research topic.

As is well-known, the average wavelength of meanders is also roughly equal to  $6B$  (Garde and Raju 1985; Yalin 1992; da Silva 2006, 2015; da Silva and Yalin 2017)—and it has since long been recognized that the occurrence of alternate bars is associated with the phenomenon of meandering. The prevailing view throughout the 1970s and 80s was that alternate bars were the cause for the initiation of meandering (see, e.g., Ackers and Charlton 1970). Yet, nowadays there is sufficient evidence that meandering can occur in alluvial streams when alternate bars are not



**Fig. 1** Alternate bars in the Rio Coto, Costa Rica; flow from left to right (from Google Earth; photo source: Digital Globe; imagery date: 3/4/2015)

present. Indeed, consider e.g. the  $(B/h; h/D)$ -plan defining the existence regions of bars (single- and multiple-row), meandering and braiding originally introduced by da Silva (1991), and which has recently been revised and updated by Ahmari and da Silva (2011) as shown in Fig. 2. Here  $D$  is grain size of the bed material. In this plan, the alternate bar region (A-region) is the region having as lower boundary the lines  $\mathcal{L}_{P,A}$  and  $\mathcal{L}_{0,1}$ , and as upper boundary, the line  $\mathcal{L}_{1,2}$ . However, meandering streams were found to plot not only in the A-region, but also below it. Hence, in Fig. 2, the regions of alternate bars and meanders have a common upper boundary (the line  $\mathcal{L}_{1,2}$ ), but different lower boundaries, with the line  $\mathcal{L}_M$  being the lower boundary of the meandering region (M-region). This provides a clear indication that alternate bars are not the cause of meanders, but merely the “catalysts” that accelerate the formation of meanders, which would take place even without them.

The similarity in length scales between alternate bars and meanders, however, cannot be ignored, and clearly suggests that these alluvial forms most likely originate as two different manifestations (or expressions) of the same phenomenon. In this context, it is important to recall that several prominent researchers were

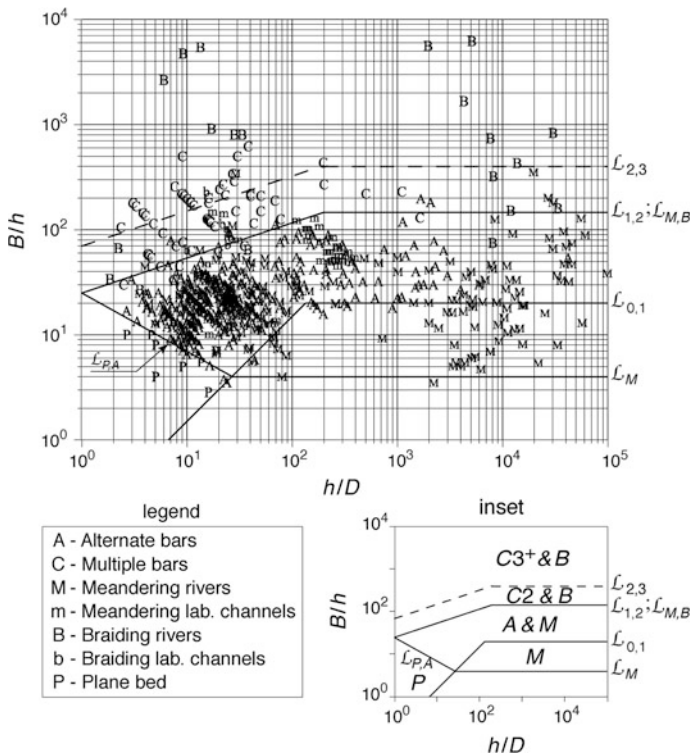


**Fig. 2** The  $(B/h; h/D)$ -plan and the related existence regions of alternate bars, multiple bars, meandering and braiding (from Ahmari and da Silva 2011, reprinted with permission from Taylor & Francis)

convinced since a long time that large-scale bed forms (bars as well as dunes) and the initiation of meandering are caused by large-scale turbulence (Matthes 1947; Velikanov 1955; Kondratiev et al. 1959; Grishnanin 1979). However, such view could not be properly elaborated before the discovery of organized motion (in turbulence) and of the related coherent structures by turbulence researchers (see, e.g., Robinson 1991 for an interesting historical review of research on coherent motions in turbulent flows). Following such a discovery, a turbulence-based explanation for the occurrence of meandering and alternate bars resting on the modern understanding of turbulence was provided by da Silva (1991) and Yalin (1992) (see also Yalin and da Silva 2001; da Silva 2006). According to these authors, alternate bars emerge in relatively shallow flows as the “imprints” on the bed of sequences of large-scale horizontal coherent structures (LSHCS’s) originating from the upper parts of the flow, near the left and right banks, and subsequently growing in lateral extent and into the flow depth, so as to occupy the entire depth of the body of fluid and spanning across the full width of the channel. They further suggested that such structures should also be present in the case of deep flows, but primarily remain at, and affect only, the upper flow regions. In this case, meandering would originate in the absence of alternate bars, as a result of direct action of the LSHCS’s on the banks. However, the existing literature on large-scale turbulence has focused almost exclusively on vertical coherent structures, as well as their morphological consequences. While evidence of the presence of LSHCS’s can be derived from the earlier measurements and observations in open-channel and river flows by Dementiev (1962), Yokosi (1967) and Grishanin (1979), to the best knowledge of the writers the first systematic studies to penetrate the characteristic scales, dynamics and morphological consequences of large-scale horizontal coherent structures have been presented by da Silva and Ahmari (2009), da Silva et al. (2012) and Kanani and da Silva (2015) (see also Kanani et al. 2010). These authors focused on a shallow, alternate bar inducing flow, conveyed in a straight channel having a flat bed. Their findings provide support to the idea that alternate bars might indeed occur as imprints on the bed of large-scale horizontal coherent structures occurring in shallow flows.

This chapter is intended as an extension of the just mentioned works to the case of deep flows. The main objective of the chapter is to present the results of the first phase of a study on LSHCS’s in deep flows presently being carried out at Queen’s University. The measurements reported here were directed at establishing the existence of LSHCS’s in deep flows, investigate their time and length scales, and provide insight into the internal structure of flow over the flow depth. In this chapter, the term shallow flow is used to imply a flow whose width-to-depth ratio is larger than the threshold value of width-to-depth ratio associated with the formation of alternate bars; and the term deep flow, to imply a flow whose width-to-depth ratio is smaller than the just mentioned threshold value. In order to make the chapter more comprehensive, the next section is devoted to the presentation of pertinent background information on the contemporary understanding of large-scale turbulence.

## 2 Background Information on Large-Scale Turbulence and Its Coherent Structures

### 2.1 General

Nowadays it is well understood that, just like in the case of other boundary-layer and wall-bounded flows, coherent structures (CS's) exist also in open-channel and river flows at a wide range of spatial and temporal scales. These vary from near-wall (small-scale) to large-scale coherent structures extending throughout the body of fluid (Yalin 1992; Nezu and Nakagawa 1993; Pope 2000; Adrian and Marusic 2012).

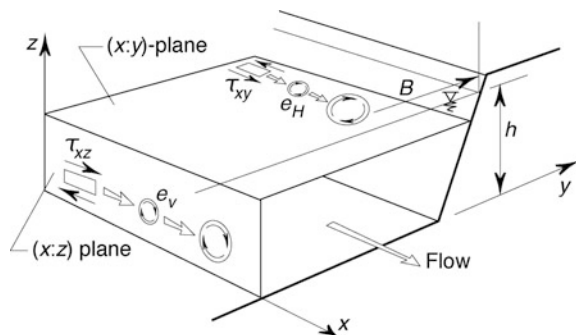
Following Hussain (1983), large-scale coherent structures can be defined as the largest conglomeration of eddies with a prevailing sense of rotation. These structures can be vertical or horizontal (Yokosi 1967; Utami and Ueno 1977; Yalin 1992; Yalin and da Silva 2001; da Silva and Ahmari 2009; Rodi et al. 2013): the former rotate in vertical ( $x; z$ )-planes around horizontal axes and scale with the flow depth, while the latter rotate in horizontal ( $x; y$ )-planes around vertical axes and scale with the flow width (see the schematic Fig. 3). Such structures are small when they first originate, then grow while being transported downstream so as to eventually occupy the body of fluid, and finally disintegrate.

The turbulence processes dealt with in this chapter, which form a “traceable” and thus deterministic component of a turbulent flow, are described below in a schematic manner—all possible deviations and distortions due to the strong “random element” ever-present in any turbulent flow are disregarded in this description. The characteristics of vertical turbulence are marked throughout this text by the subscript  $V$ ; those of horizontal turbulence, by the subscript  $H$ .

### 2.2 Large-Scale Vertical Coherent Structures

- (i) Large-scale vertical coherent structures (LSVCS's) in wall-bounded flows in general, and open-channel flows in particular, have by now been the object

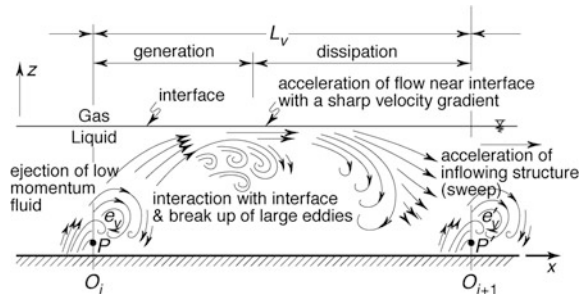
**Fig. 3** Vertical and horizontal planes of rotation of coherent structures (from Kanani and da Silva 2015, reprinted with permission from Springer)



of numerous works (for reviews, see e.g. Yalin 1992; Nezu and Nakagawa 1993; Franca 2005; Balakumar and Adrian 2007). Even though several details of how exactly these structures originate and develop remain unclear, their life-cycle can, on the basis of Blackwelder (1978), Cantwell (1981), Hussain (1983), Gad-el-Hak and Hussain (1986), Rashidi and Banerjee (1988), Jiménez (1998), and several others, be briefly synthesized as illustrated in the conceptual Fig. 4 (showing, in a stationary frame of reference, the life-cycle of a LSVCS in an open-channel flow).

A vertical coherent structure originates around a point  $P$ , at a location  $O_i$ , with the rolling-up at time  $t = 0$ , say, of an eddy  $e_V$  (“transverse vortex”). This is then ejected away from the bed, together with the fluid around it. This total fluid mass moves towards the free surface as it is conveyed by the flow downstream (*ejection phase*). In the process, the moving fluid mass continually enlarges (by engulfment) and new eddies are generated (by induction)—thus a continually growing LSVCS comes into being. When this structure becomes as large as to impinge on the free surface, it disintegrates (*break-up phase*) into a multitude of successively smaller and smaller eddies, until the size of the eddies is reduced to the last level of microturbulence (i.e. until the size of eddies become as small as the lower limit  $\nu/v_*$ , in which  $\nu$  is fluid kinematic viscosity and  $v_*$  is shear velocity), at which point their energy is dissipated by viscous action (as implied by the “Eddy-Cascade Theory”). In the process, the neutralized fluid mass moves downstream—towards the bed (*sweep stage*), with a substantially smaller velocity than that of ejection. The “break-up” of a coherent structure prompts the generation of the new eddy  $e'_V$  at  $O_{i+1}$ , which goes through the same cycle and eventually generates  $e''_V, \dots$ , and so on. The fact that the (complete) disintegration of one coherent structure coincides (in space  $x$ , and time  $t$ ) with the generation of the next, means that the coherent structures form a *sequence* along  $x$  (see Fig. 5a). It is noted here that the vertical coherent structures are, as a rule, three-dimensional, and they grow also in the cross-sectional ( $y; z$ )-planes while being conveyed downstream. The largest lateral extent of the LSVCS’s is  $\approx 2h$  (Jackson 1976; Yalin 1992; Nezu and Nakagawa 1993; Kadota and Nezu 1999; del Álamo and Jiménez 2003; etc.). It follows that a

**Fig. 4** Conceptual representation of the life-cycle of a large-scale vertical coherent structure (LSVCS); longitudinal view (from da Silva 2006, reprinted with permission from IAHR)



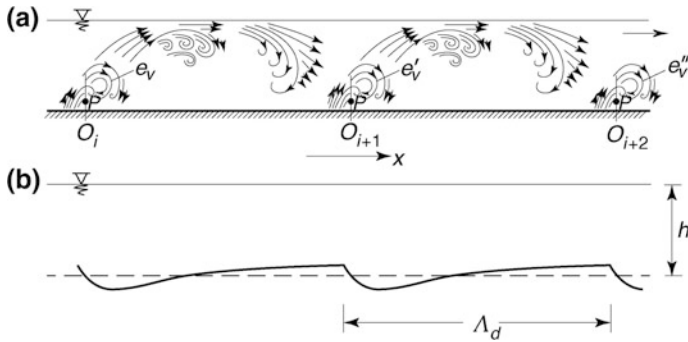


**Fig. 5** **a** Longitudinal sequence of LSVCS's in an open-channel flow past a flat bed; **b** longitudinal view of dunes. (From da Silva and Yalin 2017, reprinted with permission from CRC Press)

(longitudinal) sequence of LSVCS's is thus confined to a “corridor” of the width  $\approx 2h$  (and the height  $h$ ).

- (ii) Following del Álamo and Jiménez (2003), Franca and Lemmin (2008, 2015) and Kanani and da Silva (2015), among others, the term length scale will subsequently be used to designate the distance traveled in the streamwise direction by the (large-scale) coherent structures, from the location of their origin to that of their complete disintegration; and the term time scale, to designate the time taken by the structures to travel such a distance (i.e. to designate their “life-span”)—with the symbols  $T_V$  and  $L_V$  (see Fig. 4) being used to denote the time and length scales of the LSVCS's, respectively. Assuming, with an accuracy sufficient for all practical purposes, that the LSVCS's are conveyed downstream with the average flow velocity  $u_{av}$ , one can write

$$L_V = T_V u_{av}. \tag{1}$$

There is general agreement that the length scale of LSVCS's is proportional to the flow depth  $h$ , i.e.  $L_V = (T_V u_{av}) = \alpha_V h$ , the value of the proportionality factor  $\alpha_V$  being comparable to 6 (Jackson 1976; Yalin 1992; Nezu and Nakagawa 1993; Roy et al. 2004; Franca and Lemmin 2008, 2015). That is,

$$L_V = \alpha_V h \approx 6h. \tag{2}$$

- (iii) According to da Silva (1991) and Yalin (1992) (see also da Silva and Yalin 2017), a flow subjected to the perpetual action of a longitudinal sequence of LSVCS's (as in Fig. 5a) ‘fired’ from the (ideally speaking) same location at  $x = 0$  must inevitably cause the flow to acquire a sequence of periodic (along  $x$  and  $t$ ) non-uniformities. Consequently, the time-averaged streamlines  $s$ —averaged over a multitude of  $T_V$ —must vary periodically along  $x$  only with a



period  $T_V$ , i.e. they must acquire a wave-like pattern (in the  $(x; z)$ -planes of flow). These wave-like streamlines deform, in turn, the bed surface (as explained in greater detail in section 1.7 (iii) in da Silva and Yalin 2017), so as to produce a sequence of bed forms (dunes) whose (average) length must be the same as  $L_V$  (Fig. 5b).

As is known from research on sediment transport, the (average) length  $\Lambda_d$  of dunes (produced by fully rough flows) can indeed be expressed as  $\approx 6h$ : e.g.  $\Lambda_d = 5h$  (Yalin 1964; Allen 1985);  $\Lambda_d = 7h$  (Hino 1968);  $\Lambda_d \approx 2\pi h$  (Yalin 1977);  $\Lambda_d = 7.3h$  (van Rijn 1984);  $\Lambda_d \approx 6h$  (Yalin 1992).

- (iv) Coherent structures occur randomly in space and time. This means that under completely uniform conditions of flow and bed surface, there is an equal probability (or frequency) of occurrence of coherent structures for any region  $\Delta x$  and time interval  $\Delta t$ . Such a homogeneous or uniform distribution of coherent structures along the flow direction  $x$  cannot lead to an internal deformation of the flow that would ‘imprint’ itself as a periodic deformation of the bed surface (Yalin 1992). However, suppose that there exists in the flow a ‘location of preference’ associated with an increased frequency of occurrence of coherent structures (at that location). Since the break-up of one coherent structure (CS) triggers the generation of the next CS, such a location of preference leads also to the more frequent generation of sequences (along  $x$ ) of coherent structures initiating from it. Such an increased frequency of occurrence of CS’s at a location can be realized by means of a local discontinuity,  $d$  say (the section containing it thus becoming the preferential section  $x = 0$ , say). Under laboratory conditions, the discontinuity can be the beginning of mobile bed, an accidental ridge across the bed surface, etc. (see Yalin 1992).

### 2.3 Large-Scale Horizontal Coherent Structures

- (i) Considerable research efforts have already been devoted to the study of horizontal eddies and horizontal coherent structures originating at river irregularities, such as sudden changes in direction, confluences, bifurcations, etc. (see e.g. McLelland et al. 1996; Constantinescu et al. 2012; Konsoer and Rhoads 2014; among many others). A related, but essentially distinct process, is the occurrence of large-scale horizontal coherent structures (LSHCS’s) in rectilinear (or nearly rectilinear) channels without any such irregularities, and in which the LSHCS’s are thus not induced by them. Here we consider only the latter type, and any mention to LSHCS’s should be interpreted as referring solely to such structures.

As pointed out earlier, the LSHCS’s under consideration have so far been the object of only a few isolated studies. Yet, LSHCS’s are supposed to be the horizontal counterpart of LSVCS’s and as such should be expected in their life-cycle to follow, *mutatis mutandi*, a sequence of events similar to that

previously described for LSVCS's but instead occurring in a horizontal “flow ribbon”. The difference should be mainly in the length scale, with all “lengths” of the large-scale horizontal turbulence being proportional to the flow width  $B$  (instead of flow depth  $h$ , as is the case in large-scale vertical turbulence). LSHCS's are thus thought to originate predominantly near the banks and the free surface (i.e. in the neighbourhood of the upper corners of the flow cross-section), where horizontal shear stresses are the largest—and subsequently be conveyed downstream by the mean flow, while growing in size (see Fig. 6a). Extrapolating the sequence of events followed by LSVCS's to the case of horizontal structures, one can then say that as long as the width-to-depth ratio is not too “large”, the LSHCS's will grow until their lateral extent becomes as large as  $B$ . At this point, they will interact with the banks and disintegrate into a cascade of successively smaller and smaller eddies. The neutralized fluid mass will return to its original bank so as to arrive there at  $t = T_H$ , the (average) length scale of the LSHCS's being given by  $L_H = \alpha_H B$ . There seems to be agreement that the coherent structures forming the large-scale horizontal turbulence of a wide open channel have the shape of horizontally positioned disks (Fig. 6b, c) eventually extending (along  $z$ ) throughout the flow thickness  $h$  (Grishanin 1979; Jirka and Uijtewaal 2004; Yalin 2006; da Silva and Ahmari 2009). The disintegration of a HCS prompts the “birth” of a new HCS in the next downstream ejection point, and so on.

As pointed out by Yalin (1992), the growth rates of large-scale coherent structures in the flow direction ( $x$ ) exhibit a remarkable similarity. But if so, then the value of  $\alpha_H$  should be comparable to  $\alpha_V$ , namely 6, i.e.

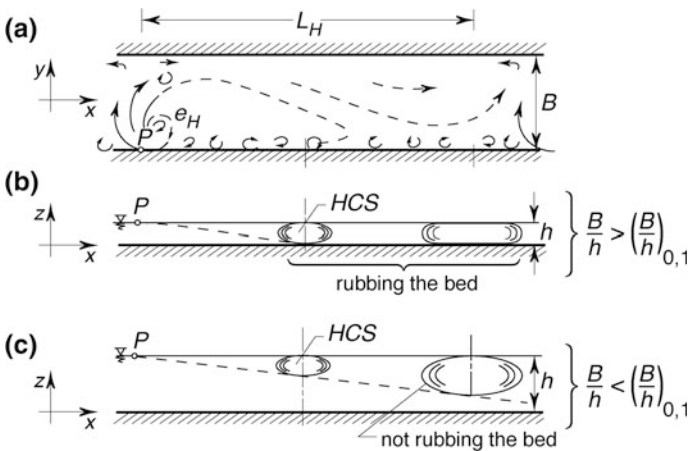


**Fig. 6** Conceptual representation of the life-cycle of a large-scale horizontal coherent structure—LSHCS (from da Silva 2006, reprinted with permission from IAHR). **a** Plan view; **b** side view in the case of “small” values of width-to-depth ratio; **c** side view in the case of comparatively larger values of width-to-depth ratio

$$L_H = \alpha_H B \approx 6B. \quad (3)$$

This expectation is in agreement with existing measurements in shallow river and open-channel flows, however few. These include the earlier measurements by Dementiev (1962), Yokosi (1967), and Grishanin (1979), as well as those in the recent works by da Silva and Ahmari (2009), da Silva et al. (2012) and Kanani and da Silva (2015) (see also Kanani et al. 2010).

On the other hand, it is known that the (average) length of alternate bars  $\Lambda_a$  is also comparable to  $6B$  (JSCE 1973; Jaeggi 1984; Ikeda 1984; Fujita and Muramoto 1985; etc.). This strongly suggests that, similarly to the case of LSVCS's and dunes, the length  $L_H$  of LSHCS's is 'imprinted' on the bed surface of a mobile bed as the alternate bar length:

$$\Lambda_a \equiv L_H \approx 6B. \quad (4)$$

- (ii) Alternate bars are anti-symmetrical in plan view with respect to the  $x$ -axis (Fig. 7c). But if so, then the sequences of LSHCS's issued from the right and left banks generating them, must also be anti-symmetrical in plan view—that is, they must be expected to be as shown in Fig. 7a, where the LSHCS's are

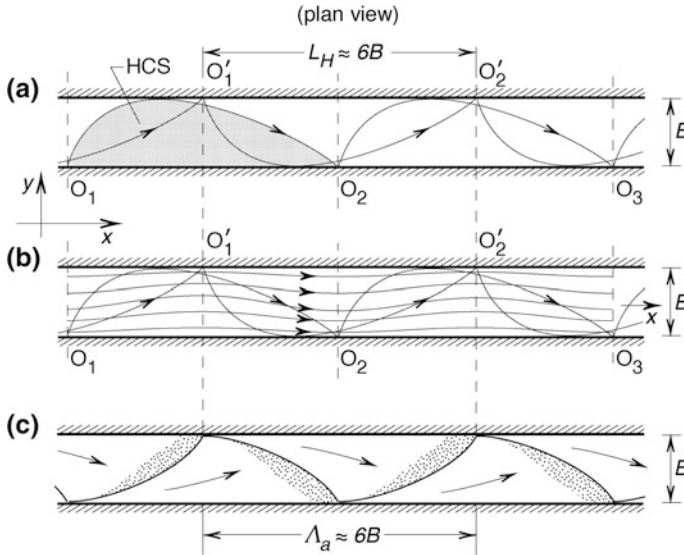


**Fig. 7** Schematic plan views of: **a** Longitudinal sequences of LSHCS's issued from the right and left bank, in flow past a flat bed; **b** wave-like streamlines resulting from the superimposition of the sequences of LSHCS's on the mean flow; **c** alternate bars. (From da Silva and Yalin 2017, reprinted with permission from CRC Press)

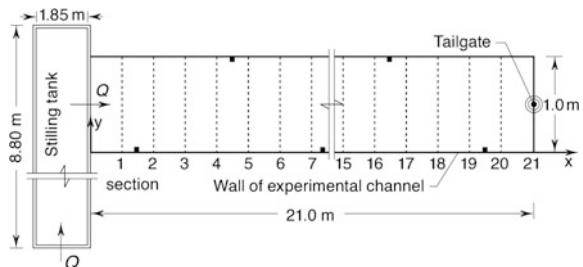
- ‘fired’ from the right bank at  $O_1, O_2$ , etc.; and from the left bank, at  $O'_1, O'_2$ , etc. Here,  $O'_1, O'_2, \dots$ , are located downstream of  $O_1, O_2, \dots$ , by  $L_H/2$ .
- (iii) Consider now the influence of the  $B/h$ -ratio on the growth of the LSHCS’s. As previously done by da Silva (1991) and Yalin (1992) (see also da Silva and Yalin 2017), we hypothesize that if  $B/h$  is small, i.e. if it is smaller than a certain value  $(B/h)_{0,1}$  say, then the LSHCS’s acquire their largest size  $B$  without rubbing the bed (Fig. 6c)—and that in this case, the LSHCS’s cannot produce any bed forms. If, however,  $B/h > (B/h)_{0,1}$ , then the LSHCS’s are rubbing the bed (Fig. 6b) and they are thus capable of producing “their” bed forms, viz alternate bars. Clearly, for any given value of  $h/D$ , the value of  $(B/h)_{0,1}$  is that of the lower boundary line of the A-region (lines  $\mathcal{L}_{P,A}$  and  $\mathcal{L}_{0,1}$  in Fig. 2).

### 3 Experimental Set-up and Description of Measurements

The present measurements were conducted in a 1 m wide, 21 m long and 0.4 m deep straight channel (Fig. 8). The channel was installed in a 7 m wide river basin of the same length, the basin being equipped with a water recirculation system. The upstream end of the river basin consisted of a 1.85 m wide and 8.8 m long stilling tank. The water entered the straight channel through a 1 m wide opening on the 0.6 m tall wall separating the stilling tank from the river basin. A tailgate was installed at the downstream end of the channel to enable control of the free surface slope. Complete details of the experimental facility are given elsewhere (Ahmari 2010; Kanani 2014).

The channel side walls were vertical and made of aluminum. The channel bed was formed by a well-sorted silica sand with average grain size  $D_{50}$  equal to 2 mm ( $D_{16} = 1.5$  mm;  $D_{84} = 2.4$  mm; specific density = 2.65). To protect the bed from erosion at the channel entrance, a 1 m long stretch of gravel with grain size of 2.5 cm was installed at the upstream end of the channel. The surface of the sand was scraped so as to produce the desired stream slope and a flat bed surface. To

**Fig. 8** Schematic representation of experimental channel. Numbers 1–20 mark cross-sections along the channel (the number of the cross-section corresponds to the distance in meters to the channel entrance); filled squares represent small “blocks” installed at the channel walls



ensure that the bed remained flat throughout the measurements, the value of the bed slope,  $S_0$ , was selected so that the bed shear  $\tau_0$  acting on the bed would be substantially below the value of the bed shear stress at the critical stage of initiation of sediment transport  $(\tau_0)_{cr}$ . It is noted that the initial aim was to conduct the measurements under uniform flow conditions ( $S_0 = S_f$  in which  $S_f$  is free surface slope). However, the operating mechanism of the tailgate did not allow the very fine adjustments that would be required to exactly match the bed and free surface slopes for such small slopes. Thus, in reality, the measurements were carried out under flow conditions that somewhat deviated from uniform, as  $S_0 = 1/2000$  and  $S_f = 1/3700$ . This deviation is inconsequential, as coherent structures exist and are often studied in natural environments where the conditions are not uniform (e.g., Roy et al. 2004; Nikora 2005; Franca and Lemmin 2015; Sukhodolov and Sukhodolova 2012).

Following the procedure by da Silva and Ahmari (2009) and Ahmari (2010) in their previous measurements on LSHCS's in shallow flows, small "blocks" were installed at regular intervals of  $6B$  along the channel walls. The blocks consisted of 15 cm long pieces of wood with  $2 \text{ cm} \times 2 \text{ cm}$  square bases. The first of the four blocks on the right wall was located 1.5 m from the channel entrance (see Fig. 8), while the first of the three blocks on the left wall was located 4.5 m from the entrance. The blocks were submerged 7 cm into the water (flow depth = 14 cm). The blocks were introduced to act as "discontinuities" in the sense of Yalin (1992) (see Sect. 2.2 (iv)). The most upstream block was used as a means to introduce a well identified (upstream) discontinuity; the remaining blocks served to perpetuate throughout the channel a more regularized flow structure, as such structure might otherwise have been present only for a limited distance downstream of the first block.

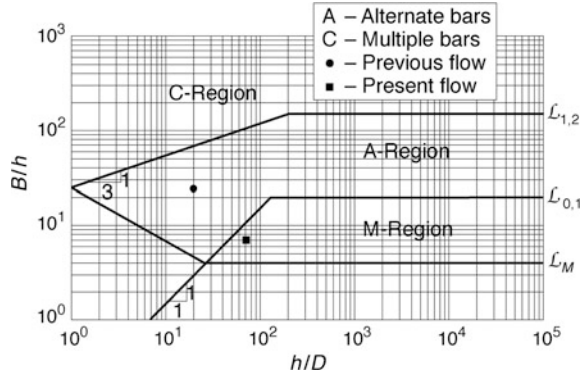
The hydraulic conditions of the investigated turbulent and sub-critical flow are summarized in Table 1. Here  $Q$  is flow rate,  $Re$  is flow Reynolds number and  $Fr$  is Froude number. The value of  $Re$  was calculated using  $\nu = 10^{-6} \text{ m}^2 \text{ s}^{-1}$ , in which  $\nu$  is fluid kinematic viscosity. The flow depth varied from 13.8 cm at cross-section 3–14.2 cm at cross-section 20. Hence the value of flow depth shown in Table 1 is to be viewed as the average flow depth in the channel. The value of the ratio  $\tau_0/(\tau_0)_{cr}$  was estimated to be 0.18 (i.e. considerably smaller than 1).

The specific combination of the values of  $h$  and  $D$  of the flow (having width  $B = 1 \text{ m}$ ) was selected so that the flow would not be of a type compatible with the occurrence of alternate bars. The present flow thus purposely plots below the lower boundary (line  $\mathcal{L}_{0,1}$ ) of the alternate bar region in the  $(B/h; h/D)$ -plan previously mentioned in this chapter (see Fig. 9, in which the present flow is plotted as a filled square). For comparison purposes, the point corresponding to the shallow flow conditions previously investigated by da Silva and Ahmari (2009), da Silva et al.

**Table 1** Hydraulics conditions of present flow ( $B = 1 \text{ m}$ ;  $D_{50} = 2 \text{ mm}$ )

$Q$ ( $\text{l s}^{-1}$ )	$h$ (cm)	$S_0$	$S_f$	$Re$	$Fr$	$B/h$	$h/D$
34.4	14.0	0.0005	0.00027	34400	0.21	7.1	70

**Fig. 9** Plot on the  $(B/h; h/D)$ -plan of present deep flow (filled square), and shallow flow (filled circle) previously investigated by da Silva and Ahmari (2009), da Silva et al. (2012) and Kanani and da Silva (2015)



(2012) and Kanani and da Silva (2015) is also plotted in the same figure (filled circle).

Flow velocity measurements (point measurements) were carried out at cross section 3–20 and in each cross section at 19 locations (i.e. different values of  $y$ ;  $y = 0$  at the right wall—see Fig. 8). The measurement locations along each cross-section were equally spaced (spacing = 5 cm), starting at 5 cm from the right wall and ending at 5 cm from the left wall. At each  $(x; y)$ -location in flow plan, the velocity was measured at three different elevations, namely  $z/h = 0.21, 0.5$  and  $0.89$  (where  $z$  is vertical direction measured from the channel bottom). The velocity measurements consisted of 180 s long records of instantaneous flow velocity. It should be clear that the complete set of 180 s velocity measurements consists of a total of 1026 velocity records (= 18 cross-sections  $\times$  19 locations in flow plan along each cross-section  $\times$  3 measurement levels). Additionally, 20 min long velocity records were collected at selected points in the flow domain, for the purpose of producing spectral density plots. All velocity measurements were accomplished with the aid of a 2D Son Tek<sup>TM</sup> Micro-ADV (velocity range = 0.03, 0.1, 1.0 and 2.5 m/s; velocity resolution =  $0.1 \text{ mm s}^{-1}$ ; accuracy = 1% of measured velocity; sampling volume =  $0.09 \text{ cm}^3$  cylinder located 0.05 m away from the sensor tip). Hence, only the longitudinal and transverse components of the flow velocity  $u$  and  $v$ , were collected. The ADV was operated at a sampling frequency of 25 Hz.

## 4 Results

### 4.1 Detection of LSHCS's

As is well-known, by applying a moving average with a given averaging time interval  $\delta t$  to a velocity oscillogram (as done e.g. by Yokosi 1967; Yalin 1992 and in more recent works by da Silva and Ahmari 2009; Konsoer and Rhoads 2014;

Kanani and da Silva 2015), then the resulting smoothed (of filtered) oscillogram contains only those velocity fluctuations whose period is larger than  $\delta t$ . This means that by selecting a sufficiently large  $\delta t$ , it is possible to reveal the longest periods (or the lowest frequencies) of the velocity fluctuations that are due to the passage of the largest structures in the flow. In this work, this simple filtering method was used first to determine whether or not LSHCS's were present in the flow. Accordingly, each 180 s long oscillogram of fluctuating longitudinal flow velocity was averaged over consecutive time intervals  $\delta t$ .

As an example of application of the just mentioned procedure, see Fig. 10, corresponding to cross-section 10,  $y/B = 0.5$ ,  $z/h = 0.89$ , and showing the original oscillogram of  $u'$  (top graph), as well as the corresponding smoothed oscillograms obtained by filtering with averaging time intervals  $\delta t = 4$  and 8 s (middle and bottom graphs in Fig. 10, respectively). In this example, the largest “periods” of the velocity fluctuation became evident when  $\delta t = 8$  s (see Fig. 10, bottom graph, where the solid line is the smoothed oscillogram and the dashed red line was manually added merely to highlight the trend of the oscillogram and its peaks (marked by crosses)). Observe that this smoothed oscillogram exhibits a rather regular cyclic pattern of velocity variation, with eight cycles between the troughs at  $t \approx 8$  and 170 s. Thus, for this example, we obtain for the average (over a sampling time of 162 s) of the periods of velocity fluctuations due to the largest structures in the flow a value of  $\approx 20.3$  s  $(= (170 \text{ s} - 8 \text{ s})/8)$ . It is noted that, on the basis of Eqs. (1) and (2), the length scale of the LSVCS's must be expected to be of the order of 3.4 s. Given that the detected oscillations are by multiple times larger than those that could be due to the passage of LSVCS's, they can only be explained if attributed to LSHCS's.

The results described in the previous paragraph are representative of those for the velocity measurements at all measurement locations. In particular, it was invariably found that the averaging time interval  $\delta t = 8$  s was adequate to reduce the velocity oscillograms to the point where the periods of the fluctuations due to the largest structures in the flow were clearly evident. Furthermore, irrespective of location, the filtered oscillograms invariably exhibited long cycles of increasing-decreasing  $u'$ , by multiples times larger than those that can be expected because of LSVCS's. The whole set of filtered velocity oscillograms thus provides a clear indication of the presence in the flow of LSHCS's.

**Fig. 10** Original and filtered oscillograms of  $u'$  corresponding to the velocity record at cross-section 10,  $y/B = 0.5$ ,  $z/h = 0.89$ : **a** Original signal; **b** filtered oscillogram using  $\delta t = 4$  s; **c** filtered oscillogram using  $\delta t = 8$  s

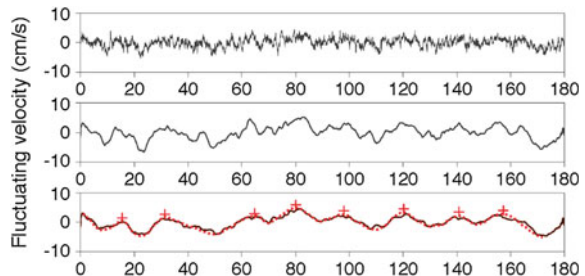
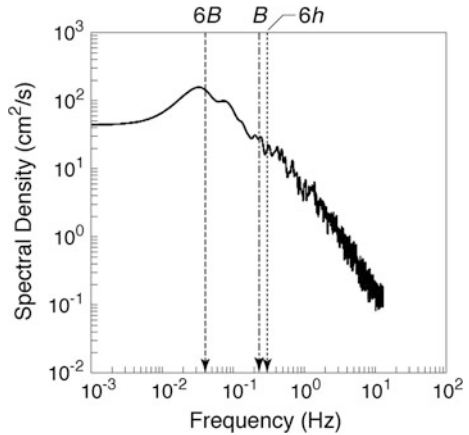


**Fig. 11** Spectral density plot of 20 min long velocity record collected at Sect. 12,  $y/B = 0.5$  (channel centerline) and  $z/h = 0.89$



As a means to complement the analysis above, spectral density plots of instantaneous longitudinal velocity were produced for the locations in the flow domain for which 20 min long records of velocity were collected. As an example, the spectral density plot corresponding to measurement cross-section 12,  $y/B = 0.5$  (channel centerline) and  $z/h = 0.89$ , is shown in Fig. 11. This was produced by adopting a Hanning filter with a window lag of  $N/25$  and zero overlap. Here  $N$  is the number of velocity measurements in the 20 min long record ( $N = 30,000$ ). It should be clear that, and adopting here the terminology by Sukhodolov and Uijtewaal (2010), this is a composite spectrum, extended to frequencies of horizontal structures. The vertical lines in Fig. 11 mark the frequencies 0.3, 0.24 and 0.04 Hz, corresponding to  $6h$ ,  $B$  and  $6B$ , respectively. As is well-known, the frequency associated with the largest coherent structures in the flow corresponds to the left end of the spectrum. In this plot this frequency is by multiple times smaller than that which can reasonably be attributed to the LSVCS's. This is in agreement with the results obtained with the simple filtering method described earlier. Note also that the frequency corresponding to the left end of the spectrum is rather close to the frequency corresponding to  $6B$ .

## 4.2 Average Time and Length Scale of LSHCS's

Since the size of individual coherent events varies in space and time, if one considers a (longitudinal) sequence of the largest structures, the length scale of each individual structure will be different from the one preceding it or following it in both space and time. That is, each individual coherent event has its own characteristic time and length. Yet, as follows from the content of Sect. 2, when considering the effect of large-scale coherent structures in the context of river



morphology and river morphodynamics, the concepts of average time and length scales acquire particular significance.

Having established in the previous section the presence of LSHCS's in the flow, we thus proceed in the following to the determination of the average time and length scales,  $T_H$  and  $L_H$ , of the LSHCS's. Continuous Wavelet Transform (CWT) is used for these purposes. As demonstrated in numerous works, CWT is particularly suitable for the treatment of non-stationary signals, known to occur in many different fields, with turbulence being a common example. In contrast to other classical methods of treatment of velocity signals, it yields the frequency components of a signal as well as their time-localization, making it a powerful tool for the study of coherent structures (see e.g. Farge et al. 1990; Farge 1992; Farge and Schneider 2001). It should be noted here that CWT has so far been seldom used in the detection and characterization of coherent structures from measurements in open-channel and river flows. Notable exceptions include Camussi (2002), Miyamoto and Kanda (2004), Franca and Lemmin (2006) and Kanani and da Silva (2015).

On the basis of Kanani and da Silva (2015), the following procedure was adopted to determine the average values of  $T_H$  and  $L_H$ :

1. Each individual 180 s long record of longitudinal flow velocity was first decomposed in the time-frequency domain using CWT. This was applied to the frequency band 0.0245–0.13 Hz, corresponding to times of 7.7–40.8 s (or lengths of  $\approx 2$ – $10B$ ). The Morlet function was used as a wavelet mother function (see Miyamoto and Kanda 2004 or Kanani and da Silva 2015 for the analytical expression of the Morlet function). Following the recommendations by Torrence and Compo (1998), the Morlet wavelet adjustable parameter  $m$  was identified with 6.
2. Subsequently, contour plots of continuous wavelet transform power (CWTP) and the global wavelet spectrum (GWS) were produced. The CWTP contour plots and the GWS graphs were used to reveal the frequency components of the signal and to localize them in time.
3. The average value of frequency of the smallest frequencies of each 180 s velocity record was then determined with the aid of the following equation:

$$\bar{f} = \frac{\sum w_i f_i}{\sum w_i}. \quad (5)$$

Here  $w_i$  is a weighting factor associated with each detected frequency  $f_i$ , defined as the time interval during which the frequency  $f_i$  itself exists in the signal.

4. After applying the procedure above to a given set of velocity records, the average time scale of the LSHCS's was obtained from the probability density function (Pdf) best fitting the resulting distribution of the average values of the smallest frequencies of individual velocity records.

To eliminate any possible entrance and tailgate effects, the analysis was carried out by using the velocity records from cross-section 9–14, representing the middle region of the stream (see Fig. 8).

Examples of the resulting CWTP contour plots in the frequency-time domain and the corresponding GWS graphs are shown in Fig. 12a, b. Here Fig. 12a results from the velocity measurements at cross-section 10,  $y/B = 0.1$ ,  $z/h = 0.89$ ; and Fig. 12b, from the measurements at cross-section 11,  $y/B = 0.25$ ,  $z/h = 0.89$ . For these examples, and as follows from the GWS graphs, the dominant frequencies in the analyzed frequency band are 0.046 Hz (21.8 s) in Fig. 12a and 0.038 Hz (26.3 s) in Fig. 12b. The related CWTP contour plots show that these exist in the velocity signal throughout most of the recording period (from  $\approx 5$  to  $\approx 155$  s in Fig. 12a and from  $\approx 5$  to  $\approx 175$  s in Fig. 12b). Therefore, for these examples, the average values of the smallest frequencies in the record can be identified with 0.046 Hz for Fig. 12a and 0.038 Hz for Fig. 12b.

**Fig. 12** Continuous wavelet transform power (CWTP) contour plots for frequency band 0.0245–0.13 Hz and corresponding global wavelet spectrum (GWS) for selected velocity records:  
**a** cross-section 10,  $y/B = 0.1$ ,  $z/h = 0.89$ ;  
**b** cross-section 11,  $y/B = 0.25$ ,  $z/h = 0.89$

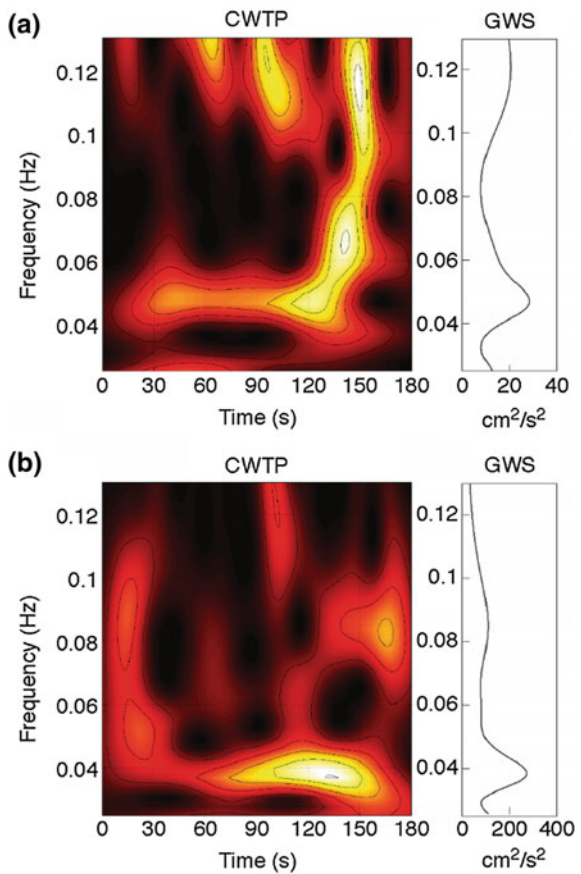
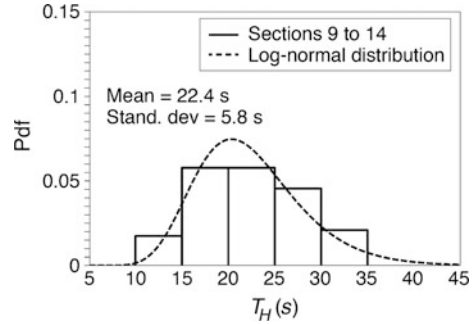


**Fig. 13** Plot of the probability density function (PDF) of the average values of the time scales of the largest coherent structures identified in individual 180 s long velocity records collected at the measurement level  $z/h = 0.89$



In general terms, the conditions in Fig. 12a, b typify those in all other velocity records—even if more complex situations could be found. For example, for the velocity measurement at section 10,  $y/B = 0.5$ ,  $z/h = 0.89$  (not included in this chapter, but readily available in Kanani 2014), the dominant (smallest) frequencies were found to be 0.033 Hz (30.3 s) and 0.049 Hz (20.4 s). The related CWTP contour plot shows that the frequency 0.033 Hz exists in the record from  $\approx 0$  s to  $\approx 65$  s and from  $\approx 130$  s to  $\approx 180$  s, while the frequency 0.049 Hz exists from  $\approx 65$  s to  $\approx 130$  s. This yields 0.0388 Hz ( $= [(65 \times 0.033) + (65 \times 0.049) + (50 \times 0.033)] / (65 + 65 + 50)$ ) as the average value of the smallest frequencies in the record.

The just described procedure was applied to the entire set of 120 s long velocity records from cross-section 9–14, and done separately for the measurements collected at each of the three different measurement levels ( $z/B = 0.21, 0.5, 0.89$ ). As example, the resulting probability density function (PDF) determined on the basis of the measurements at  $z/h = 0.89$  is shown in Fig. 13. This is well described by a log-normal distribution (see the dashed line in Fig. 13, representing the fitted distribution), with a mean value of 22.4 s. Rather similar results were obtained also for the sets of measurements at the levels  $z/h = 0.5$  and  $z/h = 0.21$ . In these cases, the mean of the fitted log-normal distributions were 23 and 20.2 s, respectively. Identifying the average time scale of the LSHCS's for the present flow with the mean of the fitted log-normal distribution in Fig. 13, yields  $T_H = 22.4$  s. This corresponds to an average length scale  $L_H = 5.5$  m (or  $L_H/B = 5.5$ ). This value is consistent with that previously determined for the shallow flow investigated by da Silva and Ahmari (2009), da Silva et al. (2012) and Kanani and da Silva (2015). It is also in agreement with the considerations in Sect. 2.

### 4.3 Effect of LSHCS's on the Mean Flow

In analogy to the case of LSVCS's, one would expect the flow subjected to the sustained action of a sequence of LSHCS's to cause the time-averaged streamlines to acquire a wave-like pattern in the ( $y$ ;  $z$ ) planes of flow (as in the schematic

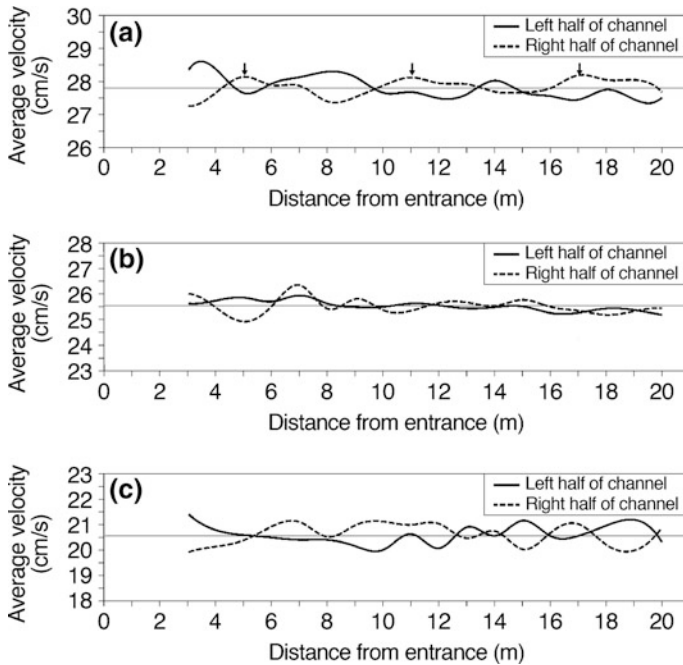


**Fig. 14** Average flow velocity in the right and left halves of the channel at the measurement levels: **a**  $z/h = 0.89$ ; **b**  $z/h = 0.5$ ; **c**  $z/h = 0.21$

Fig. 7b). Considering this, and following da Silva and Ahmari (2009) the set of 180 s long records of flow velocity collected at each different measurement level was used to produce plots of time-average flow velocity for both left and right sides of the channel versus the distance along the channel. These are shown in Fig. 14a–c, corresponding to  $z/h = 0.89, 0.5$  and  $0.21$ , respectively.

As can be inferred from Fig. 14a, at the level  $z/h = 0.89$  there is a noticeable periodic shift of the flow from one side of the channel to the other, i.e. the flow appears as internally meandering. As indicated by the arrows in Fig. 14a, the quasi-period of this cyclic shift is of the order of  $6B$ . However, at the level  $z/h = 0.5$  (Fig. 14b) such periodic shift of the flow is no longer noticeable. The deviations of the time-average flow velocity in the left and right halves of the channel are rather small (throughout most of the channel) and likely to be the result of measurement residuals. At the level  $z/h = 0.21$  (Fig. 14c) no regular pattern of behaviour is observed throughout the channel. From cross-section 5–13 the average flow velocity is consistently slightly larger on the right half of the channel than in the left half; while from section 13 onwards there is a random shift of the flow from the left to the right half of the channel. The consistent increase of average flow velocity in the left half of the channel from cross-section 5–13 suggests that in this region the bed surface was not exactly horizontal in transverse direction, but rather slightly tilted.

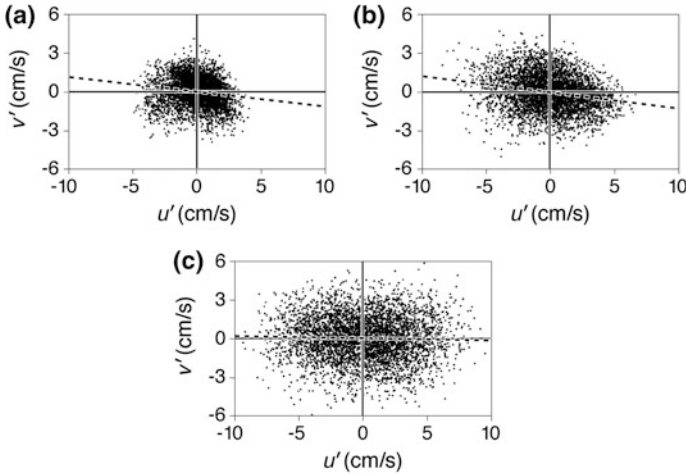


**Fig. 15** Quadrant planes corresponding to the velocity records collected at cross-section 10,  $y/B = 0.3$ , and measurement level: **a**  $z/h = 0.89$ ; **b**  $z/h = 0.5$ ; **c**  $z/h = 0.21$

#### 4.4 Turbulence Structure Over the Flow Depth

To get some insight into the variation of turbulence structure over the flow depth, quadrant analysis (Nezu and Nakagawa 1993) was applied to the entire set of 180 s long records of flow velocity, with three examples of the results being shown in Fig. 15a–c (see Kanani 2014 for the complete set of results). Since the focus is on LSHCS's, quadrant analysis is performed on the basis of the fluctuating components of longitudinal and transverse velocities,  $u'$  and  $v'$  respectively.

As is well-known, if the major axis (or transverse diameter) of the ellipse representing the data on the quadrant planes exhibits a slope (as in the example in Fig. 15a, b), then that implies the more frequent occurrence of specific events related to coherent structures out of the four following possibilities: ejection (Q2), sweep (Q4), inward (Q3) and outward (Q1) events. On the other hand, when the slope approaches zero (as in the example in Fig. 15c), i.e. when the data are almost evenly distributed in all quadrants, then that either reflects a large influence of flow structures associated with opposite shear layers (neutralized structures), or incoherent background flow structures. In other words, a smaller absolute value of the slope of the major axis of the ellipse implies weaker events. It follows that the absolute value of the aforementioned slope can be used as an index to quantify the existence of coherent structures or their tendency to possible events. Here, this index is called coherent structure existence index (CSEI). The calculated average values of CSEI for all measurement points on cross-section 9–14 are 0.178, 0.151 and 0.034 for the measurement levels  $z/h = 0.89$ , 0.5 and 0.21, respectively. Observe that the average value of CSEI at  $z/h = 0.89$  is 3.5 and 5.2 times higher than that at the levels  $z/h = 0.5$  and  $z/h = 0.21$ , respectively. These values indicate

that, for the present flow, the existence or tendency of LSHCS's to possible events decreases significantly as the distance to the free surface increases.

Together with the results in the previous sub-section, the results just described show that the structures originate towards the free surface. They further suggest that, as originally hypothesized by da Silva (1991) and Yalin (1992), in deep flows the structures primarily exist and affect the upper layers of flow. This would explain why alternate bars (i.e. the related bed deformation) cease to exist in deep flows, while meandering (i.e., the related bank deformation) can still occur.

It is interesting to notice that CWT revealed the existence of cyclic fluctuations of velocity with scales consistent with LSHCS's also at the measurement level closest to the bed ( $z/h = 0.21$ ). This may appear as contradictory with the fact that at this measurement level no internal meandering of the flow, or tendency for specific quadratic events was noticed. The writers believe that there is no contradiction, and that this is most likely due to the flow closer to the bed nonetheless being affected by the presence of the LSHCS's existing in the upper layers: the fluid motions taking place in the upper layers where the LSHCS's are present are transmitted to the lower layers where they are not present. To put it differently, the fluid in the lower flow regions "feels" what is happening in the upper flow layers and tends to behave in a correlated way—but the less and less so, the deeper into the flow.

## 5 Conclusions

Following a review of pertinent information and/or hypotheses regarding the characteristic scales, dynamics and morphological consequences of large-scale coherent structures, this chapter presents a study of large-scale horizontal coherent structures (LSHCS's) in a deep laboratory flow conveyed in a 21 m long and 1 m wide channel. The width-to-depth ratio of the flow was equal to 7.1; the channel bed was flat. The main results of the related velocity measurements can be described as follows:

1. The 180 s long records of the smoothed oscillograms of fluctuating component of longitudinal velocity were found to invariably exhibit cycles of velocity fluctuation consistent with the presence of LSHCS's occupying (or affecting) the entire body of fluid. A similar conclusion was obtained from the spectral density plots produced for selected measurement points where 20 min long records of flow velocity were collected.
2. Continuous Wavelet Transform (CWT) was used to determine the average length and time scales of the LSHCS's. This yielded  $T_H = 22.4$  s, corresponding to an average length scale  $L_H = 5.5$  m (or  $L_H/B = 5.5$ ). The result  $L_H/B = 5.5$  is consistent with that previously determined for a shallow, alternate bar inducing flow by da Silva and Ahmari (2009).

3. Plots of the time-average flow velocity for both left and right halves of the channel at the level  $z/h = 0.89$  revealed a noticeable periodic shift of the flow from one side of the channel to the other, showing that sustained longitudinal sequences of LSHCS's lead to an internal meandering of the flow. However, this internal meandering was limited to the upper flow layers, as it was not noticeable in the measurements at the levels  $z/h = 0.5$  and  $0.21$ .
4. Quadrant analysis revealed a near absence of quadratic events at the measurement level  $z/h = 0.21$ . This is in sharp contrast with the conditions at the upper flow regions. That is, the existence of quadratic events associated with the life-cycle of LSHCS's decreased significantly with submergence into the flow. This provides a clear indication that LSHCS's in deep flows exist and affect mainly the upper flow regions.

**Acknowledgements** This research was supported by funds from the Natural Sciences and Engineering Research Council of Canada, through a Discovery Grant to the first author, as well as funds from the Ontario Research and Development Challenge Fund.

## References

- Ackers P, Charlton FG (1970) The geometry of small meandering streams. In: Proceedings of the institution of civil engineers, Paper 73286S, London
- Adrian RJ, Marusic I (2012) Coherent structures in flow over hydraulic engineering surfaces. *J Hydraul Res* 50(5):451–464
- Ahmari H, da Silva AMF (2011) Regions of bars, meandering and braiding in da Silva and Yalin's plan. *J Hydraul Res* 49(6):718–727
- Ahmari H (2010) Size, dynamics and consequences of large-scale horizontal coherent structures in open-channel flows: an experimental study. PhD thesis, Queen's University, Kingston, Canada
- Allen J (1985) Principles of physical sedimentology. Chapman & Hall, London
- Balakumar BJ, Adrian RJ (2007) Large- and very-large-scale motions in channel and boundary-layer flows. *Philos Trans R Soc A Math Phys Eng Sci* 365:665–681
- Blackwelder RF (1978) The bursting process in turbulent boundary layers. In: Smith CR, Abbott DE (eds) Coherent structures in turbulent boundary layers, AFOSR/Lehigh University Workshop, Bethlehem, Penn, vol 211
- Cantwell BJ (1981) Organised motion in turbulent flow. *Annu Rev Fluid Mech* 13:457–515
- Chang HH (1988) Fluvial processes in river engineering. Wiley
- Camussi R (2002) Coherent structure identification from wavelet analysis of particle image velocimetry data. *Exp Fluids* 32(1):76–86
- Constantinescu G, Miyawaki S, Rhoads B, Sukhodolov A (2012) Numerical analysis of the effect of momentum ratio on the dynamics and sediment entrainment capacity of coherent flow structures at a stream confluence. *J Geophys Res* F04028. <https://doi.org/10.1029/2012JF002452>
- da Silva AMF, Yalin MS (2017) Fluvial processes, 2nd edn, IAHR Monograph. CRC Press, Taylor & Francis Group
- da Silva, AMF (2015) Recent advances from research on meandering and directions for future work. Chapter 14, In: Rowínsky P, Radecki-Pawlik A (eds) Rivers—physical, fluvial and environmental processes, Geoplanet: earth and planetary book series, Springer International Publishing, Switzerland, pp 373–401

- da Silva AMF, Ahmari H, Kanani A (2012) Characteristic scales and consequences of large-scale horizontal coherent structures in shallow open-channel flows. In: Environmental fluid mechanics—Memorial volume in honour of Prof. Gerhard H. Jirka, IAHR Monograph, Rodi W and Uhlmann M, Chapter 5. CRC Press, Taylor & Francis Group, pp 85–105
- da Silva AMF, Ahmari H (2009) Size and effect on the mean flow of large scale horizontal coherent structures in open-channel flows: an experimental study. *Can J Civ Eng* 36(10):1643–1655
- da Silva AMF (2006) On why and how do rivers meander. *J Hydraul Res* 44(5):579–590
- da Silva AMF (1991) Alternate bars and related alluvial processes. M.Sc. Thesis, Department of Civil Engineering, Queen’s University, Kingston, Canada
- del Álamo JC, Jiménez J (2003) Spectra of the very large anisotropic scales in turbulent channels. *Phys Fluids* 15(6):L41–L44
- Dementiev MA (1962) Investigation of flow velocity fluctuations and their influences on the flow rate of mountainous rivers. Technical report of the State Hydro-Geological Institute (GGI), vol 98, (In Russian)
- Farge M, Schneider K (2001) Analysing and computing turbulent flows using wavelets. In: Lesieur M, Yaglom AM, David F (eds) *New trends in turbulence*. Springer, Berlin
- Farge M (1992) Wavelet transforms and their applications to turbulence. *Annu Rev Fluid Mech* 24:395–447
- Farge M, Guezennec Y, Ho CM, Meneveau C (1990) Continuous wavelets analysis of coherent structures. In: *Proceedings of the summer program (1990)*. Center for Turbulence Research, Stanford University NASA-Ames, Stanford
- Franca MJ, Lemmin U (2015) Detection and reconstruction of large-scale coherent flow structures in gravel-bed rivers. *Earth Surf Proc Land* 40:93–104
- Franca MJ, Lemmin U (2008) Using empirical mode decomposition to detect large-scale coherent structures in river flows. In: Altınakar MS, Kokpinar MA, Aydin I, Cokgor S, Kirkgöz S (eds) *Proceedings of river flow 2008, 4th international conference on fluvial hydraulics*, Cesme-Izmir, Turkey, Ankara, Kubaba Congress Department and Travel Services: 67–74
- Franca MJ, Lemmin U (2006) Detection and reconstruction of coherent structures based on wavelet multiresolution analysis. In: Ferreira RML, Alves ECTL, Leal JGAB, Cardoso AH (eds) *Proceedings of River Flow 2006, 3rd international conference on fluvial hydraulics*, Lisbon, Portugal. CRC Press, Taylor & Francis Group, London, pp 181–190
- Franca MJ (2005) A field study of turbulent flows in shallow gravel-bed rivers. PhD dissertation, École Polytechnique Fédérale de Lausanne (EPFL). <https://doi.org/10.5075/epflthesis-3393>
- Fujita Y, Muramoto Y (1985) Study on the process of development of alternate bars. *Disaster Prev Res Inst Bull Kyoto Univ Jpn* 35(3):55–86
- Gad-el-Hak M, Hussain AKMF (1986) Coherent structures in a turbulent boundary layer. Part 1: Generation of “artificial” bursts. *Phys Fluids* 29(7):2124–2139
- Garde RJ, Ranga Raju KG (1985) *Mechanics of sediment transportation and alluvial stream problems*, 2nd edn. Wiley Eastern Ltd., New Delhi
- Grishanin KV (1979) Dynamics of alluvial streams. *Gidrometeoizdat*, Leningrad
- Hino M (1968) Equilibrium-range spectra of sand waves formed by running water. *J Fluid Mech* 34(3):565–573
- Hussain AF (1983) Coherent structures—reality and myth. *Phys Fluids* 26(10):2816–2850
- Ikeda S (1984) Prediction of alternate bar wavelength and height. *J Hydraul Eng* 110(4):371–386
- Jackson RG (1976) Sedimentological and fluid-dynamics implications of the turbulent bursting phenomenon in geophysical flows. *J Fluid Mech* 77:531–560
- Jaeggi MNR (1984) Formation and effects of alternate bars. *J Hydraul Eng* 110(2):142–156
- Jiménez J (1998) The largest structures in turbulent wall flows. Center for Turbulence Research Annual Research Briefs, Stanford University
- Jirka GH, Uijttewall WSJ (eds) (2004) *Shallow flows: selected papers of the international symposium on shallow flows, 16–18 June 2003, Delft, The Netherlands*. A.A. Balkema, Rotterdam, The Netherlands



- JSCE Task Committee on the Bed Configuration and Hydraulic Resistance of Alluvial Streams (1973) The bed configuration and roughness of alluvial streams. In: Proceedings of the Japan society of civil engineers, no 210, pp 65–91 (In Japanese)
- Kadota A, Nezu I (1999) Three-dimensional structure of space-time correlation on coherent vortices generated behind dune crest. *J Hydraul Res* 37(1):59–80
- Kanani A, da Silva AMF (2015) Application of continuous wavelet transform to the study of large-scale coherent structures. *J Environ Fluid Mech* 15(6):1293–1319
- Kanani A (2014) Large-scale horizontal coherent structures in a deep open channel flow: an experimental study. PhD thesis, Department of Civil Engineering, Queen's University, Kingston, Canada
- Kanani A, Ahmari H, da Silva AMF (2010) Investigation of horizontal coherent structures in a shallow open-channel flow using velocity signal decomposition. In: Dittrich A, Koll A, Aberle J, Geisenhainer P (eds) Proceedings river flow 2010, 5th international conference on fluvial hydraulics, Braunschweig, Germany, Bundesanstalt für Wasserbau (BAW), Karlsruhe, Germany, pp 1059–1066
- Kondratiev N, Lyapin AN, Popov IV, Pinikovskii SI, Fedorov NN, Yakunin II (1959) Channel processes. *Gidrometeoizdat*, Leningrad
- Konsoer KM, Rhoads BL (2014) Spatial-temporal structure of mixing interface turbulence at two large river confluences. *J Environ Fluid Mech* 14(5):1043–1070
- Matthes GH (1947) Macroturbulence in natural stream flow. *Trans Am Geophys Union* 28 (2):255–262
- McLelland SJ, Ashworth P, Best JL (1996) The origin and downstream development of coherent flow structures at channel junctions. *Coherent flow structures in open channels*. Wiley, Chichester, UK, pp 459–490
- Miyamoto H, Kanda T (2004) Extraction of coherent structure from PIV data using wavelet transform. In: Proceedings of building partnerships, joint conference on water resource engineering and water resources planning & management 2000, ASCE. [https://doi.org/10.1061/40517\(2000\)326](https://doi.org/10.1061/40517(2000)326)
- Nezu I, Nakagawa H (1993) Turbulence in open channel flow. *IAHR Monograph*. A.A. Balkema, Rotterdam, The Netherlands
- Nikora V (2005) Flow turbulence over mobile gravel-bed: spectral scaling and coherent structures. *Acta Geophys Polonica* 53(4):539–552
- Pope SB (2000) *Turbulent flows*. Cambridge University Press, UK
- Rashidi M, Banerjee S (1988) Turbulence structures in free-surface channel flows. *Phys Fluids* 31 (9):2491–2501
- Robinson SK (1991) Coherent motions in the turbulent boundary layer. *Annu Rev Fluid Mech* 23:601–639
- Rodi W, Constantinescu G, Stoesser T (2013) *Large-eddy simulation in hydraulics*. *IAHR Monograph*. CRC Press, Taylor & Francis Group
- Roy AG, Buffin-Bélanger T, Lamarre H, Kirkbride AD (2004) Size, shape and dynamics of large-scale turbulent flow structures in a gravel-bed river. *J Fluid Mech* 500:1–27
- Schweizer S, Borsuk ME, Reichert P (2007) Predicting the morphological and hydraulic consequences of river rehabilitation. *River Res Appl* 23(3):303–322. <https://doi.org/10.1002/rra.981>
- Stuart TA (1953) Spanwise migration, reproduction and young stages of loch trout. *Freshwater and salmon, fisheries research*, Scottish Home Department, Edinburgh, Scotland, Majesty's Stationary Office
- Sukhodolov AN, Sukhodolova TA (2012) Vegetated mixing layer around a finite-size patch of submerged plants: part 2. turbulence statistics and structures. *Water Resour Res* 48:W12506. <https://doi.org/10.1029/2011WR011805>
- Sukhodolov AN, Uijtewaal WS (2010) Assessment of a river reach for environmental fluid dynamics studies. *J Hydraul Eng* 136(11):880–888
- Torrence C, Compo PG (1998) A practical guide to wavelet analysis. *Bull Am Meteorol Soc* 79 (1):61–78

- Utami T, Ueno T (1977) Lagrangian and Eulerian measurement of large-scale turbulence. In: Asanuma T (ed) Proceedings of the international symposium on flow visualization I, Hemisphere, Wash
- van Rijn LC (1984) Sediment transport. Part III: bed forms and alluvial roughness. *J Hydraul Eng* 110(12):1733–1753
- Velikanov MA (1955) Dynamics of alluvial streams, vol II, Sediment and bed flow. State Publishing House for Theoretical and Technical Literature, Moscow
- Welford MR (1993) Field evaluation of empirical equations in straight alluvial channels. *Phys Geogr* 14(6):581–598
- Yalin MS (2006) Large-scale turbulence and river morphology. In: Ferreira RML, Alves ECTL, Leal JGAB, Cardoso AH (eds) Proceedings of river flow 2006, 3rd international conference on fluvial Hydraulics. CRC Press, Taylor & Francis Group, pp 1243–1249
- Yalin MS, da Silva AMF (2001) Fluvial processes. IAHR Monograph, IAHR, The Netherlands.
- Yalin MS (1992) River mechanics. Pergamon Press, Oxford
- Yalin MS (1977) Mechanics of sediment transport, 2nd edn. Pergamon Press, Oxford
- Yalin MS (1964) Geometrical properties of sand waves. *J Hydraul Div* 90(5):105–119
- Yokosi S (1967) The structure of river turbulence. *Prev Res Inst Bull Kyoto Univ Jpn* 17(2):1–29

# Ice Concerns for Hydraulic Engineering in Cold, Mountainous Terrain

Robert Ettema

**Abstract** This chapter discusses and illustrates ice concerns associated with hydraulic engineering for water conveyance systems in cold, mountainous terrain, and aims to draw attention to the potential problems that may occur when water changes from liquid to solid. Hydraulic engineering involves liquid water, and commonly comprises the design of open-water channels (or reservoirs) linked to pressurized conduits (pump-lines, penstocks, siphons, and tunnels) that pass water down, up, over, or through mountainous terrain. The topics covered herein address fundamental aspects of ice formation and behavior. An important consideration is the relationship between the freezing temperature of water and flow pressure. Flow pressure can vary substantially in closed-conduit portions of hydraulic systems. The primary engineering concern is that ice formation should not hamper the operation of the system or its component parts. Should a concern arise about the operation of the system, the concern should be mitigated by re-designing the system or its parts, and managing the system by adjusting flow rates, and by monitoring water temperature at key locations.

## 1 Introduction

Ice formation often poses challenges for hydraulic engineering activities associated with water conveyance systems in cold mountainous terrain. Mountainous areas commonly yield water and hydropower, and thus often involve extensive hydraulic engineering activities. A noteworthy feature of water conveyance systems in mountainous terrain is the combined use of open-channel and pressurized conduits. The combinations occur in the form of reservoirs and channels linked to one or more of the following conveyance-structure components:

---

R. Ettema (✉)  
Colorado State University, Fort Collins, CO 80523, USA  
e-mail: rettema@engr.colostate.edu

- pump-lines
- siphons (inverted and regular)
- water-diversion tunnels
- hydropower penstocks and turbines

Such conveyance components commonly comprise critical parts of water-conveyance systems that divert water from streams, and reservoirs in mountainous terrain. Pumps enable water to be lifted to higher elevations. Siphons and tunnels enable water to be conveyed across, or through, steep terrain. Penstocks precipitously drop water down to hydropower turbines set a lower elevation. Though these conveyance components are fairly common, little is known about their performance in mountainous terrain subject to frigid-weather conditions and, thereby, to ice. Figure 1 illustrates, for instance, a small canal conveying water to a tunnel in the Sierra Nevada Mountains, USA.

Of particular concern are problems attributable to frazil ice, which can form in several situations. The lower air temperatures and higher wind in mountainous regions may cause water in mountain streams and reservoirs to cool more quickly than at lower elevations, thereby creating conditions hastening ice formation. Consequently, pump intakes, penstocks, siphons, and tunnels linked to mountain streams and reservoirs frequently convey frigid water during winter; the severity of conditions requires that some systems be drained during such winter. The concern for frazil formation is aggravated by the swift and turbulent flow conditions prevailing in many mountain streams and rivers. Further, flow pressures in water-conveyance conduits flowing full can vary over several orders of magnitude, and thereby alter the freezing temperature of water. Together, these aspects of water flow produce situations where frazil may form in sufficient concentrations as to pose difficulties for water-conveyance systems in mountainous terrain. This chapter

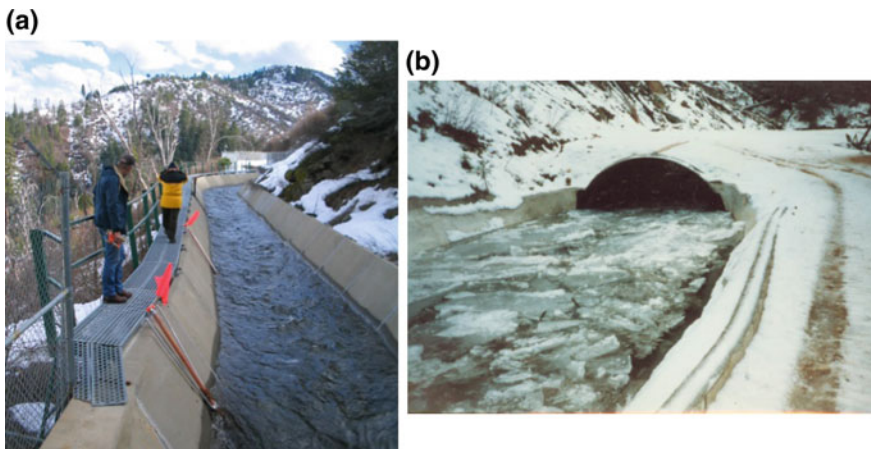


**Fig. 1** Flow along a small channel and tunnel system in mountainous terrain: **a** flow along a channel; and **b** channel flow conveying ice into a tunnel

outlines and discusses the difficulties posed by frazil and other ice forms, including snow; that hydraulic engineering projects in mountainous terrain often experience.

There is little literature on water-conveyance systems in cold mountainous regions. Though, for example, Gemperline (1990) and Billfalk (1992) usefully summarize ice considerations in the design and operation of water intakes for hydropower facilities, and Daly (1991) and Daly and Ettema (2006) do the same for water intakes generally, none of these papers tackles the ice issues complicating the overall performance of conveyance systems subject to substantial pressure variations. Gilpin's comprehensive work on freezing of water flow in pipes flows (e.g., Gilpin 1981) gives useful insights, but only for small-bore pipes and modest pressure variation. Several anecdotal accounts, and sundry ad hoc reports, however, indicate that larger-scale conveyance components in mountainous regions can encounter significant problems attributable to frazil ice and snow (e.g., Ettema et al. 2008; Ettema 2005).

## 2 Variation of Freezing Temperature with Pressure

Blockage of water intake trash-racks by frazil and other ice forms is a well-known problem (e.g., Daly 1991). Frazil accumulation can block the trash rack at the entrance to a penstock, pump-intake, siphon, and tunnel, as well as within them. Also, blockages may lead to overflow and further jamming of approach channels or pipes. Less well known are the ice problems attributable the changes in freezing temperature associated with the substantial pressure changes that water flows in pressurized conduits may undergo. The principal factor to be considered in this regard is the depression of freezing temperature as water pressure increases. This trend is illustrated in the phase diagram of water (Fig. 2a).

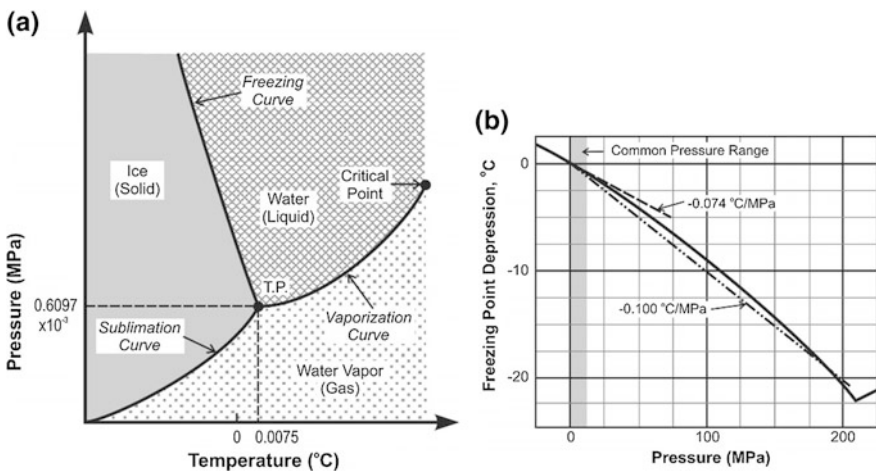


Fig. 2 Part of the phase diagram for water (a); and, freezing-point depression with pressure (b)

Pressure variation may delay or hasten freezing, and it may reconstitute ice pieces passing with water through pressurized conduits. The variation of melting/freezing temperature with gage pressure can be expressed, from the Clapyeron equation for ice-water;

$$\frac{dT_F}{dP} = T_F \frac{dV}{dH_F} \quad (1)$$

in which  $T_F$ —freezing temperature,  $P$ —pressure,  $V$ —volume of water freezing, and  $H_F$ —latent heat of water fusion. For water, with  $T_F$  in degrees Kelvin and  $P$  in MPa, the trend expressed by Eq. (1) can be illustrated graphically using a curve such as in Fig. 2b. The curve itself can be expressed as

$$T_F = 273.16 \left[ 1 - \left( \frac{P}{395.2} \right) \right]^{1/9} \quad (2)$$

Here, temperature,  $T_F$ , is in degrees Kelvin, and gage pressure,  $P$ , is in MPa. Equation (2) indicates that an increase of approximately 1 MPa pressure decreases the freezing temperature of water by about 0.074 °K (or 0.074 °C); i.e., the freezing temperature of water becomes  $-0.074$  °C. The average depression of freezing temperature for ice commonly found in nature (for ice type 1 h, typical for hydraulic engineering, Hobbs 1974) is 0.10 °C/MPa, over the pressure range associated with ice 1 h,  $0 < P < 209$  MPa. Pressure changes of the order of 0 to 2 MPa magnitude are common in closed-conduit flows associated with hydropower penstocks, pumps, siphons, though perhaps less so in tunnels. An elevation difference of 100 m produces a pressure difference of about 1 MPa.

The following two practical questions arise regarding the depression of water's freezing temperature for water flowing through hydropower penstocks, pump pipelines, and siphons:

1. Why should the depression of water's freezing temperature be of concern to the operation of these conduits?
2. How can water in these conduits attain the depressed freezing temperature?

The depression of freezing temperature can result in supercooling of water and frazil formation, with all its attendant problems of flow blockage. Accordingly, care is needed to minimize frazil formation in such conduits. To do this requires preventing water flow from actually dropping to its depressed freezing temperature, or below.

Water flowing down a conduit may cool owing to heat loss through the walls of the conduit, and through the melting of ice transported with flow into the conduits. As the freezing temperature decreases, the surface of ice melts, drawing heat from the water, thereby cooling it. The water cools to the extent that sufficient ice melts to cool the water to its freezing temperature. The amount of ice particles needed to cool frigid water from its initial freezing temperature to its adjusted freezing temperature can be calculated from the heat-balance relationship

$$\rho_{ice}\lambda(\Delta C_{ice}) = \rho_{water}C_p(\Delta T_F) \quad (3)$$

where  $\rho_{ice}$ —ice density,  $\lambda$ —latent heat of melting ice,  $C_{ice}$ —frazil ice concentration,  $C_p$ —specific heat of water and  $T_F$ —freezing temperature of water, and  $\Delta T_F = T_{F2} - T_{F1}$ ; here,  $T_{F1}$  is the freezing temperature at the higher elevation,  $T_{F2}$  is the freezing temperature at the lower elevation, and  $T_{F3}$  is the freezing temperature at the conduit's outlet. A freezing temperature drop  $T_{F,water} = 0.1$  °K requires an ice-concentration reduction of  $\Delta C_{ice} = 1.03 \times 10^{-3}$ . Assuming an initial freezing temperature,  $T_{F1} = 0$  °C, Eqs. (2) and (3) lead to a relationship between  $\Delta C_{ice}$  and net head-drop through the conveyance structure. Figure 4 shows the relationship. For instance, the change of ice concentration given in the above example corresponds approximately to a 100 m head drop. Estimates of frazil concentrations in streams and reservoirs are of the order  $10^6$  particles/m<sup>3</sup> (e.g., Daly 1991). If frazil particles in flowing water are taken to be discoids, 2 mm in diameter and 0.1 mm thick (e.g., Chen et al. 2004), a nominal volumetric frazil concentration is about  $1.6 \times 10^{-3}$ , which means that typically there is enough frazil ice to supercool water in the conveyance structures diverting water from the mountain streams and reservoirs.

Pressure-related supercooling of water occasionally occurs in the natural environments. Alley et al. (1998), for example, describe how water flowing through or beneath a deep glacier can supercool when eventually ascending a steep slope at the end of a glacier. The ascending supercooled water may freeze to the glacier's floating base, as well as to other boundaries.

### 3 Water Temperature Response to the Variation of Freezing Temperature with Pressure

The rate of change of the water temperature in response to pressure variation can be estimated by application of the one-dimensional heat transport equation. Several assumptions are required. First, the change in pressure with distance,  $x$ , along penstock can be estimated as

$$P_g = P_o + \rho gx \left[ -\frac{dz}{dx} - \frac{fU^2}{D2g} \right] = P_o + \alpha x \quad (4)$$

where  $P_g$ —the gage pressure of the flow;  $P_o$ —the initial pressure at  $x = 0$ ;  $\rho$ —the water density,  $g$ —the acceleration of gravity;  $z$ —the vertical elevation;  $f$ —the friction coefficient of the flow;  $D$ —the penstock diameter,  $U$ —the flow velocity; and  $\alpha$  is the overall rate of change of pressure with distance.

The variation of freezing temperature with position along the penstock,  $T_f(x)$  can be stated as

$$T_F(x) = T_{F(x=0)} - C\alpha x \tag{5}$$

where  $C$ —the rate of change of freezing temperature with pressure, approximately 0.074 °C/MPa (see Fig. 3); and  $T_{F(x=0)}$ —the freezing temperature at  $x = 0$ . The steady state rate of change in water temperature is then given as

$$U \frac{dT}{dx} = \frac{h_p A_p}{\rho C_p U} (T_F(x) - T) = \frac{h_p A_p}{\rho C_p U} ((T_{F(x=0)} - C\alpha x) - T) \tag{6}$$

where  $T$ —the water temperature;  $h_p$ —the heat transfer coefficient between the suspended frazil particles and the fluid;  $A_p$ —the total surface area of the particles per unit volume of the fluid; and  $C_p$ —the heat capacity of the fluid. In this case, it has been assumed that there is no heat transfer through the penstock walls, the water temperature is constant with time at every location, frictional heating can be neglected and the heat transfer rate and surface area of the particles remains constant with position along the penstock. This equation can be directly solved to arrive at the temperature as a function of distance  $x$  along the penstock

$$T(x) = T_F(x) + (T_i - T_{F(x=0)})e^{-\frac{h_p A_p}{\rho C_p U} x} + T_e \left( 1 - e^{-\frac{h_p A_p}{\rho C_p U} x} \right). \tag{7}$$

Here

$$T_e = \frac{\rho C_p U C \alpha}{h_p A_p} \tag{8}$$

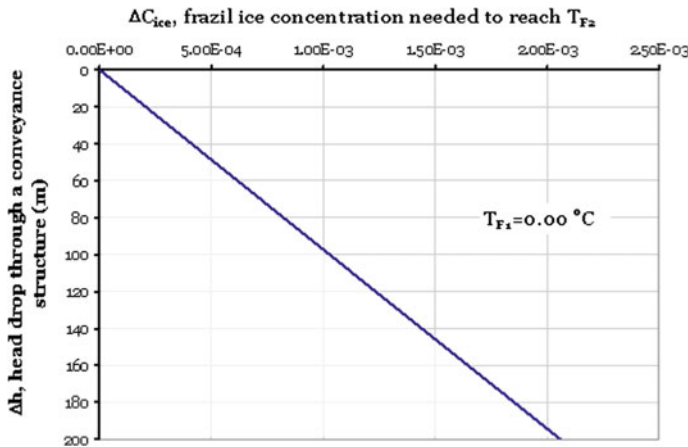


**Fig. 3** Variation of frazil conc. needed to reach freezing temperature for variable pressure-head increase



and  $T_i$ —the initial water temperature at  $x = 0$ . The product  $\rho CPUC\alpha$  can be interpreted as the rate that energy must be removed or supplied to the fluid in order that the change in water temperature matches the change in freezing temperature with distance along the penstock. In this light,  $T_e$  can be seen as the temperature difference between the fluid and the freezing temperature required to remove or supply that energy from the suspended frazil particles given the heat transfer rate from the particles,  $h_p$ , and the total area of the particles,  $A_p$ . The heat transfer rate from suspended particles is a function of the particle size relative to the Kolmogorov turbulent length scale and to a lesser degree the turbulent intensity (e.g., Daly 1984; Holland et al. 2007).

The Nusselt number, based on the particle radius and thermal conductivity of water, ranges from 1 for very small suspended particles to approximately 100 for larger particles. The area of the suspended frazil over which the heat transfer takes place depends on the number of particles, their size and shape. At initial formation, frazil ice tends to be disk shaped with a thickness roughly one tenth of their diameter; the frazil crystals then tend towards a more spherical shape as they travel downstream (Daly 1994). To illustrate the likely rate of change of water temperature along a penstock, Eq. 7 is applied to a 100 m vertical penstock flowing at 1 m/s. The parameters used are  $10^6$  spherical particles  $m^{-3}$ , and the average frazil particle size is 0.001 m. The friction losses of the flow, included in Eq. 4 are neglected and it is assumed that the water entered the penstock at the freezing temperature for zero gage pressure. The calculations are performed for three values of Nusselt number: 1, 10 and 100. This is equivalent to assuming different rates of turbulent energy dissipation in the penstock. The actual energy dissipation rate will depend on the pipe friction factor, diameter and flow velocity. The results are shown in Fig. 4.

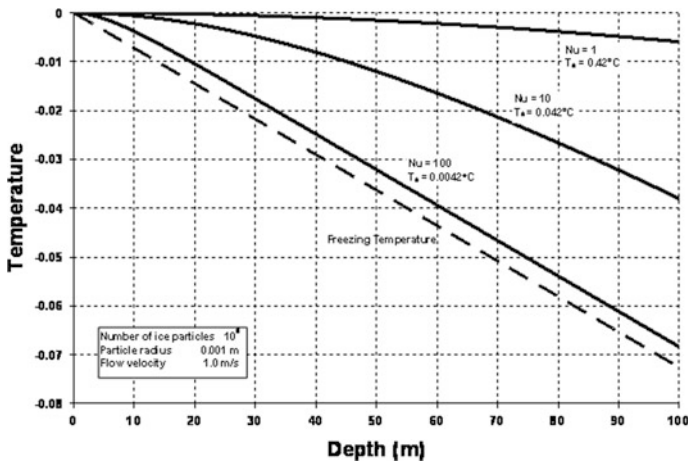
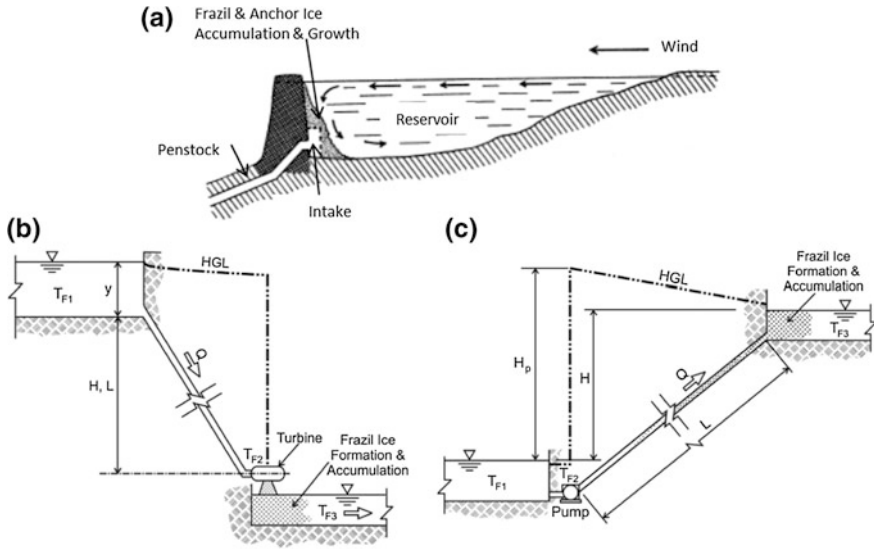


Fig. 4 Variation of water temperature along a 100 m vertical penstock assuming three values of Nusselt number,  $Nu$



**Fig. 5** Frazil and anchor ice formation and accumulation in hydro-machinery: **a** at a water intake in a reservoir; **b** at a turbine draft-tube; and, **c** at a pump-line. Here,  $T_{F1} = T_{F3} = 0.00\text{ }^{\circ}\text{C}$ ;  $T_{F2} < 0.00\text{ }^{\circ}\text{C}$

## 4 Ice Concerns in Component Hydraulics Systems

The following sections briefly discuss ice concerns often found in components of hydraulic engineering systems in mountainous terrain. Figure 5 illustrates the concerns.

### 4.1 Frazil and Anchor-Ice Blockage of Intakes

Frazil and anchor ice accumulation and anchor-ice growth on water intakes in reservoirs and canals is a common problem in cold weather conditions. The resulting blockage typically occurs abruptly and dramatically, choking the intake. Figure 5a shows how, for a reservoir, a frigid wind cools and moves water on the surface of a reservoir. Frazil may form in the water surface, as may supercooled water, and both are drawn to the intake. There, frazil may adhere to the intake and lead to growth of anchor ice. Besides choking flow from entering through the intake's trashracks, the ice blockage produces a pressure differential across the intake structure, which may collapse the trashracks.

## **4.2 Frazil Formation in Hydropower Turbines and Draft Tubes**

A penstock delivers water under pressure to a hydropower turbine, which then extracts much of the power associated with the water's flow rate and net head. For low and medium-head turbines, the water power is converted into mechanical power by means of flow momentum exchange; the flowing water remaining fully enclosed by the turbine and its draft tube, but at drastically reduced pressure. However, for high-head turbines, water surrounded by air at atmospheric pressure impacts the turbine runner, and is then discharged directly into a tailrace.

Figure 5b shows that water pressure in a penstock increases as flow moves down the penstock. A corresponding decrease in freezing temperature accompanies the pressure increase. As the water emerges from the penstock and passes through the turbine, its pressure decreases abruptly, with the consequent increase in freezing temperature, and the flow of supercooled water out of the turbine. Supercooled water is in an unstable state, and eventually (through nucleation by ice fragments in the flow) will adjust itself so as to be in a stable state. When that occurs, water releases its latent heat of fusion, and there occurs a rapid growth of frazil, which initially is in an active state. Frazil may be swept out into the tailwater channel. If the concentration of frazil is large, and the tailwater quite small, the frazil can congest the tailwater, eventually accumulating back up into the turbine, possibly eventually choking flow through the turbine. Few studies have been conducted of turbine operation when water flow is at the freezing temperature and frazil is at the verge of forming, or actually forming.

The length, or inclination, of a penstock plays a role with respect to cooling of flow through a penstock in frigid winter conditions. For a given drop in elevation, penstock length directly influences flow duration through a penstock. Greater flow duration provides more time for water to cool, by means of ice melting or heat-loss through the penstock. Accordingly, all else being equal, a longer penstock produces more frazil.

## **4.3 Frazil Formation in Pump Lines**

When water passes through a pump, water pressure suddenly rises to head  $H_p$ , as indicated in Fig. 5c then reduces along the pump-line to about the equivalent of the flow depth at the flow outlet. The freezing temperature drops correspondingly as the hydraulic grade line rises above the pipe, causing the water potentially to be supercool and the ice to melt. Actual supercooling depends on there being sufficient time for water to cool. The freezing temperature rises as the hydraulic grade line drops and approaches the water surface at the outlet.

Flow along the declining grade line is prone to form frazil. The volume of frazil formed approximately equals the volume of ice melted, and depends on additional

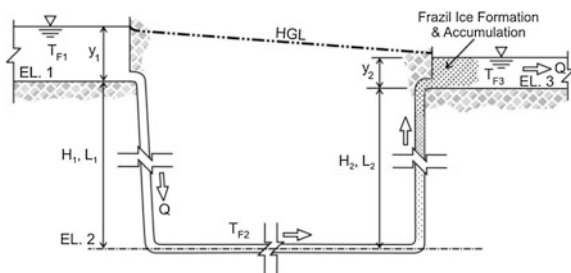
heat loss through the conduit’s walls. Frazil in supercooled water is initially in an active state whereby it can adhere to the remaining ice pieces conveyed with the flow, and agglomerating as a bolus, of ice pieces or slush that may disgorge at the outlet of the pump line. The increased flow resistance produced by the agglomerating slush may, with time, increase the flow resistance encountered by the pump. Information on ice agglomerates or boluses, discharging from a pump line is not available presently. There evidently are no document reports of their occurrence. One consideration possibly mitigating enhanced frazil occurrence during flow passage through pumps is heat emitted from the pump; this heat may reduce frazil concentration.

### 4.4 Frazil Formation in Siphons

The changes in pressure and, thereby, of freezing temperature in siphons combine the changes occurring for flow in pump discharge lines. The formation of frazil and ice agglomerates essentially is the same as for a long pump line. As described above for pump lines, and penstocks, the freezing temperature declines as pressure increases (on the siphon’s downward arm), and increases as pressure decreases (on the upward arm). Provided that the water attains the reduced freezing temperature, the flow in the upward flow is supercooled. Inverted siphons are not uncommon for mountainous terrain; the siphon has an overall U-shape form, as indicated in Fig. 5. Ice entering the siphon may largely pass through the siphon, though some ice may accumulate in the bottom, especially at locations where flow separation occurs, notably at the first bottom bend where ice in the separation region may rest against the upper side of the siphon pipe (Fig. 6).

As water descends an inverted siphon, water pressure increases and the freezing temperature of water is depressed. Water has to cool before attains its freezing temperature. In this regard, frazil and ice pieces (as well as snow) entering the siphon may partially (or entirely) melt, the heat need to melt ice being drawn from the flowing water and cooling the water. An argument can be made that the more ice entering each siphon, the greater the internal heat sink provided for the flow to supercool. The dropping water then cools, even when there is no heat transfer to the

**Fig. 6** Frazil formation in an inverted siphon;  
 $T_{F1} = T_{F3} = 0.00 \text{ }^\circ\text{C}$ ;  
 $T_{F2} < 0.00 \text{ }^\circ\text{C}$



pipe and air around the pipe. The heat generated by flow friction would be negligible compared to the heat consumed in melting ice as water drops in the siphon and flows within the siphon.

A longer siphon (all other factors equal) provides more time for water to cool more, and thereby for more frazil to be generated. The relatively long bottom section of the siphon enables considerable melting of ice entering the siphon, thereby enabling the water to attain its new freezing temperature. A longer bottom section can enable more ice to rise and accumulate along the conduit. Greater accumulation of ice would increase flow resistance, and decrease flow rate, through the siphon, thereby compounding the frazil concern.

The location where frazil first forms in each siphon depends on the air temperature and rate of heat loss from each siphon, as well as on water flow rate, and the amount of ice entering the siphon. For example, under milder weather conditions and less ice entering the siphon, frazil will form closer to the end of the siphon, and will emerge as a rather thin slush. But under more frigid weather conditions, and more ice entering the siphon, ice forms more quickly along the siphon, and would emerge from the siphon as a more agglomerated, clumpy bolus of ice.

## 4.5 *Ice in Tunnels*

Flow in most tunnels flowing full usually do not experience the great pressure fluctuations experienced by flow in penstocks, pump-lines and siphons. For most tunnels, the elevation drop is relatively modest (typically much less than 100 m), unless the tunnel includes a vertical drop. Also, tunnel-wall temperature (in tunnels flowing full) is above the freezing temperature, and warms frigid-water flows. Wall temperatures typically are between the water temperature (about 0 °C for frigid water) and the temperature of the rock at some distance from the crown of the tunnel. Rock temperatures often are estimated to be at about the yearly average air temperature of the region in which the rock is located.

Nevertheless, tunnels still can be prone to ice problems:

- ice blockage of tunnel-entrance racks
- accumulation of ice pieces drifting into a tunnel
- accumulation of frazil formed by flow turbulence within the intake entrance
- aufeis formed by freezing of water seeping into a tunnel drained during winter

The problem of entrance-rack blockage is essentially the same as that for water intakes generally, and is well documented (e.g., Gemperline 1990; Daly 1991). However, a complication for tunnel entrances in steep mountainous regions, especially in remote regions, is that the usual methods for controlling frazil blockage of intakes along rivers and lakes are infeasible or much more difficult to implement. The usual methods (e.g., Daly 1991) include facilitating the formation

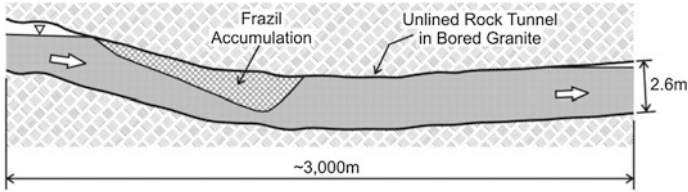


**Fig. 7** Ice accumulation along the upper portion of a tunnel

of an intact ice cover immediately upstream of the entrance, the use of warm water to heat the entrance rack, and back-flushing of flow through the entrance rack.

There are few studies documenting concerns caused by ice accumulation within water-diversion tunnels, though such problems are known to occur. Figure 7 illustrates the blockage concern. An operational difficulty is that access difficulties hinder the viewing of ice accumulations in tunnels. Ettema (2005), though, describes one instance where ice, largely frazil, accumulated in a tunnel. This instance is briefly elaborated below as a case-study example.

Lia and Carstens (1998) describe the problems caused by aufeis formation in water diversion tunnels for several Norwegian hydropower plants. The problem can be substantial for unlined tunnels in rock whose water-table lies above the tunnel. Frigid air passing through such tunnels freezes water seeping from fissures in the rock. A related further problem is snow-drift accumulation at the entrance and outlet of tunnels. Lia and Carstens (1998) describe large accumulations that practically dammed tunnels at Norwegian hydropower plants. Heavy snow falls and substantial winds can result in the formation of snow drifts. For tunnels in mountainous regions with perennial snow, the drifts can exist for several winters and consolidate.

## 5 Examples

Briefly described here are three case-study examples of frazil concerns encountered by a penstock, a siphon, and a tunnel in mountainous regions. Each example illustrates the difficulties that frazil may pose for these conveyance structures. Usefully documented examples are quite rare, and the full circumstances associated with them usually unclear. Also, several scale considerations hamper laboratory simulation of the case-study examples, or similar situations. The difficulties include the physical chemistry of water, along with the flow lengths and large pressures involved. These factors are almost prohibitively challenging to reproduce in the usual hydraulics laboratory.

### 5.1 *Frazil in a Turbine and Tailrace*

An example illustrating frazil formation and accumulation at the end of a penstock is that of a micro-hydro plant in Alaska. The plant draws water from a glacier-fed stream, and has a gross head of 90 m, and a net head of 74 m (giving  $\Delta T_F \approx -0.06$  °C). Early during its operation, a large quantity of frazil formed in the turbine and in the plant's outflow or tailrace channel. Figure 8 shows frazil being excavated from the tailrace channel.

### 5.2 *Frazil in an Inverted Siphon*

The difficulties of siphon operation in frigid winter conditions are illustrated by a siphon conveying water across an approximately 100 m-deep ravine in the Sierra Nevada Mountains, California. The siphon's operators observing flow discharging from the siphon describe how it intermittently ejects a large bolus (Fig. 9) of ice slush that adversely affects the capacity of the outlet channel to convey water. Though the literature lacks information about the formation of an ice "bolus," the size, shape, and intermittent features of a representative bolus suggests that it forms initially in flow-separation zones within the siphon; e.g., at the downstream side of the bends at the bottom of the siphon. The ice boluses tumble, consolidate, and grow within the flow separation region until reaching a size large enough to be caught by the flow and swept along the siphon, eventually emerging (whale like, as the observers report) at the siphon's outlet channel.

It is possible that several smaller boluses may merge as a single glob, and that they collect further slush as they rise relatively rapidly up the rising arm of the siphon. Bolus buoyancy, added to flow drag, propel the bolus ("like a breaching whale," as one operator characterized it) out of the siphon's outlet. There are no

**Fig. 8** Digging frazil ice away from the tailrace channel downstream



**Fig. 9** Guiding an ice bolus out of the exit of an inverted siphon



direct observations of how an ice bolus forms. There are reports (from the siphon's operators) of rumblings in the siphon's bottom section at times when the siphon is passing ice. These noises suggest that the initial ice accumulation forms along the tunnel's crown and in the flow-separation regions. Flow then drags the accumulating bolus of ice along the siphon.

Flow through the siphon is driven by the difference in water surface elevation between the siphon's inlet and the outlet. As this elevation difference decreases, such as when ice severely reduces flow through the channel, flow passes more slowly through the siphon. It is possible therefore that ice difficulties in the channel become aggravated as they progress, because flow slows through the siphon, ice in the siphon forms larger boluses, which in turn have greater difficulty in passing through the channel.

### ***5.3 Frazil Accumulation in a Diversion Tunnel***

As is likely with frazil accumulation in most tunnels, the general circumstances associated with frazil passage into the tunnel described here are known in only approximate terms. Direct observations of the processes resulting in the accumulation are incomplete, for various reasons including a lack of observations about ice conditions along the canal conveying water to the tunnel. The manner whereby ice passage and accumulation in the tunnel, nonetheless, can be inferred from the data obtained from several sources, from what is known in the literature about the formation of similar accumulations in rivers and streams, and from photos of drained tunnels, such as Fig. 10. Here, the frazil accumulation was akin to a hanging frazil "dam," such as described for rivers (e.g., Ashton 1986; Beltaos 1995), and shown by Fig. 7. The main differences from hanging frazil dams in rivers are:



**Fig. 10** Accumulated ice on the floor of a water-diversion tunnel after the tunnel was drained



- The accumulated frazil rested against the tunnel's rock crown
- As the frazil accumulation thickened, the constrained flow path narrowed and velocities increased

A construction problem had resulted in the tunnel not following a steady downward invert grade that would have facilitated the free-surface flow of water along its entire length. The tunnel's initial gradient was over-steep, and an alignment correction was needed. Accordingly, the tunnel had a mild kink at about its mid-point, where the tunnel's grade became mildly upward so that the tunnel would reach the required exit at an outlet channel location. Frazil entering the tunnel, and possibly forming in an initial portion of tunnel, accumulated near the location where the tunnel's slope begins to arc gently upwards towards its outlet. In this region, the free-surface flow of water along the downward reach of the tunnel gradually occupies practically the full flow cross section of the tunnel. The frazil accumulation did not block flow, which continued to pass through the tunnel. Considerations related to critical velocity for erosion of accumulated frazil slush infer that the tunnel likely would not block owing to frazil accumulation.

## 6 Concluding Remarks

Ice is an under-appreciated concern for many water-conveyance systems, but nowhere more so than for systems in mountainous terrain. Mountainous terrain is more likely to have colder weather, swift-flowing streams, and to have limited accessibility. The combined considerations of temperature and flow speed increase the likelihood of ice concerns. Limited accessibility aggravates the concern.

Also, because water-conveyance systems in mountainous terrain often entail the combined use of open-channel and pressurized conduits, a further mechanism compounds frazil difficulties in mountainous terrain. The mechanism arises when

frigid water flowing in a conduit undergoes major pressure increase, and then reduction. Increased pressure depresses water's freezing temperature, and thereby results in the supercooling of water that subsequently flows with decreasing pressure. If the water cools to the depressed freezing temperature, frazil quickly forms when water flows at reduced pressure. Flows through a penstock and hydropower turbine, a pump line, or a siphon, produce cycles of increased then decreased pressure, thereby exposing these flow components to frazil. Water flowing at increased pressure may cool as ice transported in the water melts, and also by heat loss through the conduit walls. A longer conduit (all else equal) provides more time for water to cool to its depressed freezing temperature. Also, more ice entering a pressurizing flow enables water to cool more quickly to the depressed freezing temperature.

## References

- Alley RB, Lawson DE, Evenson EB, Strasser JC, Larson G (1998) Glaciohydraulic supercooling: a freeze-on mechanism to create stratified, debris-rich basal ice: II. *Theor J Glaciol* 44(148): 563–569
- Ashton GD (1986) River and lake ice hydraulics. Water Resource Publications, Littleton, CO, USA
- Beltaos S (1995) River ice jams. Water Resource Publications, Littleton, CO, USA
- Billfalk L (1992) Ice effects and control for hydropower production. In: Proceedings of the 11th symposium on ice. IAHR'92, Banff, Canada, pp 671–682
- Chen Z, Ettema R, Lai Y (2004) Laboratory and numerical experiments of frazil ingestion by submerged intakes. *ASCE J Hydraul Eng* 130(3):101–111
- Daly SF (1984) Frazil ice dynamics. US Army Corps of Engineers, Cold Regions Research & Engineering Laboratory, Hanover, NH
- Daly SF (1991) Frazil ice blockage of intake trash racks. Cold regions technical digest, no 91–1. US Army Corps of Engineers, Cold Regions Research & Engineering Laboratory, Hanover, NH 03755
- Daly SF (1994) Report on frazil ice, prepared by IAHR research working group on thermal regimes. U.S. Army Corp of Engineers, Cold Regions Research and Engineering Laboratory, Special Report#SR 43, 43, Hanover, NH
- Daly S, Ettema R (2006) Frazil-Ice blockage of intakes in the U.S. Great Lakes. *ASCE J Hydraul Eng* 132(8):814–824
- Ettema R (2005) Ice concerns associated with the Mill-Bull Tunnel in the El Dorado Canal system. Report, Ettema Consulting, Iowa City, IA 52245
- Ettema R, Kirkil G, Daly S (2008) Frazil ice concerns for channels, pump-lines, penstocks, siphons, and tunnels in mountainous regions. *Cold Reg Sci Technol* 55(2):202–211
- Gemperline E (1990) Considerations in the design and operation of hydro power intakes. In: Ryan WL, Crissman RD (eds) Cold regions hydrology and hydraulics. ASCE, New, York, pp 517–556
- Gilpin RR (1981) Modes of ice formation and flow blockage that occur while filling a cold pipe. *Cold Reg Sci Technol* 5:163–171
- Hobbs PV (1974) Ice physics. Clarendon Press, Oxford, Britain
- Holland PR, Feltham DR, Daly SF (2007) On the nusselt number for frazil ice growth. *J Hydraul Res* 45(3):421–423
- Lia L, Carstens T (1998) Snow and ice blocking of tunnels. In: Shen HT (ed) Proceedings of the IAHR ice symposium, Balkema, Rotterdam, Netherlands, pp 85–91

# Where “Small Is Beautiful”—Mathematical Modelling and Free Surface Flows

John D. Fenton

**Abstract** Mathematical and computational models in river and canal hydraulics often require data that may not be available, or it might be available and accurate while other information is only roughly known. There is considerable room for the development of approximate models requiring fewer details but giving more insight. Techniques are presented, especially linearisation, which is used in several places. A selection of helpful mathematical methods is presented. The approximation of data is discussed and methods presented, showing that a slightly more sophisticated approach is necessary. Several problems in waves and flows in open channels are then examined. Complicated methods have often been used instead of standard simple numerical ones. The one-dimensional long wave equations are discussed and presented. A formulation in terms of cross-sectional area is shown to have a surprising property, that the equations can be solved with little knowledge of the stream bathymetry. Generalised finite difference methods for long wave equations are presented and used. They have long been incorrectly believed to be unstable, which has stunted development in the field. Past presentations of boundary conditions have been unsatisfactory, and a systematic exposition is given using finite differences. The nature of the long wave equations and their solutions is examined. A simplified but accurate equation for flood routing is presented. However, numerical solution of the long wave equations by explicit finite differences is also simple, and more general. A common problem, the numerical solution of steady flows is then discussed. Traditional methods are criticised and simple standard numerical ones are proposed and demonstrated. A linearised model for the surface profile of a stream is obtained, also to give solutions without requiring detailed bathymetric knowledge.

**Keywords** Approximation • Boundary conditions • Finite differences  
Gradually-varied flow equation • Interpolation • Kinematic • Long wave  
equations • Numerical methods • Reservoir routing • Resistance  
Obstacles • Telegraph equation

---

J. D. Fenton (✉)  
Institute of Hydraulic and Water Resources Engineering, Vienna University of Technology,  
Karlsplatz 13/222, 1040 Vienna, Austria  
e-mail: JohnDFenton@gmail.com

© Springer International Publishing AG 2018  
M. B. Kalinowska et al. (eds.), *Free Surface Flows and Transport Processes*,  
GeoPlanet: Earth and Planetary Sciences,  
[https://doi.org/10.1007/978-3-319-70914-7\\_3](https://doi.org/10.1007/978-3-319-70914-7_3)

## 1 Introduction

The originator of the expression “small is beautiful” was Leopold Kohr, an Austrian philosopher and economist. The expression was adopted, used, and popularised in the title of a 1973 book “Small Is Beautiful: A Study of Economics As If People Mattered” by a student of Kohr, Ernst Friedrich Schumacher, a German economist and statistician who spent most of his life in Britain.

The present author can lay a small claim to some association with the idea. In 1974, the year after publication of the book, he went on a weekend workshop to discuss its economic and political messages in Windsor Great Park near London. It was a pleasant and optimistic era for some. Subsequently, however, in the first phase of his career, the author honoured “small is beautiful”, in the words of Shakespeare’s *Hamlet*: “more in the breach than the observance”, meaning, usually *not* honouring it. Or even doing the opposite: one of his first publications was entitled “A ninth-order solution for the solitary wave”. Then, after working for some 25 years in coastal and ocean engineering, where the problems are complex enough that it is difficult to keep matters simple, the author gradually moved onshore and up the rivers and streams of the terrestrial environment and onto land. Gradually he thought he saw that many things were done, sometimes wrongly, sometimes too complicatedly, and that complexity often obscured the meaning and understanding of what was being done. He tried to publish papers, but found that contrary and simple views were not welcome. He has now spent some 20 years travelling in a direction transverse to the flow of the canonical science, trying to place obstacles in the flow. Now as he approaches the end of his career, he wonders, whether he might not end like Siddhartha in Hermann Hesse’s Buddhist novel of the same name, and act as a ferryman, still crossing and defying the river of conventional thought, but helping people by carrying them to and fro with him, pointing out how things might otherwise be done.

Initially here we will present several mathematical methods which are of some generality and application to the title of this work—and will be used in the remainder. It is pointed out that there are a number of methods or formulae in river engineering which are wrong, silly, and/or unnecessarily complicated. Corrections are suggested and some new results are presented, which the author hopes will justify reading this work.

## 2 Virtues of Simplicity

Mathematics is a problem for many people, and can lead to early alienation and the internalising of a sense of failure and of ignorance. However, one should be confident of one’s own patient thought processes—and remember Newton: “If I have ever made any valuable discoveries, it has been due more to patient attention, than to any other talent”. Concerning simplicity, Newton wrote, admittedly not very simply by twenty-first century standards:

- “Nature is pleased with simplicity, and affects not the pomp of superfluous causes”, and
- “Truth is ever to be found in the simplicity, and not in the multiplicity and confusion of things”.

In this advocacy of simplicity, Newton had long been preceded by William of Ockham, a medieval monk and philosopher, who developed the principle known as *Ockham’s Razor*, which states that if something can be explained without a further assumption, there is no reason for that. Any explanation should be in terms of the fewest factors or parameters. This was paraphrased, possibly even better, by Albert Einstein as “Make things as simple as possible, but not simpler”. He also said: “If you can’t explain it simply, you don’t understand it well enough.” Therein lies some of the benefits of teaching for researchers: to teach properly one must understand it—and to make it as simple as possible for the students—while revealing any underlying complexity.

We consider some thoughts on the nature of mathematics and simplicity:

- Mathematics is like learning another language—a certain body of knowledge is necessary. Something can sit unused in the brain, but when a problem is required to be solved, it can leap to the front. It helps remembrance if one has understanding. And simplicity helps understanding.
- An aspect of mathematics and simplicity is the symbiotic relationship between mathematics and visual perception and understanding. Many scientists and engineers have highly-developed visual-spatial abilities, which can help.
- An important aspect of simplicity is the ease of disproof, in the sense of Karl Popper: if something is complicated, it is likely to be more difficult for people to understand it and to disprove it. If something has been expressed in simple mathematics, it is likely to be more correct because it has withstood attempts to disprove it.
- A formal process of mathematical modelling provides some structure and discipline to our thought processes: one should make the simplest possible model and if it works, good, but if not, refine it, and repeat if necessary, reflecting the above quote by Einstein on making things as simple as possible, but not too much so.
- An important problem is the mismatch between data and mathematical models available, whether too much data or too little. One might have all the cross-sectional data of a stream at every 100 m, and be tempted to include all that in a numerical model—while knowing the resistance coefficient only to some  $\pm 30\%$ . The sensible thing would be to abandon the detailed data and use an approximate model. Or, one might have little cross-sectional data, but because a public or private organisation requires the use of a certain computer program (HEC-RAS comes to mind), it might be necessary to arrange an expensive field survey. It would be better if managers had more scientific judgement about when *not* to believe detailed results.
- In research rather than applications, the processes by which it is evaluated and judged are hostile to simplicity. The author has written a critique of peer review

and publishing processes in Fenton (2016, §4.4). Trying to publish something simple seems to be very difficult—reviewers are pleased to discover something that they can understand and then criticise it severely, whereas something complicated that is beyond their understanding is likely to be accepted, then replicated, and expanded upon *ad infinitum*. Faddish, fashionable, and complicated techniques are certainly good for publishing and a career in research.

### 3 Approximate Solutions—Linearising and the Use of Series

Often there is much less detailed information known about a problem than the governing equations require. In such cases, approximations are highly justified and reveal to us rather more the real nature of the problem. The most common way is to *linearise* the problem, considering a quantity to be relatively small, and writing series in that quantity, manipulating only to first order. Or, a function can be approximated by using a finite number of terms of its Taylor series calculated from the function's derivatives at a single point. Here a brief revision of some elementary series operations is given, and then a physical example is presented, the interaction between an obstacle such as a bridge pier and a stream flow. Below, in Sects. 7.2 and 9.5 linearised versions of the unsteady and steady long wave equations will be presented, with a number of results.

#### 3.1 Series—Revision and Notation for Accuracy

**Taylor series:** An example of a Taylor series for a function of two variables:

$$\begin{aligned} f(x + \Delta x, t + \Delta t) \\ = f(x, t) + \Delta x \left. \frac{\partial f}{\partial x} \right|_{(x,t)} + \Delta t \left. \frac{\partial f}{\partial t} \right|_{(x,t)} + \frac{1}{2!} \left( \Delta x \frac{\partial}{\partial x} + \Delta t \frac{\partial}{\partial t} \right)^2 f \Big|_{(x,t)} + \dots \end{aligned}$$

**Binomial theorem:**

$$(x + \Delta x)^n = x^n \left( 1 + \frac{n}{1!} \frac{\Delta x}{x} + \frac{n(n-1)}{2!} \left( \frac{\Delta x}{x} \right)^2 + \dots \right),$$

where if  $n$  is a positive integer, the series terminates.

**Big O notation:** Usually series are truncated and it is often convenient to use the Big O symbol for the order of accuracy. A theory or numerical solution is said to be  $n$ th-order accurate if the error of the neglected terms is proportional to a quantity  $\Delta$  to the  $n$ th power,  $C\Delta^n$ , where  $C$  is independent of  $\Delta$ . The value of  $C$  is not important,

so that one writes the neglected terms instead using the Big O (“order of”) notation  $O(\Delta^n)$ . The implication is that this will be the largest such term, others being of higher order such that in the limit when  $\Delta \rightarrow 0$  they are smaller in magnitude.

**Combination of series:** Having converted all the individual parts of a mathematical expression to series, they must be combined, usually by multiplication, ignoring terms higher than the truncation level chosen. Algebraic operations using the Big O notation are simple and obvious, for example,  $\frac{1}{2}\Delta \times O(\Delta^n) = O(\Delta^{n+1})$ . A simple product of two short series is, for example:

$$(a_0 + a_1\Delta)(b_0 + b_1\Delta) = a_0b_0 + \Delta(a_0b_1 + a_1b_0) + O(\Delta^2) .$$

### 3.2 Example—Linear Solution for the Effects of an Obstacle on a Stream

As an example we consider an obstacle such as a bridge pier or piers in a stream, where the water surface  $\eta$  in a stream rises by a small amount  $\Delta\eta$ , as shown in Fig. 1. Consider the conservation of momentum equation between an upstream Sect. 1 and a downstream Sect. 2. On the left of the equation the force on the body is given by the conventional expression for the drag force on a bluff body, and on the right is the difference in momentum flux. All terms have been divided by fluid density:

$$\frac{1}{2}\gamma C_D \frac{Q^2}{A_1^2} a_1 = \left( gA\bar{h} + \beta \frac{Q^2}{A} \right)_1 - \left( gA\bar{h} + \beta \frac{Q^2}{A} \right)_2 . \quad (1)$$

In this  $\gamma$  is a necessary coefficient as for some types of obstacle the velocity that impinges on it is not necessarily equal to the mean velocity in the flow  $Q/A_1$ , where  $Q$  is discharge and  $A_1$  is cross-sectional area upstream. Other terms include:  $C_D$  is the drag coefficient,  $a_1$  is the blockage area of the object measured transverse to the flow with water level that at Sect. 1,  $g$  is gravitational acceleration,  $\bar{h}$  is the depth of the centroid of the flow cross-section below the surface, and  $\beta$  is a Boussinesq momentum coefficient. A typical problem is in sub-critical flow, where the downstream water level  $\eta_2$  is given, and we want to know how much the water level will be raised upstream if a bridge is built. As both  $A_{1,2}$  and  $\bar{h}_{1,2}$  are functions of the surface elevations  $\eta_{1,2}$ , conditions at 2 can be evaluated. The equation is then a nonlinear transcendental equation for the unknown  $\eta_1$ , which could be solved numerically, but it is non-trivial.

If the depth change is small, as usual, then an explicit approximate solution can be obtained. Consider the stream cross-section shown in Fig. 2, with a small change in water level  $\Delta\eta$ , such that  $\eta_1 = \eta_2 + \Delta\eta$ . We now use geometry to obtain expressions for quantities at 1 in terms of those at 2. It is easily shown that

$$A_1 = A_2 + B_2 \Delta\eta + O((\Delta\eta)^2) , \text{ and } (A\bar{h})_1 = (A\bar{h})_2 + A_2 \Delta\eta + O((\Delta\eta)^2) ,$$

**Fig. 1** The physical problem of a flow obstruction, showing the mean backwater with  $\Delta\eta$  just upstream of the obstacle and the actual surface on its axis and sides

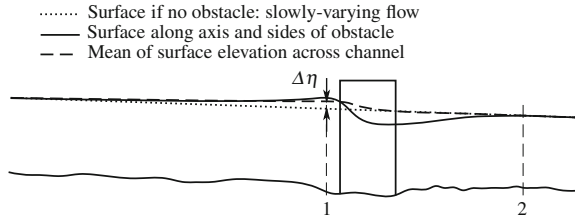
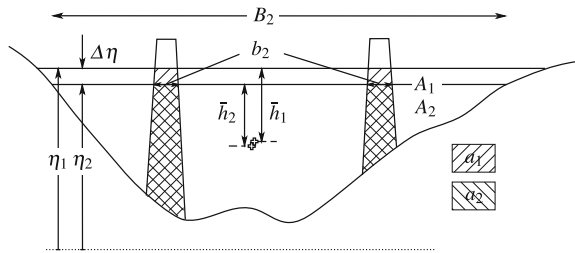


**Fig. 2** Cross-section of channel showing dimensions, the change of area due to an elemental surface height increase, and the depth of the centroid for the original and increased surface heights



and similarly we write for the blockage area:

$$a_1 = a_2 + b_2 \Delta\eta + O((\Delta\eta)^2) ,$$

where  $b_2$  is the surface width of the obstacle (which for a submerged obstacle would be zero).

Substituting these expressions for the quantities at 1 into the momentum equation (1), expanding each side as a power series in  $\Delta\eta$ , and neglecting terms like  $(\Delta\eta)^2$ , gives a linear equation which can be solved to give an explicit approximation for the dimensionless drop across the obstacle  $\Delta\eta / (A_2/B_2)$ , where  $A_2/B_2$  is the mean downstream depth:

$$\frac{\Delta\eta}{A_2/B_2} = \frac{\frac{1}{2} \gamma C_D F_2^2 a_2}{1 - \beta F_2^2 A_2} . \tag{2}$$

This explicit approximate solution has revealed the important quantities of the problem to us and how they affect the result: downstream Froude number  $F_2^2 = Q^2 B_2 / g A_2^3$  and the relative blockage area  $a_2/A_2$ . For subcritical flow  $\beta F_2^2 < 1$  the denominator in (2) is positive, and so is  $\Delta\eta$ , so that the surface drops from 1 to 2, as we expect. If the flow is supercritical,  $\beta F_2^2 > 1$ , we find  $\Delta\eta$  negative, and the surface rises between 1 and 2. If the flow is near critical  $\beta F_2^2 \approx 1$ , the change in depth will be large, which is made explicit, and the theory will not be valid.

Another benefit of the approximate analytical solution is that it shows that such an obstacle forms a control in the channel, so that the finite sudden change in surface elevation  $\Delta\eta$  is a function of  $Q^2$ , or  $Q$  a function of  $\sqrt{\Delta\eta}$ , in a manner analogous to a weir. In numerical river models it should ideally be included as an internal boundary



condition between different reaches as if it were a type of fixed control. The mathematical step of linearising has revealed much to us about the nature of the problem.

## 4 Mathematical Tools

Some familiar and some less-familiar methods will now be explained—how to use direct iteration for solution of transcendental equations and how to obtain more accurate results from simple methods with Richardson and Aitken extrapolation. The common problem of the approximation of data is considered, and after a simple recipe for interpolation, it is demonstrated, in contradiction to the main thesis of this work, how simple polynomial methods may not work and orthogonal functions are required. It is suggested that the formulation and solution of many problems using optimisation is simple and powerful. Finally, revision of basic numerical methods for ordinary differential equations is given, as sometimes in water engineering these seem not to be known.

### 4.1 *Direct Iteration Solution of Transcendental Equations*

Consider a common problem where it is required to solve an equation for  $x$  such that  $f(x) = 0$ , in which the function is transcendental such that it cannot be solved analytically. There are several well-known methods for solving such equations, such as Newton’s, Secant, and Bisection methods. The simplest is that of Direct Iteration, which however, fails in about 50% of cases and numerical analysts warn against it! The reason why we present it here is that such a scheme is simple and can be incorporated easily into hydraulic software. We will investigate the general conditions for it to succeed, and using the knowledge so obtained, as an example we will later devise a scheme for the computation of normal depth in steady uniform flow.

We re-arrange  $f(x) = 0$  in the form  $x = g(x)$ , where  $g(x)$  is some function of  $x$ . This gives the iteration scheme

$$x_{m+1} = g(x_m),$$

where  $m$  is the iteration number. We assume some initial value  $x_0$ , evaluate  $g(x_0)$  and use this value as the next estimate  $x_1$  and so on. Conditions for which this works can be explained graphically. Solving the equation  $x = g(x)$  is equivalent to solving the pair of simultaneous equations  $y = x$  and  $y = g(x)$ , so that if we plot the two relationships, the first is simply a straight line of gradient 1 passing through the origin, and the problem is to determine where the second curve crosses it.

The iteration procedure for different cases is shown in Fig. 3, where the open circles show a possible initial estimate, and the full circles show the solution. In Case A, the function  $g(x)$  has a negative gradient that is greater than 1 in magnitude,

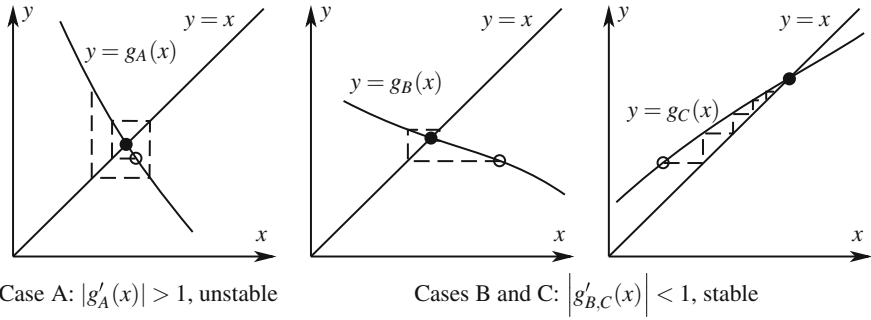


**Fig. 3** Unstable and stable behaviour of direct iteration scheme for different function gradients

and although we start near the solution, we are taken away from it. In the next Case B the function still has a negative slope, but its magnitude is less than 1 and it can be seen how the solution spirals in to converge. The last Case C is for a positive slope which is less than 1, and the process also converges. These figures suggest the condition for convergence that the direct iteration scheme is stable if

$$\left| \frac{dg}{dx}(x) \right| < 1, \text{ in the vicinity of the solution.}$$

*Example 1* Use direct iteration to solve the equation  $x^3 - x - 1 = 0$

We consider two schemes. The most obvious one is  $x_{m+1} = x_m^3 - 1$ . Immediately there seems to be trouble, as the derivative of the right side,  $g'(x) = 3x^2$ , may well be greater than 1. We start with  $x_0 = 1$ , and obtain the diverging results shown in columns 2 and 3 of the table. By a different rearrangement,  $x_{m+1} = (x_m + 1)^{1/3}$ , and columns 4 and 5 show that the process converges quite well.

		Unstable scheme		Stable scheme	
$m$	$x_m$	$x_{m+1} = x_m^3 - 1$	$x_m$	$x_{m+1} = (x_m + 1)^{1/3}$	
0	1	$1^3 - 1 = 0$	1	$(1 + 1)^{1/3} = 1.259$	
1	0	$0^3 - 1 = -1$	1.259	$(1.259 + 1)^{1/3} = 1.3121$	
2	-1	$-1^3 - 1 = -2$	1.3121	$(1.3121 + 1)^{1/3} = 1.3223$	
3	-2	$-2^3 - 1 = -9$	1.3223	$(1.3223 + 1)^{1/3} = 1.3243$	
4	-9	$-9^3 - 1 = -730$	1.3243	$(1.3243 + 1)^{1/3} = 1.3246$	

**The computation of normal depth in a prismatic channel**

Consider the Gauckler-Manning equation for steady uniform flow

$$Q = \frac{1}{n} \frac{A^{5/3}(h)}{P^{2/3}(h)} \sqrt{S}, \tag{3}$$

where  $Q$  is discharge,  $n$  is the Manning resistance coefficient,  $A$  is cross-sectional area and  $P$  is wetted perimeter of the channel section, both shown as functions of the maximum depth  $h$ , and  $S$  is the channel slope. A common problem is the determination of  $h$  for a given discharge. Commonly, channels are rather wider than they are deep, and neither the wetted perimeter  $P$  nor the surface width  $B$  nor the mean width  $A(h)/h$  vary strongly with  $h$ . We use the insight obtained above to re-write the equation in a form for  $h$  where the right side as a function of  $h$  varies slowly, so that if plotted as in Fig. 3 the curve would be almost horizontal and convergence rapid. Firstly, we divide  $A^{5/3}(h)$  by  $h^{5/3}$  which, as it is the mean width raised to that power, is often a relatively slowly-varying function of  $h$ ; then we multiply by the same quantity  $h^{5/3}$ :

$$Q = \frac{\sqrt{S} (A(h)/h)^{5/3}}{n P^{2/3}(h)} \times h^{5/3}.$$

Most of the variation with  $h$  is contained in the last term  $h^{5/3}$ . By solving for that we have the equation in a form suitable for direct iteration

$$h_{m+1} = \left( \frac{Qn}{\sqrt{S}} \right)^{3/5} \times \frac{P^{2/5}(h_m)}{A(h_m)/h_m}, \quad (4)$$

where the first term on the right is a constant for any particular problem, and the whole right side varies slowly with depth. Experience with typical trapezoidal sections shows that this works well and is quickly convergent. For small flows and depths in sewers this is not so, and a more complicated method has to be used.

For an initial estimate we suggest applying the formula, making a more extreme wide channel approximation of constant width, where we are probably able to make a rough estimate of the approximate width  $B_0$  and so, setting  $A(h)/h \approx B_0$  and  $P(h) \approx B_0$ , in the general scheme of (4) gives

$$h_0 = \left( Qn/B_0\sqrt{S} \right)^{3/5}. \quad (5)$$

*Example 2* Calculate the normal depth in a trapezoidal channel of slope 0.001, Manning’s coefficient  $n = 0.04$ , bottom width 10 m, with batter slopes (H:V)  $\gamma = 2$ , carrying a flow of  $20 \text{ m}^3 \text{ s}^{-1}$ .

For a trapezoidal section, with bottom width  $W$  and side slopes  $\gamma$  (H:V), the scheme is, from (4):

$$h_{m+1} = \left( \frac{Qn}{\sqrt{S}} \right)^{3/5} \frac{\left( W + 2\sqrt{1 + \gamma^2} h_m \right)^{2/5}}{W + \gamma h_m}.$$

Starting with the rough approximation  $B_0 = W = 10 \text{ m}$ , the wide-channel Gauckler-Manning formula (5) gives  $h_0 = 1.745 \text{ m}$ , and then the more general formula (4)

gives the sequence of approximations to the normal depth: 1.629 and 1.638 m, already having converged to this four-figure accuracy.

## 4.2 Accurate Results with Simple Methods—Richardson and Aitken Extrapolation

### 4.2.1 Richardson Extrapolation

Consider the numerical value of any part of a computational solution for some physical quantity  $\phi$  obtained using a time or space step  $\Delta$ , such that we write  $\phi(\Delta)$ . Let the computational scheme be of known  $n$ th order such that the *global* error of the scheme at any point or time is proportional to  $\Delta^n$ , then if  $\phi(0)$  is the exact solution, we can write the expression in terms of the error at order  $n$ :

$$\phi(\Delta) = \phi(0) + b\Delta^n + \dots, \quad (6)$$

where  $b$  is an unknown coefficient, and where the neglected terms vary like  $\Delta^{n+1}$ . If we have two numerical simulations or approximations with two different  $\Delta_1$  and  $\Delta_2$  giving numerical values  $\phi_1 = \phi(\Delta_1)$  and  $\phi_2 = \phi(\Delta_2)$  then we write (6) for each:

$$\phi_1 = \phi(0) + b\Delta_1^n + \dots, \quad (7a)$$

$$\phi_2 = \phi(0) + b\Delta_2^n + \dots. \quad (7b)$$

These are two linear equations in the two unknowns  $\phi(0)$  and  $b$ . Eliminating  $b$ , which is not important, between the two equations and neglecting the terms omitted, we can solve for  $\phi(0)$ , an approximation to the exact solution:

$$\phi(0) = \frac{\phi_2 - r^n \phi_1}{1 - r^n} + O(\Delta_1^{n+1}, \Delta_2^{n+1}), \quad (8)$$

where  $r = \Delta_2/\Delta_1$ . The errors are now proportional to step size to the power  $n + 1$ , so that we have gained a higher-order scheme without having to implement any more sophisticated numerical methods, just with a simple numerical calculation. This procedure, where  $n$  is known, is called *Richardson extrapolation to the limit*.

#### Example 3 Richardson extrapolation

Consider the numerical solution by Euler's method (well known—and presented here below in Sect. 4.5) of the differential equation  $dy/dt = e^t$ , with  $y(0) = 1$ , as far as  $t = 1$ . The differential equation has the exact solution  $y = e^t$  and so the exact result for  $y(1) = e = 2.718281828$ . Calculating first 10 steps with  $\Delta_1 = 0.1$  and then 20 steps,  $\Delta_2 = 0.05$ , then using  $r = \frac{1}{2}$  in (8) with  $n = 1$  as it is a first-order method:

	Numerical result	Relative error (%)
$N = 10$	2.805628	3.2
$N = 20$	2.761597	1.6
Richardson	2.717566	<b>0.026</b>

### 4.2.2 Aitken Extrapolation

Aitken’s  $\Delta^2$  method can be used where we do not know the value of  $n$ , the order of the scheme. As that is one more unknown, we have to do a computation with a third step so that we can write a third equation in addition to (7a) and (7b):

$$\phi_3 = \phi(0) + b\Delta_3^n + \dots \tag{7c}$$

The equations that we now have to solve are nonlinear (the  $n$  occurs in an exponent) but they can still be solved. The  $b$  can be eliminated to give two equations

$$\frac{\phi_1 - \phi(0)}{\phi_2 - \phi(0)} = \left(\frac{\Delta_1}{\Delta_2}\right)^n \quad \text{and} \quad \frac{\phi_2 - \phi(0)}{\phi_3 - \phi(0)} = \left(\frac{\Delta_2}{\Delta_3}\right)^n \tag{9}$$

It is possible to eliminate  $n$  between these two equations to give a single equation for  $\phi(0)$ , but for arbitrary  $\Delta_1$ ,  $\Delta_2$ , and  $\Delta_3$  it is a transcendental equation which cannot be solved simply. However, if we choose the ratios of the steps to be the same,  $\Delta_1/\Delta_2 = \Delta_2/\Delta_3$ , which is usually possible, the right sides of the equations are equal, we can equate the two left sides and solve for  $\phi(0)$ :

$$\phi(0) \approx \phi_3 - \frac{(\phi_3 - \phi_2)^2}{\phi_1 + \phi_3 - 2\phi_2}, \quad \text{for} \quad \frac{\Delta_1}{\Delta_2} = \frac{\Delta_2}{\Delta_3}.$$

The solution is written here as a correction to  $\phi_3$ . Even if the top and bottom of the fraction go to zero as the process converges, as it is a correction the whole expression is less-susceptible to error than if it were written as a single fraction.

*Example 4* Aitken extrapolation

Apply the Trapezoidal rule to approximate the integral

$$\int_0^\pi \frac{1}{2} \sin x \, dx.$$

The Trapezoidal rule is of second order,  $n = 2$ , but initially we pretend neither to know this nor to use it.

	Numerical result	Relative error (%)
$N = 8$	0.987116	1.29
$N = 12$	0.994282	0.57
$N = 18$	0.997460	0.25
Aitken	0.999994	<b>0.0006</b>

### 4.2.3 Use of Aitken Extrapolation to Test Computations and Software

Sometimes a result for  $n$  is important, to know whether a method or program is as accurate as it should be. For three different computational steps, having computed a value of  $\phi(0)$ , and now with numerical values for all terms in either of the Eq. (9), we can solve for  $n$ . In the example just considered, we obtain  $n = 2.005$ , not exact because the equations have higher order neglected terms. Now admitting that we know that the answer should be  $n = 2$ , this provides us with welcome evidence that we have not made a gross mistake in the programming. This was a short and simple example. The same method can be used to provide a check on any calculation, however long. The author uses it to test programs for tasks like the numerical solution of the long wave equations: one computes the flow or surface height at a particular point in space at a single particular time for three different values of time step  $\Delta t$ , computing  $n$  for the time approximation. Then the process can be repeated, this time using the space step  $\Delta x$  and computing  $n$  for the space approximation. If the values obtained are numerically close to theoretical expectations, even for that single point, it is again evidence that the program is correct. If not, there is work ahead—unfortunately the method does not tell us *where* the error might be!

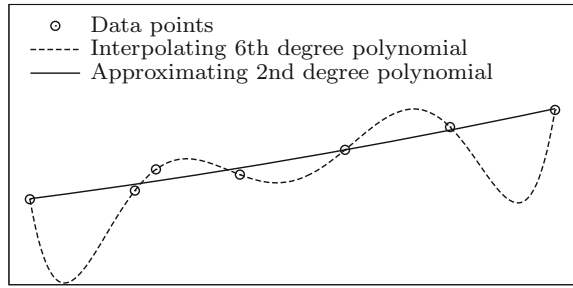
## 4.3 Interpolation and Approximation

Consider the representation of a number of data points  $(x_n, y_n)$  for  $n = 0, \dots, N$  by a continuous function  $y = p(x)$  composed of a linear combination of a number of specified functions  $p_m(x)$ , each multiplied by an unknown coefficient  $a_m$ :

$$p(x) = \sum_{m=0}^M a_m p_m(x) = a_0 p_0(x) + a_1 p_1(x) + \dots + a_M p_M(x). \quad (10)$$

If the number of the  $M + 1$  coefficients is equal to the number of data points  $N + 1$  then the function passes through every data point such that it *interpolates* them. If  $M < N$  then the function *approximates* the data points. In general this is to be preferred, for if we use global interpolation with  $M = N$ , irregularities can lead to the approximating function varying unreasonably everywhere. In Statistics this is called *overfitting*. The difference is demonstrated in Fig. 4.

**Fig. 4** Comparison between interpolation and approximation of seven data points



### 4.3.1 Polynomial Interpolation and Differentiation—Newton’s Method

Before considering approximation, firstly we consider interpolation, as it is commonly useful especially for plotting purposes. The problem becomes complicated very quickly for more than the trivial case of two points. Here we present Newton’s very simple way of solving the problem, even for high degree interpolation.

We wish to pass a polynomial of degree  $N$  through  $N + 1$  points. We might write the polynomial in *power* form in terms of  $x - x_*$ , where  $x_*$  is in the range of the data points, probably at one of them, typically  $x_* = x_0$ :

$$p(x) = c_0 + c_1 (x - x_*) + c_2 (x - x_*)^2 + \dots + c_N (x - x_*)^N . \tag{11}$$

The problem is to determine the coefficients  $c_0, \dots, c_N$ , by requiring  $p(x_n) = y_n$  for  $n = 0, \dots, N$ , which needs the solution of  $N + 1$  simultaneous equations. Even for quadratic interpolation,  $N = 2$ , the problem with three equations is non-trivial. For larger  $N$  one would have to use software for the solution of systems of linear equations.

A much simpler solution is available, although initially it does not seem to be so! One could describe it using the French expression *retirer pour mieux sauter* (“draw back so as to be better able to leap forward”). We use a *nested* form, the *Newton polynomial*:

$$p(x) = a_0 + (x - x_0) (a_1 + (x - x_1) (a_2 + \dots (a_{N-1} + a_N (x - x_{N-1})) \dots)) , \tag{12}$$

where the  $n$ th term, starting counting from zero, is a product of all the  $x - x_k$ , up to  $k = n - 1$ . The coefficients

$$a_n = y [x_0, \dots, x_n] ,$$

are the *divided differences* (all starting with  $x_0$ ) of the table of function values (Conte and de Boor 1980, p. 42), which we now define and the coefficients are easily obtained. The zeroeth-order differences are

$$y[x_n] = y_n, \quad n = 0, \dots, N .$$

The first-order differences are

$$y[x_n, x_{n+1}] = \frac{y[x_{n+1}] - y[x_n]}{x_{n+1} - x_n} = \frac{y_{n+1} - y_n}{x_{n+1} - x_n}, \quad n = 0, \dots, N - 1.$$

The first second-order difference is

$$y[x_0, x_1, x_2] = \frac{y[x_1, x_2] - y[x_0, x_1]}{x_2 - x_0},$$

and so on. The higher-order divided differences are obtained from the recursion formula

$$y[x_n, \dots, x_{n+k}] = \frac{y[x_{n+1}, \dots, x_{n+k}] - y[x_n, \dots, x_{n+k-1}]}{x_{n+k} - x_n},$$

where this quantity is known as the “ $k$ th divided difference at  $x_n$ ”.

The table shows how simply this can be programmed, for arbitrary  $N$ :

---

Divided difference table – With initial values  $a_n = y_n$ , for  $n = 0, \dots, N$ :

---

```
for i from 1 to N do
  for j from N to i step -1 do
    a[j] := (a[j] - a[j - 1]) / (x[j] - x[j - i])
```

---

This makes higher order polynomial interpolation simple. To evaluate the Newton interpolating polynomial in the nested form of (12) the following simple procedure can be followed:

---

```
Evaluate Newton polynomial  $p(X)$ 
p := a[N]
for j from N - 1 to 0 step -1 do
  p := a[j] + p * (X - x[j])
```

---

Conte and de Boor (1980) provide similar procedures for calculating derivatives.

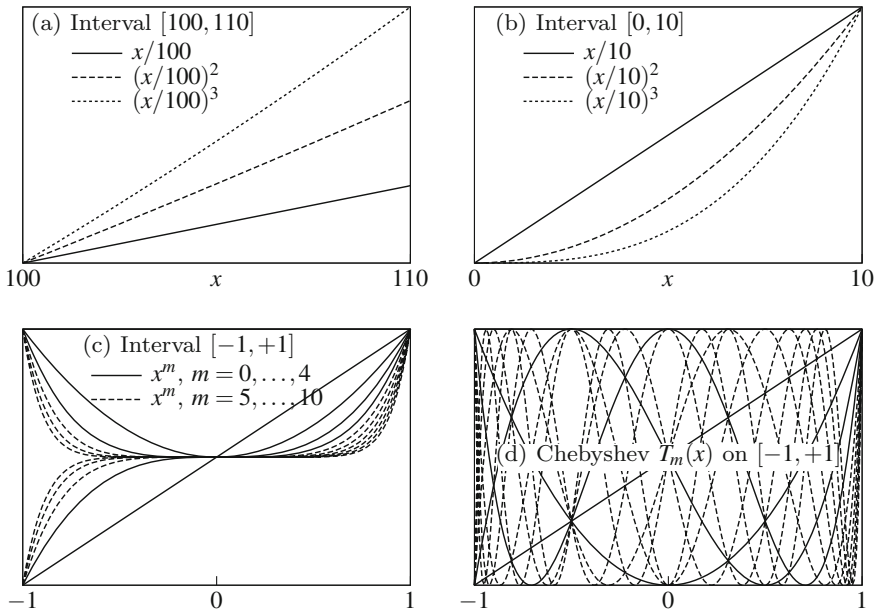
### 4.3.2 Global Interpolation and Approximation

The procedure that we just followed, of computational effort proportional to  $N^2$ , can be used for many, indeed all, interpolation points. However, using it for *all* data points, global interpolation, has some important difficulties. We will see that some care has to be taken with the functions used, and rapid local variation anywhere can make matters difficult. The following applies to both interpolation and approximation. We will, somewhat loosely, use the term “approximation” to apply to both.

#### Inadequacy of the monomial basis functions

The simplest approximating function is a polynomial, whether written in the form of (10), (11), or (12). Here we initially consider the form of (10) with the individual contributions  $p_m(x)$  to be the monomials  $x^m$ . Figure 5 shows different aspects of the approximation:





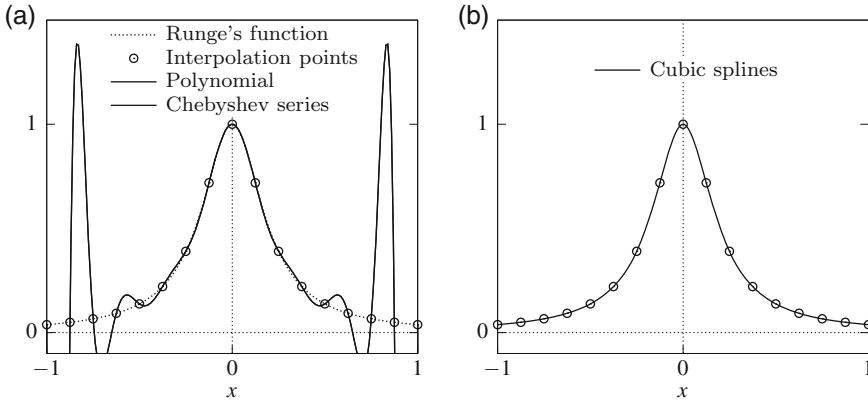
**Fig. 5** Comparison of the first three monomials on the intervals [100, 110] and [0, 10] and the first ten monomials and Chebyshev polynomials on [-1, +1]

Figure 5a shows the first three monomials (after  $p_0(x) = x^0 = 1$ ) on the interval [100, 110], scaled for plotting purposes. It can be seen that all three look almost like straight lines on such an interval. If the function to be approximated had any curvature, those functions would have to work very hard, in the form of large oscillating values of the coefficients  $a_m$ .

Figure 5b shows what happens if we were to transform the interval to [0, 10] using  $x_* = 100$  in (11), where the basis functions now look less similar, and as a result they could better approximate a more general function with curvature. That holds only to a limited extent, however, as seen in the right half of the next figure.

Figure 5c shows a better solution where the interval of approximation has been transformed to [-1, +1], and the first 4 or 5 monomials are really quite different, however for larger values of  $m$  they all start to look similar to each other, making general approximation more difficult. That would be especially so if we were to consider just the interval [0, 1] in the right half of the figure.

Figure 5d shows possibly the best solution of all, to use orthogonal Chebyshev polynomials,  $T_m(x) = \cos(m \arccos(x))$ ,  $T_0(x) = 1$ ,  $T_1(x) = x$ ,  $T_2(x) = 2x^2 - 1$ , etc. They all show behaviour quite different from each other, and hence have the ability to describe arbitrarily varying quantities.



**Fig. 6** Runge's problem: comparison between **a** Global polynomial interpolation and **b** Piecewise-continuous interpolation with cubic splines

### Runge's problem—global approximation with rapid local variation

Now we consider an example that shows an important problem of global approximation. If anywhere the data to be approximated shows sudden local variation, then the global approximation can be bad almost everywhere.

A famous function was devised by Runge:  $1/(1 + 25x^2)$  on  $[-1, +1]$ , with large curvature near  $x = 0$ . Figure 6a shows the global polynomial interpolation of the function using 17 data points, by a 16th degree polynomial and a 16th degree Chebyshev series. It can be seen that the better numerical properties of the Chebyshev functions have been no advantage here, coinciding with those from simple monomial approximation, both giving very bad results, which only become worse if the degree of approximation is increased! On the other hand, using piecewise-continuous approximation, which approximates locally, the problems can be overcome, as is shown by Fig. 6b using cubic splines, to be described in Sect. 4.3.3.

### The need for orthogonal functions in global polynomial approximation

Now we consider a practical problem which supports our earlier arguments in Fig. 5 and shows how very extreme the consequences of not using an orthogonal basis set can be. The example comes from river engineering, and is that of a *Rating Curve*, one which approximates a number of measurement pairs of river heights  $h$  at a gauging station and the corresponding measured flows  $Q$ . The data is from a gauging station on the Ganges River in 1992. We apply global approximation using four series of different basis functions following the sequence of functions shown in Fig. 5. Results are shown in Fig. 7 and are remarkably coincident, apparently quite satisfactory in spite of our expectations based on the behaviours shown in Fig. 5.

Surprisingly, when we consider the details of the approximations, most are revealed to be unsatisfactory and quite in accordance with the deductions from Fig. 5. Figure 8 shows the contribution of different terms in the four different 10-term series at  $h = h_{\max}$ , which obtained the numerically coincident results for the maximum

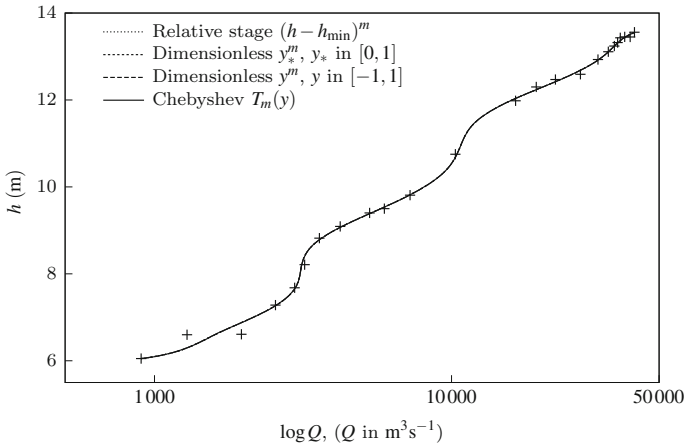


**Fig. 7** Approximation of river rating data by four different sets of basis functions—results visually coincident

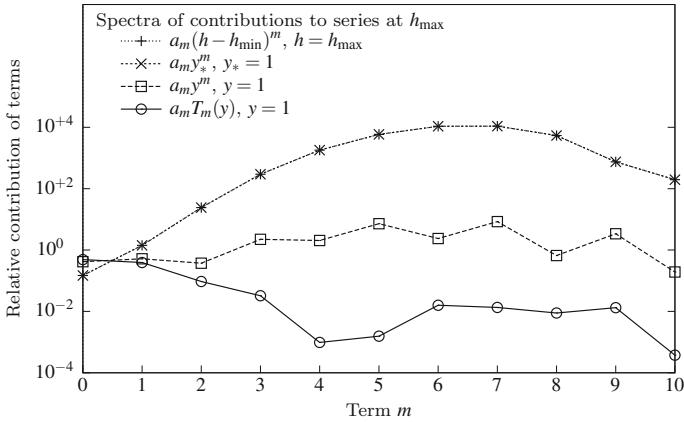


**Fig. 8** The relative contributions of terms in polynomials with different basis functions, for the single case of calculating an approximation to  $Q$  using the maximum stage of Fig. 7. The two top curves are coincident

flow point in the previous figure. All results have been scaled by the discharge so that they sum to 1, and the points show the actual relative contributions.

Firstly, we consider the results shown in the coincident two top curves, from the unscaled polynomials in  $(h - h_{\min})$  and using the scaled variable  $y_*$  in  $[0, 1]$ . To the author’s surprise, the scaling has had no effect, but to the author’s much greater surprise, the individual contributions are actually huge, of order  $10^4$  (oscillating in sign of course). In Fig. 7 we were not to know that we were looking at the results of a sum, each term some  $\pm 10000$  times that of the final sum!

If we use the monomials  $y^m$  with the simple difference that the  $y$  are now defined on  $[-1, +1]$ , with the greater diversity of behaviour shown on Fig. 5c, we find that the individual contributions to the series are now approximately  $10^0 = 1$ , summing to about 1, very much better, but still not so desirable from a computational point of view.

Finally, for Chebyshev polynomials the contributions of the terms in the series are smaller, and as  $m$  increases, typical contributions are  $\approx 10^{-2}$ , showing that the process is converging. This is the sort of behaviour one would want from a series representation.

The bad behaviours shown in the simple polynomial representations here could be a problem for *all* approximation problems. Within a particular computer program, as we found, the results seemed to be good, but if one were reporting results or transferring between programs, unless using Chebyshev polynomials, the greatest care would have to be taken to specify coefficients to high accuracy. It is ugly and dangerous to have such sums with hugely oscillating contributions.

As a general rule, we make the deduction, suggested by the diverse behaviour of the Chebyshev polynomials in Fig. 5d and dramatically confirmed in Fig. 8: *for global polynomial approximation of data one should use orthogonal functions such as Chebyshev polynomials—or, one can use piecewise-continuous approximation as we now describe.*

### 4.3.3 Splines—Piecewise-Continuous Local Interpolation and Approximation

Instead of global interpolation, with its problems that we have encountered—but substantially overcome—we consider a different approach, using a connected sequence of local functions. Splines are a sequence of piecewise-continuous low-degree polynomials that interpolate data points and are very useful in calculating an accurate value of the interpolating function, or indeed, a derivative. Figure 9 shows the principal behind spline interpolation. Between each pair of data points is a cubic polynomial which agrees in function value at the data points. At all internal data points, the first and second derivatives from both neighbouring splines to left and right are required to agree, as shown. The method is described in many books (for example, de Boor 2001) and included in software packages. One has to be careful however, for many years spline packages required the imposition of either first or second derivatives at the two end points. A better way, following de Boor, is to use a single cubic polynomial over the first two intervals and another over the last two intervals so that at the first and last *internal* points, the third derivative also is continuous, as shown in the figure. Using such a spline package means that one hardly has to think again in matters of obtaining information from smooth data and plotting it.

The author has recently developed a spline package for *approximating* irregular data rather than interpolating it, but will not be described here.

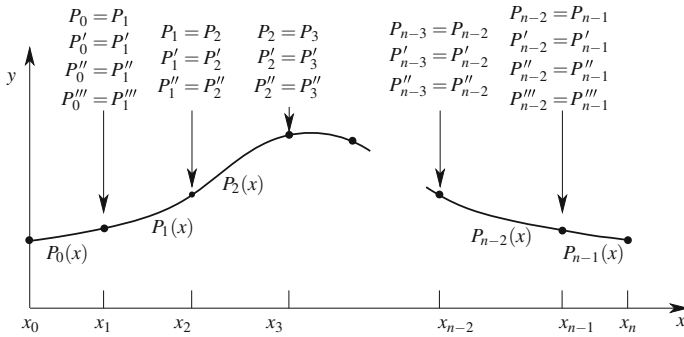


Fig. 9 Spline interpolation by a sequence of piecewise continuous cubic polynomials

### 4.4 Mathematical Formulation of Problems and Solution by Optimisation

Often one has to solve a number of simultaneous equations, for which there may be several difficulties. A major problem is if the equations are nonlinear, when it can be very difficult to obtain a solution. In problems of linear approximation of data the equations are poorly conditioned and the results from algebra packages unreliable. Another difficulty is if there is a mis-match between the number of equations and the number of unknowns. A practical difficulty is that setting up the equations for software is often complicated, for example calculating matrix coefficients.

The use of optimising software can overcome all these difficulties. If the system of equations to be solved is written  $f_m(x_n, n = 1, \dots, N) = 0$ , for  $m = 1, \dots, M$ , where the  $x_n$  are the unknowns, optimising software takes the sum of the squares of the equations:

$$e = \sum_{m=1}^M f_m^2,$$

and obtains values of the unknowns  $x_n$ , by minimising  $e$ . Figure 10 shows a typical search procedure, here for two variables only. The search paths are straight lines in the space of variables  $(x_1, x_2)$ ; the curves show the vertical projections of those lines onto the error surface. A search in three dimensions is easily visualised (e.g. the hottest point in a room, successive straight lines in physical space); a search in many ( $N$ ) dimensions can almost be visualised by analogy. An initial point is chosen, whether an approximate solution or an arbitrary one, then a search along an arbitrary direction proceeds until a minimum is found, then a search direction perpendicular to that one in  $N$ -dimensional space is determined and the process repeated. Whereas the actual equations may not even have an exact solution, the minimising procedure will almost always find an appropriate solution—for example, where the error, the sum of absolute residual errors of a number of equations, is not zero but is minimised.

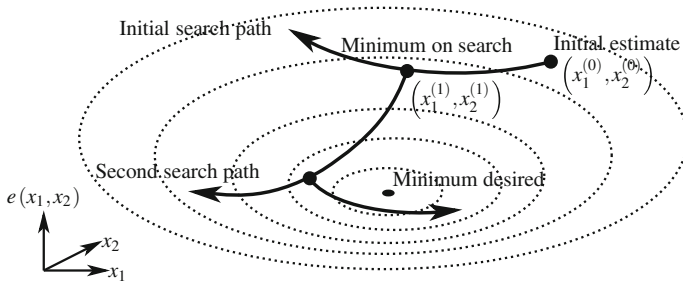


**Fig. 10** The process of optimisation—finding the values of the independent variables at which the error is a minimum—here for two variables only

With black box software to do the solving, one really just has to be able to write down the governing equations. The setting up of the equations provides a useful exercise in itself, providing some formal modelling which can lead to understanding and insight. There is little need for the obtaining and storing of matrix coefficients, as with linear algebra programs. The methods are powerful, even for nonlinear problems, and the software can be used without a great deal of knowledge of the program details. There are optimisation programs in many software packages. The most widely available are the Solver modules in spreadsheets.

### 4.5 Simple Numerical Methods for Differential Equations

In hydraulic engineering and hydrology it has often not been recognised that processes can be expressed and solved as differential equations. Instead, complicated implicit methods have been developed based on finite approximations to conservation laws. Here, we describe two simple and obvious methods for solving ordinary differential equations, and then present the example of reservoir routing, which for many years was solved using a complicated implicit method.

#### Euler’s method

This is the simplest but least accurate of all methods—yet it might be appropriate for open channel problems where quantities may only be known approximately. One can use simple modifications such as Heun’s method to gain better accuracy, or use Richardson extrapolation—or even more simply, just take smaller steps. Consider a problem where the governing differential equation is

$$\frac{dy}{dx} = f(x, y) \quad \text{with boundary condition} \quad y(x_0) = y_0 .$$

Euler’s method is, where  $\Delta x$  is a step from a point  $x_i$  to the next at  $x_{i+1}$ :

$$y_{i+1} = y_i + \Delta x f(x_i, y_i) + O((\Delta x)^2) , \tag{13}$$

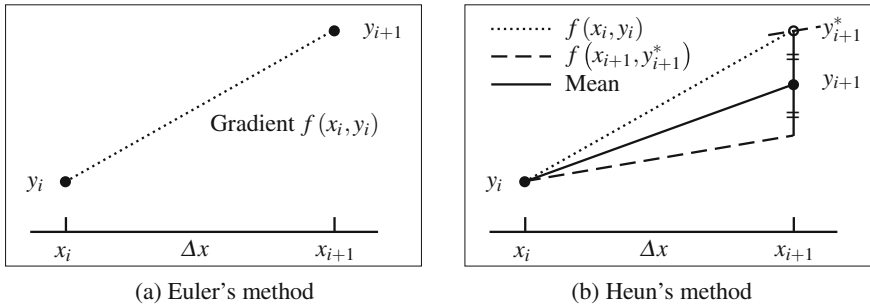


**Fig. 11** The two simplest methods for numerical solution of ordinary differential equations

and is shown in Fig. 11a. To reach a certain value of  $x$ , the number of steps necessary is proportional to  $1/\Delta x$ , each with error  $O(\Delta x^2)$ , with the result that the error at the final point is  $O(\Delta x)$  such that this is a first-order method, which knowledge is useful if Richardson extrapolation is then used.

**Heun’s method**

This scheme is shown in Fig. 11b. The value of  $y_{i+1}$  calculated from Euler’s method, (13) is used as a first estimate of the solution at the next point,  $y_{i+1}^*$ , then the value of the derivative  $dy/dx$  at that point  $(x_{i+1}, y_{i+1}^*)$  is calculated, shown by a short dashed line. Heun’s method is to use the mean of the two slopes, the initial value at  $x_i$  shown by the dotted line and that at the other end of the interval calculated by the Euler step, shown as a dashed line, the mean shown by the solid line:

$$y_{i+1}^* = y_i + \Delta x f(x_i, y_i) , \tag{14a}$$

$$y_{i+1} = y_i + \frac{\Delta x}{2} (f(x_i, y_i) + f(x_{i+1}, y_{i+1}^*)) + O((\Delta x)^3) . \tag{14b}$$

Here the error at any point  $x$  is proportional to  $1/\Delta x \times \Delta x^3 = \Delta x^2$ , a second order scheme.

**Predictor-corrector method–Trapezoidal method**

This is simply an iteration of Heun’s method, whereby the step in (14b) is repeated several times, at each stage taking the updated value of  $y_{i+1}$  and setting  $y_{i+1}^*$  equal to it. While also formally second order, it is more accurate than Heun’s method.

**Higher-order methods**

There are sophisticated methods such as high-order Runge-Kutta and predictor-corrector methods. However, in the case of open channel hydraulics there will usually be some variation of parameters or uncertainties such that such sophistication is unnecessary.

**Reservoir routing**

We now consider a problem where traditionally it has not been recognised that the governing process is described simply by a differential equation. Consider a reser-

voir or a storage tank, where a generally unsteady inflow  $I(t)$  enters and we have to calculate what the outflow  $Q(t)$  is. The action of the reservoir is usually to store water and to release it more slowly, so that the outflow is delayed and the maximum value is less than the maximum inflow. Some reservoirs, notably in urban areas, are installed just for this purpose, and are called detention reservoirs or storages. The procedure of solving the problem is also called *Level-pool Routing*.

### Formulation as a differential equation

It is simple and obvious to write down the relationship

$$\frac{d\eta}{dt} = \frac{I(t) - Q(\eta, t)}{A(\eta)}, \quad (15)$$

where  $\eta$  is the free surface elevation, the equation stating that the rate of surface rise  $d\eta/dt$  is equal to the net rate of volume increase divided by surface area  $A$ . This is a differential equation for the surface elevation itself. It requires knowledge of the dependence  $A(\eta)$ , possibly given by interpolation from planimetric information from contour maps, and the dependence of outflow  $Q$  on  $\eta$ , which is usually a simple expression from a weir flow formula or the like, while the dependence on  $t$ , as shown, is to allow for gate movement, varying the form of that formula.

### The traditional “Modified Puls” method

The traditional method of solving the problem, described in almost all books on hydrology, is to ignore the fact that it can be set up as a differential equation, and to give an unnecessarily complicated method, derived without any consideration of it being a continuous process. What for us would be a differential equation is approximated by a forward difference approximation of the rate of change of storage volume  $\mathcal{V}$  and then a trapezoidal approximation for the right side, the mean of net outflow, but where  $Q$  is considered a function of storage  $\mathcal{V}$ , as the dependent variable, rather than surface elevation:

$$\frac{\mathcal{V}(t + \Delta t) - \mathcal{V}(t)}{\Delta t} = \frac{1}{2} (I(t) + I(t + \Delta t)) - \frac{1}{2} (Q(\mathcal{V}(t + \Delta t), t + \Delta t) + Q(\mathcal{V}(t), t)),$$

where  $\Delta t$  is a finite step in time. The equation is then a transcendental one for the single unknown quantity  $\mathcal{V}(t + \Delta t)$ , the storage volume at the next time step. The formulation is awkward, and even introductory textbooks are forced to present procedures which tend to obscure with mathematical and numerical detail the underlying simplicity of reservoir routing. At an advanced level, practical difficulties may arise including specifying outflow as a function of storage volume, which is often known only coarsely. It is simpler and more fundamental to treat the problem as a differential equation.

*Example 5* Routing a flood through a reservoir by solving the differential equation

Consider a small detention reservoir, square in plan, with dimensions 100 m by 100 m, with water level origin  $\eta = 0$  at the crest of a sharp-crested weir of length



$b = 4$  m, where the outflow over the sharp-crested weir is given by the formula

$$Q(\eta) = 0.6\sqrt{g}b\eta^{3/2} ,$$

where  $g = 9.8 \text{ ms}^{-2}$ . The surrounding land has a slope (V:H) of about 1:2, so that the length of a reservoir side is  $100 + 2 \times 2 \times \eta$ , where  $\eta$  is the surface elevation relative to the weir crest, and

$$A(\eta) = (100 + 4\eta)^2 .$$

The inflow hydrograph is assumed to be

$$I(t) = Q_{\min} + (Q_{\max} - Q_{\min}) \left( \frac{t}{T_{\max}} e^{1-t/T_{\max}} \right)^5 , \tag{16}$$

where the event starts at  $t = 0$  with  $Q_{\min}$  and has a maximum  $Q_{\max}$  at  $t = T_{\max}$ . This mimics a typical storm. In the present example we consider a typical local storm event, with  $Q_{\min} = 1 \text{ m}^3 \text{ s}^{-1}$ , and  $Q_{\max} = 20 \text{ m}^3 \text{ s}^{-1}$  at  $T_{\max} = 1800$  s.

Results are shown in Fig. 12. The problem was first solved with an accurate 4th-order Runge-Kutta scheme to provide a basis for comparison, shown as a solid line. Next, Euler’s method (13) was used with 30 steps of 200 s, with results that are barely acceptable. Halving the time step to 100 s and taking 60 steps gave the slightly better results shown. It seems, as expected from knowledge of the behaviour of the global error of the Euler method, that it has been halved at each point. Next, applying Richardson extrapolation, (8) with  $r = \frac{1}{2}$ , gave the results shown by the circular points. They almost coincide with the accurate solution, and the solution crosses the inflow hydrograph with an apparent horizontal gradient, as required when inflow is equal to outflow  $I = Q$ , Eq. (15) gives  $d\eta/dt = 0$ , and the reservoir level is momentarily not changing. The less-accurate results do not quite show this.

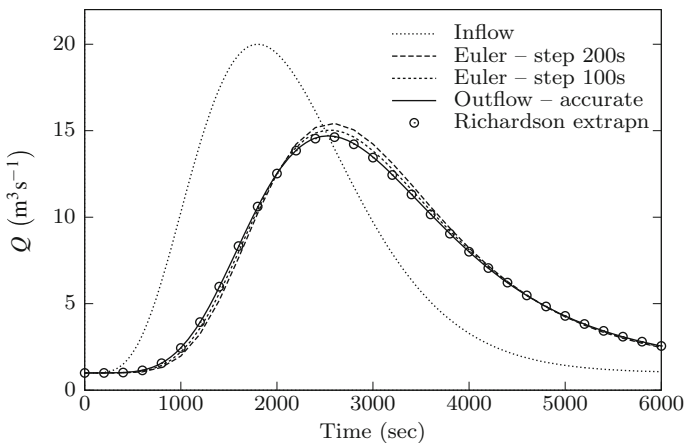


**Fig. 12** Computational results for the routing of a storm flow through a small detention reservoir

## 5 The One-Dimensional Long Wave Equations

The most important terms in the equations, the gravitational driving force and the resistance force, will now be obtained and discussed. The resistance contributions are presented in generalised terms, incorporating rating measurements in real streams as well as well-known resistance formulae. The equations are presented also with cross-sectional area as one dependent variable, when an interesting and surprising discovery is made that they require very little knowledge of the stream bathymetry, which might be useful in practice. The conventional use of surface elevation as the corresponding dependent variable means that quantities in the equations such as cross-sectional area and wetted perimeter require detailed bathymetric knowledge.

An old self-referential mathematical joke goes “We will model a cow – we assume it to be spherical”. That might be a rough first approximation. In our case, we look at the typical dimensions of a river or canal and we observe that its lateral dimensions are very much smaller than its longitudinal one, and so we will assume a one-dimensional stream, where everything is averaged across the section at any point. This is a sensible first step, but will tell us nothing about secondary currents, for example. We might think that we have to include meandering of the stream, however Fenton (2015, §1.3.7) showed that the effects of horizontal curvature are small and can usually be neglected.

We use a mass conservation equation and could use either momentum or energy conservation. Fenton (2010, Appendix B) found that momentum was simpler: using energy required more coefficients to approximate integrals, and there was the difficulty of approximating various forms of energy dissipation which occur throughout the fluid rather than just momentum loss at the boundary.

Here we will not go into details of the derivations, but we discuss the calculation of the most important two terms in the momentum equation, one using not-so-simple mathematics but which gives a very simple method of evaluating the pressure force contributions, and the other is the not-particularly-mathematical but physically-simple modelling of the resistance force around the boundary.

### 5.1 *The Driving Force Term Due to Gravity*

It is simpler to use cartesian coordinates, with the  $x$  axis horizontal and straight along our supposedly-straight river, rather than bed-oriented axes, which introduce mathematical complications. As gravity acts vertically, there is no explicit contribution from it to horizontal momentum. It appears from the pressure gradient in the fluid due to the surface slope, which we now evaluate.

#### **Evaluating the net pressure force on an arbitrary closed surface**

To evaluate terms in momentum conservation equations one might have to consider difficult control surfaces, such as one bounded below by the stream bed, two or maybe four (depending on how many horizontal dimensions considered) stationary

vertical planar faces and the free surface which can move and the control surface moves with it. The total pressure force acting on the fluid within a control surface is  $-\int_{CS} p \hat{\mathbf{n}} dS$ , where  $p$  is the pressure,  $\hat{\mathbf{n}}$  is the unit vector directed outwards normal to the element  $dS$  of the control surface CS, and the negative sign shows that the local force acts opposite to it, on the fluid inside the surface. In this form it is difficult to evaluate, as the pressure and the non-constant unit vector have to be integrated over all the submerged faces of the control surface. In some books and papers one can find several pages of difficult mathematics evaluating it.

A considerably simpler derivation is obtained if the term is evaluated using what one might call the *Archimedes/Lagrange/Gauss/Ostrogradsky/Green Divergence Theorem*, replacing the integral over the rather complicated control surface by a simpler volume integral. It is well known, and can be found in any book on vector calculus. Here we consider it in the form

$$\text{Net force} = - \int_{CS} p \hat{\mathbf{n}} dS = - \int_{CV} \nabla p dV, \quad (17)$$

where  $\nabla$  is the gradient operator such that  $\nabla p$  is a vector whose components are the pressure gradients in each direction, and  $dV$  is an element of the control volume CV. In a stationary fluid or one flowing with a surface gradient of very small slope, the pressure is given by  $p = \rho g (\eta - z)$ , where  $\rho$  is fluid density,  $g$  is gravitational acceleration,  $\eta(x, y)$  is free surface elevation and  $z$  is the vertical coordinate. Evaluating  $\nabla p$ :

$$\nabla p = \rho g \left( \frac{\partial \eta}{\partial x}, \frac{\partial \eta}{\partial y}, -1 \right).$$

Archimedes, not unreasonably, limited himself to the horizontal surface of a bath, and found, as we would do here by substituting the vertical component into (17), the total vertical force on a body to be  $+\rho g \mathcal{V}$ , the force on the fluid displaced, with the correct sign, upwards. For the one-dimensional channel flow problem of a control surface which is a vertical slice of thickness  $\delta x$  across a channel where the free surface is horizontal such that  $\partial \eta / \partial x$  is constant across the channel and  $\partial \eta / \partial y = 0$ , the integration on the right side of (17) is trivial and we obtain

$$\text{Net force} = -\rho g A \left( \frac{\partial \eta}{\partial x}, 0, -1 \right) \delta x,$$

where  $A$  is the cross-sectional area. Usually we are only concerned with the first component, the longitudinal  $x$  one, and dividing by  $\rho \delta x$  gives the horizontal force per unit length divided by density:

$$\text{Gravitational contribution} = -g A \frac{\partial \eta}{\partial x}. \quad (18)$$

The result is so simple that we are tempted to say that it could have just been written down. However, if one considers a channel with arbitrarily-varying boundaries, could we have been certain that contributions cancel to give such a simple result?

## 5.2 Resistance Force

The other most important contribution to horizontal momentum is that of resistance around the boundary.

**Weisbach resistance:** Using the Weisbach form for the forces of the boundary on the flow makes incorporation of the resistance more rational than the Gauckler-Manning form. Consider the expression for the magnitude of the shear force  $\tau$  on a pipe wall (e.g. §6 of White 2009):

$$\tau = \frac{\lambda}{8} \rho V^2, \quad (19)$$

where the Weisbach coefficient  $\lambda$  is a dimensionless resistance factor, and  $V$  is the mean velocity in the pipe. The denominator 8 follows from the original introduction of  $\lambda$  in the Darcy-Weisbach formula for head loss in a pipe, with a term  $2g$  in the expression for head and a term 4 in the relationship between head loss and  $\tau$ . We will avoid it in open channel flows by using the symbol  $\Lambda$  for the dimensionless resistance coefficient:

$$\Lambda = \frac{\lambda}{8} = \frac{g}{C^2}, \quad (20)$$

where  $\lambda$  is the mean value around the wetted perimeter of the channel at a section, and we have shown how it is related to  $C$ , the Chézy coefficient. We usually have little idea of the variation of  $\lambda$  around the section.

Now for a channel on a small slope we assume  $V = Q/A$  and replace  $V^2$  by  $-Q|Q|/A^2$  in (19), allowing for possible change of flow direction, such that the resisting force is always opposite to the flow direction. Multiplying the stress by the wetted perimeter  $P$  and dividing by density  $\rho$ , gives the contribution

$$\text{Resistance force per unit length divided by density} = -\Lambda P \frac{Q|Q|}{A^2}. \quad (21)$$

In this form the nature of the contributions are explicit and obvious: a resistance coefficient multiplied by the square of the velocity multiplied by the wetted perimeter around which resistance acts.

For steady uniform flow with  $\partial\eta/\partial x = -S$ , where  $S$  is bed slope, algebraically combining the gravity and resistance terms (18) and (21) gives the Chézy-Weisbach formula for discharge:

$$Q = \sqrt{\frac{gA^3}{\Lambda P}} S.$$

It is interesting to re-write this in terms of Froude number  $F$  as

$$F^2 = \frac{Q^2 B}{g A^3} = \frac{S B}{\Lambda P},$$

and as  $B \approx P$  for wide channels, we see that the square of the Froude number is approximately equal to the ratio of bed slope  $S$  to resistance coefficient  $\Lambda$ , giving some significance and physical feeling for  $\Lambda$ . This means that for a particular reach of river, where slope  $S$  is effectively independent of flow, where  $B/P$  also does not vary much with the flow and  $\Lambda$  often does not vary much, the Froude number  $F$  does not change much with flow. While a flood might look more dramatic than a more-common low flow, because it is faster and higher, the Froude number is roughly the same for both.

**Gauckler-Manning formula:** Here, starting with the Gauckler-Manning formula (3) for steady uniform flow

$$Q = \frac{1}{n} \frac{A^{5/3}}{P^{2/3}} \sqrt{S},$$

assuming resistance proportional to the square of the velocity and requiring the resistance term to yield the Gauckler-Manning formula when combined with the pressure/gravity term for steady uniform flow, the resistance term here would be written:

$$\text{Alternative resistance force contribution} = -gn^2 \frac{P^{4/3} Q |Q|}{A^{7/3}}. \quad (22)$$

It appears as being proportional to perimeter  $P^{4/3}$ , and not to  $P$  which one would expect, and which leads one to fear that using the Gauckler-Manning resistance is not so fundamental.

**General terminology and Rating Curves:** We want to develop a general terminology for use in the resistance term, so we write a generalisation of (21) and (22):

$$\text{Generalised resistance force contribution} = -\Omega Q |Q|, \quad (23)$$

where the coefficient  $\Omega$ , of dimensions  $L^{-3}$ , is a function of resistance coefficient, cross-sectional area, and wetted perimeter.

As an alternative we also consider the common case where we know the rating curve at a particular station, which is where the discharge is known as a function of the stage (surface elevation) relative to an arbitrary datum. Here if we want to use the rating curve along the channel, assuming that the relationship holds at other points in the stream, it is more convenient to express it in terms of area, as that does not require an arbitrary datum. In any case, in the determination of the rating curve, the cross-sectional area  $A$  is also measured for every point. This use of a discharge-area relationship measured at one point but used for a channel reach might be a better approximation than any use of assumed values of resistance coefficients  $\Lambda$  in the Chézy-Weisbach formula or  $n$  in the Gauckler-Manning formula.

Ideally, all measurements leading to the rating relationship would have been for steady quasi-uniform flow. The functional relationship for the rated discharge is written here as  $Q_r(A)$ .

To incorporate this into our resistance terminology, it is assumed that for points on the rating curve, flow is assumed to be uniform and steady, and we add the gravity and resistance terms (18) and (23) algebraically. If no slope measurements exist, we have to assume that the slope of the free surface in the gravity term is  $\partial\eta/\partial x = -\tilde{S}$ , the mean stream bed slope. Combining the two terms:

$$-\Omega Q_r^2(A) + gA\tilde{S} = 0, \quad (24)$$

which can be solved for  $\Omega$ . Comparison of the expressions (21), (22), (23) and (24) gives the alternative definitions of  $\Omega$

$$\Omega = \begin{cases} gA\tilde{S}/Q_r^2(A), & \text{in terms of rated discharge } Q_r(A); \\ \Lambda P/A^2, & \text{Chézy-Weisbach, where } \Lambda = \lambda/8 = g/C^2; \\ n^2 g P^{4/3}/A^{7/3}, & \text{Gauckler-Manning.} \end{cases} \quad (25)$$

In fact, use of the symbol  $Q_r$  is helpful in different presentations of the equations too, so that we write it in its different forms, as measured, and also as could be calculated:

$$Q_r(A) = \begin{cases} \text{Measured,} & \text{for rated discharge;} \\ \sqrt{gA^3/\Lambda P(A)}\sqrt{S}, & \text{Chézy-Weisbach;} \\ 1/n \times (A^{5/3}/P^{2/3}(A))\sqrt{S}, & \text{Gauckler-Manning.} \end{cases} \quad (26)$$

**Misleading terminology with  $S_f$ :** We note here the misleading terminology in many presentations of the momentum equation, when the resistance term is written  $-gAS_f$ . The symbol  $S_f$  does not reveal the nature of the term. It is usually described as being the slope of a line representing the variation of total head, the energy grade line, which it is in an energy equation. In a momentum equation, however, it is actually *the ratio of resistance force to gravitational force, both per unit length*. The notation has led to mistakes made in some works where  $S_f$  has been assumed constant, independent of  $Q$  and  $A$ .

**Compound resistance:** One advantage of the Weisbach formulation, being directly related to stress and force, is that one can linearly superimpose force contributions, so that in a more complicated situation, where there may be bedforms, vegetation, and/or different boundary parts such as floodplains contributing to the resistance, the forces can be added and we can write, for contributions from various parts

$$\Lambda P = \sum_i \gamma_i A_i P_i. \quad (27)$$

The  $\gamma_i$  are velocity correction factors, as the relevant square of velocity for each part of a compound section is not simply  $(Q/A)^2$ , in terms of the mean velocity.

When the Gauckler-Manning form is used for resistance there has been much irrationality. Yen (2002, Table 8) lists 26 different formulae for compound or composite sections. Some of them just weight contributions according to individual areas  $A_i$ , some just according to perimeters  $P_i$ . Most do not include allowance for the local velocity being different from the mean of the whole section. Some do not weight different contributions at all, but combine them imaginatively. Almost all such formulae are nonsense.

### 5.3 The Equations

The long wave equations are well-known. We consider them as presented by Fenton (2010, 2015; §1.3.7), here making the usual approximation that river curvature can be neglected. The symbols used, with some repetition of those already introduced are:

**Independent variables:**  $x$  is a horizontal cartesian co-ordinate along the line of the river,  $t$  is time.

**Dependent variables:** Cross-sectional area  $A$  or surface elevation  $\eta$ , and discharge  $Q$ .

**Other quantities:**  $B$ —surface width,  $i$ —lateral inflow volume rate per unit length of river,  $\beta$ —Boussinesq momentum coefficient, slightly greater than 1,  $\Omega$ —general resistance coefficient defined in (25) and  $\tilde{S}$ —local mean downstream slope of the stream bed evaluated across the section,

$$\tilde{S} = -\frac{1}{B} \int_B \frac{\partial Z}{\partial x} dy, \quad (28)$$

where the bed elevation is  $z = Z(x, y)$ , with  $y$  the transverse co-ordinate. The definition includes a negative sign such that in the usual situation where the bed slopes downwards in the direction of  $x$  so that  $Z$  decreases,  $\tilde{S}$  will be positive. If the bottom geometry is precisely known, this can be precisely evaluated and it incorporates the non-prismatic contribution. Often the geometry is only approximately known and a typical bed slope of the stream is used.

#### 5.3.1 Equations with $\eta$ and $Q$ as Dependent Variables

The use of water elevation  $\eta$  is more useful for practical problems, but it is necessary to know enough information about the bathymetry such that the functional dependencies of  $A$ ,  $B$ , and  $P$  on  $\eta$  can be determined for any  $x$ . This is simple for a prismatic channel, but otherwise is a demanding requirement. With no vertical diverging/converging walls and  $\beta$  constant, the equations are:

$$\frac{\partial \eta}{\partial t} + \frac{1}{B} \frac{\partial Q}{\partial x} = \frac{i}{B}, \quad (29a)$$

$$\frac{\partial Q}{\partial t} + 2\beta \frac{Q}{A} \frac{\partial Q}{\partial x} + \left( gA - \beta \frac{Q^2 B}{A^2} \right) \frac{\partial \eta}{\partial x} = \beta \frac{Q^2 B}{A^2} \tilde{S} - \Omega Q |Q|. \quad (29b)$$

### 5.3.2 Use of $A$ and $Q$ and Application to Streams of Unknown Bathymetry

For theoretical purposes the equations in this form are more useful. And, as we are about to discover, there is a simplicity about this form which might make it more useful also practically:

$$\frac{\partial A}{\partial t} + \frac{\partial Q}{\partial x} = i, \quad (30a)$$

$$\frac{\partial Q}{\partial t} + \frac{\partial}{\partial x} \left( \beta \frac{Q^2}{A} \right) + \frac{gA}{B} \frac{\partial A}{\partial x} = gA \tilde{S} - \Omega Q |Q|. \quad (30b)$$

The simplicity of this form in  $A$  is that the only places where the bathymetry appears are in the three relatively weakly-varying quantities: slope  $\tilde{S}$ , surface width  $B(A)$ , and wetted perimeter  $P(A)$ . This suggests that using this form of the long wave equations in terms of  $A$  has advantages. Few details are required to solve a problem numerically: an approximate mean value of slope  $S$ , approximate (linear?) relationships  $B(A)$  and  $P(A)$  for the expected limited range of variation, and, where the greatest uncertainty enters anyway, a value of resistance coefficient  $\Lambda$  or  $n$  or the relationship  $Q_r(A)$ .

It is a surprising result that such a solution of the long wave equations can be carried out almost independently of how the underwater topography varies and that we can do so much with so little information. As  $Q$  is also a dependent variable, in flood routing studies, the discharge hydrograph  $Q(x_i, t)$  at any point  $x_i$  is obtained as part of the computations. However, if one needed a value of surface elevation  $\eta$  at such a point, it would be necessary to know cross-sectional details there to go from the computed value of  $A$  to  $\eta$ .

In many places throughout the rest of this document, except for the steady-flow equations, the traditional  $(\eta, Q)$  form will be used so as to relate any new results to known ones. In many places it would be possible to replace  $A$  with  $\eta$  or the long wave equations (30) for those in (29).

## 6 Numerical Solution of the Long Wave Equations

The simplest numerical method will be now presented, that of finite differences forward in time and with quadratic variation in space. Schemes are introduced for arbitrary point distribution along a stream. Initial and boundary conditions are discussed



and generalised finite difference expressions introduced for a systematic treatment of various upstream and downstream boundary conditions. A simple approach to open downstream boundaries is proposed, which seems to work well.

### 6.1 *Numerical Solution by Explicit Generalised Finite Differences*

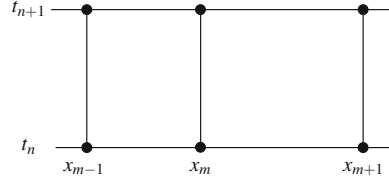
A great complication was made when Liggett and Cunge (1975, p. 111) stated that the simplest and most obvious finite difference numerical scheme, Forward in Time and Central in Space (FTCS) was unconditionally unstable and named it “The Unstable Scheme”. This may have contributed to the extensive use of implicit methods throughout river hydraulics, such as the Preissmann Box scheme, and a culture that complicated is good. Such schemes are stable and allow large time steps, but they are much more complex and require many more calculations, including the solution at each time step of a system of nonlinear equations, the number of equations being equal to the number of space steps. This complexity may have contributed to computational hydraulics, once being a cottage industry with skilled people, similarly to the tendencies of the industrial revolution, becoming dominated by large software houses and the down-skilling of ordinary practitioners.

The author (Fenton 2014, §6) has shown that the deductions of Liggett and Cunge concerning the simple explicit method are wrong. A linear stability analysis showed that the scheme has a quite acceptable stability limitation, and it opens up the possibility of this as a much simpler method for computations of floods and flows in open channels. When compared with computations over a wide range of slopes and roughnesses encountered in practice, the stability limit found gave quite a sharp estimate of the allowable time step in practical calculations. Instead of presenting it here, we suggest the obvious procedure: if the computations become unstable, halve the computational time step, and if that does not work, halve again. And so on.

The theoretical stability criteria and practical computations show that the FTCS method is quite capable of simulating flows and waves in open channels. The time steps allowed might be less than for implicit schemes, but the simplicity is an important advantage. Such small time steps do not seem to be a problem in practice. A typical run time on a personal computer for the examples shown below is only a second or two.

We consider a generalised computational module as shown in Fig. 13 with two time levels and three arbitrarily spaced points in  $x$ , so that we can use forward differences for derivatives in time  $t$  and generalised expressions using quadratic variation for derivatives in space  $x$ , giving **Forward-Time-Quadratic-Space** schemes. With the use of this approximation, over possibly unequally-spaced points and left- and right-sided as well as centred, we propose the acronym FTQS as a generalisation of FTCS encountered previously. At any of the three computational points  $(x_{m+k}, t_n)$ ,  $k = -1, 0, +1$  we approximate the time derivative by the forward difference approx-

**Fig. 13** Generalised computational module for Forwards-Time-Quadratic-Space approximation



imation, where  $f$  is any of the dependent quantities  $A$ ,  $\eta$  or  $Q$ :

$$\left. \frac{\partial f}{\partial t} \right|_{(m+k,n)} \approx \frac{f(x_{m+k}, t_{n+1}) - f(x_{m+k}, t_n)}{t_{n+1} - t_n}. \quad (31)$$

For the  $x$  derivatives at any point of the three-point module, we use the divided difference formulae introduced above, assuming quadratic variation. For the actual partial differential equations in the interior of a computational reach, one would use the centre of three points, but sometimes, particularly in the satisfaction of boundary conditions, it is necessary to have expressions at the first and last points also. We form the divided differences

$$a_{m-1} = f_{m-1}, \quad a_m = \frac{f_m - f_{m-1}}{x_m - x_{m-1}}, \quad a_{m+1}^* = \frac{f_{m+1} - f_m}{x_{m+1} - x_m}, \quad \text{and} \quad a_{m+1} = \frac{a_{m+1}^* - a_m}{x_{m+1} - x_{m-1}}, \quad (32)$$

using the temporary symbol  $a_{m+1}^*$  shown. The general expression for the derivative at any of the three computational points is then

$$\left. \frac{\partial f}{\partial x} \right|_{m+k} = a_m + (2x_{m+k} - x_{m-1} - x_m) a_{m+1}. \quad (33)$$

For the usual case of equally spaced points  $x_{m-1} = x_m - \Delta x$  and  $x_{m+1} = x_m + \Delta x$  we obtain

$$a_{m-1} = f_{m-1}, \quad a_m = \frac{f_m - f_{m-1}}{\Delta x}, \quad \text{and} \quad a_{m+1} = \frac{f_{m-1} + f_{m+1} - 2f_m}{2\Delta x^2},$$

giving

$$\left. \frac{\partial f}{\partial x} \right|_{m-1} = \frac{-3f_{m-1} + 4f_m - f_{m+1}}{2\Delta x} \quad (34a)$$

$$\left. \frac{\partial f}{\partial x} \right|_m = \frac{f_{m+1} - f_{m-1}}{2\Delta x} \quad (34b)$$

$$\left. \frac{\partial f}{\partial x} \right|_{m+1} = \frac{f_{m-1} - 4f_m + 3f_{m+1}}{2\Delta x}. \quad (34c)$$

If it were necessary, the second derivative is given by  $\partial^2 f / \partial x^2 = 2a_{m+1}$ . The centred expression (34b) is familiar. We will use the derivatives at the end points when we consider boundary conditions.

**The FTQS computational scheme:** Replacing derivatives in the long wave equations (29) by the finite difference approximations of (31) and (33) or (34) gives the equations

$$\frac{\eta_{m+k,n+1} - \eta_{m+k,n}}{t_{n+1} - t_n} = \frac{i}{B} - \frac{1}{B} \frac{\partial Q}{\partial x} \Big|_{m+k,n}, \quad (35a)$$

$$\frac{Q_{m+k,n+1} - Q_{m+k,n}}{t_{n+1} - t_n} = -2\beta \frac{Q}{A} \frac{\partial Q}{\partial x} - \left( gA - \beta \frac{Q^2 B}{A^2} \right) \frac{\partial \eta}{\partial x} + \beta \frac{Q^2}{A^2} B \tilde{S} - \Omega Q |Q| \Big|_{m+k,n}. \quad (35b)$$

Both expressions can be re-arranged to give explicit formulae for the values of  $\eta$  and  $Q$  at point  $m+k$  at the next time level  $n+1$ . All terms on the right are evaluated at  $(m+k, n)$  as shown, each derivative  $\partial \eta / \partial x$  and  $\partial Q / \partial x$  at that point evaluated using the divided difference expression in terms of the three values at  $m-1$ ,  $m$  and  $m+1$ .

To advance the solution for interior points, we use the two expressions with  $k=0$ , the centre point of our computational module. At the two end points, the expressions for  $k = \pm 1$  will be seen to be useful in the subsequent section on boundary conditions.

## 6.2 Initial Conditions

**Initial conditions in a real stream:** The simplest method of obtaining initial conditions over a variable computational reach is to assume an approximate solution with constant discharge and something like linear free surface variation, and use the unsteady program to compute until all waves generated by that incorrect solution have left the system, and then use the results as the real initial conditions. One could use the methods for steady flows described below in Sect. 9, but if one has the unsteady program operating, using it would be simplest.

**Initial conditions in an idealised stream:** If one has a geometry, flow and boundary conditions such that the initial conditions are a uniform flow, one can use the direct iteration scheme described in Sect. 4.1 to calculate the constant normal depth.

## 6.3 Boundary Conditions

In books on open channel hydraulics and numerical methods, there are few practical results or physical insights for finite difference boundary conditions. Most books

that do treat the subject include an extensive discussion of the characteristic formulation of the long wave equations but provide few concrete results. Writers seem convinced that the characteristic formulation is more fundamental than the equations themselves. This has led to complicated presentations and paradoxically to oversimplified and less-accurate numerical approximations, because it is more difficult to approximate the characteristics to higher than first order.

We propose to take an approach of common sense. In particular, our approach will almost everywhere disagree with the often-cited contributions of Liggett and Cunge (1975, pp. 135–142) and Cunge et al. (1980, pp. 72–3, p. 198). We will be ignoring their many warnings about finite difference expressions. We will not be making any appeal to the method of characteristics. We believe it is not superior to the long wave equations themselves and is not “the only general technique for finding boundary conditions for explicit finite difference schemes”. This means that we can very simply develop numerical approximations for boundary conditions that are as accurate as the partial differential equations and more accurate than many characteristics-based formulae. To do this we will be using left and right three-point differencing at boundaries, without any apparent problems. Amongst other things, we will go on to introduce a new type of open downstream boundary condition which enables the accurate simulation of waves leaving a truncated computational domain.

### 6.3.1 Boundaries Where the Stage or Discharge Hydrograph Is Known

Where the discharge hydrograph,  $Q$  as a function of time  $t$ , is known, we can use the FTQS mass conservation equation (35a) to calculate  $\eta$  at the next time step, and symmetrically, if the stage hydrograph,  $\eta$  as a function of time  $t$  is known, we can use the FTQS momentum conservation equation (35b) to calculate  $Q$  at the next time step. All  $x$  derivatives are calculated using the three-point formula (33) or the equi-spaced alternatives in (34). At the upstream boundary, denoted by  $x_0$  here, the formulae are implemented with  $m = 1$  and  $k = -1$  in the above notation, using point values at  $x_0, x_1$  and  $x_2$  to calculate derivatives. Similarly at the downstream boundary, denoted here by  $x_M$ , we would use  $m = M - 1$  and  $k = +1$ , namely points  $x_{M-2}, x_{M-1}$ , and  $x_M$  for the derivatives. The four alternatives are detailed in Table 1.

**Upstream boundary:** In supercritical flow it is obvious that at an upstream boundary one has to provide hydrographs of flow  $Q(t)$  and surface elevation  $\eta(t)$ . In the more usual subcritical case, if the stream is blocked at the upstream boundary such as by a dam, waves cannot propagate further upstream, then our approach seems to be a good model of reality. If the start of the computational reach is an open boundary where the channel is not blocked, there may not be complete correspondence between the physical problem and computational model. If the input condition were an actual measured stage hydrograph, the computed discharge there might be different from the unsteady discharge which had entered from upstream in reality. If the condition were an inferred discharge hydrograph from a rating curve, then the procedure giving that is just an approximate model anyway of unsteady non-uniform

**Table 1** Schemes for incorporation of boundary condition if stage or discharge hydrograph is known at the upstream or downstream boundary

Inflow hydrograph known $Q(x_0, t) = Q_0(t)$
$Q(x_0, t_{n+1}) = Q_0(t_{n+1})$
$\eta(x_0, t_{n+1})$ from (33) and (35a) using $m = 1, k = -1$
Upstream stage hydrograph known $\eta(x_0, t) = \eta_0(t)$
$\eta(x_0, t_{n+1}) = \eta_0(t_{n+1})$
$Q(x_0, t_{n+1})$ from (33) and (35b) using $m = 1, k = -1$
Outflow hydrograph known $Q(x_M, t) = Q_M(t)$
$Q(x_M, t_{n+1}) = Q_M(t_{n+1})$
$\eta(x_M, t_{n+1})$ from (33) and (35a) using $m = M - 1, k = +1$
Downstream stage hydrograph known $\eta(x_M, t) = \eta_M(t)$
$\eta(x_M, t_{n+1}) = \eta_M(t_{n+1})$
$Q(x_M, t_{n+1})$ from (33) and (35b) using $m = M - 1, k = +1$

reality. Alternatively, if a theoretical model hydrograph were specified, then this is arbitrary in any case. All such cases seem to be unavoidable consequences of a model with a finite domain.

**Downstream boundary:** In supercritical flow no downstream boundary conditions can be specified. For subcritical flow the procedure described above for a specified stage hydrograph would be necessary in cases such as a lake, reservoir, or the sea, where the water surface elevation downstream is specified as constant or a function of time. The case where a downstream flow hydrograph is known might occur where recorded gauge data is available and the model is being calibrated to a specific flood event, however this seems relatively rare.

### 6.3.2 Known Downstream Stage-Discharge Relationship

Most commonly this is where there is a downstream control structure such as a spillway, weir, gate, or flume, and there is a functional relationship between flow and surface elevation that we denote by  $Q = F(\eta)$ . It does not include the case that we will consider subsequently where the end point is actually an open one.

We assume that the  $Q = F(\eta)$  relationship is not affected by unsteadiness and non-uniformity, which probably holds for relatively short control structures mentioned. Our approach, however, has a potential difficulty. In principle we have one equation too many. We have the FTQS mass and momentum conservation formulae (35a and 35b) which we could use to calculate the updated boundary values  $\eta(x_M, t_{n+1})$  and  $Q(x_M, t_{n+1})$ , but we also have the relation between them

$$Q(x_M, t_{n+1}) = F(\eta(x_M, t_{n+1})) . \quad (36)$$

In fact, a sudden change in section where a typical spillway, weir, gate, or flume is placed violates a fundamental assumption of the long wave momentum equation, that variation in the channel is slow and long. Hence we can ignore the momentum equation near such a sudden change. Fortunately, the mass conservation equation is still valid and (35a) for  $\eta(x_M, t_{n+1})$  requires only the assumption that water surface is horizontal across the channel. We use that, and then simply use the discharge formula (36) for  $Q(x_M, t_{n+1})$ .

### 6.3.3 Open Downstream Boundary

A common boundary condition is where the computational domain is truncated at an arbitrary point in the stream, and no computations are performed downstream of that point. HEC-RAS (2010, pp. 2–47) calls this the Normal Depth boundary and advocates using the Gauckler-Manning equation to give a stage considered to be normal depth if uniform flow conditions existed downstream. As that is not correct, they suggest that the computational domain be artificially extended and this boundary condition be used far enough downstream from the study area such that it does not affect the results there.

There is a simple and rational alternative. However it goes in the opposite direction from the conventional understanding of open channel hydraulics, where an oft-repeated principle is “one boundary condition has to be given for every characteristic entering through the boundaries of the solution domain” (Cunge et al. 1980, p. 31). In this way, conventionally a boundary condition is applied even at an open boundary at a truncated position in the stream. However, if one can truncate the computational domain then it must be because downstream the region is unimportant and no significant information is coming back from there.

We advocate simply doing away with the downstream boundary condition if the boundary is an open one. Instead we suggest simply treating the end point as if it were an ordinary point in the stream and numerically solving the long wave equations there also, but instead of the approximations centred on the mid point, using the three-point leftwards approximations for the last point  $x_M$  in terms of values at  $x_{M-2}$ ,  $x_{M-1}$ , and  $x_M$ . If the boundary condition is open, most important information is coming from upstream, as the waves that are input at the upstream boundary progress downstream. To use upstream or backward differences seems sensible. For streams on small slopes, where downstream effects diffuse upstream more, this may be less accurate, but in the example we are about to show, that is not noticeable.

The open treatment of the downstream boundary condition was tested in several model cases. The results of one are presented here: a relatively flat stream of slope 0.0001 where downstream boundary effects are likely to be more important, of length 100 km, of rectangular section with no side resistance, so all results are per unit width, with a Manning  $n = 0.05$ . An initial flow of  $q = 1 \text{ m}^2 \text{ s}^{-1}$  was increased smoothly to  $q = 10 \text{ m}^2 \text{ s}^{-1}$  and back down to the original flow using the model inflow hydrograph, Eq. (16). Four calculations were performed, two using a uniform flow boundary at 50 km and 100 km and two using the open boundary condition

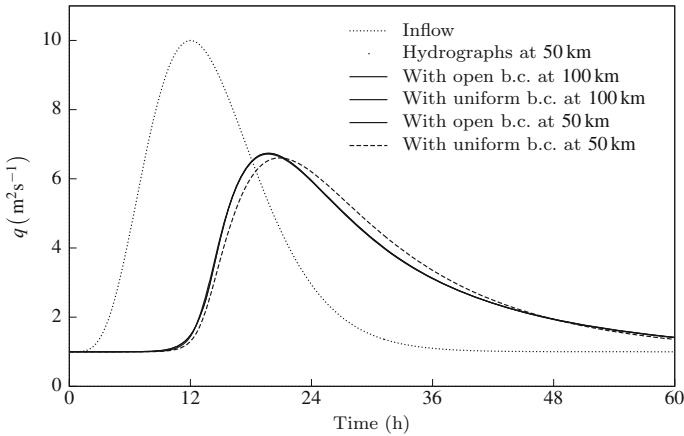


**Fig. 14** Computed hydrographs at 50 km with two different boundary conditions applied at two points, 50 km itself and one 50 km further downstream: where results are coincident the same line type is used

suggested here at both points. Results are shown in Fig. 14. Three of the results agree closely: where the boundary condition was applied a further 50 km downstream, both the uniform flow boundary condition and the open boundary condition agreed closely, as we might expect. Most happily, results for the open boundary condition applied at the 50 km point also agreed with them. However, results from the uniform flow boundary condition applied at that point differed somewhat. The simple result is pleasing that it is possible just to use the long wave equations with three-point leftwards differences at the downstream boundary, and not to have to arbitrarily add on a region of uniform flow.

The apparent success of this approach follows the essential nature of the physical problem, but not that dictated by the characteristic formulation. We suggest that the rule stated by other authors above, of requiring one boundary condition for each entering characteristic, is too rigid. A more pragmatic approach is possible, that boundary conditions should be provided where they make physical sense.

#### 6.4 An Example of the Performance of the FTQS Schemes

As a test of some of these methods and formulae in practice, we conducted simulations for the same stream as has just been considered. Results are shown in Fig. 15. The first three methods considered all used a uniform flow downstream boundary condition (DS BC): the Preissmann Implicit Box scheme, the Method of Characteristics (actually with quadratic  $x$  variation), and the FTQS finite difference scheme. All agreed closely with each other at both the mid-point of the computations and at the downstream boundary.

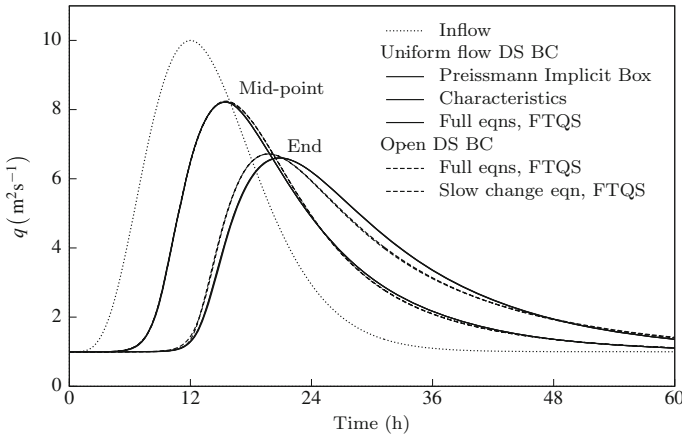


**Fig. 15** Comparison of different computational methods: where results are coincident the same line type is used

The next two methods considered used the open boundary condition at the downstream point, the FTQS finite difference scheme and the simpler slow-change equation using upstream volume to be presented below (Eq. 47). At that downstream boundary, the three schemes that used the uniform flow boundary condition no longer agreed with those from the two schemes that used the open boundary, one of which we have already seen in Fig. 14 is accurate even at the boundary. The conclusion we draw is that the simple explicit FTQS scheme, both for the full equations and the slow-change equation, works well, agreeing with traditional well-known methods where it should, and better than them when it used the open downstream boundary condition. One example, of course, does not provide a definitive test.

## 7 Nature of Wave Propagation

The concept of Upstream Volume will now be introduced. It is shown how it can simplify theoretical and practical operations. Using it, the long wave equations are linearised and reduced to a Telegraph equation, containing first derivatives which are more important for slower-rising flood waves, and second derivatives which are important for disturbances created by rapid gate movements. The traditional “kinematic” approximation is shown to be no such thing—instead it is a very long wave approximation. In an alternative approach, by non-dimensionalising the equations and introducing the idea that it is the time scales of waves imposed by boundary conditions that determine the nature of waves, the same result is obtained. A simplified single equation in terms of upstream volume is obtained for intermediate and long waves. However, it is asserted that finite difference methods for the full long wave equations are simple enough and are satisfactory.



## 7.1 The Use of Upstream Volume

There is a quantity that can make the relating of equations and computational results between area  $A$  and discharge  $Q$  simpler, as well as in the incorporation of boundary conditions. For theoretical and some computational studies it is easier to consider a single equation in terms of the total volume of fluid  $V$  upstream of a point that will pass the point during the course of computations.

Consider the total volume of fluid upstream of a point  $x$  at a time  $t$ , denoted by  $V(x, t)$ :

$$V(x, t) = \int^x A(x', t) dx' .$$

This is a slightly different and simpler definition from that used in Fenton (2015, §1.5.5) where  $V$  was defined as the volume in the channel between an initial point  $x_0$  and  $x$ . In this the present  $V$  includes that water which will enter the channel from further upstream as well. From simple calculus, the derivative of volume with respect to distance  $x$  gives the cross-sectional area:

$$A = \frac{\partial V}{\partial x} . \quad (37)$$

The time rate of change of  $V$  at a point is equal to the total rate upstream at which the volume is increasing, which is  $\int^x i dx'$ , minus  $Q$ , the volume rate which is passing the point  $x$  and hence being no longer upstream. Hence,

$$Q = -\frac{\partial V}{\partial t} + \int^x i(x') dx' . \quad (38)$$

Substituting these expressions for  $A$  and  $Q$  into the volume conservation equation (30a):

$$\frac{\partial}{\partial t} \left( \frac{\partial V}{\partial x} \right) + \frac{\partial}{\partial x} \left( -\frac{\partial V}{\partial t} - \int^x i(x') dx' \right) = i ,$$

and evaluating the left side we see that the equation is satisfied identically, which the total volume of fluid should do. We have one quantity  $V$  instead of two,  $A$  and  $Q$ , and now we have only the momentum equation to satisfy. Equation (30b) becomes, using the resistance formulation in terms of  $Q_r$ , and after taking all terms to the left side

$$\frac{\partial^2 V}{\partial t^2} + 2\beta \frac{Q}{A} \frac{\partial^2 V}{\partial x \partial t} + \left( \beta \frac{Q^2}{A^2} - \frac{gA}{B(A)} \right) \frac{\partial^2 V}{\partial x^2} + gA\tilde{S} \left( 1 - \left( -\frac{\partial V / \partial t}{Q_r(A)} \right)^2 \right) = 0 , \quad (39)$$

where for notational simplicity, symbols  $Q$  and  $A$  have been retained in coefficients of derivatives, and for conciseness the resistance term has been shown in terms of the usual unidirectional flow result  $Q^2$  rather than  $Q|Q|$ . The momentum equation has

become a second-order partial differential equation in terms of the single variable  $V$ . It could be used for flood routing and wave propagation studies, but as it is a second-order equation, in computations one would probably proceed by introducing an intermediate variable  $\partial V/\partial t$ , which is the reverse of the direction from which we have come. The equation is probably more useful in theoretical works and where approximations can be made, as we now do.

## 7.2 *The Telegraph Equation and the Nature of Long Wave Propagation*

The momentum equation (39) is linearised by considering relatively small disturbances about a uniform flow with area  $A_0$  and discharge  $Q_0$ . We substitute the series

$$V = A_0x - Q_0t + \varepsilon v, \quad A = A_0 + \varepsilon v_x, \quad Q = Q_0 - \varepsilon v_t, \quad \text{and} \quad Q_r(A) = Q_0 + Q'_r(A) \varepsilon v_x,$$

where  $\varepsilon v$  is a disturbance volume in which  $\varepsilon$  is a small quantity,  $v_t = \partial v/\partial t$ ,  $v_x = \partial v/\partial x$ , and  $Q'_r(A) = dQ_r/dA|_{A_0}$ . Performing power series operations to order  $\varepsilon$ , and taking the coefficient of  $\varepsilon$  we obtain the linearised momentum equation, a *Telegraph equation*:

$$\sigma_0 \left( \frac{\partial v}{\partial t} + c_0 \frac{\partial v}{\partial x} \right) + \frac{\partial^2 v}{\partial t^2} + 2\beta U_0 \frac{\partial^2 v}{\partial x \partial t} - (C_0^2 - \beta^2 U_0^2) \frac{\partial^2 v}{\partial x^2} = 0, \quad (40)$$

where:

$\sigma_0$ —Resistance parameter/Inverse time scale:

$$\sigma_0 = \frac{2gA_0S_0}{Q_0} = 2 \frac{gS_0}{U_0}, \quad (41)$$

which is simply the derivative of the resistance term with respect to  $Q$  evaluated for the underlying uniform flow. The resistance term in the momentum equation (30b) has magnitude  $\Omega Q^2$ , the derivative is  $2\Omega Q$ , giving  $\sigma_0 = 2\Omega_0 Q_0$  for the uniform flow. However for that flow with gravity and resistance terms balancing, we have  $\Omega_0 Q_0^2 = gA_0 S_0$ . Using this to obtain  $\Omega_0$  gives the result for  $\sigma_0$  in (41). For our purposes this is simple and satisfactory, but we could substitute for  $Q_0$  in terms of other channel parameters. We could argue by a rough electrical analogy that the resistance term in the momentum equation is equivalent to potential difference or voltage, while discharge  $Q$  is equivalent to current, so that  $\sigma_0$  can be thought of as a *resistance parameter* in our nonlinear case. It will be found below that as an inverse time scale, it is actually an important channel parameter, determining the nature of wave behaviour and computational solution properties.

$c_0$ —wave speed:  $c_0 = dQ_r/dA|_0$ , which is a well-known general result, but where  $c_0$  has been known as the kinematic wave speed. We will see that it is actually the speed of waves that are very long and no “kinematic” approximation has been made. Substituting the Chézy-Weisbach and Gauckler-Manning expressions from Eq. (26) for  $Q_r$  into this we obtain

$$c_0 = \begin{cases} dQ_r/dA|_0, & \text{General expression ;} \\ \frac{3}{2}U_0 \left(1 - \frac{1}{3}A_0P'_0/P_0\right), & \text{ChézyWeisbach ;} \\ \frac{5}{3}U_0 \left(1 - \frac{2}{5}A_0P'_0/P_0\right), & \text{Gauckler-Manning .} \end{cases}$$

$U_0$ —mean fluid velocity:  $U_0 = Q_0/A_0$ .

$C_0$ —the speed of not-so-long waves:

$$C_0 = \sqrt{gA_0/B_0 + (\beta^2 - \beta) U_0^2} .$$

In most textbooks this is written, not unreasonably, with  $\beta = 1$  such that  $C_0 = \sqrt{gA_0/B_0}$ , which is usually said to be the “long wave speed” or “dynamic wave speed”. Below it will be shown that, in paradoxical contradiction to its traditional names, it is actually the speed of waves only in the limit of shorter waves, short in terms of the time scale of our resistance-determined quantity  $\sigma_0$ , but still long enough that the hydrostatic approximation holds. We call these “not-so-long” waves. They occur when waves are due to rapid gate movements, for example.

We now obtain some simple solutions to the Telegraph equation (40) in two limits, and briefly consider the general case.

### Very long waves

For disturbances that have a very long time scale, such that  $\partial^2/\partial t^2 \ll \sigma_0\partial/\partial t$ , which we will call “very long waves”, the last three terms in (40) can be neglected, and the equation becomes the advection equation

$$\frac{\partial v}{\partial t} + c_0 \frac{\partial v}{\partial x} = 0 ,$$

with a general solution  $v = f_1(x - c_0t)$ , where  $f_1(\cdot)$  is an arbitrary function given by the upstream conditions, and which is a wave propagating downstream at speed  $c_0$ . The equation has been widely known as the “kinematic wave equation” and  $c_0$  the “kinematic wave speed”, because the approximation has previously been believed to be such that terms of order  $F^2$  in the momentum equation have been neglected. Here the only approximation has been that the wave period is long. No approximation has been made by neglecting dynamical terms. A better name is the *Very Long Wave Equation*, VLWE.

### Not-so-long waves

In the other limit, for disturbances which are shorter, such that  $\partial^2/\partial t^2 \gg \sigma_0 \partial/\partial t$ , for which we use the term “not-so-long” waves, (40) becomes

$$\frac{\partial^2 v}{\partial t^2} + 2\beta U_0 \frac{\partial^2 v}{\partial x \partial t} - (C_0^2 - \beta^2 U_0^2) \frac{\partial^2 v}{\partial x^2} = 0,$$

which is a second-order wave equation with solutions

$$v = f_{21}(x - (\beta U_0 + C_0)t) + f_{22}(x - (\beta U_0 - C_0)t),$$

where  $f_{21}(\cdot)$  and  $f_{22}(\cdot)$  are arbitrary functions determined by boundary conditions both upstream and downstream. In this case the solutions are waves propagating upstream and downstream at velocities of  $\beta U_0 \pm C_0$ , such that in the usual terminology  $C_0$  is the “long wave speed”, and the waves travel relative to an advection velocity  $\beta U_0$ , where the presence of  $\beta$  is slightly surprising. This shows that  $C_0$  is the speed of waves that are actually not so long, apparently paradoxically—they are long enough that the pressure distribution in the fluid is still hydrostatic, but they are short in terms of time scales given by the resistance characteristics.

### Intermediate period waves

In the general case, solutions of the long wave equations, as shown by the general linear approximation of (40) show wave propagation characteristics, velocity and rate of decay, that depend on the period of the waves, so that the waves are actually diffusive and dispersive. There is no such thing as “a long wave speed”. One can obtain solutions for the propagation behaviour in terms of wave period, but the operations are not particularly small or simple, and they are not included here. The widespread belief is wrong, that all waves obeying the long wave equations travel at a speed  $C \approx \sqrt{gA/B}$ . The behaviour is much more complicated.

## 7.3 Non-dimensional Long Wave Equations and the Nature of Approximations

Here we examine the nature of the long wave equations in a different light, by scaling them without linearising, and extracting what terms are important and the conditions for that. The results obtained here are complementary to the previous ones obtained from the Telegraph equation.

Consider Eqs. (30a) and (30b) in terms of  $A$  and  $Q$ . We introduce dimensionless quantities denoted by asterisks, such that the independent variables are written  $t = t_* T$  and  $x = x_* L$ , where  $T$  and  $L$  are time and length scales respectively. The dependent variables are scaled as  $A = A_* A_0$  and  $Q = Q_* U_0 A_0$ , where  $A_0$  is a cross-sectional area scale and  $U_0$  is the scale of the mean velocity in a steady uniform reference flow, and all subsequent quantities with subscript 0 are those of that flow. For channel width we use the width scale  $B_0$  such that  $B = B_* B_0$ , and for the perime-

ter we write  $P = P_* P_0$ , in terms of a perimeter scale  $P_0$ , which could well be the same as  $B_0$  but it gives a simpler result if we use a different symbol. The quantity  $Q_r$ , the uniform flow for a given cross-sectional area (or the rating curve flow) is written as  $Q_r = Q_{r*} U_0 A_0$ . In addition we write the channel slope as  $\bar{S} = S_* S_0$  even though it is already dimensionless. The equations become, where all starred (\*) quantities have a scale of order 1:

$$\frac{\partial A_*}{\partial t_*} + \frac{U_0 T}{L} \frac{\partial Q_*}{\partial x_*} = 0, \quad (42a)$$

$$\frac{U_0}{g S_0 T} \left( \frac{\partial Q_*}{\partial t_*} + \frac{U_0 T}{L} \frac{\partial}{\partial x_*} \left( \frac{\beta Q_*^2}{A_*} \right) \right) + \frac{A_0/B_0}{S_0 L} \frac{A_*}{B_*} \frac{\partial A_*}{\partial x_*} + A_* S_* \left( \frac{Q_*^2}{Q_{r*}^2} - 1 \right) = 0. \quad (42b)$$

The traditional approach has been to assume that the wavelength  $L$  is fundamental and that the wave period  $T$  is determined by the mean fluid velocity, such that  $T = L/U_0$ . There are two problems with this. The first is that the wave speed connecting  $T$  and  $L$  is not necessarily proportional to  $U_0$ ; in the case of not-so-long waves above it is determined more by  $C_0 = \sqrt{gA_0/B_0}$ , often in the past believed to be the speed at which all long waves propagate. The second problem is caused by the presumption that  $L$  is an important length scale leading to the setting of  $T = L/U_0$  in the coefficient in front of the first two terms bracketed, the first row of (42b). In that case the coefficient becomes  $U_0^2 / (gS_0L)$  and multiplying through, it can be written in terms of the Froude number  $F_0^2 = U_0^2 / (gA_0/B_0)$ . The conclusion drawn from this has been that ignoring the terms in brackets in the first row is a small Froude number approximation. Hence, the equation with the remaining terms has been called the “kinematic” or “low inertia” approximation.

Here it is asserted that the important quantity is not  $L$ , but the time scale  $T$  of disturbances which are imposed on the stream from outside such as that of a flood hydrograph or gate movements. The lengths of waves in the channel are merely a response to that. To see this, consider a problem where a boundary condition can be written as a function  $F(t/T)$ , where  $T$  is the time scale. Now any wave motion in the channel with a propagation velocity of  $c$ , whether this is the very long wave speed  $c_0$  or the  $\beta U_0 \pm C_0$  of not-so-long waves or any other value, to be called a travelling wave it must, partially at least, contain a function of  $x - ct$ , or in the present context,  $t - x/c$ . As this solution should satisfy the inflow boundary condition  $F(t/T)$ , the wave must have a solution looking like  $F(t/T - x/cT)$  everywhere in the channel. The  $x$  scale of motion is then  $L = cT$ , determined by the propagation speed. More important is the fact that everywhere in the stream, time variation is like  $t/T$ , determined by the boundary condition as we hypothesised.

Here, taking  $T$  as fundamental, if the first terms of the momentum equation (42b) are neglected, it is the coefficient  $U_0 / (gS_0T)$  which must be small. This can be expressed simply using a result obtained above in (41) for the definition of  $\sigma_0$ ; the coefficient becomes simply  $2 / (\sigma_0 T)$  and Eq. (42b) becomes

$$\frac{2}{\sigma_0 T} \left( \frac{\partial Q_*}{\partial t_*} + \frac{U_0 T}{L} \frac{\partial}{\partial x_*} \left( \frac{\beta Q_*^2}{A_*} \right) \right) + \frac{A_0/B_0}{S_0 L} \frac{A_*}{B_*} \frac{\partial A_*}{\partial x_*} + A_* S_* \left( \frac{Q_*^2}{Q_{r*}^2} - 1 \right) = 0. \quad (43)$$

Hence we have shown that the common approximation of neglecting the time derivative and fluid inertia terms, those in the brackets in the first row of (42b) and termed the “kinematic approximation” is not a low inertia approximation for  $F_0^2$  small, but is actually valid when  $\sigma_0 T$  is large, as we already showed in Sect. 7.2. Again we have shown that the well-known approximation of neglecting the time derivative and fluid inertia terms in the equation is actually a *slow change approximation*, expressing the behaviour in time brought about by boundary conditions.

For upstream propagation problems where a downstream boundary condition changes, such as tides in the sea, water levels in a reservoir, or downstream gate operations, then the wave velocity is negative, and both it and the wavelength can become small if the waves struggle against the current. This means that  $U_0 T/L$  in (43) becomes large and the fluid momentum term can no longer be neglected. For the moment we change our terminology and suggest the nomenclature for the approximation to the momentum equation as the *slow-change-and-for-upstream-propagation-slow-flow* approximation, simplified to *slow-change/slow flow approximation*.

## 8 The Slow-Change Nonlinear Routing Equation

A fully-nonlinear advection-diffusion routing equation will now be obtained based on the approximation that boundary condition changes are sufficiently slow, satisfied by most flood propagation problems. As a single equation in a single unknown it is conceptually simple. It has been found to have some advantages for starting flows in irrigation ditches. However, an evaluation concludes that usually one may as well use finite difference solutions of the long wave equations.

### 8.1 Derivation of the Equation

Now making the approximation that has just been described, the non-dimensional equation (43) for very long period waves such that  $2/\sigma_0 T$  is small becomes

$$\frac{A_0/B_0}{S_0 L} \frac{A_*}{B_*} \frac{\partial A_*}{\partial x_*} + A_* S_* \left( \frac{Q_*^2}{Q_{r*}^2} - 1 \right) = 0. \quad (44)$$

As all starred quantities have a magnitude of 1, the importance of the first term is measured by the depth/drop quantity  $(A_0/B_0)/(S_0 L)$ , where  $A_0/B_0$  is the mean depth and  $S_0 L$  is the amount by which the bed drops in a wavelength. For steeper streams where the water is not deep, the term is small, and the only important terms in

the momentum equation are the gravity and resistance terms, combined with brackets as shown.

Returning to the physical equation (30b) in  $(A, Q)$  but using (44) to suggest retaining just the corresponding last three terms, for sufficiently long waves the momentum equation becomes:

$$\frac{1}{B} \frac{\partial A}{\partial x} = \tilde{S} \left( 1 - \frac{Q|Q|}{Q_r^2} \right).$$

We will now consider only unidirectional flow, such that  $Q$  is not negative, ruling out disturbances created by downstream boundary changes. Replacing  $Q|Q|$  by  $Q^2$  and solving for  $Q$  the momentum equation becomes:

$$Q = Q_r \sqrt{1 - \frac{1}{\tilde{S}B} \frac{\partial A}{\partial x}}. \quad (45)$$

Then, substituting into the mass conservation equation (30a),  $\partial A/\partial t + \partial Q/\partial x = i$ , we obtain

$$\frac{\partial A}{\partial t} + \frac{\partial}{\partial x} \left( Q_r(A) \sqrt{1 - \frac{1}{\tilde{S}B(A)} \frac{\partial A}{\partial x}} \right) = i, \quad (46)$$

an equation with just  $A$  as dependent variable. This could be used for numerical simulation, but it has two problems. First, performing the differentiation with respect to  $x$  would give a rather more complicated equation. Second, and a more difficult problem, is that upstream boundary conditions are often where  $Q$ , and not  $A$ , is given as a function of time.

Those problems are avoided by using Upstream Volume  $V$  as defined in Eqs. (37) and (38). The mass conservation equation is identically satisfied, as already shown, while the simplified momentum equation (45) gives the single equation in the single dependent variable  $V$ , where both breadth  $B$  and  $Q_r$  can be written as functions of area  $A = \partial V/\partial x = V_x$ , to give

$$\frac{\partial V}{\partial t} + Q_r(V_x) \sqrt{1 - \frac{1}{\tilde{S}B(V_x)} \frac{\partial^2 V}{\partial x^2}} = 0. \quad (47)$$

The only approximation relative to the long wave equations has been that the variation with time is slow, such that  $\sigma_0 T$  is large. The equation is a fully nonlinear advection-diffusion equation. Its nature as an advection equation is clear, if one recognises that the term  $Q_r(V_x)$  when evaluated using the Chézy-Weisbachor Gauckler-Manning formulae, Eq. (26), contains  $V_x = \partial V/\partial x$  raised to a power greater than one, such that it is a nonlinear advection term. Its nature as a nonlinear diffusion equation comes from the second derivative term under the square root.

For numerical solution, boundary conditions involving  $Q$  and  $\eta$  and their derivatives can be incorporated, using (37) and (38) and the geometrical relationship be-

tween  $A$  and  $\eta$  at a point. The apparent difference between the right sides of (46) and (47) is not inconsistent, the inflow  $i$  in the first is included with the time derivative on the left of the second (see Eq. 38).

Equation (47) has been used by Soroush et al. (2013) to simulate flows in irrigation ditches. They suggested the name *Slow-change routing equation* for waves moving downstream. In that work it had some advantages in treating starting flows with an infinitesimal starting depth, when the long wave equations would have had problems. However, for stability it was found that it was better to use implicit numerical schemes.

If (47) is linearised as we did more generally in Sect. 7.2, the well-known advection-diffusion approximation is simply obtained:

$$\frac{\partial v}{\partial t} + c_0 \frac{\partial v}{\partial x} - \frac{Q_0}{2B_0 S_0} \frac{\partial^2 v}{\partial x^2} = 0. \quad (48)$$

Fenton (2015, §1.5.3) showed that this advection-diffusion equation was a good model for the Telegraph equation over a wide range of wave periods such that  $\sigma_0 T \gtrsim 20$ . The criterion is easily satisfied for most flood propagation problems. As no magnitude approximations have been made, this means that the fully-nonlinear equation (47) should also be a good approximation to the fully-nonlinear long wave equations also for wave periods satisfying the condition.

## 8.2 A Computational Example

Figure 16 shows results from the slow-change routing equation for two different boundary resistances, Manning's  $n = 0.015$  for a smooth artificial boundary and  $n = 0.050$  for a natural boundary. The channel was rectangular with no resistance on the sides, with an initial discharge per unit width of  $q = 1 \text{ m}^2 \text{ s}^{-1}$  rising to  $10 \text{ m}^2 \text{ s}^{-1}$ . The channel slope was  $S = 0.0005$  and the length was 50 km, the hydrographs being for the outflow at the end.

The aim was to demonstrate the accuracy of the slow-change routing equation, even for finite Froude numbers, and that it really is a slow-change approximation: the Froude number of the initial flow for the first case was the finite value of  $F_0 = 0.46$ , and for the more natural boundary was the small value of  $F_0 = 0.15$ .

The value of  $\sigma_0 T$  was the same in both cases. Using the calculated value of  $\sigma_0 \approx 0.016 \text{ s}^{-1}$ , and choosing a value of  $T = 12 \text{ h}$ , the time of rise of the flood wave, gives  $\sigma_0 T \approx 700$ , certainly large enough for the flood wave to be considered a very long wave, given the suggestion above that waves could be considered to be very long for  $\sigma_0 T > 20$ .

The figure shows how the approximate method seems to work for the Froude numbers considered here. In our zeal to show this, the choice of a smooth channel with  $n = 0.015$  has given results showing that steepening of the flood wave has occurred, rising rather more quickly at 50 km than at the input, and such that an oscillation near



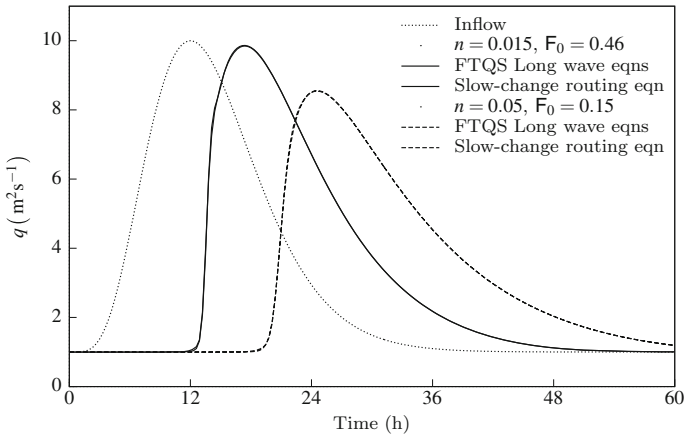


**Fig. 16** Comparison of results from the slow-change routing equation and the long wave equations, both using Forward-Time-Quadratic-Space approximation including at the downstream open boundary. Where results are coincident the same line type has been used

the crest can be seen. For this case we would not be able to use the present equations much further down the channel, as a bore is forming, which our equations cannot describe.

### 8.3 Evaluation and Comparison

- The nonlinear slow-change routing equation (47) is conceptually slightly simpler than the two long wave equations.
- It has the advantages of the  $(A, Q)$  formulation of the long wave equations, that relatively little detailed bathymetry knowledge is necessary. Both forms, the long wave equations and the routing equation require knowledge of the same quantities: resistance in the form of  $Q_r(A)$ , slope  $\tilde{S}$ , and surface breadth  $B(A)$ .
- The single equation has been found to be better for studying starting flows in irrigation canals, however implicit numerical methods were necessary. All advection-diffusion equations can have demanding stability criteria for explicit finite difference methods.

To conclude, the nonlinear slow-change routing equation, a single equation in a single unknown, is an interesting alternative, but has few advantages over the use of the FTQS scheme for the long wave equations. They and the numerical scheme are actually quite simple and have no slow-change limitation as does the routing equation. On balance, they are to be preferred.

## 9 Steady Flow and the Gradually-Varied Flow Equation (GVFE)

One of the most common computational tasks in river and canal engineering is to calculate the free surface elevation along a steadily flowing stream. The problem is simply that of the solution of a first-order differential equation but that is often obscured in writings on the subject. In this part, first an alternative approach is suggested, using cross-sectional area as the dependent variable. That requires little knowledge of the details of the underwater topography. The conventional use of GVFEs in terms of water depth is then described. A review of traditional textbook methods finds the situation unsatisfactory. Of the two usual methods presented, the “Standard Step” method is unnecessarily complicated and the “Direct Step” method is incorrect. Application of the simplest explicit numerical methods is described. Other than the method mentioned above using area, for non-prismatic streams all require much data. Often that is not available. An approximate linearised model of flow in a river is made in which it is possible to obtain an explicit general solution for arbitrary variation of slope and resistance parameters. This gives us insight into the nature of the problem, as well as giving simple approximate answers.

### 9.1 The Differential Equations

#### 9.1.1 Use of Area $A$ and Application to Streams of Unknown Bathymetry

For steady flow where  $Q$  is constant so that  $\partial Q/\partial t$  and  $\partial Q/\partial x$  are zero, the long wave momentum equation (30b) in terms of cross-sectional area  $A$ , gives one version of the GVFE:

$$\frac{dA}{dx} = B \frac{\tilde{S} - Q^2/K^2}{1 - \beta F^2}. \quad (49)$$

In the resistance term we have introduced another symbol  $K$ , the *conveyance*, which is a function of section properties and makes the presentation simpler;  $K$  is related to quantities introduced above for the resistance term, in the form in which it almost everywhere appears here,  $1/K^2$ , as

$$\frac{1}{K^2} = \frac{\Omega}{gA} = \frac{\tilde{S}}{Q_r^2} = \frac{\Lambda P}{gA^3} = \frac{n^2 P^{4/3}}{A^{10/3}}. \quad (50)$$

The conveyance  $K$  has the property that  $Q_r = K\sqrt{\tilde{S}}$  and in the Chézy-Weisbach and Gauckler-Manning flow formulae it contains the resistance coefficient and dependence on area and perimeter as shown.

The ordinary differential equation (49) is valid also for non-prismatic channels, being written in terms of the mean bed slope at a section  $\tilde{S}$ , which can be evaluated from (28). The slope is, however, usually poorly known and is often just estimated, like the other parameters of the problem;  $\beta$  might be something like 1.1. The resistance coefficients in the Chézy-Weisbach and Gauckler-Manning flow formulae used for  $1/K^2$  from (50) are also usually poorly known. More accurate would be the case where a rating curve has been determined.

In the differential equation there are strongly-varying functions of the dependent variable itself,  $A^3$  and possibly  $A^{10/3}$ , plus the usually slowly-varying functions  $B(A)$  and  $P(A)$ . This suggests that using the GVFE in terms of  $A$  has an important advantage: one needs few details of the under-water topography. It is not necessary to know the precise details of the underwater bathymetry other than those weakly-varying functions, for which the obvious approximation could be made that they are constant and equal; river width often does not vary much.

To start numerical solution, one would need to know the area at a control where surface elevation might be known. The solution in terms of area might be enough, to give an idea of how far upstream the effects of a structure or channel changes extend. It is surprising that we can do so much with so little information. However, if one needed a value of surface elevation  $\eta$  at a certain value of  $x$ , one would then need cross-sectional details there to go from the computed  $A$  to  $\eta$ .

### 9.1.2 Customary Use of a Quantity $h$ Called the “Water Depth”

The long wave momentum equation (29b) in terms of surface elevation  $\eta$ , for  $Q$  constant so that  $\partial Q/\partial t$  and  $\partial Q/\partial x$  are zero and  $Q/|Q| = Q^2$ , gives another version of the GVFE:

$$\frac{d\eta}{dx} = \frac{\tilde{S}\beta F^2 - Q^2/K^2}{1 - \beta F^2}. \quad (51)$$

On the right side of the differential equation, the geometric quantities  $A$  and  $P$  would need to be known as a function of the local elevation  $\eta$  along the channel for this differential equation to be solved. That is possible, but in no textbook is it suggested. Instead, prismatic sections with a well-defined invert are used and the problem posed in terms of  $h$ , the *maximum* depth at any section. For irregular bathymetry the concept of  $h$  becomes vague indeed and is rarely addressed, although it must be in commercial software.

Here we introduce a longitudinal axis with elevation  $Z_0(x)$  and a depth-like quantity  $h = \eta - Z_0$ . Of course, in prismatic channels we would choose the axis to be on the invert of the channel, as in textbooks.

As the use of  $h$  seems to be standard, however, we will now present a number of results for that, criticising and correcting numerical methods used in textbooks, and pointing out the fact, known to some textbook authors, that any simple standard method for the numerical solution of ordinary differential equations can be used.

The GVFE (51) becomes

$$\frac{dh}{dx} = \frac{S_0 + \beta (\tilde{S} - S_0) F^2 - Q^2/K^2}{1 - \beta F^2},$$

where  $S_0 = -dZ_0/dx$ , the slope of the reference axis, positive downwards. We almost never know the details of  $\tilde{S}$  so here we assume that  $\tilde{S} = S_0$ , which we now write as  $S$ , giving

$$\frac{dh}{dx} = \frac{S - Q^2/K^2}{1 - \beta F^2}, \tag{52}$$

where in general both  $K$  and  $F$  are functions of both  $x$  and  $h$ , while in a prismatic channel, they are functions just of  $h$ . This is the form usually presented in textbooks. It is a differential equation of first order, and to obtain numerical solutions it is necessary to have a boundary condition  $h = h_0$  at a certain  $x = x_0$ , which will be provided by a control.

### 9.2 Traditional Numerical Methods

Here we present the two “step” methods as they are given in textbooks. Both use the energy formulation, for which the derivation is remarkably simple. The first uses a complicated implicit method of solution which must have confused and troubled many students. The second is an inconsistent approximation and is not accurate.

The almost trivial energy derivation, ignoring non-prismatic effects, is that the rate of change of total head  $H$  is given by the empirical expression for the energy gradient

$$\frac{dH}{dx} = -\frac{Q^2}{K^2(x, h)}. \tag{53}$$

The total head  $H$  is given as a function of position  $x$  and depth  $h$  by

$$H = Z_0(x) + h + \alpha \frac{Q^2}{2gA^2(x, h)}, \tag{54}$$

using symbols as above, but where  $\alpha$  here is a Coriolis energy coefficient.

**“Standard step” method—depth calculated from distance:** The differential equation given by Eqs. (53) and (54) is approximated over an interval in  $x$  by a forward difference expression for the derivative on the left and the *mean* of the resistance term on the right at beginning and end of the interval:

$$\frac{H(x_{i+1}, h_{i+1}) - H(x_i, h_i)}{x_{i+1} - x_i} = -\frac{1}{2} \left( \frac{Q^2}{K^2(x_i, h_i)} + \frac{Q^2}{K^2(x_{i+1}, h_{i+1})} \right). \tag{55}$$

For the common case of subcritical flow, one would probably use a convention that  $i$  increases upstream, such that  $x_{i+1} - x_i$  is negative. The unknown  $h_{i+1}$  appears in two different nonlinear functions  $H$  and  $K$ , so that this is an *implicit* method, requiring numerical solution of a transcendental equation at each step. It is complicated, and one can imagine the clean-cut young male students of the pre-calculator and pre-computer 1950s and early 1960s, such as the author, having to work very hard on their slide rules to apply the method to problems like Example 10-9 of Chow (1959, p. 267) and then probably using trial and error rather than a systematic approach. Although the method is accurate and stable, and suitable for commercial software, the author considers it far too complicated for teaching and everyday purposes. Over the years it has caused many unnecessary hours of human effort.

**“Direct step” method—distance calculated from depth:** This is applied by taking steps in the water depth and calculating the corresponding step in  $x$ . It has some advantages, in that iterative methods are not necessary, unlike the Standard step method. Practical disadvantages are such that it is applicable only to prismatic sections, results are not obtained at specified points in  $x$ , and as uniform flow is approached the steps become infinitely large.

We will show that it contains an error which means that the traditional version is not accurate, despite claims. A corrected version is obtained here, but is not recommended for teaching or practice.

We introduce the “specific head”, that relative to the local channel bottom, denoted here by  $H_0$ :

$$H_0(h) = H(h) - Z_0.$$

Using this in the differential equation (53) and inverting each side:

$$\frac{dx}{dH_0} = \frac{1}{S - Q^2/K^2}. \quad (56)$$

The differential equation is now approximated, the left side by a finite difference expression  $(x_{i+1} - x_i) / (H_{0,i+1} - H_{0,i})$ . For the right side the Direct step method as set out in textbooks is to take the mean of the denominator at beginning and end points, and so to write

$$x_{i+1} = x_i + \frac{H_{0,i+1} - H_{0,i}}{\frac{1}{2}(S_i - Q^2/K_i^2) + \frac{1}{2}(S_{i+1} - Q^2/K_{i+1}^2)}. \quad (57)$$

Steps are taken in  $h_i$ , the corresponding  $H_0$  calculated, and the  $x_i$  found. While this is a plausible approximation, it is not mathematically consistent and hence not accurate. What should be done is not to take the mean of just the denominator of the right side of the differential equation (56) at beginning and end points, but to use the mean value of the whole right side there. This is Heun’s method as presented in (14), which leads to the scheme

$$x_{i+1} = x_i + \frac{H_{0,i+1} - H_{0,i}}{2} \left( \frac{1}{S_i - Q^2/K_i^2} + \frac{1}{S_{i+1} - Q^2/K_{i+1}^2} \right). \quad (58)$$

The accuracy of these two direct step methods, original and corrected, will be compared with others below. The original will be found to be quite defective.

### 9.3 Using Standard Numerical Methods for Differential Equations

Here the methods are presented where the dependent variable is the maximum depth  $h$  as favoured by textbooks, here using Eq. (52). If one were to use the area  $A$  with GVFE (49), corresponding numerical schemes could be simply written down.

**Euler's method:** The simplest scheme to advance the solution from  $(x_i, h_i)$  to  $(x_{i+1}, h_{i+1})$  is, using (13):

$$h_{i+1} = h_i + (x_{i+1} - x_i) \frac{S_i - Q^2/K^2(x_i, h_i)}{1 - \beta F^2(x_i, h_i)}. \quad (59)$$

The expression here, and throughout other equations following, is general, whether the convention is chosen that  $i$  increases upstream or downstream. Euler's method is the simplest method. It is of first-order accuracy, yet it might be appropriate for open channel problems where quantities may only be known approximately. One can use simple modifications such as Heun's method to gain better accuracy, or use Richardson extrapolation—or even more simply, just take smaller steps in  $x$ .

**Heun's method:** The scheme of (14) becomes:

$$h_{i+1}^* = h_i + (x_{i+1} - x_i) \frac{S_i - Q^2/K^2(x_i, h_i)}{1 - \beta F^2(x_i, h_i)}, \quad (60a)$$

$$h_{i+1} = h_i + \frac{x_{i+1} - x_i}{2} \left( \frac{S_i - Q^2/K^2(x_i, h_i)}{1 - \beta F^2(x_i, h_i)} + \frac{S_{i+1} - Q^2/K^2(x_{i+1}, h_{i+1}^*)}{1 - \beta F^2(x_{i+1}, h_{i+1}^*)} \right). \quad (60b)$$

It is second-order accurate.

Often hydraulics textbooks do not present these two methods as alternatives, yet they are simple and flexible, and reveal the nature of what we are doing. The step in  $x$  can be varied at will, to suit possible irregularly spaced cross-sectional data.

**Predictor-corrector method–Trapezoidal method:** This is simply an iteration of the last method, whereby the step in (60b) is repeated several times, at each stage setting  $h_{i+1}^*$  equal to the updated value of  $h_{i+1}$ . This gives a highly accurate method.

**Higher-order methods:** One of the aims here has been to emphasise that all that is being done is to solve a differential equation numerically, and any method can be

used. There are sophisticated methods such as high-order Runge-Kutta and predictor-corrector methods. However, in the case of open channel hydraulics there will usually be some variation of parameters along the channel that such sophistication is unnecessary.

## 9.4 Comparison of Schemes

To compare the performance of the various numerical schemes, Example 10-1 of Chow (1959, p. 250) was solved using each. All quantities specified by Chow were converted to *SI* units and rounded to the numbers shown here: a flow of  $11.33 \text{ m}^3 \text{ s}^{-1}$  passes down a trapezoidal channel of gradient  $S = 0.0016$ , bed width 6.10 m and channel side slopes  $H:V = 2$ ,  $g = 9.8 \text{ m s}^{-2}$ , the quantity  $\alpha$  or  $\beta = 1.1$ , and Manning’s  $n = 0.025$ . At  $x = 0$  the flow is backed up to a depth of 1.524 m, and the backwater curve was computed for 1000 m. Some results from three schemes for the water surface profile are shown in Fig. 17, with relatively few computational steps for each scheme giving coarse spacing such that the finite errors can be seen. The symbol  $\Delta x$  is the magnitude of the constant point spacing. The solid line is from an accurate Runge-Kutta 4th order method. It is not recommended here as a method, however, as it makes use of information from three intermediate points at each step, which in non-prismatic channels is usually not available. The Euler scheme (59) was applied with two different step sizes, and then Richardson extrapolation (8) used to improve the results, which can be seen to be accurate. Several other methods were applied, and the results summarised in Fig. 18. It shows the errors of the various methods that have been described here, and how they vary with step size. The bases for comparison were the results from the Runge-Kutta 4th-order method. Euler’s method, (59), was the least accurate, as expected. As it is a first-order scheme, halving the step size halved the error. Then applying Richardson extrapolation, (8), gave the third most accurate of all the methods, more than enough for practical purposes. The most accurate of all were the Standard step method and the Trapezoidal method, namely using Heun’s method, (60a), and iterating the second step, (60b). It is clear that there is something wrong with the conventional Direct step method (57) as we have suggested, while the corrected scheme (58) is highly accurate. In any case, calculating results for  $x$  seems to be a poor way of solving the problem. It was a good idea if one believed that the only alternative was the implicit standard step method. This has been emphasised here as not to be the case.

## 9.5 A Mathematical Model of Steady Flow in a River

Often the precise details of a stream are not known, and it is quite appropriate to make further modelling approximations. In addition, these might give us more insight and understanding of the problem. Now a model is made where the GVFE is linearised

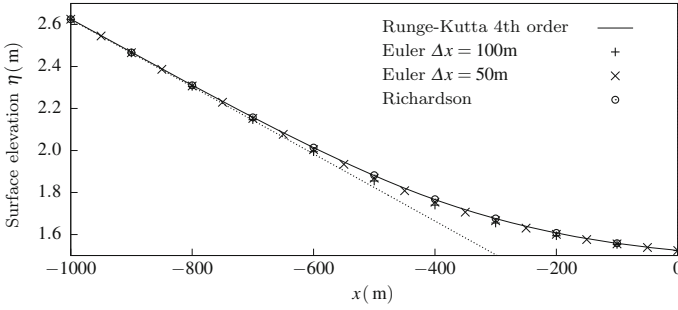


**Fig. 17** Backwater curve computed with various schemes; the dotted line is the surface for uniform flow

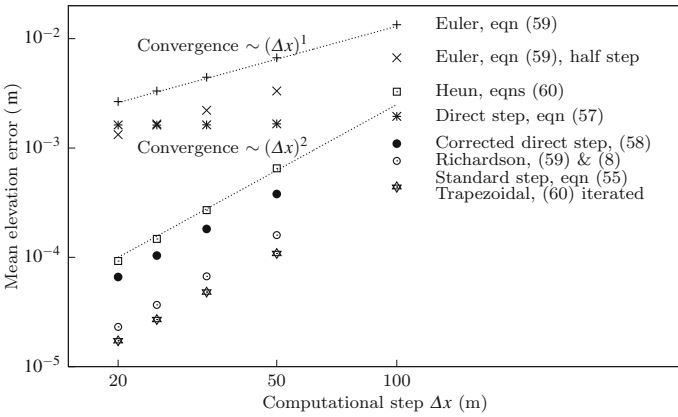


**Fig. 18** Convergence of numerical schemes for solving the GVFE—logarithmic axes

and a general solution obtained so that one can calculate an approximate solution for a whole stream if the variation in the resistance coefficient and geometry are known or can be estimated. The GVFE (52) is

$$\frac{dh}{dx} = \frac{S - Q^2/K^2(x, h)}{1 - \beta F^2(x, h)} .$$

We consider small perturbations about an underlying uniform flow of slope  $S_0$  and depth  $h_0$ , such that we write

$$h = h_0 + \varepsilon h_1(x) + \dots ,$$

where  $\varepsilon$  is a small quantity expressing the magnitude of deviations from uniform. Similarly we also let the possible non-constant slope be



$$S = S_0 + \varepsilon S_1(x) + \dots .$$

In a real stream varying along its length, both  $K$  and  $F$  are functions of  $x$  and  $h$ . We write  $K$  as the two-dimensional Taylor series to first order:

$$K = K_0 + \varepsilon K_1(x) + \varepsilon h_1(x) K_{h_0} + O(\varepsilon^2) ,$$

where  $K_1$  is a change caused by a change in the channel properties in  $x$ , whether the resistance coefficient or the cross-section, and  $K_{h_0} = dK/dh|_0$  expresses the change of conveyance with water depth. We also write

$$F^2 = F_0^2 + O(\varepsilon) + \dots ,$$

in which we will find that terms in  $\varepsilon$  are not necessary. Multiplying the differential equation through by  $1 - \beta F^2$ , substituting the Taylor series, expanding, using power series, setting  $dh_0/dx$  to zero for uniform flow, and neglecting terms in  $\varepsilon^2$ :

$$\varepsilon (1 - \beta F_0^2) \frac{dh_1(x)}{dx} = S_0 + \varepsilon S_1(x) - \frac{Q^2}{K_0^2} \left( 1 - 2\varepsilon \frac{K_1(x)}{K_0} - 2\varepsilon h_1(x) \frac{K_{h_0}}{K_0} \right) .$$

At zeroeth order  $\varepsilon^0$  we obtain

$$S_0 - Q^2/K_0^2 , \tag{61}$$

identically satisfied as  $Q = K_0 \sqrt{S_0}$ . At  $\varepsilon^1$ , we eliminate  $Q$  by using  $Q^2 = S_0 K_0^2$  but leave  $F_0^2$  as its significance is very clear and we know we will often be able to neglect it:

$$(1 - \beta F_0^2) \frac{dh_1}{dx} - 2S_0 \frac{K_{h_0}}{K_0} h_1 = S_1(x) + 2S_0 \frac{K_1(x)}{K_0} .$$

We write this linear differential equation as

$$\frac{dh_1}{dx} - \gamma h_1 = \phi(x) , \tag{62}$$

where  $\gamma$  is a constant:

$$\gamma = 2 \frac{S_0 K_{h_0}/K_0}{1 - \beta F_0^2} = \frac{S_0}{1 - \beta F_0^2} \times \begin{cases} 2 \frac{dK/dh|_0}{K_0}, & \text{General expression;} \\ 3 \frac{B_0}{A_0} - \frac{dP/dh|_0}{P_0}, & \text{Chézy - Weisbach;} \\ \frac{10}{3} \frac{B_0}{A_0} - \frac{4}{3} \frac{dP/dh|_0}{P_0}, & \text{Gauckler-Manning;} \end{cases} \tag{63}$$

assuming that neither resistance coefficient  $\Lambda$  nor  $n$  vary with depth, and using  $dA/dh|_0 = B_0$ . The forcing term on the right of (62) is

$$\phi(x) = \frac{S_0}{1 - \beta F_0^2} \left( \frac{S_1(x)}{S_0} + \frac{2K_1(x)}{K_0} \right), \tag{64}$$

expressed in terms of fractional changes in slope  $S$  and conveyance  $K$ .

**Solving the differential equation**

The differential equation (62) is in *integrating factor* form, and can be solved by multiplying both sides by  $e^{-\gamma x}$  and writing the result

$$\frac{d}{dx} (e^{-\gamma x} h_1) = e^{-\gamma x} \phi(x),$$

which can be integrated to give

$$h_1 = e^{\gamma x} \left( \int^x e^{-\gamma x'} \phi(x') dx' + \text{Constant} \right),$$

where  $x'$  is a dummy variable. Returning to physical variables,  $h = h_0 + \varepsilon h_1$  gives the solution

$$h = h_0 + H e^{\gamma x} + \int^x e^{\gamma(x-x')} \phi(x') dx'. \tag{65}$$

The part of the solution  $H e^{\gamma x}$  is that obtained by Samuels (1989), giving the solution for backwater level in a uniform channel by evaluating the constant of integration using a downstream boundary condition  $h = h_0 + H$  at  $x = 0$ . It shows how the surface decays upstream at a rate  $e^{\gamma x}$  as  $x$  becomes increasingly negative, because  $\gamma$  is positive.

For a wide channel, the second terms in  $dP/dh$  in (63) are unimportant (and are often not well known), so that  $A_0/B_0 \approx h_0$ , the channel depth, and for small Froude number this gives

$$\gamma \approx 3 \frac{S_0}{h_0}, \tag{66}$$

which is a very simple expression for us to estimate how far upstream backwater effects occur. It shows that the rate of exponential decay is small for gently sloping and deep streams and greatest for steep and shallow ones.

Consider the distance  $x_{1/2}$  upstream for the effect of a downstream surface elevation to diminish by a factor of 1/2. Then  $\exp(-\gamma x_{1/2}) = 1/2$ , or

$$x_{1/2} = \frac{\ln 2}{\gamma} \approx \frac{\ln 2}{3} \frac{h_0}{S_0} \approx 0.2 \frac{h_0}{S_0}, \tag{67}$$

and so for a gently-sloping river 2 m deep and  $S_0 = 10^{-4}$ , the effect of any backwater decreases by 1/2 in a distance of 4 km. To diminish to 1/16, say, the distance is 16 km. For a steeper river, say  $S_0 = 0.0016$  from the example in Fig. 17, where  $h_0 \approx 1$  m, the “half-length” is about 150 m. This is roughly in agreement with the computed results in Fig. 17. If the approximate exponential decay solution were shown on that figure, it would not agree closely with the computed results, because the checked-up disturbance is as large as 50% of the depth, when the linear solution is not accurate. The utility of the approximate solution lies in its ability to give a simple estimate and an appreciation of the quantities that affect the length of backwater.

In the more general solution here, (65), the integral expresses the effect of all downstream channel variations, expressed as a convolution integral of the disturbance function  $\phi$  and the exponential decay function with the same  $\gamma$ . Here we will neglect any boundary conditions and consider just the solution due to the forcing function  $\phi$  due to channel changes:

$$h = h_0 - \int_x^\infty e^{\gamma(x-x')} \phi(x') dx', \tag{68}$$

having reversed the order of integration and placed a minus sign in front. This shows that at our general point  $x$ , in subcritical flow, the disturbance is due to the integrated effects of the disturbance function  $\phi$  for all downstream points, from  $x$  to  $\infty$ .

*Example 6* The effect on a river of a finite length of greater resistance

Consider, as an example, a case where over a finite length  $L$  of river, the carrying capacity is reduced by the conveyance  $K$  decreasing by a relative amount  $K_1/K_0 = -\delta$ , such as by local deposition of material, between  $x = 0$  and  $x = L$ , and constant in that interval. Assume  $F_0^2$  negligible and the river wide. From (64) we have:

$$\phi(x) = \begin{cases} 0, & \text{if } x \leq 0; \\ -2S_0\delta, & \text{if } 0 \leq x \leq L; \\ 0, & \text{if } x \geq L. \end{cases}$$

- For  $x$  downstream,  $x \geq L$ ,  $\phi(x) = 0$ , and  $h = h_0$ , which is correct in this sub-critical flow, there are no downstream effects.
- For  $x$  in the section where the changes occur,  $0 \leq x \leq L$ , the solution is

$$h = h_0 + 2S_0\delta \int_x^L e^{\gamma(x-x')} dx' = h_0 + \frac{2S_0\delta}{\gamma} (1 - e^{\gamma(x-L)}). \tag{69}$$

- For  $x$  upstream,  $x \leq 0$ , where there is no extra resistance,

$$h = h_0 + 2S_0\delta e^{\gamma x} \int_0^L e^{-\gamma x'} dx' = h_0 + \frac{2S_0\delta}{\gamma} e^{\gamma x} (1 - e^{-\gamma L}). \tag{70}$$

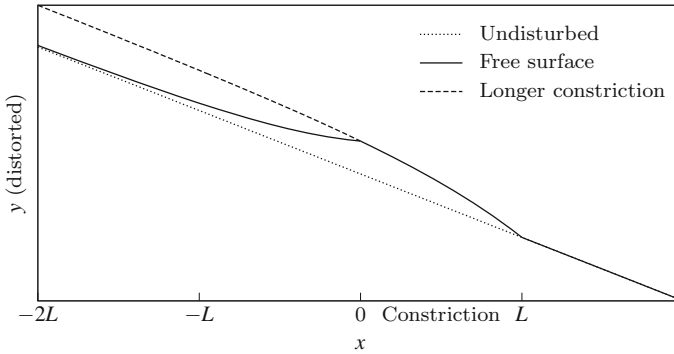


**Fig. 19** The effect of a finite length of increased resistance modelled by the approximate analytical solution to the GVFE

In the reach of increased resistance the surface is raised, as one expects and shows an exponential approach to the changed depth  $2S_0\delta/\gamma$  if  $L \rightarrow \infty$ . With no extra resistance further upstream, the surface then decays exponentially to  $h_0$ , as shown by (70).

These solutions are all shown in Fig. 19 with an arbitrary vertical scale such that the slope is exaggerated. The calculations were performed for  $S_0 = 0.0005$ ,  $h_0 = 1$  m, and with a constricted length of  $L = 1000$  m, with a 5% decrease in conveyance there, such that  $\delta = 0.05$ . Using these figures, and with  $\gamma = 3S_0/h_0$ , the computed backwater at the beginning of the constriction calculated according to (69) or (70) was 2.6 cm. The figure shows the nature of our mathematical approximation—if we consider going from downstream to upstream, immediately the section of greater resistance is encountered the surface starts to rise, making an exponentially decaying adjustment to the extra resistance, assuming that it will last for ever, as shown by the dashed line. When we enter the end of the extra resistance, it adjusts again with another exponential decay curve. The abrupt changes of gradient violate the physical assumptions of the long wave equations, but they and the model give us a clear picture of what happens, possibly obvious in retrospect, but hopefully of assistance.

## References

- Chow VT (1959) *Open-channel hydraulics*. McGraw-Hill, New York
- Conte SD, de Boor C (1980) *Elementary numerical analysis*, 3rd edn. McGraw-Hill Kogakusha, Tokyo
- Cunge JA, Holly FM, Verwey A (1980) *Practical aspects of computational river hydraulics*. Pitman, London
- de Boor C (2001) *A practical guide to splines*, revised edn. Springer, New York
- Fenton JD (2010) The long wave equations. Technical report, *Alternative Hydraulics Paper 1*. <http://johndfenton.com/Papers/01-The-long-wave-equations.pdf>

- Fenton JD (2014) Long waves in open channels—their nature, equations, approximations, and numerical simulation. In: Proceedings of the 19th IAHR-APD congress, Sept 2014, Hanoi, Vietnam
- Fenton JD (2015) Basic physical processes in rivers. In: Rowiński PM, Radecki-Pawlik A (eds) Rivers—physical, fluvial and environmental processes. Springer, chapter 1
- Fenton JD (2016) Hydraulics: science, knowledge, and culture. *J Hydraul Res* 54(5):485–501
- HEC-RAS (2010) HEC-RAS River Analysis System Hydraulic Reference Manual. Report CPD-69, Version 4.1, US Army Corps of Engineers, Institute for Water Resources, Hydrologic Engineering Center. <http://www.hec.usace.army.mil/software/hec-ras/documentation.aspx>
- Liggett JA, Cunge JA (1975) Numerical methods of solution of the unsteady flow equations. In: Mahmood K, Yevjevich V (eds) Unsteady flow in open channels, vol 1. Water Resources Publications, Fort Collins, chapter 4
- Samuels PG (1989) Backwater lengths in rivers. *Proc Inst Civ Eng, Part 2* 87:571–582
- Soroush F, Fenton JD, Mostafazadeh-Fard B, Mousavi SF, Abbasi F (2013) Simulation of furrow irrigation using the slow-change/slow-flow equation. *Agric Water Manag* 116:160–174. <https://doi.org/10.1016/j.agwat.2012.07.008>
- White FM (2009) Fluid mechanics, 7th edn. McGraw-Hill, New York
- Yen BC (2002) Open channel flow resistance. *J Hydraul Eng* 128(1):20–39

# Application of the AISA Hyperspectral Image for Verification of Sediment Transport Results Obtained from CCHE2D Hydrodynamic Model—Zegrze Reservoir Case Study, Poland

Artur Magnuszewski, Anita Sabat, Anna Jarocińska  
and Łukasz Sławik

**Abstract** Zegrze Reservoir was built on the Narew River and its tributary Bug River in the period 1957–1963. The hydraulic conditions at the Bug River mouth had been studied with the use of hydrodynamic two dimensional model CCHE2D. Distribution of the sediment transport was recorded by the AISA hyperspectral scanner and shown as a remote sensing index of Red Edge Normalized Difference Vegetation Index—NDVI<sub>705</sub> and Total Suspended Solids—TSS. Results of suspended sediments concentration from the CCHE2D model had been converted to a graphical (vector) form and compared with remote sensing indexes. Relationship between remote sensing indexes and CCHE2D model simulation results had been evaluated using statistical method of Spearman correlation.

## 1 Introduction

In the studies of large reservoirs we encounter the problem of water body scale. Limited speed of the research boat versus distance to go along the reservoir and usually complex pattern of the sampling points make it impossible to obtain synoptic data in a short time. Field measurements may record different states of the reservoir influenced by the changing meteorological conditions, work of hydropower

---

A. Magnuszewski (✉)

Faculty of Geography and Regional Studies, Department of Hydrology,  
University of Warsaw, Krakowskie Przedmieście 30, 00-927 Warsaw, Poland  
e-mail: asmagnus@uw.edu.pl

A. Sabat · A. Jarocińska · Ł. Sławik

Faculty of Geography and Regional Studies, Department of Geoinformatics,  
Cartography and Remote Sensing, University of Warsaw, Krakowskie Przedmieście 30,  
00-927 Warsaw, Poland

© Springer International Publishing AG 2018

M. B. Kalinowska et al. (eds.), *Free Surface Flows and Transport Processes*,  
GeoPlanet: Earth and Planetary Sciences,  
[https://doi.org/10.1007/978-3-319-70914-7\\_4](https://doi.org/10.1007/978-3-319-70914-7_4)

structures, or unsteady flow. There is a considerable progress in Computational Fluid Dynamics (CFD) methods, which are able to simulate the water and sediment flow down the reservoir. For practical reasons, hydrodynamic models available are solved in 2D mesh, which makes it possible to calculate velocity field and related hydraulic parameters.

Some of the CFD models solve the equations representing sediment transport in the fluvial environment. Results of the model after the verification can be used in the studies on hydrology of the reservoir. Another approach is the application of remote sensing, usually aerial photographs or high resolution satellite images. Remote sensing approach is useful since it records simultaneously the whole water body, showing its optical properties in a visible and near infrared spectrum of the light. There is a growing use of the hyperspectral images which records specific ranges of the electromagnetic spectrum corresponding to the absorption of radiation by suspended sediments and phytoplankton. Open problem in application of CFD methods for sediment transport is the model results verification. Xiaoling et al. (2010) doing research on application of MERIS image in the Bohai Sea together with hydrodynamic modeling came to conclusion that remote sensing images can record the instantaneous states periodically, and numerical simulation can complement the deficiency.

In case of water flow it is possible to verify model results by comparison to physical measurements. A water surface elevation calculated by the model can be compared to leveling results or water stage at hydrological gauge. Distribution of water velocity can be compared to current meter measurements. Much more difficult it is to verify sediments distribution calculated by the model. In such a task, a possible solution can be to compare the model results with the hyperspectral images. On the other hand, the remote sensing data need to be interpreted using some physical reference data as a so-called "ground truth". Hydrodynamic model results showing suspended sediments distribution can be used as a reference data for image interpretation. In this paper we show this relationship on the example of CCHE2D model results and hyperspectral image recorded by the AISA scanner. As a case study we use mouth of the Bug River which discharges to the Zegrze Reservoir. The confluence of these two rivers is interesting since the waters of these rivers do not mix with each other and show characteristic pattern in suspended sediments distribution.

## 2 Description of the Study Area

Zegrze Reservoir was built in the years 1957–1963 by the dam across the Narew River located in the Dębe village on 28.3 km of the river course. It is the only one completed structure from the planned cascade of reservoirs forming the so-called East-West waterway. The idea of building this waterway was proposed by the Russian engineers in 1910 as connection between catchment of Dniepr River and Wisła River. That connection could extend the European system of navigable rivers and canals to Russia.

The dam at Dębe had created reservoir which tames water from three rivers, Bug, Narew and Rządza (Fig. 1). The maximum water head at the Dębe dam is 7.10 m, the average head is 6.8 m. The dam consist of hydroelectric power station (20 MW), section of 5 weirs and earth dam. Backwater from the dam has the length of 39 km on the Narew River and 25 km on the Bug River. The volume of the reservoir is  $94.3 \times 10^3 \text{ m}^3$ , the area is  $30 \text{ km}^2$ , and the coast line length is 219 km (Dojlido and Gromiec 2003; MPHP 2010).

River basin closed by the Dębe Dam has an area of  $69.7 \times 10^3 \text{ km}^2$ . The average discharge (years 1951–2010) of the Bug River at Wyszków gauge was  $162 \text{ m}^3 \text{ s}^{-1}$ , and Narew River at Zambski Kościelne gauge  $139 \text{ m}^3 \text{ s}^{-1}$ .

Water head at the Dębe dam is maintained at the constant elevation of 79.02 m a.s.l. and does not exceed the limits of 78.60–79.10 m a.s.l. The continuous level of damming is maintained to supply drinking water intake facility in Wieliszew and to provide transit depth at Żerański shipping channel.

Bathymetry of the reservoir is known from the measurements done in the year 2004 by MGGP surveying company with the use of echo-sounder and GPS receiver. The set of measurements consists of about 311 thousand  $x, y, z$  points, where  $x$  and  $y$  are the plane coordinates of the points and  $z$  is the reservoir bottom elevation in m a.s.l. Sounding lines were spaced every 50 m and sounding points were recorded every 1 m along the profile. Using this set of data, a bathymetric map of the reservoir has been drawn as contour lines. The map has been updated by the

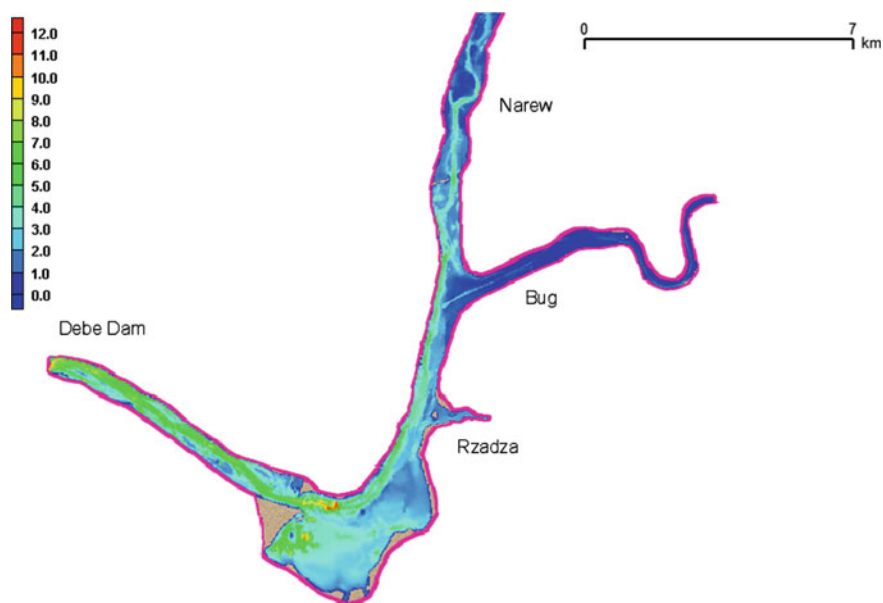


**Fig. 1** Bathymetric map (m) of the Zegrze reservoir calculated from 2004 and 2012 soundings (data provided by the courtesy of Warsaw regional water management authority—RZGW Warszawa)



newer results of bathymetric measurements done at the mouth of the Bug River in 2012. Both sets of data were provided by the Regional Water Authority in Warsaw.

The initial state of the reservoir bottom can be obtained from the design plans and large scale topographic maps. Contour maps showing initial and recent state of the reservoir bottom relief had been converted to DEM raster model of the resolution 5 m. The comparison of both DEMs shows that the main river channel of the Narew River is still visible and forms the main thalweg. Deepest parts of the reservoir are mining pits resulting from the gravel exploitation by dredging in the 1970s. The most intensive sedimentation takes place at the mouth of Bug River (Magnuszewski 2014).

### 3 Materials and Methods

For computer simulation of the Zegrze Reservoir water and sediment flow, two-dimensional model CCHE2D has been used; it was developed at the National Center for Computational Hydroscience and Engineering of the University of Mississippi, USA (Altinakar et al. 2005). The model solves vertically-averaged Navier-Stokes equations using a modified finite element method, using a control-cell technique. The model was successfully tested on field and laboratory measurements as well as applied to many case studies, as presented in Jia et al. (2002). Using the vector map of the Zegrze Reservoir coast line, a computing mesh having the resolution of  $i = 435$  by  $j = 899$  nodes was created. The subdomains with a higher grid density were created for Narew River tributaries—Bug River and Rządza River. The spatial resolution of the curvilinear grid of irregular quadrangles is higher in the Bug River and Rządza River mouths ( $15 \times 20$  m) and lower in the main basin ( $40 \times 60$  m). Sediment transport has been calculated by the Wu et al. (2000) equation, which has been confirmed as appropriate for lowland rivers by Popek (2006).

For the upper boundary of the model, long term average discharge of the Bug River (Wyszków gauge) and Narew (Zambski Koscielne gauge) have been selected. The lower boundary of the model is the normal water head level of 79.02 m a.s.l. at the Dębe dam. A steady flow and weather without wind have been assumed. Simulation time—800,000 s, time step—60 s. A single value of  $n = 0.025$  for the Manning coefficient of roughness was used for the entire reservoir.

Corresponding to that, characteristic discharges the upper boundary conditions for sediment transport at Bug and Narew River were the following: suspended sediments concentration for Bug River  $C_s = 0.0230 \text{ kg m}^{-3}$  and for Narew River  $C_s = 0.0130 \text{ kg m}^{-3}$ , intensity of the bedload transport for Bug River  $q_r = 0.032 \text{ kg s}^{-1} \text{ m}^{-1}$  and for Narew River  $q_r = 0.022 \text{ kg s}^{-1} \text{ m}^{-1}$ . The size of grains of suspended sediment was taken as  $d_{50} = 0.02$  mm and bedload  $d_{50} = 0.386$  mm.

Values of these boundary conditions are taken from hydrological yearbooks published by the Institute of Meteorology and Water Management (IMGW) while data on suspended sedimentation concentration and bedload transport rate from the literature (Nawalany 1999; Skibiński 1976).

Aerial hyperspectral image was recorded on August 3, 2013, by the AISA scanner from the deck of FPK Piper Navajo airplane and provided by the courtesy of MGGP Aero company. During the flight, the discharge of Bug River was  $132 \text{ m}^3 \text{ s}^{-1}$  while for Narew River it was  $78 \text{ m}^3 \text{ s}^{-1}$ , and there was no wind.

The patch recorded by the scanner was oriented in S-N direction covering part of the reservoir's main bay and mouth of the Bug River. The hyperspectral image had been corrected by improving geometry and reducing the influence of atmosphere (Sabat et al. 2016). There is a long list of the indexes which can be used for water quality estimation, namely: Total Suspended Solids (TSS), Coloured Dissolved Organic Matter (CDOM), Secchi Disk Depth (SDD), Total Phosphorus (TP), Chlorophyll a (Chl a), Turbidity (T) and Photochemical Reflectance Index (PRI), Red Edge Normalized Difference Vegetation Index (NDVI<sub>705</sub>). The formulas used to calculate these indexes are discussed in many works, for instance, Osińska-Skotak (2010). In Sweden, extensive studies on the possibilities to monitor lake water quality by remote sensing Compact Airborne Spectrographic Imager (CASI) were performed on lakes Erken and Malaren in the project SALMON (Östlund et al. 2001).

From the long list of remote sensing indexes, in this paper we have chosen and calculated the values of NDVI<sub>705</sub> and Total Suspended Solids—TSS. The NDVI<sub>705</sub> was used to estimate chlorophyll content and indirectly the organic matter content. The TSS index was used to acquire information about the total content of mineral and organic suspended. Zegrze Reservoir has properties of both lacustrine and riverine environment. In the riverine environment, significant is the transport of suspended sediments which can be visualized by the TSS index. In the lacustrine environment, more important are biotic processes manifested by the growth of phytoplankton, that characteristic can be visualized by NDVI<sub>705</sub>.

NDVI<sub>705</sub> index is a modification of the very popular in remote sensing Normalized Difference Vegetation Index used to study the vigor and condition of the terrestrial vegetation. It is used in hyperspectral image analysis since it shows the content of chlorophyll in the phytoplankton (Zagajewski et al. 2010), and is calculated from the formula:

$$\text{NDVI}_{705} = (\rho_{750} - \rho_{705}) / (\rho_{750} + \rho_{705}) \quad (1)$$

where  $\rho_{705}$  is the spectral reflectance of wavelength 705 nm (in case of AISA scanner, channel No. 67 records wavelength 702.59 nm), and  $\rho_{750}$  is the spectral reflectance of wavelength 750 nm (in case of AISA scanner, channel No. 77 records the wavelength 749.98 nm).

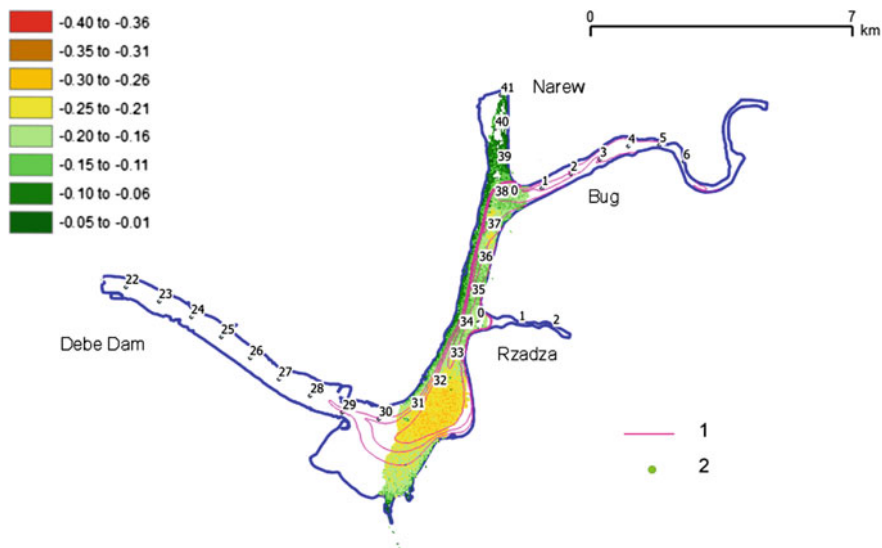


**Fig. 2** Map showing the  $NDVI_{705}$  index calculated from AISA image recorded over Zegrze reservoir on August 3, 2013, by MGGP Aero, (1) contour lines of suspended sediment calculated by CCHE2D model, (2) river length

The  $NDVI_{705}$  index (Fig. 2) is dimensionless and has a value from  $-1$  to  $1$ . High value of the index corresponds to high concentration of the chlorophyll in the phytoplankton.

Total Suspended Solids—TSS (Fig. 3) is used to estimate the total content of mineral and organic sediments suspended in the water (Östlund et al. 2001; Osińska-Skotak 2010). Particles of the suspended material cause high reflectance in the visible range of the light spectrum. Index TSS is unitless and is calculated according to the formula:

$$TSS = 1.92 + 4.49 (\rho_{614.5 \div 625.2}) \quad (2)$$

where  $\rho_{614.5 \div 625.2}$  is the reflectance of wavelengths between 614.5 and 625.5 nm (in case of AISA scanner, channel No. 49 records wavelength 618.07 nm).

Formula (2) was developed for a Lake Erken in Sweden, which has similar environmental properties (climate, concentration of suspended sediments) to Zegrze Reservoir.

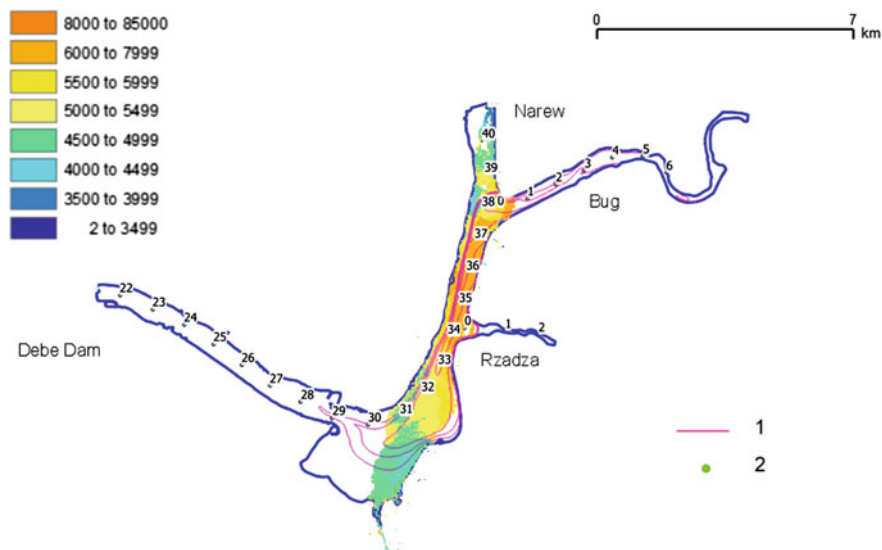


**Fig. 3** Map showing the TSS index calculated from AISA image recorded over Zegrze reservoir on August 3, 2013, by MGGP Aero, (1) contour lines of suspended sediment calculated by CCHE2D model, (2) river length

Hydrodynamic model results show the different zones of the reservoir according to a water velocity. Bug River has the velocities characteristic for a lowland river,  $0.2\text{--}0.5\text{ m s}^{-1}$ , then the flow slows down to velocity of  $0.1\text{ m s}^{-1}$  at the mouth of the river. Water velocities in the main part of the reservoir are in the range of few  $\text{cm s}^{-1}$ .

The spatial distribution of the suspended sediments concentration in the Zegrze Reservoir calculated by the CCHE2D model is shown in Fig. 4. The values of suspended sediment concentration calculated at computing mesh nodes had been exported from the hydrodynamic model results file and used in Surfer program to interpolate the contour lines. These contour lines then were displayed on top of the raster images of  $\text{NDVI}_{705}$  and TSS index (Figs. 2 and 3).

## 4 Discussion of Results

Airborne imaging spectrometry has the advantage of good spatial resolution and the precise spectral information. The limiting factors for a frequent use of that technique are high cost of the image recording and, in case of hydrological applications, narrow weather window conditions. The hyperspectral remote sensing indexes are semi quantitative and they are not able to exchange completely the traditional ground measurements.

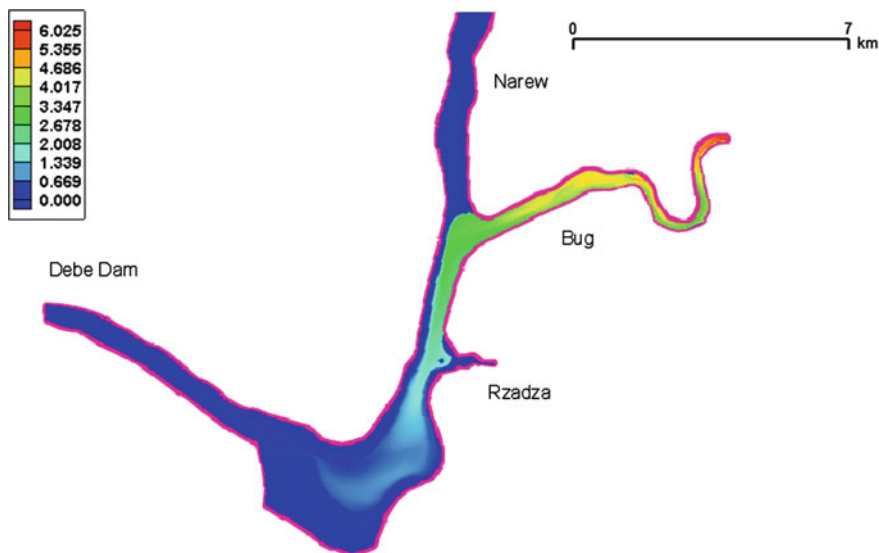


**Fig. 4** Distribution of suspended sediment concentration  $\text{gm}^3$  calculated by CCHE2D model in Zegrze reservoir for conditions of long-term average discharge and average conditions of the sediment transport shown as a raster map

The hydrodynamic model result of suspended sediment concentration calculated by the CCHE2D model can be verified by comparison to hyperspectral remote sensing indexes  $\text{NDVI}_{705}$  and TSS. The comparison can be done visually by displaying contour lines of sediments concentration from the model on top of the raster images of the indexes. Between 31 and 38 km there is visible a sharp gradient in the sediments concentration between the two water fluxes from Narew and Bug Rivers (Figs. 1 and 2). Below the km 31 the sediments transported by the Bug River start to mix with the Narew River in the widest part of the reservoir (Fig. 4).

The  $\text{NDVI}_{705}$  index (Fig. 2) shows another interesting pattern: in the mouth of Bug River the high velocity of water flow and high suspended mineral sediment concentration obstruct the growth of the phytoplankton. In the main basin of the Zegrze Reservoir there is a good condition for a growth of the phytoplankton which is manifested by the higher level of chlorophyll content.

The correlation between both data sources (hydrodynamic model and hyper-spectral image) can be analyzed also by a statistical method. In the study of Östlund et al. (2001) there was calculated a correlation between the reflectance values of a single band and chlorophyll content field measurements (23 sample points). In our study we deal with 391,065 model mesh nodes, about 48,000 of them lying in the image area. Since the distributions of analyzed variables do not approach a normal distribution, it was decided to calculate the Spearman rank correlation coefficient with the level of significance of 0.05. Data representing hydrodynamic model fields (suspended matter concentration, water velocities, bedload transport rate) are stored

**Table 1** Spearman correlation coefficient calculated between selected hydrodynamic CCHE2D model results and AISA scanner hyperspectral image indexes

AISA index/CCHE2D model results	NDVI <sub>705</sub>	TSS
Suspended sediments concentration	-0.49	0.55
Flow velocity	0.22	0.40
Bedload transport rate	0.06	0.59

in a tabular format representing results of calculation in nodes of computing mesh. Knowing coordinates of the nodes, it is possible to correlate the hydrodynamic model results with remote sensing indexes written as a geo-referenced image. From about 48000 model nodes in the image area there had been selected randomly 400 points for calculating the correlation coefficients. It was impossible to use the whole number of points, because of different spatial resolution of the data and numerical constrains. 400 selected points of the model were located on the image and in these places the average values were calculated from 9 pixels to avoid the errors related to radiometric noise. Such a procedure increases the radiometric resolution by lowering the spatial resolution. Results are shown in Table 1.

In the case of application of remote sensing to study the water properties we encounter the problem of very weak reflectance signal, and in lake environment different types of substances may modify the spectral signature. A very high correlation coefficient between remote sensing indexes and physical parameters in Lake Erken study is warned to be related to the very few observations (Östlund et al. 2001).

It was found that there is a moderate relationship between the TSS index and suspended sediments concentration as well as bedload transport rate calculated by the hydrodynamic model CCHE2D. The negative relationship between suspended sediments concentration and NDVI<sub>705</sub> confirms the information that high concentration of the mineral suspended material transported by the Bug River hampers the growth of the phytoplankton at the mouth of the river. Water without sediments having a low velocity at the main part of the reservoir favors the growth of the phytoplankton. Values of the correlation between hydraulic and remote sensing parameters (Table 1) are low because the variables used to calculate them were obtained by different scheme of averaging. Remote sensing indexes are averaged on the water surface, while hydraulic parameters are averaged in the reservoir verticals.

Results of this study show the potential use of hyperspectral aerial imagery for two-dimensional hydrodynamic model verification. On the other hand, hydrodynamic model results are very helpful in interpretation of the remote sensing indexes and classifications.

**Acknowledgements** Hyperspectral image recorded by the AISA scanner was provided on the basis of scientific cooperation by MGGP Aero company. We thank Professor Mustafa Altınakar from The Center for Computational Hydroscience and Engineering (CCHE) at The University of Mississippi for making available to us the newest version of CCHE2D hydrodynamic model. We acknowledge RZGW Warszawa for the data used for bathymetric map creation.

## References

- Altınakar MS, Czernuszenko W, Rowiński P, Wang SY (eds) (2005) Computational modeling for the development of sustainable water resources systems in Poland. Publications Institute of Geophysics, Polish Academy of Sciences, E-5 (387)
- Dojlido J, Gromiec M (2003) Rzeka Bug—zasoby wodne i przyrodnicze, IMGW. Wyższa Szkoła Ekologii i Zarządzania, Warszawa
- Jia Y, Wang, SSY, Xu Y (2002) Validation and application of a 2D model to channels with complex geometry. *Int J Comput Eng Sci* 3(1):57–71
- Magnuszewski A (2014) Procesy korytowe w Jeziorze Żegrzyńskim. Monografie Komitetu Gospodarki Wodnej PAN XX:299–306
- MPHP (2010) Mapa Podziału Hydrograficznego Polski. IMGW, Warszawa
- Nawalany M (1999) Opracowanie komputerowego modelu ekosystemu wodnego Zbiornika Żegrzyńskiego. Instytut Systemów Inżynierii Środowiska PW, Warszawa
- Osińska-Skotak K (2010) Metodyka wykorzystania super i hiperspektralnych danych satelitarnych w analizie jakości wód śródlądowych, Oficyna Wydawnicza Politechniki Warszawskiej, Warszawa
- Östlund C, Flink P, Strömbeck N, Pierson D, Lindell T (2001) Mapping of the water quality of Lake Erken, Sweden, from imaging spectroscopy and landsat thematic mapper. *Sci Total Environ* 268(1–3):139–154
- Popek Z (2006) Warunki ruchu rumowiska wlezonego w małej rzece nizinnej. Rozprawy naukowe i monografie, Wydawnictwo SGGW, Warszawa
- Sabat A, Jarocińska A, Magnuszewski A, Sławik Ł, Zagajewski B, Ochtyra A, Niedzielko J (2016) Wykorzystanie technik hiperspektralnych do kartowania wód Jeziora Żegrzyńskiego. *Prace i Studia Geograficzne* 62(2):85–103
- Skibiński J (1976) Próba ilościowej oceny intensywności transportu rumowiska wlezonego w rzekach środkowej Polski. *Zeszyty Naukowe SGGW AR* 74
- Wu W, Wang S, Jia Y (2000) Nonuniform sediment transport in alluvial rivers. *J Hydraul Res* 38 (6):427–434
- Xiaoling C, Jianzhong L, Tingwei C, Wensheng J, Liqiao T, Liqiong C, Wenjing Z (2010) Coupling remote sensing retrieval with numerical simulation for SPM study—Taking Bohai Sea in China as a case. *Int J Appl Earth Obs Geoinf* 12:203–211
- Zagajewski B, Jarocińska A, Olesiuk D (2010) Metody i techniki badań geoinformatycznych, Warszawa

# Natural and Anthropogenic Changes of the Vistula Outlet to the Sea

Wojciech Majewski

**Abstract** The Vistula (Wisła) is the largest Polish river, which flows from the south to north through the whole Poland. Its source is in the south in the mountains and the mouth in the north at the Baltic Sea. The Vistula catchment includes 54% of Polish territory. The river was always a very important economic, cultural and even defensive axis of the country. The whole course of the river was changing through the time, but most important changes appeared within its estuary area in the XIX century. These were natural and anthropogenic changes, which resulted mainly from severe ice jam floods, very complicated hydraulic course of the Vistula over its estuary area and severe hydro-meteorological conditions. They caused high social and economic losses. The engineering solution to solve this problem was in the form of an artificial Direct Channel (Przekop) to the sea. This well designed and realized engineering solution serves well till the present time. Development of Direct Channel had to be accompanied by efficient ice-breaking and additional hydraulic structures. The paper presents the description of the Vistula River and its catchment, its estuary area called Żuławy, floods in the XIX century in this area, and finally the design and execution of Direct Channel together with other engineering structures. The paper ends with conclusions concerning the past, present and future.

## 1 Introduction

Important changes of the Vistula along its course were present in XIX and XX century. These were natural and anthropogenic, which appeared in various parts of the Vistula and on its tributaries. The most visible natural and in consequence anthropogenic change was observed in the XIX century and included the estuarine area of the Vistula called Żuławy. This flat lowland terrain has very important agricultural and cultural value. It is also the area of Poland that is most endangered

---

W. Majewski (✉)

Institute of Meteorology and Water Management, State Research Institute, Warsaw, Poland  
e-mail: wmaj@ibwpan.gda.pl; wojciech.majewski@imgw.pl

© Springer International Publishing AG 2018

M. B. Kalinowska et al. (eds.), *Free Surface Flows and Transport Processes*,

GeoPlanet: Earth and Planetary Sciences,

[https://doi.org/10.1007/978-3-319-70914-7\\_5](https://doi.org/10.1007/978-3-319-70914-7_5)



by flooding. In XVII and XVIII century the Vistula was one of the most navigable rivers in Europe. About 250 thousand tons of agricultural products, wood and raw materials were transported on the Vistula to and from the harbor of Gdańsk, which was Poland's window to the world. At the end of XVIII century, Poland was partitioned by Prussia, Russia and Austria. In the same way the Vistula was divided into three separate sections and thus lost its previous significance, while other European rivers, like Rhein, Danube, Rodan and Seine, were developing rapidly providing possibilities for transportation, water supply and production of energy. During this time significant changes were performed over the lower section of Vistula, which belonged to Prussia.

## 2 The Vistula River

The Vistula River basin comprises almost the whole eastern part of Poland. The whole basin has the area of 194 thousand km<sup>2</sup>, of which 87% (169 thousand km<sup>2</sup>) is on the terrain of Poland. Remaining part of the basin is on the terrain of neighbouring countries: Belarus, Ukraine, and Slovakia. The basin of the Vistula, which is in Poland, covers 54% of the country area. It has important social and economic significance, where large urban and industrial centres are located. The Vistula basin is inhabited by more than half of Poland's population. The course of the river from its sources to the mouth is shown in Fig.1. Both the Vistula and its basin are very differentiated along their course. This diversity can be observed in terms of the terrain configuration, climate, water resources, hydraulic infrastructure as well as economy.

The whole length of the Vistula is 1,047 km. Data concerning discharges are from the Institute of Meteorology and Water Management (IMGW) records (1951–1970). In 1970 barrage Włocławek on the Lower Vistula was commissioned, which changed the flow regime. The barrage created run-of-river reservoir, 50 km long, with the initial volume of 400 million m<sup>3</sup>. Average discharge of Vistula at the mouth is 1,080 m<sup>3</sup> s<sup>-1</sup>, minimum recorded discharge is 253 m<sup>3</sup> s<sup>-1</sup>, while the maximum was 7.840 m<sup>3</sup> s<sup>-1</sup>. Discharge of the probability of 1% was evaluated as 9.190 m<sup>3</sup> s<sup>-1</sup>. After commissioning of Włocławek barrage, the maximum discharge did not exceed 6.000 m<sup>3</sup> s<sup>-1</sup> and minimum flow dropped even to 200 m<sup>3</sup> s<sup>-1</sup> (drought 2015). The summer flood hazard on the Vistula initiates in the mountains, southern part of catchment, due to high precipitation, while the main flood hazard in the Lower Vistula appears in the beginning of winter by the formation of various forms of ice and in spring during ice breakup and ice run.

From hydrographical point of view, we distinguish three sections of the Vistula and its basin: the upper, middle, and lower. This division is determined by a significant change in the Vistula River discharge caused by the tributaries. The River San (right hand tributary) marks the boundary of the Upper Vistula River. From the tributary San to the tributary Narew we have the Middle Vistula River, and from the tributary Narew to the Vistula mouth to the sea we have Lower Vistula.

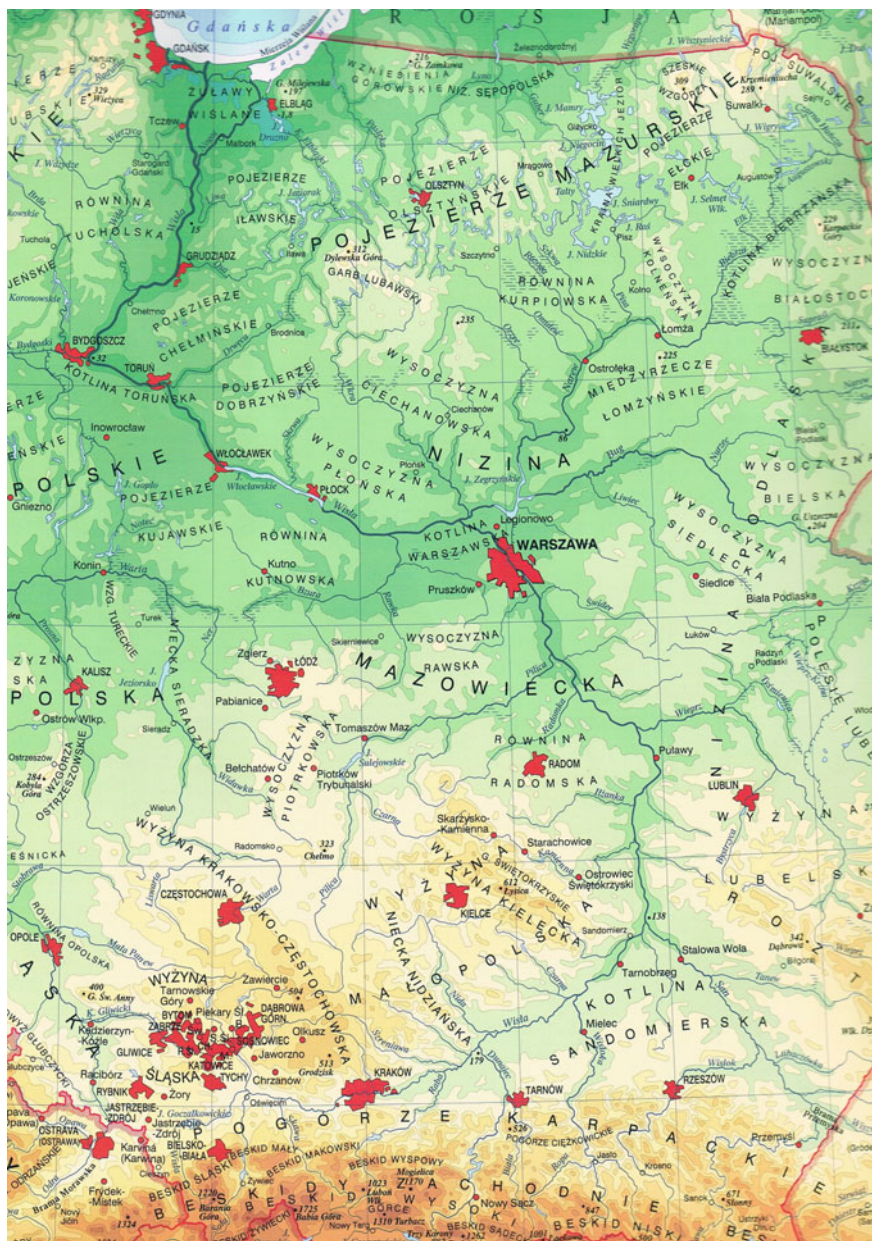


Fig. 1 The Vistula River and its catchment

The ecologists consider the Vistula as a natural river and would like to keep it in this state forever. The water resources specialists consider the Vistula as a degraded river bringing no profits to the economy and the society, and causing very high economic and social losses during floods. The degradation of the Vistula is constantly progressing. Most of the course of the Vistula valley is under the Program NATURA 2000, which significantly limits any new hydraulic structures, except those which fulfil the aim of preventing the flood hazard.

### 3 Żuławy Wiślane—Estuary Delta of the Vistula

Żuławy is a flat delta area of about 1,700 km<sup>2</sup> located at the mouth of the Vistula (Czarnecka and Kowalski 2015). Żuławy, as practically every river delta, was transformed by natural and also anthropogenic activity of people who inhabited this area. Within this area there are depressions (about 2 m below sea level) which cover about 450 km<sup>2</sup>. Żuławy can be divided into 3 separate parts (Fig. 2). These are: (i) Żuławy Gdańskie situated on the west side of the main Vistula channel. They include Gdańsk Water Node, which is a complicated system of rivers and channels. (ii) Żuławy Wielkie, called also Żuławy Malborskie, which are located between main Vistula channel and Nogat River. (iii) The third part is called Żuławy Elbląskie, which extend to the east from the Nogat River. Żuławy are characterized by very fertile soil and very high standard of agriculture, which was brought here by Mennonites, who came from the Netherlands and settled there.

Fig. 2 The map of Żuławy Wiślane

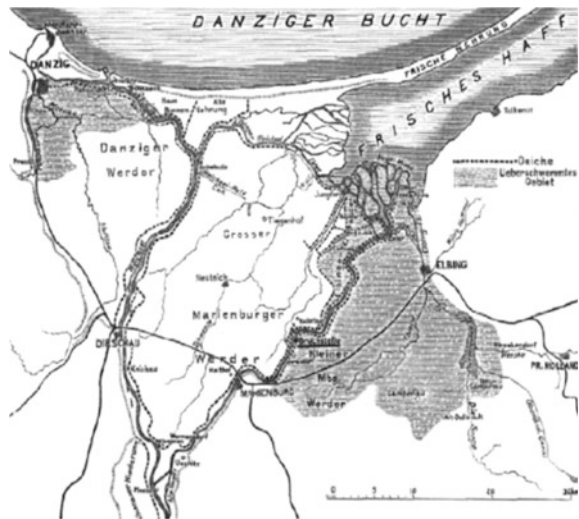


### 4 The Vistula Outlet to the Sea

The present Vistula outlet to the sea (Fig. 2) is different from that which existed in the XVIII century (Fig 3) and is shown on an old map.

The first right-hand branch from the main Vistula channel is the Nogat River, which has a connection with Zalew Wiślany. Farther to the north, the Vistula divides into two separate channels. Wisła Gdańska (Gdańsk Vistula) flows to the west and Szkarpawa or Wisła Elbląska (the Elbląg Vistula), which turns to the east and has connection with Zalew Wiślany in a similar way as Nogat. None of these three branches had any control structure, and the division of the Vistula discharge was very difficult to predict. This complicated hydraulic layout of the Vistula resulted in numerous ice jam floods. It was very difficult to predict where an ice jam and flood will appear. If during spring ice run, an ice jam formed on the Nogat River then the whole discharge was directed to the north, and it was difficult to predict whether it will flow through the Gdańsk Vistula or through Elbląg Vistula. All three parts of Żuławy were subject to flooding. Floods appeared in this area in the XIX century practically every 3–4 years. This was caused by complicated hydraulic layout of the Vistula, severe winters and springs with very high discharges. An additional fact was the flow direction of the Vistula—from south to north. Very often when spring and snow melting occurred in the south, in the northern region there was still winter and solid ice cover. Some floods which happened in the XIX century were very devastating and caused natural modifications of the Vistula channel. The most devastating floods are described in Sect. 5 Majewski (2015).

Fig. 3 The old map of Żuławy Wiślane



## 5 Floods in XIX Century

### 5.1 Flood 1829

This flood appeared at the end of April after long and severe winter, with large amounts of snow and ice. Ice thickness on the Lower Vistula reached even 1 m. The thaw started in the south, thus creating large discharge of the Vistula, which was estimated as 10 thousand  $\text{m}^3 \text{s}^{-1}$ . The left hand flood dykes of the Vistula were breached in several places and the river flow turned, over flat area of Żuławy Gdańskie, towards the Vistula outlet near the fortress Wisłoujście. A large ice jam formed there and the main Vistula channel turned further to the west, thus forming a new natural outlet. This way a new area called Westerplatte was formed (famous from the Second World War). This new outlet was later used as Gdańsk harbor. Large area of  $340 \text{ km}^2$  was flooded encompassing the city of Gdańsk, where water level reached the first floor. About 10 thousand people were homeless and economic and social losses were very high. Flooded area is marked by a dark color in Fig. 3. It was the first sign that something should be done with the Vistula outlet.

### 5.2 Flood 1840

This flood was caused by a very large ice jam which formed at the end of January on Gdańsk Vistula and resulted in a significant increase of water level and breaching of sand dunes along the coastline. This way new natural outlet of the Vistula to the sea was formed. Later it was called Wisła Śmiała (Bold Vistula). Economic and social losses were not large; however, the new layout of the Vistula channel was formed and changed the existing flow pattern.

### 5.3 Flood 1855

This flood formed in late spring after a long and severe winter. Discharge of the Vistula was very high, similar to the flood of 1829 (about 10 thousand  $\text{m}^3 \text{s}^{-1}$ ). Ice thickness on the Lower Vistula reached 0.9 m. Nearly the whole Żuławy Wielkie were flooded by the Vistula water flowing through the breached right hand flood dykes. The area of about  $600 \text{ km}^2$  was flooded and nearly 100 people lost their life. Economic and social losses were very high. Most of the flooded area were depressions, which required pumping of flood water. The first proposals to change outlet section of the Vistula appeared; however, decisions were not taken, because of very high cost of such a project.

## 5.4 Flood 1888

The scenery of this flood was similar to the cases of 1829 and 1855. This winter was very long, cold, with large amount of snow. On the main Vistula channel, the ice cover was 0.4 m thick, but on the Nogat this thickness ranged from 0.6 to 0.8 m. The thaw in the south of Poland started in the second decade of March, while in the north there was still strong winter. Large discharge of water and ice flowing in Vistula to the north met solid ice cover on the main channel of the Vistula and flow was directed to Nogat breaking the existing ice cover. This caused several ice jams and flood over the whole part of Żuławy Elbląskie. Flooded was 400 km<sup>2</sup> of fertile land, including all depressions. Losses were large and included the whole drainage system with channels and pump stations. Estimated economic losses were comparable with the cost of new project to mitigate flood hazard over the whole area of Żuławy

## 6 Design of the Direct Channel to the Sea (Przekop Wisły)

In XIX century there were many projects how to solve the difficult flood situation over the area of Żuławy. They usually appeared after each devastating flood. One of the projects was the design of Alsen and Fahl from 1877. It was a very comprehensive project, which included not only the direct channel to the sea, but also training of the whole section of Vistula, which was on Prussian territory, mainly from Bydgoszcz (tributary of Brda) to the sea. This training had the two aims: navigation and flood protection. It was also necessary to separate Nogat in Biała Góra from the main Vistula channel by means of navigation lock and flood gate, to separate Gdańsk Vistula and Elbląg Vistula in the place Gdańska Głowa from the main Vistula Channel. These additional structures were developed subsequently after the main Direct Channel was completed. This total project was a gigantic engineering undertaking requiring large amounts of money, engineering skills, and enterprises, which could complete this important project. In 1891 the whole technical documentation was complete. Decision was taken by the Cesar of Prussia, and engineering works started.

Direct Channel was 7.1 km long and its widths varied from 250 m in the beginning, to 400 m in the final section. The bottom elevation of the channel ranged from 1.3 to 1.9 m below average sea level. The layout of the Direct Channel is shown in Fig. 4.

The final section of the channel, which was directed through sand dunes (about 20 m high) was 1.4 km long and had the width of 50 m only. At the end of this narrow channel there was the earth closure. It was assumed that flowing water will enlarge the channel to the required dimensions. On both sides of the channel were flood dykes with crest level ranging from 8 to 9 m above sea level. The view of the channel is in Fig. 5.

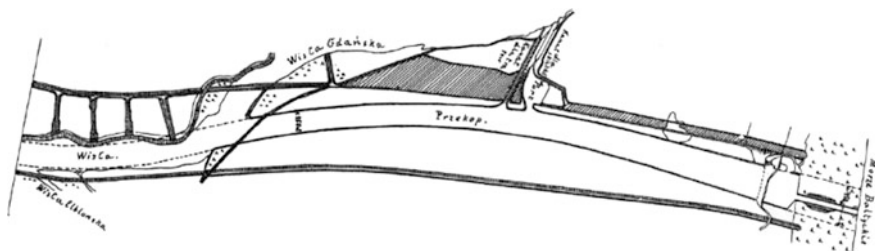


**Fig. 4** The layout of direct channel (Przekop)



**Fig. 5** The view of direct channel construction

In summer 1894 all engineering works were completed and in the autumn the water was introduced to the main channel. It was assumed that first water will flow through the channel after spring ice run in 1895. However, the ice jam which formed in the vicinity of Tczew endangered the construction of Direct Channel and it was decided to start its operation on 31 March 1895. The opening was done by the President of East Prussia at the request of Emperor of Prussia Wilhelm II (Fig. 6).

## 7 First Discharge Through DC

The earth closure was removed and the first water of the Vistula flew initially as a small stream to the sea. After 45 min the narrow channel widened to 100 m. After 3 h its widths increased to 200 m, and after 16 h its widths reached 300 m mainly through sand dunes, which were along the sea coast. Till the end of April the



**Fig. 6** Opening ceremony of the direct channel

Direct Channel reached its designed dimensions. It was estimated that during final operation of the opening of Direct Channel 9 million m<sup>3</sup> of sediment was moved towards the sea.

## **8 Consequences of Direct Channel (Przekop)**

Realization of the Direct Channel resulted in the shortening of the Vistula course of approximately 10 km and thus increased the slope of the final river section. Decreased was also the catchment of the Vistula by excluding some areas which were cut off by means of control structures. The most important change, however, was the initiation of sedimentation cone, which was formed by the sediment load carried by the Vistula. Now it is estimated that approximately 1.5 million m<sup>3</sup> is deposited at the mouth of the Vistula in an average hydrological year. During past 120 years of the Direct Channel operation, the coastline moved towards the sea by about 3 km (Fig. 7).

## **9 Follow up Actions**

Design and execution of the Direct Channel was in fact only the beginning of a very comprehensive project. First of all it was necessary to secure ice breaking over the final section of the Vistula, including Direct Channel, starting from the Vistula mouth to allow the outflow of crushed ice to the Gdańsk Bay. The fleet of





**Fig. 7** Present view of the direct channel

icebreakers consisted of more than 10 vessels, some of them still with steam engine propulsion. The next step was the formation of navigation route connecting the harbor of Gdańsk with German waterways via Vistula, Brda, Brda channel, Noteć, Warta, Odra and Havela channel. This was accomplished by means of river training consisting of about 2000 groins, which concentrated the river flow. Transport of goods, timber and other products was very intensive. In addition, hydraulic structures were developed separating Nogat, the Gdańsk Vistula, now called Dead Vistula (Martwa Wisła), and the Elbląg Vistula from the main Vistula channel by means of navigation locks. One of these structures is shown in Fig. 8. They were developed consequently during next years after completing the Direct Channel.



**Fig. 8** The view of navigation lock in Gdańska Głowa separating the Elbląg Vistula

The Direct Channel project fulfilled its assumptions and during time after its completion there was no flood in the final section of the Vistula and Żuławy. Freight navigation between Gdańsk harbor and Germany was very intensive. Operation of icebreakers secured the area of Żuławy from the formation of ice jams and floods. Sedimentation cone developed gradually and dykes at the end of both sides of the channel were gradually extended.

Devastating flood happened, however, in 1945 over the area of Żuławy, which was caused by military action. The whole Żuławy were flooded for nearly 3 years.

## 10 Present State of DC Project

During the past hundred and twenty years since the realization of Direct Channel Project, many factors have changed. There is new national division of the area, new water administration system, new economic requirements, and new hydrologic conditions resulting from climate changes. In every case when new engineering change is included into existing hydrologic system, detailed observation of this system is necessary.

First of all we now observe the decrease of discharge in the final section of the Vistula despite the fact that precipitation over its catchment did not change. The explanation of this situation is a higher evaporation due to the increase of air temperature and higher water consumption along the river. Thus both minimum, average, and maximum discharges decreased. Navigation locks which were constructed to separate main Vistula channel from Nogat, Gdańsk Vistula, and Elbląg Vistula are operating properly and serve now mainly for pleasure navigation. There is practically no freight navigation, because there is no sufficient depth for such a navigation. Groins which were constructed for river training in the past are not maintained and deteriorate. During low discharge, the depth of the Vistula is only about 1 m, which is not sufficient for freight navigation. Flood dykes are in a very bad state and their total deterioration is constantly progressing.

The development of sedimentation cone required the construction of two parallel dykes on both sides of the outlet. These dykes were consequently extended to form stable channel for navigation and icebreakers. Dredging was often necessary to secure proper depth for icebreakers (about 1.8 m). These constructions coincide with present ecological requirements as in the vicinity of the outlet there is birds sanctuary and a lot of seals. Present outlet view from the sea side is shown in Fig. 9.

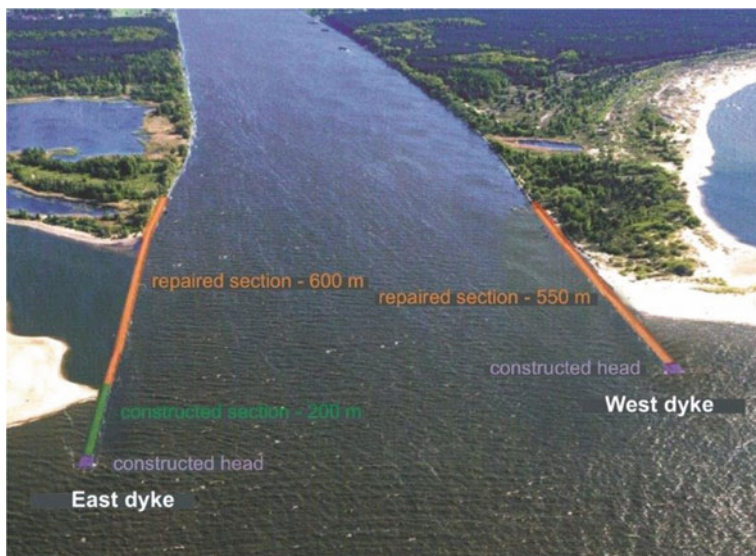


**Fig. 9** The view of the outlet of direct channel—Vistula (Przekop). *Source* Czarnecka and Kowalski (2015)

## 11 Conclusions

In the XIX and XX century, the final section of the Vistula has undergone many changes, which were of natural and anthropogenic character. Natural changes resulted from extreme hydrologic and meteorological conditions and were in the form of the change of the river course caused by extremely high water levels caused by ice jams accompanied by very high discharge. These were: change of the Vistula channel near the Vistula Mouth fortress and formation of new Vistula outlet to the sea. Both these cases were accompanied by severe floods, which resulted in very high economic and social losses.

Anthropogenic changes resulted from economic and technical considerations of how to reduce flood losses by means of new engineering structures. Here the Direct Channel must be mentioned. It has been one of very important, well designed and properly executed engineering undertakings in the Vistula catchment and till today serves the aim which was assumed in the project. It requires, however, constant maintenance and repairs. Today probably this project could not be realized because of the shortage of finances and protests of ecologists.

## References

- Czarnecka H, Kowalski P (2015) The Żuławy project, flood protection of Żuławy and Gdańsk, history and present. In: Scientific and technical conference, main technical organization (NOT), Mar 2015 (in Polish)
- Majewski W (2015) Vistula direct channel and its significance for flood protection of Żuławy, flood protection of Żuławy and Gdańsk, history and present. In: Scientific and technical conference, main technical organization (NOT), Mar 2015 (in Polish)

# Numerical Analysis of Steady Gradually Varied Flow in Open Channel Networks with Hydraulic Structures

Wojciech Artichowicz and Dariusz Gašiorowski

**Abstract** In this paper, a method for numerical analysis of steady gradually varied flow in channel networks with hydraulic structures is considered. For this purpose, a boundary problem for the system of ordinary differential equations consisting of energy equation and mass conservation equations is formulated. The boundary problem is solved using finite difference technique which leads to the system of non-linear algebraic equations. The arising system is solved with modified Picard method. The presented methodology is applicable to any channel network type and any type of hydraulic structure.

## 1 Introduction

One-dimensional steady gradually varied flow (SGVF) in open channels is one of the most frequently considered flow types in hydraulic engineering. As it is one of the basic problems, it seems to be well recognized (Chow 1959; Cunge et al. 1979; French 1985; Chanson 2004; Szymkiewicz 2010). However, practical modeling of this kind of flow in channel networks still remains an issue. In the literature, two approaches to this problem can be found. From formal viewpoint, both of them require formulation of the boundary problem for the governing equations describing SGVF. Both approaches have their advantages and drawbacks. One of the approaches is based on the shooting method. Such approach is, for example, implemented in HEC-RAS software (US Army Corps of Engineers 2010). However, this method has it difficult to converge in cases where looped channel networks are considered, which makes it useless for flow modelling in irrigation canals. Some improvements were introduced to this approach by Misra (1995, 1996, 1998) which allowed to work around the convergence problem. The second approach is based on the finite difference method (Schulte and Chaudhry

---

W. Artichowicz (✉) · D. Gašiorowski  
Faculty of Civil and Environmental Engineering, Gdansk University of Technology, ul.  
G. Narutowicza 11/12, 80-233 Gdańsk, Poland  
e-mail: wojartic@pg.gda.pl

1987; Szymkiewicz and Szymkiewicz 2004). This approach offers an elegant mathematical formulation of the problem as well as unified description of the issue. In this approach, a global system of equations for the entire channel network is formulated. This method allows to perform computations for looped and dendric channel networks without distinction. However, it does not allow to perform simulations of the mixed flow regime, which is possible in the first case.

In this paper, the second approach is evaluated. The method introduced by Szymkiewicz and Szymkiewicz (2004) for SGVF modelling is adjusted for SGVF modelling in channel networks of any type, including hydraulic structures. This work is the expansion of the considerations presented in Szymkiewicz and Artichowicz (2016).

## 2 Governing Equations

The modelling of the one-dimensional SGVF in open channels is based on the system of two ordinary differential equations derived from the system of the Saint-Venant equations (Artichowicz 2015; Szymkiewicz 2010):

$$\frac{dQ}{dx} = 0, \quad (1)$$

$$\frac{dE}{dx} = -S \quad (2)$$

where  $Q$  denotes the flow discharge,  $x$  is the spatial coordinate,  $E$  is the mechanical energy of the flow, and  $S$  is the energy slope. The first equation represents the mass conservation principle, whereas the second one represents the energy conservation principle. In the presented form the mass conservation equation states that no lateral flow is taken into consideration. However, including lateral inflow or outflow does not influence the presented solution methodology. The flow energy in Eq. (2) is expressed as follows

$$E = h + \frac{\alpha Q^2}{2gA^2}, \quad (3)$$

where  $h$  is the water stage level,  $\alpha$  is the energy correctional coefficient,  $A$  is the active flow area and  $g$  is the gravitational acceleration. The energy slope can be estimated using Manning's formula:

$$S = \frac{n^2 Q^2}{A^2 R^{4/3}}, \quad (4)$$

in which  $n$  denotes the roughness coefficient and  $R$  is the hydraulic radius.

### 3 Boundary Value Problem for Energy Equation and Its Numerical Solution with Finite Difference Method

If flow discharge in a channel is known, then to obtain the flow profile it is necessary to formulate and solve the initial value problem for the energy equation. Such problem is a typical one and has been widely described in the literature (Cunge et al. 1979; French 1985; Szymkiewicz 2010). However, if the flow discharge in a channel is unknown then, to find the water profile, a boundary problem for the system of ordinary differential Eqs. (1) and (2) has to be stated. Its solution provides the flow discharge value and flow profile in the considered channel (Fig. 1). To formulate the boundary problem for Eqs. (1) and (2) it is necessary to impose the boundary conditions at both ends of the considered channel reach. It means that water stage levels in the first ( $h_0$ ) and the last ( $h_L$ ) cross-section of the channel reach have to be imposed (Fig. 1).

The energy equation has to be approximated with numerical scheme. At least formally, the numerical solution of the boundary problem can be obtained by any numerical approach like collocation method, shooting method, finite difference method etc. In this work, the finite difference method (FDM) will be used. Application of the FDM to Eq. (2) yields:

$$\frac{E_{i+1} - E_i}{\Delta x_i} + \frac{1}{2}(S_i + S_{i+1}) = 0. \tag{5}$$

In fact the FDM approximation is identical to implicit trapezoidal rule (Artichowicz and Prybytak 2015; Ascher and Petzold 1998). Substitution of Eqs. (3) and (4) into Eq. (5) yields:

$$-\left(h_i + \frac{\alpha_i Q^2}{2gA_i^2}\right) + \left(h_{i+1} + \frac{\alpha_{i+1} Q^2}{2gA_{i+1}^2}\right) + \frac{\Delta x_i}{2} \left(\frac{Q^2 n_i^2}{A_i^2 R_i^{4/3}} + \frac{Q^2 n_{i+1}^2}{A_{i+1}^2 R_{i+1}^{4/3}}\right) = 0. \tag{6}$$

This form of the equation allows to consider the flow in one direction only. However, when channel networks are considered it is sometimes impossible to

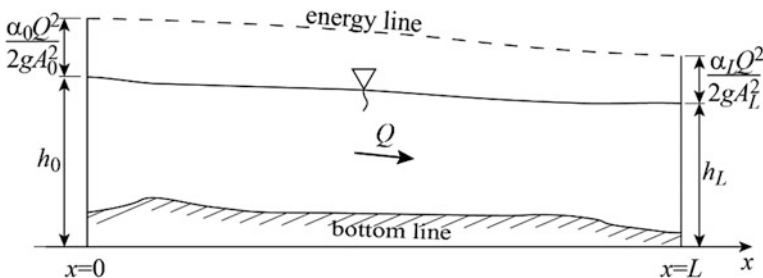


Fig. 1 Boundary problem for Eqs. (1) and (2) in a channel reach





$$a_{1,1} = 1 \text{ and } a_{M+1,M} = 1, \tag{11a, b}$$

whereas other elements are resulting from Eq. (7):

$$a_{i,i-1} = -1, a_{i,i} = 1, \\ a_{i,M+1} = \frac{Q}{2g} \left( -\frac{\alpha_i}{A_i^2} + \frac{\alpha_{i+1}}{A_{i+1}^2} \right) + \frac{|Q|\Delta x_i}{2} \left( \frac{n_i^2}{A_i^2 R_i^{4/3}} + \frac{n_{i+1}^2}{A_{i+1}^2 R_{i+1}^{4/3}} \right). \tag{12a, b, c}$$

The elements of the unknown vector are

$$x_i = h_i, \text{ and } x_{M+1} = Q, \tag{13a, b}$$

for  $i = 1, \dots, M$ . The elements of the right-hand side vector are equal to

$$b_1 = h_0, b_i = 0, \text{ and } b_{M+1} = h_L, \tag{14a, b, c}$$

for  $i = 2, 3, \dots, M$ . The obtained system of Eqs. (10) is an algebraic non-linear one. It can be successively solved using modified Picard method (Szymkiewicz and Szymkiewicz 2004). Let us rewrite Eq. (9) in a form introducing iteration index  $k$ :

$$\mathbf{A}^* \mathbf{x}^{(k+1)} = \mathbf{b}, \tag{15}$$

where the modified system matrix  $\mathbf{A}^*$  is computed based on the mean values of two previous iterations of the solution vector:

$$\mathbf{A}^* = \mathbf{A} \left( \frac{\mathbf{x}^{(k-1)} + \mathbf{x}^{(k)}}{2} \right). \tag{16}$$

In the first iteration (for  $k = 0$ ), the matrix is computed based on the starting point only  $\mathbf{x}^{(0)}$ :

$$\mathbf{A}^* = \mathbf{A} \left( \mathbf{x}^{(k)} \right). \tag{17}$$

The iterative process is considered as finished when the following criteria are fulfilled:

$$\left| h_i^{(k+1)} - h_i^{(k)} \right| < \varepsilon_h, \text{ and } \left| Q^{(k+1)} - Q^{(k)} \right| < \varepsilon_Q, \tag{18a, b}$$

for  $i = 1, 2, \dots, M$ , where  $\varepsilon_h$  and  $\varepsilon_Q$  are the required solution accuracies of water stage levels and flow discharge, respectively.

## 4 Including the Hydraulic Structures

The method presented in the previous section can be applied to a channel with one or multiple hydraulic structures as well. An example of such a channel is presented in Fig. 3.

In such a situation, the elements of the system (10) corresponding to channel section with the hydraulic structure will be replaced. Instead of elements resulting from Eq. (7), the ones resulting from the formulas describing the hydraulic structure will be used. In general, such a formula can be written as

$$Q = Q(h_j, h_{j+1}), \quad (19)$$

meaning that water stage levels around the structure and the flow discharge are involved.

To include Eq. (19) into system (9) it has to be rearranged to a form allowing the extraction of the unknown water stage levels and flow discharge into the vector of unknowns  $\mathbf{x}$ . The rearrangement will be presented on the examples of two most common hydraulic structures: weir and orifice.

### 4.1 Weir

The hydraulic scheme for submerged weir is presented in Fig. 4. In literature there are many formulas for estimating flow discharge of such structures as weirs. For simplicity let us consider rectangular sharp-crested weir. Expression for the discharge of such weir is

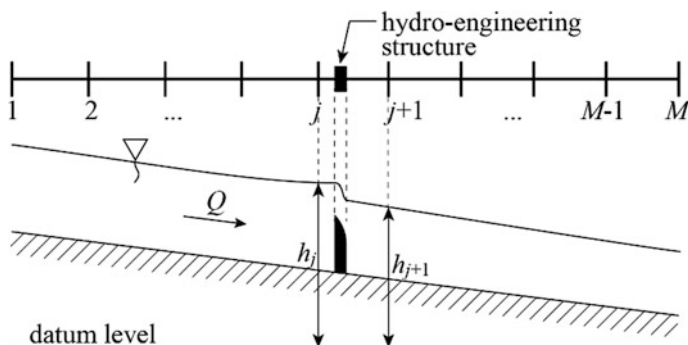


**Fig. 3** The top view and longitudinal cross-sectional view to the schematic of the channel with hydraulic structure

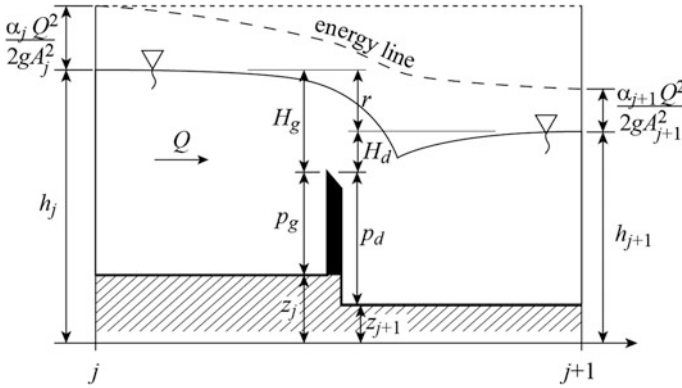


Fig. 4 The computational scheme for weir discharge computations

$$Q = \frac{2}{3} \mu B \sqrt{2g} \left[ \left( H_g + \frac{\alpha_j Q^2}{2gA_j^2} \right)^{3/2} - \left( \frac{\alpha_j Q^2}{2gA_j^2} \right)^{3/2} \right] \sigma, \tag{20}$$

where  $\mu$  is the weir discharge coefficient,  $H_g$  the water level above the crest before the weir,  $p_g$  the crest level over the bottom before the weir,  $B$  the weir width, and  $\sigma$  is the submergence coefficient, which can be expressed as (Kubrak and Kubrak 2010)

$$\sigma = 1.05 \left( 1 + 0.02 \frac{H_d}{p_d} \right)^3 \sqrt{\frac{H_g - H_d}{H_g}}, \tag{21}$$

in which  $H_d$  is the water level above the crest behind the weir, and  $p_d$  is the crest level over the bottom behind the weir.

Formula (20) is valid if  $0.25 < (H_g - H_d/p_d) < 0.75$ . If the weir is not submerged, then the value of the coefficient is taken as  $\sigma = 1$ .

To include Eq. (20) into system of Eq. (9) it has to be rearranged in such way that it will be possible to extract from it  $h_j$ ,  $h_{j+1}$  and  $Q$  into the vector of unknowns. If the weir is not submerged, the rearranged Eq. (20) will take the form:

$$-Uh_j + Q = U \left( \frac{\alpha_j Q^2}{2gA_j^2} - z_j - p_g \right) - W, \tag{22}$$

where

$$U = \frac{2}{3} \mu B \sqrt{2g \left( H_g + \frac{\alpha_j Q^2}{2gA_j^2} \right)},$$

$$W = \frac{2}{3} \mu B \sqrt{2g} \left( \frac{\alpha_j Q^2}{2gA_j^2} \right)^{3/2}.$$

In such case, the resulting matrix and right-hand side vector will be expressed with the following formulas:

$$a_{j,j} = -U, a_{j,j+1} = 0, a_{j,M+1} = 1, \quad (23a, b, c)$$

$$b_j = U \left( \frac{\alpha_j Q^2}{2gA_j^2} - z_j - p_g \right) - W, \quad (24)$$

If the weir is submerged, Eq. (20) will be written as follows:

$$-\sigma U h_j - \left( T \frac{0.021}{p_d} \sqrt[3]{\frac{r}{H_g}} \right) h_{j+1} + Q = T \left( 1.0291 - 0.021 \frac{z_{j+1}}{p_d} \right) \sqrt[3]{\frac{r}{H_g}}, \quad (25)$$

with

$$T = U \left( \frac{\alpha_j Q^2}{2gA_j^2} - z_j - p_g \right) - W.$$

In such a situation, the resulting matrix and right-hand side vector will be expressed with the following formulas:

$$a_{j,j} = -\sigma U, a_{j,j+1} = -T \frac{0.021}{p_d} \sqrt[3]{\frac{r}{H_g}}, a_{j,M+1} = 1, \quad (26a, b, c)$$

$$b_j = T \left( 1.0291 - 0.021 \frac{z_{j+1}}{p_d} \right) \sqrt[3]{\frac{r}{H_g}}. \quad (27)$$

If necessary, it is possible to include the variability of the weir coefficient  $\mu$ .

## 4.2 Unsubmerged Orifice

Similarly as the weir, an orifice can be considered. The formula for the discharge of the small unsubmerged orifice is (Fig. 5):

$$Q = \mu A_o \sqrt{2gH_o}. \quad (28)$$

where  $\mu$  is the orifice discharge coefficient,  $A_o$  the area of the orifice,  $H_o$  the water level above the centre of the orifice area, and  $p$  is the distance between the bottom

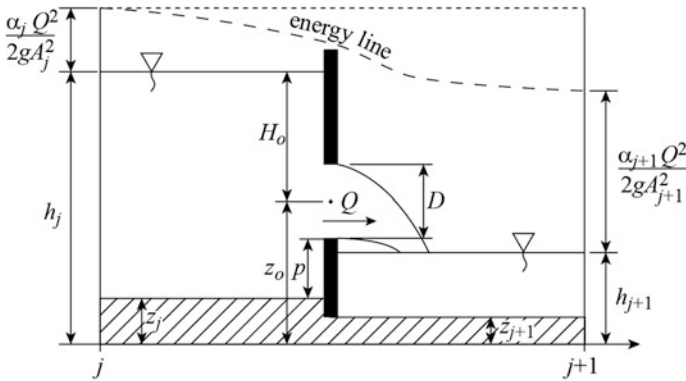


**Fig. 5** The computational scheme for unsubmerged orifice discharge computations

and the bottom edge of the orifice. As previously, to include Eq. (28) in the system of Eq. (9) it has to be rearranged. To this order, let us notice that in case of the circular or rectangular orifice it can be written that

$$z_o = z_j + p + \frac{D}{2}, \tag{29}$$

and

$$H_o = h_j - z_o. \tag{30}$$

To rearrange Eq. (28) for suitable form to be included in the system (9) it is convenient to raise its both sides to the power of two. Equation (28), after rearrangement, will take the form:

$$Q^2 - 2g(\mu A_D)^2 h_j = -2g(\mu A_D)^2 z_o, \tag{31}$$

which leads to resulting matrix and right-hand side vector elements:

$$a_{j,j} = -2g(\mu A_D)^2, a_{j,j+1} = 0, a_{j,M+1} = Q, \tag{32a, b, c}$$

$$b_j = -2g(\mu A_D)^2 z_o. \tag{33}$$

### 4.3 Submerged Orifice

If the orifice is submerged, then the formula describing its discharge is (Fig. 6)

$$Q = \mu A_o \sqrt{2g\Delta H}, \quad (34)$$

where  $\Delta H = h_j - h_{j+1}$  is the difference between the water level before and behind the orifice. As previously, it is convenient to raise both sides of formula (34) to the power of two:

$$Q^2 - 2g(\mu A_D)^2 h_j + 2g(\mu A_D)^2 h_{j+1} = 0. \quad (35)$$

The elements of the matrix and the right-hand side vector are

$$a_{j,j} = -2g(\mu A_D)^2, a_{j,j+1} = 2g(\mu A_D)^2, a_{j,M+1} = Q, \quad (42a, b, c)$$

$$b_j = 0. \quad (36)$$

#### 4.4 Example

To illustrate the FDM method and its accuracy let us consider a laboratory flume with adjustable bottom slope. The flume has the following parameters: length  $L = 10$  m, width  $B = 0.38$  m, bed slope  $s = 0.001745$ . The Manning's roughness coefficient of the channel is constant and equal to  $n = 0.0185$  s m<sup>-1/3</sup>. At the distance of  $x_{ovf} = 2.0$  m, the sharp crested weir of height  $p_g = p_d = 0.24$  m is situated. The sketch of the laboratory station is presented in Fig. 7.

The flow discharge was set to  $Q = 0.0133$  m<sup>3</sup> s<sup>-1</sup>. The corresponding measured water stage levels at the first ( $x = 0$  m) and last ( $x = 9$  m) cross-sections were  $h_0 = 1.31$  m,  $h_L = 1.26$  m, respectively. The above-mentioned FDM method was applied to simulate the flow in the flume. The initial discharge value was taken as  $Q_0 = 0.01$  m<sup>3</sup> s<sup>-1</sup>. The initial water stage was taken as the stage corresponding to

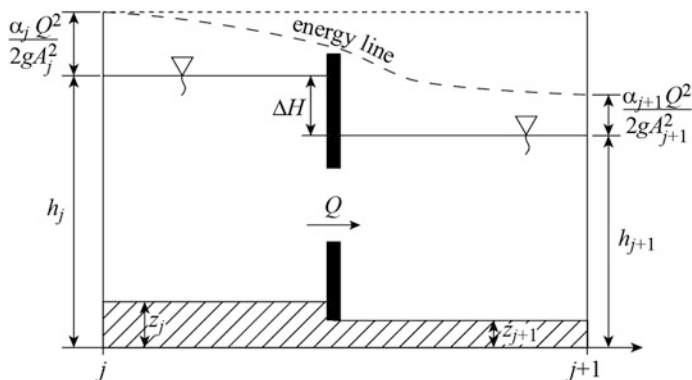


Fig. 6 The computational scheme for submerged orifice discharge computations

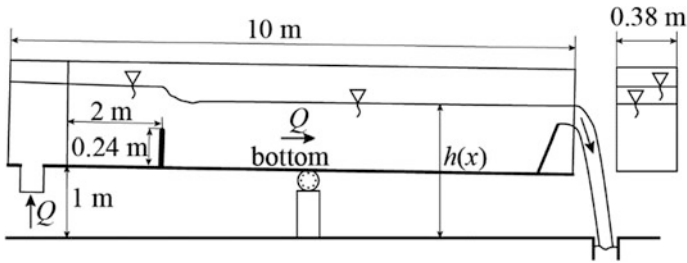


Fig. 7 The sketch of the laboratory flume

mean value of the depths resulting from the imposed boundary conditions. The weir discharge coefficient was computed using the following formula

$$\mu = 0.615 \left( 1 + \frac{1}{1000H_g + 1.6} \right) \left[ 1 + 0.5 \left( \frac{H_g}{H_g + p_g} \right)^2 \right]. \quad (37)$$

The computations required 6 iterations to finish with demanded accuracy  $\epsilon_h = 0.0001 \text{ m}$  and  $\epsilon_Q = 0.0001 \text{ m}^3 \text{ s}^{-1}$ . The obtained flow discharge value is  $Q_c = 0.0142 \text{ m}^3 \text{ s}^{-1}$ , which means the relative error  $\epsilon = |Q - Q_c|/Q \cdot 100\% = 6.76\%$ . The outcome of the measurements and computations was presented in Fig. 8. The computed water stage levels are very similar to the measured values, which confirms the efficacy of the presented methodology.

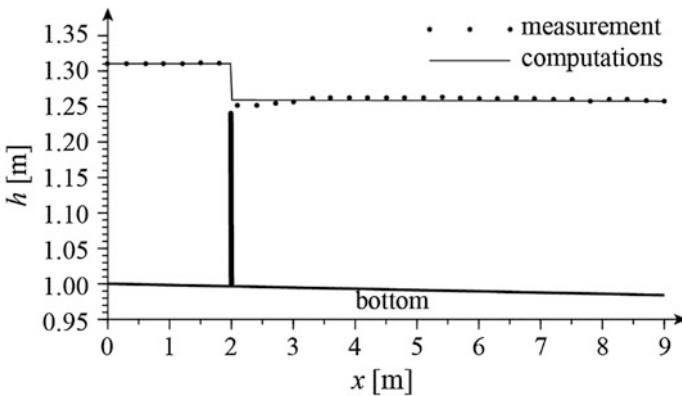


Fig. 8 The comparison of the measurements and computations outcome

## 5 Channel Networks

The presented methodology can be applied seamlessly to channel networks of any type. To perform the computations in such a case, each channel has to be divided into computational cross-sections in the same manner as presented in the case of the single channel. However, to close the arising system of equations, additional equations are required. Those equations are representations of the mass conservation principle and the energy stage equality applied to junctions.

The scheme of the typical channel junction and its computational representation is displayed in Fig. 9.

It is possible to include any number of channels in a junction representation, however, in practice, junctions with more than three channels are very rare. The equation representing the mass conservation principle is

$$\sum_P Q_P = 0. \quad (38)$$

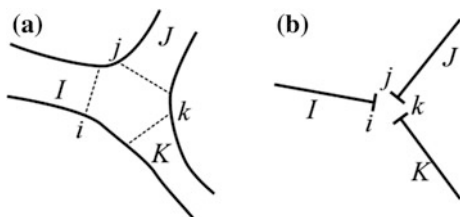
with  $P$  becoming the index of each channel included in the junction. For the situation presented in Fig. 9 it would mean that  $P = I, J, K$ . Equation (38) means that the volume of the water flowing into the junction and flowing out of the junction is identical. To include Eq. (38) in the arising global system of equations it is necessary to assume the flow directions in each channel of the considered network. The flow direction is then represented with the sign of the discharge value as previously mentioned. The equations representing the equality of the energy in the junction can be written as

$$h_i + \frac{\alpha_i Q_I^2}{2gA_i^2} = h_j + \frac{\alpha_j Q_J^2}{2gA_j^2} = h_k + \frac{\alpha_k Q_K^2}{2gA_k^2}, \quad (39)$$

which means that the flow energy in each of the cross sections included in junction is the same. Equation (39) in fact represents two equations resulting from the situation presented in Fig. 9. In a general case in which  $P$  channels are included in the junction to express the equality of the energy in the junction  $P-1$  equations will arise, where  $P$  means the number of channels included in the joint.

The resulting global system of equations will include subsystems written for each channel expressed by system (10) and from Eqs. (38) and (39) representing

**Fig. 9** **a** The sketch of the channel junction and **b** its typical computational representation





the junctions. If there are hydraulic structures in the channels included in the network they can be included in the model with the methodology described in Sect. 4 without any changes. In each step of the computational process, the flow direction in the channels can change, which has to be taken into consideration when writing the equations describing the hydraulic structures. The resulting system of non-linear algebraic equations, as previously, can be solved using the modified Picard method.

### 5.1 Example

Let us consider an imaginary channel network consisting of eleven channels (Fig. 10). All channels in the network are rectangular and have width equal to  $B = 5$  m. Also roughness coefficient is identical in all channels and is equal to  $n = 0.03 \text{ s m}^{-1/3}$ . The bed slopes  $s$  and lengths  $L$  of the channels are given in Table 1. The channel network contains four identical rectangular weirs (denoted in Fig. 10 as  $wr$  1–4 situated in channels 2, 3, 5 and 7). The parameters of the weirs have the following values: the width  $B_{wr} = 5$  m, the crest levels over the bottom  $p_g = p_d = 1$  m. The discharge  $\mu_{wr}$  coefficient is computed using Eq. (37). The orifice parameters are: width  $B_{orf} = 2.5$  m, height  $D = 0.3$  m, discharge coefficient  $\mu_{orf} = 0.67$ , the bottom edge of the orifice is at the level of the channel bed thus  $p = 0$  m. The orifice is situated in channel 4. All hydraulic structures are positioned in the half of the channel lengths.

The network contains pairs of identical channels placed symmetrically: 2 and 3, 5 and 7, 9 and 10. The channel network is thus symmetrical with regard to the channels 1, 4 and 11.

The imposed boundary conditions are water stage levels corresponding to the given water depths  $H_{B1} = 2$  m,  $H_{B2} = 1.2$  m,  $H_{B3} = H_{B4} = 1.3$  m. The imposed starting values for iterative process were the same for all the channels and were equal to  $H^{(0)} = 5$  m and  $Q^{(0)} = 0.1 \text{ m}^3 \text{ s}^{-1}$ . It took 16 iterations to obtain the demanded accuracy  $\epsilon_h = 0.001$  m and  $\epsilon_Q = 0.001 \text{ m}^3 \text{ s}^{-1}$ . The computed flow discharges are presented in Table 1.

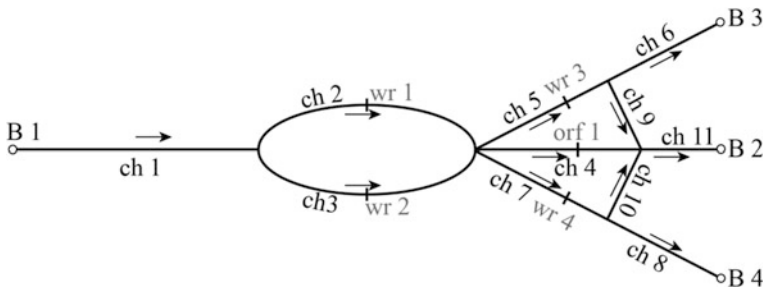
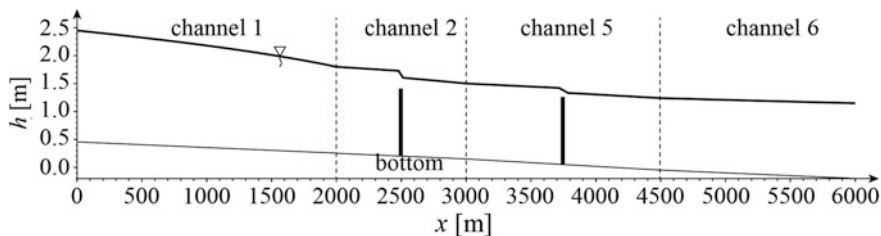


Fig. 10 The schematic of the considered channel network

**Table 1** The parameters of the channel network and the computed discharges

No.	$s$ [-]	$L$ [m]	$Q$ [m <sup>3</sup> s <sup>-1</sup> ]
1	0.0001	2000	5.502
2	0.0001	1000	2.751
3	0.0001	1000	2.751
4	0.0001	1500	1.087
5	0.0001333	1500	2.207
6	0.0001	1500	1.477
7	0.0001333	1500	2.207
8	0.0001	1500	1.477
9	-0.00005	1000	0.730
10	-0.00005	1000	0.730
11	0.0002	1000	2.547

The water profiles in paths consisting of channels 1–2–5–6, 4–11 and channel 9 are presented in Figs. 11, 12 and 13, respectively. As the network is symmetrical, the flow profiles in the remaining channels are identical as in the presented paths (Fig. 10).



**Fig. 11** The flow profile in the path connecting channels 1–2–5–6

**Fig. 12** The flow profile in the path connecting channels 4–11

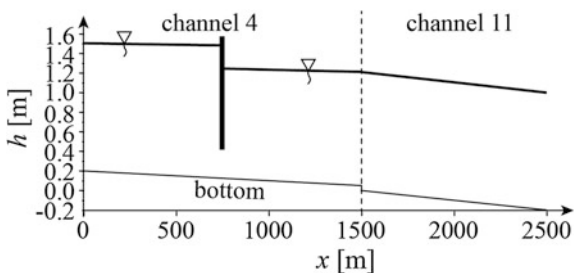
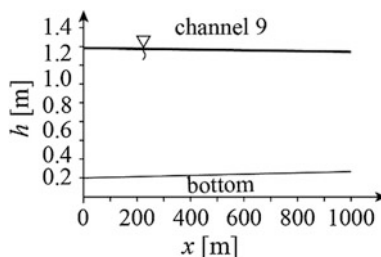


**Fig. 13** The flow profile in channel 9



## 6 Conclusions

In this paper, the methodology for SGVF modeling in channel networks with hydraulic structures of any type was presented. The core of the presented methodology is the system of ordinary differential equations consisting of the continuity and energy equations representing the one-dimensional SGVF in open channels. This system was approximated with finite difference method, which led to non-linear system of algebraic equations. If the network branches include hydraulic structures, the rows of this system corresponding to the cross-sections embracing the structures have to be modified. For such cross-sections the algebraic formulas involving discharge and water stage values before and behind the structure are used instead of the equations resulting from the approximation of the energy equation. The resulting system is closed by adding the equations representing the boundary conditions written for the pending cross-sections, and equations representing the energy line equality and mass conservation principle in the network junctions. The resulting system can be successively solved with modified Picard method.

The efficacy of this methodology was tested with imaginary examples as well as against experimental outcome.

## References

- Ascher UM, Petzold LR (1998) Computer methods for ordinary differential equations and difference-algebraic equations. SIAM, Philadelphia
- Artichowicz W, Prybytak D (2015) Impact of energy slope averaging methods on numerical solution of 1D steady gradually varied flow. Arch Hydro-Eng Environ Mech 62(3–4):101–119. Gdańsk 2015. <https://doi.org/10.1515/heem-2015-0022>
- Chanson H (2004) The hydraulics of open channel flow: an introduction, 2nd edn. Elsevier
- Chow VT (1959) Open-channel hydraulics. McGraw-Hill / Kogakusha Company LTD, Tokyo
- Cunge JA, Holly FM, Verwey A (1979) Practical aspects of computational river hydraulics. Pitman Advanced Publishing Program, Boston, London, Melbourne
- French RH (1985) Open channel hydraulics. McGraw-Hill, New York
- Kubrak E, Kubrak J (2010) Podstawy obliczeń z mechaniki płynów w inżynierii i ochronie środowiska. SGGW, Warszawa
- Misra R (1995) Steady flow simulation in irrigation canals. SADHANA Acad Proc Eng Sci Part 6 20:955–969

- Misra R (1996) Spatially varied steady flow in irrigation canals. *Agric Water Manag* 30:217–235
- Misra R (1998) Recursive algorithm for steady flow in a canal network. *Adv Eng Softw* 29(1):77–86 (1998)
- Schulte AM, Chaudhry MH (1987) Gradually-varied flows in open channel networks. *J Hydraul Res* 25(3)
- Szymkiewicz R (2010) *Numerical modeling in open channel hydraulics*. Springer
- Szymkiewicz A, Szymkiewicz R (2004) Method to solve the non-linear systems of equations for steady gradually varied flow in open channel network. *Commun. Numer Methods Eng* 20(4)
- Szymkiewicz R, Artichowicz W (2016) Modelowanie przepływu ustalonego niejednostajnego w sieciach kanałów otwartych z uwzględnieniem obiektów hydrotechnicznych. In: Sroka Z, Tschuschke W (eds) *A chapter in monography: modelowanie przepływów w ośrodkach porowatych oraz w sieciach rzecznych*. Bogucki Wydawnictwo Naukowe, Poznań
- US Army Corps of Engineers (2010) *HEC-RAS hydraulic reference*

# Lattice Boltzmann Method for the Numerical Simulations of the Melting and Floating of Ice

Ayurzana Badarch and Hosoyamada Tokuzo

**Abstract** In this paper, an extension to a recently introduced model for liquid-solid phase changes in free surface flow is explored by adding a new floating body simulation algorithm. The algorithm, based on the immersed boundary formulation of the Lattice Boltzmann method, is applied over a time dependent, arbitrary shaped, floating or immersed body in a free surface flow. Here, simulation and laboratory experiment of a floating ice cylinder was carried out to examine the accuracy of the proposed model. Numerical results confirm that the proposed algorithm satisfies the mass conservation, which has been difficult to be handled, and computes the involved free surface and heat transfer with reasonable accuracy.

## 1 Introduction

The physical interaction of ice in a river can be decomposed into the processes of heat transfer between ice and water, liquid-solid phase changes of water, free surface flow and floating body mechanics. Thus, this interaction is considered to be a problem based on the liquid-solid phase changes occurring in a free surface flow. Few studies regarding the problem have been done numerically (Iwasaki et al. 2010), since the problem has been a cause challenging the existing numerical tools due to the complexity of a free surface condition and liquid-solid phase changes.

In this regard, the Lattice Boltzmann method (LBM) has been taking a huge relevance to solve fluid problems instead of the Navier-Stokes equation. Even though the popularity of the LBM is low in the hydraulic community (Karpinski et al. 2013), the LBM has been well introduced and tested for the most complicated

---

A. Badarch (✉)

Graduate School of Engineering, Nagaoka University of Technology,  
1603-1 Kamitimioka, Nagaoka 940-2188, Japan  
e-mail: ayur\_426@yahoo.com

H. Tokuzo

Department of Civil and Environmental Engineering, Nagaoka University  
of Technology, 1603-1 Kamitimioka, Nagaoka 940-2188, Japan

© Springer International Publishing AG 2018

M. B. Kalinowska et al. (eds.), *Free Surface Flows and Transport Processes*,  
GeoPlanet: Earth and Planetary Sciences,  
[https://doi.org/10.1007/978-3-319-70914-7\\_7](https://doi.org/10.1007/978-3-319-70914-7_7)

hydraulics problem in recent years. Since the LBM has been particularly effective in heat transport, phase changes and free surface flows, a new combination of lattice Boltzmann (LB) models for this kind of problems is introduced. In addition, a new immersed boundary based algorithm for a freely moving floating body in a free surface flow that considers heat transfer and body shape changes over time is proposed. The proposed model is applied in an ice melting simulation in order to show the phase changes in a free surface flow. Additionally, to examine the floating body simulation algorithm, comparison between experiment and simulation, which consisted in plunging an ice cylinder into water, was performed.

## 2 Numerical Models

### 2.1 LBM for Free Surface Flow

Avoiding the repetition of underlying physics of the LBM, the discretized Boltzmann equation with the BGK collision operator (Bhatnagar et al. 1954) and the immersed boundary modification (Noble and Torczynski 1998) can be written as

$$f_i(\mathbf{x} + \mathbf{c}_i \delta t, t + \delta t) - f_i(\mathbf{x}, t) = - \frac{\delta t(1 - \beta)}{\tau_{tot}} (f_i(\mathbf{x}, t) - f_i^{eq}(\mathbf{x}, t)) + \beta f_i^m(\mathbf{x}, t) + \delta t F_i, \tag{1}$$

where  $f_i(\mathbf{x}, t)$ —density distribution function (DF) at time  $t$  (see lower layer of the Fig. 1b),  $\mathbf{x} = (y, z)$ —position vector (m),  $\mathbf{c}_i = (c_x, c_y)$ —discrete velocity,  $\delta t$ —lattice time step,  $\tau_{tot}$ —total relaxation time,  $\beta$ —immersed boundary parameter,  $f_i^{eq}(\mathbf{x}, t)$ —equilibrium distribution function,  $f_i^m(\mathbf{x}, t)$ —additional collision term for immersed boundary influence on the fluid flow,  $F_i$ —force term.

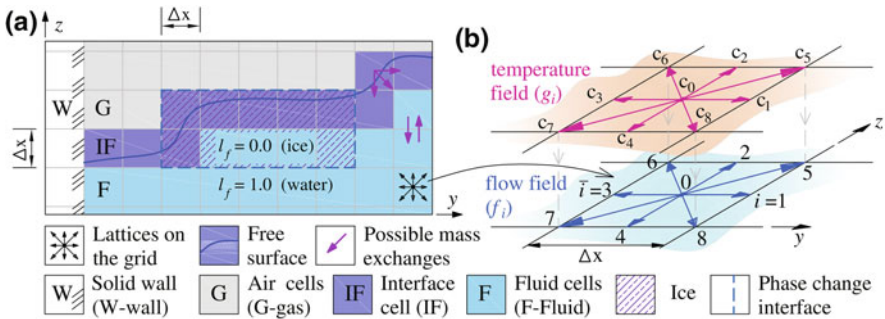


**Fig. 1** Schematic description of a numerical model: **a** free surface representation with cell types and the possibilities of mass exchange between cells, **b** a description of two distribution functions model for flow and temperature field

The total relaxation describes turbulence for fluid flow and it can be expressed by the function of the kinematic and eddy viscosity term (Hou et al. 1994) as

$$\tau_{tot} = \frac{3\Delta t}{\Delta x^2}(\nu + C\Delta^2|S|) + \frac{1}{2}, \quad (2)$$

where  $\Delta t$ —time step (s),  $\Delta x$ —lattice space (m),  $\nu$ —viscosity of fluid ( $\text{m}^2 \text{s}^{-1}$ ),  $C$ —Smagorinsky constant,  $\Delta$ —filter width (m),  $S$ —the magnitude of the large-scale strain rate tensor. The immersed boundary parameter, which modifies a collision term in Eq. (1), is defined by

$$\beta(l_f, \tau_{tot}) = \frac{(1-l_f)(\tau_{tot}-0.5)}{l_f + (\tau_{tot}-0.5)}, \quad (3)$$

where  $l_f$ —liquid fraction (see Sect. 2.2) and the additional collision term (Strack and Cook 2007) can be given as

$$f_i^m(\mathbf{x}, t) = f_i(\mathbf{x}, t) - f_i(\mathbf{x}, t) + f_i^{eq}(\rho, \mathbf{u}_s) - f_{\bar{i}}^{eq}(\rho, \mathbf{u}), \quad (4)$$

where  $\mathbf{u}_s$ —velocity of moving solid body and  $\bar{i}$  is the opposite direction to direction  $i$  (see Fig. 1b). A force scheme described in Karpinski et al. (2013) is used to account for the body forces and the force,  $\mathbf{F}$ , in the scheme consists of the acceleration of gravity and non-Boussinesq approximation for the buoyance force as

$$\mathbf{F} = \mathbf{g} \left( 1 - \alpha_V (\theta - \theta_o)^2 \right), \quad (5)$$

where  $\mathbf{g}$  ( $=\mathbf{g}_R \Delta t^2 / \Delta x$ )—lattice gravitation,  $\mathbf{g}_R$ —acceleration of gravity ( $\text{m s}^{-2}$ ) and R subscript denotes a real physical value,  $\alpha_V$ —thermal volume expansion of water,  $\theta_o$ —dimensionless reference temperature, which is the temperature at the maximum density inversion point of water. Since the variables and constants contributing in Eq. (1) must be in dimensionless form, the thermal volume expansion can be obtained by the Rayleigh number (Ra) definition. The equilibrium distribution function for the fluid flow can be determined by the expansion of the Maxwell distribution functions (Chen and Doolen 1998). The macroscopic variables, density and velocity, can be computed by the moments of the distribution functions as

$$\rho = \sum_{i=0}^8 f_i, \quad \rho \mathbf{u} = \sum_{i=0}^8 \mathbf{c}_i f_i + \frac{\mathbf{F} \delta t}{2}. \quad (6)$$

Equation (1) need to be solved on the fluid and interface cells by two steps called the streaming and the collision. Fluid (F) and interface cells (IF), depicted in Fig. 1a, can be water cells, which are able to be frozen into ice or to remain water itself. Ice and water states among the water cells are distinguished by the liquid fraction value,  $l_f$ , which takes value 1 for water, 0 for ice and between 0 and 1 for an interface or mushy zone between two phases, as shown in Fig. 1a.

As mentioned above, there are four types of cells in computational domain indicating materials, such as motionless wall (W), air (G) and water (F and IF). The cells W and G are only used to impose boundary conditions on the wall and free surface, respectively. We have adopted the free surface LB model introduced by Thurey et al. (2005) in our model. The interface cell has a responsibility to represent free surface transformation depending on the changes of the volume fraction of water on the cell. For instance, the cell that has 0 value of volume fraction will be G cell. If a volume fraction of the cell is 1, then the cell will be F, and between 0 and 1 refers to IF cell. The value of the volume fraction of water on the cell can be expressed as the ratio of mass to density of the cell defined by Eq. (6), i.e.,  $\epsilon(\mathbf{x}) = m(\mathbf{x})/\rho(\mathbf{x})$ . As the values of the volume fraction changes the position of the IF cells, which are chained side by side of cells, the changes of the cell mass on an IF cell are computed by the mass exchanges between water cells as

$$m(\mathbf{x}, t + \Delta t) = m(\mathbf{x}, t) + \sum_{i=1}^8 \Delta m_i(\mathbf{x}, t + \Delta t), \quad (7)$$

where  $\Delta m_i$ —mass exchange value, which is allowed to be defined between IF cells with their neighboring water cells, as marked in Fig. 1a. Note that the water cells are IF and F cells, whose liquid fraction is  $l_f = 1.0$ . Therefore, IF and F cells turning into ice cells cannot exchange mass with water IF cells. The mass exchange values between IF and F cells are easily computed by the difference between the distribution functions entering to and leaving from the cell, whereas in the mass exchanges between IF cells, the volume fraction of water of the mass exchanging pairs must be considered. The neighboring information of the IF cell (see Table 4.1 in thesis of Thurey 2007) is also needed to be considered. The cell mass is updated with Eq. (7) for the entire domain, and then the usual operation of the LBM for flow and temperature field can be performed. Since the density has been defined at a new time step, the transformation of IF cells can be tracked with the following criteria

$$\begin{aligned} \text{IF} \rightarrow \text{F} & \text{ when } m(\mathbf{x}, t + \Delta t) > (1 + k)\rho(\mathbf{x}, t + \Delta t) \text{ or} \\ \text{IF} \rightarrow \text{G} & \text{ when } m(\mathbf{x}, t + \Delta t) < (-k)\rho(\mathbf{x}, t + \Delta t), \end{aligned} \quad (8)$$

where  $k = 10^{-3}$ —threshold of judgment for emptied or filled cells. This transformation of IF cells lead the changes of flagging of neighboring F and G cells in order to satisfy continuities of IF cells, as shown in Fig. 2b and c. Those neighboring cells are newly changed cells and need appropriate amount of mass due to the excess mass distribution from the transformed IF cells, as follows:

$$m(x + \mathbf{c}_i) = m(x + \mathbf{c}_i) + m^{ex}(\eta_i/\eta_{tot}), \quad (9)$$

where  $m^{ex}$ —positive or negative excess mass of filled or emptied IF cells,  $\eta_{tot}$ —sum of the weights,  $\eta_i$ —weight for  $i$  direction, each of which is estimated by the discrete velocity and the normal vector  $\mathbf{n}$  on the free surface (Thurey 2007).



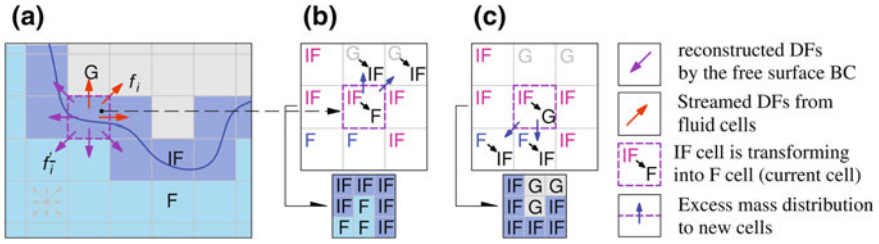


**Fig. 2** Free surface movement: **a** Free surface boundary condition, **b** IF cell is being filled and neighboring G cells recognized to change into IF cells and **c** IF cell is being emptied and neighboring F cells recognized to change into IF cells

The filled or emptied IF cell as well as newly changed cell can receive a new flagging of cell after the excess mass distribution and the reinitialization of the newly changed cells. To do so, after judging IF cells with Eq. (8) and defining the newly changed cells, temporal flags are imposed for IF cells. With temporal flags, DFs are reinitialized on the newly stated G cells, which are going to be new IF cells, with the equilibrium distribution functions:

$$\begin{aligned}
 f_i(\mathbf{x}, t) &= f_i^{eq}(\rho^{av}, u^{av}) \text{ for fluid flow and} \\
 g_i(\mathbf{x}, t) &= g_i^{eq}(\theta^{av}, u^{av}) \text{ for heat transport,}
 \end{aligned}
 \tag{10}$$

where  $g_i(x, t)$ —thermal distribution function for the temperature field and average variables in Eq. (10) can be computed using the surrounding non-gas cells.

A free surface boundary condition must be imposed on an IF cell in order to reconstruct distribution functions that would be streamed from G cells during the streaming step, if the following condition holds:

$$\varepsilon(\mathbf{x} + \mathbf{c}_i) = 0 \text{ or } \mathbf{n} \cdot \mathbf{c}_i > 0, \text{ where } \mathbf{n} = \frac{1}{2} \begin{pmatrix} \varepsilon(\mathbf{x}_{y-1,z}) - \varepsilon(\mathbf{x}_{y+1,z}) \\ \varepsilon(\mathbf{x}_{y,z-1}) - \varepsilon(\mathbf{x}_{y,z+1}) \end{pmatrix}.
 \tag{11}$$

Satisfying an air pressure on the water surface, the free surface boundary condition reconstructs DFs on the IF cells, as shown in Fig. 2a, with the following DF

$$f'_i(\mathbf{x}, t + \Delta t) = f_i^{eq}(\rho_A, \mathbf{u}) + f_i^{eq}(\rho_A, \mathbf{u}) - f_i(\mathbf{x}, t),
 \tag{12}$$

where  $\rho_A$ —air density in lattice form, which often assumed to be unit. The bounce forward scheme is imposed on the motionless wall to express smooth surface. If water is at the rest and the depth of water is considerable for computation, the hydrostatic pressure condition must be given in initial condition to balance the force field. This initial condition can be expressed in terms of density derived from the barometric formula using  $c_s = 1/\sqrt{3}$  and  $\rho_0 = 3P_0$ :

$$\rho(z) = \rho_0 e^{3gz}, \quad (13)$$

where  $z$ —depth of water in initial state,  $P_0$ —reference pressure at the free surface.

## 2.2 LBM for Heat Transport and Phase Changes

A temperature field is a widely used approach in the simulation of heat transport processes instead of internal energy. The thermal Boltzmann equation (Huber et al. 2008), which is able to reduce heat transport equation with latent heat source, is used to define the temporal evolution of thermal distribution functions, as depicted in the top layer of Fig. 1b, as

$$g_i(\mathbf{x} + \mathbf{c}_i \delta t, t + \delta t) - g_i(\mathbf{x}, t) = \frac{g_i^{eq}(\mathbf{x}, t) - g_i(\mathbf{x}, t)}{\tau_h} - w_i \frac{L_h(l_f(\mathbf{x}, t - \delta t) - l_f(\mathbf{x}, t))}{c_p}, \quad (14)$$

where  $g_i^{eq}(\mathbf{x}, t)$ —equilibrium distribution function for temperature field,  $\tau_h = 3 + 0.5$ —dimensionless relaxation time with respect to the dimensionless thermal diffusivity  $\alpha$ ,  $L_h$ —dimensionless latent heat of ice,  $c_p$ —dimensionless thermal capacity. The specific heat capacity and thermal diffusivity of ice and water must be defined exactly on the cell depending on their occupation as

$$\phi = (1 - l_f(\mathbf{x}))\phi^{ice} + l_f(\mathbf{x})\phi^{water}, \quad (15)$$

where  $\phi$ —physical properties, such as  $\alpha$  and  $c_p$ . The specific heat capacity of water in dimensionless form can be obtained from the Stefan number,  $St_R = St_L = (c_p^{water} \Delta\theta) / L_h$ , and can be used to obtain the specific heat capacity of ice as  $c_p^{ice} / c_p^{water} = c_{pR}^{ice} / c_{pR}^{water}$ , where subscript  $L$  stands for the lattice physical constants. The thermal diffusivity of water is related to the kinematic viscosity of water in definition of the Prandtl number (Pr) (Ayurzana and Hosoyamada 2016). The equilibrium distribution function for the temperature field is

$$g_i^{eq} = w_i \theta \left[ 1 + \frac{\mathbf{c}_i \mathbf{u}}{c_s^2} \right], \text{ where } \theta = \sum_{i=0}^8 g_i. \quad (16)$$

The plain temperature of water and ice can be estimated from the dimensionless temperature  $\theta$  using the relation:

$$T(\mathbf{x}) = \frac{T_{max} - T_{melt}}{\theta_{max} - \theta_{melt}} (\theta - \theta_{melt}) + T_{melt}. \quad (17)$$

The local enthalpy is estimated using the dimensionless temperature and the latent heat of melting as  $En(\mathbf{x}) = c_p\theta + l_f(\mathbf{x}, t - \delta t)L_h$  and it is used to linearly interpolate the liquid fraction value on a cell,

$$l_f(\mathbf{x}) = \begin{cases} 1 & \text{for } En > En_s + L_h = En_l \\ 0 & \text{for } En < En_s = c_p\theta_{melt} \\ \frac{En - En_s}{En_l - En_s} & \text{for } En_s \leq En \leq En_l. \end{cases} \quad (18)$$

The liquid fraction value defines the water and the ice cells in the computational domain. If the ice floats on the free surface, cells interacting with G cells must be IF cells due to the free surface definition, which is detailed in Sect. 2.3.

Motionless walls are assumed to be adiabatic. The proposed thermal LB model for temperature field can account for conjugate heat transfer at the interface between ice and water, since the model uses the exact thermal properties for the liquid and solid phases. At the free surface, we use a boundary condition with a constant temperature to satisfy the presence of an air thermal condition, which can also be given by a constant flux boundary condition.

### 2.3 Modeling of a Floating Ice

A moving solid body in the fluid flow can be effectively simulated with the immersed boundary (IB) modification (Strack and Cook 2007) into the discrete Boltzmann equation (see Eq. (1)). A Noble and Torczynski's version of IB method generates the smooth hydrodynamic force for the fluid flow and the solid motion. We propose an algorithm to use the IB-LBM to the floating object in the single phase free surface LBM. First, the force and the torque acting on an ice covering  $n$  cells are simply modified as:

$$\begin{aligned} \mathbf{F}_f &= s \frac{\Delta x^2}{\Delta t} \sum_n \beta \sum_{i=0}^8 f_i^m \mathbf{c}_i \text{ and} \\ \mathbf{T}_f &= s \frac{\Delta x^2}{\Delta t} \sum_n (\mathbf{x}_n - \mathbf{x}_c) \left( \beta \sum_{i=0}^8 f_i^m \mathbf{c}_i \right), \end{aligned} \quad (19)$$

where  $s$ —submerged volumetric percent of floating ice body (Fig. 3c),  $\mathbf{x}_n$ —coordinate of the current cell,  $\mathbf{x}_c$ —coordinate of the central cell of the floating body, as shown in Fig. 3b. The hydrodynamic force acting on the submerged part depends on the situation of the body position.

The motion of the ice body is resolved by the equation of motion:

$$m \frac{d^2 \mathbf{x}}{dt^2} = \mathbf{F}_f + \mathbf{F}_b \text{ and } I \frac{d\omega}{dt} = \mathbf{T}_f, \quad (20)$$

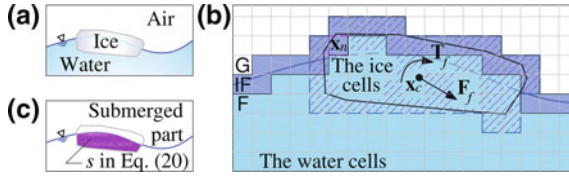


**Fig. 3** Floating ice on the free surface: **a** A general view, **b** discretization into 2D grid and **c** the representation of submerged part implying displaced water by the floating ice

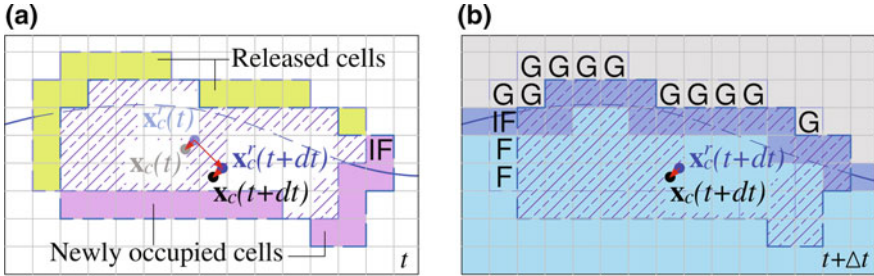


**Fig. 4** The movement of ice body: **a** Released and newly occupied cells and the centers, **b** letter flags on the cells show their changes due to the movement of ice body

where  $m$ —ice mass (kg),  $I$ —moment of inertia of the body ( $\text{kg m}^2$ ),  $\omega$ —angular velocity ( $\text{rad s}^{-1}$ ),  $\mathbf{F}_b = \mathbf{g}(\rho_{ice} A_{ice} - \rho_{water} A_{sub})$ —buoyancy force in two-dimensional space (N),  $A_{sub}$ —area of the submerged part the floating body ( $\text{m}^2$ ).

If phase changes of water take place around the interface between ice and water, mass and shape of the ice body will be changed over time. The changes of the body will affect the values of every physical variable of the body at each time step. To enable body shape changes over time or to simulate arbitrarily shaped body, an algorithm must use the body shape of previous time step for the computations in current time step. In addition, the staircase discretization of body may generate an error and accumulation of the error leads unphysical body shape changes for the moving body. To avoid this unphysical body shape changes and to reduce error accumulation on the body shape, an integer center of mass for the moving body is introduced in Eq. (19) and it must be resided on the lattice node in order to discretize ice body into the computational domain. The integer center of mass  $\mathbf{x}_c$  should be obtained from the real center of mass  $\mathbf{x}_c^r$  defined by Eq. (20), see Fig. 4a. Moreover, the movement of the ice body requires special care for the cell types. When the ice body moves to a new position, previous cells, which are released from the occupied cells by the ice body, need to be converted into appropriate cell types (Fig. 4b). As ice moves, newly occupied cells by the ice body are correctly initialized with the thermal and physical variables of the ice at the current time step. For instance, a temperature field of ice must be translated and rotated with the ice body movement to maintain the fields inside the ice. The same numerical

procedure should be applied for the thermal distribution functions, as well as physical and numerical variables unique for the ice cells. This translation and rotation of the variables can be done by storing variables into temporal polar coordinate fields originated at the integer center of the ice body. Then the variables initialization for the cells of new position of moved ice body uses the stored variables in the polar coordinate after the ice movement. This is most critical implementation of the moving body algorithm, since the phenomena inside the solid body are major for the computation.

If gas cells are newly occupied by the ice body discretization, as shown in Fig. 4a, they mainly become IF cells and distribution functions for them need to be reinitialized with Eq. (10). The mass of released IF cells, which are going to be G cells, need to be distributed among the neighboring IF cells as Eq. (9) in order to ensure the mass conservation. This algorithm for floating object is also applicable for the fully immersed body simulation, such as bed forming and sedimentation.

### 3 Numerical Simulations

#### 3.1 Melting of Motionless Ice in Free Surface Flow

Validations and the application of the free surface LBM can be found in Badarch et al. (2016). Numerical tests and applications for the heat transport and phase changes with and without the free surface flow can also be found in Ayurzana and Hosoyamada (2016, 2017). The numerical simulations of liquid-solid phase changes in free surface water flow in laboratory scale have been analyzed with experiments in our recent works. To demonstrate applicability of the proposed model for the phase changes in free surface flow, an ice bed melting with flow over a sharp crested weir is simulated. In this simulation, the ice bed is fixed. Thus, ice does not move, even if it melts into several parts, so that velocity in Eq. (4) set to zero. Initially, the ice bed thickness was 0.06 m and the temperature was  $-30\text{ }^{\circ}\text{C}$ . The water temperature at inflow boundary was maintained to be  $30\text{ }^{\circ}\text{C}$ , whereas ambient air temperature set to  $20\text{ }^{\circ}\text{C}$ . A selected grid number for the weir height gave a grid spacing and a time step as  $\Delta x = 2.5 \times 10^{-3}\text{ m}$  and  $\Delta t = 5.41 \times 10^{-3}\text{ s}$ . Dimensionless number for the simulation were  $\text{Pr} = 11.59$ ,  $\text{Ra} = 10^5$  and  $\text{Fr} = 0.13$ , where  $\text{Fr}$  is the Froude number.

The simulation properly predicts the flow and temperature field in domain, as shown in Fig. 5. The total melting time of the ice bed was 3.25 min and the melting rate of ice mass was around  $42.46\text{ kg min}^{-1}$ . We measured the local Nusselt number ( $\text{Nu}$ ) through the melting interface of ice to evaluate convective heat transport. The average Nusselt number ( $\text{Nu}_{\text{av}}$ ) was around 60–110, which gives the heat convection coefficient  $h_c = \text{Nu}_{\text{av}} k_R^{\text{ice}} / L_m \approx 648$  to  $1188\text{ (W K}^{-1}\text{ m}^{-2})$ , where  $k_R^{\text{ice}}$ —thermal conductivity of ice ( $\text{W K}^{-1}\text{ m}^{-1}$ ),  $L_m$ —characteristic water depth on the ice surface (m). Melting interface morphology in Fig. 5 shows that the nappe flow has been playing a significant role of melting the ice.

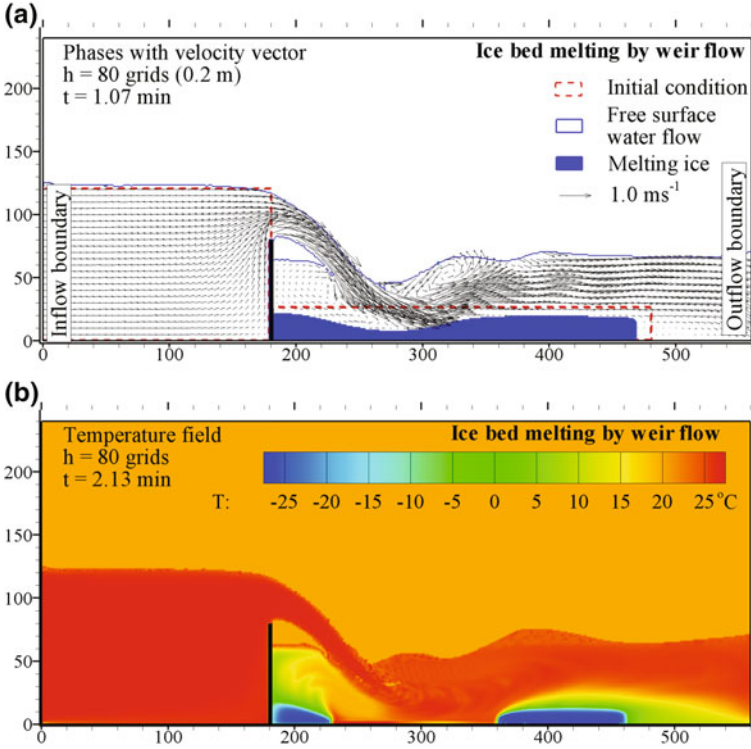


**Fig. 5** Snapshots of the forced melting of the ice bed: **a** Phases with the velocity vectors at  $t = 1.07$  min, **b** the temperature field at  $t = 2.13$  min after the simulation started

### 3.2 Floating of an Ice Cylinder

The floating of ice bodies is an important part of simulation of ice in the free surface flow. For simplicity, a simulation of an ice cylinder floating on the free surface is performed and compared with an experiment in order to demonstrate the proposed algorithm for floating body simulation. The ice cylinder with diameter  $D = 3$  cm, initially positioned above the free surface at a distance  $h = D + D/2$ , falls into stagnant water and then floats on the water surface. The initial temperature of ice was  $-25$   $^{\circ}\text{C}$ , whereas the water temperature was  $30$   $^{\circ}\text{C}$ . We tried to provide same condition for the experiment and simulation. A grid spacing  $\Delta x = 1.0 \times 10^{-3}$  m and a time step  $\Delta t = 4.57 \times 10^{-5}$  s are used for the simulation. The simulation time was shorter than the melting of the ice cylinder.

In Fig. 6a, we compare the coordinate of the center of the ice cylinder measured as a function of time in the simulation and laboratory experiment. Overestimates of position can be observed at the turnings of the ice cylinder position, which might be caused by the underestimates of the hydrodynamics force in simulation. By contrast, initial flow field might be affected on the ice cylinder movement in the

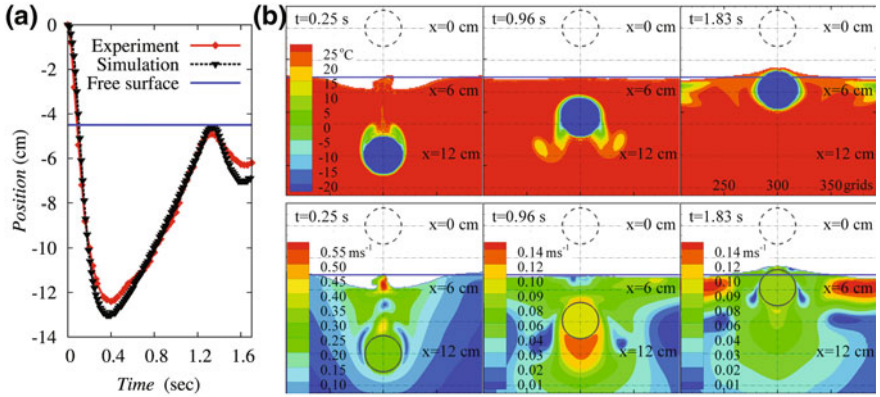


**Fig. 6** Falling and floating ice: **a** The comparison of the displacement of the ice cylinder measured in the simulation and lab experiment, **b** The computed temperature field (top) and flow field (bottom) at specific times

experiment. Another source of the overestimates might be the choice of the Rayleigh number. Figure 6 shows the numerical results at  $Ra = 10^4$ . When  $Ra$  is greater than  $Ra = 10^4$ , the convective flow become active than the inertial flow induced by the movement of the ice body.

The temperature and velocity field shows symmetries except of the splash during the ice cylinder plunging into the water in Fig. 6b. The shape of the cylinder at the end of simulation was same as the initial shape of the cylinder and the mass of system was conserved during the simulation.

### 4 Conclusions

Conclusively, a proper introduction and demonstration of the applicability of a liquid-solid phase change model for a free surface flow was achieved. In addition, a novel algorithm for the simulation of a time dependent arbitrary shaped floating body was attained. The model integrates a non-iterative enthalpy based method for phase changes, a heat transfer model, a free surface model and a floating body algorithm in the LB framework. Specifically, an ice bed melting due to flow over a weir was the demonstration of ice melting in the free surface flow. Subsequently, the main contribution of this paper was to show the accuracy of the proposed algorithm over a floating body simulation based on the IB-LB approach. This was confirmed with the simulation of a floating ice cylinder. Here, the proposed algorithm conserves the mass and shows less accumulated error for stepwise spatial discretization of the body. Finally, it can be said that the proposed model is not only capable of simulating ice dynamics in a free surface flow, but also capable of simulating dissolving related problems.

## References

- Ayurzana B, Hosoyamada T (2016) Phase change simulations of water near its density inversion point by Lattice Boltzmann method. In: Proceedings of the 23rd IAHR International Symposium on ice, pp 1–8
- Ayurzana B, Hosoyamada T (2017) Application of the lattice Boltzmann method to liquid-solid phase change in free surface flow: an example of Mongolian small hydropower plant. *J Jpn Soc Civil Eng Ser B1* 73(4): I\_607–I\_612
- Badarch A, Tokuzo H, Narantsogt N (2016) Hydraulics application of the free-surface lattice Boltzmann method. In: 11th International forum on strategic technology (IFOST), pp 195–199
- Bhatnagar PL, Gross EP, Krook M (1954) A model for collision processes in gases. I: small amplitude processes in charged and neutral one-component system. *Phys Rev* 94:511–525
- Chen S, Doolen GD (1998) Lattice Boltzmann method for fluid flows. *Annu Rev Fluid Mech* 30(1):329–364
- Hou S, Sterling J, Chen S, Doolen GD (1994) A lattice Boltzmann subgrid model for high Reynolds number flows. [arXiv:comp-gas/9401004](https://arxiv.org/abs/comp-gas/9401004)
- Huber C, Parmigiani A, Chopard B, Manga M, Bachmann O (2008) Lattice Boltzmann model for melting with natural convection. *Int. J Heat Fluid Flow* 29(5):1469–1480
- Iwasaki K, Uchida H, Dobashi Y, Nishita T (2010) Fast particle-based visual simulation of ice melting. In: Computer graphics forum, vol 29, no 7, pp 2215–2223
- Karpiński M, Bialik RJ, Rowiński PM (2013) Application of Lattice Boltzmann Method for generation of flow velocity field over river bed-forms. Experimental and computational solutions of hydraulic problems. Springer, Berlin Heidelberg, pp 327–335
- Noble DR, Torczynski JR (1998) A lattice-Boltzmann method for partially saturated computational cells. *Int J Mod Phys C* 9(08):1189–1201
- Strack OE, Cook BK (2007) Three-dimensional immersed boundary conditions for moving solids in the lattice-Boltzmann method. *Int J Numer Methods Fluids* 55(2):103–125
- Thürey N, Körner C, Rüde U (2005) Interactive free surface fluids with the lattice Boltzmann method. Technical report 05-4. University of Erlangen-Nuremberg, Germany
- Thürey N (2007) Physically based animation of free surface flows with the lattice Boltzmann Method. Ph.D. thesis, University of Erlangen-Nuremberg



# Simulation of Flow Characteristics Through Emerged Rigid Vegetation Over a Perturbed Bed

Paromita Chakraborty and Arindam Sarkar

**Abstract** Flow through submerged vegetation has been an active area of research due to its immense importance in the field of flood control, storm water management, soil erosion control, natural and manmade wetlands. But in situations of lower flow rate, the vegetation emerges out of the flow, rendering it the case of flow through emerged vegetation which also plays a significant role in the above-mentioned cases of practical applications. In the present study, the flow through rigid, emerged vegetation over a sinusoidal bed with small amplitude has been investigated. Biot's equation of poro-elasticity has been applied to get the governing equations of the 2-D flow which have been solved analytically by the perturbation method to get the velocity field. Further, the solutions for the vertical shear stress distribution and the bed shear stress are obtained and the effects of the vegetation density on the velocity and shear stress are analyzed. The results indicate that the bed form also affects the longitudinal component of velocity significantly when the vegetation is less dense. The difference between the maximum and minimum velocity of flow near the trough and crest is almost 30%.

## 1 Introduction

Flow through submerged as well as emerged vegetation has always been an active area of research due its widespread applications in the fields of sediment transport, erosion of river bed, restoration of the ecological systems etc. The presence of emergent rigid and flexible floodplain vegetation increases the flow resistance and enhances the sediment deposition process (Aberle and Järvelä 2013) which, in the long run, can significantly change the bed forms resulting in the formation of ripples, dunes etc. On many occasions, manmade wetlands are constructed for flood control, storm water management etc. Numerous researchers (Rowinski and Kubrak

---

P. Chakraborty (✉) · A. Sarkar  
School of Infrastructure, Indian Institute of Technology Bhubaneswar,  
Bhubaneswar 751013, Odisha, India  
e-mail: pc10@iitbbs.ac.in

© Springer International Publishing AG 2018  
M. B. Kalinowska et al. (eds.), *Free Surface Flows and Transport Processes*,  
GeoPlanet: Earth and Planetary Sciences,  
[https://doi.org/10.1007/978-3-319-70914-7\\_8](https://doi.org/10.1007/978-3-319-70914-7_8)

2002; Hsieh and Bolton 2007; Huai et al. 2009a, b; Zhao et al. 2012; Hsieh 2013) carried out both theoretical and experimental investigations to predict the qualitative as well as quantitative response of the wetland flow for varying flow situations and evaluated velocity, shear stress, bed shear for these cases. However, investigators divided the flow into outer and inner regions of emerged vegetation for the determination of the velocity field (Huai et al. 2009a, b). Abt et al. (1994) carried out experimental investigation to study the effect of vegetated streambeds on sediment deposition and concluded that the sediment deposited depends greatly on the vegetation length. Fairbanks (1998) conducted experiments to investigate the effect of vegetation array on sediment transport and reported that alternate crest and trough formation takes place at the upstream and downstream of the vegetation stems. Nepf (1999) studied the effect of vegetation patch on the flow and reported that the turbulence intensity is significantly affected by the interaction of the patches resulting in the greater sediment transport rate. The effect of vegetation on bed load transport has been studied experimentally by Yager and Schmeckle (2013), and formation of the scour hole is reported due to the increased turbulence intensities near the bed. The effect of vegetation density on flow and scour hole was also studied experimentally by Chen et al. (2012) and the dune height, scour depth, length of the scour hole were reported to bear an inverse relation with the vegetation density. Bed roughness significantly affects the flow velocity in case of erodible beds, which has attracted numerous researchers to study the effect of bed forms and vegetation on flow velocity, turbulence intensity, and Reynold stress. Several analyses (Liu et al. 2008; Stoesser et al. 2008; Dehsorkhi et al. 2011) have been carried out to understand the effect of bed form and vegetation on velocity, shear and turbulence intensity in an open channel flow.

In most of the previous research works, the effects of vegetation on Manning's coefficient, Darcy's friction factor and vegetation drag coefficient were investigated, but the effects of bed forms on flow field and shear stress were seldom reported. More detailed understanding of velocity, shear stress and energy distribution in submerged as well as emerged flow over different bed forms is required. Moreover, most of the previous investigations were experimental or numerical. Further, for clear understanding of the physical situation, analytical solutions are always preferred. Some of the analytical studies based on the porous media flow theory (Zhao et al. 2012; Hsieh 2013) are available, but they have not considered the flow through vegetation over erodible beds and various bed forms. Chakraborty and Sarkar (2016) first proposed an analytical solution over a sinusoidal bed for rigid and submerged vegetation in a wetland. The poro-elastic flow theory has been applied (Heish and Shiu 2006; Zhao et al. 2012) and laminar flow condition has been considered to get the analytical solution for flow through submerged and emerged vegetation over inclined plane bed. From the literature, it is evident that the effect of vegetation on longitudinal velocity component has been extensively studied, but few investigations have been carried out to study the effect of bed forms on the vegetated flow through submerged and emerged vegetation. In the present study, an analytical approach for the laminar water flow through emerged

vegetation over a sinusoidal bed is proposed, focusing on the influences of vegetation and bed forms on the flow process through an emerged wetland.

## 2 Model Formulation

Flow through rigid, emergent vegetation over a sinusoidal bed has been considered in the present study.  $H$  is the total depth of flow from the mean line of the perturbed bed up to the free water surface,  $x$ ,  $y$ ,  $z$  are the co-ordinates in the longitudinal, vertical and transverse direction (m), respectively, and  $\theta$  is the bed angle, as shown in Fig. 1.

### 2.1 Governing Equations

The flow through emergent rigid vegetation is modeled by a set of continuity and momentum equations implementing Biot's theory of poro-elasticity (Biot 1956). In the present study, flow through the wetland is considered to be steady, laminar, 2-D and incompressible. For the sake of brevity, directly the non-dimensional governing equations are written by defining the following non-dimensional variables:

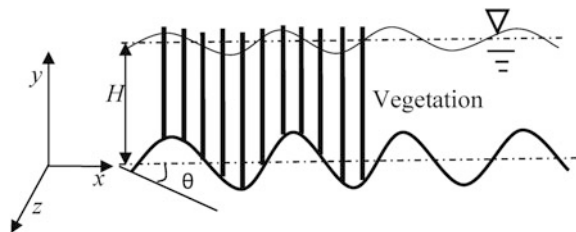
$$\hat{x} = \frac{x}{H}, \hat{y} = \frac{y}{H}, \hat{u} = \frac{u}{u_0}, \hat{v} = \frac{v}{u_0}, \hat{P} = \frac{P}{P_0} \quad (1)$$

where  $u$ ,  $v$  are the velocity components in the  $x$  and  $y$  direction ( $\text{m s}^{-1}$ ), respectively, and  $P$  is the pressure.  $u_0$  and  $P_0$  are the velocity scale ( $\text{m s}^{-1}$ ) and pressure scale ( $\text{kg m}^{-1} \text{s}^{-2}$ )

$$\frac{\partial \hat{u}}{\partial \hat{x}} + \frac{\partial \hat{v}}{\partial \hat{y}} = 0 \quad (2)$$

$$R_e \left( \hat{u} \frac{\partial \hat{u}}{\partial \hat{x}} + \hat{v} \frac{\partial \hat{u}}{\partial \hat{y}} \right) = - \frac{\partial \hat{P}}{\partial \hat{x}} + \left( \frac{\partial^2 \hat{u}}{\partial \hat{x}^2} + \frac{\partial^2 \hat{u}}{\partial \hat{y}^2} \right) + \frac{\rho g H^2 \sin \theta}{\mu u_0} - T_3 \quad (3)$$

**Fig. 1** Schematic for flow through emerged vegetation over sinusoidal bed



$$R_e \left( \hat{u} \frac{\partial \hat{v}}{\partial \hat{x}} + \hat{v} \frac{\partial \hat{v}}{\partial \hat{y}} \right) = - \frac{\partial \hat{P}}{\partial \hat{y}} + \left( \frac{\partial^2 \hat{v}}{\partial \hat{x}^2} + \frac{\partial^2 \hat{v}}{\partial \hat{y}^2} \right) - \frac{\rho g H^2 \cos \theta}{\mu u_0} - T_4 \quad (4)$$

where

$$R_e = \frac{u_0 H \rho}{\mu}, T_3 = \frac{H^2 \eta \hat{u}}{k_p}, T_4 = \frac{H^2 \eta \hat{v}}{k_p}. \quad (5)$$

The vegetation porosity parameter is found from the analytical study of Hsieh and Shiu (2006).  $\hat{P}$  is the non dimensional pressure,  $g$  is the acceleration due to gravity.  $\hat{x}, \hat{y}$  are the non-dimensional longitudinal and vertical co-ordinates, respectively.  $\hat{u}, \hat{v}$  are the non-dimensional longitudinal and vertical velocity, respectively,  $R_e$  is the Reynolds number,  $\mu$  is dynamic viscosity ( $\text{kg m}^{-1} \text{s}^{-1}$ ),  $\eta$  is vegetation porosity and is defined as the ratio of water volume to the total volume of each layer.  $k_p$  is the porous medium permeability ( $\text{m}^2$ ),  $\rho$  is the density of the fluid ( $\text{kg m}^{-3}$ ). The effect of inertia is considered to be negligible, and the flow is mainly gravity driven rendering the order of the gravity force and viscous force to be same. Equating these forces, the scales for velocity  $u_0$  and pressure scale  $P_0$  have been obtained.

## 2.2 Profile of the Perturbed Bed

For solving the equations, perturbation method is applied (Kang and Chen 1995). The amplitude of the sinusoidal bed is assumed to be small compared to the total flow depth and may be represented in non-dimensional form as follows:

$$\hat{y} = \varepsilon \sin \alpha \hat{x}, \quad \varepsilon = \frac{a}{H} \quad \text{where} \quad \alpha = \frac{2\pi H}{\lambda} \quad (6)$$

where  $a$  and  $\lambda$  are the amplitude (m) and wave length (m) of the sinusoidal bed, respectively,  $\alpha$  is the non-dimensional wave number. The ratio  $\varepsilon$  of amplitudes of the bed and total flow depth is small and may be regarded as the perturbation parameter. Depending on the bed profile, a series solution may be assumed for all the flow variables (Kang and Chen 1995) and all the variables are expanded with respect to the small perturbation parameter as follows:

$$\begin{aligned} \hat{u} &= \hat{u}_0 + \varepsilon \hat{u}_1 + \varepsilon^2 \hat{u}_2 + \dots, \quad \hat{v} = \hat{v}_0 + \varepsilon \hat{v}_1 + \varepsilon^2 \hat{v}_2 + \dots, \\ \hat{P} &= \hat{P}_0 + \varepsilon \hat{P}_1 + \varepsilon^2 \hat{P}_2 + \dots, \quad g(\hat{x}) = \varepsilon g_1(\hat{x}) + \varepsilon^2 g_2(\hat{x}) \dots, \\ \hat{\tau} &= \hat{\tau}_0 + \varepsilon \hat{\tau}_1 + \varepsilon^2 \hat{\tau}_2 + \dots \end{aligned} \quad (7)$$

where  $\hat{u}_0$  and  $\hat{v}_0$  are the non-dimensional longitudinal and vertical velocity components;  $\hat{P}_0$  is the non-dimensional pressure; and  $\hat{\tau}_0$  is the non-dimensional shear

stress. The sub index number indicates the 0th, 1st and 2nd order, respectively. The equation of the free surface in non-dimensional form is given as follows:

$$\hat{y} = 1 + g(\hat{x}) \quad (8)$$

where  $g(\hat{x})$  represents the disturbances in the free surface. Substituting Eq. (7) in Eqs. (2)–(5) and equating the coefficient of  $\varepsilon^0$  and  $\varepsilon^1$  from the resulting equations, the following 0th order and 1st order equations are obtained:

$$\frac{\partial \hat{u}_0}{\partial \hat{x}} = 0 \quad (9)$$

$$\frac{d^2 \hat{u}_0}{d\hat{y}^2} = -\frac{\rho g H^2 \sin \theta}{\mu u_0} + T_3 \quad (10)$$

$$\frac{d\hat{P}_0}{d\hat{y}} = -\frac{\rho g H^2 \cos \theta}{\mu u_0} \quad (11)$$

$$\frac{\partial \hat{u}_1}{\partial \hat{x}} + \frac{\partial \hat{v}_1}{\partial \hat{y}} = 0 \quad (12)$$

$$\frac{\partial^2 \hat{u}_1}{\partial \hat{x}^2} + \frac{\partial^2 \hat{u}_1}{\partial \hat{y}^2} - \frac{\partial \hat{P}_1}{\partial \hat{x}} - T_3 = 0 \quad (13)$$

$$\frac{\partial^2 \hat{v}_1}{\partial \hat{x}^2} + \frac{\partial^2 \hat{v}_1}{\partial \hat{y}^2} - \frac{\partial \hat{P}_1}{\partial \hat{y}} - T_4 = 0. \quad (14)$$

### 2.3 Boundary Conditions and Solutions

The variables on the bed are expanded with respect to  $\varepsilon = 0$ , and at each order of  $\varepsilon$  these boundary conditions are applied on the mean position of the bed. The same procedure is used for the free surface, resulting in the following boundary conditions:

No slip condition at the bed and zero shear stress at the free surface are considered for the 0th order.

Again for the 1st order, no slip condition at the bed and kinematic boundary condition have been applied at the free surface. Considering no infiltration through the bed gives

$$\hat{u}_1 + \frac{d\hat{u}_0}{d\hat{y}} \sin \alpha \hat{x} = 0, \hat{v}_1 = 0. \quad (15)$$

Considering zero shear and continuity of normal stress at the free surface

$$\hat{g}_1 \frac{d^2 \hat{u}_0}{d\hat{y}^2} + \frac{\partial \hat{u}_1}{\partial \hat{y}} + \frac{\partial \hat{v}_1}{\partial \hat{x}} = 0, -\frac{d\hat{P}_0}{d\hat{y}} g_1 - \hat{P}_1 - 2 \frac{\partial g_1}{\partial \hat{x}} \left( \frac{d\hat{u}_0}{d\hat{y}} \right) + 2 \frac{\partial \hat{v}_1}{\partial \hat{y}} = 0 \quad (16)$$

Solving the continuity and momentum Eqs. (9)–(11), the 0th order solution is obtained

$$\hat{u}_0 = c_1 e^{m_2 \hat{y}} + c_2 e^{-m_2 \hat{y}} + \frac{1}{m_2^2} \quad (17)$$

where  $c_1$  and  $c_2$  are the constants of integration. Applying the 0th order boundary conditions, the solutions of the 0th order problem are obtained for various values of porosity parameters  $m_2^2$  and these values are used for the solution of the 1st order problem.

The boundary conditions for the 1st order Eqs. (15)–(17) suggest the solution of the Eqs. (12)–(14) to be assumed as follows:

$$\hat{u}_1 = \hat{U}_1(\hat{y}) e^{j\alpha \hat{x}}, \hat{v}_1 = \hat{V}_1(\hat{y}) e^{j\alpha \hat{x}}, g_1 = A e^{j\alpha \hat{x}}, \hat{P}_{11} = \hat{P}_1(\hat{y}) e^{j\alpha \hat{x}} \quad (18)$$

where  $j = \sqrt{-1}$  and  $A$  and  $B$  are complex constants, and  $\hat{U}_1$ ,  $\hat{V}_1$ ,  $\hat{P}_1$  are the non dimensional function of  $\hat{y}$ . Here only the real parts of the variables are to be considered. Substituting the above Eq. (18) in the continuity and momentum Eqs. (12)–(14) and simplifying, the following ordinary differential equations and their respective solutions are

$$\left. \begin{aligned} \hat{U}_1^{IV} - (2\alpha^2 + m_2^2) \hat{U}_1^{II} + (\alpha^4 + \alpha^2 m_2^2) \hat{U}_1 &= 0 \\ \hat{U}_1 &= A_1' e^{(\sqrt{\alpha^2 + m_2^2}) \hat{y}} + B_1' e^{-(\sqrt{\alpha^2 + m_2^2}) \hat{y}} + C_1' e^{\alpha \hat{y}} + D_1' e^{-\alpha \hat{y}} \end{aligned} \right\} \quad (19)$$

$$\left. \begin{aligned} \hat{V}_1^{IV} - (2\alpha^2 + m_2^2) \hat{V}_1^{II} + (\alpha^4 + \alpha^2 m_2^2) \hat{V}_1 &= 0 \\ \hat{V}_1 &= A_2' e^{(\sqrt{\alpha^2 + m_2^2}) \hat{y}} + B_2' e^{-(\sqrt{\alpha^2 + m_2^2}) \hat{y}} + C_2' e^{\alpha \hat{y}} + D_2' e^{-\alpha \hat{y}} \end{aligned} \right\} \quad (20)$$

where  $\hat{U}_1^{IV}$ ,  $\hat{U}_1^{II}$ ,  $\hat{V}_1^{IV}$  and  $\hat{V}_1^{II}$  are fourth-order and second-order derivatives of  $\hat{U}$  and  $\hat{V}$ , respectively. The final expression for the shear stress is as follows

$$\tau_b = \frac{d\hat{u}_{20}}{d\hat{y}} \Big|_{\hat{y}=0} + \varepsilon \left[ \left( \frac{\partial \hat{u}_{21}}{\partial \hat{y}} + \frac{\partial \hat{v}_{21}}{\partial \hat{x}} \right) \Big|_{\hat{y}=0} + \frac{d^2 \hat{u}_{20}}{d\hat{y}^2} \Big|_{\hat{y}=0} \sin \alpha \hat{x} \right] \quad (21)$$

where  $\hat{\tau}_b$  is the bed shear stress and shear stress scale is  $\tau_0 = \frac{\mu u_0}{H}$ , where  $\tau_0$  is the shear stress scale ( $\text{kg m}^{-1} \text{s}^{-2}$ ).

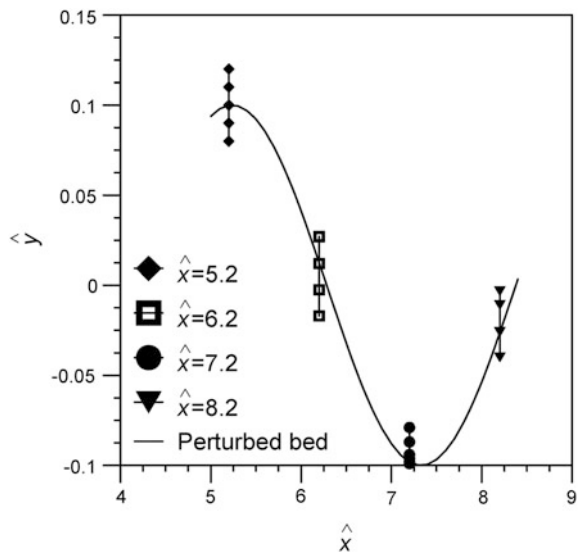
### 3 Results and Discussions

The model which is proposed in the present study is being applied to a typical wetland flow, with 0.4 m total flow depth, a vegetated layer of 0.2 m height and longitudinal bed slope of 0.0001. The pore specific area and the perturbation parameter have been assumed to be  $100 \text{ m}^{-1}$  and 0.1, respectively. Typical values of  $C_s = 3$ ,  $T_0 = 2$ ,  $\rho = 1000 \text{ kg m}^{-3}$ ,  $\mu = 0.001 \text{ Ns m}^{-2}$ ,  $g = 9.81 \text{ m s}^{-2}$  are considered (Zhao et al. 2012). From Eq. (12), solutions have been obtained for longitudinal and vertical components of velocity profile for rigid emerged vegetation. All the results reported in the following correspond to the vertical profile, from the mean bed to the mean free surface height. The velocity profiles have been presented in the selected sections on the perturbed sinusoidal bed, depicted in Fig. 2. The experimental result (run 3) of Rowiński and Kubrak (2002) is superposed on the longitudinal velocity distribution of the present study in Fig. 3 to show the effects of vegetation distribution on the velocity profiles. Although the flow and bed conditions in two situations are not similar, yet the similar trend is found.

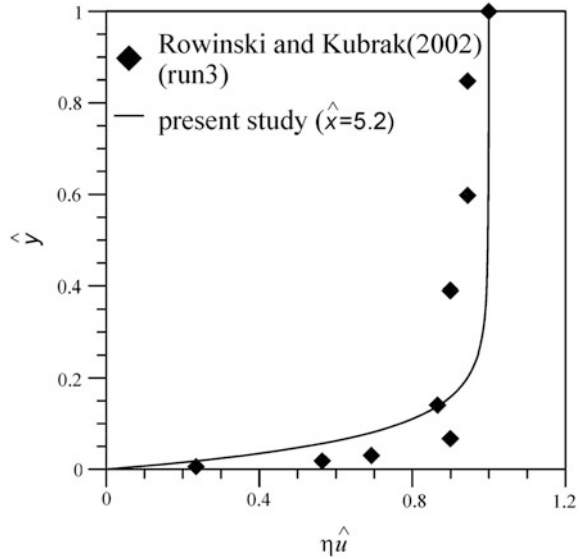
#### 3.1 Velocity Distribution and Bed Shear Stress

Figure 4 depicts the horizontal velocity distribution at different non-dimensional sections ( $\hat{x} = 5.2, 6.2, 7.2, 8.2$ ) of the sinusoidal bed for different values of vegetation porosity ( $\eta = 0.8, 0.85$ ). Increase in  $\eta$  signifies more water volume fraction offering less flow resistance resulting in higher velocity. For lower values of  $\eta$ , the vegetation drag increases which causes significant reduction in the horizontal

**Fig. 2** Different sections over the sinusoidal bed



**Fig. 3** Longitudinal velocity distribution at the crest

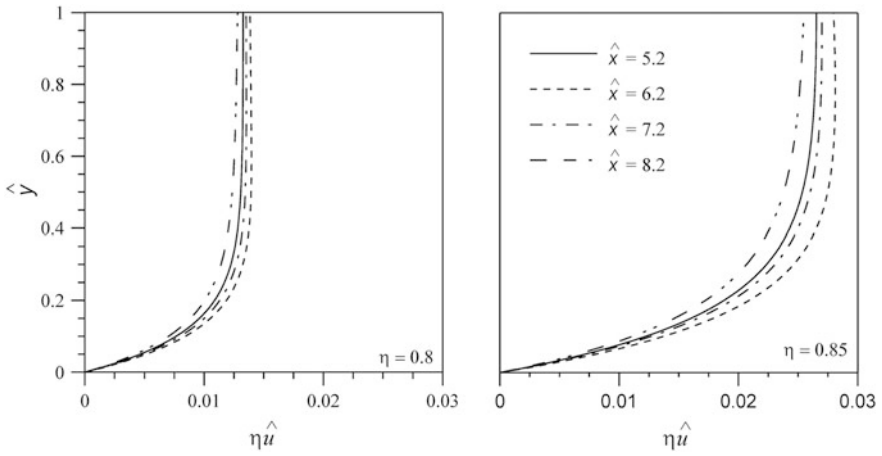


velocity. However, for higher values of  $\eta$ , the variations of the velocities at different sections are quite significant. While flowing towards the trough, the gravity force assists the flow which causes an increase in the velocity. It is important to note down that the velocity is not maximum at the trough as the effect of the upward slope's flow resistance is felt here. Therefore, the velocity will reach its maximum near the middle of the downward slope portion ( $\hat{x} = 6.2$ ). This is also evident from the figure. The velocity will be minimum near the middle of the upward slope portion as the effect of the opposing gravity is greater in that part. At the crest, the effect of the start of the downward slope will also act on the fluid and flow velocity will not be minimum. This is evident in Fig. 4.

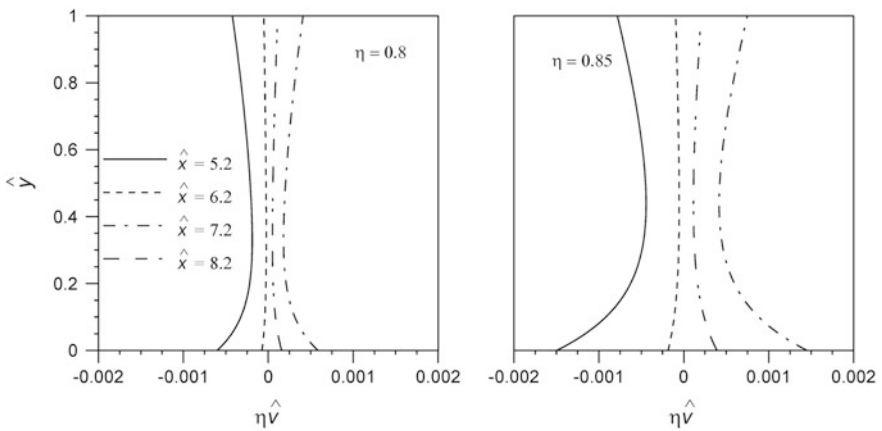
Figure 5 represents the vertical velocity distributions at different sections ( $\hat{x} = 5.2, 6.2, 7.2, 8.2$ ) for different vegetation porosity values  $\eta = 0.8$  and  $0.85$ . It is observed that at the crest and trough, vertical components of velocity are showing opposite trend, as shown in Fig. 5. At the trough, the transverse velocity is in the upward direction and at the crest it is in the downward direction. Near the middle of the downward and upward slopes, the transverse velocity is minimum. For higher values of vegetation porosity,  $\eta = 0.85$ , the velocities at all sections increase. Distributions of vertical component of velocity at different sections are shown for different values of  $\eta$ .

Figure 6 depicts the bed shear variation along the longitudinal direction for different values of  $\eta$ . It is evident that the magnitude of the bed shear increases with the decrease in the vegetation density. As the vegetation density decreases, the velocity of flow increases, resulting in higher drag on the bed applied by the fluid. Bed shear also follows a periodic pattern and its amplitude depends on vegetation





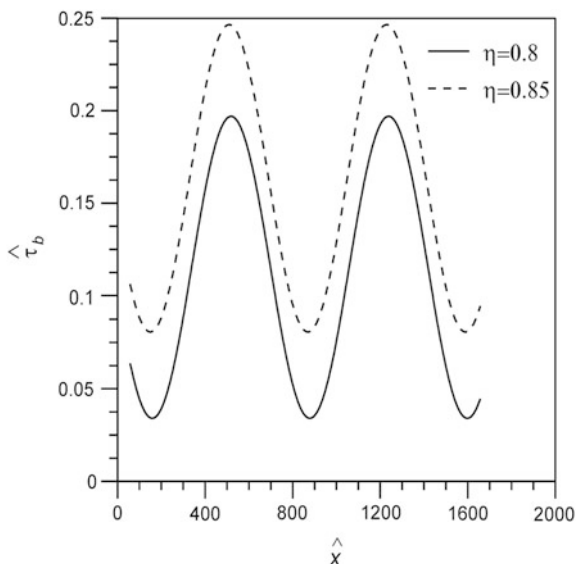
**Fig. 4** Vertical distributions of longitudinal velocity at different sections for various values of  $\eta$



**Fig. 5** Vertical distribution of vertical velocity at different sections for different values of  $\eta$

density. It may be observed that a 7% decrease in vegetation density increases the bed shear stress by nearly 20%. Vertical shear stress has also been analysed and it is observed that shear stress is more at the bed for lower vegetation density. At the trough, shear at the bed is greater. As the velocity is greater in the trough, change of velocity with respect to depth is higher near the bed at the trough, resulting in a higher shear stress.

**Fig. 6** Variation of the bed shear along the bed for different values of  $\eta$



## 4 Conclusions

Flow through emerged, rigid vegetation over a sinusoidal bed is considered and a 2-D analytical model has been proposed considering the amplitude of the bed to be small. The equations governing the flow are solved by the perturbation method and velocity and shear stress have been obtained. It is observed that the velocity and bed shear increase with the decrease in vegetation density. The bed form also affects the velocity significantly when the vegetation is less dense. The difference between the maximum and minimum velocity of flow near the trough and crest is almost 30%. It is also observed that a 7% decrease in vegetation density increases the bed shear stress by nearly 20%.

## References

- Aberle J, Järvelä J (2013) Flow resistance of emergent rigid and flexible floodplain vegetation. *J Hydraul Res* 51(1):33–45
- Abt SR, Clary WP, Thornton CI (1994) Sediment deposition and entrapment in vegetated streambeds. *J Irrig Drain Eng* 120(6):1098–1111
- Biot MA (1956) Theory of propagation of elastic waves in a fluid-saturated porous solid. *J Acoust Soc Am* 28(1):168–191
- Chakraborty P, Sarkar A (2016) Flow characteristics through submerged rigid vegetation over a sinusoidal perturbed bed. *Int J River Basin Manag* 4(3):255–266
- Chen SC, Chan HC, Li YH (2012) Observations on flow and local scour around submerged flexible vegetation. *Adv Water Resour* 43:28–37

- Dehsorkhi EN, Afzalimehr H, Vijay PS (2011) Effect of bed forms and vegetated banks on velocity distributions and turbulent flow structure. *J Hydrol Eng* 16:495–507
- Fairbanks JD (1998) Velocity and turbulence characteristics in flows through rigid vegetation. M. Tech Thesis. Virginia Polytechnic Institute & State University
- Hsieh PC, Bolton S (2007) Laminar surface water flow over vegetated ground. *J Hydraul Eng* 133(3):335–341
- Hsieh PC (2013) Direct analytical solution of turbulent surface water flow on a slope. *J Hydrol Eng* 18(8):976–982
- Hsieh PC, Shiu YS (2006) Analytical solutions for water flow passing over a vegetal area. *Adv Water Resour* 29(9):1257–1266
- Huai WX, Chen ZB, Han J (2009a) Mathematical model for the flow with submerged and emerged rigid vegetation. *J Hydrodyn* 21(5):722–729
- Huai WX, Zeng YH, Xu ZG, Yang ZH (2009b) Three-layer model for vertical velocity distribution in open channel flow. *Adv Water Resour* 32(4):487–492
- Kang F, Chen K (1995) Gravity driven two layer flow down a slightly wavy periodic incline at low Reynolds numbers. *Int J Multiph Flow* 21(3):501–513
- Liu D, Diplas P, Fairbanks JD, Hodges CC (2008) An experimental study of flow through rigid vegetation. *J Geophys Res* 113(12):1–16
- Nepf HM (1999) Drag, turbulence, and diffusion in flow through emergent vegetation. *Water Resour Res* 35(2):479–489
- Rowinski PM, Kubrak J (2002) A mixing-length model for predicting vertical velocity distribution in flows through emergent vegetation. *J Hydrol Sci* 47(6):893–904
- Stoesser TM, Braun C, Garcia M, Rodi WM (2008) Turbulence structures in flow over two-dimensional dunes. *J Hydraul Eng* 134(1):42–55
- Yager EM, Schmeeckle MW (2013) The influence of vegetation on turbulence and bed load transport. *J Geophys Res Earth Surf* 118:1585–1601
- Zhao M, Huai W, Han J, Xie Z, Guo J (2012) Uniform laminar wetland flow through submerged and floating plants. *J Hydraul Res* 50(1):52–59

# Numerical Study of Sedimentation in Uniformly Vegetated Wetlands

Eleonora Dallan, Andrea Bottacin-Busolin, Nima Sabokrouhiyeh,  
Matteo Tregnaghi and Andrea Marion

**Abstract** Constructed wetlands for wastewater treatment are increasingly recognized as a valid alternative to conventional water treatment methods with a high ecological value. Sediment transport and deposition processes play a key role in determining the treatment performance and the morphological evolution of a wetland, and must be carefully considered both in the design and the maintenance phase. This work presents a 2-D numerical study of the effect of vegetation density on sedimentation in wetlands. A depth-averaged hydrodynamic and mass transport model was applied to a rectangular wetland with uniform vegetation density and flat topography. Sediment settling and resuspension are represented in the model by a first-order source/sink term that depends on grain size and shear velocity. Results show that, for the same inflow discharge, the removal efficiency for relatively small grain sizes is lower in wetlands with higher vegetation density. This is a consequence of the more uniform flow distribution found in more densely vegetated wetlands. However, the condition of total removal of suspended sediment is

---

E. Dallan (✉) · N. Sabokrouhiyeh · M. Tregnaghi · A. Marion  
Department of Industrial Engineering, University of Padua, via F.  
Marzolo 9, 35131 Padua, Italy  
e-mail: eleonora.dallan@phd.unipd.it

N. Sabokrouhiyeh  
e-mail: nima.sabokrouhiyeh@unipd.it

M. Tregnaghi  
e-mail: matteo.tregnaghi@unipd.it

A. Marion  
e-mail: andrea.marion@unipd.it

A. Bottacin-Busolin  
School of Mechanical, Aerospace and Civil Engineering, University of Manchester,  
Manchester M13 9PL, UK  
e-mail: andreabottacin@gmail.com

achieved for higher grain sizes in more sparsely vegetated wetlands, meaning there is a range of relatively large grain sizes for which the removal efficiency is higher for higher vegetation densities.

## 1 Introduction

Free water surface constructed wetlands (FWS CWs) have received increasing attention in recent years due to their potential for treatment of municipal, agricultural, industrial wastewater and storm water. Although CWs can improve water quality significantly, satisfactory performance depends on an efficient wetland design. The development of more effective criteria and protocols based on measurable physical and ecological parameters requires an improved understanding of contaminant removal processes in these complex environments.

In the last decades, growing interest in the construction and restoration of wetlands (Marion et al. 2014) has led to an increasing development of conceptual, analytical and numerical models for wetlands. Initial studies analyzed wetland performance using continuously stirred tank reactor (CSTR) models (Kadlec and Knight 1996; Stone et al. 2004). Subsequent studies used experimental, numerical and analytical methods to analyze wetland processes. Most of the mechanistic models presented in the literature have been developed for urban wastewater treatment in subsurface flow CWs (SSFCWs), e.g. Constructed Wetlands 2D (CW2D) (Langergraber 2001), whilst models for free water surface constructed wetlands (FWSCWs) remain fewer (Gargallo et al. 2016). Since the fate of contaminants in wetlands depends on the heterogeneity of various factors such as vegetation, two- or three-dimensional models appear more appropriate to describe wetland processes. Recent 2D modeling approaches combine shallow water depth-averaged hydrodynamic models with advection-dispersion models for mass transport. These approaches have been applied to investigate the effect of wetland geometry and vegetation distribution (Musner et al. 2014; Savickis et al. 2016; Sabokrouhiyeh et al. 2016). Wetland contaminant removal is also influenced by sediment transport processes, because they influence soil particles retention, water transparency, interactions between pathogens and dissolved oxygen exchanges across the water-sediment interface.

The aim of this study is to analyze the deposition of suspended sediment in FWSCWs. Numerical simulations are performed using the model presented by Musner et al. (2014), adapted to include a first simplified description of sediment transport, settling and resuspension. The analysis focuses on the effect of grain size and vegetation density on sediment removal in a uniformly vegetated wetland. The overarching aim of this research is to develop practical criteria for optimal wetland design based on an improved physical understanding of the fate of sediments in free surface wetlands.

## 2 Theoretical Background

### 2.1 Two-Dimensional Wetland Model

A two-dimensional numerical model of a wetland was developed to simulate flow dynamics and transport of suspended sediment. Assuming that vertical gradients are smaller than the horizontal gradients, the transport of a solute in a wetland can be represented by a two-dimensional depth-averaged model. This assumption has often been used in wetland studies (Somes et al. 1999; Arega and Sanders 2004; Jenkins and Greenway 2005) and is consistent with the simplified wetland topography and geometry analyzed in this work.

The hydrodynamic model solves the 2-D shallow-water equations, whereas the transport model solves the advection-dispersion equation with a source/sink term. In the hydrodynamic model, the effect of vegetation is represented as an equivalent flow resistance that depends on vegetation density, stem diameter and submerged stem length. The solute transport model relies on the velocity field predicted by the hydrodynamic model and takes into account the additional mechanical and turbulent dispersion induced by vegetation via an appropriately defined dispersion tensor. In the next paragraphs an abridge description of the mathematical formulation of the model is presented. The detailed formulation can be found in Musner et al. (2014). The model flow and solute transport equations are solved using a Finite Element formulation with quadratic shape functions.

#### 2.1.1 Hydrodynamic Model

The governing equations include mass conservation Eq. (1) and the conservation of linear momentum in the horizontal plane Eqs. (2)–(3). Assuming hydrostatic pressure, stationary flow, negligible wind and Coriolis forces, the depth-averaged velocity field and water depth can be described by the following equations (Wu 2007):

$$\frac{\partial(hU_x)}{\partial x} + \frac{\partial(hU_y)}{\partial y} = 0 \tag{1}$$

$$\frac{\partial(hU_x^2)}{\partial x} + \frac{\partial(hU_xU_y)}{\partial y} = -gh \frac{\partial(z_s)}{\partial x} - \frac{\tau_{bx}}{\rho} - \frac{\tau_{vx}}{\rho} \tag{2}$$

$$\frac{\partial(hU_xU_y)}{\partial x} + \frac{\partial(hU_y^2)}{\partial y} = -gh \frac{\partial(z_s)}{\partial y} - \frac{\tau_{by}}{\rho} - \frac{\tau_{vy}}{\rho} \tag{3}$$

where  $U_x$ ,  $U_y$ —velocity components along the  $x$ - and  $y$ -direction, respectively,  $h$ —water depth,  $z_s$ —water surface elevation,  $\rho$ —water density,  $\tau_{bx}$  and  $\tau_{by}$ —bed shear

stresses,  $\tau_{vx}$  and  $\tau_{vy}$ —vegetation drag stresses in the  $x$ - and  $y$ -direction, respectively. Equations (2)–(3) assume that Reynolds stresses are negligible compared to bed and vegetative resistance.

Bed shear stresses are determined from the following equations (Kadlec and Wallace 2008):

$$\tau_{bx} = \rho C_b U_x \sqrt{U_x^2 + U_y^2} \quad (4)$$

$$\tau_{by} = \rho C_b U_y \sqrt{U_x^2 + U_y^2} \quad (5)$$

in which the bed-drag coefficient,  $C_b$ , is defined as:

$$C_b = \frac{3\mu}{h\rho\sqrt{U_x^2 + U_y^2}} + \frac{M^2 g}{h^3} = \frac{3}{Re_b} + \frac{M^2 g}{h^3} \quad (6)$$

where  $\mu$ —water dynamic viscosity, and  $M$ —Manning friction coefficient. In Eq. (6) the first term dominates under laminar and transitional flow ( $Re \leq 500$ ), whereas the second one becomes significant for larger Reynolds numbers ( $Re \geq 1250$ ).

Vegetation drag is modeled using the following expressions for the drag exerted by the stems (Kadlec and Wallace 2008):

$$\tau_{vx} = \frac{1}{2} \rho C_{vD} n_v d l U_x \sqrt{U_x^2 + U_y^2} \quad (7)$$

$$\tau_{vy} = \frac{1}{2} \rho C_{vD} n_v d l U_y \sqrt{U_x^2 + U_y^2} \quad (8)$$

where  $C_{vD}$ —vegetation-drag coefficient (dimensionless),  $n_v$ —number of vegetation stems per unit area,  $d$ —cylinder diameter of vegetation,  $l$ —submerged stem length (here taken as equal to water depth  $h$ ). The coefficient  $C_{vD}$  is expressed as:

$$C_{vD} = \frac{10\mu}{\rho d \sqrt{U_x^2 + U_y^2}} + 1 = \frac{10}{Re_d} + 1 = \frac{10}{Re_h} \frac{h}{d} + 1 \quad (9)$$

where  $Re_d = Ud/\nu$  is the stem Reynolds number.

### 2.1.2 Solute Transport Model

The transport of suspended sediment is simulated using the 2D depth-averaged advection-dispersion equation with a first-order source/sink term:

$$\begin{aligned} \frac{\partial(hC)}{\partial t} + \frac{\partial(hU_x C)}{\partial x} + \frac{\partial(hU_y C)}{\partial y} &= \frac{\partial}{\partial x} \left( hE_{xx} \frac{\partial C}{\partial x} + hE_{xy} \frac{\partial C}{\partial y} \right) \\ &+ \frac{\partial}{\partial y} \left( hE_{yx} \frac{\partial C}{\partial x} + hE_{yy} \frac{\partial C}{\partial y} \right) - KC \end{aligned} \quad (10)$$

where  $C$ —depth-averaged sediment concentration, and the source term represents sediment settling and resuspension (Sect. 2.1.3). The coefficients  $E_{ij}$  account for both turbulent diffusion and shear dispersion due to vertical velocity gradients (Arega and Sanders 2004), and are expressed in terms of the transverse diffusivity ( $E_T$ ) and longitudinal dispersion coefficient ( $E_L$ ):

$$E_{xx} = E_L + (E_L - E_T) \frac{U_x^2}{U_x^2 + U_y^2} \quad (11)$$

$$E_{xy} = E_{yx} = (E_L - E_T) \frac{U_x U_y}{U_x^2 + U_y^2} \quad (12)$$

$$E_{yy} = E_T + (E_L - E_T) \frac{U_y^2}{U_x^2 + U_y^2}. \quad (13)$$

Transverse diffusion for flow through emergent vegetation is expressed as a combination of mechanical and turbulent diffusion as proposed by Nepf (1999):

$$\frac{E_T}{U_x d} = \alpha_h (C_{vD} a d)^{\frac{1}{3}} + \frac{\beta^2}{2} a d \quad (14)$$

where  $\alpha_h$  and  $\beta$  are  $o(1)$  factors,  $a$ —plant area projected on a plane perpendicular to the flow direction per unit volume ( $\text{m}^{-1}$ ) and  $a = n_v d$  for cylindrical stems. Based on experimental data, Nepf (1999) suggested  $\alpha_h = 0.81$  and  $\beta = 1$ .

The longitudinal dispersion  $E_L$  includes the effects of stem-scale longitudinal dispersion and the dispersion induced by vertical velocity gradients. The non-dimensional form of the coefficient  $E_L$  is written as a combination of the stem-scale and the depth-scale dispersion process as (Lightbody and Nepf 2006):

$$\frac{E_L}{U_x d} = \frac{1}{2} (C_{vD})^{\frac{3}{2}} + \frac{U_x h}{D_z} \Gamma \quad (15)$$

where  $D_z = \alpha_z (C_{vD} a d)^{\frac{1}{3}} U d$  is the vertical turbulent diffusion coefficient,  $\alpha_z = 0.1$ , and  $\Gamma$ —non-dimensional velocity shape factor. Typically the first term in Eq. (15) is smaller than the second term.

For the range of stem Reynolds numbers investigated in this study it is reasonable to consider only the first term of Eq. (14) and the second term of Eq. (15).



### 2.1.3 Sediment Transport Processes

Sediment transport is represented in the model considering the processes of deposition and resuspension that affect the concentration  $C$  of suspended particles. These are represented by an effective deposition rate  $K(x, y)$  in Eq. (10) expressed as:

$$K = k_s - k_r \quad (16)$$

where  $k_s$ —settling rate, and  $k_r$ —resuspension rate. The settling rate  $k_s$  depends on the fall velocity  $w_s$  and water depth  $h$ :

$$k_s = \frac{w_s}{h}. \quad (17)$$

Since variations in water depth within the wetland are negligible in this study,  $k_s$  is taken as constant for a given class size.

The fall velocity  $w_s$  can be expressed using the Newton-Stokes formula. A particle suspended in a still fluid is subjected to the opposite forces of submerged weight  $W$  and viscous drag  $R_D$ :

$$W = (\rho_s - \rho_f)gV \quad (18)$$

$$R_D = C_D \frac{\rho_f w_s^2 A}{2} \quad (19)$$

where  $\rho_s$  and  $\rho_f$ —sediment and fluid density,  $V$ —particle volume,  $C_D$ —drag coefficient,  $A$ —projected particle area perpendicular to the direction of motion. The terminal particle settling velocity is found by imposing the equilibrium of the forces:

$$w_s = \sqrt{\frac{2gV(\rho_s - \rho_f)}{C_D \rho_f A}}. \quad (20)$$

For a spherical particle of diameter  $D$ , Eq. (20) becomes (Newton's Law):

$$w_s = \sqrt{\frac{4g(\rho_s - \rho_f)D}{3C_D \rho_f}}. \quad (21)$$

The drag coefficient  $C_D$  is function of the particle Reynold number,  $Re_p = \frac{w_s D}{\nu}$ . For spherical particles:

$$C_D = \frac{24}{Re_p} + \frac{3}{\sqrt{Re_p}} + 0.34 \quad (22)$$

The last two terms on the right-hand side of Eq. (22) can be neglected if  $Re_p < 1$ , and Eq. (21) can be expressed as (Stoke’s law):

$$w_s = \frac{8g(\rho_s - \rho_f)D^2}{18\mu_f}. \tag{23}$$

If  $Re_p > 1$ , the value of  $w_s$  obtained from Eq. (21) is used as a first approximation of an iterative procedure to determine  $C_D$  from Eq. (22) and  $w_s$  from Eq. (23).

As a first conceptual approximation, resuspension is modelled as a threshold process dependent on the Rouse number  $r$ ,

$$r = \frac{w_s}{ku^*} \tag{24}$$

where,  $k$ —von Karman coefficient ( $k = 0.4$ ),  $u^*$ —bed shear velocity. In general,  $r > 2.5$  corresponds to a condition of very little to no suspended sediments. For  $2.5 < r < 1.8$  a partial suspension takes place. For  $r < 1.8$  there is full suspension. The largest size of suspended material is determined from the condition  $r = 2.5$ , which leads to:

$$w_s = u^*. \tag{25}$$

This condition is used in the model as a threshold for determining whether a given grain size will be in suspension or not. This provides a threshold condition in terms of the bed shear stress: if  $u^* < u_{th}^*$ , there is no resuspension of sediments and the resuspension rate is equal to zero. If  $u^* \geq u_{th}^*$ , it is assumed that  $k_r = k_s$ . This condition applies locally as a function of the shear velocity:

$$u^* = \sqrt{\frac{\tau_b}{\rho}} \tag{26}$$

where the bed shear stress  $\tau_b = \sqrt{\tau_{bx}^2 + \tau_{by}^2}$  is calculated from Eqs. (4)–(5). The effective settling rate is therefore:

$$K = k_s - k_r = \begin{cases} k_s & \text{if } u^* < u_{th}^* \\ 0 & \text{if } u^* \geq u_{th}^* \end{cases} \tag{27}$$

When the bed shear velocity exceeds the threshold shear velocity, non-cohesive sediments are resuspended and, according to the assumption above,  $K = 0$ . When the bed shear velocity becomes lower than the threshold, suspended sediments are deposited with a settling rate  $K = k_s$ .

**Table 1** Diameter  $D$  and fall velocity  $w_s$  of sediment particles used in the simulations. For the particle density a value of  $\rho_s = 2600 \text{ kg m}^{-3}$  has been used

$D (\times 10^{-6} \text{ m})$	1	2	3	4	5	6	7	8	9	10
$w_s (\times 10^{-6} \text{ m s}^{-1})$	0.9	3.5	7.8	13.9	21.8	31.4	42.7	55.8	70.6	87.1

### 3 Model Application

Simulations are performed for a rectangular wetland of width  $B = 50 \text{ m}$ , length  $L = 200 \text{ m}$  and flat topography with zero bed slope. The wetland inlet and outlet are positioned symmetrically around the wetland central axis, and are both  $10 \text{ m}$  in width. The boundary conditions are given by the inflow at the inlet,  $Q_{in} = 0.83 \text{ m}^3 \text{ s}^{-1}$ , and the water depth at the outlet,  $0.5 \text{ m}$ . The value of the flow rate is chosen so that the nominal residence time,  $t_n = V/Q$ , is approximately 7 days and the Reynolds numbers  $Re < 100$ . Bottom resistance is represented by a uniform value of the Manning's roughness coefficient,  $M = 0.02 \text{ m}^{-1/3} \text{ s}$  (Musner et al. 2014), whereas a no-slip condition is applied at the walls of the computational domain. The vegetation shear stresses are determined by Eqs. (7)–(8) assuming a stem diameter  $d = 10 \text{ mm}$ , which is typical of many constructed FWS wetland (Serra et al. 2004). Simulations are performed for 4 different values of uniform vegetation densities  $n_v = 1, 10, 100, 1000 \text{ stems m}^{-2}$ .

The transport equation (Eq. 10) is solved for a constant concentration  $C_{in}$  at the inlet, an open boundary condition at the outlet, and the no-flux condition on the remaining part of the flow boundary. The sediment particles are considered uniform, spherical, with no mutual interaction. Fall velocity is prescribed as an input parameter. Table 1 shows the grain sizes considered in the simulations and their fall velocity, determined as described in Sect. 2.1.3. Although the diameters chosen belong to the category of cohesive sediments, they have been treated as non-cohesive under the assumption of instant resuspension.

The outlet concentration of the suspended solid is used to estimate the removal efficiency of the wetland for the different grain sizes and vegetation densities. The removal efficiency  $E$  is taken as the ratio between the outlet concentration  $C_{out}$  and the inlet concentration  $C_{in}$ :

$$E = \frac{C_{out}}{C_{in}}. \quad (28)$$

### 4 Results and Discussion

The efficiency values obtained from the numerical simulations are presented in Table 2 and Fig. 1.

**Table 2** Removal efficiency obtained from the numerical simulations for different grain diameters,  $D$ , and vegetation densities,  $n_v$

$D (\times 10^{-3})$	1	2	3	4	5	6	7	8	9	10
$w_s (\times 10^{-6} \text{ m s}^{-1})$	0.9	3.5	7.8	13.9	21.8	31.4	42.7	55.8	70.6	87.1
$E(\%, n_v \text{ 1 stems m}^{-2})$	1.3	1.3	2.4	6.1	12.6	22.9	36.5	55.9	100.0	100.0
$E(\%, n_v \text{ 10 stems m}^{-2})$	1.5	1.5	1.7	3.3	7.9	16.4	29.9	67.9	100.0	100.0
$E(\%, n_v \text{ 100 stems m}^{-2})$	1.2	1.2	1.3	2.4	4.5	9.8	22.6	100.0	100.0	100.0
$E(\%, n_v \text{ 1000 stems m}^{-2})$	0.9	0.9	1.0	1.4	3.2	6.2	17.4	100.0	100.0	100.0

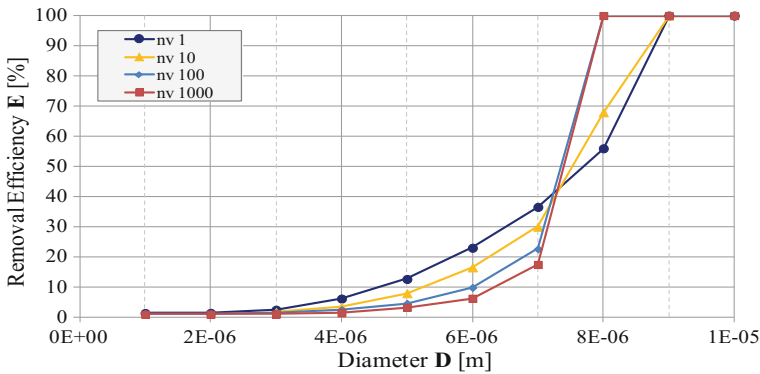


**Fig. 1** Calculated removal efficiency,  $E$ , versus grain diameter,  $D$ , and vegetation density,  $n_v$

The curves show a common behavior: efficiency increases slowly with sediment size for very small particles, whereas the slope increases for higher grain sizes until the condition of complete removal is achieved. This behavior is similar for all the vegetation densities. For the highest density, the difference between the first and the final part of the graph is more evident: a slight increase in efficiency up to  $D = 6 \mu\text{m}$  followed by a significant increase in the slope of the curve. Figure 2 shows the steady-state concentration distribution obtained for 2 different diameters. Up to  $D = 6 \mu\text{m}$  the concentration of suspended sediment is significantly different from zero over most of the wetland and the average concentration at the outlet is close to the inlet concentration. Conversely, for  $D = 8 \mu\text{m}$  most of the sediment is detained inside the wetland.

The efficiency curves in Fig. 1 exhibit an unexpected behavior: for the same inflow discharge, efficiency decreases as vegetation density increases. In the final part of the curves, just before the condition of total removal is achieved ( $E = 100\%$ ), this trend is reversed: wetlands with higher vegetation density have higher efficiency and achieve total removal of suspended sediment for finer grain sizes. This behavior can be understood by looking at the spatial distribution of the

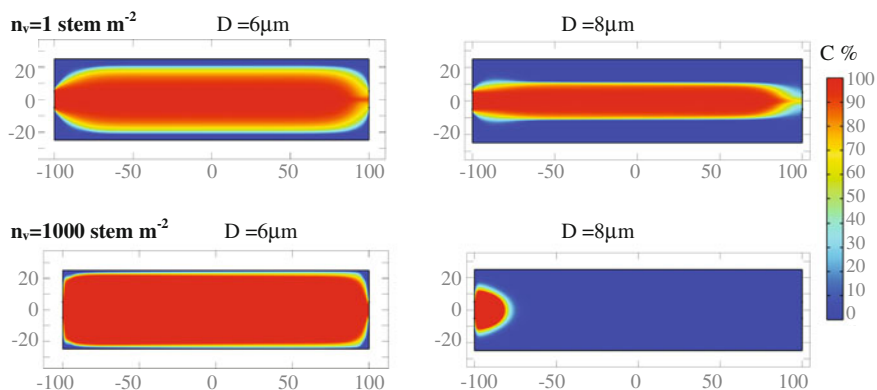


**Fig. 2** Steady-state concentration distributions of suspended sediment in the wetland, for two different grain diameters,  $D = 6 \mu\text{m}$  (left side) and  $D = 8 \mu\text{m}$  (right side) and two vegetation densities ( $n_v = 1 \text{ stems m}^{-2}$  and  $n_v = 1000 \text{ stems m}^{-2}$ )

shear velocity. Although the shear velocity (as well as the flow velocity) decreases as vegetation density increases, in the case where  $n_v = 1 \text{ stems m}^{-2}$  (shown in Fig. 3), the flow occurs mostly in a narrow central strip of the domain. Thus, for lower vegetation densities, the flow is more channelized, and the shear velocity averaged over the entire wetland,  $u^*_{\text{mean}}$ , is lower, whereas the shear velocity at the center of the wetland  $u^*(0, 0)$  is higher (see Table 3). As the vegetation density increases, the mean shear velocity  $u^*_{\text{mean}}$  increases because the flow distribution becomes more uniform, whereas the value at the middle point  $u^*(0, 0)$  decreases. In the simulations, the velocity distribution is symmetrical and the velocity in proximity of the middle point represents the minimum velocity along the central streamline. If sediments can pass the central section at  $x = 0$ , they are more likely to reach the outlet. Hence, for higher vegetation densities, corresponding to smaller values of  $u^*(0, 0)$ , the condition of complete removal is achieved for smaller grain diameters (see  $E = 100\%$  in Fig. 4). The shear velocity  $u^*_{\text{mean}}$  can explain the general trend of efficiency: for finer grain sizes, efficiency is lower in more densely vegetated wetlands because the velocity distribution is more uniform (hence  $u^*_{\text{mean}}$  is higher). Figure 5 shows the behavior of the efficiency and the mean shear velocity versus vegetation density for a few grain diameters: removal efficiency decreases with increasing mean shear velocity, which increases with increasing vegetation density.

The results show that the presence of vegetation in a wetland affects its capacity to remove suspended sediment particles. Under a few simplifying assumptions on the settling/resuspension rate, it has been shown that the presence of vegetation may cause a greater amount of fine sediment particles to remain in suspension as compared to the case of a less densely vegetated wetland. In contrast, more densely vegetated wetlands achieve complete settling for smaller particle sizes.

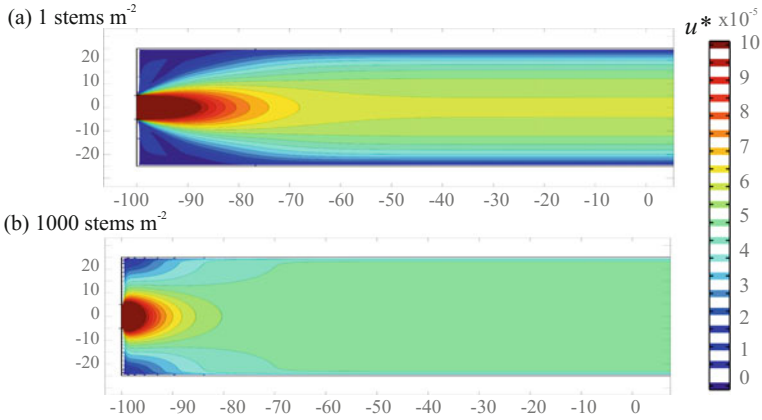


**Fig. 3** Spatial distribution of shear velocity (in the first half of the wetland domain) for two different vegetation densities: **a** 1 stems  $m^{-2}$  and **b** 1000 stems  $m^{-2}$

**Table 3** Shear velocity for different vegetation densities,  $n_v$ . The values reported in the table are the average shear velocity  $u^*_{mean}$  and the shear velocity in the center of the wetland,  $u^*(0, 0)$

$n_v$ (stems $m^{-2}$ )	1	10	100	1000
$u^*_{mean}$ ( $\times 10^{-6}$ m $s^{-1}$ )	48.9	49.6	50.5	50.8
$u^*(0, 0)$ ( $\times 10^{-6}$ m $s^{-1}$ )	60.6	56.4	52.2	50.8

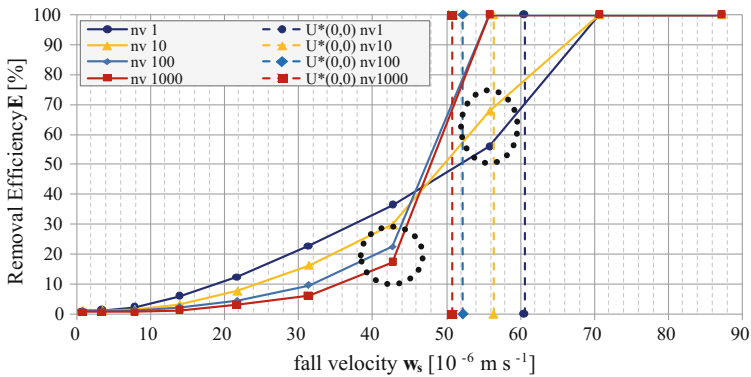


**Fig. 4** Comparison between removal efficiency  $E$  and shear velocity in the middle of the wetland,  $u^*(0, 0)$ , for different vegetation densities  $n_v$ . The dotted circles highlight the largest sediment size, among those considered, for which there is a significant sediment concentration at the outlet. These have threshold shear velocity (equal to their fall velocity) just lower than  $u^*(0, 0)$ . For higher  $n_v$ ,  $u^*(0, 0)$  decreases, and total removal is achieved for lower diameters

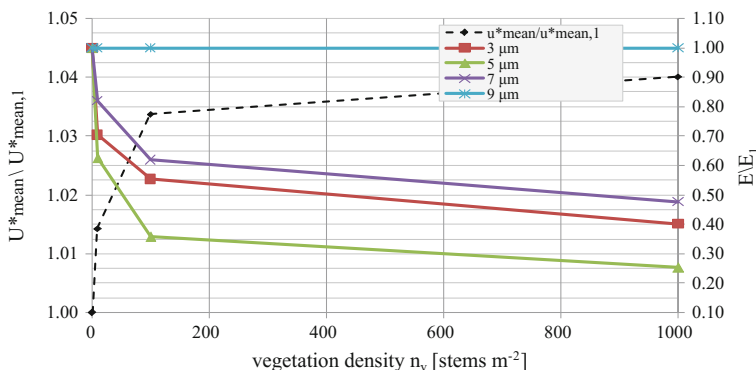


**Fig. 5** Comparison between removal efficiency for some diameters and average shear velocity  $u^*_{mean}$  as function of  $n_v$ . Values are normalized by the average shear velocity,  $u^*_{mean,1}$ , and removal efficiency,  $E_1$ , obtained for  $n_v = 1$  stems  $m^{-2}$

## 5 Conclusion

This study has analyzed the removal of suspended sediment in a vegetated wetland. The analysis is based on a simplified model in which settling and resuspension is represented by a first-order source/sink term in the advection-dispersion equation. This term depends on the definition of a settling/resuspension rate,  $K$ , which is expressed as a function of sediment diameter and vegetation density.

The removal efficiency  $E$  as a function of grain size exhibits an unexpected behavior for different vegetation densities. For very fine particles,  $E$  decreases as vegetation density increases. However, in the final part of the efficiency curve, where  $E$  approaches 100%, this trend is reversed:  $E$  is higher for higher vegetation densities and  $E = 100\%$  for finer grain sizes. This can be explained by the spatial distribution of velocity (and shear velocity) in wetlands with different vegetation densities. More densely vegetated wetlands are characterized by more uniform velocity distributions, resulting in a greater value of the average shear velocity. A larger amount of sediment remains in suspension and can reach the outlet. On the other hand, since the maximum velocity is smaller, total removal (by settling) is achieved for smaller grain sizes.

The proposed model is intended as a possible conceptual model to study sediment transport processes in constructed wetlands. In particular, the formulation of the settling and the resuspension rate is based on a few simplifying assumptions that will need to be tested and further refined in a future study. More detailed numerical simulations and improved theoretical models of sediment transport in wetlands will underpin the development of improved criteria for wetland design.

## References

- Arega F, Sanders BF (2004) Dispersion model for tidal wetlands. *J Hydraul Eng* 130(8):739–754
- Gargallo S, Martín M, Oliver N, Hernández-Crespo C (2016) Sedimentation and resuspension modelling in free water surface constructed wetlands. *Ecol Eng* 98:318–329. <https://doi.org/10.1016/j.ecoleng.2016.09.014>
- Jenkins GA, Greenway M (2005). The hydraulic efficiency of fringing versus banded vegetation in constructed wetlands. *Ecol Eng* 25:61–72. <https://doi.org/10.1016/j.ecoleng.2005.03.001>
- Kadlec R, Knight R (1996) *Treatment wetlands*. CRC Press, Boca raton, FL
- Kadlec R, Wallace S (2008) *Treatment wetlands*, 2nd edn. CRC Press, Boca raton, FL
- Langergraber G (2001). *Development of a simulation tool for subsurface flow constructed wetlands*. PhD thesis. Wiener Mitteilungen 196, Vienna, Austria
- Lightbody AF, Nepf HM (2006) Prediction of velocity profiles and longitudinal dispersion in salt marsh vegetation. *Limnol Oceanogr* 51:218–228. <https://doi.org/10.4319/lo.2006.51.1.0218>
- Marion A, Nikora V, Puijalon S, Bouma T, Koll K, Ballio F, Tait S, Zaramella M, Sukhodolov A, Hare O, Wharton G, Aberle J, Tregnaghi M, Davies P, Parker G, Statzner B (2014) Aquatic interfaces: a hydrodynamic and ecological perspective. *J Hydraul Res* 52:744–758. <https://doi.org/10.1080/00221686.2014.968887>
- Musner T, Bottacin-Busolin A, Zaramella M, Marion A (2014). A contaminant transport model for wetlands accounting for distinct residence time bimodality. *J Hydrol* 515:237–246. <https://doi.org/10.1016/j.jhydrol.2014.04.043>
- Nepf HM (1999) Drag, turbulence, and diffusion in flow through emergent vegetation. *Water Resour Res* 35:479–489. <https://doi.org/10.1029/1998WR900069>
- Sabokrouhiyeh N, Bottacin-Busolin A, Nepf H, Marion A (2016). Effects of vegetation density and wetland aspect ratio variation on hydraulic efficiency of wetlands. In: *Hydrodynamic and mass transport at freshwater aquatic interfaces*, pp 101–113
- Savickis J, Bottacin-Busolin A, Zaramella M, Sabokrouhiyeh N, Marion A (2016) Effect of a meandering channel on wetland performance. *J Hydrol* 535:204–210. <https://doi.org/10.1016/j.jhydrol.2016.01.082>
- Serra T, Fernando HJS, Rodríguez RV (2004) Effects of emergent vegetation on lateral diffusion in wetlands. *Water Res* 38:139–147. <https://doi.org/10.1016/j.watres.2003.09.009>
- Somes NLG, Bishop WA, Wong THF (1999) Numerical simulation of wetland hydrodynamics. *Environ Int* 25:773–779. [https://doi.org/10.1016/S0160-4120\(99\)00058-6](https://doi.org/10.1016/S0160-4120(99)00058-6)
- Stone K, Poach M, Hunt P, Reddy G (2004) Marsh-pond-marsh constructed wetland design analysis for swine lagoon waste water treatment. *Ecol Eng* 23:127–133
- Wu W (2007) *Computational river dynamics*. CRC Press



# An Acoustic Technique to Measure the Velocity of Shallow Turbulent Flows Remotely

Giulio Dolcetti, Anton Krynkin, Kirill V. Horoshenkov  
and Simon J. Tait

**Abstract** Methods to estimate the mean surface velocity of shallow turbulent flows remotely are advantageous with respect to traditional measurement techniques because of their low cost, and little maintenance requirements. The measurement of the airborne acoustic field scattered by the water surface in time allows the reconstruction of the surface elevation at one location, based on the stationary phase method. Experimental data presented in this paper shows that when the mean surface velocity is larger than the minimum phase velocity of gravity capillary waves, the frequency power spectra of the free surface elevation in these flows scale almost linearly with the product of the wavenumber of the stationary waves and of the mean surface velocity. This scaling is exploited in order to estimate the mean surface velocity remotely, based on the remote acoustic measurement of the elevation with two ultrasonic transducers. This observation paves the way for the development of a new range of acoustic sensors that can measure the mean surface velocity of shallow turbulent flows remotely for a range of sub critical flow conditions.

## 1 Introduction

Non-contact methods to measure the velocity of shallow turbulent flows remotely could provide an attractive alternative to traditional Doppler based methods, because of their lower costs, safer access, and less likelihood of damage from floating debris (Fujita et al. 2007; Plant et al. 2005), but their range of applications so far has been limited. Optical methods such as the Space-Time Image Velocimetry (Fujita et al. 2007) rely on the illumination conditions, and do not take into account the dispersion

---

G. Dolcetti (✉) · A. Krynkin · K. V. Horoshenkov  
Department of Mechanical Engineering,  
The University of Sheffield, Sheffield, UK  
e-mail: g.dolcetti@sheffield.ac.uk

S. J. Tait  
Department of Civil and Structural Engineering,  
The University of Sheffield, Sheffield, UK

© Springer International Publishing AG 2018  
M. B. Kalinowska et al. (eds.), *Free Surface Flows and Transport Processes*,  
GeoPlanet: Earth and Planetary Sciences,  
[https://doi.org/10.1007/978-3-319-70914-7\\_10](https://doi.org/10.1007/978-3-319-70914-7_10)

of free surface gravity-capillary waves. Methods based on the Doppler spectrum of backscattered radar depend strongly on the dynamics of short waves on the water surface, which is still largely unknown (Plant et al. 2005).

The application of the stationary phase method to reconstruct the water surface elevation based on the measurement of the airborne ultrasound scattered by the surface was demonstrated in (Wang et al. 1991) for a flat layer of water, and extended in (Nichols et al. 2013) to the measurement of the dynamic patterns on the surface of shallow turbulent water flows over a homogeneously rough bed. A study presented in (Dolcetti et al. 2016) has shown that when the flow mean surface velocity is larger than the minimum phase velocity of gravity-capillary waves, these patterns are dominated by the stationary waves generated by the interaction with the rough bed. The same study showed that the frequency power spectra of the surface elevation scale consistently with the product of the wavenumber of the stationary waves and of the mean surface velocity.

Here the measurements of the frequency spectra of the surface elevation obtained with a conductance wave probe and shown previously in (Dolcetti et al. 2016) are compared with new data obtained remotely with an airborne acoustic technique, in the same flow conditions. The relation with the mean surface velocity is characterised empirically over a range of sub critical shallow turbulent flows. A new analysis that allows the estimation of the mean surface velocity from either the wave probes or the acoustic measurement of the frequency spectra of the elevation is presented.

## 2 Experimental Setup

### 2.1 Experimental Conditions

The data presented here were obtained in a 12.6 m long and 0.459 m wide rectangular laboratory flume. A sketch of the flume and of the measurement setup is shown in Fig. 1a. The bed of the flume was covered with three layers of hexagonally packed plastic spheres with the diameter of  $d = 25.4$  mm. The flow conditions were defined by the mean flow depth,  $H$ , and by the mean surface velocity,  $U_0$ . Different flow conditions were obtained with different settings of the flow discharge and of the flume bed slope,  $s$ . In each flow condition the mean depth was maintained homogeneous along the channel by accurately setting the inclination of an adjustable gate at the end of the flume.

The depth of the flow was measured with a set of manual point gauges at five streamwise locations between 7.43 and 10.1 m from the inlet, at the flume centreline and at half the distance between the centreline and each side wall. The mean depth was calculated as the average across three measurements at each location, with the estimated uncertainty of  $\pm 0.7$  mm. The depth datum was set at the distance  $d/4$  below the crest of the top layer of spheres. The mean surface velocity was measured in each flow condition by timing the passage of buoyant particles across a streamwise

distance of 1.53 m.  $U_0$  was defined as the average of 10 independent measurements, with the standard deviation smaller than 3.5% of  $U_0$ .

It was shown in (Dolcetti et al. 2016) that the dynamics of the free surface over the same range of flow conditions as the ones investigated here are approximated well by a model of gravity-capillary waves, propagating in a flow where the time averaged streamwise velocity profile is described by

$$U(z) = U_0 (z/H)^n, \tag{1}$$

where  $U(z)$  is the time averaged streamwise flow velocity at the depth  $z$  above the datum. The value of the exponent  $n = 1/3$  was found to be representative of the surface dynamics across the whole range of conditions, with an error comparable with the measurement resolution. In a flow where the time averaged streamwise velocity profile is described by Eq. 1, the wavenumber of the stationary waves,  $k_0$ , is found numerically by the solution of (Burns 1953; Fenton 1973)

$$k_0 \frac{I_{-1/2-n}(k_0 H)}{I_{1/2-n}(k_0 H)} = \frac{g + \frac{\gamma}{\rho} k_0^2}{U_0^2}, \tag{2}$$

where  $g$  is the gravity constant,  $\gamma$  is the surface tension,  $\rho$  is the density of water, and  $I_n$  is the modified Bessel function of order  $n$ .

Equation 2 has real solutions only when  $U_0$  is larger than the minimum phase velocity of gravity-capillary waves, which is approximately  $0.23 \text{ m s}^{-1}$ . In this case the frequency spectra of the surface elevation scale linearly with the characteristic frequency  $k_0 U_0$  (Dolcetti et al. 2016). If  $U_0 < 0.23 \text{ m s}^{-1}$ , the stationary waves cannot form, and the frequency spectra have a different scaling. The parameters of each flow condition investigated here are reported in Table 1. The flow conditions have been ordered according to the value of  $k_0 H$ , which represents the squared inverse of a characteristic Froude Number. In Table 1,  $\sigma$  is the standard deviation of the free surface elevation measured with the conductance wave probe,  $Re$  is the Reynolds Number based on the mean surface velocity and on the mean flow depth, and  $F$  is the Froude Number defined as  $F = U_0 / \sqrt{gH}$ .  $L_F$  and  $\kappa$  are the size of the Fresnel zone and the acoustic wavenumber, respectively, and are defined in Sect. 3.

## 2.2 Wave Probe Setup

The conductance wave probe used in this study was installed at the distance of 9 m from the flume inlet, at the flume centreline. The probe comprised of two 0.24 mm thick tin-copperd wires, which were anchored to the flume bed and to a fixed frame installed above the flume. The two wires were slightly tensioned, and were aligned along the transverse direction at a distance of 13 mm from each other. An alternating current was passed through the wires. The change of the water depth causes the linear

**Table 1** Experimental flow conditions

Flow condition	$H$ (mm)	$s$ (-)	$U_0$ (m s <sup>-1</sup> )	$F$ (-)	$Re$ (-)	$\sigma$ (mm)	$k_0$ (rad m <sup>-1</sup> )	$k_0 H / \pi$ (-)	$k_0 \sigma / 2\pi$ (-)	$k_0 L_F / 2\pi$ (-)	$\kappa \sigma / 2\pi$ (-)
1	72.9	0.001	0.35	0.41	$2.5 \times 10^4$	0.33	89.7	2.08	0.0047	0.24	0.038
2	101.0	0.001	0.41	0.41	$4.1 \times 10^4$	0.29	63.6	2.05	0.0029	0.17	0.033
3	42.2	0.002	0.30	0.47	$1.3 \times 10^4$	0.23	131.5	1.77	0.0048	0.36	0.027
4	101.3	0.002	0.49	0.49	$4.9 \times 10^4$	2.05	45.1	1.45	0.0147	0.12	0.024
5	43.0	0.003	0.34	0.52	$1.5 \times 10^4$	0.37	99.7	1.36	0.0058	0.27	0.042
6	73.1	0.002	0.46	0.54	$3.4 \times 10^4$	1.24	52.4	1.22	0.0104	0.14	0.142
7	40.5	0.004	0.36	0.57	$1.5 \times 10^4$	0.31	89.5	1.15	0.0044	0.24	0.035
8	43.4	0.005	0.40	0.61	$1.7 \times 10^4$	0.44	72.6	1.00	0.0051	0.20	0.050
9	99.0	0.003	0.60	0.61	$5.9 \times 10^4$	2.33	31.4	0.99	0.0116	0.09	0.267
10	72.4	0.003	0.54	0.64	$3.9 \times 10^4$	1.20	39.4	0.91	0.0076	0.11	0.138
11	43.1	0.006	0.43	0.66	$1.8 \times 10^4$	0.52	63.8	0.88	0.0052	0.17	0.059
12	73.2	0.004	0.58	0.68	$4.2 \times 10^4$	1.07	34.8	0.81	0.0059	0.09	0.123

variation of the conductivity of water in between the two wires, and therefore of the voltage at their free ends. The wave probe was calibrated in still water at six different depths between 30 and 130 mm, with the flume slope of  $s = 0$ . The sensitivity of the probe was equal to  $0.134 \text{ V mm}^{-1}$ .

The wave probe data was obtained via a Churchill Controls WM1A wave monitor. The data was digitised and acquired with a National Instruments PXIe-8108 control system with LabView. The accuracy of the data acquisition system was 0.3 mV, which corresponds to a resolution of 0.002 mm based on the measured sensitivity. The sampling frequency was originally equal to 500 Hz, but was reduced to 50 Hz by downsampling in order to reduce the computational cost of the analysis. The data was recorded continuously for 10 min for each flow conditions. The 10 min long time series were later split into 59 segments, each with the length of 10 s. The linear trend was removed from each 10 s long segment, in order to eliminate the effect of the constant depth. The standard deviation of the surface elevation,  $\sigma$ , was calculated from the 10 min long time series.

### 2.3 Acoustic Setup

The remote measurement of the free surface elevation was obtained with a pair of ultrasonic transducers based on the stationary phase method, as described in (Nichols et al. 2013). Two TR-89B Series Type 40 ultrasonic transducers manufactured by Massa Product Corporation, with the diameter of 25.4 mm, were employed. These can be used as an acoustic source and emit ultrasound at a fixed frequency if connected to a function generator, or they can be used as ultrasonic receivers if connected to an amplifier and acquisition system. The source transducer was driven directly by a Tektronix AFG 3022C function generator with a sinusoid with peak-to-peak amplitude of 10 V and the frequency of 39 kHz. The receiver was connected to a set of purpose built amplifiers, and the output was digitised and recorded by the same National Instruments data acquisition system used for the conductance wave probe.

The transducers were fitted in a rectangular frame composed of one rigid layer of Perspex and one layer of porous rubber foam. The transducers were only in contact with the porous layer so to avoid transmission of vibrations to the frame, and their active surface was accurately aligned with the front porous surface of the frame. This was installed at the distance of 200 mm from the mean surface level, with the transducers aligned along the flume centreline and pointing down towards the flow surface. The source transducer was located at the distance of 8 m from the flume inlet. The distance between the two transducers was equal to  $D = 70 \text{ mm}$ , and the receiver was closer to the inlet than the source. This distance was chosen as a compromise between the accuracy of the reconstruction of the surface elevation and the signal to noise ratio.

### 3 Remote Measurement of the Surface Elevation with the Stationary Phase Method

The principle of the reconstruction of the free surface elevation with the stationary phase method from the scattering of airborne ultrasound is described, for example, in (Krynkina et al. 2014). Here a simplified interpretation is presented for the case of a two-dimensional rough water surface. A diagram of the acoustic setup for this case is shown in Fig. 1b. In this figure, the acoustic source and receiver have the coordinates  $(x_1, z)$  and  $(x_2, z)$ , respectively, where the  $x$ -axis is parallel to the streamwise direction and the origin is on the plane that corresponds to the mean water surface elevation.

Based on the stationary phase approximation, one assumes that the dominant contribution to the scattered acoustic field measured by the acoustic receiver comes from the reflection at the stationary phase point,  $x_s$ . When the spatial gradient of the water surface is small, the location of the stationary phase point is approximated by  $(x_1 + x_2)/2$ , like in Fig. 1b. The recorded acoustic signal has the analytic form  $P_2 = A_2 e^{i\phi}$ , where  $A_2$  and  $\phi$  are the amplitude and the phase, respectively. The input signal which drives the source has the analytic form  $P_1 = A_1 e^{i2\pi f_a t}$ , where  $f_a$  is the acoustic frequency and  $t$  represents time. The phase of the signal  $\phi$  is equal to the phase of the signal emitted by the source, plus a term proportional to the length of the path between the source and the stationary phase point, and between the stationary phase point and the receiver. With reference to Fig. 1b, when the surface is flat this path has the length  $R_1 + R_2$ , and the measured phase is

$$\phi = \kappa[R_1 + R_2] + 2\pi f_a t, \tag{3}$$

where  $\kappa = 2\pi f_a / c_a$  is the acoustic wavenumber, and  $c_a$  is the speed of sound in air. When the surface is dynamically rough, the path length is  $R'_1 + R'_2$ , which differs from the previous case by an amount that depends on the free surface elevation  $\zeta$  at the stationary phase point. If  $\kappa R_1 \gg 1$ , and the free surface elevation is small in comparison to  $R_1$  and  $R_2$ , the phase is then approximated by

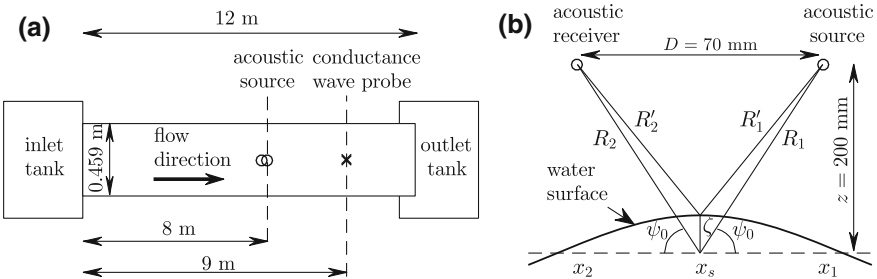


**Fig. 1** a Schematic of the laboratory flume. b Diagram of the acoustic setup. Dimensions are not to scale

$$\phi = \kappa[R'_1 + R'_2] + 2\pi f_a t \approx 2\kappa R_1[1 - \sin(\psi_0)\zeta(t)/R_1] + 2\pi f_a t, \quad (4)$$

where  $\psi_0 = \tan^{-1}(2z/D)$ . The surface elevation  $\zeta(t)$  can be found as

$$\zeta(t) = -\frac{1}{2\kappa \sin \psi_0} \left\{ \Im \left[ \log \left( \frac{P_2}{P_1} \right) \right] - \left\langle \Im \left[ \log \left( \frac{P_2}{P_1} \right) \right] \right\rangle \right\}, \quad (5)$$

where  $\Im$  represents the imaginary part, and  $\langle \rangle$  denotes averaging in time. It is noted that the phase is defined only in the interval between  $-\pi$  and  $\pi$ . When the amplitude of the surface fluctuations is comparable with the acoustic wavelength, the phase needs to be unwrapped in order to represent the full range of  $\zeta$ .

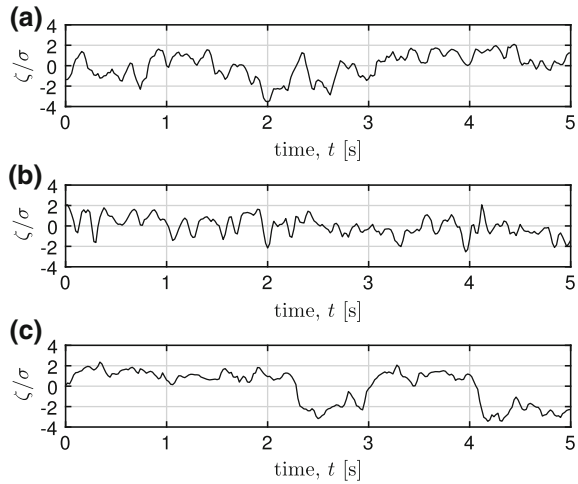
In the measurements reported here, the acoustic pressure at the receiver and the direct output from the function generator were recorded simultaneously with the sampling frequency of 500 kHz, for 5 min in each flow condition. The analytic form of the signal was obtained by a Hilbert transform, with the same procedure described in (Nichols et al. 2013). The transform was applied to short segments of data with the duration of 1 ms, sampled at the constant rate of 100 Hz. The phase and amplitude of the transformed signals were averaged across each 1 ms long segment. The unwrapping was performed in time with the *unwrap* function available in Matlab 2015b. The free surface elevation was calculated with Eq. 5 at the frequency of 100 Hz, then downsampled to 50 Hz. The time-series of the reconstructed surface elevation was split into 29 segments, each with the length of 10 s.

In (Dolcetti et al. 2016) it was shown that when  $U_0 > 0.23 \text{ m s}^{-1}$  the characteristic horizontal scale of the free surface of a shallow turbulent flow over a homogeneous rough bed is represented by the wavelength of the stationary waves,  $2\pi/k_0$ . The amplitude of the surface elevation is represented by its standard deviation,  $\sigma$ . The characteristic spatial gradient is then  $k_0\sigma/2\pi$ . The size of the Fresnel zone is defined as (Bass and Fuks 1979, p.120)

$$L_F = \sqrt{R_1/\kappa \sin^2 \psi_0}, \quad (6)$$

The Fresnel zone corresponds to the region of the free surface where the phase of the scattered acoustic waves varies slowly, and which contributes more strongly to the scattered acoustic field. If the spatial gradient is large, or if the size of the Fresnel zone is large compared to the characteristic horizontal scale of the water surface, then the location of the stationary phase point deviates more largely from that of the intermediate point  $(x_1 + x_2)/2$ . In these conditions the acoustic reconstruction of the surface elevation becomes inaccurate. Small amplitudes of the elevation  $\sigma$  are also characterised by larger relative errors of the reconstruction, in relation with the resolution of the phase measurements. In (Nichols et al. 2013) the conditions for the validity of the reconstruction based on these three effects were expressed mathematically as

**Fig. 2** Examples of the reconstruction of the surface elevation based on the stationary phase method applied to the scattered acoustic field for **a** condition 2, **b** condition 3, and **c** condition 6.  $\zeta/\sigma$  is the surface elevation normalised by its standard deviation measured with the conductance wave probe



$$k_0 L_F / 2\pi < 1, \quad (7)$$

$$k_0 \sigma / 2\pi < 0.005, \quad (8)$$

$$\kappa \sigma / 2\pi > 0.01. \quad (9)$$

The values of the parameters of Eqs. 7–9 are reported in Table 1 for each flow condition. The condition of Eq. 8 was found to be more stringent, as it was satisfied only in flow conditions 1, 2, 3, and 7.

Figure 2 shows three examples of the reconstruction of the free surface elevation obtained for flow conditions 2, 3, and 6. These conditions are representative of a range of the parameters of Eqs. 7–9. The reconstruction for condition 6 presented in Fig. 1c shows intervals of time during which the surface elevation has relatively small variations (e.g., between  $t = 0.2$  s and  $t = 2.2$  s, and between  $t = 3.2$  s and  $t = 4$  s), separated by intervals where the elevation is shifted rapidly to a smaller average value. The large shifts of the reconstructed elevation in Fig. 1c were associated with the large gradient of the surface,  $k_0 \sigma / 2\pi$ , which affected the accuracy of the method. A similar behaviour was observed in all flow conditions except conditions 1, 2, 3, and 5. Condition 7 had very similar surface parameters compared to condition 1 and it satisfied Eqs. 7–9, but contrarily to condition 1 it showed large shifts of the reconstruction similar to those displayed in Fig. 2c. This was explained by the larger Froude Number for condition 7, which is associated with a larger relative amplitude of short waves (Dolcetti et al. 2016). Therefore, condition 7 was excluded from the acoustic analysis, which was only applied for conditions 1, 2, 3, and 5.



## 4 Estimation of the Mean Surface Velocity from the Frequency Spectrum of the Surface Elevation

A procedure for the estimation of the mean surface velocity based on the measurement of the frequency power spectra of the free surface elevation is suggested here. The method is based on the observation reported in (Dolcetti et al. 2016), that the frequency power spectra of the water surface elevation measured in sub critical shallow turbulent flows scale with the frequency  $k_0 U_0$ , whenever  $U_0$  is larger than the minimum phase velocity of gravity-capillary waves in still water, which is equal to approximately  $0.23 \text{ m s}^{-1}$ .  $k_0 U_0$  is the characteristic frequency of the stationary waves with the wavenumber  $k_0$  when they are advected rigidly at the mean surface velocity.

The frequency power spectrum  $S(\omega)$  of the surface elevation is calculated as the square of the absolute value of the Fourier transform of the elevation in time.  $\omega$  is the radian frequency of the surface elevation. The spectra are normalised such that

$$\frac{T}{2\pi} \int S(\omega) d\omega = 1, \quad (10)$$

where  $T$  is the duration of the measurements in time, and the integral can be calculated numerically with a trapezoidal method. In the measurements reported here  $T$  was equal to 10 s.

The characteristic frequency of the frequency power spectra is quantified in terms of the first spectral moment, defined as

$$s_1 = \frac{T}{2\pi} \int \omega S(\omega) d\omega. \quad (11)$$

The linear scaling of the spectra with the frequency  $k_0 U_0$  observed by Dolcetti 2016 is represented here by the relation

$$s_1 = m k_0 U_0, \quad (12)$$

where  $m$  is a calibration coefficient that can be found by a least squares fitting of the measured values of  $s_1$  in a representative set of flow conditions. It is noted that the calibration only requires the measurement of the mean surface velocity and of the mean flow depth, and the estimate of the exponent  $n$  of the time averaged streamwise velocity profile. In fact,  $k_0$  is calculated based on these quantities by means of Eq. 2.

It is suggested to use Eq. 12 with the measured calibration coefficient  $m$  together with Eq. 2 in order to estimate the mean surface velocity from the measurement of the spectral moment  $s_1$ . The procedure comprises of two steps. At the first step  $k_0$  is calculated numerically after substitution of Eq. 12 into Eq. 2, which results in

$$\sqrt{k_0 \left( g + \frac{\gamma}{\rho} k_0^2 \right) \frac{I_{1/2-n}(k_0 H)}{I_{-1/2-n}(k_0 H)}} = \frac{s_1}{m}. \quad (13)$$

At the second step the mean surface velocity is estimated as

$$\tilde{U}_0 = s_1 / m k_0. \quad (14)$$

The procedure requires the knowledge of the mean flow depth  $H$  and of the exponent of the time averaged streamwise velocity profile  $n$ . The measurement of the mean flow depth can be obtained remotely with the same acoustic technique described in (Wang et al. 1991), or by measuring the time of flight of short acoustic pulses (Haynes and Margison 1992). The exponent  $n$  depends on the flow Reynolds Number and on the relative submergence (Cheng 2007).  $n$  may be estimated, or it may be determined by iterations based on the measured mean flow depth and the recursive calculation of the mean surface velocity.

## 5 Experimental Results

The procedure described in Sect. 4 was applied to the measurements of the free surface elevation obtained both with a conductance wave probe and with the acoustic reconstruction technique. The average frequency power spectra of the elevation are shown as a function of the non-dimensional frequency  $\omega/k_0 U_0$  in Fig. 3a and b. Figure 3a shows the average over 59 measurements of the spectra obtained for all conditions with the conductance wave probe. Figure 3b shows the average over 29 measurements of the spectra obtained for conditions 1, 2, 3, and 5 with the acoustic reconstruction technique. These were the only conditions where the reconstructed elevation did not display the large shifts observed in Fig. 2c.

The power spectra shown in Fig. 3a and b scale consistently with the frequency  $k_0 U_0$ , as observed in (Dolcetti et al. 2016). The decay of the spectra at the frequency larger than  $k_0 U_0$  is slower for the conditions with the larger Froude Number, shown in magenta in Fig. 3a. The spectra obtained from the reconstruction with the acoustic technique shown in Fig. 3b decay less rapidly at the higher frequencies. This can be explained by the uncertainty of the reconstruction, or by the smaller sensitivity of the wave probe to short surface waves. The first spectral moment shown in Fig. 3c grows approximately linearly with  $k_0 U_0$  for both types of measurement. The best fit with Eq. 12 was determined for the measurements with the wave probe only, because of the limited number of measurements with the acoustic reconstruction technique. For the conditions investigated here the best fit was found with the coefficient  $m = 0.61$ .

The estimation of the mean surface velocity based on the procedure described in Sect. 4 was performed in all the measured conditions for each 10 s long measurement of the surface elevation obtained with the conductance wave probe and with the acoustic reconstruction technique. In solving Eq. 13, the measured values of the

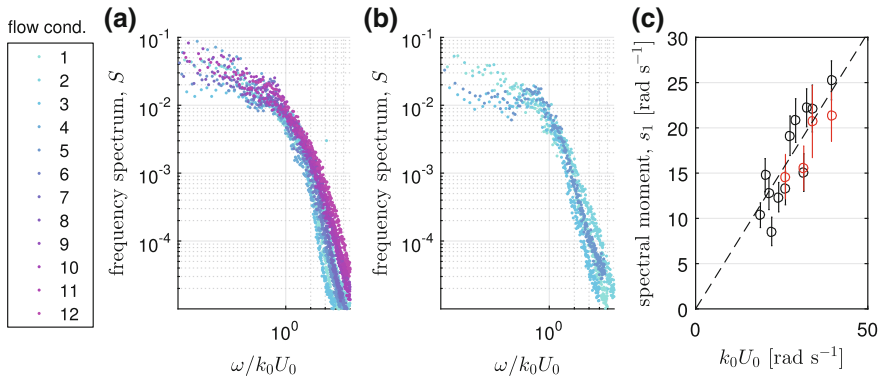


**Fig. 3** **a, b** The average frequency power spectra of the surface elevation **a** measured with the conductance wave probe, **b** reconstructed with the acoustic method.  $\omega/k_0U_0$  is the radian frequency normalised by the characteristic frequency of the stationary waves,  $k_0U_0$ . **c** The first spectral moment measured with both methods. The circles are the average across all measurements, and the errorbars are  $\pm$  the standard deviation. (black) Measured with the conductance wave probe, (red) reconstructed with the acoustic method, (dashed line)  $s_1 = 0.61k_0U_0$

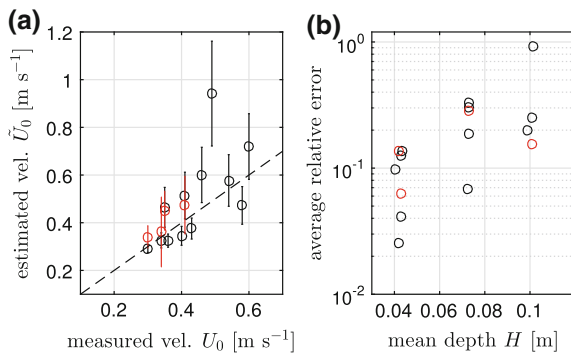


**Fig. 4** **a** The estimation of the mean surface velocity,  $\tilde{U}_0$ , based on the first spectral moment of the surface elevation (black) measured with the conductance wave probe, (red) reconstructed with the acoustic method. The circles are the average across all estimates, and the errorbars are  $\pm$  the standard deviation. (dashed line) the measured mean surface velocity  $U_0$ . **b** The average relative error of the estimation. The average relative error was defined as the absolute difference between the average estimated velocity  $\tilde{U}_0$  and the measured value of  $U_0$ , divided by the latter

depth  $H$  and the value of the exponent  $n = 1/3$  were used. The value of the coefficient  $m = 0.61$  obtained by the linear fitting of the wave probes data was used for both types of measurement of the surface elevation. Figure 4a shows the estimated mean surface velocities compared with the measured velocity of the buoyant particles. The average relative error of the estimates is represented in Fig. 4b, as a function of the flow depth  $H$ .

Figure 4b shows that the method was able to determine the mean surface velocity with the uncertainty of at most  $\pm 14\%$  in the conditions where the mean depth was between 40.5 and 43.4 mm. The average relative error was smaller than  $\pm 33\%$  in the conditions where the mean depth was between 72.4 and 101.0 mm, with the exception of condition 4 where the mean depth was 101.3 mm and the absolute error was 92% of  $U_0$ . The accuracy was similar for the measurements with the conductance wave probe and with the acoustic reconstruction technique. The best estimate was found for condition 3 based on the measurement with the wave probe, where the average relative error was less than 3%. The acoustic reconstruction yielded an average relative error of 29% in condition 1, 16% in condition 2, 14% in condition 3, and 6% in condition 5. In these conditions the average relative errors obtained with the wave probe were 33%, 25%, 3%, and 4%, respectively.

The reasons for the larger error which was found for condition 4, and for the apparent increase of the error when the mean flow depth was increased above 43.4 mm are not fully understood, and deserve further investigations. It is noted that in condition 4 the empirical relation of Eq. 12 overestimated  $s_1$  by 57%, which suggests that the proposed linear scaling between  $s_1$  and  $k_0 U_0$  may need to be modified for deeper and slower flows in order to improve the accuracy.

## 6 Conclusions

The first result of this study was the development of a parametric quasi-empirical relation (Eq. 12) that expresses the relation between the frequency spectra of the free surface elevation and the flow mean surface velocity, observed for a range of subcritical shallow turbulent flows over a homogeneous rough bed. This scaling had been previously observed in (Dolcetti et al. 2016), but only qualitatively. As a second result, a numerical procedure that exploits the suggested relation in order to estimate the mean surface velocity from the measurement of the free surface elevation in time at one location has been proposed. The estimation requires the knowledge of the mean flow depth and of the exponent of the time averaged streamwise velocity profile. The depth can be measured remotely using an acoustic setup similar to the one described here (Haynes and Margison 1992; Wang et al. 1991), while the exponent of the velocity profile can be estimated or calculated iteratively. As a third result, it was shown that the frequency spectra of the surface elevation can be measured remotely based on the scattering of ultrasound emitted and recorded above the water surface with two transducers, although the method was found to be accurate only in a limited range of flow conditions. In these conditions, the acoustic measurements combined with the proposed numerical procedure allow the estimate of the mean surface velocity of shallow turbulent flows remotely.

Across the range of tested flow conditions, the acoustic reconstruction of the frequency spectra was stable only in four conditions, which had the Froude Number smaller than 0.54. It is suggested that the accurate choice of the acoustic frequency could extend the range of validity of the method to a wider range of flow conditions.

The uncertainty of the numerical procedure to estimate the mean surface velocity was tested on a wider range of flow conditions by including the measurements obtained with a conductance wave probe. The uncertainty was found to be smaller than  $\pm 33\%$  in all conditions except in the small-velocity, high-submergence condition 4, where the uncertainty was as large as 92%. In the flows with small submergence, the maximum uncertainty was 14%. The uncertainty appears to increase with the mean flow depth, suggesting a more complex relation between the surface spectra and the mean surface velocity than the one which was suggested here, especially for flows with a large submergence and small velocity.

In comparison, the uncertainty of velocity measurements obtained with non-contact Doppler radar sensors is usually between 10 and 30%, with the larger uncertainty found in flows with a small submergence (Welber et al. 2016). Doppler sensors perform better in high flow conditions, when the water surface is rougher (Plant et al. 2005). In contrast, the non-contact acoustic method proposed here performs better in low-submergence flows with a small amplitude of the water surface roughness. If the scaling of the frequency spectra observed here was confirmed outside of the controlled laboratory conditions, the method would represent a simple and inexpensive technique to estimate the mean surface velocity of shallow turbulent flows such as small rivers remotely, thus complementing the existing Doppler techniques. It will be of interest in the future to test the performance of the method in real small rivers. The proposed method has only been demonstrated over a limited range of flow conditions. Future studies about the spectra of the water surface elevation over wider range of conditions would help generalise the development of the technique presented here.

**Acknowledgements** This work was supported by EPSRC grant EP/N029437/1. The authors are grateful to an anonymous referee whose comments helped to improve the quality of this paper.

## References

- Bass FG, Fuks IM (1979) Wave scattering from statistically rough surfaces. In: Oxford Pergamon Press international series on natural philosophy, vol 93
- Burns JC (1953) Long waves in running water. In: Mathematical proceedings of the Cambridge philosophical society, vol 49, No 04, pp 695–706. Camb Univ Press, Cambridge
- Cheng N-S (2007) Power-law index for velocity profiles in open channel flows. *Adv Water Resour* 30:1775–1784
- Dolcetti G, Horoshenkov KV, Krynkina A, Tait SJ (2016) Frequency-wavenumber spectrum of the free surface of shallow turbulent flows over a rough boundary. *Phys Fluids* 28(10):105105
- Fenton JD (1973) Some results for surface gravity waves on shear flows. *IMA J Appl Math* 12:1–20
- Fujita I, Watanabe H, Tsubaki R (2007) Development of a non-intrusive and efficient flow monitoring technique: the space-time image velocimetry (STIV). *Int J River Basin Manag* 5(2):105–114
- Haynes KM, Margison SE (1992) Ultrasonic level detector. US Patent No. 5,131,271
- Krynkina A, Horoshenkov KV, Nichols A, Tait SJ (2014) A non-invasive acoustical method to measure the mean roughness height of the free surface of a turbulent shallow water flow. *Rev Sci Instrum* 85(11):114902

- Nichols A, Tait SJ, Horoshenkov KV, Shepherd S (2013) A non-invasive airborne wave monitor. *Flow Meas Instrum* 34:118–126
- Plant WJ, Keller WC, Hayes K (2005) Measurement of river surface currents with coherent microwave systems. *IEEE T Geosci Remote* 43(6):1242–1257
- Wang Y, Mingotaud C, Patterson LK (1991) Noncontact monitoring of liquid surface levels with a precision of 10 micrometers: a simple ultrasound device. *Rev Sci Instrum* 62(6):1640–1641
- Welber M, Le Coz J, Zolezzi G, Zamlar D, Dramais G, Hauet A, Salvaro M (2016) Field assessment of noncontact stream gauging using portable surface velocity radars (SVR). *Water Resour Res* 52(2):1108–1126

# A CFD Based Comparison of Mixing Due to Regular and Random Cylinder Arrays

Mahshid Golzar, Fred Sonnenwald, Ian Guymer and Virginia Stovin

**Abstract** Numerous studies have focused on flow and mixing within cylinder arrays because of their similarity to vegetated flows. Randomly distributed cylinders are considered to be a closer representation of the natural distribution of vegetation stems compared with regularly distributed arrays. In this study the flow fields associated with two arrays of regularly and randomly distributed cylinders are modelled in two dimensions, using ANSYS Fluent 16.1. The RSM turbulence model is used to model the turbulence closure, and all the variables are discretized using the second order upwind method. The resulting flow fields are used to run the solute transport model to characterize mixing within each geometry. For the same stem diameter and solid volume fraction, greater dispersion is evident in the random cylinder array compared with the regular array. Dispersion coefficient values are compared with those reported in the literature and a good agreement is shown. Turbulence length scales estimated from the velocity profiles and optimized dispersion coefficients are close to the cylinder diameter, which is in agreement with theories in the literature.

## 1 Introduction

Flow past a cylinder is a classic case study from a fluid mechanics point of view, and numerous detailed studies have been done to fully explore all characteristics of the flow past one single or an array of cylinders. Zdravkovich (2003) provides a relatively complete collection of experimental and practical studies on flow past cylinders.

Certain aquatic vegetation types are approximately cylindrical (Tanino and Nepf 2009), which makes the cylinder an ideal choice for a basic study of vegetated flow.

---

M. Golzar (✉) · F. Sonnenwald · V. Stovin  
Department of Civil and Structural Engineering, University of Sheffield, Sheffield, UK  
e-mail: mgolzar1@sheffield.ac.uk

I. Guymer  
School of Engineering, University of Warwick, Coventry, UK

There are a considerable number of experimental and computational studies on flow and mixing within regularly spaced cylinder arrays (e.g. Zhou et al. 2015; Anagnostopoulos and Seitanis 2014). To make the models closer to natural distributions of vegetation, several studies have employed random distributions of cylinders (e.g. White and Nepf 2003, Tanino and Nepf 2008). The main mixing processes within vegetated flows are turbulent diffusion, differential advection, and molecular diffusion. Their overall effect is summed up and usually expressed as a single dispersion coefficient, in each direction. In this study 2D models are considered and longitudinal and transverse dispersion coefficients are investigated. The two-dimensional advection-dispersion equation is shown as Eq. 1:

$$\frac{\partial C}{\partial t} + u \frac{\partial C}{\partial x} + v \frac{\partial C}{\partial y} = D_x \frac{\partial^2 C}{\partial x^2} + D_y \frac{\partial^2 C}{\partial y^2}; \quad (1)$$

where  $C$  is the depth-averaged tracer concentration;  $u$  is the depth-averaged longitudinal velocity;  $v$  is the depth-averaged transverse velocity,  $t$  is time;  $x$  is the longitudinal distance;  $D_x$  is the longitudinal dispersion coefficient, and  $D_y$  is the transverse dispersion coefficient.

### ***1.1 Aims of This Study***

Despite the availability of studies on flow and mixing within regular and random cylinder arrays, no study has directly compared the mixing characteristics due to random and regular arrays. Regular arrays cause a repeating, predictable pattern in the velocity field, which can result in specific solute transport characteristics. By introducing a random pattern of cylinders, a random flow field develops, for which dispersion is no longer predictable. This flow field can exhibit a wide range of solute transport features depending on the relative spacing of cylinders.

This study aims to examine the capability of CFD modeling, i.e. the Reynolds Stress Model (RSM), for simulating flow and solute transport within regular and random cylinder arrays. It will compare the velocity fields that develop within these two different geometries, leading to a detailed comparison between mixing characteristics of each. The effect of cylinder distribution and flow field are to be investigated via changing the injection point location, and comparing the resultant transverse and longitudinal tracer distribution and corresponding quantified mixing coefficients. The results of this study will indicate the applicability of 2D RSM-based models, along with the scalar transport, for modelling flow and mixing within various distributions of cylinder arrays.



## 2 Methods

Two 1.5 m long, 0.5 wide channels consisting of regular and random distributions of 0.004 m diameter cylinders were defined, both with the same stem density of  $N = 398$  cylinders/m<sup>2</sup>, solid volume fraction,  $\phi = 0.005$ , and frontal facing area,  $a = 0.016$  cm<sup>-1</sup>. This density was initially chosen to reproduce the laboratory results of West (2016). The geometries of the regular and random arrays, along with the channel dimensions, are shown in Fig. 1a and b, respectively.

Both models were meshed using a 0.001 m triangular mesh (confirmed to be mesh-independent) with approximately  $1.6 \times 10^6$  cells for each array. The inlet and outlet were modelled using a periodic boundary condition. The walls were modelled using the enhanced wall function option available in ANSYS Fluent 16.1 (ANSYS, Inc 2015). Turbulence closure was modelled using the Reynolds Stress Model (RSM), while all the variables were discretized using the second order upwind method and the turbulent Schmidt number was set to 1.0. For an explanation of the flow equations and turbulence closure, refer to Versteeg and Malalasekera (1995).

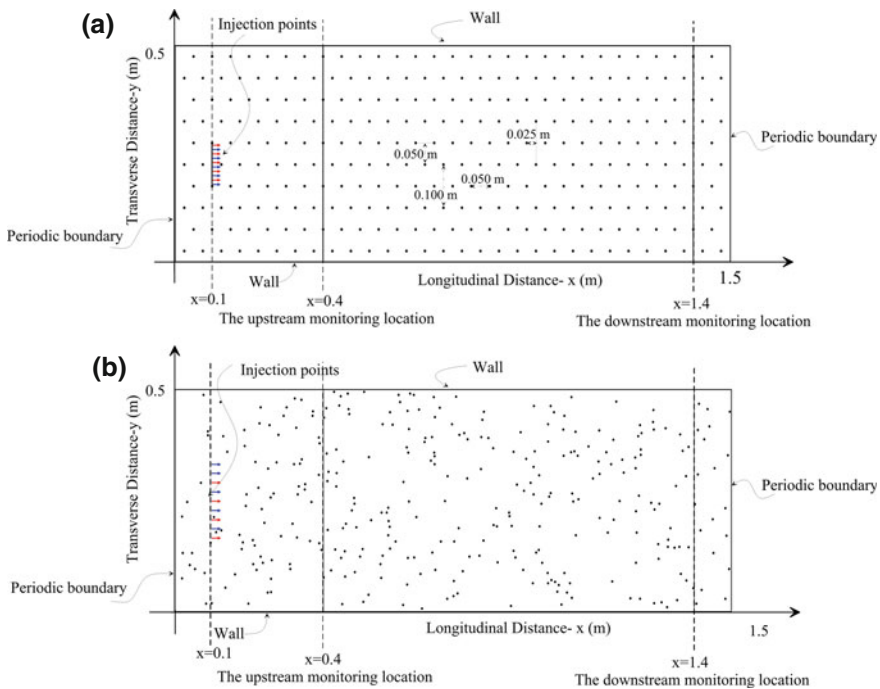


**Fig. 1** Channel dimensions, boundary conditions and injection points: **a** the regular array, **b** the random array

After solving the flow field in steady conditions for both regular and random arrays, the models were switched to transient mode and a pulse of 1 s duration tracer of user defined scalar was injected into the flow at the upstream end of the channel i.e. at  $x = 0.1$  m from the inlet at different transverse locations. In the regular channel, the tracer was injected at 0.01 m transverse intervals between  $y = 0.18$  m and  $y = 0.28$  m, i.e. spanning one repeat of the cylinder pattern (Fig. 1a). To sample the different possible conditions for the injected tracer in the random flow field, the middle one-third of the channel was divided into 8 equal segments and tracer was injected at each of the 9 points, as shown in Fig. 1b.

The concentration of the tracer was recorded as it passed the two transverse monitoring lines at  $x = 0.4$  m and  $x = 1.4$  m from the inlet. The monitoring locations are shown in Fig. 1. The resulting upstream and downstream tracer distributions versus time and versus transverse distance were used to estimate the longitudinal and transverse dispersion coefficients, respectively. Longitudinal dispersion coefficient, i.e.  $D_x$ , was estimated based on Eq. 2 and the transverse dispersion coefficient, i.e.  $D_y$ , was estimated based on the transverse equivalent of Eq. 2,

$$C(1.4, t) = \int_{\alpha = -\infty}^{\infty} \frac{C(0.4, \alpha)}{\sqrt{4\pi D_x (T_2 - T_1)}} \exp\left[-\frac{u^2 (T_2 - T_1 - t + \alpha)^2}{4D_x (T_2 - T_1)}\right] d\alpha; \quad (2)$$

where  $C(0.4, t)$  is the width-averaged concentration as a function of time at  $x = 0.4$  m;  $C(1.4, t)$  is the predicted width-averaged concentration as a function of time at  $x = 1.4$ ,  $T_1$  and  $T_2$  are the mean times of passage at  $x = 0.4$  m and  $x = 1.4$  m, respectively, and  $\alpha$  is the dummy time variable of integration. For further explanation, refer to Rutherford (1994).

### 3 Results

The inlet mass flow for both models was set based on a mean velocity of  $0.017 \text{ ms}^{-1}$ , which corresponds to a Reynolds number of  $Re_d = 67.2$ , based on the cylinder diameters. The longitudinal velocity contours are shown in Fig. 2a and b for the regular and random arrays, respectively. Comparable velocity results for the regular array were validated against laboratory measurements by Sonnenwald et al. (2016).

It can be seen that the random velocity field covers a wider range of velocity values and has a higher maximum value than the regular one. The negative values correspond to the wake zones downstream of each cylinder. In general, each cylinder causes the velocity to decrease to the minimum value and then it returns to its local maximum in the gap between the cylinders. The resulting shear can have a determining effect on the mixing coefficients. In order to compare the shear in each flow field, transverse profiles of longitudinal velocity,  $u$ , and transverse velocity,  $v$ ,

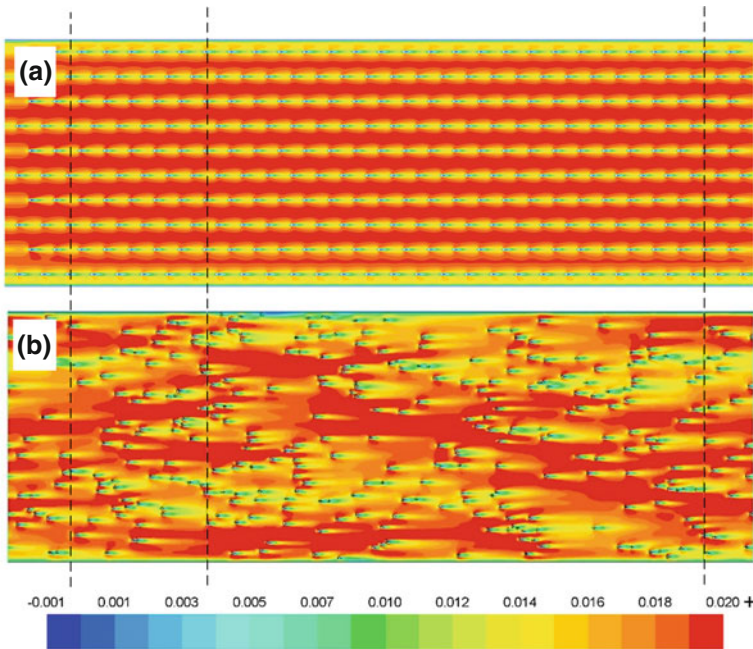


**Fig. 2** Longitudinal velocity,  $u$  contours: **a** regular array, **b** random array; the maximum value is  $0.027 \text{ m s}^{-1}$

recorded at  $x = 0.4 \text{ m}$  for both regular and random fields are shown in Fig. 3a and b, respectively.

The regular array results in a regular flow field with fast flow between the cylinders and dead zones behind the cylinders, whereas the random array results in a random distribution of peak velocity values. In order to quantify the corresponding velocity shear in each flow field, the rates of changes in longitudinal velocity values over the channel width, i.e.  $ldu/dyl$ , were calculated between adjacent cells on 21 cross-sections ( $0.4 \text{ m} \leq x \leq 0.6 \text{ m}$ ) in each flow field. The mean and standard deviation of velocity shear,  $ldu/dyl$ , for each cross-section are shown in Fig. 4.

Although the mean values of the velocity shear in both arrays are very close to each other, the randomly distributed array has a higher standard deviation of velocity shear,  $ldu/dyl$ , over most of the cross-sections. Higher dispersion coefficients are therefore expected for the random array.

It was expected that the transverse position of the tracer injection would influence the tracer’s path and in turn affect its transverse and longitudinal distribution. These effects are dependent on whether the injection point falls immediately behind a stem or within the fast flow. Therefore, the injection point location was varied systematically within the mid-section of each channel, as shown in Fig. 1a and b.

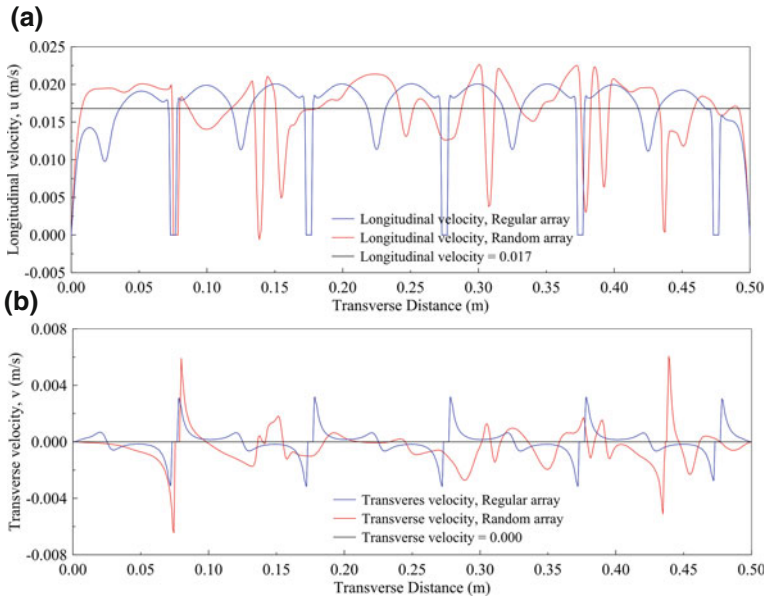


Fig. 3 Transverse velocity profiles at  $x = 0.4$  m: **a** longitudinal velocity,  $u$ ; **b** transverse velocity,  $v$

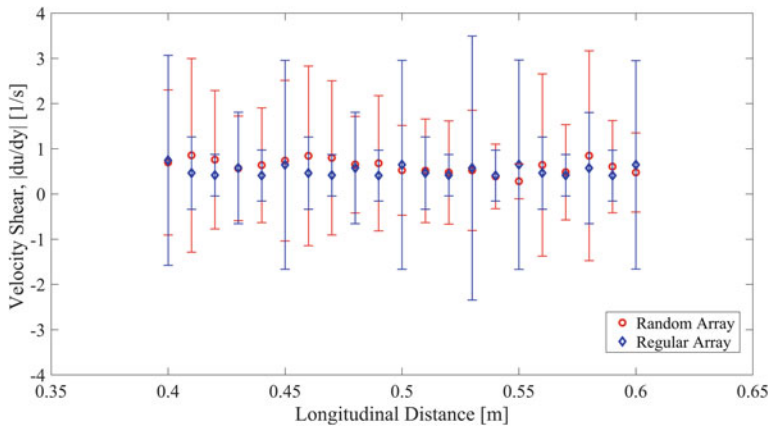


Fig. 4 Mean and standard deviation of velocity shear,  $|du/dy|$

### 3.1 Longitudinal Dispersion Coefficient, $D_x$

Temporal width-averaged concentration profiles are presented in Fig. 5a and b for the regular and random arrays, respectively. The predicted downstream concentration distributions for the tracer released at  $y = 0.22$  m for the regular array and at  $y = 0.25$  m for the random array are included to illustrate the typically good fit between observed profiles and those predicted from the fitted value of  $D_x$ . It should be noted that the profiles for the tracers released in the regular array between  $y = 0.24$  m and  $y = 0.28$  m are not presented considering the symmetric nature of the velocity field. And also some of the concentration distributions of the random array are not included for sake of readability.

The longitudinal distributions of tracer released at different lateral injection points in the regular array are quite similar, except for those released at  $y = 0.20$  m, which corresponds to the maximum longitudinal velocity value. Moving with the maximum longitudinal velocity, the tracer particles released at  $y = 0.20$  m pass the monitoring positions before those released from other injection points. The same effect can be seen in the random array for tracer released at  $y = 0.208$  m, which also corresponds to a high longitudinal velocity. A mean value for each dispersion coefficient has been calculated to represent the whole domain, Fig. 7.

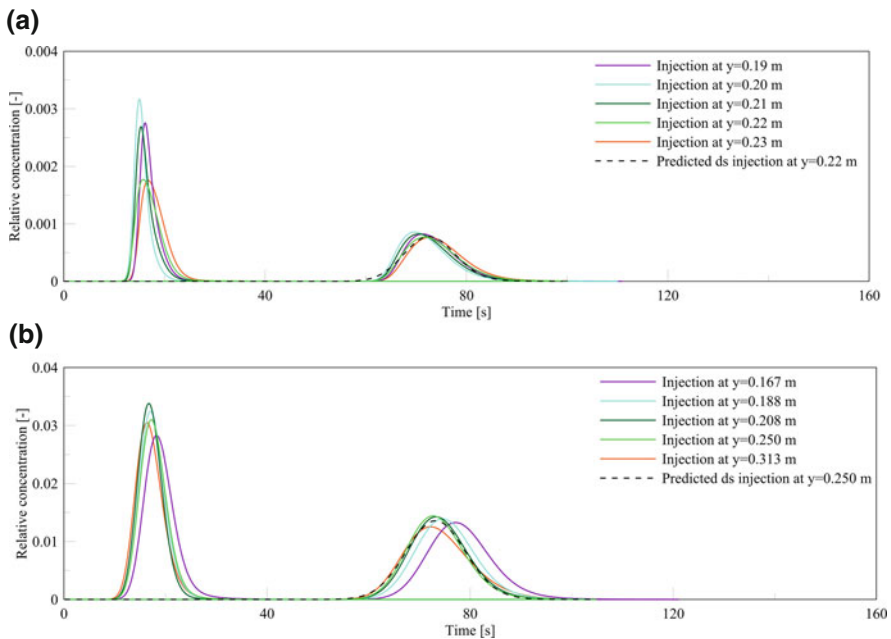


Fig. 5 Width-averaged concentration versus time **a** for the regular array, **b** for the random array

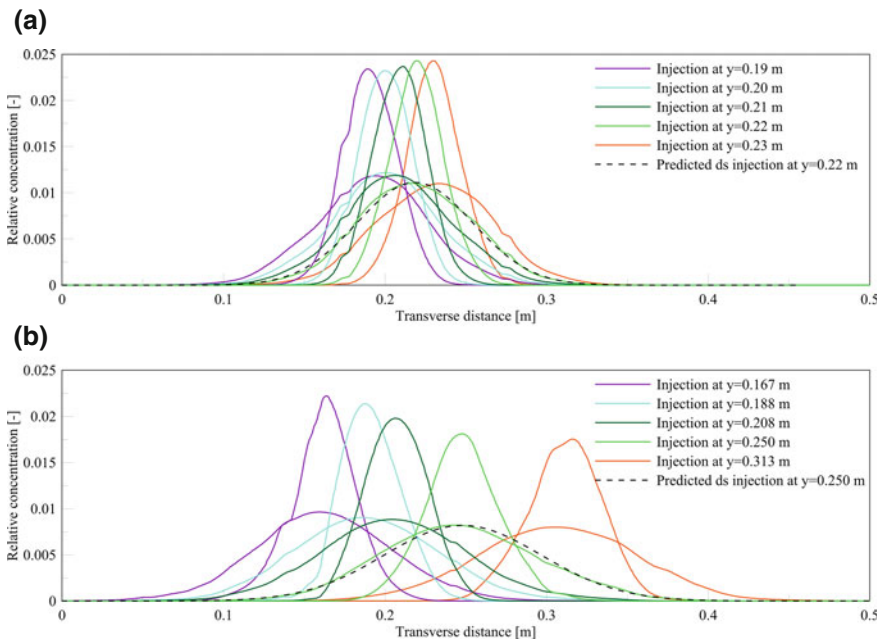
### 3.2 Transverse Dispersion Coefficient, $D_y$

Figure 6a and b show the transverse distributions of time-averaged tracer over the width of the channel at both the downstream and the upstream monitoring locations for the regular and random arrays, respectively. Some of the concentration distributions are not included for sake of readability.

The transverse and longitudinal dispersion coefficients for the regular and random arrays, along with their mean values, are presented in Fig. 7. The laboratory values of dispersion coefficients for the regular array (West 2016) are also included.

The mean longitudinal dispersion coefficient is approximately 1.2 times greater in the random array compared with the regular array. The  $D_y$  values are approximately one fifth of the  $D_x$  values, but again the random array exhibits greater transverse dispersion when compared with the regular array.

Comparing the laboratory measured values for the dispersion coefficients, which were measured in a regular array similar to the regular array in this study by West (2016), with those estimated in this study shows that both the longitudinal and the transverse dispersion coefficients are underestimated in this study. This could be a limitation of the two-dimensional CFD modelling and not considering the effect of



**Fig. 6** Time-averaged concentration versus transverse distance **a** for the regular array, **b** for the random array

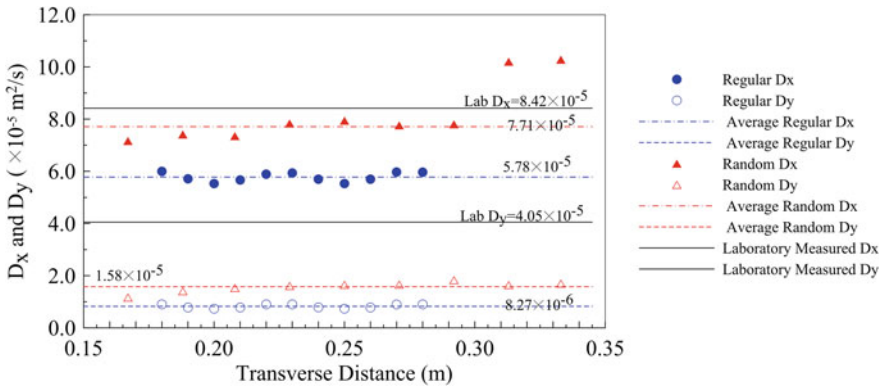


**Fig. 7** Longitudinal and transverse dispersion coefficients for the random and regular arrays

vertical velocity distribution over the channel depth. Other sources of error could be the turbulence model’s approximations and ignoring the roughness of cylinders and channel walls. Also it should be considered that in the model used in this study the tracer had only 0.3 m to be dispersed before the upstream monitoring location, whereas in the laboratory the tracer was injected 1 m before the upstream monitoring location.

### 4 Discussion

The comparison between the regular and random arrays’ flow fields showed the effect of randomness on velocity distribution. The random flow field had higher local maximum longitudinal velocity values, and higher values of velocity shear,  $|du/dy|$ , which is consistent with the higher longitudinal dispersion coefficients.

Both the longitudinal and transverse dispersion coefficients were underestimated in this study, but the estimation for the longitudinal coefficient was closer to the laboratory measured value comparing to the transverse one.

Nepf et al. (1997) reported values of transverse dispersion measured within random cylinder arrays, for a solid volume fraction of 0.006—which is very close to the one used in the current study—but with higher  $Re_d$  numbers, i.e. 192, 390, 588 and 786 and cylinder diameter of  $d = 0.006$  m. Considering a linear relation between normalized dispersion coefficient and  $Re_d$ , these values can be used to estimate a  $D_y$  value for the current study. The linear extrapolation results in a normalized transverse dispersion coefficient of  $D_y/jud = 0.16$  which in turn results in  $D_y = 8.9 \times 10^{-6} \text{ m}^2 \text{ s}^{-1}$ , which is approximately 0.6 of the estimated value of  $D_y$  in the current study.

The relation between transverse eddy viscosity, transverse turbulent length scale, and the rate of longitudinal velocity change over the width of the channel can be described by Eq. 3 (Rutherford 1994):

$$D_y = L_t^2 \left| \frac{du}{dy} \right|; \quad (3)$$

where  $L_t$  is the transverse turbulent length scale.

Using the mean values of velocity shear,  $|du/dy|$ , over all the cross-sections for the regular and the random arrays, i.e.  $0.513 \text{ s}^{-1}$  and  $0.619 \text{ s}^{-1}$ , respectively, and the mean value of transverse dispersion coefficients, i.e.  $D_{y(\text{regular})} = 8.27 \times 10^{-6} \text{ m}^2 \text{ s}^{-1}$  and  $D_{y(\text{random})} = 1.58 \times 10^{-5} \text{ m}^2 \text{ s}^{-1}$ , results in estimated  $L_t$  of 0.004 m and 0.005 m for the regular and the random array, respectively. The estimated value for the regular array is almost exactly equal to the cylinder diameter i.e.  $d = 0.004 \text{ m}$ , which helps to confirm the numerical accuracy of the RSM turbulence model. The slightly higher estimated mixing length scale for the random array is likely to be due to the combined effects of turbulent diffusion with transverse mechanical dispersion, as suggested by Tanino and Nepf (2008). The regular array would not be expected to exhibit significant mechanical dispersion due to its regular geometry.

## 5 Conclusions

- A direct comparison between flow and mixing within two regularly and randomly distributed cylinder arrays was performed. Both transverse and longitudinal dispersion were found to be greater in the random array compared with the regular array. These differences may be attributed to greater levels of velocity shear.
- The mixing length scales calculated suggest that the model is accurate and is able to model the effects of mechanical dispersion taking place within the random cylinder arrays.
- The CFD 2D RSM turbulence model along with scalar transport, was shown as a useful tool in modelling mixing within cylinder arrays, highlighting the potential to consider other distributions with different cylinder diameter/distance and with different solid volume fractions.



## References

- Anagnostopoulos P, Seitanis SA (2014) Numerical study of aperiodic phenomena past two staggered rows of cylinders in cross-flow. *Ocean Eng* 92:212–233
- ANSYS, Inc (2015) ANSYS Fluent® Academic Research, Release 16.1
- Nepf HM, Sullivan JA, Zavistoski RA (1997) A model for diffusion within emergent vegetation. *Limnol Oceanogr* 42(8):1735–1745
- Rutherford JC (1994) River mixing. John Wiley & Son Ltd
- Sonnenwald F, Guymier I, Marchant A, Wilson N, Golzar M, Stovin V (2016) Estimating stem-scale mixing coefficients in low velocity flows. *Sustainable hydraulics in the era of global change—Epicum et al. (eds) © 2016 Taylor & Francis Group, London, ISBN 978-1-138-02977-4*
- Tanino Y (2008) Flow and solute transport in random cylinder arrays: a model for emergent aquatic plant canopies. Doctoral dissertation, Massachusetts Institute of Technology
- Tanino Y, Nepf HM (2008) Laboratory investigation of mean drag in a random array of rigid, emergent cylinders. *J Hydraul Eng* 134(1):34–41
- Tanino Y, Nepf HM (2009) Laboratory investigation of lateral dispersion within dense arrays of randomly distributed cylinders at transitional Reynolds number. *Phys Fluids* 21(4):046603-10. © 2009 American Institute of Physics
- Versteeg HK, Malalasekera W (1995) An introduction to computational fluid dynamics. Longman Scientific & Technical, New York
- West PO (2016) Quantifying solute mixing across low velocity emergent real vegetation shear layers. Doctoral dissertation, University of Warwick, School of Engineering
- White BL, Nepf HM (2003) Scalar transport in random cylinder arrays at moderate Reynolds number. *J Fluid Mech* 487:43–79
- Zdravkovich MM (2003) Flow around circular cylinders: Volume 2: Applications. Oxford University Press
- Zhou B, Wang X, Guo W, Gho WM, Tan SK (2015) Experimental study on flow past a circular cylinder with rough surface. *Ocean Eng* 109:7–13

# Turbulence Flow Modeling of One-Sharp-Groyne Field

Oscar Herrera-Granados

**Abstract** Groyne arrangements had been subject of numerous studies, which demonstrate that the first groyne plays a crucial role on the hydraulic behavior of the whole arrangement. This contribution presents the application of two 3D numerical techniques (RNG and LES) to compute one single sharp-groyne field in a rectangular channel. In the laboratory, flow velocities and water levels were measured in order to calibrate and verify the accuracy of the numerical models. Two turbulence parameters, namely the Reynolds Shear Stresses in the  $XY$ -plane and the Turbulent Kinetic Energy, were estimated and compared. Both numerical techniques present good agreement with the time average velocity components recorded in the laboratory. Nonetheless, as expected, the Large Eddy Simulation (LES) is more appropriate for the computation of turbulence characteristics, but more expensive in terms of computational costs.

## 1 Introduction

Groynes are river training structures that can fulfill multiple objectives such as controlling mass transport processes, scouring process along river banks, maintaining channels for navigation or restoring fish habitats (McCoy et al. 2008). These structures come in various shapes depending on the characteristics of the specific river and on historical developments. Therefore, to understand the physical processes that involve the interaction between groynes and free surface flows is of interest of hydraulic scientists and engineers.

Previously, Ouillon and Dartus (1997) performed a numerical simulation of flow behavior downstream a lateral structure using the well known Reynolds-average Navier-Stokes (RANS)  $k$ - $\epsilon$  model. Their study demonstrated that the RANS-based methods present good agreement between modeled water surface elevations and

---

O. Herrera-Granados (✉)

Faculty of Civil Engineering, Wrocław University of Science & Technology, Wyb. Wyspiańskiego 27, 50-370 Wrocław, Poland  
e-mail: Oscar.Herrera-Granados@pwr.edu.pl

© Springer International Publishing AG 2018

M. B. Kalinowska et al. (eds.), *Free Surface Flows and Transport Processes*,  
GeoPlanet: Earth and Planetary Sciences,  
[https://doi.org/10.1007/978-3-319-70914-7\\_12](https://doi.org/10.1007/978-3-319-70914-7_12)

207

those measured in the laboratory. It also demonstrated that RANS models are useful to analyze sediment transport phenomena downstream one groyne. McCoy et al. (2008) investigated the dynamics of the main coherent structures in the flow around two vertical submerged groynes using a Large Eddy Simulation (LES). Also, using the same technique, they investigated the flow hydrodynamics in a straight open channel containing a multiple-embayment groyne field on one of its sides. They found that the flow inside the main recirculation eddy in the embayments can be characterized as being quasi-two dimensional. Also they found that the flow inside the mixing layer region between the embayments and the channel is strongly non-uniform over the depth. Constantinescu et al. (2009) investigated the exchange of dissolved matter between a straight open channel and a series of shallow embayments. The direct link between the mechanism of mass exchange and the dynamics of coherent structures was demonstrated. Also, it has been shown that the eddies lose progressively their coherence as they are convected toward the sidewall. Kashyap et al. (2010) used LES to elucidate the main features of a 3D turbulent flow field around submerged groynes in a sharp channel bend with a flat bed. They showed that flow at the inner bank of a curved bend is characterized by strong streamwise oriented vortices that can locally erode the bed and the channel sidewalls. Yu et al. (2010) proposed a two-dimensional lattice Boltzmann model coupled with a LES and applied it to flows around a non-submerged groyne in a channel. Their coupled model successfully predicted the flow characteristics and water depth distributions with the compared experimental data with reasonable accuracy and reliability. Brevis et al. (2014) provided a description of the three-dimensional flow induced by a sequence of lateral obstacles with flat bathymetry. The flow structure was experimentally characterized by Particle Image Velocimetry (PIV) measurements in a laboratory flume and simulated using three-dimensional LES. The mean flow within the dead zone is characterized by a large recirculation region and several additional vortex systems. They observed that the hydraulic behavior in the dead zones is sensitive to the aspect ratio, which is indirectly dependent on the length of the groyne field. Fang et al. (2014) implemented a direct-forcing immersed boundary method (IBM) to approximate complex boundaries around groynes with round heads and carried out measurements with PIV to validate the LES model to investigate the impact of groyne parameters on the flow properties. Model results showed that a rectangular-headed groyne generates higher turbulence intensities and larger vortices than a round-headed groyne.

In this contribution, the Renormalized Group (RNG) and a LES (Smagorinsky 1963) models are applied to analyse turbulence characteristics of a single sharp-groyne field. The output of the models is compared with measurements carried out in the laboratory to calibrate and verify the models. Main differences between natural flow behavior (measured in the laboratory) and the numerical discretizations are highlighted.

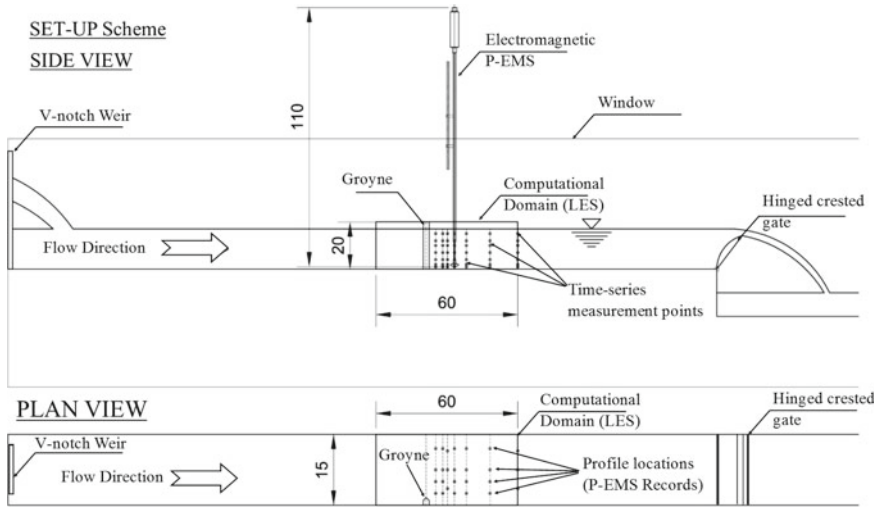


**Fig. 1** General scheme of the experimental setup, the location of the P-EMS and the computational domain (dimensions in cm)

## 2 Laboratory Works

A rectangular channel without slope was used for the experiments. The general dimensions of the flume are 5.0 m length, 0.5 m width and up to 0.8 m height. Figure 1 depicts the general scheme of the experimental set-up, the groyne, the electromagnetic P-EMS, the V-notch weir, the hinged crest gate, the flow direction as well as the spatial location of the computational domain (for the LES) and its dimensions. The roughness coefficients of the walls and bed were estimated as  $0.025 \text{ s m}^{-1/3}$  for the bed as well as for the left wall (taking as reference the flow direction) and  $0.018 \text{ s m}^{-1/3}$  for the right wall.

The hydrodynamic conditions of the experiments were controlled with a Thomson Weir (upstream) and with a hinged crest gate (downstream). The shallow water flow rate was calculated with the calibrated rating curve of the Thomson weir and with a piezometer indicating the hydraulic head acting on this weir. A flow rate of  $Q_e = 3.8 \text{ dm}^3 \text{ s}^{-1}$  was used for the experiments presented in this contribution. Also, the water surface elevation in the hinge of the gate was measured with a piezometer. For this  $Q_e$ , the Froude number of the bulk open-channel flow was approx.  $F = 0.20$  and the Reynolds number  $Re$  had a value around 10000. The water surface elevations were measured with a point gauge along the channel and registered from the hinged crest gate up to 2 m upstream the location of the groyne. The registered hydraulic gradient of the free surface elevation along the experimental zone was approximately 0.0015.

Several time velocity series were recorded with a programmable Electromagnetic Liquid Velocitymeter (P-EMS) and its accessories E-30. This apparatus is able to

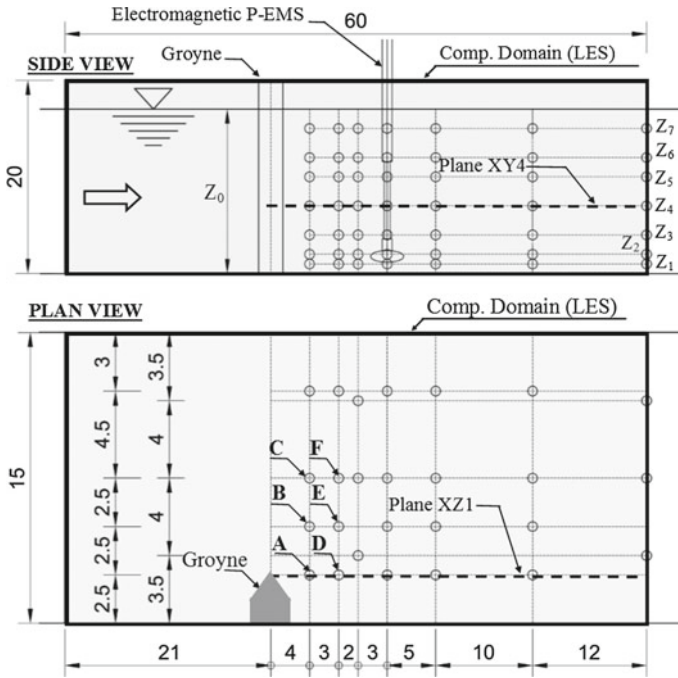


**Fig. 2** Location of the points and profiles where the velocity time series were recorded in the laboratory within the computational domain (dimensions in cm)

measure simultaneously the flow velocity components in two (mutually perpendicular) different directions with an accuracy of  $0.001 \text{ m s}^{-1}$  and a frequency of 10 Hz in the point where the probe is fixed (Herrera-Granados 2013). Twenty six velocity profiles were observed and for each profile, time series at seven different elevations were recorded (Elevations  $Z_1$  to  $Z_7$  in Fig. 2). For this contribution, six profiles were analyzed and compared. These profiles are denominated with the letters A to F in Fig. 2. The duration of the recorded time-series was in the range from one to three minutes. It was demonstrated that for the P-EMS velocimeter, the duration of the time series is sufficient to capture the turbulence characteristics for production and dissipation of the energy cascade (Herrera-Granados 2012).

### 3 Numerical Models

For these analyzes, the commercial code Flow-3D, developed by Flow Science, its standard RANS-RNG and LES models together with the Fractional Area-Volume Obstacle Representation (FAVOR) technique were applied. To discretize the govern-

ing equations, the computer software uses the generalized minimum residual method (Herrera-Granados and Kostecki 2016).

### 3.1 RNG Model

The 3D dimensional model was based on the modification of the continuity and momentum equations, the very well known RANS equations. In the RANS technique, the time-averaged velocity field may be defined by ensemble averaging, which is represented in the following system of equations (Pope 2000):

$$\frac{\partial \bar{u}_i}{\partial t} + \bar{u}_j \frac{\partial \bar{u}_i}{\partial x_j} = -\frac{1}{\rho} \frac{\partial \bar{p}}{\partial x_i} + \nu \frac{\partial^2 \bar{u}_i}{\partial x_j \partial x_j} - \frac{\partial}{\partial x_j} R_{ij} \quad (1)$$

$$\frac{\partial \bar{u}_i}{\partial x_i} = 0 \quad (2)$$

where  $\bar{u} = u - u'$  is the time-averaged velocity,  $u$  is the instantaneous velocity,  $u'$  is the velocity fluctuation,  $\bar{p}$  is the time-averaged pressure,  $\nu$  is the molecular viscosity and  $R_{ij}$  is the Reynolds stress tensor defined by (3)

$$R_{ij} = \overline{u'_i u'_j} \quad (3)$$

The turbulent stresses can be modeled with the following equation:

$$-\overline{u'_i u'_j} = \nu_T \left( \frac{\partial \bar{u}_i}{\partial x_j} + \frac{\partial \bar{u}_j}{\partial x_i} \right) - \frac{2}{3} k \delta_{ij} \quad (4)$$

where  $k$  is the Turbulent Kinetic Energy or TKE,  $\delta_{ij}$  is the Kronecker delta and  $\nu_T$  is the Eddy viscosity which plays a profound role in turbulence modeling.

The renormalization group model (RNG) was developed by Yakhot et al. (1992) to *renormalise* the Navier-Stokes Equations (NSE) and account for the effects of smaller scales of motion. In the standard  $k$ - $\epsilon$  model the eddy viscosity is determined from a single turbulence length scale, so the calculated turbulent diffusion is that which occurs only at the specified scale. The RNG approach results in a modified form of  $\epsilon$  (the dissipation rate of  $k$ ) which attempts to account for the different scales of motion through changes to the production term. Equations for  $k$  and  $\epsilon$  are:

$$\frac{\partial k}{\partial t} + \bar{u}_i \frac{\partial k}{\partial x_i} = \frac{\partial}{\partial x_j} \left[ \left( \nu + \frac{\nu_T}{\sigma_k} \right) \frac{\partial k}{\partial x_j} \right] + P_k - \epsilon \quad (5)$$

$$\frac{\partial \epsilon}{\partial t} + \bar{u}_i \frac{\partial \epsilon}{\partial x_i} = \frac{\partial}{\partial x_j} \left[ \left( \nu + \frac{\nu_T}{\sigma_\epsilon} \right) \frac{\partial \epsilon}{\partial x_j} \right] + C_{1\epsilon} \frac{\epsilon}{k} P_k - C_{2\epsilon}^* \frac{\epsilon^2}{k} \quad (6)$$

**Table 1** Constants of the RNG model

Constant	$C_\mu$	$\sigma_k$	$\sigma_\epsilon$	$C_{1\epsilon}$	$C_{2\epsilon}$	$\eta_0$	$\beta$
Value	0.0845	0.719	0.719	1.42	1.68	4.38	0.012

where  $C_{2\epsilon}^* = C_{2\epsilon} + \frac{C_\mu \eta^3 (1 - \eta/\eta_0)}{1 + \beta \eta^3}$ ,  $\eta = Sk/\epsilon$  and  $S$  is the modulus of the mean rate-of-strain tensor, defined as  $S \equiv \sqrt{2S_{ij}S_{ij}}$  and  $P_k = -\overline{u'_i u'_j \frac{\partial \bar{u}_i}{\partial x_j}}$  is the production of turbulence by shear. The constants of the RNG model are listed in Table 1.

### 3.2 LES Model

The aim of LES is to filter the NSE, insert a closure approximation, supply boundary conditions (called a Near Wall Model), discretize appropriately and perform a simulation (Berselli et al. 2006). In LES, the flow variables are decomposed into a *large-scale* component (or a resolved part), denoted by an overbar, and a *subgrid* scale (SGS) component. This decomposition is formally achieved by a filtering operation. The resolved part of the field represents the large eddies, while the subgrid part of the velocity represents the small scales whose effect on the resolved field is included through the SGS.

The filtering process can be understood as the convolution of a flow variable (in this case velocity) in one dimension  $\bar{u}$  is defined by:

$$\bar{u}(\mathbf{x}) = \int_{-\infty}^{+\infty} G(x, x') \bar{u}(x') dx' \quad (7)$$

where  $\bar{u}$  represents the resolved part of  $u$  and  $G$  is the kernel filter depending on the mapping function  $x' = (\mathbf{x})$ . Substituting in the decomposition filtering  $u = u'_i + \bar{u}_i$  and  $p = p'_i + \bar{p}_i$  in the NSE derives equations of motion for the resolved field, known as the Filtered Navier-Stokes Equation (FNSE).

$$\frac{\partial \bar{u}_i}{\partial t} + \bar{u}_j \frac{\partial \bar{u}_i}{\partial x_j} = -\frac{1}{\rho} \frac{\partial \bar{p}}{\partial x_i} + \frac{\partial}{\partial x_j} \left( [\nu + \nu_{SGS}] \frac{\partial \bar{u}_i}{\partial x_j} \right), \quad (8)$$

where  $\nu_{SGS}$  is the subgrid-scale turbulent viscosity, equivalent to the eddy viscosity of the RANS models. The most popular SGS model was proposed by Smagorinsky (1963). This model relates the grid size  $\bar{\Delta}$  as the length scale (or filter cutoff length scale) to the resolved strain rate  $\bar{S}_{ij}$ .  $\nu_{SGS}$  is modeled by

$$\nu_{SGS} = (C_s \bar{\Delta})^2 \left| \bar{S}_{ij} \right| \quad (9)$$

where  $\overline{S_{ij}}$  is the rate-of-strain tensor for the resolved scale defined by

$$\overline{S_{ij}} = \frac{1}{2} \left( \frac{\partial \bar{u}_i}{\partial x_j} + \frac{\partial \bar{u}_j}{\partial x_i} \right) \quad (10)$$

the filter length is usually calculated as  $\bar{\Delta} = V^{1/3}$ , where  $V$  is the volume of the computational cell. The Smagorinsky constant  $C_s$  usually has the value 0.1 – 0.2.

### 3.3 Meshing, Boundary Conditions and Calibration

For the RNG approach, one numerical hexahedron mesh, built with uniform cubic elements, was used in order to simulate the water flow from the beginning of the flume (2.0 m upstream the location of the groyne) up to the location of the hinged crested gate. For the LES, two numerical meshes (one large and one nested), were applied. The first mesh covered the computational domain (see Fig. 1). The nested mesh was used to simulate the flow behavior beside and downstream the groyne. The meshes' dimensions and parameters of the computational domains are summarized in Table 2. For the case of the RNG model, the size of the mesh was chosen in order that the streamwise velocity profile can follow the logarithmic law in the center of the channel upstream the location of the groyne. For the LES, the mesh size was defined using the computed turbulent length scale from the RNG model.

In the RNG model, the value  $Q_e$  was defined as the upstream boundary condition while the water surface measured in the laboratory was established as the downstream boundary condition. The RNG model was calibrated using the measured water surfaces with the point gauge and changing the values of the Manning coefficients of the walls and bed.

The boundary conditions of the LES were established with the computed velocity values of the calibrated RNG model. Once the LES model was run, the values that were recorded in the laboratory, namely the streamwise time-averaged velocity  $V_x$ , were compared with the values computed with both numerical models. The parameters of the numerical methods (e.g. time step controls and selection of the pressure solver) were modified in order to carry out a new verification of the numerical approaches. The comparison of the  $V_x$  profiles for the locations A to F (See

**Table 2** Parameters of the computational domains and meshes

Model	Length (m)	Width (m)	Height (m)	Cell size (m)	No. of cells
RNG	4.0	0.15	0.2	0.005	960000
LES-main	0.6	0.15	0.2	0.0025	1152000
LES-nested	0.4	0.10	0.2	0.001	8000000



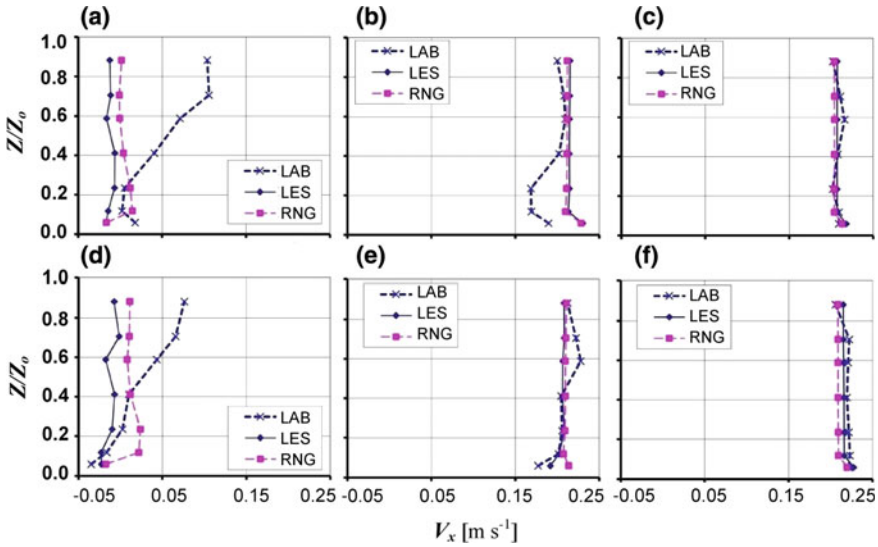


**Fig. 3** Verification of the numerical models using the measured  $V_x$  values (Profiles A-F)

Fig. 2) are presented in Fig. 3. The model and the experimental values present good agreement. Nonetheless, as depicted in Fig. 3, there are some discrepancies in the profiles located close to the tip of the groyne (A, B & D).

### 4 Output of the Models and Discussion

The comparison of the output of the models is depicted in Figs. 4 and 5. Regardless of the fact that the RNG model attempts to account for the different scales of turbulent motion, the LES computes the vorticity field, where vorticity is defined as the curl of the velocity field  $\omega = \nabla \times \mathbf{v}$  (Kostecki 2008), in a more proper way.

Figure 4 depicts the streamwise vorticity field and the 2D velocity vectors in the plane XY downstream the groyne at the elevation  $Z_4$  of Fig. 4. Figure 5 depicts the same variables for the XZ plane where the points A and D were located.

Evident differences between the output of the models can be noticed. In the case of the RNG, the values of the computed vorticity were in the range between  $-1.1$  up to  $16.3 \text{ s}^{-1}$  where the maximal values were computed in the upstream base of the groyne (positive) and downstream the sharp groyne head (negative). For the LES, the values of the computed vorticity were in the range between  $-47$  up to  $41 \text{ s}^{-1}$  and both maximal negative and positive values were computed in the interfacial region downstream the groyne. Nonetheless, the time-averaged computed velocities did not differ too much in the two models, as presented in Fig. 3.

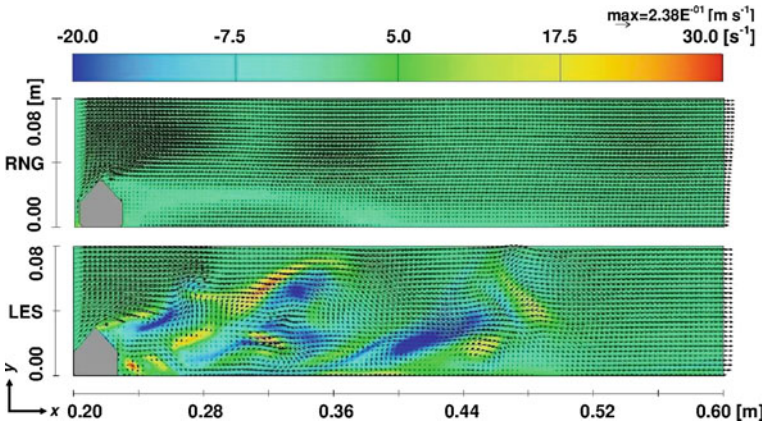


Fig. 4 Comparison of the computed vorticity field (Above-RNG and below-LES) in streamwise direction and computed velocity vectors in the plane XY4

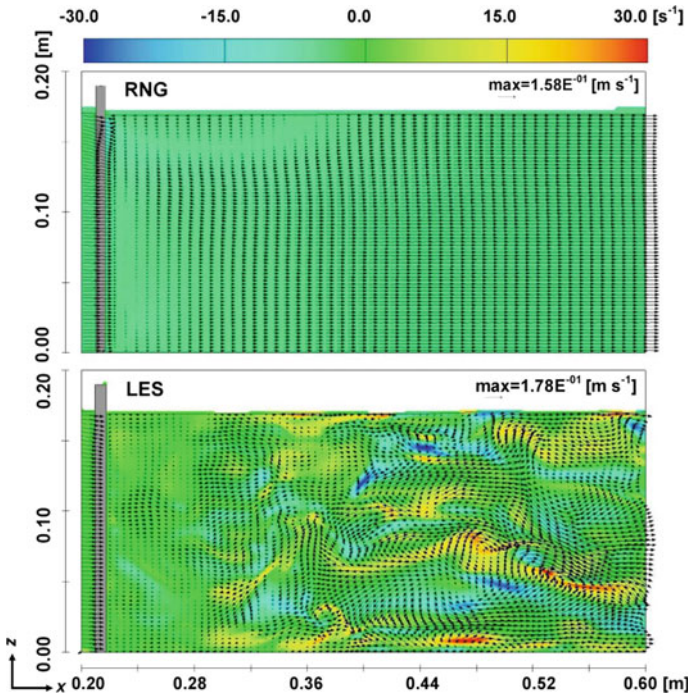


Fig. 5 Comparison of the computed vorticity field (Above-RNG and below-LES) in streamwise direction and computed velocity vectors in the plane XZ1

### 4.1 Comparison of the Simulations with the Laboratory Records

Observed Reynolds shear stresses in the XY-plane and TKE were estimated by analyzing the instantaneous velocity fluctuations of the recorded time-series. The Re Stresses were calculated directly from the velocity fluctuations as:

$$\tau_{xy} = -\overline{\rho v'_x v'_y} \tag{11}$$

while TKE was calculated by:

$$k \approx \frac{1.33}{2} (v_x'^2 + v_y'^2) \tag{12}$$

where  $v_x'^2$  and  $v_y'^2$  are the variance of the flow velocity components in two directions: x-streamwise and y-spanwise (Herrera-Granados 2012).

Figures 6 and 7 depict the profiles of the shear stresses in the plane XY and TKE, respectively, in the six different profiles (A-F) recorded in the laboratory. Also, using the output of the numerical models and Eqs. 11 and 12, the same profiles were estimated and compared with the experiments.

The LES model is capable to predict the non-isotropic behavior of the velocity fluctuations close to the tip of the groyne. This situation is more evident in the calculated profiles of the TKE. The accuracy of the LES decreases in the case of the profiles C and F, located in the center of the channel. In both cases, the RNG pro-

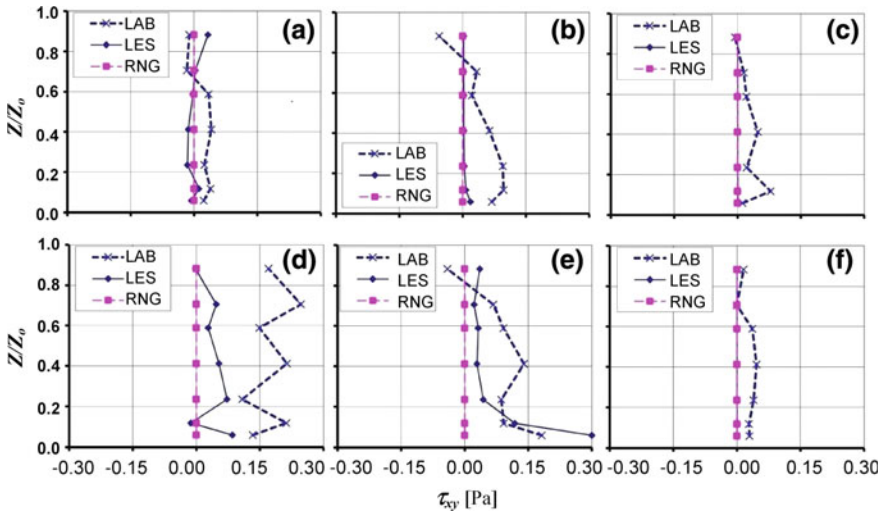


**Fig. 6** Comparison of the Re stresses computed with the numerical models and the values measured in the laboratory (Profiles A-F)

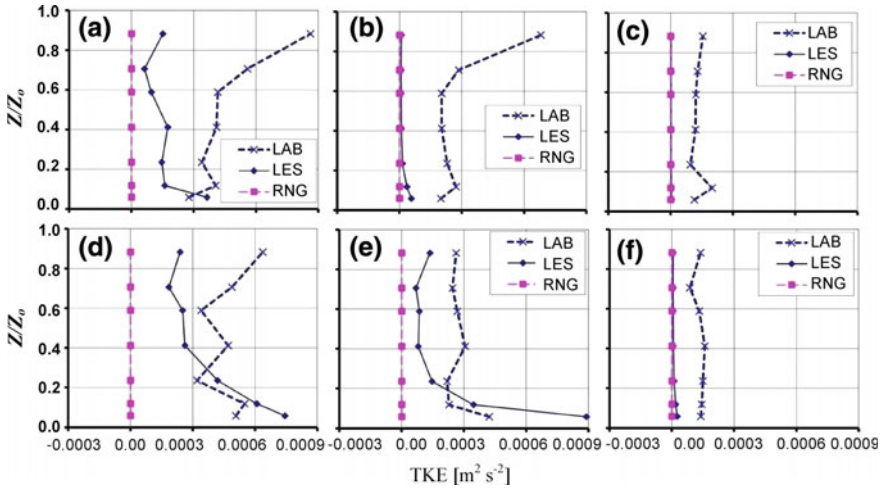


Fig. 7 Comparison of the TKE computed with the numerical models and the values measured in the laboratory (Profiles A-F)

files present an isotropic behavior. The differences between the model and the time-averaged velocity profiles are in the range from 0.001 to  $0.116 \text{ m s}^{-1}$  in the profiles A and D. For the other four profiles (B, C, E and F), the time averaged velocity profiles presented very good agreement with the measurements recorded in the laboratory, The differences of the computed Reynolds shear stresses vary from 0.033 to 0.096 Pa and for the TKE are in the range from 0.0001 to  $0.0007 \text{ m}^2 \text{ s}^{-2}$ . The discrepancies between the output of both models are lower.

## 5 Conclusions

Due to the fact that river flows practically always in turbulent regime, the importance of understanding the water-structure interaction is a key role to increase the reliability of our engineering CFD calculations. In the present contribution, full three-dimensional numerical modeling was used to predict the velocity field of a single sharp-crest groyne. The laboratory measurements demonstrated that LES is a more proper tool to analyze the behavior of water downstream the groyne. The LES model (as expected) predicts more accurately the velocity field downstream the lateral obstruction, where some turbulent structures can be identified. Discrepancies were found in the upper part ( $Z/Z_0 > 0.4$ ) of the computed velocity profiles and the laboratory measurements of the profiles located close to the tip of the groyne (A and D). Nonetheless, the presented LES depicts the flow behavior in the interfacial and dead zones with good accuracy, in a similar way as Brevis et al. (2014) presented it for long aspect ratios.

On one hand, and after analyzing the time-averaged turbulence parameters of this contribution, it is possible to state that the obtained TKE results from both RNG and LES models differ between each other. Thus, the effects of turbulence can be much better represented in a numerical model if those large eddies are resolved, such as Large Eddy Simulations. On the other hand, the computed Reynolds shear stresses do not vary drastically. Thus, taking in the balance “accuracy vs computational costs”, it is difficult to state that LES is a better option to analyze the groyne-water interaction for engineering purposes, e.g. sediment transport phenomena. Thus, for larger-scale river engineering problems, the RNG approach seems to be a feasible technique to predict flow behavior with lateral structures, such as Ouillon and Dartus (1997) demonstrated with a single groyne and the  $k-\epsilon$  model.

## References

- Berselli LC, Ilescu T, Layton WJ (2006) *Mathematics of large eddy simulation of turbulent flows*. Springer, Berlin-Heidelberg
- Brevis W, García-Villalba M, Niño Y (2014) Experimental and large eddy simulation study of the flow developed by a sequence of lateral obstacles. *Environ Fluid Mech* 14:873–893
- Constantinescu G, Sukhodolov A, McCoy A (2009) Mass exchange in a shallow channel flow with a series of groynes: LES study and comparison with laboratory and field experiments. *Environ Fluid Mech* 9:587–615
- Fang H, Bai J, He G, Zhao H (2014) Calculations of nonsubmerged groin flow in a shallow open channel by large-eddy simulation. *J Eng Mech* 140(5):04014,016–1–11
- Herrera-Granados O (2012) *Seepage influence on river dynamics*. PhD thesis, Wrocław University of Science and Technology, Wrocław, Poland
- Herrera-Granados O (2013) *Statistical analysis of seepage’s influence on open-channel turbulence*. In: *Experimental and computational methods in hydraulic research*. Springer, Berlin Heidelberg, pp 147–158
- Herrera-Granados O, Kostecki S (2016) Numerical and physical modeling of water flow over the ogee weir of the new Niedów barrage. *J Hydrology Hydrodyn* 64(1):67–74
- Kashyap S, Rennie C, Townsend R, Constantinescu G, Tokyay T (2010) Flow around submerged groynes in a sharp bend using a 3D LES model. In: *River Flow 2010*, Bundesanstalt für Wasserbau, pp 643–650
- Kostecki S (2008) Numerical modelling of flow through moving water-control gates by vortex method. Part I problem formulation. *Arch Civ Mech Eng* 8(3):73–89
- McCoy A, Constantinescu G, Weber L (2008) Numerical investigation of flow hydrodynamics in a channel with a series of groynes. *J Hydraul Eng* 134(2):157–172
- Ouillon S, Dartus D (1997) Three-Dimensional computation of flow around groyne. *J Hydraul Eng* 123(11):962–970
- Pope S (2000) *Turbulent flows*. Cambridge University Press, Cambridge, UK
- Smagorinsky J (1963) General circulation experiments with the primitive equations. *Mon Weather Rev* 91:99–164
- Yakhot V, Orszag S, Thangam S, Gatski T, Speziale C (1992) Development of turbulence models for shear flows by a double expansion technique. *Mon Weather Rev* 4(7):1510–1520
- Yu X, Tang X, Wang W, Wang F, Chen Z, Shi X (2010) A lattice Boltzmann model coupled with a Large Eddy Simulation model for flows around a groyne. *Int J Sedim Res* 25(3):271–282

# Sensitivity Analysis for the Water-Air Heat Exchange Term

Monika B. Kalinowska, Magdalena M. Mrokowska  
and Paweł M. Rowiński

**Abstract** A term expressing heat exchange between water and air is often present in models of thermal pollution spreading in rivers. The importance of this term depends strongly on temporal and spatial scale of the process as well on meteorological and hydrological conditions. Although heat exchange between the water and atmosphere has been studied for many years, its determination is still difficult in practical cases, and different simplifications are considered in practice. The objective of this study was to verify which of the input data needed for the net heat flux calculations are of utmost importance and which of them influences its final value most significantly. The analyses have been performed for several data sets collected in natural conditions.

## 1 Introduction

River temperature is governed by atmospheric conditions, its topography, water discharge and the streambed and it is one of key variables responsible for the health of aquatic ecosystem. It is of crucial importance to be able to predict the fate of a thermal plume in a stream in situations when significantly warmer or significantly colder water inflows the main stream, causing locally an abrupt change in thermal conditions of a river. It is a complex process and one of key questions to be answered when models of thermal pollution in rivers are constructed is which of additional heat sources should be included in such models. Which of them, if any, are finally taken into account depends on the analyzed situation and particularly on the temporal and spatial scale of the process and input data availability and accuracy (Kalinowska and Rowiński 2015; Kalinowska et al. 2016). A significant heat exchange between the water and its environment occurs through the water-air interface (Evans et al. 1998; Webb and Zhang 1999). The net heat flux— $Q_A$

---

M. B. Kalinowska (✉) · M. M. Mrokowska · P. M. Rowiński  
Institute of Geophysics, Polish Academy of Sciences, Ksiecia Janusza, 64, 01-452 Warsaw,  
Poland  
e-mail: Monika.Kalinowska@igf.edu.pl

[W m<sup>-2</sup>]*—*results from the energy balance at the water-air interface, and it includes several processes, like (Chapra 1997; Edinger et al. 1974; Rutherford et al. 1993):

- shortwave solar radiation ( $q_s$ ),
- longwave atmospheric radiation ( $q_a$ ),
- longwave water back radiation—emitted by the water surface ( $q_b$ ),
- evaporation and condensation ( $q_e$ ),
- conduction and convection ( $q_h$ ).

The net heat flux is defined as follows:

$$Q_A = q_s + q_a - q_b \pm q_e \pm q_h. \quad (1)$$

It may be calculated based on water temperature and set of meteorological data. There are many different (more or less complicated) formulae available in the literature that can be used to compute each term in Eq. (1). Generally, all the described processes turn out to be functions of water temperature  $T_w$  [°C], air temperature  $T_a$  [°C], air humidity  $Rh$  [%], air pressure  $p_a$  [mb = HPa], measured shortwave solar radiation  $q_{SR}$  [W m<sup>-2</sup>] and wind speed  $u$  [m s<sup>-1</sup>], i.e.:  $q_s = f(q_{SR})$ ,  $q_a = f(T_a, Rh)$ ,  $q_b = f(T_w)$ ,  $q_e = f(p_a, u, T_a, T_w)$  and  $q_h = f(p_a, u, T_a, T_w)$ . The following relations have been applied herein to estimate each term of Eq. (1):

$$q_s = q_{SR}(1 - A), \quad (2)$$

$$q_a = \varepsilon_a \sigma (T_a + 273.15)^4 (1 - r), \quad (3)$$

$$q_b = \varepsilon_w \sigma (T_w + 273.15)^4, \quad (4)$$

$$q_e = f(u)(e_s - e_a), \quad (5)$$

$$q_h = C_b \frac{p_a}{p_0} f(u)(T_w - T_a), \quad (6)$$

where:  $A$ —water albedo [–] (= 0.06),  $\varepsilon_a$ —emissivity of atmosphere [–],  $r$ —reflection coefficient (= 0.03),  $\varepsilon_w$ —emissivity of water [–] (= 0.97 has been assumed in the paper),  $\sigma$ —the Stefan-Boltzmann constant (=  $5.67 * 10^{-8}$  W m<sup>-2</sup> K<sup>-4</sup>),  $e_a$ —actual vapor pressure (water vapor pressure in the air) [mb],  $e_s$ —saturation vapor pressure at the water surface [mb],  $C_b$ —Bowen coefficient (= 0.62 mb °C<sup>-1</sup>),  $p_0$ —reference air pressure (= 1013 mb),  $f(u)$ —wind speed function [W m<sup>-2</sup> mb<sup>-1</sup>]. For the atmospheric emissivity the formula proposed by Brunt (1932) has been chosen:

$$\varepsilon_a = a_1 + a_2 \sqrt{e_a} \quad (7)$$

where:  $a_1$  [–] and  $a_2$  [mb<sup>-1/2</sup>] are empirical coefficients. Note that there are many different formulae available in the literature that can be used here (see, e.g.: Iziomon et al. 2003; Flerchinger et al. 2009). The actual vapor pressure may be expressed as:

$$e_a = e_{sat} \frac{Rh}{100}, \quad \text{where: } e_{sat} = r_1 \exp\left(\frac{r_2 T_a}{T_a + r_3}\right). \quad (8)$$

$e_{sat}$  is a saturation vapor pressure in the air, and  $r_1, r_2, r_3$  are empirical coefficients. The saturation vapor pressure at the water surface is equal to:

$$e_s = r_1 \exp\left(\frac{r_2 T_w}{T_w + r_3}\right). \quad (9)$$

For the wind speed function, even more problematic variable, usually the following empirical relation is applied (Zhen-Gang 2008):

$$f(u) = b_0 + b_1 u + b_2 u^2, \quad (10)$$

where  $b_0, b_1, b_2$  are empirical coefficients, that may take different values.

As a result, Eq. (1) becomes a complicated nonlinear function with many empirical coefficients. This makes calculations, together with the problem with availability and accuracy of input data, difficult. Several variants and empirical formulae with different coefficients have been applied to the case studies described in the paper. For the results presented in the paper, the following empirical coefficients have been chosen:  $a_1 = 0.55$ ,  $a_2 = 0.065$  (Brant 1932);  $r_1 = 6.12$ ,  $r_2 = 17.27$ ,  $r_3 = 237.3$  (Chapra 1997; Raudkivi 1979);  $b_0 = 6.9$ ,  $b_1 = 0$ ,  $b_2 = 0.34$  (Ahsan and Blumberg 1999; Zhen-Gang 2008).

The primary objective of this study was to find which input data are of utmost importance, and which of them influence the final value of net heat flux most. Another issue was to find whether the change of empirical coefficients or change in meteorological and hydrological conditions may alter qualitatively the results.

## 2 Methods—Sensitivity Analysis

Sensitivity analysis aims to describe to what extent the output values are affected by changes in the input values. One of its measures is the so-called sensitivity coefficient. In hydrological research the application of sensitivity coefficient may be found in the studies of Mrokowska et al. (2013), Gong et al. (2006), Hupert and Vanclooster (2001) and Qiu et al. (1998). Given an output variable  $y$  and input variables  $x_i$ , *sensitivity coefficient* of  $x_i$  on  $y$  is defined as (Gutenbaum 1992; ISO 1999):

$$S_i = \frac{\partial y}{\partial x_i}; \quad (11)$$

and expresses the effect of a small perturbation of input variable  $x_i$  on output variable  $y$ . Very often, like in the case of net heat flux calculations, we deal with



many input variables with different dimensions and different ranges of values. In such cases, the non-dimensional so-called *relative sensitivity coefficient* should be used (Gutenbaum 1992; McCuen 1973; Beven 1979):

$$S_i^R = \frac{\partial y}{\partial x_i} \frac{x_i}{y}. \quad (12)$$

In this paper, the sensitivity coefficients have been applied in order to assess the impact of six input variables:  $T_w$ ,  $T_a$ ,  $Rh$ ,  $p_a$ ,  $q_{SR}$  and  $u$  on the net heat flux  $Q_A$  for sample data presented in the next section. The absolute values of the sensitivity coefficients are considered, as we are interested only in the magnitude of impact of input variable on the result, not in the direction of this impact. Additionally, percentage of the relative sensitivity coefficient has been evaluated for each time instant to make the results easier to compare.

### 3 Input Data

The analysis has been performed for sample data sets from several measurement campaigns carried out in two lowland rivers in Poland, namely, Świder and Narew. The chosen rivers have different hydrological settings (see Table 1). Detailed description of both of them may be found in Rajwa et al. (2014) and Rajwa-Kuligiewicz et al. (2015). Additionally, in the case of the River Świder analyses have been performed for different periods of the year. These studies have included, among others, measurements of selected meteorological and hydrological data.

The following data have been used in further calculations: water temperature, atmospheric pressure, air temperature, measured solar shortwave radiation, humidity, and wind speed. Most of these data have been measured every minute, for some data sets every 5 min. Values averaged over 30 min have been used for calculations. The analyses have been performed for the following data sets:

- Set I—the River Narew for 24 h (16.10 00:00–17.10.2013 00:00);
- Set II—the River Świder for 24 h (26.09 00:00–27.09.2013 00:00);
- Set III—the River Świder for 24 h (02.05 00:00–03.05.2016 00:00);
- Set IV—the River Świder for 24 h (30.07 00:00–31.07.2016 00:00).

**Table 1** Hydraulic characteristics of considered rivers' sections during the measurements in 2013

River	$B$ [m]	$H$ [m]	$S$ [-]	$R$ [m]	$Q$ [m <sup>3</sup> s <sup>-1</sup> ]	$U_*$ [m s <sup>-1</sup> ]	$U$ [m s <sup>-1</sup> ]
Narew	20	1.8	0.0001	1.16	11.0	0.03	0.3
Świder	20	0.3	0.0023	0.26	3.0	0.07	0.5

$B$ —width,  $H$ —cross-sectionally averaged depth,  $S$ —slope,  $R$ —hydraulic radius,  $Q$ —discharge,  $U_*$ —shear velocity,  $U$ —mean velocity in the cross-section

All data sets are illustrated in Figs. 1, 2, 3 and 4, respectively. In case of Set I, measured water temperature has been complemented by meteorological data from the Narew National Park Weather Station which is the nearest meteorological station ([http://meteo.npn.pl/](http://meteo.npn.pl), 53°06'17.56"N 22°47'51.84"E, 114 m above sea

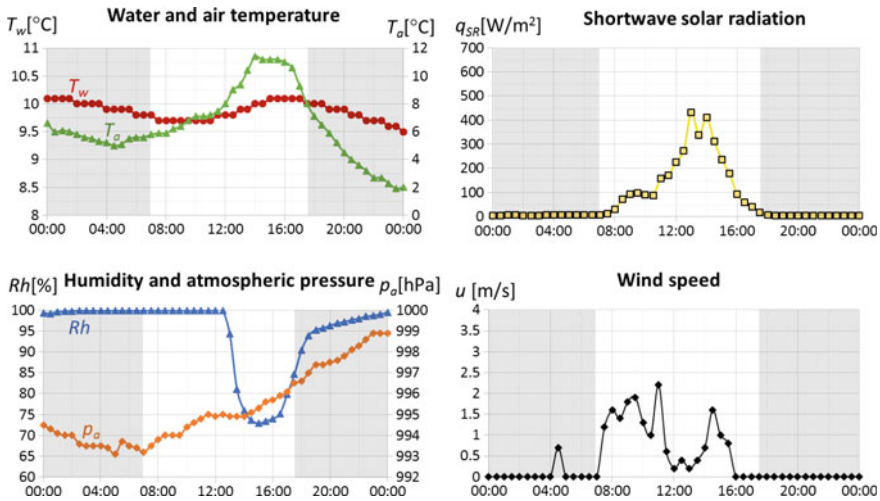


**Fig. 1** Input data for evaluating heat budget for the River Narew—Set I (16.10.2013). On the horizontal axis, the time is given; additionally, day (white color) and night (grey color) are indicated

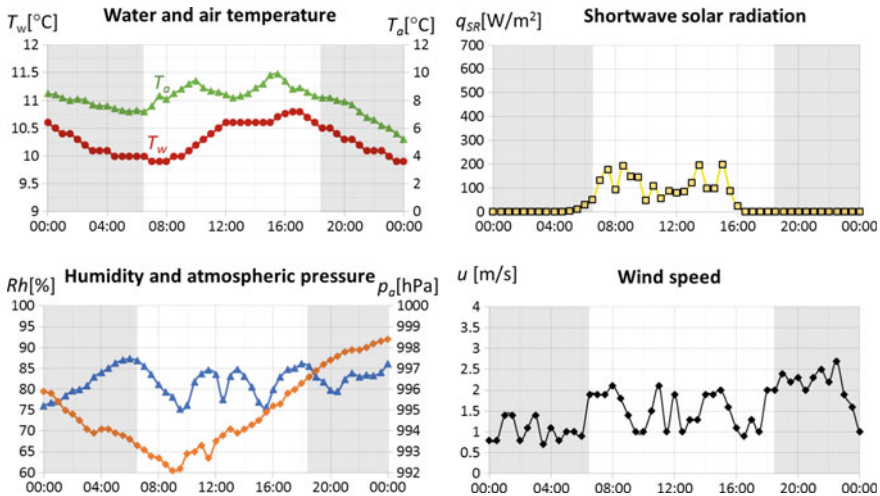


**Fig. 2** Input data for evaluating heat budget for the River Świder—Set II (26.09.2013). On the horizontal axis, the time is given; additionally, day (white color) and night (grey color) are indicated

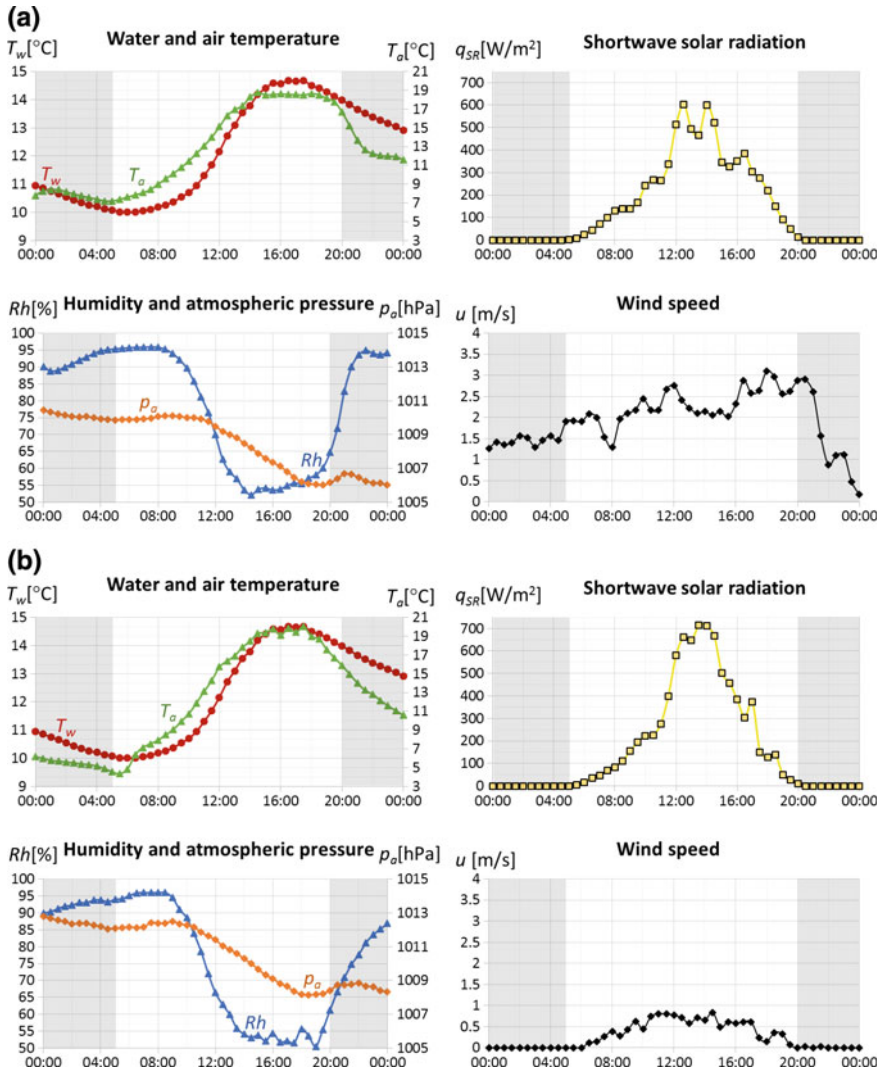


**Fig. 3** Input data for evaluating heat budget for the River Świder—Set III (02.05.2016). On the horizontal axis, the time is given meteorological; additionally, day (white color) and night (grey color) are indicated. **a** Meteorological data from Warsaw Meteo Station; **b** meteorological data measured directly on the river bank

level). In case of Set II, the meteorological data from IGF UW Meteorological observatory (<http://metobs.igf.fuw.edu.pl/>, 52°12'42.7"N 20°58'59.5"E, 148 m above sea level) have been used. For Set III, two sources of meteorological data have been used: data from Warsaw Meteo Station (<http://www.meteo.waw.pl/>, 52°10'53"N 20°52'13"E 110 m above sea level) and data measured directly on the

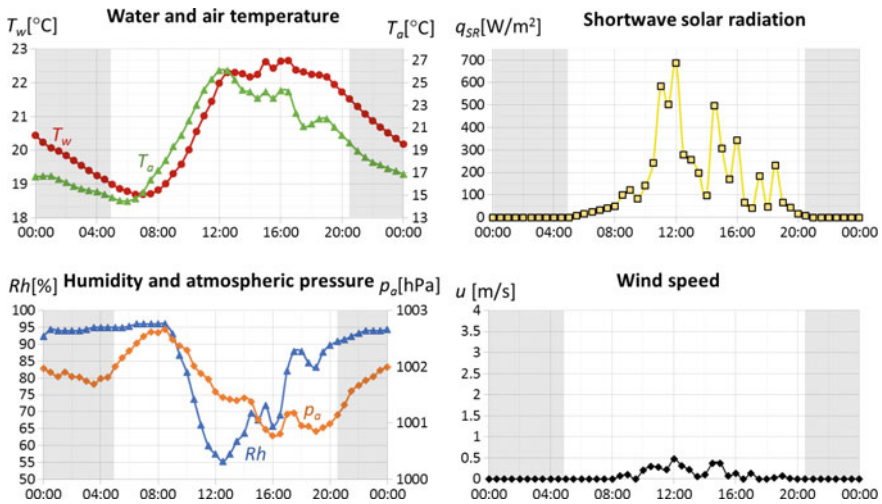


**Fig. 4** Input data for evaluating heat budget for River Świder—Set IV (30.07.2016). On the horizontal axis the time is given; additionally, day (white color) and night (grey color) are indicated

river bank together with the water temperature measurements. Meteorological data have been measured using the Davis Vantage Pro2 Weather Station (Wireless), the water temperate and atmospheric pressure using the Handheld Optical Dissolved Oxygen Meter (ProODO, YSI) equipped with water temperature sensor, barometric pressure sensor and an optical dissolved oxygen sensor. For Set IV the meteorological data measured directly on the river bank have been used.

## 4 Results—Sensitivity of the Net Heat Flux on Input Variables

### 4.1 Heat Flux with All Processes Included

The sensitivity analysis has been performed for the net heat flux taking into account all processes included in Eq. (1). In order to estimate the significance of input variables for each time instant, the percentage of the relative sensitivity coefficient has been evaluated. The results for different data sets (Set I, Set II, Set III a), Set III b) and Set IV) are presented in Figs. 5, 6, 7, 8 and 9, respectively. From all the figures it is seen that water temperature, air temperature and humidity are significant during the 24 h, while solar radiation is significant during the daytime only. Atmospheric pressure is less significant and wind speed is the least significant variable, but it should be noted that for higher values of wind speed (noted during

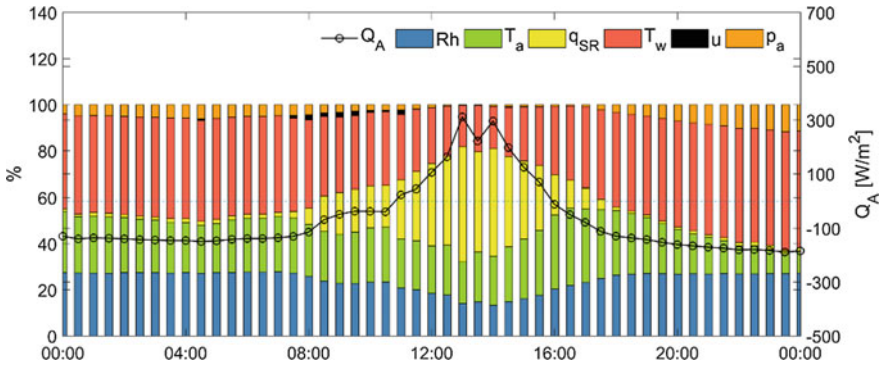


**Fig. 5** Diurnal percentage of relative sensitivity coefficient for the River Narew—Set I (16.10.2013)

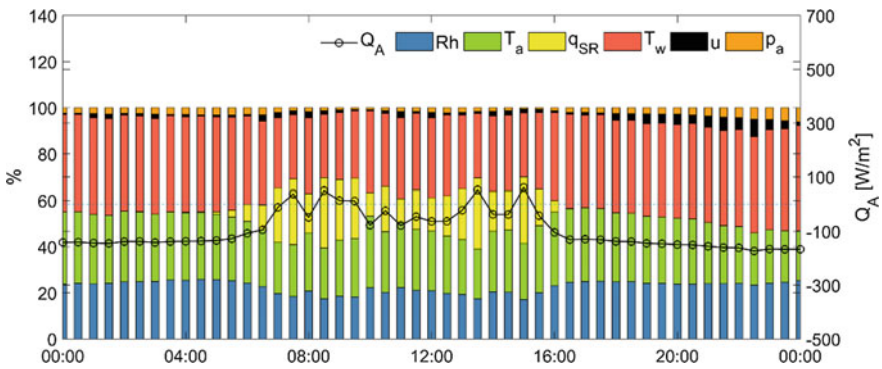


**Fig. 6** Diurnal percentage of relative sensitivity coefficient for the River Świder—Set II (26.09.2013)

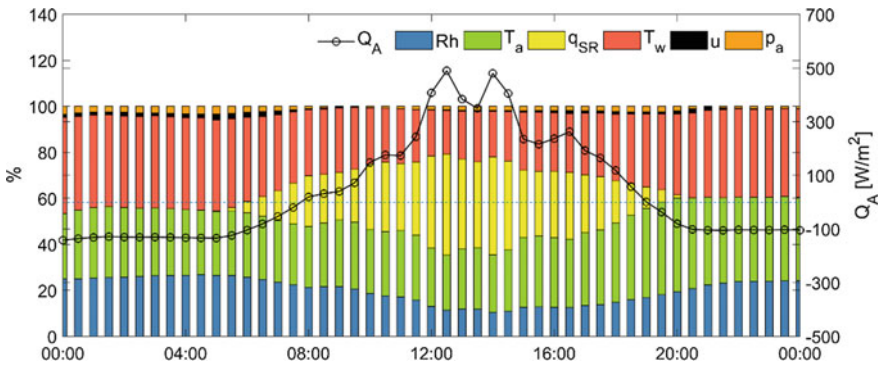


**Fig. 7** Diurnal percentage of relative sensitivity coefficient for the River Świder—Set III a (02.05.2016); meteorological data from Warsaw Meteo Station

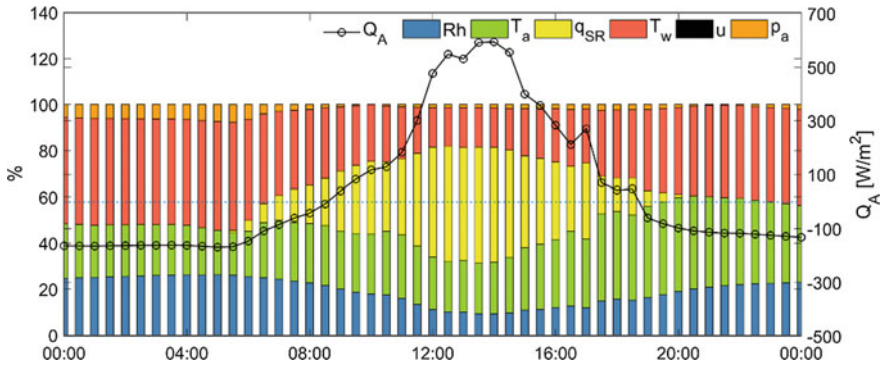


**Fig. 8** Diurnal percentage of relative sensitivity coefficient for the River Świder—Set III b (02.05.2016); meteorological data measured directly on the river bank

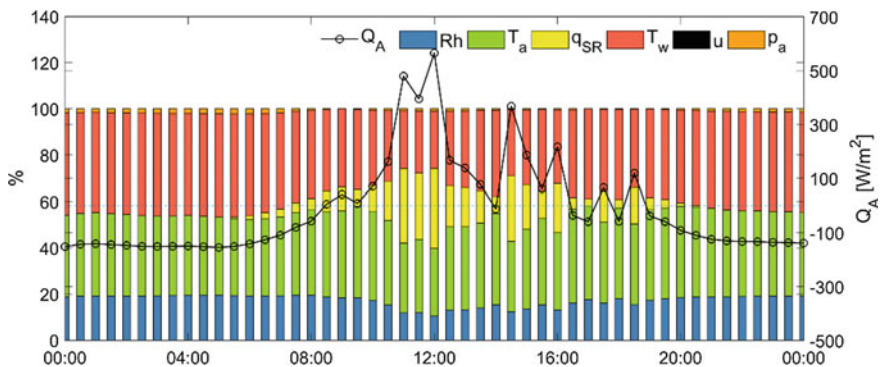


**Fig. 9** Diurnal percentage of relative sensitivity coefficient for the River Świder—Set IV (30.07.2016)

the measurements in case of Set II—Fig. 6 and Set III a—Fig. 7), the wind speed is just as important (or even more) as the atmospheric pressure.

Considering various parts of the day, it could be concluded that in the evening, night and morning the water temperature is the most significant in all the cases, next goes the temperature of air and humidity that are similarly significant (with some exception, e.g. in case of Set IV the air temperature is more important than humidity). During the day, the temperature of air and its humidity, temperature of water and shortwave radiation are meaningful. Usually about the midday, the measured solar radiation is the most significant variable and it is connected with its higher value at the same time. The exception may be observed in case of Set II where there is no maximum of  $q_{SR}$  at midday. From Figs. 5, 6, 7, 8 and 9 we can see that the  $q_{SR}$  is the most significant at these times of the day when it takes the greatest values.

### 4.2 Heat Flux with Omission of Terms Independent of Water Temperature

While modeling thermal pollution spreading in rivers we are usually interested in possible changes in ambient water temperature (usually its increase) caused by artificial heat sources. In such cases it is useful to compute the temperature change ( $\Delta T$ ) instead of the actual water temperature ( $T$ ) (see e.g. Kalinowska and Rowiński 2012; Kalinowska et al. 2012). The calculation of the net heat flux may then be simplified to:

$$Q_A = -q_b \pm q_e \pm q_h. \tag{13}$$

The terms that do not depend on water temperature, such as the shortwave solar radiation and the longwave atmospheric radiation, may be omitted during the calculation. They simply counterbalance each other while computing the temperature difference ( $\Delta T$ ), since they are the same for different water temperatures.

The sensitivity analysis has been repeated for the simplified net heat flux (Eq. 13) for all data sets. The percentage of relative sensitivity coefficient for selected cases for the Narew and the Świder Rivers (Set I and Set II) are presented in Figs. 10 and 11. In comparison to the results for full net heat flux there are no large fluctuations of the results during the day. It should be noted that for the simplified form, the net heat flux ( $Q_A$ ) is negative for the whole day in both cases. Similarly to the calculation for the full net heat flux, water and air temperature and humidity have the highest impact on  $Q_A$  over the whole 24 h period. The biggest

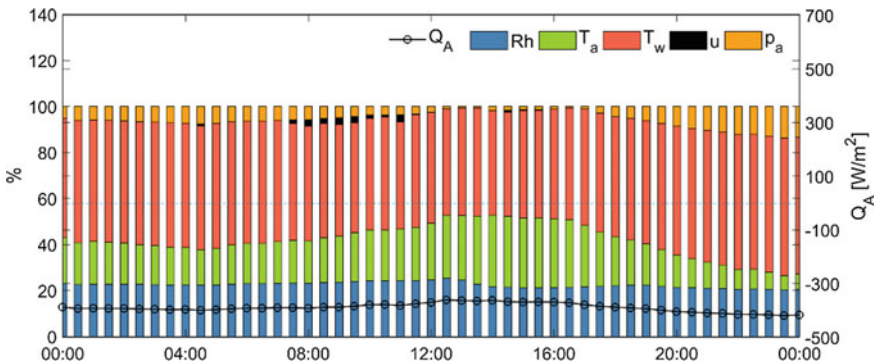


**Fig. 10** Diurnal evolution of the percentage of relative sensitivity coefficient for simplified net head flux for the River Narew—data Set I

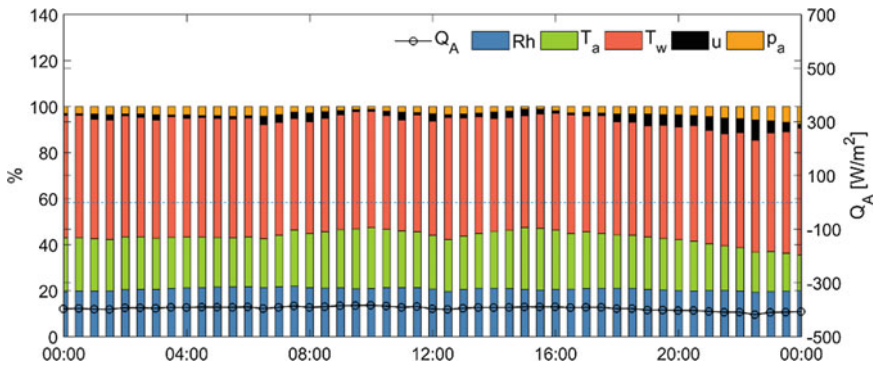


**Fig. 11** Diurnal evolution of the percentage of relative sensitivity coefficient for simplified net head flux for the River Świder—data Set II

impact of air temperature may be noted for the time of the day when the highest air temperatures are noted. The impact of air temperature decreases when the air temperature approaches zero in favor of the water temperature and the air pressure. In case of the River Narew, significance of air temperature varies along the day, and is the largest between 12 am and 4 pm. Wind velocity is the least significant variable. In case of the River Świder, the impact of the wind velocity is similar to the impact of atmospheric pressure. Both have little impact on  $Q_A$ .

### 4.3 Heat Flux Calculated for Different Empirical Coefficients

As it has been described in Sect. 1, there are many empirical coefficients that have to be estimated before calculation of the net heat flux. It would be profitable to calibrate all coefficients based on experimental investigations but this is in most cases infeasible. One of the most problematic coefficients are those occurring in the wind speed function (see Eq. 10) that is used to compute the evaporation/condensation and convection/conduction heat fluxes. For rivers the problem is particularly important. Many empirical formulae are available in the literature, but most of them have been derived for lakes and reservoirs and then adapted to rivers. The sensitivity analysis has been performed for different empirical formulae for wind speed function. In Figs. 12 and 13 the results for the selected cases for the Narew and the Świder rivers with selected wind speed formulae (described in Table 2) have been presented. By changing the wind speed function we can observe that the wind speed ( $u$ ) may be of different importance. Two “new” formulae taken from (Czernuszenko 1990), where they had been used for rivers, were selected for further considerations. Those wind speed function formulae ( $f_2(u)$  and  $f_3(u)$ ) caused the increase of the impact of the wind velocity on the net heat flux comparing to the



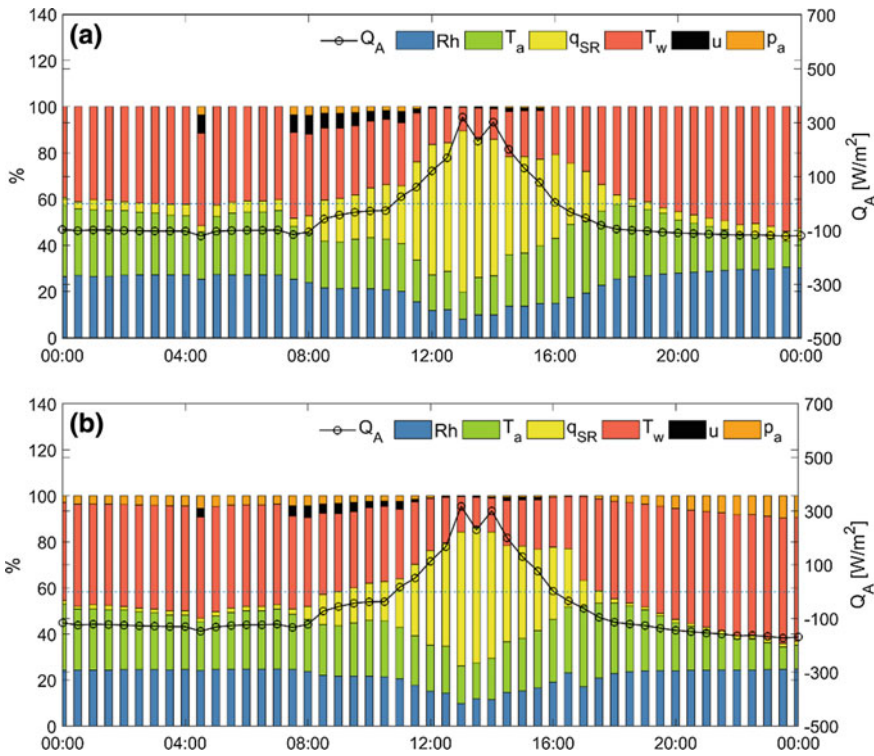


**Fig. 12** Diurnal evolution of the percentage of relative sensitivity coefficient for River Narew—data Set I. Different formulae for wind speed function have been used (see Table 2): **a**  $f_2(u)$ , **b**  $f_3(u)$ ; results for  $f_1(u)$  have been presented in Fig. 5

$f_1(u)$  (also used for rivers, Zhen-Gang, 2008) wind speed function applied in all previous figures. The wind velocity is at least as important as the air pressure. Additionally we can notice that the value of air pressure value is completely ignored while using the wind speed function formula  $f_2(u)$  when the wind velocity is 0 (see Fig. 12a). At the same time, while using the  $f_1(u)$  and  $f_3(u)$  functions, no wind conditions cause the disregard of air pressure value.

Similar analysis may be performed for other coefficients and empirical formulae, for example, for different ways of computation of longwave atmospheric radiation. But they do not affect the final results as much as changing of speed function does.

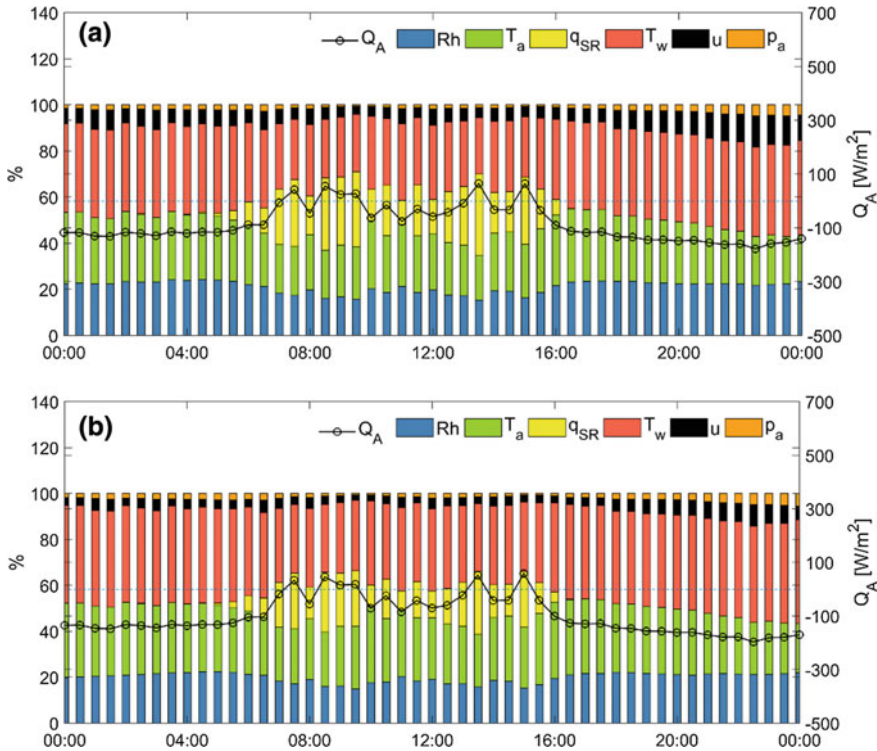


**Fig. 13** Diurnal evolution of the percentage of relative sensitivity coefficient for River Świder—data Set II. Different formulae for wind speed function have been used (see Table 2): **a**  $f_2(u)$ , **b**  $f_3(u)$ ; results for  $f_1(u)$  have been presented in Fig. 6

**Table 2** Coefficients for selected wind speed function empirical formulae used in the paper

Empirical formula for wind speed function	$b_0$ [ $\text{W m}^{-2} \text{ mb}^{-1}$ ]	$b_1$ [ $\text{W m}^{-3} \text{ mb}^{-1} \text{ s}$ ]	$b_2$ [ $\text{W m}^{-4} \text{ mb}^{-1} \text{ s}^2$ ]
$f_1(u)$ (Ahsan and Blumberg 1999; Zhen-Gang 2008)	6.9	0	0.34
$f_2(u)$ (Czernuszenko 1990)	0	3.75	0
$f_3(u)$ (Czernuszenko 1990)	$A(T_w - T_a)^{1/3}$	3.2	0

$A$ —parameter for free convection,  $A = 2.7$  [ $\text{W m}^{-2} \text{ mb}^{-1} (\text{°C})^{-1/3}$ ]

## 5 Conclusions

In this study, the significance of six input variables—water temperature, air temperature, humidity, atmospheric pressure, solar radiation, and wind speed velocity—on the net heat flux  $Q_A$  has been assessed. It may be concluded that water and air

temperature and humidity have the highest impact on  $Q_A$  for both rivers—Świder and Narew for different data sets and different seasons. During night and morning, water temperature is the most significant input value in all cases; next, the temperature of air and humidity are similarly significant. During the day, the temperature of air, humidity, temperature of water and shortwave radiation are significant. Wind speed velocity and atmospheric pressure are the least significant variables, but we can observe that the wind speed may be of different importance depending on the chosen wind speed function.

**Acknowledgements** This study has been partly supported by the grant IP2012 028772 from the Polish Ministry of Science and Higher Education and supported within statutory activities No. 3841/E-41/S/2017 of the Ministry of Science and Higher Education of Poland. The authors would like to thank Krzysztof Markowicz for sharing data from IGF UW Meteorological observatory the Narew National Park for sharing data from Narew National Park Weather Station.

## References

- Ahsan AKMQ, Blumberg AF (1999) Three-dimensional hydrothermal model of Onondaga Lake, New York. *J Hydraul Eng* 125(9):912–923. [https://doi.org/10.1061/\(ASCE\)0733-9429\(1999\)125:9\(912\)](https://doi.org/10.1061/(ASCE)0733-9429(1999)125:9(912))
- Beven K (1979) A sensitivity analysis of the Penman-Monteith actual evapotranspiration estimates. *J Hydrol* 44:169–190
- Brunt D (1932) Notes on radiation in the atmosphere. *Q J R Meteorol Soc* 58:389–420
- Chapra SC (1997) Surface water-quality modeling. Waveland Press Inc, Long Grove, Illinois
- Czernuszenko W (1990) Dispersion of pollutants in flowing surface water. In: Encyclopedia of fluid mechanics, surface and groundwater flow phenomena, vol 10, Chap 4. Gulf Publishing Company, pp 119–168
- Edinger JE, Brady DK, Geyer JC (1974) Heat exchange and transport in the environment. Electric Power Research Institute, Palo Alto, California
- Evans EC, McGregor GR, Petts GE (1998) River energy budgets with special reference to river bed processes. *Hydrol Process* 12:575–595
- Flerchinger GN, Xaio W, Marks D, Sauer TJ, Yu Q (2009) Comparison of algorithms for incoming atmospheric long-wave radiation. *Water Resour Res* 45:W03423. <https://doi.org/10.1029/2008WR007394>
- Gong L, Xu C, Chen D, Halldin S, Chen Y (2006) Sensitivity of the Penman-Monteith reference evapotranspiration to key climatic variables in the Changjiang (Yangtze river) basin. *J Hydrol* 329:620–629
- Gutenbaum J (1992) Mathematical modeling of systems. Omnitech Press, Warsaw
- Hupert F, Vanclooster M (2001) Effect of the sampling frequency of methodological variables on the estimation of the reference evapotranspiration. *J Hydrol* 243:192–204
- ISO (1999) Guide to expression of uncertainty in measurement, ISO, 1995. Polish translation, Central Office of Measures
- Iziomon MG, Mayer H, Matzarakis A (2003) Downward atmospheric longwave irradiance under clear and cloudy skies: Measurement and parameterization. *J Atmos Sol Terr Phys* 65:1107–1116
- Kalinowska MB, Mrokowska MM, Rowiński PM (2016) Role of heat exchange between water and atmosphere in models of thermal pollution in rivers. In: 12th international conference on hydrosience and engineering, Hydro-science and engineering for environmental resilience, November 6–10, 2016, Tainan, Taiwan

- Kalinowska MB, Rowiński PM (2015) Thermal pollution in rivers—modelling of the spread of thermal plumes. In: Rowiński PM, Radecki-Pawlik A (eds) *Rivers—physical, fluvial and environmental processes*, Series: GeoPlanet: Earth and planetary sciences. Springer, Berlin, pp 591–613
- Kalinowska MB, Rowiński PM (2012) Uncertainty in computations of the spread of warm water in a river—lessons from Environmental Impact Assessment case study. *Hydrol Earth Syst Sci* 16:4177–4190
- Kalinowska MB, Rowiński PM, Kubrak J, Mirosław-Swiątek D (2012) Scenarios of the spread of a waste heat discharge in a river—Vistula River case study. *Acta Geophys* 60:214–231
- McCuen R (1973) The role of sensitivity analysis in hydrologic modeling. *J Hydrol* 18:37–53
- Mrokowska MM, Rowiński PM, Kalinowska MB (2013) The uncertainty of measurements in river hydraulics—the case of the friction velocity evaluation based on an unrepeatable experiment. In: Rowiński P (ed) *Experimental and computational solutions of hydraulic problems*, Series: GeoPlanet: Earth and planetary sciences. Springer, Berlin, pp 195–206. <https://doi.org/10.1007/978-3-642-30209-1>
- Qiu GY, Yano T, Momii K (1998) An improved methodology to measure evaporation from bare soil based on comparison of surface temperature with a dry soil surface. *J Hydrol* 210:93–105
- Rajwa A, Rowiński PM, Bialik RJ, Karpiński M (2014) Stream diurnal profiles of dissolved oxygen—case studies. In: 3rd IAHR Europe congress, Porto
- Rajwa-Kuligiewicz A, Bialik RJ, Rowiński PM (2015) Dissolved oxygen and water temperature dynamics in lowland rivers over various timescales. *J Hydrol Hydromech* 63(4):353–363
- Raudkivi AI (1979) *Hydrology*. Pergamon, Oxford, England
- Rutherford JC, Macaskill JB, Bryan LW (1993) Natural water temperature variations in the lower Waikato River, New Zealand. *J Mar Freshw Res* 27(1):71–85
- Webb BW, Zhang Y (1999) Water temperatures and heat budgets in Dorset chalk water courses. *Hydrol Process* 13:309–321
- Zhen-Gang J (2008) *Hydrodynamics and water quality: modeling rivers, lakes, and estuaries*. Wiley. <https://doi.org/10.1002/9780470241066>

# Time Variation of Scour at Downstream Pier for Two Piers in Tandem Arrangement

Shivakumar Khaple, Prashanth Reddy Hanmaiahgari  
and Subhasish Dey

**Abstract** A semi-empirical model is presented to estimate the time variation of scour depth at downstream of pier when two piers are arranged in tandem arrangement under clear water scour condition with uniform sediments. The methodology developed for computing the time variation of scour depth is based on the concept of the conservation of mass of sediment, considering the primary horseshoe vortex system to be the main agent of scouring and assuming a layer-by-layer scouring process. The proposed model agrees closely with the reported experimental data of time variation of scour depth at downstream piers in tandem pier arrangements under clear water condition with uniform sediments.

**Keywords** Bridge piers · Local scour · Analytical model · Sediment transport  
Time variation

## 1 Introduction

It may be stated that a bridge is secure only as long as there is no excessive scour at piers. A large percentage of bridge catastrophes are recognized due to failure of foundations affected by scour. The obstruction to the flowing stream by a bridge pier causes a three-dimensional separation of approaching flow forming a turbulent flow field around the pier resulting in local scour at the pier (Dey et al. 1995).

Most of the rivers carry a considerable amount of sediment during floods, which causes an increase or decrease in flow depending on a change in width, depth, slope and meander pattern. The interference of a bridge will cause the river to replace either the original regime or a substitute which is consistent with the obstruction and then obeys the fundamental laws of “mobile” boundary hydraulics. The sediment

---

S. Khaple (✉) · P. R. Hanmaiahgari · S. Dey  
Department of Civil Engineering, Indian Institute of Technology,  
Kharagpur 721302, West Bengal, India  
e-mail: shivabku@gmail.com

may be transported in a number of ways: as suspended load, bed load, saltation load, wash load, or as dissolved load.

In the past, the bridge superstructures were designed precisely from the structural point of view, whereas the hydraulic design of the piers and abutments was based on imprecise empirical rules. Undermining of structures because of scour around them, is still a challenging problem to civil, hydraulic, and bridge engineers etc. Failure of bridges due to local scour at pier foundations is a common occurrence.

Local scour can be defined as erosion of bed elevation in the vicinity of an obstacle owing to the removal of bed material by the erosive action of flowing water. The local scour is classified based on the mode of sediment transport occurring in the approaching flow, as clear water scour and live bed scour. Clear water scour occurs only when sediment is eroded from the scour hole but there is no supply of sediment by the approaching flow, whereas live bed scour occurs not only at scour hole but throughout the channel by the action of an approaching flow.

Melville and Raudkivi (1996) presented design relationships and introduced the concept of an effective pier size for the estimation of maximum scour depth at nonuniform piers. Dey (1997a, b) introduced a brief review of the literature on scour around pier and also gave comprehensive bibliographical references. The time-variation of scour at piers in tandem arrangement is an important aspect. Many investigators have previously carried out the time-variation of scour at a single pier (Chabert and Engeldinger 1956; Raudkivi and Ettema 1983; Yanmaz and Altinbilek 1991; Dey 1999; Dey and Raikar 2007; Kothiyari and Kumar 2012). Dey and Barbhuiya (2005) developed a numerical model for the time variation of scour depth at short abutments. Lu et al. (2011) proposed a semi-empirical model to compute the temporal variation of scour depth at non-uniform circular piers with unexposed foundations. Kothiyari and Kumar (2012) developed a mathematical model to compute the temporal variation of scour depth at circular compound bridge piers for all possible cases of footing positions with respect to the common level of the bed. Laboratory study for the time variation of scour at piers in tandem arrangement has been carried out by Khaple et al. (2017). However, a complete analytical solution for the temporal variation of scour at piers in tandem arrangement seems to be inadequate because only a few analytical solutions have been given for isolated single pier analysis in clear water scour condition.

Previous research works were just focused on obtaining an analytical solution for time variation of scour at an isolated pier. However, time variation of scour caused by two piers in tandem arrangement is considered in this paper. The aim of this paper is to present the new findings of an analytical model for the piers arranged in tandem arrangement to estimate the temporal variation of scour depth under clear water scour condition with uniform sediments. The model is developed based on the sediment continuity equation for the scour hole at piers in tandem arrangements. The analytical model solution can effectively be used by bridge engineers to design bridge pier foundations for the piers arranged in tandem. The experimental data reported by Khaple et al. (2017) is used to compare the results obtained by the present analytical model. Only the details of experimental setup and

procedure were given by Khaple et al. (2017). The proposed study presents analytical model in detail, which is a new addition.

## 2 Mathematical Model

### 2.1 Model Background

The semiempirical model of the temporal variation of scour at two piers in tandem arrangements under clear water scour conditions is derived based on the following assumptions:

- (a) The primary vortex upstream of the pier base is the basic cause of scouring,
- (b) Sediment particles are picked up from the upstream flat semicircular region where the maximum scour depth appears,
- (c) The scour profiles are geometrically similar with time as scouring progresses layer by layer,
- (d) The rate of change of sediment mass in the scour hole equals the difference between the sediment mass removal rate from the scour hole and the sediment mass inflow rate by the approaching flow into the scour hole.

### 2.2 Formulation of Model

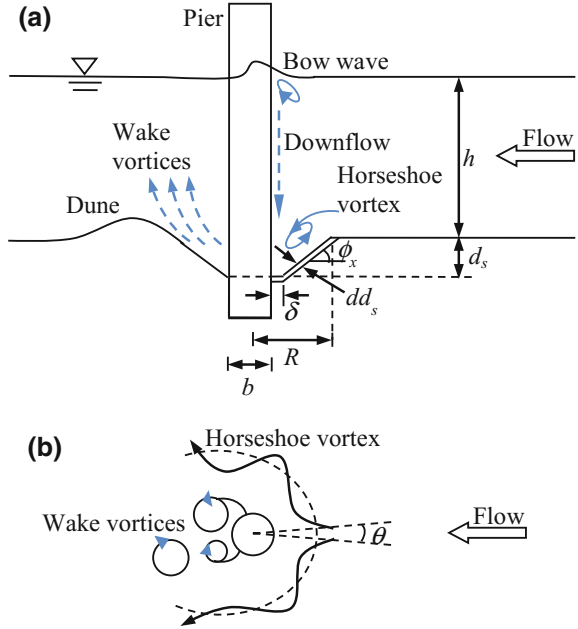
Figure 1 shows the schematic diagram of the scouring process in time  $t$ , as was idealized by Dey et al. (1995). Considering a small angle  $\theta$  to the axis of symmetry of the scour hole upstream, the mass rate of sediment picked up from the flat semicircular region during a small interval of time  $dt$  is

$$dm_1 = 0.5\theta\delta(\delta + b)Edt, \quad (1)$$

where  $b$  is the pier diameter,  $\delta$  is the average width of the upstream flat region where the sediment pick up takes place, and  $E$  is the sediment pick up rate at the base of the pier in time  $t$ .

The effective pick up rate of the sediment that leaves the scour hole is actually considered to be  $E$ . The sediment particles have a characteristic kinetic energy assumed proportional to  $\tau_b d_{50}^3$ . Here,  $\tau_b$  is the bed shear stress in the scour hole at the pier base and  $d_{50}$  is the median sediment size. On the other hand, the potential energy of the sediment particles corresponding to the scour depth  $d_s$  is proportional to  $\rho\Delta g d_{50}^3 d_s$ , where  $\rho$  is the mass density of water,  $\Delta$  is  $s - 1$ ,  $s$  is the relative density of sediment, and  $g$  is the gravitational constant.

**Fig. 1** Definition sketch of scouring at a pier: **a** elevation view; **b** top view



The width of the flat semicircular region  $\delta$  (Fig. 1) can be expressed as a fraction of the radial length of the scour hole from the pier boundary at the original bed level upstream

$$\delta = \varepsilon(R - 0.5b), \tag{2}$$

where  $\varepsilon$  is a geometric factor, and  $R$  is the radius of the scour hole at the original bed level upstream in time  $t$ , thus  $R$  is given by

$$R = \left[ \frac{d_s}{(1 - \varepsilon)} \right] \cot \phi_x + 0.5b, \tag{3}$$

where  $d_s$  is the scour depth in time  $t$ . Substituting Eqs. (2) and (3) in Eq. (1) yields

$$dm_1 = 0.5\theta \frac{\varepsilon}{1 - \varepsilon} d_s \cot \phi_x \left( \frac{\varepsilon}{1 - \varepsilon} d_s \cot \phi_x + b \right) E dt. \tag{4}$$

The sediment pick up rate  $E$  at the base of the pier due to scouring, determined using the equation suggested by Van Rijn (1984a, b), is given by

$$E = 0.00033 \rho_s (\Delta g d_{50})^{0.5} D_*^{0.3} T_s^{1.5}, \tag{5}$$

where  $\rho_s$  is the mass density of sediment,  $D_*$  is the particle parameter, that is,  $d_{50}(\Delta g/\nu^2)^{1/3}$ ,  $\nu$  is the kinematic viscosity of water,  $T_s$  is the transport-stage



parameter due to scouring, that is  $(\tau_b - \tau_{bc})/\tau_{bc}$ ,  $\tau_b$  is the bed shear stress in the scour hole at the pier base,  $\tau_{bc}$  is the critical bed shear stress in the scour hole ( $= \xi\tau_{cr}$ ),  $\tau_{cr}$  is the critical bed shear stress on a plane bed for the median sediment size of  $d_{50}$ , and  $\xi$  is a factor depending on turbulent agitation and oscillation of horseshoe vortex. The local bed shear stress  $\tau_b$  at the pier base is calculated from the empirical formula given by Kothyari et al. (1992) as

$$\tau_b = 4\tau_0 \left[ \left( \frac{2}{\pi} \right) \left( \frac{d_s}{d_v} \right)^2 \cot \phi_x + 1 \right]^{-0.57}, \quad (6)$$

where  $\tau_0$  is the bed shear stress of approaching flow, and  $d_v$  is the diameter of the horseshoe vortex at the beginning of scouring, determined from the empirical formula proposed by Kothyari et al. (1992) as

$$d_v = 0.28h^{0.15}b^{0.85}. \quad (7)$$

Here,  $h$  is the approaching flow depth. The critical bed shear stress  $\tau_{cr}$ , being given in the Shields diagram, can be determined from the empirical formula proposed by Van Rijn (1984a, b) as

$$\tau_{cr} = \Delta\gamma d_{50}\theta_{cr}, \quad (8)$$

where  $\gamma$  is the specific weight of water ( $= \rho g$ ), and  $\theta_{cr}$  is the nondimensional critical shear stress that is,  $\tau_{cr}/(\Delta\gamma d_{50})$ . The relationship between  $\theta_{cr}$  and  $D^*$  was given by Van Rijn (1984a, b). The bed shear stress  $\tau_0$  of the approaching flow can be expressed as a function of dynamic pressure due to an average velocity  $U$  of flow as

$$\tau_0 = \frac{\lambda_D}{8} \rho U^2, \quad (9)$$

where  $\lambda_D$  is the Darcy-Weisbach friction factor. The value of  $\lambda_D$  can be determined using an explicit form of the Colebrook-White equation was given by Haaland (1983),

$$\frac{1}{\lambda_D^{0.5}} = -0.782 \ln \left[ \left( \frac{k_s P}{14.8A} \right)^{1.1} + \frac{6.9}{R_e} \right], \quad (10)$$

where  $A$  is the flow area,  $P$  is the wetted perimeter, and  $R_e$  is the flow Reynolds number.

Here, the average velocity  $U$  of flow downstream of the upstream pier is determined from the quadratic equation obtained experimentally in Khaple et al. (2017), as a function of spacing between two piers, as

$$\frac{U}{U_a} = 0.2053 + 0.1491 \left( \frac{S}{b} \right) - 0.0078 \left( \frac{S}{b} \right)^2, \quad (11)$$

where  $S$  is the spacing between two piers in tandem arrangement, and  $U_a$  is the approaching flow velocity.

Applying the concept of geometrical similarity of the scour profiles with time, the reduction of the sediment mass due to an increase in scour depth  $dd_s$  in time  $dt$  is expressed as

$$dm_2 = -0.5(1 - \rho_0)\rho_s\theta \times \{ \delta(\delta + b) + \cot \phi_x \times [(R^2 - 0.25b^2) - \delta(\delta + b)] \} dd_s, \quad (12)$$

where  $\rho_0$  is the porosity of sediment. The right-hand side of the above equation is negative due to the reduction of sediment mass. Substituting Eqs. (2) and (3) into Eq. (12) yields

$$dm_2 = -0.5(1 - \rho_0)\rho_s\theta \frac{d_s}{1 - \varepsilon} \times \left[ \varepsilon \cot \phi_x \left( \frac{\varepsilon}{1 - \varepsilon} d_s \cot \phi_x + b \right) + \frac{(1 + \varepsilon)d_s \cot \phi_x + (1 - \varepsilon)b}{\sin \phi_x} \right] dd_s. \quad (13)$$

The fundamental equation to describe the scouring process can be obtained from the basic concept of conservation of the mass of sediment as

$$dm_1 + dm_2 = 0. \quad (14)$$

Substituting Eqs. (4) and (13) in to Eq. (14) we obtain the following first-order differential equation of temporal variation of scour depth at downstream of pier when two piers are in tandem arrangements in nondimensional form:

$$(1 - \rho_0) \left[ \varepsilon \cot \phi_x \left( \frac{\varepsilon}{1 - \varepsilon} \hat{d}_s \cot \phi_x + 1 \right) + \frac{(1 + \varepsilon)\hat{d}_s \cot \phi_x + (1 - \varepsilon)}{\sin \phi_x} \right] \frac{d\hat{d}_s}{d\hat{t}} = \varepsilon \cot \phi_x \left( \frac{\varepsilon}{1 - \varepsilon} \hat{d}_s \cot \phi_x + 1 \right) \hat{b}\phi_p \quad (15)$$

where  $\hat{d}_s = d_s/b$ ,  $\hat{t} =$  time parameter, that is  $td_{50}\sqrt{(\Delta g d_{50})}/b^2$ ,  $\hat{b} = b/d_{50}$ , and  $\phi_p =$  sediment pick up function due to scouring, that is  $E/\rho_s\sqrt{(\Delta g d_{50})}$ .

From the point of view of pier scour, time parameter  $\hat{t}$  is physically important, as it includes scour related parameters, such as pier size and sediment size. Equation (15) is a first-order differential equation, which can be solved by the fourth-order Runge-Kutta method to determine the variation of  $\hat{d}_s$  with  $\hat{t}$ . The geometric factor  $\varepsilon$  was taken as 0.1.

The parameters of porosity,  $\rho_0$ , and angle of repose,  $\phi_x$ , are small for the sediments commonly available in the field. Hence,  $\rho_0$  and  $\phi_x$  were assumed to be 0.40 and  $37^\circ$ , respectively, as was used by Dey (1991), in the present analysis.

### 3 Results and Discussion

For two piers in tandem arrangement, it is important to identify that the scour depth at downstream pier oscillates over a period of time due to the formation of dune at downstream of the upstream pier. The effect of transporting bed sediment or dune results in decrease of scour depth at downstream of the pier, depending on whether

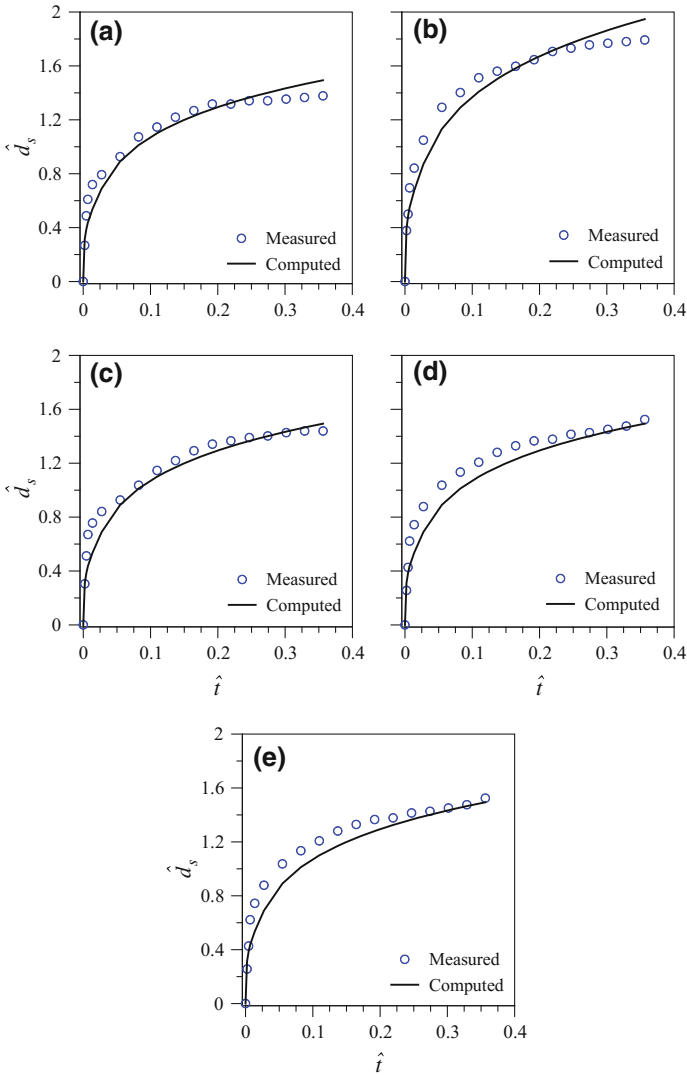


**Fig. 2** Temporal variation of scour depth at downstream of piers in tandem pier arrangements: **a**  $S/b = 3$ , **b**  $S/b = 5$ , **c**  $S/b = 7$ , **d**  $S/b = 9$ , **e**  $S/b = 11$

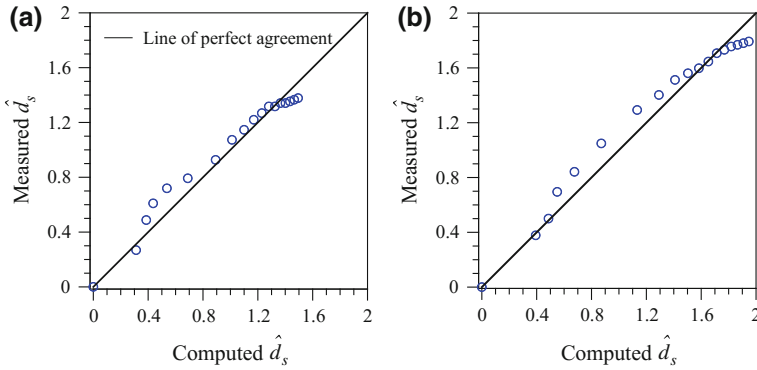


**Fig. 3** Comparison of computational data with measured data: **a**  $S/b = 3$  and **b**  $S/b = 5$

the crest or trough of the bed form is transporting through the scour hole at downstream pier. For two piers in tandem arrangement, the scour depth at the downstream pier is less than that of the upstream pier. As the distance between the piers increases, the scour depths at downstream pier decrease with time. Figures 2a–e show the temporal variation of  $\hat{d}_s$  with  $\hat{t}$  in uniform sediments under clear water scour condition for two piers arranged in tandem. The analytical results agree satisfactorily with the experimental data. It is observed that the computed value of sediment pick-up rate  $E$  from the scour hole area is inversely proportional to the scour depth  $d_s$ . In all the experiments (Fig. 2a–e), the initial rate of sediment pick-up is very high, resulting in a rapid growth of the scour depth. The present analytical model shows a tendency of underestimating scour depth particularly in the initial periods of scouring process and good agreement in the final periods of scouring. In addition, the experimental data reported by Khaple et al. (2017) for pier diameter  $b = 8.2$  cm and two piers arranged in tandem arrangements were analysed and compared with the computed model results in Fig. 3a and b for spacing ( $S/b$ ) 3 and 5, respectively. It is evident from the Fig. 3a and b that computed and measured all data points are laid on line of perfect agreement and also it shows that the experimental data are in good agreement with the model data. Finally, the reasonable agreement between model predicted and experimentally measured temporal variation of scour depth illustrates the satisfactory performance of the model.

## 4 Conclusions

The temporal variation of scour depth at piers in tandem arrangements under clear-water scour condition in uniform sediments has been analytically modeled. The process of scouring at downstream pier has been defined using the concept of conservation of the mass of sediment that leads to a first-order differential equation,

which has been solved numerically by the fourth-order Runge-Kutta method to compute the time-variation of scour depth. The temporal variation of scour depths computed using the present model is in reasonable agreement with the measured data.

**Acknowledgements** The present study is the part of doctoral research work of Shivakumar Khaple under the supervision of Prof. Subhasish Dey and Prof. H. Prashanth Reddy. The authors also thank the Late Kana Dey, mother of Prof. Subhasish Dey, for her well wishes during the presentation of manuscript.

## References

- Chabert J, Engeldinger P (1956) Etude des affouillements autour des piles de ponts. Serie A. Laboratoire National d'Hydraulique, Chatou, France (in French)
- Dey S (1991) Clear water scour around circular bridge piers: a model. PhD thesis, Department of Civil Engineering, Indian Institute of Technology, Kharagpur, India
- Dey S, Bose SK, Sastry GLN (1995) Clear water scour at circular piers: a model. *J Hydraul Eng* 121(12):869–876
- Dey S (1997a) Local scour at piers, part 1: a review of development of research. *Int J Sediment Res* 12(2):23–46
- Dey S (1997b) Local scour at piers, part II: bibliography. *Int J Sediment Res* 12(2):47–57
- Dey S (1999) Time variation of scour in the vicinity of circular piers. *Proc Inst Civ Eng Wat Marit Energy* 136(2):67–75
- Dey S, Barbhuiya AK (2005) Time variation of scour at abutments. *J Hydraul Eng* 131(1):11–23
- Dey S, Raikar RV (2007) Characteristics of horseshoe vortex in developing scour holes at piers. *J Hydraul Eng* 133(4):399–413
- Haaland SE (1983) Simple and explicit formulas for the friction factor in turbulent flow. *J Fluids Eng* 105(5):89–90
- Kothyari UC, Ranga Raju KG, Garde RJ (1992) Live-bed scour around cylindrical bridge piers. *J Hydraul Res* 30(5):701–715
- Khaple S, Hanmaiahgari PR, Gaudio R, Dey S (2017) Interference of an upstream pier on local scour at downstream piers. *Acta Geophys* 65(1):29–46
- Kothyari UC, Kumar A (2012) Temporal variation of scour around circular compound piers. *J Hydraul Eng* 138(11):945–957
- Lu JY, Shi ZZ, Hong JH, Lee JJ, Raikar RV (2011) Temporal variation of scour depth at nonuniform cylindrical piers. *J Hydraul Eng* 137(1):45–56
- Melville BW, Raudkivi AJ (1996) Effects of foundation geometry on bridge pier scour. *J Hydraul Eng* 122(4):203–209
- Raudkivi AJ, Etema R (1983) Clear-water scour at cylindrical piers. *J Hydraul Eng* 109(3):338–350
- Van Rijn LC (1984a) Sediment pick-up functions. *J Hydraul Eng* 110(10):1494–1502
- Van Rijn LC (1984b) Sediment transport, part I: bed load transport. *J Hydraul Eng* 110(10):1431–1456
- Yanmaz AM, Altinbilek HDGA (1991) Study of time-dependent local scour around bridge piers. *J Hydraul Eng* 117(10):1247–1268

# Geometry Description of Local Scouring Process in Various Laboratory Water Structure Models

Marta Kiraga and Zbigniew Popek

**Abstract** Water structures are usually used to stabilise river bed, although they also are a cause of degradation processes like erosion and scouring. The aim of this study was to correlate scour geometry, characterized by the scour medium and maximal depth and its length with hydraulic and granulometric properties. The study presents results obtained for three laboratory models (with and without weir flow) with partially or totally erodible bed, with median grain size  $d_{50} = 0.91$  mm in clear-water and live-bed conditions. The experiment duration was sufficient to obtain equilibrium, stable scour shape. Analysed relationships were parameterized using linear and exponential functions. The intensity of the sediment transport was investigated using the modified principle of fluvial hydraulics—the Lane’s relation, originally derived from basic rules of the sediment transport as a qualitative expression.

## 1 Introduction

Water structures are usually used to stabilise river bed, although they also are a cause of degradation processes like erosion and scouring. The downstream erosion not only causes morphological changes, but also could be dangerous for structure safety because of the erosion of foundations and loss of structure stability (Petts 1977).

Many studies have been devoted to the problem of local scouring near different hydraulic structures. Laboratory experiments allowed to develop many formulas and more complex numerical models of this process. However, all the methods used in practical applications are still very inaccurate, because of the complexity of the

---

M. Kiraga (✉) · Z. Popek  
River Engineering Division, Department of Hydraulic Engineering, Warsaw University  
of Life Sciences, 159 Nowoursynowska Street, Post code 02-787 Warsaw, Poland  
e-mail: marta\_kiraga@sggw.pl

Z. Popek  
e-mail: zbigniew\_popek@sggw.pl

transport processes and the fact that there is no general equation, so far, for describing a local scour geometry. Some attempts using real *in situ* data (Lenzi et al. 2003; Pagliara et al. 2016) revealed the problem of unknown initial conditions, such as the shape of a river bed before the scour was formed.

A comprehensive analysis was performed for mountain rivers—the study dealing with scour process analysis occurring downstream of block ramps located in river bends was presented by Pagliara et al. (2016). Studies proved that the river curvature is the most important parameter affecting the maximum scour depth occurring downstream the structure. Mountain river experiments indicated differences even up to 300% between laboratory measurements and results of calculations with scour forecasting formulas (Ślizowski and Radecki-Pawlik 2003).

The case of local scouring in a bed made of sequences of sills is well recognized and described in the literature. Gaudio et al. (2000) used dimensional analysis to obtain predictive formulae for clear-water conditions of scour hole dimensions for rivers with a moderate slope. It was emphasized that maximum scour depth and the scour hole length could be described as functions of ‘morphological jump’ (defined as the multiplication outcome of difference between initial and equilibrium bed slopes and the distance between subsequent sills), critical specific energy, relative submerged grain density and median grain size with  $r = 0.98$  correlation coefficient. Gaudio et al. (2000) attempt was confirmed by others (Lenzi et al. 2002) for mountain high-gradient streams (for non-uniform sediments with presence of protruding cobbles), however the best fit to experimental data was obtained for the non-linear equation, both for scour length and maximum scour depth, with the 0.99 and 0.95 correlation coefficients. Other experiment results (Gaudio and Marion 2003) confirmed the validity of Gaudio’s method for maximum depth of scour assessment for mild bed slopes, with correlation coefficient 0.94—the outcome of the study was a linear formula describing maximal scour depth geometry using the hydraulic, morphological and granulometric variables proposed by Gaudio et al. (2000). Although Gaudio’s experiment gave good results, the accuracy of the proposed methods is still inadequate in other experimental flume model variants (Ben Meftah and Mossa 2006). The general conclusion for bed sills sequence experiments was that the maximal scour depth and length strongly depend on the distance between sills and that maximal scour depth and length are not correlated (Ben Meftah and Mossa 2006; Gaudio et al. 2000; Gaudio and Marion 2003; Lenzi et al. 2002).

It was shown that for mild energy grade line slopes the maximal scour depth could be described as a function of dimensionless shear stress with correlation coefficient of 0.67 for laboratory flumes with a rectangular cross-section, in which the solid bottom transforms into sandy bottom in the intake part. Due to the increase of flow resistance on the whole length of the bed, resulting from varied roughness of the solid and sandy bottom, the hydraulic gradient increases causing an increase of shear stress on the bottom (Kiraga and Popek 2016). The present paper comprises an extension of this experimental case.

All the above-mentioned experiments (Gaudio et al. 2000; Lenzi et al. 2002; Gaudio and Marion 2003; Ben Meftah and Mossa 2006; Kiraga and Popek 2016)

were conducted with no sediment feeding system adopted, namely, in clear water conditions. Live-bed conditions case is still an undeveloped branch of experimental research, the present paper attempts to fulfil.

The aim of this paper is to complement Gaudio et al. (2000) and Kiraga and Popek (2016) attempts, in a scope of three experimental test stands with or without hydraulic structure (stone weir) in the laboratory flume for moderate energy grade lines, including live-bed conditions. Besides the maximal scour depth and length, the medium scour depth was also included. It was an attempt made to find functional correlations between hydrodynamic parameters of water and sediment discharge and geometrical parameters of local scour holes in various physical models. Inter alia, modified cause-and-effect Lane's relation was included, commonly used to describe river and valley morphology formation.

## 2 Methods

### 2.1 Initial Assumptions

For clear water conditions, Gaudio et al. (2000) proposed the following formulas:

$$\left(\frac{z_{max}}{H_s}\right) = c \frac{a_1}{sd_{50}} + d, \quad (1)$$

$$\left(\frac{l_s}{H_s}\right) = f \frac{a_1}{sd_{50}} + j, \quad (2)$$

where  $c$ ,  $d$ ,  $f$ ,  $j$  stand for linear coefficients,  $z_{max}$  the maximal scour depth (in equilibrium conditions) (m),  $l_s$  for scour hole length (m),  $s$  for relative particle density (–) and  $d_{50}$  for median grain size (m).  $H_s = 1.5^3 \sqrt{q^2/g}$  stands for the critical specific energy in proximity of the water structure (m) with  $q$  for unit discharge ( $\text{m}^3 \text{s}^{-1} \text{m}^{-1}$ ) and  $g$  for gravity acceleration ( $\text{m s}^{-2}$ ).  $a_1 = (S_0 - S_{eq})L$  stands for the morphological jump,  $S_0$  and  $S_{eq}$  denote, respectively, the initial and the final longitudinal bed slope (–) and  $L$  is the distance between two successive sills (m). Equations (1) and (2) are recognized to be valid in the range  $1.3 \leq a_1/(s d_{50}) \leq 9.1$  with the correlation coefficient  $r = 0.98$ . For the stone weir investigated in the present paper, the above equations were modified—'morphological jump' was substituted by 'energy grade line jump', using total working section length instead of the distance between the sills, and the initial and equilibrium longitudinal bed slopes were substituted by, respectively, initial and equilibrium longitudinal energy grade line slopes.

The original Lane's relation (Lane 1955),  $Q_s d \sim Q_w S$ , involves bedload transport discharge  $Q_s$ , particle diameter  $d$ , water discharge  $Q_w$  and energy grade line slope  $S$  and comprises a qualitative expression because of incompatibility of



units. Despite its simplified character, original Lane's principle serves well to describe the process of forming alluvial stream channels. Additionally, it was demonstrated on physical model in which the solid bottom transforms into sandy bed in the intake part in clear-water conditions, that it is possible to correlate multiplication outcome of bedload transport discharge, grain parameter  $D_* = d_{50}[(s-1)g/\nu^2]^{1/3}$  (–) (Van Rijn 1993), considering kinematic viscosity parameter  $\nu$  ( $\text{m}^2 \text{s}^{-1}$ ) and width-to-depth ( $W/H$ ) ratio with multiplication outcome of water discharge and equilibrium longitudinal energy grade line slope  $S$  with  $r = 0.95$  correlation coefficient (Kiraga and Popek 2016):

$$Q_s D_* (W/H)^{-1} = 0.158(Q_w S) - 1.459. \quad (3)$$

Relationship (3) was examined in praxis for the water maximum discharge of  $5.06 \text{ m}^3 \text{ s}^{-1}$  during a flood event in Zagożdżonka River (Poland) on the grounds of in situ measurements. The river channel properties were similar to laboratory model—the solid bottom precedes sandy bed, and the formation of local scour takes place in clear-water conditions. The results are satisfactory because of the same order of magnitude (Kiraga and Popek 2016). It was established that miscalculation could result from the lack of knowledge of exact bottom shape before the flood occurrence, the variability of water surface level during flood conditions and variable energy grade line slope in natural flow conditions. The newly introduced form of Eq. (3), including local scour geometry properties (medium scour depth  $z_m$  and  $l_s$  scour length) eventually takes the form of linear empirical equation with parameters  $a$  and  $b$ :

$$Q_s D_* (W/H)^{-1} \left( \frac{z_m}{l_s} \right) = a Q_w (S - S_0) + b. \quad (4)$$

It was also demonstrated that maximal scour depth could be expressed as a function of dimensionless shear stress in bed region,  $z_{max} = f(\theta)$  (with  $r = 0.67$  correlation coefficient, as a linear function) (Kiraga and Popek 2016); however, re-examination of data suggested better correlation if function would be expressed as exponential (correlation coefficient  $r = 0.82$ ). To determine the hydraulic radius of the sandy bottom part in the chosen cross-section, necessary for bed shear stress calculations, the Einstein's division of the velocity field was used (for detailed description, see Kiraga and Popek 2016).

It was investigated if it is possible to delineate the non-linear formula including medium scour depth-to-length ratio. The function would eventually take the following form, with exponential function parameters  $k$  and  $m$ :

$$\left( \frac{z_m}{l_s} \right) = k e^{m\theta}, \quad (5)$$

Equations (1), (2), (4) and (5) were analysed using three models of the flume structure.

## 2.2 Experimental Set-up

The research of local scours properties was conducted in the hydraulic laboratory of Warsaw University of Life Sciences (Poland). The experiment was performed on three test stands with and without water structure and it included 13 runs for each stand. The flume of the rectangular cross-section was 0.58 m wide and 0.60 m high. For the full description of the laboratory flume and hydraulic system, see Kiraga and Popek (2016). The sediment used in all tests was sand with the median diameter  $d_{50} = 0.91$  mm and relative submerged density  $s = 2.61$ .

The first model (I) had the following bottom construction: about 4-meter long solid bottom that transforms in the intake part into the sandy bottom, long for  $L = 2.18$  m (Fig. 1a). The experimental conditions in this study may be compared to a case of the transport continuity being disrupted by the accumulation of the bedload material in the retention reservoir located in the upstream (Dust and Wohl 2012; Huang et al. 2014). Due to the increase of flow resistance along the whole flume, resulting from varied roughness of solid and sandy bottom, the hydraulic gradient increases, also causing the increment of shear stress at the bottom. After exceeding the critical shear stress, the motion of sediment grains starts, followed by gradual scouring of the bed. The experiment was carried out until the scour hole shape stabilized. Then, the local scour hole obtained its equilibrium length  $l_s$ , medium depth in clear-water scour conditions  $z_m$  and maximal depth  $z_{max}$  (Kiraga and Popek 2016).

In the second (II) and third model (III), water structure was introduced in the flume with a totally or partially sandy bed (Fig. 1b, c); the weir was made of stone with four slots (summary area of slots  $A_{sII} = 0.018$  m<sup>2</sup> and  $A_{sIII} = 0.035$  m<sup>2</sup>). The weir was situated downstream the 4.0 m section of the sandy bed. In the third model, a 0.35 m long section of the bottom, immediately downstream the weir was reinforced. Upstream the weir, the thickness of the sand layer was 5 cm, while downstream it was 25 cm. Sandy bed above the structure was washed out by the approaching flow and the sediment load was moved out from the upper part towards the lower part of the water structure, ensuring live-bed conditions. Velocity of the flowing water in the structure's slots is increased because of flow area reduction. Therefore, in this case, the shear stress reinforcement is a result not only of roughness variability of material, but also of the velocity increment. Local scour was allowed to form gradually, until live-bed equilibrium conditions were obtained, just to achieve a stable shape, characterized by geometrical parameters such as length  $l_s$ , medium and maximal depth  $z_m$  and  $z_{max}$  (Fig. 4).

During an experimental research, there were few cases in which the scour length  $l_s$  had seemed to be slightly longer than the total length of erodible part of the bed

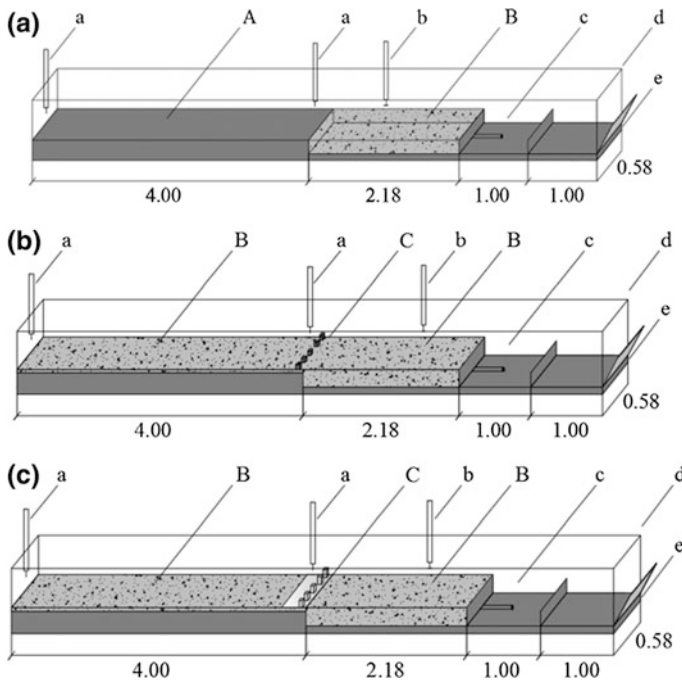


**Fig. 1** Experimental channel schemes: model I (a); model II (b), and model III (c) (all dimensions in meters), where: A—solid bottom; B—working section with washout bed (sandy); C—stone weir (with or without solid bottom); a—pin water gauge; b—disc probe; c—collection chamber; d—glass panels, e—the regulatory gate

$L$  (Fig. 2)—i.e. the scour hole would have been longer if erodible bed had been longer too. In such cases, its value was extrapolated.

All four equations' parameters were identified for each experiment (Eqs. 1, 2, 4, and 5). Tables 1, 2 and 3 report conditions of each run: water discharge  $Q_w$  and water depth  $H$  in control profile, situated in the nearest region of the weir (in  $D-D$  cross section), observed directly after reaching equilibrium conditions (during total time of experiment  $t_t$ ). After the flume was drained, the volume of sand captured in the collection chamber  $V_t$  was measured, providing information on the total volume of scour, that was transformed into sediment transport discharge by dividing it by the total time. Besides the bed shape and water surface elevation, allowing initial and equilibrium energy grade slope line appointment  $S_0$  and  $S$ , also temperature  $T$  was measured in each time step during each experiment and the kinematic viscosity parameter  $\nu$  was assigned (Kiraga and Popek 2016). The  $S$  slope was specified while obtaining stable scour shape, i.e. when local scouring equilibrium was ensured.

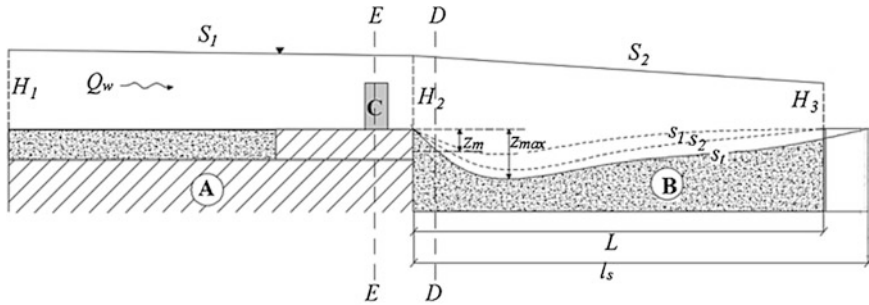


**Fig. 2** Scheme of local scour forming in washable area of sandy bed in model III, where: A—solid bottom; B—sandy washout bed; C—stone weir;  $H_1, H_2, H_3$ —water depths;  $Q_w$ —water flow discharge;  $S_1, S_2$ —energy grade line slope;  $z_{max}$ —maximal depth of local scour while achieving stabilization in time  $t_t$  with  $s_t$  scour shape (live-bed equilibrium scour depth);  $s_1, s_2, s_r$ —bed elevation below the weir while duration of experiment in time,  $D-D$ —computational cross-section,  $E-E$ —cross section in water structure’s region for water velocity calculations

### 3 Results and Discussion

Four empirical equations were verified in the scope of three test stands with 13 experimental runs for each. Two of them (Eqs. 1 and 2) were originally derived from the relations specified for bed sills sequences. Because the hydraulic structure inserted into the flume was a single stone weir, there was a necessity to modify original equations. The third of them (Eq. 4) is modified Lane’s relation, applicable so far in dynamic balance conditions in the context of alluvial rivers, and the fourth (Eq. 5) is an extension for previously conducted experiment (Kiraga and Popek 2016). The obtained relations are shown in Figs. 3, 4, 5 and 6 with regression lines sketched and  $r$  correlation coefficient remarked. In few experimental series, performed on test stand I, it was noticed that the initial energy grade line slope exceeded the final slope. When a stable scour shape was obtained, the bump was formed in the bed downstream the scour hole, which led to water surface level lifting. Those cases interfered with the general conclusion about the regressions obtained for this test stand.

The following equations were obtained for each test stand:

(1) For test stand I

$$\left(\frac{z_m}{l_s}\right) = 0.003e^{25.6\theta}; r = 0.82. \tag{6}$$

(2) For test stand II

$$\left(\frac{z_{max}}{H_s}\right) = 0.145 \frac{a_1}{sd_{50}} + 0.256; r = 0.86; \tag{7}$$

Table 1 Main parameters of the first test case

No	$Q_w$ ( $\text{m}^3 \text{s}^{-1}$ )	$H$ (m)	$t_r$ (h)	$V_r$ ( $\text{m}^3$ )	$z_m$ (m)	$z_{max}$ (m)	$l_s$ (m)	$S_0$ (-)	$S$ (-)	$T$ ( $^{\circ}\text{C}$ )	$\nu$ ( $10^{-6} \text{m}^2 \text{s}^{-1}$ )
1	0.020	0.10	7.25	0.00153	0.0016	0.0042	0.20	0.0005	0.0005	16.8	1.086
2	0.025	0.10	10.50	0.01841	0.0150	0.0341	2.20	0.0008	0.0007	16.5	1.094
3	0.025	0.12	6.50	0.00151	0.0016	0.0041	0.26	0.0004	0.0003	16.1	1.104
4	0.030	0.10	5.00	0.03701	0.0293	0.0474	2.35	0.0013	0.0014	16.5	1.094
5	0.030	0.15	6.00	0.00151	0.0016	0.0047	0.19	0.0004	0.0004	16.7	1.089
6	0.035	0.12	8.50	0.04681	0.0372	0.0564	2.20	0.0011	0.0010	16.3	1.099
7	0.035	0.15	7.50	0.00404	0.0032	0.0217	1.00	0.0005	0.0005	15.9	1.109
8	0.040	0.10	9.25	0.09746	0.0783	0.1182	2.35	0.0012	0.0013	16.0	1.107
9	0.040	0.12	10.50	0.05500	0.0443	0.0928	2.29	0.0010	0.0010	17.2	1.076
10	0.040	0.15	8.00	0.01900	0.0150	0.0423	0.55	0.0008	0.0009	17.0	1.081
11	0.040	0.20	6.00	0.00240	0.0016	0.0059	0.44	0.0002	0.0002	16.8	1.086
12	0.043	0.12	8.50	0.06800	0.0538	0.0764	2.20	0.0013	0.0012	16.6	1.091
13	0.045	0.15	8.50	0.04500	0.0356	0.0629	2.31	0.0008	0.0009	16.0	1.107

**Table 2** Main parameters of the second test case

No	$Q_w$ ( $m^3 s^{-1}$ )	$H$ (m)	$t_r$ (h)	$V_r$ ( $m^3$ )	$z_m$ (m)	$z_{max}$ (m)	$l_s$ (m)	$S_0$ (-)	$S$ (-)	$T$ (°C)	$\nu$ ( $10^{-6} m^2 s^{-1}$ )
1	0.020	0.10	8.00	0.00151	0.0016	0.0200	0.78	0.0010	0.0010	16.7	1.089
2	0.025	0.10	8.00	0.01560	0.0076	0.0323	1.60	0.0023	0.0032	16.3	1.099
3	0.025	0.12	8.00	0.00300	0.0025	0.0220	1.20	0.0012	0.0014	15.9	1.109
4	0.030	0.10	8.00	0.04800	0.0133	0.0400	1.80	0.0023	0.0026	16.8	1.086
5	0.030	0.15	8.00	0.00151	0.0124	0.0457	1.70	0.0010	0.0012	16.6	1.091
6	0.035	0.12	8.00	0.16000	0.0491	0.0520	1.80	0.0040	0.0067	16.0	1.107
7	0.035	0.15	8.00	0.00550	0.0040	0.0274	1.40	0.0012	0.0014	16.3	1.099
8	0.040	0.10	8.00	0.13450	0.0440	0.0850	3.10	0.0056	0.0085	15.9	1.109
9	0.040	0.12	8.00	0.20400	0.0644	0.0770	2.70	0.0060	0.0090	16.8	1.086
10	0.040	0.15	8.00	0.02050	0.0110	0.0304	2.00	0.0017	0.0019	16.5	1.094
11	0.040	0.20	8.00	0.00200	0.0042	0.0150	1.00	0.0013	0.0016	16.8	1.086
12	0.043	0.12	8.00	0.19000	0.0634	0.0832	3.00	0.0050	0.0077	16.8	1.086
13	0.045	0.15	8.00	0.05050	0.0063	0.0300	1.91	0.0020	0.0024	16.5	1.094

Table 3 Main parameters of the third test case

No	$Q_w$ ( $\text{m}^3 \text{ s}^{-1}$ )	$H$ (m)	$t_r$ (h)	$V_r$ ( $\text{m}^3$ )	$z_m$ (m)	$z_{max}$ (m)	$l_s$ (m)	$S_0$ (-)	$S$ (-)	$T$ (°C)	$\nu$ ( $10^{-6} \text{ m}^2 \text{ s}^{-1}$ )
1	0.020	0.10	8.00	0.01000	0.0199	0.0613	1.35	0.0052	0.0063	16.0	1.107
2	0.025	0.10	8.00	0.04800	0.0397	0.0872	2.60	0.0066	0.0082	16.8	1.086
3	0.025	0.12	8.00	0.01400	0.0206	0.0592	1.12	0.0039	0.0047	16.0	1.107
4	0.030	0.10	8.00	0.07480	0.0479	0.0843	2.31	0.0059	0.0073	16.7	1.089
5	0.030	0.15	8.00	0.00040	0.0050	0.0270	0.53	0.0013	0.0015	16.8	1.086
6	0.035	0.12	8.00	0.07900	0.0457	0.0809	2.44	0.0061	0.0075	16.8	1.086
7	0.035	0.15	8.00	0.01340	0.0192	0.0472	1.68	0.0026	0.0027	16.6	1.091
8	0.040	0.10	8.00	0.11200	0.0562	0.0870	2.03	0.0081	0.0092	16.3	1.099
9	0.040	0.12	8.00	0.12400	0.0516	0.0826	2.29	0.0053	0.0066	17.0	1.081
10	0.040	0.15	8.00	0.03600	0.0281	0.0516	1.86	0.0027	0.0028	16.3	1.099
11	0.040	0.20	8.00	0.00065	0.0014	0.0142	0.28	0.0002	0.0003	16.8	1.086
12	0.043	0.12	8.00	0.14452	0.0596	0.0868	2.38	0.0085	0.0099	16.7	1.089
13	0.045	0.15	8.00	0.06000	0.0144	0.0235	1.80	0.0013	0.0015	16.1	1.104

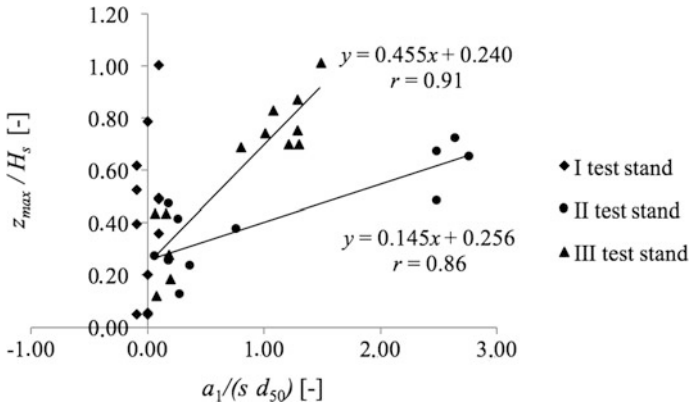


Fig. 3 Regression of equation  $\left(\frac{z_{max}}{H_s}\right) = c \frac{a_1}{sd_{50}} + d$  (Eq. 1)

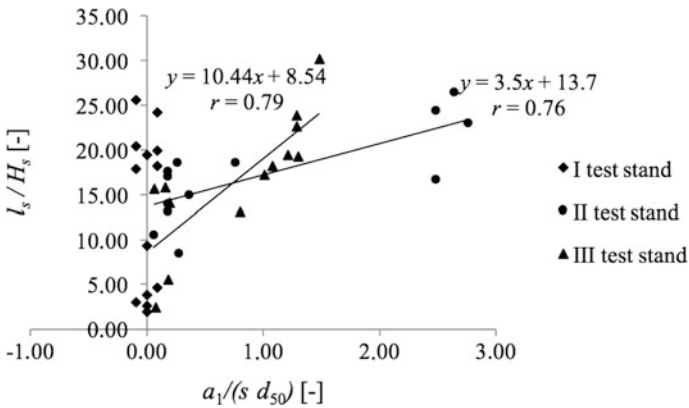


Fig. 4 Regression of equation  $\left(\frac{l_s}{H_s}\right) = f \frac{a_1}{sd_{50}} + j$  (Eq. 2)

$$\left(\frac{l_s}{H_s}\right) = 3.50 \frac{a_1}{sd_{50}} + 13.7; r = 0.76; \tag{8}$$

$$Q_s D_* \left(\frac{W}{H}\right)^{-1} \left(\frac{z_m}{l_s}\right) = 0.005 Q_w (S - S_0) - 0.033; r = 0.91; \tag{9}$$

$$\left(\frac{z_m}{l_s}\right) = 0.002 e^{6.4\theta}; r = 0.87. \tag{10}$$



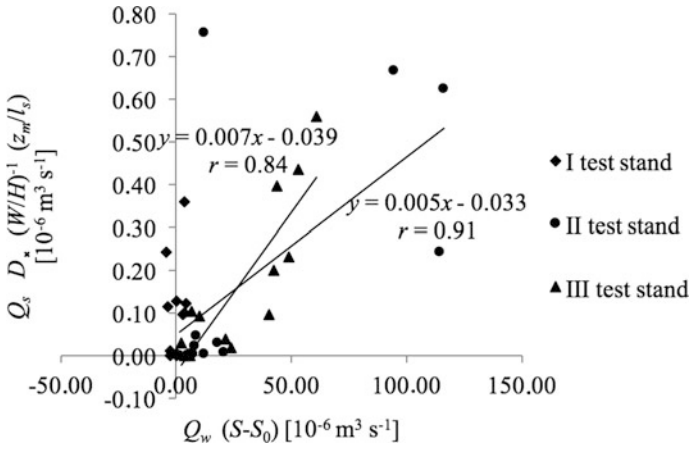


Fig. 5 Regression of equation  $Q_s D_* (W/H)^{-1} \left(\frac{z_m}{l_s}\right) = a Q_w (S - S_0) + b$  (Eq. 4)

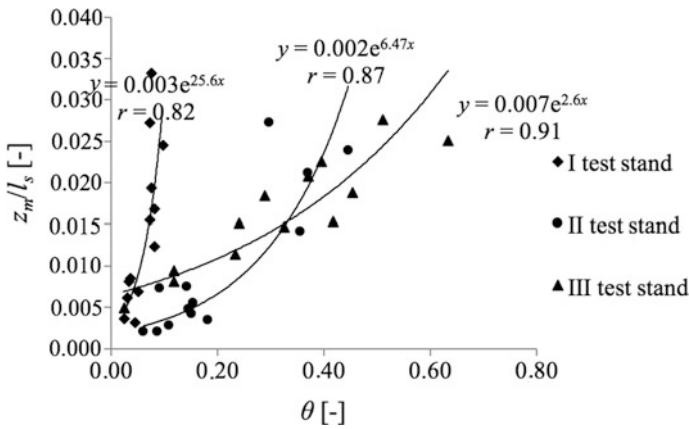


Fig. 6 Regression of equation  $\left(\frac{z_m}{l_s}\right) = k e^{m\theta}$  (Eq. 5)

(3) For test stand III

$$\left(\frac{z_{max}}{H_s}\right) = 0.455 \frac{a_1}{sd_{50}} + 0.240; r = 0.91; \tag{11}$$

$$\left(\frac{l_s}{H_s}\right) = 10.4 \frac{a_1}{sd_{50}} + 8.54; r = 0.79; \tag{12}$$

$$Q_s D_* \left( \frac{W}{H} \right)^{-1} \left( \frac{z_m}{l_s} \right) = 0.007 Q_w (S - S_0) - 0.038; r = 0.84; \quad (13)$$

$$\left( \frac{z_m}{l_s} \right) = 0.007 e^{2.6\theta}; r = 0.91. \quad (14)$$

## 4 Conclusions

The experiment including a total of thirty-nine test runs, performed on three test stands (13 test runs for each stand), was conducted in the hydraulic laboratory to investigate the local scours properties, aiming at relating scour geometry with hydrodynamic parameters of water and sediment discharge. Measurements were taken when the scour hole has obtained its stable shape in clear-water and live-bed conditions. One non-uniform sand was used as a bed material with  $d_{50} = 0.91$  mm. Test stands included total and partially sandy bed with and without the water structure (stone weir).

According to initial assumptions, four empirical formulas—Eqs. (1), (2), (4) and (5)—were confirmed to predict the medium scour depth  $z_m$ , maximal scour depth  $z_{max}$  and the length of the scour hole  $l_s$ , as far as correlation coefficient  $r > 0.70$  signalizes satisfying match and  $r > 0.80$  good match of data in test cases with the stone weir. It must be mentioned that the local scour geometrical properties are strongly responsive to the difference between the equilibrium and initial energy grade line slope. The exponential and linear functions were identified, hence there was no general equation for cases with water structure input into the flume. The obtained values of linear function coefficients  $c, d, f, j$  are similar to those proposed by Gaudio et al. (2000) and Gaudio and Marion (2003). Further development could involve higher energy grade slopes (the high equilibrium energy slope line surplus to the initial slope) or different stone weir configurations, for example, similar to the water structure presented in this research, with diminished slots area to intensify scour forming processes in the proposed test run conditions.

## References

- Ben Meftah M, Mossa M (2006) Scour holes downstream of bed sills in low-gradient channels. *J Hydraul Res* 44(4):497–509
- Dust D, Wohl E (2012) Conceptual model for complex river responses using an expanded Lane's relation. *Geomorphology* 139–140:109–121
- Gaudio R, Marion A, Bovolin V (2000) Morphological effects of bed sills in degrading rivers. *J Hydraul Res* 38(2):89–96
- Gaudio R, Marion A (2003) Time evolution of scouring downstream of bed sills. *J Hydraul Res* 41 (3):271–284

- Huang HQ, Liu X, Nanson GC (2014) Commentary on a Conceptual model for complex river responses using an expanded Lane's diagram by David Dust and Ellen Wohl *Geomorphology*, vol 139–140, pp 109–121. *Geomorphology* 209:140–142
- Kiraga M, Popek Z (2016) Using a modified Lane's relation in local bed scouring studies in the laboratory channel. *Water* 8(16):1490–1509
- Lane EW (1955) The importance of fluvial morphology in hydraulic engineering. In: *Proceedings of American society of civil engineers*, New York, USA, pp 1–17
- Lenzi MA, Marion A, Comiti F, Gaudio R (2002) Local scouring in low and high gradient streams at bed sills. *J Hydraul Res* 40(6):731–739
- Lenzi MA, Marion A, Comiti F (2003) Local scouring at grade-control structures in alluvial mountain rivers. *Water Resour Res* 39(7):1176–1188
- Pagliara S, Radecki-Pawlik A, Palermo M, Plesiński K (2016) Block ramps in curved rivers: morphology analysis and prototype data supported design criteria for mild bed slopes. *River Res Appl*. Wiley
- Petts GE (1977) Channel response to flow regulation: the case of the river Derwent, Derbyshire. In: Gregory KJ (ed) *River channel changes*. Wiley, Chichester, Great Britain
- Ślizowski R, Radecki-Pawlik A (2003) Weryfikacja formuł do obliczania rozmoczonego dna poniżej budowli wodnej na podstawie pomiarów laboratoryjnych. *Acta Scientiarum Polonorum—Formatio Circumiectus*, 2(2):25–34. (in Polish)
- Van Rijn LC (1993) *Principles of sediment transport in rivers, estuaries and coastal seas*. Aqua Publications, Amsterdam, The Netherlands

# An Experimental Investigation of Pressure Wave Celerity During the Transient Slurry Flow

Apoloniusz Kodura, Michał Kubrak, Paweł Stefanek  
and Katarzyna Weinerowska-Bords

**Abstract** Transportation of slurries in pressure pipelines is an example of a complex flow due to specific parameters of transported medium. For practitioners, the economy of designing and maintenance is usually the most important factor. For this reason, most of hydrotransport installations are fairly simple; however, they become more vulnerable to negative effects of the transient flow which can occur in pressure pipelines. As the consequence, the phenomenon may cause major damage, and thus, it should be precisely described. A deep analysis of transients in slurries is crucial, both from theoretical and practical points of view. In this paper, the experimental investigation of pressure wave celerity during the transient flow of slurries in the high density polyethylene pressure pipe was described. The value of this celerity has a significant influence on the pressure changes in the pipeline, and thus, its correct determination is crucial to calculate the actual maximal pressure increases or decreases. To achieve the aim, two sets of the physical tests were performed. The first series were carried out with use of a physical model, enabling the measurements of pressure characteristics caused by a rapid valve closure. The experiments were accomplished both for slurries of different densities and for water. The second series were carried out in a real hydrotransport installation. The analysis of the experimental data was compared with the theoretical equation for the wave celerity. Experimental data indicates a huge difference compared to the theoretical values of celerity. The results confirm the necessity for revision of the theoretical expression for the wave celerity.

---

A. Kodura (✉) · M. Kubrak  
Faculty of Building Services, Hydro and Environmental Engineering,  
Warsaw University of Technology, 20 Nowowiejska Str., 00-653 Warsaw, Poland  
e-mail: apoloniusz.kodura@pw.edu.pl

P. Stefanek  
Tailings Management Division, KGHM Polska Miedź, 52 Polkowicka Str.,  
59-305 Rudna, Poland

K. Weinerowska-Bords  
Department of Civil and Environmental Engineering, Gdańsk University of Technology,  
11-12 Gabriela Narutowicza Str., 80-233 Gdańsk, Poland

## 1 Introduction

Over the years, the hydrotransport has become more widespread method of transportation of fine solid materials. This occurred as the result of a development of new energy-efficient methods of pumping. One of the greatest advantages of that method is the continuity of the transport, with fluent possibility of mass intensity regulations. In continuous industry processes this property is crucial. The most common materials transported by water in pressure systems are: iron concentrate and tailings, phosphorus concentrate and tailings, coal, coal ash and limestone (Han et al. 1998).

The flow of the slurry strongly depends on the concentration of the mixture, sizes of solid particles, weight of the solid phase and the parameters of the system—pipes, pumps and fittings. The model of a quasi-steady flow for slurries is more complicated than for water. Theoretically, the models for non-Newtonian fluids are recommended to be used. Solid particles can be transported as a homogenous mixture or as a two-phase liquid. For the second case, the problem of different velocities of water and a solid phase (often creating the benthic zone) leads to the need of simplification of the mathematical description.

The transient flow of slurries becomes even more complex, compared to the steady case. As the result of the rapid changes of velocity, kinetic energy is transformed into pressure energy. That process is observed in a form of the pressure wave that spreads in pipelines with a very high celerity. A shock wave can exceed the safety pressure level for installation, and thus the process has to be taken under consideration during design studies. Due to the properties of water hammer, the process is more dangerous in long pipelines. Unfortunately, the hydrotransport installations are usually designed as relatively simple long pipelines.

One of the most important parameters of water hammer is wave celerity. Its value describes additionally a magnitude of a rapid pressure change. The following parameters of water: density and bulk modulus, and the parameters of the pipe: diameter, wall thickness and Young modulus, have an influence on the wave celerity. In the case of the slurry transport, additionally the parameters of the solid phase should be analyzed. However, due to a significant variability of the solid phase, this analysis should be performed individually, for the specific installations of hydrotransport (Cristoffanini et al. 2014; Lan et al. 2013).

In this paper, an experimental investigation of the value of the wave celerity was carried out. To achieve the results, two series of experiments were performed. The first one was done in a laboratory. A variable concentration of slurries was analyzed during the tests. The second one was carried out in the real hydrotransport installation. For both experiments, the same kind of solid phase was used. However, due to the operating limitation in the Company, the field tests were performed for the of-the-moment mixture concentration.

The results of the experiments were analyzed and compared with the values resulting from the theoretical equation for the wave celerity.

## 2 Water Hammer Phenomenon

### 2.1 Wave Celerity for Transient Water Flow

The water hammer phenomenon is one of the most common examples of the transient flow in pressure pipelines. Since the first published equation—the Joukowsky equation (in 1898)—a lot of improvements in description of this phenomenon have been done. However, still the value of the maximum pressure change due to the rapid water hammer can be calculated with a high accuracy from the previous formula (Wylie et al. 1993):

$$\Delta p = \Delta v \rho a, \quad (1)$$

where:  $\Delta v$ —velocity change,  $\rho$ —liquid density,  $a$ —wave propagation celerity.

Practically, the Joukowsky formula can be considered by engineers as the maximum pressure change estimation in the case of rapid water hammer. This formula was appointed based on three factors. The first two parameters: velocity change and density, are easy to determine in the case of water. The third parameter—the pressure wave celerity, can be expressed as a relationship of the pipe length and the time of the reflected wave returning (Mitosek 1993; Fox 1977):

$$a = \frac{2L}{T_R}, \quad (2)$$

where:  $a$ —wave propagation celerity,  $L$ —pipeline length,  $T_R$ —reflected wave returning time.

By using Eq. (2), the celerity of the wave propagation can be estimated by means of physical experiments. The reflected wave returning time is used to determine the types of water hammer. When the time of velocity change is no longer than  $T_R$ , the rapid water hammer occurs. This type leads to the biggest changes of pressure.

The second way to determine the wave celerity is to use the Korteweg equation (Parmakian 1955; Wylie et al. 1993):

$$a = \frac{\sqrt{\frac{K}{\rho}}}{\sqrt{1 + \frac{D K}{e E}}}, \quad (3)$$

where:  $a$ —wave propagation celerity,  $K$ —bulk modulus of liquid,  $E$ —modulus of elasticity of pipe material,  $D$ —diameter of pipeline,  $e$ —wall thickness,  $\rho$ —liquid density.

According to this equation, the celerity is affected by both, the liquid (bulk modulus and density) and the pipeline parameters (modulus of elasticity, cross-section diameter and wall-thickness of the pipe). However, this formula can be used only for Newtonian liquids.

## 2.2 Wave Celerity for Transient Slurries Flow

In the case of slurries, the Korteweg equation is useless. A new approach to the wave celerity estimation should be developed. However, in the literature a few examples of solutions to this problem can be found.

Theoretically, two kinds of flow may occur—quasi-homogenous slurries and heterogeneous slurries. In the first case, the mixture has overall constant density and the distribution of the solid phase is almost uniform. These slurries can be described as liquids, but with different (modified) density and viscosity. The second group of slurries is defined by uneven solid phase distribution. This fact implies the necessity of a different description of the phenomenon. A modified form of the Korteweg equation is expected. This issue was one of the aims of the study of Wenlinag et al. (1998), who presented the equation for the wave propagation celerity in the case of a heterogeneous flow:

$$a_{he} = \frac{\sqrt{K \left( \frac{C_V}{\rho_S} + \frac{1-C_V}{\rho_L} \right)}}{\sqrt{1 - C_V + \frac{K}{E_S} C_V + \frac{K D}{E e}}}, \quad (4)$$

where:  $a_{he}$ —wave propagation celerity for heterogeneous slurry,  $K$ —bulk modulus of liquid (water),  $E$ —modulus of elasticity of pipe material,  $D$ —diameter of pipeline,  $e$ —wall thickness,  $\rho_L$ —liquid density,  $C_V$ —volume concentration of slurry,  $E_S$ —bulk modulus of solid phase,  $\rho_S$ —solid phase density.

Comparison of the two equations, (3) and (4), shows a significant difference. The density of the liquid is replaced by the density of the mixture, dependent on the relationship between the amount of the solid and liquid phase. According to the literature (Wenlinag et al. 1998), Eq. (4) was tested in experiments carried out for hydrotransport of fine grains of coal.

One of the targets of this paper is to explore the possibility of using Eq. (4) to calculate the wave celerity for different kind of slurries. A description of the relationship between the wave celerity and the volume concentration of slurries by means of experiments would be desirable.

## 3 Experiments

### 3.1 Laboratory Tests

The experiments were divided into two series. The first was performed in laboratory conditions. A unique physical model, shown in Fig. 1, was built. The model consisted of a high density polyethylene (HDPE) pressure pipeline of 16.24 m length and 25 mm external diameter (1) and a pressure tank (2). At the downstream

end of the pipe, a ball valve (3) was equipped by a unique system to register an angle of closing in time. Two pressure transducers (4) located close to the valve, were connected to a PC computer (5) via an analog-digital card (6) to store the experimental data. An additional ball valve (7) was located downstream to set a constant value of discharge during a steady flow. Just downstream of ball valve, a short section of pipe made of plexiglass was installed (8). This section was used to observe flows during steady conditions. The discharge was measured by means of a vessel (9), with use of the volumetric method. From the capacitive vessel, liquid was pumped via returning pipe to the pressure tank (2). This vessel was equipped with a mixer, whose rotation was deliberately added to obtain the steady density of the slurry. The air pressure above the liquid surface was maintained by a compressor, to obtain the steady pressure in the vessel.

The experiments were made for both, water and slurries flow, for comparable conditions of average flow velocities. The slurry samples were taken from the company KGHM Polska Miedź Tailings Management Division, where the hydro-transport is used for transportation of the waste fine grained rock, produced in the process of obtaining copper from ore water, into a settling tank. Experiments were performed with the use of real material.

For each case of the transient flow, the characteristic of pressure change was stored and analyzed. The example of the analyzed characteristic is presented in Fig. 2. The significant influence of the volumetric concentration on the phenomenon run was observed. For the slurry flow, the pressure wave has shorter duration time and higher increase. The increase of the returning wave time is also noticeable.

In Fig. 3, the correlation between the average flow velocity before the water hammer and the pressure increase for the measured slurry and water flow is presented. Similarly, for water and slurries the comparable linear relation is observed.

For each of the collected pressure characteristics, the wave celerity was calculated. The calculated values were compared with the ones obtained from the theoretical equation. Results are presented in Fig. 4. A noticeable influence of the solid phase to the significant slowdown in the pressure celerity is visible. The calculated (with use of the Eq. (4)) pressure celerity is also presented in the chart. The analysis of this graph indicates significant differences between the measured and calculated data. Equation (4) shows lesser sensitivity of the wave celerity to the changes of the slurry concentration than the experimental data.

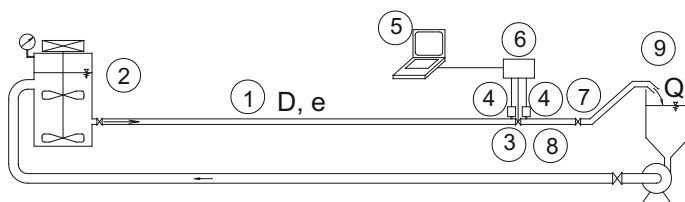
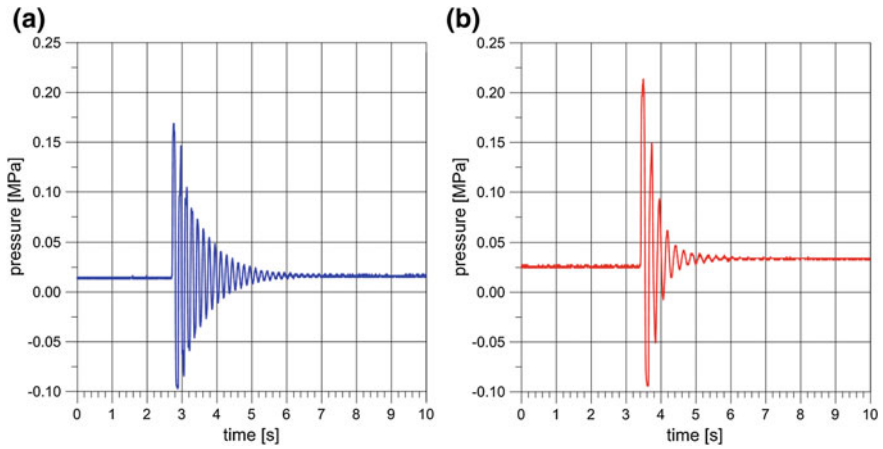
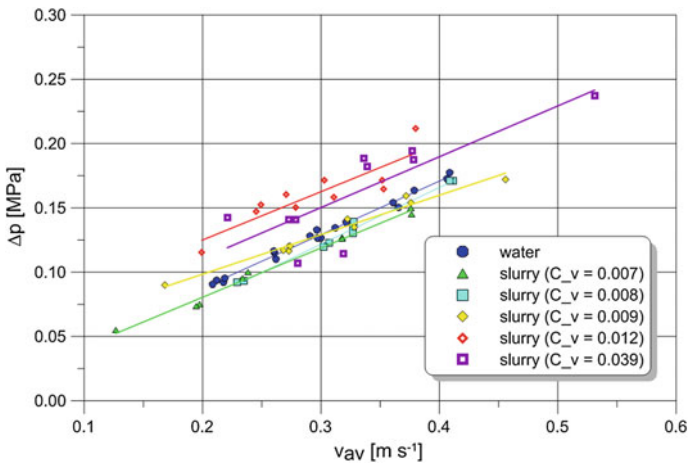


Fig. 1 Laboratory model scheme (labels explained in the text)





**Fig. 2** Pressure characteristic during transient flow: **a** water; **b** slurry ( $C_v = 0.012$ )



**Fig. 3** The relationship between the average flow velocity and pressure rise obtained depending on the concentration of the mixture

### 3.2 Field Tests

The field tests were performed in the existing slurry system of Tailings Management Division. This pressure system consists of three pumping stations ('Lubin', 'Rudna' and 'Polkowice') and more than 120 km of pressure conduits of diameter higher than 600 mm. The field tests were done with use of the unique system of pressure transducers. Two sections of the pipelines were selected: one in the pipeline transporting the slurry from 'Lubin', and the second one—in the pipeline

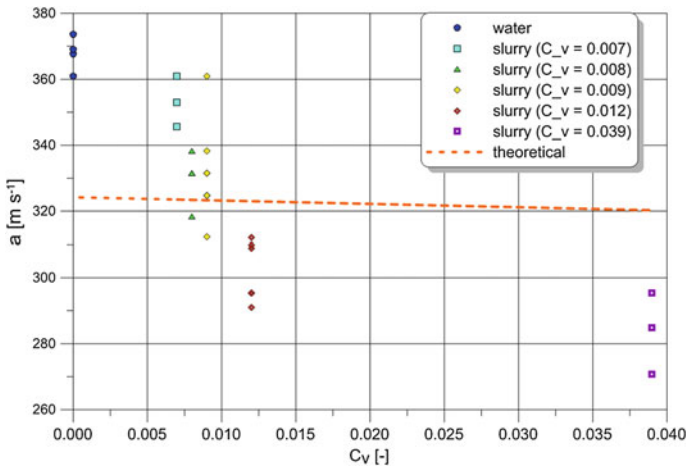


Fig. 4 Impact of mixture concentration on the speed of the pressure wave

from ‘Rudna’ and ‘Polkowice’ pumping stations. Two cross-sections (upstream and downstream) were installed in each of the selected sections. The distances between the cross-sections were 3.250 km and 4.350 km, respectively. The HDPE pipelines had an external diameter of 1300 mm and 76 mm wall thickness.

The unique system of pressure measurement consists of the pressure transducers and the electronic controllers, which were used to provide electric power transducers and collect data. Before the experiments, the coordination of time on both controllers was checked.

The tests were restricted by the limitations of the temporary change of typical work of the system. The pumping station staff manually steered the operation of the system, to obtain short periods of decreasing and increasing pressure of the transported slurry. Their steering was observed as the pressure wave, which spread in the pressure system. The stored data in the form of pressure characteristics (Figs. 5 and 6) were analyzed. The wave celerity was calculated by measuring shifts between the time of the occurrence of the pressure change in upstream and downstream cross-sections of the selected pipeline section.

The values of the measured and calculated wave celerity are presented in Table 1. An average volumetric concentration is in range from 0.046 for ‘Lubin’ pumping station to 0.071 for ‘Polkowice’, pumping station. For ‘Rudna’, volumetric concentration is equal to 0.065; however, due to specific conditions of the flow (sludge with air), the wave celerity for these experiments achieves visibly smaller values.

As it was mentioned, due to technical problems of air-sludge mixture flow from ‘Rudna’, results for that flow should be analyzed separately. For two proper data series, ‘Polkowice’ and ‘Lubin’, the measured pressure wave celerity is in the relation with the volumetric concentration. However, this relationship is completely different from that in the case of laboratory measurements. During the field test, the

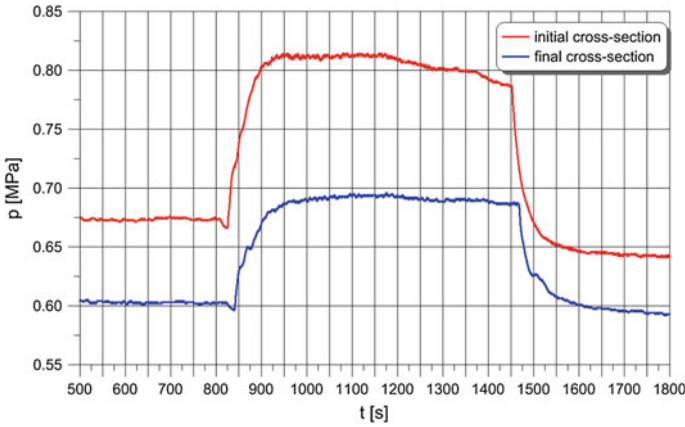


**Fig. 5** Example of measured pressure characteristic in pressure slurry system—“Rudna” pumping station

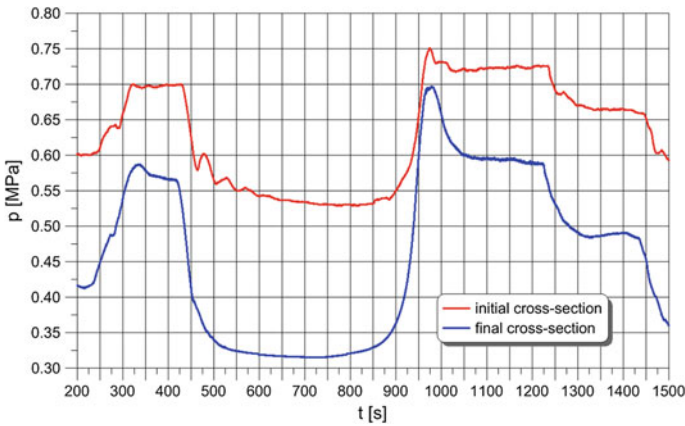


**Fig. 6** Example of measured pressure characteristic in pressure slurry system—“Polkowice” pumping station. Additional pressure disturbances are visible, as a result of spreading wave in the complex pipelines system

growth of the volume concentration is accompanied by an increase in celerity. One of the most important reasons of this situation are the conditions of flow. In the laboratory, each series of measurements for a given concentration was preceded and finished with flushing the pipe by water. In addition, the steady flow duration was relatively short. For the real installation, the slurry was transported through the analyzed pipeline for several weeks. Due to the heterogeneous nature of the flow, a layer of a quasi-constant depth was formed at the bottom of the pipeline. The bottom layer, that fills the pipeline with different thickness, has immeasurable influence on the wave celerity.

**Table 1** Pressure wave celerity

Pumping station	Measured wave celerity (m s <sup>-1</sup> )	Average wave celerity (m s <sup>-1</sup> )	Volumetric concentration	Calculated wave celerity (m s <sup>-1</sup> )
Lubin	383.9 359.3 376.1 380.1	374.8	0.046	307.2
Polkowice	441.6 469.7 413.6 482.4 433.8 519.4 472.4	461.8	0.071	305.2
Rudna	286.1 281.1 266.4 262.5 251.8 247.2 246.7 291.6 281.6 285.9 258.6 273.5 271.5 266.5	269.4	0.065	305.8

The second important observation is the fact that the obtained wave celerity for two pumping stations ('Polkowice' and 'Lubin') is higher than during the laboratory tests. The most probable reason of this difference is a geometric size of the pipeline and additional stiffness of the real system conduits.

The comparison with the values calculated with use of the theoretical formula shows that the measured values are significantly higher. That fact will lead to much higher pressure increase. The tested theoretical formula gives much understated values for the tested sludge. The obtained difference indicates that the analyzed equation does not take into account all the factors affecting the value of the celerity.

The analysis of the pressure characteristic (Figs. 5 and 6) indicates differences in the phenomenon course. The pressure characteristic for sludge from 'Polkowice' (Fig. 6), particularly for the upstream cross-section, shows additional visible small pressure changes. They are a result of spreading of the wave in pipes connection, that is localized near to initial cross-section. For the slurry from 'Rudna' pumping station (Fig. 5), the pressure increase demonstrates the quasi-constant value, without additional pressure oscillations. This is a result of water hammer energy dissipation in some amount of air (Mitosek and Szymkiewicz 2012). For this

pumping station, small bubbles of air were detected during measurements. This fact may be a result of the nature of the technical process in the pumping station. Even a slight volume of air leads to a significant decrease of the pressure wave celerity. This may be confirmed by lower values of wave celerity, which were indicated for slurry from 'Rudna' pumping station (Table 1). This fact can affect the results of data analysis.

During the measurements, changing the value of the sludge concentration was not possible due to technological processes. Because of a very complex character of flow, the measured value of volumetric concentration was additionally fraught with high measurement uncertainty.

## 4 Conclusions

The conducted analysis of the theoretical equations and the experimental data leads to a conclusion that, both for water and slurries, the pressure increase during the transient flow is in linear relationship to the steady-flow velocity. In both cases the pressure wave is formed, which spreads in the installation with a certain velocity. The observed pressure raise for slurries increases with the raising volumetric concentration. However, the time of the phenomenon duration is shorter.

A similar influence of the flow velocity on the pressure increase allows the use of Joukovsky formula to determine the maximum pressure change. However, the value of the wave celerity should be properly determined.

The laboratory and field tests have shown a significant influence of volumetric concentration of slurry on the wave celerity. The growth of the volumetric concentration is accompanied by the drop in celerity. That relationship is more complicated than theoretical. The comparison of the measured and calculated values for the analyzed slurries shows the significant reduction in the celerity calculated by means of the theoretical equations.

The wave celerity calculated from the field test results is higher than that obtained during the laboratory tests. The most probable reason is a geometric size of the pipeline and additional stiffness of the real system conduits. The stiffness is determined by a layer of soil that covers the pipeline and by the bottom layer of variable thickness, which fills the pipeline.

During the field test, the significant influence of slight amount of air on pressure wave decrease was observed.

The relationship between the wave celerity and the volumetric concentration obtained during the field test is different from that observed during the laboratory experiments. A different nature of the flow and the occurrence of quasi-solid bottom layer, are another argument for the necessity to seek a new equation of wave celerity. Formulation of a new equation enabling determination of the wave celerity for slurries is a challenge for scientists. At the moment it is advisable to determine the celerity each time in the way of experiments.

**Acknowledgements** This study has been performed due to help of KGHM Polska Miedź Tailings Management Division.

## References

- Cristoffanini C, Karkare M, Aceituno M (2014) Transient simulation of long distance tailings and concentrate pipelines for operation training. In: Proceedings of SME annual meeting/exhibit, February 24–26, 2014, Salt Lake City, UT, USA
- Fox JA (1977) Hydraulic analysis of unsteady flow in pipe networks. The MacMillian Press LTD, London and Basingstoke
- Han W, Dong Z, Chai H (1998) Water hammer in pipelines with hyperconcentrated slurry flows carrying solid particles, vol 41, no 4 Science in China (Series E) August 1998
- Lan G, Jiang J, Li DD, Yi WS, Zhao Z, Nie LN (2013) Research on numerical simulation and protection of transient process in long-distance slurry transportation pipelines. In: 6th international conference on pumps and fans with compressors and wind turbines IOP publishing IOP conference series: materials science and engineering 52 072008. <https://doi.org/10.1088/1757-899X/52/7/072008>
- Mitosek M, Szymkiewicz R (2012) Wave damping and smoothing in the unsteady pipe flow. ASCE J Hydraul Eng 138:619–628
- Mitosek M (1993) Oscillatory liquid flow in elastic porous tubes. Acta Mech 102:139–153
- Parmakian J (1955) Water hammer analysis. Prentice-Hall Inc, New York
- Wylie BE, Streeter VL, Suo L (1993) Fluid transients in systems. Prentice Hall, Englewood Hills, NJ

# Numerical Modeling of Water Flow Conditions with Spatial Distribution of Boulders in Main Channel

Leszek Książek, Maciej Wyrębek, Mateusz Strutyński  
and Agnieszka Woś

**Abstract** The article presents a study on the influence of spatial distribution of boulders placed in the main channel on parameters of flow conditions. Restoration guidelines recommend boulders structures but engineering solutions must be individually adapted to local situation. The depth-averaged 2D numerical model of unsteady, free-surface flow in open channels was used to calculate spatial distribution of velocity magnitude, slope of water surface level and water depth. The impact of individual boulder on the flow conditions in river channels increases through the group arrangement. Model of the Wisłoka River section was changed by implementation of boulders in various configurations: a group of three or four placed in triangles or rhomboids, openwork deflectors, groups located by the banks, groups located alternately to form a curvilinear thalweg. The effect of boulders structure on velocity spatial distribution along the channel was calculated for discharge  $Q_{10\text{-day}} = 15 \text{ m}^3 \text{ s}^{-1}$ . Impact of single boulder structures on flow velocity is visible up to 20–30 m and increases for multiple single boulders structures up to 30–60 m. In addition, stability of individual boulder for discharge  $Q_{1\%}$  and influence the flood hazard were tested.

**Keywords** Boulders structure · Numerical modeling · River restoration

## 1 Introduction

Economic use of rivers led to transformation of river valleys and river channels. Uncontrolled exploitation of bedload and extracting single boulder from a river channel on a wide scale caused a disturbance of natural channel morphology. Negative outcomes of human activity causing degradation of river channels

---

L. Książek (✉) · M. Wyrębek · M. Strutyński · A. Woś  
Faculty of Environmental Engineering and Land Surveying, Department of Hydraulic Engineering and Geotechnics, University of Agriculture in Krakow,  
Al. Mickiewicza 24/28, 30-059 Krakow, Poland  
e-mail: rmksiazek@cyf-kr.edu.pl

© Springer International Publishing AG 2018  
M. B. Kalinowska et al. (eds.), *Free Surface Flows and Transport Processes*,  
GeoPlanet: Earth and Planetary Sciences,  
[https://doi.org/10.1007/978-3-319-70914-7\\_17](https://doi.org/10.1007/978-3-319-70914-7_17)

(Korpak 2007; Wyżga et al. 2016) comprise formation of local depressions, destroying of the riverbed armouring layer (Michalik and Książek 2009), incision of the channel (Lach and Wyżga 2002), lowering of groundwater level and a change of bedload granulometric composition or its total washout. The consequence was a disappearance of places favouring the existence and reproduction of ichthyofauna. For example, sources from the turn of the 19th and 20th century registered 35 fish species occurring in the Wisłoka River. In the 1970s, the presence of 25 fish species was registered. During investigations of ichthyofauna in the middle and lower course of the river, 22 fish species were caught (Jelonek et al. 2002).

Preventing the deterioration of the current state and in further perspective, its improvement was reflected in the Water Framework Directive. In this context, recognizing the principle of equivalence between hydraulic structures and environment protection becomes important.

Restoration activities denote restoring a previous, close to natural, state of the river, i.e. the state before the regulation or existing in nature prior to human interference. Restituting biological continuum of watercourses concerns both making possible negotiating the impoundment elevations by aquatic organisms and ensuring hydrodynamic and ecological balance in watercourse channels along their whole length. The restoration measures in the watercourse channel comprise:

- restoration of continuity of bedload transport along the channel length and in the cross-section to activate river structures: islands, point bars, promontories or bays but also improvement of the bed material,
- restructuring of the horizontal pattern of the watercourse through diversification of the river course, including the oxbow lakes or variability of the watercourse width,
- correction of the longitudinal profile owing to liquidation of transversal obstacles, diversification of local longitudinal slope and bankfull discharge,
- change of cross-sections, i.e. diversification of the shape and dimension along the channel, ensuring an appropriate water depth.

The elements which change water flow conditions and enrich the diversity of habitat conditions are local obstacles such as fallen trees, wood or gravels which upthrust of the bed. Despite stream habitat, restoration guidelines describe boulder placement methods but engineering solutions must be individually adapted to local situation (Ward 1997; Saldi-Caromile et al. 2004).

This study shows an example of determination of advantageous flow characteristics in rivers from the point of view of ecological state of the river ecosystem.

The aim of this paper is to assess the hydraulic conditions of flow around spatially distributed boulders structures deposited in the bed of the main channel.



## 2 Materials and Methods

### 2.1 Research Area

The Wisłoka River is a right bank tributary to the Vistula, about 164 km long and with the catchment area of over 4.1 thousand km<sup>2</sup>. The reach under investigations, from the Mokrzec to Pustkow, is 30 km long (km 43–73). At the Dębica cross-section km 55 + 850, the discharges of 50 and 1% annual exceedance probability are  $Q_{50\%} = 381 \text{ m}^3 \text{ s}^{-1}$  and  $Q_{1\%} = 1334 \text{ m}^3 \text{ s}^{-1}$ .

Hydromorphological assessment comprises evaluation of the main channel, banks, littoral zone and inundation area (PN EN 2008). It was stated that along the studied Wisłoka River section the effect of hydrotechnical structures on hydromorphological quality of the watercourse declines along the length of c.a. 5 km. In the areas classified as heavily modified regarding their morphology, sections of high morphological quality may occur, whereas in the area of natural morphology, long straight sections of greatly decreased ecological usability are possible (Hawryło and Leja 2012).

Evaluation of the state of the river on the basis of zoobenthos or ichthyofauna indicates a good ecological state of the river ecosystem. Coarse and fine gravel prevail on the channel bottom, with definitely lower share of stone fraction, particularly cobbles and boulders. At the same structure of the bottom, the conditions for development of invertebrates are fulfilled, however the conditions for ichthyofauna development are not fair enough for the species which occurred in the Wisłoka in the past. The requirement for an improvement of the ecological state is restoration of habitat conditions (stony sections and boulders) which determine the increase in the number of large fish species and their specimens.

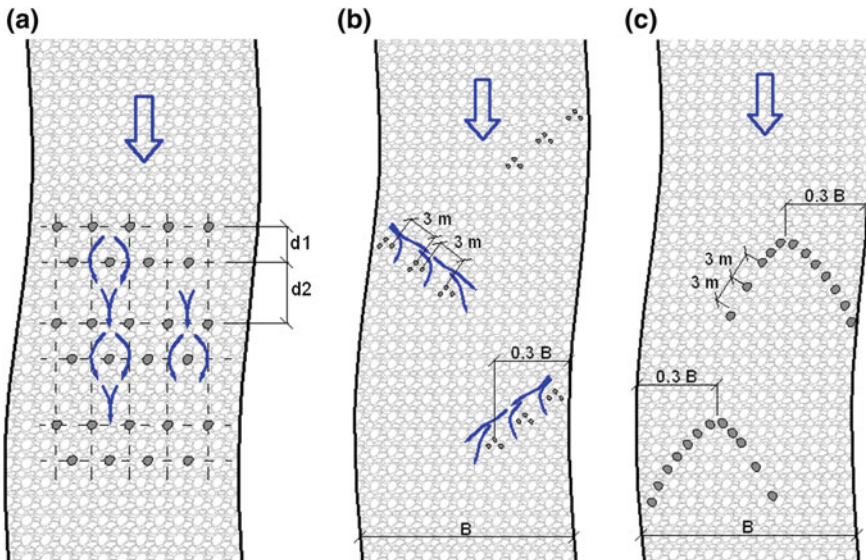
### 2.2 Methods

Diversification of water discharge conditions was achieved owing to placing structures into the channel and deposition of bedload in the river channel (Table 1). Studies on the way of placing single boulders and their grouping (Fig. 1) were conducted by numerous authors. Yaworski and Fee (1982) stated that a boulder below 0.6 m may become buried in the riverbed because of the potholes forming around the grains. Therefore, the authors recommend using boulders with larger diameters or their grouping. They also suggest to add a bedload with finer graining in the boulder vicinity to stabilize the riverbed in the area of boulder presence. The method is not recommended for rivers with fine bedload because the boulders may become dug deeply into the bottom (Saldi-Caromile et al. 2004).

In case of riverbed incised into alluvial units, without inundation terraces, the computed height of deflectors (Fig. 2) for discharge  $Q_{50\%}$  may prove too high. In this case, it is recommended to establish the maximum current deflector height for

**Table 1** Structures in river channel

Structures	Description	Changes
Openwork boulders	The distance between the boulders is no smaller than 0.7 m. The degree of obscuring the cross-section is no higher than 20–30%	Deceleration of flow velocity. Breaking of stream flow. Diversification of flow conditions and bed material transport
Group boulders	The distance between the grain groups c.a. 3–5 m. Grain groups placed on the length equal to 1–2 channel width	Creating: diversified bedload and flow conditions in the group vicinity; point bars in form of mounts in the downstream zone—spawning grounds for <i>Salmo salar</i> (fine material, mount); Conditions for fish rest, i.e. shadow of grain groups
Current deflectors	The degree of deflector protruding: 1/3 of the channel width; inclination 20–30 degrees with reference to the river bank line; slope 2–7% towards the middle of the river	Diversification of the thalweg and change the horizontal course. Forming quiet zones in the shadow of the deflector

**Fig. 1** Structures of boulders: **a** openwork arrangement, **b** boulders in groups, **c** openwork—deflector;  $B$ —channel width

summer flow (García de Jalón and Gortázar 2007). Local material originating from the pits and exposures of the contemporary inundation terraces will be used for the Wisłoka River channel. Minimum dimensions of single boulder vary from 0.6 to

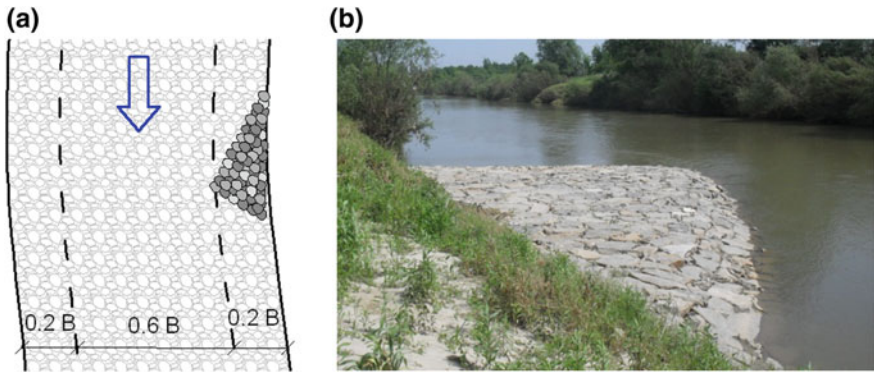


**Fig. 2** Structure and dimensions of the current deflector, the Wisłoka River: **a** layout, **b** view

0.8 m (diameter *b*) with shapes approximate to spherical—the boulder shape coefficient should range from 0.6 to 1.0.

On the basis of field measurements including survey measurements, bedload granulometric composition and water surface level, hydraulic parameters of water flow conditions were calculated using a two-dimensional numerical model CCHE2D. The model is a depth-averaged 2D numerical model for simulating unsteady, turbulent, free-surface flow in open channels with alluvial bed (Jia and Wang 1998; Tena et al. 2013). The numerical modeling procedure requires creating a mesh ( $2.34 \times 10^5$  cells,  $11.1 \text{ nodes m}^{-2}$  in the main channel,  $5.6 \text{ nodes m}^{-2}$  at floodplain), define initial and boundary conditions, setup of model parameters (time step  $\Delta t = 0.5 \text{ s}$ ), running of numerical solutions and visualization of modeling results.

The created model was calibrated through comparing the measured and computed water surface levels. Flow hydraulic parameters were calculated using 2D model for discharge of  $Q_{10\text{-day}} = 15 \text{ m}^3 \text{ s}^{-1}$ . In accordance with Tennant’s (1976) procedure, the discharge (about 40% of mean annual flow) was evaluated as good for fish, wildlife, recreation and related environmental resources in streams flow. Also Bartnik et al. (2011) recommend ten-day discharges as conducive for fish migration. For various patterns and location of boulder placement in the channel, the types of hydromorphological units corresponding to different flow conditions were determined: from still water to rapids.

The following variants were taking into account:

- version 1—present state;
- version 2—placing boulders in various configurations (Fig. 3):
  - a bow curved towards the tail water;
  - a group of three or four gravels placed in triangles or rhomboids;

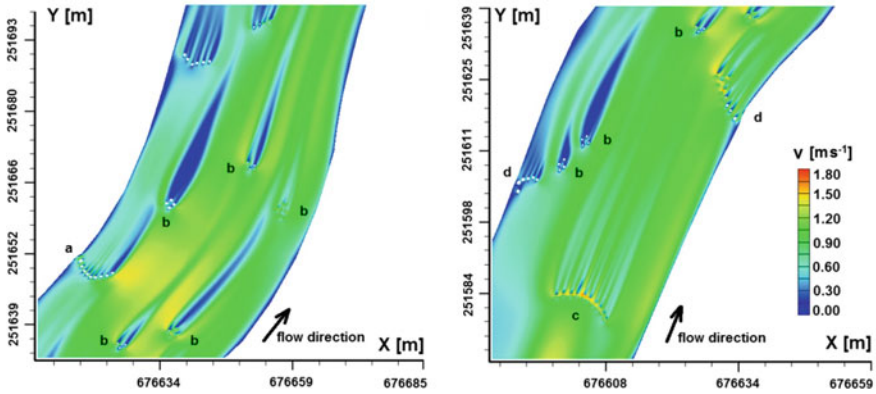
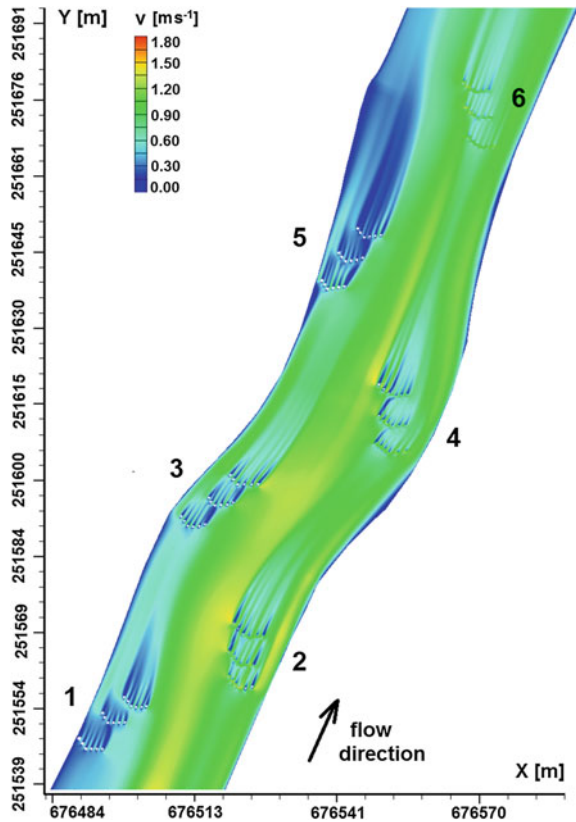


**Fig. 3** Spatial distributions of flow velocity; **a** and **c**—flow direction oriented openwork-deflector, **b**—group of three or four gravels, **d**—boulders at the banks, version 2

**Fig. 4** Spatial distributions of flow velocity, 1–6 boulders in groups on both banks, version 3



- a bow curved towards the head water;
- groups of boulders located by the banks;
- version 3—placing boulders in groups alternately—on the left and right bank to form a curvilinear thalweg (Fig. 4).

### 3 Results and Discussion

Boulders are placed in the main channel in an openwork arrangement causing a breakdown of the flowing stream of water. While flowing around the individual boulder, water decelerates and diversifies the hydraulic flow conditions.

At the discharge of  $15 \text{ m}^3 \text{ s}^{-1}$ , the length of impact zone of single structures of boulder arrangement is visible up to 20–30 m (Table 2). Arranging single boulders structures in groups causes their interaction (Fig. 4). In this case, zones with decreased velocity elongate and are visible for up to 30–60 m. In comparison with undisturbed flow phenomena, the presence of boulders in the main channel for discharge of 40% ratio to the mean annul flow, reduces the mean flow velocity magnitude, by 37% (SD = 7%) in average (Table 3).

Increasing flow resistance caused by the presence of boulders in the cross section leads to change in a water surface level (WSL). For the discharge of  $Q = 15 \text{ m}^3 \text{ s}^{-1}$  WSL increase does not exceed  $\Delta h = 0.08 \text{ m}$ . Basing on the results of one-dimension modeling, it may be stated that for the discharge  $Q_{1\%}$  the mean change of water depth along the Wistoka River section is 0.5% in relation to the discharge without boulder implementation (Bartnik et al. 2015). So the assumption that the gravel implementation does not influence the flood hazard was fulfilled.

The second assumption was that the individual boulders will be stable for the discharge  $Q_{1\%}$ . The stability of an individual boulder was a guarantee of stability of its structures. The initial bed conditions in the model were defined as stable so the critical conditions of bed movement were calculated based on shear stresses. To see if initial bed conditions are exceeded, the normal  $\tau_0$  and critical  $\tau_{cr}$  shear stresses were calculated. Normal shear stress  $\tau_0$  [ $\text{N m}^{-2}$ ] was evaluated using the classical formula  $\tau_0 = \gamma h I$ , while critical shear stress  $\tau_{cr}$  [ $\text{N m}^{-2}$ ] from equation  $\tau_{cr} = \Delta \gamma_s f_i d_i$ ; where  $h$

**Table 2** Results of numerical modeling for discharge of  $15 \text{ m}^3 \text{ s}^{-1}$ , version 2

Structure of boulders	$v$ [ $\text{m s}^{-1}$ ]	$h$ [m]	Zones with decreased velocity	
			Width [m]	Length [m]
v.2 a	0.3–0.5	0.40	7	20
v.2 b	0.1	0.45–0.60	1–3	8–30
v.2 c	0.6–0.8	0.70	13	23
v.2 d	0.1–0.7	0.40–0.60	4–8	12

**Table 3** Comparison of basic hydraulic parameters for discharge of  $15 \text{ m}^3 \text{ s}^{-1}$ , versions 1 and 3

No	$v \text{ [m s}^{-1}\text{]}$ version 1	$v \text{ [m s}^{-1}\text{]}$ version 3	$h \text{ [m]}$ version 3	Length of reduced velocity	
				Width [m]	Length [m]
1	0.4–0.8	0.0–0.4	0.42–0.48	12	36
2	1.0	0.6–0.8	0.57–0.70	9	35
3	0.9	0.1–0.6	0.42–0.50	9	26
4	1.0	0.4–0.6	0.60–0.80	7	30
5	0.5	0.1–0.3	0.30–0.50	10	60
6	1.0	0.4–0.6	0.80–1.20	5	30

is the water depth [m],  $I$  the slope of energy line,  $f_i$  the Shields parameter [-], and  $d_i$  is the diameter [m]. For the assumed size of boulders (diameter  $b$ :  $d_i = 0.8 \text{ m}$ , shape factor  $0.6 - 1.0$ ,  $f_i = 0.033 - 0.047$ ), critical shear stresses vary from  $425$  to  $605 \text{ N m}^{-2}$ . The critical shear stress values were calculated using equation  $\tau_{cr} = 2.66.80^{1.213} = 541 \text{ N m}^{-2}$  (range up to  $500 \text{ cm}$ ) (O'Connor 1993). For discharge  $Q_{1\%}$ , normal shear stress does not exceed  $95 \text{ N m}^{-2}$ , so such conditions provide the stability of boulder:  $\tau_0 < \tau_{cr}$ .

The matter differs for movement of bedload material. In that case, initial conditions of bedload transport may be exceeded. The presence of boulders in the channel causes changes in the flow hydraulics. Immediately around grains, the bed material is washed out which leads to diversification of depth. In their shadow there is a zone of increased flow turbulence which is connected with water flow around the grain. Its size depends on the size, shape and degree of single boulder exposure above the cover (Strutyński et al. 2013). The occurrence of boulders in the channel diversifies the amount of bedload forming the bottom cover. Vortexes and turbulence caused by their presence lead to deposition of fine bedload which is not washed out. Intensified turbulence behind a boulder causes that fine material sediment immediately behind it is only locally suspended but not transported downstream.

The unsteady flow conditions around boulder favour reconstruction of the substratum for spawning as well as support armouring phenomena. In result of bed material deposition, the movable central bars are formed changing morphological conditions of the river. Once the flood wave is over, the bar changes its geometry, creating new morphological conditions.

From the hydraulic perspective, measures suggested for the main stream rely on exchange of steady flow to variable flow movement to diversify the flow and bankfull discharge conditions and modify the habitat conditions. The main elements changing the stream of flowing water are boulders arranged in structures with various configurations. The impact of a single boulder on flow conditions is local. The effect of boulders arranged in groups on the flow conditions covers a larger area. Arrangement of boulders groups into clusters still increases the area.

Depending on their configuration they may fragment the stream into single rivulets, change the direction of flow altering the mainstream course into curvilinear and concentrate the thalweg in a part of the cross-section.

## 4 Conclusions

In order to realize conceptual activities aimed at restoration of fish habitats along the Wisłoka River reach from the weir in Mokrzec to Pustkow, spatial distribution of boulder structures were tested. Restoration guidelines describe boulders placement methods but each sector of a river must be individually investigated. The set of parameters which have been taken into account includes flow conditions, river morphology as well as requirements of fish. The effect of impact of an individual boulder in the cross-section can be strengthened by placing boulders in clusters which break the streamlines, differentiate both water velocity and depth in the cross-section and longitudinal profile, i.e. creating variable conditions of water flow. On the basis of numerical simulation of the Wisłoka River reach, it may be stated that the boulders placement does not affect flood safety conditions. After the boulders implementation, an average change of water surface level for discharge  $Q_{1\%}$  on the studied section of the Wisłoka River does not exceed few centimeters. The bed initial conditions of gravels were evaluated using shear stresses. Both assumptions were fulfilled: the individual boulder will be stable for discharge  $Q_{1\%}$  and the gravel implementation does not influence the flood hazard.

An assessment of water flow conditions was possible by using a two-dimensional numerical model. The numerical model bases on the momentum and continuity equations; the computational domain covers the whole river reach, not only the cross-sections. Furthermore, it is a useful tool in the process of restoration of the rivers understood as creating an ecological corridor free from barriers to migration, reducing the fragmentation of the catchment and restoring the integrity of the Natura2000 area.

**Acknowledgements** The study has been financial supported by the PIOS-05.02.00-00-182-09-00 project.

## References

- Bartnik W, Epler P, Jelonek M, Klaczak A, Książek L, Mikołajczyk T, Nowak M, Popek W, Sławińska A, Sobieszczyk P, Szczerbik P, Wyrębek M (2011) Fisheries management with relations to the restoration of connectivity of the little and the upper Vistula River basins. Infrastructure and ecology of Rural areas—Monograph 4, Polish Academy of Sciences Krakow Branch, 13 (in Polish)
- Bartnik W, Książek L, Jelonek M, Sobieszczyk P, Florek J, Hawryło A, Leja M, Strużyński A, Strutyński M, Wałęga A, Wyrębek W, Wiśniewolski W, Parasiewicz P, Prus P, Adamczyk M,

- Depowski R (2015) Warunki przywracania struktury siedlisk dla ryb na odcinku rzeki Wisłoka w km 73 + 200 & #x00F7; 42 + 600. *Gospodarka Wodna* 5:147–152 (in Polish)
- García de Jalón D, Gortázar J (2007) Evaluation of instream habitat enhancement options using fish habitat simulations: case-studies in the river Pas. *Aquat Ecol* 41:461–474 (in Spain)
- Hawryło A, Leja M (2012) Hydromorphological evaluation of the Wisłoka River section from Mokrzec to Pustków. *Episteme* 14:85–91 (in Polish)
- Jia, Y, Wang SS (1998) Capability assessment of CCHE2D in channel flow simulations. *Proc Adv HydroSci Eng* 3
- Jelonek M, Żurek R, Klich M (2002) Ichtiofauna rzeki Wisłoki w rejonie nowo powstałego zbiornika Mokrzec (Starostwo Dębica). *Suppl ad Acta Hydrobiol* 3:69–78 (in Polish)
- Korpak J (2007) The influence of river training on mountain channel changes (Polish Carpathian Mountains). *Geomorphology* 92(3–4):166–181
- Lach J, Wyźga B (2002) Channel incision and flow increase of the upper Wisłoka River, southern Poland, subsequent to the reafforestation of its catchment. *Earth Surf Proc Land* 27(4):445–462
- Michalik A, Książek L (2009) Dynamics of water flow on degraded sectors of polish mountain stream channels. *Pol J Environ Stud* 18(4):665–672
- O'Connor JE (1993) Hydrology, hydraulics, and geomorphology of the bonneville flood. *Geol Soc Am Spec Pap* 274:1–84
- PN-EN 14614 (2008) Jakość wody—Wytyczne do oceny hydromorfologicznych cech rzek, Polski Komitet Normalizacyjny, Warszawa (in Polish)
- Saldi-Caromile KK, Bates K, Skidmore P, Barenti J, Pineo D (2004) Stream habitat restoration guidelines: final draft. In: Co-published by the Washington departments of fish and wildlife and ecology and the U.S. fish and wildlife service. Olympia, Washington, June 2010
- Strutyński M, Strużyński A, Kulesza K (2013) The influence of large roughness elements on natural morphological changes in a mountain river bed. In: Rowiński P (ed) *Experimental and computational solutions of hydraulic problems*. GeoPlanet, Earth and Planetary Sciences, pp 237–247
- Tena A, Książek L, Vericat D, Batalla RJ (2013) Assessing the geomorphic effects of a flushing flow in a large regulated river. *River Res Appl* 29(7):876–890. <https://doi.org/10.1002/rra.2572>
- Tennant DL (1976) Instream flow regime for fish, wildlife, recreation and related environmental resources. *Fisheries* 1(4):6–10. [https://doi.org/10.1577/1548-8446\(1976\)001<0006:IFRFFW>2.0.CO;2](https://doi.org/10.1577/1548-8446(1976)001<0006:IFRFFW>2.0.CO;2)
- Ward BR (1997) Using boulder clusters to rehabilitate juvenile salmonid habitat. In: Slaney PA, Zaldokas D (eds) *Fish habitat rehabilitation procedures, watershed restoration technical circular 9*. Ministry of Environment, Lands and Parks, Vancouver
- Wyźga B, Kundzewicz ZW, Ruiz-Villanueva V, Zawiejska J (2016) Flood generation mechanisms and changes in principal drivers. In: Kundzewicz ZW, Stoffel M, Niedźwiedz T, Wyźga B (eds) *Flood risk in the upper vistula basin*. GeoPlanet, Earth and Planetary Sciences, pp 55–75
- Yaworsky B, Fee J (1982) Boulder introduction to enhance salmonid. Reading habitat Scott Creek, Ministry of Environment, Victoria



# Analysis of Pressure Wave Velocity in a Steel Pipeline with Inserted Fiber Optic Cable

Michał Kubrak, Apoloniusz Kodura and Szymon Imielowski

**Abstract** The paper presents the analysis of the water hammer phenomenon in a steel pipeline with inserted fiber optic cable. Specifically, pressure wave velocity of the phenomenon is considered. The derivation of formula, which is presented, allows to calculate pressure wave velocity in the case where a cable with different Young's modulus compared to the elasticity of the pipeline is inserted into it. The derivation was carried out using the mass balance. The results of experimental tests conducted using three different fiber optic cables are presented. Experimental studies show that inserting a cable into a pipeline has an attenuating effect on water hammer phenomenon.

## 1 Introduction

Development of internet and telecommunication services results in the need for infrastructure development. Creating new conventional networks in densely built-up city areas causes many technical, economic and legal problems (Andrzejewski and Szeląg 2011). One of the solutions to this issue is to use the existing infrastructure of pipeline networks to carry fiber optic telecommunication cables. The most developed underground network is the water supply system, which reaches almost all the buildings and can be successfully used for routing of fiber optic cables. The idea of using water pipelines to carry fiber optic telecommunication cables requires a diagnose of the effect of putting cable into a pipeline on water flow conditions, both in transient and steady water flow. Inserting the fiber optic cable into the existing pipe causes a decrease of the cross-section and changes the shape of the stream. This has an impact on hydraulic flow conditions. Due to the fact that the cause of the vast majority of water pipeline failures is water hammer, it is necessary in this case to explain the impact of different elasticity of fiber optic cable

---

M. Kubrak (✉) · A. Kodura · S. Imielowski  
Faculty of Building Services, Hydro and Environmental Engineering,  
Warsaw University of Technology, Nowowiejska 20, 00-653 Warsaw, Poland  
e-mail: [michal.kubrak@pw.edu.pl](mailto:michal.kubrak@pw.edu.pl)

compared to the elasticity of the pipeline on this phenomenon. The aim of this paper is to analyze the influence of inserting fiber optic cable into a steel pipeline on the water hammer phenomenon. In particular, the influence of the cables on the pressure wave is considered. The article covers theoretical and experimental research.

## 2 Theoretical Description of Water Hammer Effect in a Pipeline Without Fiber Optic Telecommunication Cable Inserted into It

Water hammer is a pressure wave which occurs when a fluid in motion is forced to change its velocity. It commonly occurs when a valve closes or opens at the end of a pipeline system, or a pump starts or stops. As a consequence, a pressure wave propagates in the pipe (Mambretti 2014).

The pressure increase during water hammer is described with Joukovsky's equation:

$$\Delta p = \rho c \Delta v, \quad (1)$$

where  $\Delta p$ —pressure increase [Pa],  $\rho$ —density of water [ $\text{kg m}^3$ ],  $c$ —pressure wave velocity [ $\text{m s}^{-1}$ ],  $\Delta v$ —change in flow velocity [ $\text{m s}^{-1}$ ].

The pressure wave velocity is described with Korteweg-Joukovsky equation:

$$c = \frac{\sqrt{\frac{K}{\rho}}}{\sqrt{1 + \frac{KD}{Ee}}}, \quad (2)$$

where  $K$ —water compressibility [Pa],  $D$ —pipe diameter [m],  $e$ —pipe wall thickness [m],  $E$ —Young's modulus of pipe wall [Pa].

## 3 Theoretical Description of Water Hammer Effect in a Pipeline with Inserted Fiber Optic Telecommunication Cable

Theoretical analysis was conducted under the assumption that the pipe is thin-walled and hoop stress is of crucial importance (Bergant et al. 2008). It was assumed that the pipeline has an inner diameter  $D_1$  and Young's Modulus  $E_1$ . Inserted fiber optic cable has diameter  $D_2$  and modulus of elasticity  $E_2$  (Fig. 1).

The cross-sectional area of liquid stream in the pipeline with inserted fiber optic cable is:

**Fig. 1** Scheme of placement of fiber optic cable in the pipe

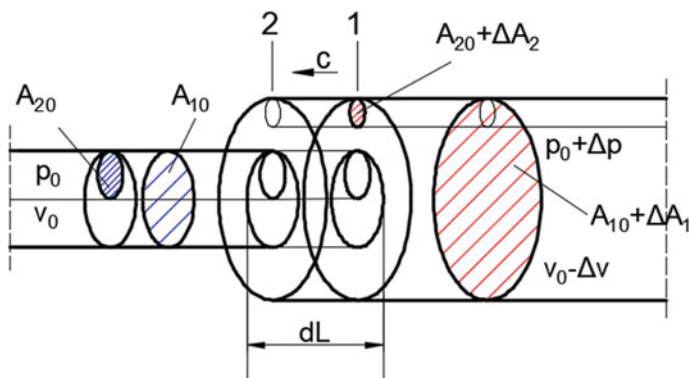
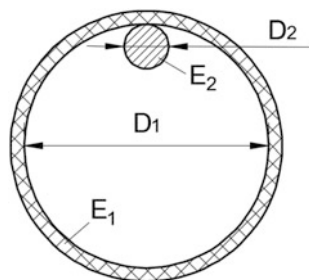


**Fig. 2** Scheme of the course of water hammer phenomenon in the pipeline with inserted cable

$$A = A_1 - A_2 \tag{3}$$

where  $A_1$ —cross-sectional area of pipe of diameter  $D_1$  [ $m^2$ ],  $A_2$ —cross-sectional area of the cable  $D_2$  [ $m^2$ ].

It was assumed that on the right hand side of cross-section 1 there are flow conditions just after initiating water hammer phenomenon and flow conditions on the left hand side of cross-section 2 have not yet changed (Fig. 2). Hence:

$$A_0 = A_{10} - A_{20}, \tag{4}$$

where  $A_0$ —cross-sectional area of the pipeline with inserted fiber optic cable before the initiation of the phenomenon [ $m^2$ ],  $A_{10}$ —cross-sectional area of the pipeline of diameter  $D_1$  before the initiation of the phenomenon [ $m^2$ ],  $A_{20}$ —cross-sectional area of the fiber optic cable before the initiation of the phenomenon [ $m^2$ ]; and:

$$A_1 = A_{10} + \Delta A_1, \tag{5}$$

where  $\Delta A_1$ —increase of cross-sectional area of pipeline of diameter  $D_1$  [ $m^2$ ].

Similarly, the change of cross-sectional area of the fiber optic cable can be expressed as follows:

$$A_2 = A_{20} + \Delta A_2, \quad (6)$$

where  $\Delta A_2$ —the change of the cross-sectional area of the fiber optic cable with a diameter  $D_2$  [m<sup>2</sup>].

The increase of water pressure causes stretching of the pipe wall, which results in an increase in its cross-sectional area. At the same time, the pressure increase causes the compression of the fiber optic cable inserted in the pipeline. Hence:

$$\Delta A_2 < 0. \quad (7)$$

The mass increase in an elementary section of the pipeline with the length of  $dL$  is equal to the mass of the inflow and outflow of the liquid from this section:

$$[\rho(A_1 - A_2) - \rho_0(A_{20} - A_{10})]dL = [\rho_0(A_{10} - A_{20})v_0 - \rho(A_1 - A_2)v]dt. \quad (8)$$

Combining Eqs. (3) and (4), the left hand side of (8) can be written as:

$$[(\rho_0 + \Delta\rho)(A_1 - A_2) - \rho_0(A_{20} - A_{10})]dL. \quad (9)$$

After multiplication, substituting the Eqs. (5) and (6), omitting  $\Delta\rho\Delta A_1$  and  $\Delta\rho\Delta A_2$ , the left hand side of (8) becomes:

$$[\rho_0(\Delta A_1 - \Delta A_2) + \Delta\rho(A_{20} - A_{10})]dL. \quad (10)$$

The right hand side of (8) for the pipeline with inserted fiber optic cable can be written:

$$[\rho_0(A_{10} - A_{20})v_0 - (\rho_0 + \Delta\rho)(A_{10} + \Delta A_1 - A_{20} - \Delta A_2)(v_0 - \Delta v)]dt. \quad (11)$$

After multiplication, all the terms with  $\Delta\rho$ ,  $\Delta A_1$  and  $\Delta A_2$  were omitted. The right hand side of (8) becomes:

$$[\rho_0\Delta v(A_{10} - A_{20})]dt. \quad (12)$$

Hence:

$$[\rho_0(\Delta A_1 - \Delta A_2) + \Delta\rho(A_{20} - A_{10})]dL = [\rho_0\Delta v(A_{10} - A_{20})]dt. \quad (13)$$

Substituting  $dL = cd t$  results with:

$$c = \frac{\rho_0\Delta v(A_{10} - A_{20})}{\rho_0(\Delta A_1 - \Delta A_2) + \Delta\rho(A_{10} - A_{20})}. \quad (14)$$

Using the definition of elasticity of the liquid (Mitosek 2014), (14) can be expressed as follows:

$$c = \frac{\frac{K}{\Delta p} \Delta \rho \Delta v (A_{10} - A_{20})}{\frac{K}{\Delta p} \Delta \rho (\Delta A_1 - \Delta A_2) + \Delta \rho (A_{10} - A_{20})}. \tag{15}$$

Expressing  $\Delta p$  in the numerator of (15) by (1) results in:

$$c = \sqrt{\frac{\frac{K}{\rho}}{1 + \frac{K}{\Delta p} \left( \frac{\Delta A_1 - \Delta A_2}{A_{10} - A_{20}} \right)}}. \tag{16}$$

In the thin-walled pipe, in the area of linear elastic deformation, the increase of cross-sectional area of the pipeline can be expressed as follows (Mitosek 2014):

$$\Delta A_1 = A_{10} \frac{\Delta p D_1}{E_1 e_1}. \tag{17}$$

Unlike the pipeline, the inserted fiber optic cable is not thin-walled pipe, but a conduit with solid cross-section. For this reason, when determining the elastic energy, which is equal to the mechanical work of reduction of the cable, the average reduction in circumference  $\Delta l$  should be considered as follows:

$$\Delta l = \frac{1}{2} \pi D \frac{\Delta p}{E_2}. \tag{18}$$

Due to the fact that fiber optic cable is compressed during the phenomenon (7), the relative variation of the cross-sectional area can be written as:

$$\frac{\Delta A_2}{A_{20}} = - \frac{\Delta p}{E_2}. \tag{19}$$

Combining (17) and (19) with (16) results in:

$$c = \sqrt{\frac{\frac{K}{\rho}}{1 + \frac{K}{\Delta p} \left( \frac{A_{10} \frac{\Delta p D_1}{E_1 e_1}}{A_{10} - A_{20}} + \frac{A_{20} \frac{\Delta p}{E_2}}{A_{10} - A_{20}} \right)}}. \tag{20}$$

Expressing  $A_{10}$  with  $A_1$  and  $A_{20}$  with  $A_2$ , we can write:

$$c = \sqrt{\frac{\frac{K}{\rho}}{1 + \frac{K}{\Delta p} \left( \frac{(A_1 - \Delta A_1) \frac{\Delta p D_1}{E_1 e_1}}{A + \Delta A_1 - \Delta A_2} + \frac{(A_2 - \Delta A_2) \frac{\Delta p}{E_2}}{A + \Delta A_1 - \Delta A_2} \right)}}. \tag{21}$$

After omitting  $\Delta A_1$  and  $\Delta A_2$  the final form of the pressure wave velocity equation can be expressed as follows:

$$c = \sqrt{\frac{\frac{K}{\rho}}{1 + \frac{A_1}{A} \frac{KD_1}{E_1 e_1} + \frac{A_2}{A} \frac{K}{E_2}}} \quad (22)$$

From (22) it follows that the pressure wave velocity in the pipeline with inserted fiber optic cable depends on the diameter and elasticity of the cable. In order to verify the above equation, the experimental study was conducted.

#### 4 Experimental Tests of Water Hammer Phenomenon in a Steel Pipeline with Inserted Fiber Optic Telecommunication Cable

Designed measuring stand for transient water flow in a steel pipeline with inserted fiber optic telecommunication cable is shown in Fig. 3.

The measuring stand consists of the following components:

1. The steel pipe with a diameter of 0.0531 m and wall thickness of 0.0035 m in which fiber optic cables with diameters of 5.3, 6.0 and 6.5 mm were inserted;
2. Pressure tank;
3. Pressure sensors;
4. Recorder of pressure samples—portable computer;
5. Analog-to-digital card;
6. Valve closure time meter;
7. Inductive flowmeter;
8. Valve;
9. Valve of initiating the water hammer phenomenon;
10. Water flow regulation valve.

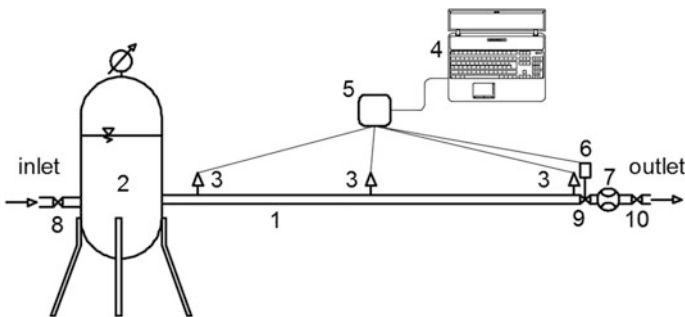


Fig. 3 Scheme of the measuring stand

In the experimental model, a steel pipeline of 48 m length consisted of 16 equal sections. Due to the necessity of inserting fiber optic telecommunication cables into the pipe, sections of the pipe were connected so that its rapid disconnection was possible. Pipe sections were connected using Camlock fittings.

The steel pipeline was supplied with a pressure tank connected to the water supply. Three connections with screwed-in pressure sensors welded to the pipeline were installed. The water pressure in the pipeline was measured directly by a set of three CL1-L type pressure sensors (Fig. 3) adapted to measure the pressure ranging from  $-0.1$  to  $1.2$  MPa. Pressure changes recorded by the sensor were converted into an electrical signal transmitted through the analog-to-digital card connected to a computer. The computer was equipped with a special software to collect digital results of measurements. Pressure changes in the pipe were recorded at the frequency of  $500$  Hz. Continuous measurement of pressure lasted  $20$  s. At that time, a set of  $500 \text{ s}^{-1} \cdot 20 \text{ s} = 1000$  pressure values were saved on each sensor. A valve was closed by hand. The closing time (approx.  $0.065$  s) was shorter than the pressure wave period. Experimental tests were conducted for volumetric flow rate  $Q = 60 \text{ dm}^3 \text{ s}^{-1}$ .

## 5 Results of the Experiment

The obtained data was used to make the characteristics of the pressure as a function of time. The analysis of measurements was carried out based on the data recorded by the sensor installed near the valve initiating the phenomenon. The results were put in one chart (Fig. 4) in order to compare the course of the phenomenon of water hammer in the pipeline with and without fiber optic cables.

The characteristic of pressure for each experiment was prepared so as to have the same initiation time—the pressure increase caused by the rapid closure of the valve begins at  $t = 0.5$  s. The first  $2.5$  s were analyzed, i.e. approx. 17 periods of the wave. Figure 4 shows that insertion of fiber optic cable does influence the course of the water hammer phenomenon. It is worth noting the pressure drop in the middle of the peak. This is due to the occurrence of reverse flow during pressure rise, which was experimentally explained by Brunone et al. (2000).

A fiber optic cable attenuates the pressure wave (shown in Fig. 4 magnified window), and consequently reduces the duration of the phenomenon. It should be noted, however, that amplitudes of pressure as a function of time for all the experiments overlap, which indicates a constant pressure wave velocity. For all measurements—with and without fiber optic cable—the same pressure wave velocity of  $1263 \text{ m s}^{-1}$  was obtained. The same pressure wave velocity generates the same maximum pressure increase for the flow with and without fiber optic cable. The maximum pressure increase in all cases amounted to approx.  $0.56$  MPa.

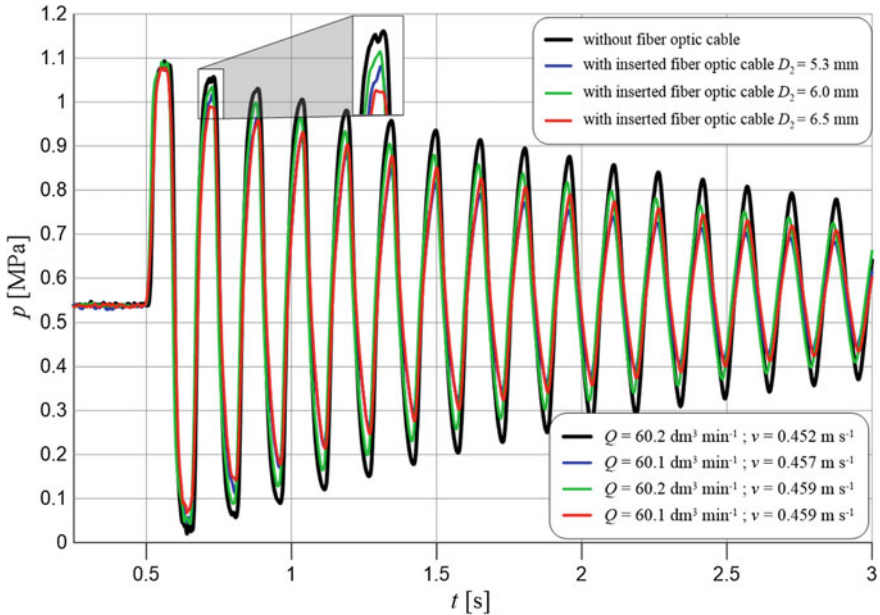


**Fig. 4** Changes of pressure as a function of time recorded during water hammer phenomenon in the pipeline with and without fiber optic cable

## 6 Theoretical Analysis of Pressure Wave Velocity During the Water Hammer Phenomenon in a Pipeline with Inserted Fiber Optic Cable

Equation (22) shows that the pressure wave velocity in a pipeline with inserted fiber optic cable depends on the cable's diameter and flexibility. Assuming that an inner diameter equals that of the pipeline used in the experiments,  $D_1 = 0.0531$  m, and assuming the same diameter of fiber optic cables, the pressure wave velocity was calculated for fiber optic cables of various flexibility. For the purpose of theoretical analysis, Young's modulus of steel from which the pipeline is made was calculated using the derived Eq. (2), assuming that the wave propagation velocity in the pipeline without a cable equals  $1263$  m s<sup>-1</sup>. Thus,  $E_1 = 119.3$  GPa. The calculated values of pressure wave velocity in a pipeline with inserted fiber optic cable are shown in the chart—Fig. 5.

Figure 5 shows that the larger the diameter and the lower the stiffness of the fiber optic cable, the greater effect it has on reducing the pressure wave velocity (and hence the attenuation of the water hammer phenomenon). The dotted line in the chart shows the pressure wave velocity in a pipeline without fiber optic cable as equal to  $1263$  m s<sup>-1</sup>. It should be noted that the insertion of fiber optic cable, with modulus of elasticity equaling  $\sim 10$  GPa, into a pipeline, causes small changes in



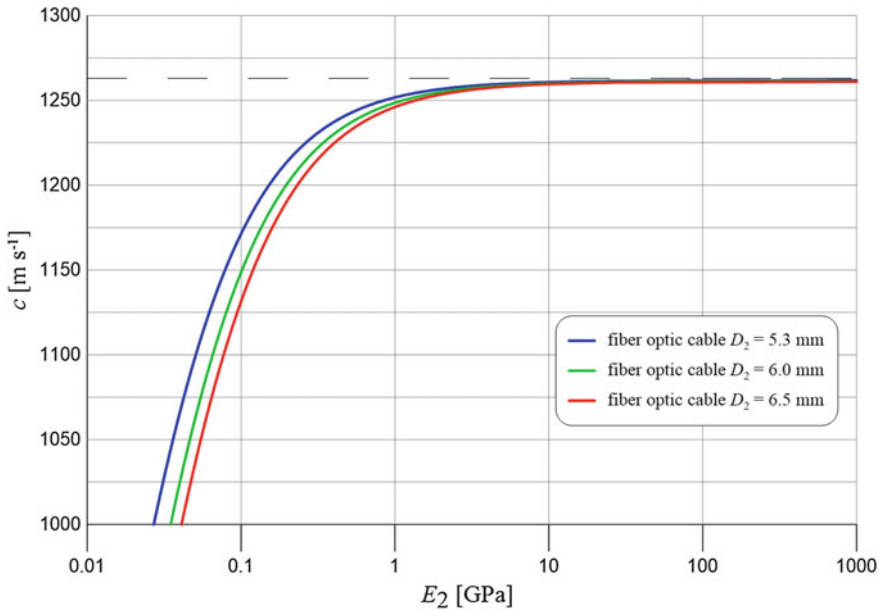


**Fig. 5** Pressure wave velocity as a function of cable’s Young’s modulus for different diameters of the fiber optic cables

pressure wave propagation velocity—amounting to less than 1%. It can therefore be supposed that the Young’s modulus of the fiber optic cable is greater than 10 GPa and thereby does not cause a noticeable reduction of the pressure wave velocity (Fig. 4).

In order to analyze how cable’s diameter influences the course of the water hammer phenomenon, derived Eq. (22) was used to calculate the pressure wave propagation velocity for fiber optic cables of 4 different elastic modules. Pipeline diameter used was  $D_1 = 0.0531$  m. The results as a function of the cable’s diameter are shown in Fig. 6.

Figure 6 shows that the insertion of the cable of low stiffness might have a significant impact on reducing pressure wave velocity. The chart shows that the insertion of a cable with Young’s modulus  $E_2 = 0.1$  GPa and a diameter  $D_2 = 0.008$  m into a steel pipeline with a diameter  $D_1 = 0.0531$  m may reduce the wave velocity from 1263 to 1030  $m\ s^{-1}$ , i.e. approx. by 19%.

It should be noted that the insertion of the cable into a pipeline reduces its diameter, thus increasing the average water flow velocity. This leads to higher pressure changes in case of the water hammer phenomenon.

In order to examine how the insertion of the cable into a pipeline affects the pressure increase in the event of a rapid water hammer,  $\Delta p_{f.o.c.}/\Delta p$  ratios were calculated, where  $\Delta p_{f.o.c.}$ —pressure increase in the pipeline with inserted fiber optic cable,  $\Delta p$ —pressure increase in the pipeline without fiber optic cable. The

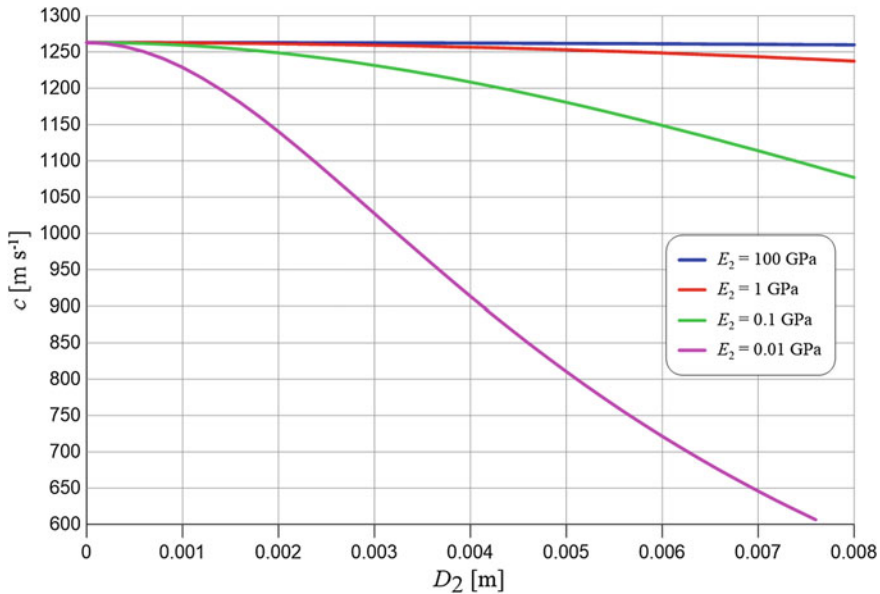


Fig. 6 Pressure wave velocity as a function of fiber optic cable’s diameter of different elasticity

maximum pressure increase  $\Delta p$  for a pipeline without inserted fiber optic cable was calculated using Joukovsky’s Eq. (1). Pressure wave velocity of  $c = 1263 \text{ m s}^{-1}$  was used for the calculations. Maximum pressure increase  $\Delta p_{f.o.c}$  for pipeline with inserted fiber optic cable was calculated from the same Eq. (1), taking into account the velocity determined from (22) and different (higher) average water flow velocity for the same flow rate. The same diameter of the pipeline as in the experiments, i.e.  $D_1 = 0.0531 \text{ m}$ , was used in these calculations. Calculations were done for five different modules of elasticity of the cable. The calculation results are shown in the chart—Fig. 7.

Figure 6 shows that the insertion of the fiber optic cable with a Young’s modulus  $E_2 \geq 1 \text{ GPa}$  into a steel pipeline has a negative impact on the water hammer phenomenon, i.e. pressure increase. Inserting the cable with modulus of elasticity  $E_2 \leq 0.1 \text{ GPa}$  into a pipeline reduces pressure increase during the rapid valve closure. To a certain point—the larger the diameter of the cable, the greater its influence on the attenuation of the water hammer.

The growth of the relative pressure increase for cables of Young’s modules  $E_2 = 0.1 \text{ GPa}$  and  $E_2 = 0.01 \text{ GPa}$  for diameters above  $D_2/D_1 = 0.8$  stems from the reduction of a pipeline’s cross-section and the thus increased average water flow velocity. Therefore, a cable with a constant Young’s modulus might be selected in order to attenuate the water hammer as much as possible. For example, the insertion of the cable with Young’s modulus  $E_2 = 0.1 \text{ GPa}$  and a diameter  $D_2 = 0.1 D_1$  into a steel pipeline with a diameter of  $D_1$  reduces the pressure increase by 40% in relation to a pipeline without inserted cable.

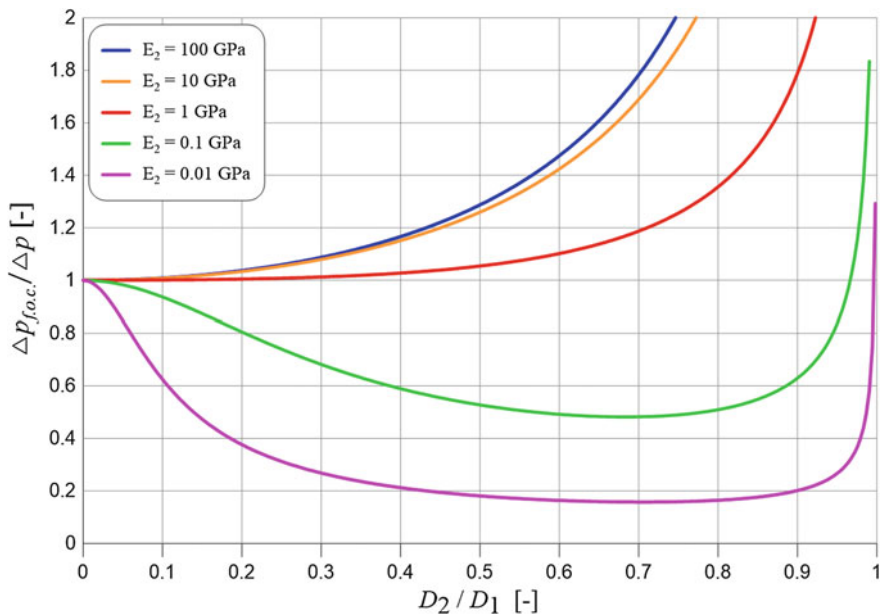


Fig. 7 Ratios of pressure increase during water hammer phenomenon in steel pipeline with and without fiber optic cable

### 7 Conclusion and Summary

The conducted theoretical considerations indicate that the pressure wave velocity in the pipeline with inserted fiber optic cable depends on the diameter and elasticity of the cable. The greater the diameter and the lower cable’s Young’s modulus, the greater its effect on reducing pressure wave velocity. The calculations performed for assessed diameters revealed that if the fiber optic cable has a similar elasticity compared to the pipe’s material, its effect on the pressure wave velocity is practically negligible. On the basis of derived pressure wave velocity equation, it can be concluded that inserting a cable with a low Young’s modulus can have a significant impact on reducing the increase of pressure caused by water hammer. Inserting the cable with modulus of elasticity  $E_2 \leq 0.1$  GPa into a steel pipeline, despite a reduction in its cross-sectional area and increase of the average water flow speed, reduces the pressure increase caused by sudden valve closure. In practice, using this kind of solution may protect the pipeline system against negative effects of water hammer phenomenon. On the other hand, experimental studies show that inserting fiber optic cables into a steel pipeline has an attenuating effect on water hammer phenomenon.

In order to additionally verify the derived theoretical formula, other experimental studies, using cables of different diameters and materials, will be performed.

Furthermore, the insertion of cable into pipeline increases head loss, which also affects the pressure changes during the water hammer phenomenon. Estimating its value will be the next stage of the research.

## References

- Andrzejewski M, Szelaǳ B (2011) Metody układania kabli telekomunikacyjnych w obiektach podziemnej infrastruktury miejskiej 14–15 (in Polish)
- Bergant A, Tijsseling A, Vitkovsky J et al (2008) Parameters affecting water-hammer attenuation, shape and timing—part I: mathematical tools 377
- Brunone B, Karney B et al (2000) Velocity profiles and unsteady pipe friction in transient flow 238–242
- Mambretti S (2014) Water hammer simulations: 9–11
- Mitosek M (2014) Mechanika plynów w inżynierii i ochronie środowiska: 16:206–207 (in Polish)

# Equilibrium Time of Scour Near Water Engineering Structures on River Floodplains

Oskars Lauva and Boriss Gjunsburgs

**Abstract** The differential equation of the bed sediment movement in clear-water scour conditions was used and a new method for equilibrium time of scour calculation at water engineering structures with flow separation at the structure in clear-water scour conditions was elaborated. The proposed threshold criteria for equilibrium time of scour known from the literature are only depending on the size of the hydraulic structure, and not on hydraulic parameters of the flow. Ratio of the recalculated critical flow velocity to the local one at the head of the water engineering structure was proposed as the hydraulic threshold criterion in equilibrium time of scour calculation. Calculated test data revealed that with an increase in flow contraction rate and with an increase in approach flow Froude number, equilibrium time of scour increases as well. To verify the developed equilibrium time of scour evaluation method, calculated time of scour values were compared to computer modelled ones, and the results showed good agreement. This calculation method can be applied to water engineering structures with flow separation at the structure at steady-flow and clear-water conditions.

## 1 Introduction

The European Environment Agency (EEA) identifies river flooding together with wind related storms as the most important natural hazards in the EU in terms of economic loss. The spatial distribution of high and very high flood hazard risk did not change significantly from 2002 to 2012. However, flood occurrence is projected to increase even further with climate change. The main reason for high flood occurrence is the general increase in winter precipitation, apparent in almost all regions of Europe except in the Mediterranean (Territorial Dynamics in Europe 2013).

---

O. Lauva (✉) · B. Gjunsburgs

Civil Engineering Faculty, Water Engineering and Technology Department,  
Riga Technical University, Kipsalas street 6A/B, 263, Riga LV-1048, Latvia  
e-mail: lauva.oskars@gmail.com

© Springer International Publishing AG 2018

M. B. Kalinowska et al. (eds.), *Free Surface Flows and Transport Processes*,  
GeoPlanet: Earth and Planetary Sciences,  
[https://doi.org/10.1007/978-3-319-70914-7\\_19](https://doi.org/10.1007/978-3-319-70914-7_19)

From the year 1997 up to nowadays, Europe has suffered over 100 major damaging floods. Economic losses because of extreme flood events have been dramatic. The 1997 floods in Poland and Czech Republic were responsible for losses of about EUR 5.2 billion. In 2000, Italy, France and Switzerland experienced losses of EUR 9.2 billion. In 2002 the material flood damage recorded in Germany, Czech Republic and Austria of EUR 17.4 billion has been higher than in any single year before. Moreover, the cost of floods in the UK in summer 2007 has been estimated at around EUR 4.3 billion. The annual average flood damage in Europe in the last few decades is about EUR 4 billion per year (Barredo 2007).

Without efforts to reduce emissions, resulting in changes to rainfall and streamflow mean that across Europe, extreme floods are likely to double in frequency within the next three decades. For example, floods that used to happen about every 100 years will start to occur every 50 years instead. A doubling in frequency of these extreme events corresponds to a tripling in the expected damage by the end of the century in Europe (Alfieri et al. 2015).

The amount of water flowing in large European rivers will increase in 73% of the study area by 2080. Considering the size of the rivers and the projected changes, this corresponds to an average increase in water flow of 8% by 2080 compared with 1990 (Alfieri et al. 2015).

Despite the significant investment of researchers in local scour investigation, hydraulic structures in rivers still fail due to scouring processes. It is believed that this is partially a consequence of scouring processes simplification, application of empirical methods, inadequacies between laboratory conditions and the reality in nature, and the present state of knowledge about some aspects of hydraulic and scouring complexity.

For the last two decades, many studies, particularly those dealing with clear-water conditions (without general bed sediment motion), report experiments that might not have lasted long enough to reach the equilibrium scour holes, whose depth and shape no longer significantly evolve with time. Since then, most studies claim the contrary, i.e., to have reached the equilibrium in long lasting experiments. With few exceptions, such studies refer to steady flows, although in nature, long lasting steady flows seldom exist; unsteadiness is particularly important during floods (Fael and Cardoso 2008).

Since the scouring process at hydraulic structures is never ending, threshold criteria are used for equilibrium time of scour evaluation. Threshold criteria, proposed and known from the literature are, when in a 24 h period: (i) the depth of scour increases less than 5% of the pier diameter (Melville and Chiew 1999); or (ii) less than 5% of the flow depth or abutments length (Coleman et al. 2003); or (iii) less than 5% of the 1/3 of the pier diameter (Grimaldi et al. 2006). The proposed threshold criteria for equilibrium time of scour known from the literature are only depending on the size of the hydraulic structure, and not on hydraulic parameters of the flow. Time to equilibrium,  $t_e$ , is defined as the time corresponding to the end of the principal phase, and the onset of the equilibrium phase.

## 2 Method

The differential equation of equilibrium for the bed sediment movement in clear-water conditions has the form:

$$(1-p) \frac{dW}{dt} = Q_s, \quad (1)$$

where  $p$ —porosity of riverbed material [-],  $W$ —volume of the scour hole [ $\text{m}^3$ ],  $t$ —time [s], and  $Q_s$ —sediment discharge out of the scour hole [ $\text{m}^3 \text{s}^{-1}$ ].

Volume and shape of the scour hole are independent of the contraction rate of the flow (Gjunsburgs et al. 2006a, b).

The left-hand part of Eq. (1) can be written as:

$$(1-p) \frac{dW}{dt} = \frac{1}{2} \pi m^2 h_s^2 \frac{dh_s}{dt} = a h_s^2 \frac{dh_s}{dt}, \quad (2)$$

where  $a = 1/2 \pi m^2$ ,  $m$ —steepness of the scour hole [deg.], and  $h_s$ —scour depth [m].

The sediment discharge was determined by the Levi (1969) formula:

$$Q_s = ABV_l^4, \quad (3)$$

where  $A$ —a parameter in the Levi (1969) formula [-],  $B = mh_s$  describes the width of the scour hole [m], and  $V_l$ —local flow velocity at the structure [ $\text{m s}^{-1}$ ].

The discharge across the width of a scour hole before and after the scour at water engineering structures is determined as follows (Gjunsburgs and Neilands 2001):

$$Q_f = Q_{sc} k, \quad (4)$$

where  $Q_f$ —discharge across the width of the scour hole with a plain bed [ $\text{m}^3 \text{s}^{-1}$ ],  $Q_{sc}$ —discharge across the scour hole with a scour depth  $h_s$  [ $\text{m}^3 \text{s}^{-1}$ ], and  $k$ —coefficient of changes in discharge because of scour, which depends on the flow contraction (Gjunsburgs and Neilands 2001) [-].

From Eq. (4) we have:

$$mh_s h_f V_l = k \left( mh_s h_f + \frac{mh_s}{2} h_s \right) V_{lr}, \quad (5)$$

where  $h_f$ —water depth in the floodplain [m], and  $V_{lr}$ —local flow velocity at the water engineering structure at a scour depth  $h_s$  [m].

Now from Eq. (5) we find the local flow velocity  $V_{lr}$  at the water engineering structure for any depth of scour (Gjunsburgs and Neilands 2001):

$$V_{lr} = \frac{V_1}{k \left( 1 + \frac{h_s}{2h_f} \right)}. \quad (6)$$

The critical flow velocity  $V_0$  at the water engineering structure at plain bed can be determined by the Studenitnikov (1964) formula:

$$V_0 = 1.15 \sqrt{g} d_i^{0.25} h_f^{0.25}, \quad (7)$$

where  $g$ —acceleration due to gravity [ $\text{m s}^{-2}$ ], and  $d_i$ —grain size of the bed material [m].

From Eq. (7), calculating the square root of  $g$  and multiplying it by 1.15, we get  $3.6 \text{ m}^{0.5} \text{ s}^{-1}$ ; afterwards, this is inserted into Eq. (7) and  $V_0 = 3.6 d^{0.25} h_f^{0.25}$ . The critical flow velocity  $V_{0r}$  at the water engineering structure for any depth of scour  $h_s$  and for the flow bended by the structure is:

$$V_{0r} = 3.6 \beta d_i^{0.25} h_f^{0.25} \left( 1 + \frac{h_s}{2h_f} \right)^{0.25}, \quad (8)$$

where  $\beta$ —reduction coefficient of the critical flow velocity at the bended flow determined by using the Rozovskyi (1956) approach [-],  $h_m = h^{0.25}(1 + h_s/2h_f)^{0.25}$ —mean depth of the scour hole [m], and  $h$ —approach flow depth [m].

At a plain riverbed, the formula for  $A = A_1$  is presented as (Eq. 3):

$$A = \frac{5.62}{\gamma} \left( 1 - \frac{\beta V_0}{V_1} \right) \frac{1}{d_i^{0.25} h_f^{0.25}}, \quad (9)$$

where  $\gamma$ —specific weight of sediments [ $\text{t m}^{-3}$ ].

The parameter  $A$  depends on scour, local flow velocity  $V_1$ , and recalculated critical flow velocity  $\beta V_0$ , and grain size of the bed material, which changes during floods.

$A_i$  at any depth of scour is:

$$A_i = \frac{5.62}{\gamma} \left[ 1 - \frac{k \beta V_0}{V_1} \left( 1 + \frac{h_s}{2h_f} \right)^{1.25} \right] \frac{1}{d_i^{0.25} h_f^{0.25} \left( 1 + \frac{h_s}{2h_f} \right)^{0.25}}, \quad (10)$$

where  $\frac{\beta V_{0r}}{V_{lr}} = \frac{\beta V_0}{V_1} \left( 1 + \frac{h_s}{2h_f} \right)^{1.25}$ .

Then we replace  $V_1$  in Eq. (3) with the local flow velocity at any depth of scour  $V_{lr}$  from Eq. (6). The parameter  $A$  in Eq. (3) is replaced with the parameter  $A_i$  from Eq. (10). The sediment discharge upon the development of scour is:



$$Q_s = A_i m h_s V_{lt}^4 = b \frac{h_s}{k^4 \left(1 + \frac{h_s}{2h_f}\right)^4}, \tag{11}$$

where  $b = A_i m V_1^4$ .

The hydraulic characteristics, such as the contraction rate of the flow, flow velocities  $\beta V_0$  and  $V_1$ , grain size in different bed layers, sediment discharge, and the depth, width and volume of the scour hole, varied during floods.

Considering Eqs. (2) and (11), Eq. (1) can be written in the form:

$$a h_s^2 \frac{dh_s}{dt} = b \frac{h_s}{k^4 \left(1 + \frac{h_s}{2h_f}\right)^4}. \tag{12}$$

After separating the variables and integrating Eq. (12), we have:

$$t = D_i \int_{x_1}^{x_2} h_s \left(1 + \frac{h_s}{2h_f}\right)^4 dh_s, \tag{13}$$

$$D_i = \frac{k^4 a}{b} = \frac{1}{2} \frac{\pi m k^4}{A_i V_1^4}, \tag{14}$$

where  $D_i$ —constant parameter in short time interval [-],  $x_1 = 1 + h_{s1}/2h_f$  and  $x_2 = 1 + h_{s2}/2h_f$  are relative depths of scour [-].

After integration of Eq. (13) and with new variables  $x = 1 + h_s/2h_f$ ,  $h_s = 2h_f(x - 1)$ , and  $dh_s = 2h_f dx$ , we obtain:

$$t = 4D_i h_f^2 (N_i - N_0), \tag{15}$$

where  $N_i = 1/6x_i^6 - 1/5x_i^5$  [-], and  $N_0 = 1/6x_0^6 - 1/5x_0^5 = -0.033$ —parameter to calculate scour formed during the previous time step [-].

Using Eqs. (10), (14) and (15), which contain equilibrium depth of scour, it is therefore possible to find the equilibrium time of scour near a water engineering structure:

$$t_{\text{equil}} = 4D_{\text{equil}} h_f^2 (N_{\text{equil}} - N_0), \tag{16}$$

where  $D_{\text{equil}} = 1/2(\pi m k^4)/(A_{\text{equil}} V_1^4)$  [-],  $N_{\text{equil}} = 1/6x_{\text{equil}}^6 - 1/5x_{\text{equil}}^5$  [-],  $x_{\text{equil}} = 1 + h_{\text{equil}}/2h_f$  [-], and  $h_{\text{equil}}$ —equilibrium scour depth [m].

The value of  $h_{\text{equil}}$  is determined by Gjunsburgs and Neilands (2001):

$$h_{\text{equil}} = 2h_f \left[ \left( \frac{V_1}{k \beta V_0} \right)^{0.8} - 1 \right] k_\alpha k_m, \tag{17}$$

where  $k_\alpha$ —a coefficient depending on the flow crossing angle (when  $\alpha = 90^\circ$ ,  $k_\alpha = 1$ ) [-], and  $k_m$ —a coefficient depending on the side-wall slope of the water engineering structure ( $k_m = 1$ ) [-].

Using the value of  $h_{\text{equil}}$ , it is possible to find values of  $A_{\text{equil}}$ ,  $D_{\text{equil}}$ ,  $N_{\text{equil}}$  and finally  $t_{\text{equil}}$ .

When the local flow velocity  $V_{lr}$  becomes equal to the recalculated critical flow velocity  $\beta V_{0r}$ , then  $A_{\text{equil}} = 0$ ,  $D_{\text{equil}} = \infty$  and  $t_{\text{equil}} = \infty$ . Criteria to evaluate the threshold are needed to appoint to calculate equilibrium time of scour near water engineering structures.

## 2.1 Threshold Criterion

Since the scouring process at hydraulic structures is never ending, threshold criteria are used for equilibrium time of scour calculation. The proposed threshold criteria for equilibrium time of scour known from the literature are only depending on the size of the structure, and not on hydraulic parameters of the flow. A new threshold criterion is needed to be proposed, depending on hydraulic parameters of the flow to calculate the equilibrium time of scour values for water engineering structures.

Ratio of the recalculated critical flow velocity to the local flow velocity at the head of the water engineering structure is proposed as the hydraulic threshold criterion in equilibrium time of scour calculations for water engineering structures.

Per computer-modeling results, the scour stops when the local flow velocity  $V_{lr}$  becomes equal to the recalculated critical flow velocity  $\beta V_{0r}$  or the ratio of those velocities becomes equal to 1, and the equilibrium is equal to infinity. Different values of the ratio of recalculated critical flow velocity to local flow velocity at the head of the water engineering structure were presumed for equilibrium time of scour calculation to find the best fit between computer modeled and calculated equilibrium time of scour values. Thus, the proposed equilibrium time of scour calculation threshold criterion for water engineering structures that showed the best agreement is equal to:

$$\frac{\beta V_{0r}}{V_{lr}} = \frac{\beta V_0}{V_1} \left( 1 + \frac{h_{\text{equil}}}{2h_f} \right)^{1.25} = 0.985. \quad (18)$$

## 3 Experiment Set-up

Tests for water engineering structures were carried out at the Transport Research Institute (Russia) in a flume 3.5 m wide and 21 m long (see Fig. 1). The tests were carried out under open-flow conditions, while studying the flow distribution between the channel and the floodplain. Tests were performed with rigid and sand

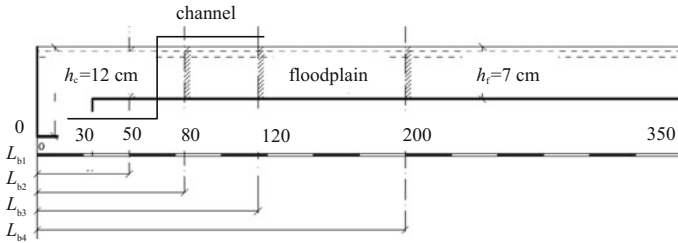


**Fig. 1** Cross-section view of the experiment flume

beds. The fixed bed tests were performed for different flow contractions and Froude numbers to investigate flow velocity and water level changes near the water engineering structure. The aim of the tests with a sand bed was to study scour processes, changes in flow velocity with time, effect of hydraulic parameters and contraction rate of the flow, grain size of the bed material, and scour development in time.

If the shape of a water engineering structure is rectangular, the flow is separated at the upstream edge of the structure; this creates water level changes at the structure and a backwater.

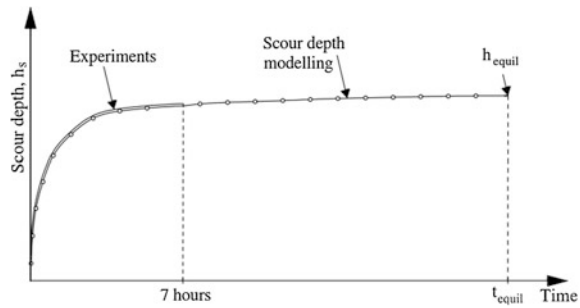
The openings of the water engineering structure model were 50, 80, 120, and 200 cm (see Fig. 1). Flow contraction rate  $Q/Q_b$  (where  $Q$  is the flow discharge, and  $Q_b$  is the discharge in the bridge opening under open-flow conditions) varied from 1.56 to 5.69 for the floodplain depth of 7 cm, and the Froude numbers varied from 0.078 to 0.124; the slope of the flume was 0.0012. The Froude number is calculated with the following equation:

$$Fr = \frac{V}{\sqrt{gh_f}}, \tag{19}$$

where  $V$ —mean approach flow velocity [ $m\ s^{-1}$ ].

The sand bed tests were carried out under clear-water conditions. The sand was placed 1 m up and down the contraction of the flume. The mean grain size was  $d_1 = 0.24$  mm and  $d_2 = 0.67$  mm. The condition that  $Fr_R = Fr_f$  was fulfilled, where  $Fr_R$  and  $Fr_f$  are the Froude numbers for the plain river and for the flume, respectively. The tests in the flume lasted for 7 h, the length scale was 50 and the time scale was 7. With respect to the real conditions, the test time was equal to 2 days. This was the mean duration of time steps into which the flood hydrograph was divided. Scour development was examined with different flow parameters in time intervals within one 7 h step and within two steps of the hydrograph, 7 h each. The tests were carried out with one floodplain model and one side contraction of the flow.

**Fig. 2** Scour computer-modelling principle



Experiment data by Gjunsburgs and Neilands (2001) and method for estimation of scour development in time during floods by Gjunsburgs and Neilands (2006), and Gjunsburgs et al. (2004, 2005) were used for computer modelling of scour depth development in time. Method for estimation of scour development in time during floods was confirmed by the experiment data of laboratory tests with duration of 7 h (Gjunsburgs and Neilands 2001).

By using computer modelling (see Fig. 2), the duration of water engineering structure laboratory tests of 7 h was prolonged until the scour depth development reached the equilibrium stage.

At the end of each time interval, there is a change in local flow velocity and in critical flow velocity, because of the changes in scour hole in the previous time interval. It means that with an increase of scour depth at the end of each time interval, current cross section increases, decreasing local flow velocity; on the other hand, critical flow velocity increases because of an increase of the total flow depth—sum of the initial flow depth and the scour depth developed in the previous time interval (see Fig. 3).

Since there is a necessity to re-calculate the scour depth in every time interval, in addition, time to reach the equilibrium stage can be up to a few days, the calculation of the scour depth development by the method of Gjunsburgs et al. (2004, 2005) is

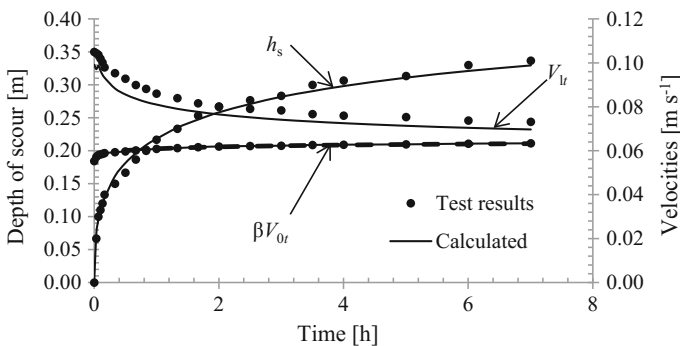


**Fig. 3** Change of local and critical flow velocities during scour development in time

mathematically complicated and long lasting; therefore, the program RoBo was used (Gjunsburgs et al. 2006). RoBo is a simple but powerful tool with a mathematical algorithm written in Microsoft® Excel® program. The following parameters must be put in: initial flow depth in the floodplain, flow contraction rate, maximum backwater, grain size, specific weight of the bed material, and thickness of the bed layers. After the calculation, we have: local flow velocity, critical flow velocity, and scour depth changes at the end of each time interval, as well as the calculated velocity coefficient, and the coefficient depending on flow contraction.

By using computer modelling (Gjunsburgs et al. 2006), the number of time intervals and duration of the simulations are not restricted. The key consideration here is to determine an appropriate criterion that limits the changes of scour depth in time to define the equilibrium stage for each of the experiment tests.

## 4 Results

For the same approach flow velocity and approach flow Froude number, but increasing contraction rate of the flow, relative depth of scour is increasing as the scour depth is increasing as well. Equilibrium time of scour is increasing as the scour depth keeps increasing as well for the same approach flow Froude number and increasing flow contraction (see Table 1).

Calculated values of equilibrium time of scour show a good agreement with the computer modeled equilibrium time of scour values, with sand grain size  $d_1 = 0.24$  mm (see Table 1).

However, taking a closer look at Table 1, several estimated equilibrium time of scour values from Tests AL4, AL8 and AL12 seem to be over and under evaluated (by more than 10%) in comparison with the computer modeled equilibrium time of scour values, since their percent relative error is 15.63%, 10.88% and  $-10.39\%$ , respectively.

**Table 1** Computer modeled and calculated results, sand grain size  $d_1 = 0.24$  mm

TEST	$Q/Q_b$	$h_{equil}/h_f$	$Fr$	$t_{comp}$ [h]	$t_{form}$ [h]	$t_{form} / t_{comp}$	$\varepsilon$ [%]
AL1	5.27	2.31	0.078	99.00	95.93	0.97	-3.10
AL2	5.69	3.04	0.103	190.00	183.66	0.97	-3.34
AL3	5.55	3.30	0.124	228.00	238.78	1.05	4.73
AL4	3.66	1.69	0.078	103.00	119.10	1.16	15.63
AL5	3.87	2.33	0.103	144.00	152.02	1.06	5.57
AL6	3.78	2.83	0.124	172.00	158.37	0.92	-7.92
AL7	2.60	0.96	0.078	48.00	46.85	0.98	-2.40
AL8	2.69	1.58	0.103	93.00	103.12	1.11	10.88
AL9	2.65	1.98	0.124	100.80	95.63	0.95	-5.13
AL10	1.56	0.38	0.078	12.40	11.42	0.92	-7.90
AL12	1.67	0.77	0.124	36.00	32.26	0.90	-10.39

On the other hand, the rest of the calculated equilibrium time of scour values from Table 1 show a very close agreement with the computer modeled ones, particularly highlighting estimated equilibrium time of scour values from Tests AL1, AL2 and AL7, where the percent relative error in comparison with the experimentally derived ones is just  $-3.10\%$ ,  $-3.34\%$  and  $-2.40\%$ , respectively.

The average percent relative error for data set of water engineering structure tests with sand grain size  $d_1 = 0.24$  mm is  $7.0\%$  (see Table 1).

### 4.1 Theoretical Analysis

To analyze the equilibrium time of scour estimation method for water engineering structures, Eqs. (14) and (16) are transformed to a form that shows clearly that they contain dimensionless parameters and characteristics of the flow and riverbed:

$$N_{\text{equil}} = \frac{t_{\text{equil}}}{4D_{\text{equil}}h_f^2} + N_0. \tag{20}$$

Equation (20) is transformed into a more detailed form, expressing the parameter  $D_{\text{equil}}$ :

$$N_{\text{equil}} = \frac{2t_{\text{equil}}A_{\text{equil}}\varphi^4g^2\Delta h^2}{\pi mk^4 h_f^2} + N_0. \tag{21}$$

In general form, Eq. (21) for water engineering structures can be written as:

$$N_{\text{equil}} = \frac{2A_{\text{equil}}\varphi^4g^2h^2}{\pi mk^4 h_f^2} \frac{1}{\left(\frac{d}{h_f}\right)^{0.25}}, \tag{22}$$

$$\left\{ \frac{P_k}{2} \left[ \left(\frac{Q}{Q_b}\right)^2 - 1 \right] + \frac{1}{2}P_{kb} \sqrt{\frac{1}{Fr}} \left[ \left(\frac{Q}{Q_b}\right)^2 + 1 \right] + P_{kb} \right\}^2 t_{\text{equil}} + N_0$$

where  $P_k = V_k^2/gh$ —kinetic parameter of flow in contraction in open-flow conditions [-],  $V_k$ —flow velocity in contraction [ $\text{m s}^{-1}$ ],  $P_{kb} = V^2/gh_f$ —kinetic parameter of the open flow in natural conditions [-],  $Fr/i$ —ratio of the Froude number to the river slope [-], and  $d/h_f$ —dimensionless sand grain size [-].

From Eq. (22), the equilibrium time of scour is expressed and it reads as follows:

$$t_{\text{equil}} = \frac{(N_{\text{equil}} - N_0)(\pi mk^4 h_f^2) \left(\frac{d}{h_f}\right)^{0.25}}{\left\{ \frac{P_k}{2} \left[ \left(\frac{Q}{Q_b}\right)^2 - 1 \right] + \frac{1}{2}P_{kb} \sqrt{\frac{1}{Fr}} \left[ \left(\frac{Q}{Q_b}\right)^2 + 1 \right] + P_{kb} \right\}^2 2A_{\text{equil}}\varphi^4g^2h^2}. \tag{23}$$

In general form, the equilibrium time of scour is a function of the following parameters:

$$t_{\text{equil}} = f\left(\frac{Q}{Q_b}; P_k; P_{kb}; \frac{Fr}{i}; \frac{d}{h_f}; \frac{\beta V_0}{V_1}; \frac{h}{h_f}; \frac{h_{\text{equil}}}{h_f}\right). \tag{24}$$

Theoretical analysis of the developed equilibrium time of scour calculation method (Eq. 16) was made and it showed that equilibrium time of scour depends on flow contraction rate, kinetic parameter of flow in contraction in open-flow conditions, kinetic parameter of the open flow, ratio of the Froude number to the river slope, dimensionless sand grain size, ratio of the recalculated critical flow velocity to the local flow velocity, relative flow depth, and relative scour depth (Eq. 24).

### 4.2 Graphical Analysis

Laboratory experiment data (Gjunsburgs and Neilands 2001) and calculation results of the suggested equilibrium time of scour estimation method (Eq. 16) for water engineering structures were used to show the impact of hydraulic and riverbed parameters on equilibrium time of scour.

The points in the graphs (Figs. 4, 5, 6 and 7) indicate the calculated and computer modeled equilibrium points, where equilibrium time and scour have been achieved.

Flow contraction creates a series of events that also have an impact on equilibrium time of scour; thereby, if the flow contraction rate increases, equilibrium time of scour increases as well; consequently, the greater the contraction rate of the flow value is, the greater the equilibrium time of scour value becomes. Since finer sand particles are more easily scoured away, it takes longer time to achieve equilibrium stage than it is with coarse sand (see Fig. 4).

When the scouring process continues in the scour hole, it takes longer time to achieve time to equilibrium scour. In the case of coarse sand, the depth of scour is achieved faster, thus resulting in a lesser relative depth of scour and at the same time lesser time to equilibrium scour; however, with fine sand on the contrary, it takes more time to achieve equilibrium scour depth, since the scour depth continues

**Fig. 4** Contraction rate of the flow impact on equilibrium time of scour

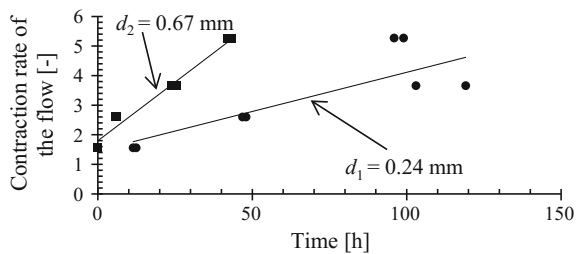


**Fig. 5** Relative depth of scour impact on equilibrium time of scour

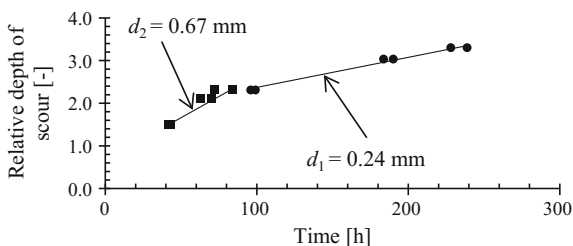


**Fig. 6** Froude number influence on equilibrium time of scour

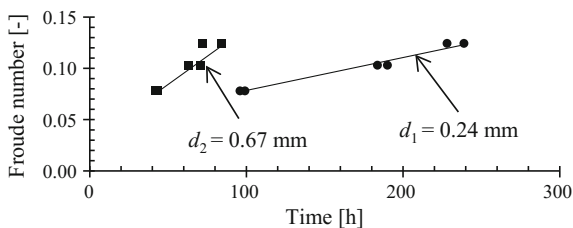
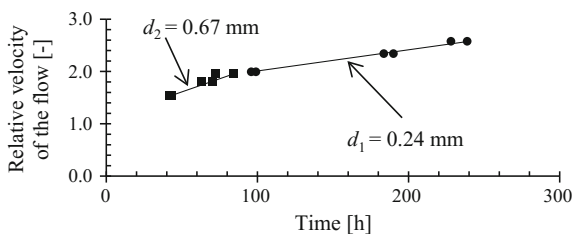


**Fig. 7** Relative velocity of the flow influence on equilibrium time of scour



to increase, consequently increasing the relative depth of scour. The relative depth of scour relates to equilibrium time of scour in a direct way—if the relative depth of scour becomes greater, the equilibrium time of scour increases as well (see Fig. 5).

With an increase in Froude number, there is also an increase in equilibrium time of scour; the greater the Froude number value becomes, the further the scouring process continues in the scour hole, resulting also in an increased equilibrium time of scour. With fine sand, the equilibrium time is greater, and the scouring process takes longer to achieve the equilibrium stage; with coarse sand, on the other hand, the scouring process ends more quickly, resulting in lesser equilibrium time of scour value (see Fig. 6).

Since coarse sand particles are heavier, it takes more energy to scour them away, so with an increase of relative velocity of the flow the increase in equilibrium time of scour is medium, while for fine sand the increase in equilibrium time is more accelerating with an increase of relative velocity of the flow. So, the greater the local flow velocity is and, at the same time, the smaller the recalculated critical flow velocity for the fine sand is, the greater the equilibrium time of scour will become (see Fig. 7).



## 5 Conclusions

The proposed threshold criteria for the equilibrium time of scour known from the literature are only depending on the size of the hydraulic structure, and not on hydraulic parameters of the flow.

The differential equation of the bed sediment movement in clear-water conditions was used and a new equilibrium time of scour evaluation method for water engineering structures with and without flow separation at the structure in river floodplains was worked out (Eq. 16).

Ratio of the recalculated critical flow velocity to the local one at the head of the water engineering structure was proposed as the hydraulic threshold criterion in equilibrium time of scour calculation, equal to  $\beta V_{Or} / V_{lr} = 0.985$  (Eq. 18).

Calculated and computer modeled water engineering structure test data revealed that with an increase in flow contraction rate and with an increase in approach flow Froude number, equilibrium time of scour increases as well (Table 1). Calculated and computer modeled equilibrium time of scour value comparison showed good agreement.

Theoretical analysis of the developed calculation method (Eq. 16) showed that equilibrium time of scour depends on: flow contraction rate; kinetic parameter of flow in contraction in open-flow conditions; kinetic parameter of the open flow; ratio of the Froude number to the river slope; dimensionless sand grain size; ratio of the recalculated critical flow velocity to the local flow velocity; relative flow depth; and relative scour depth (Eq. 24).

Graphical hydraulic and riverbed parameter dependence analysis of the developed calculation method results showed that equilibrium time of scour depends on: flow contraction rate; relative depth of scour; Froude number; and relative velocity of the flow (Figs. 4, 5, 6 and 7).

## References

- Alfieri L, Burek P, Feyen L, Forzieri G (2015) Global warming increases the frequency of river floods in Europe. *Hydrol Earth Syst Sci* 19(5):1119–1152
- Barredo JI (2007) Major flood disasters in Europe: 1950–2005. *Nat Hazards* 42(1):125–148
- Coleman SE, Lauchlan CS, Melville BW (2003) Clear water scour development at bridge abutments. *J Hydraul Res* 43(4):445–448
- Fael C, Cardoso A (2008) Evolution of scour at comparatively long vertical-wall abutments under clear-water flow conditions. *River Flow 2008*:1593–1599
- Gjunsburgs B, Neilands R (2006) Local velocity at bridge abutments on plain rivers. *Proc Int Conf Fluv Hydraul River Flow 2*:1649–1655
- Gjunsburgs B, Neilands R (2001) Scour development on time at the abutment of the bridge on plain rivers. *Proc Conf Environ Res Eng Manag* 1(15):8–11
- Gjunsburgs B, Neilands R, Kreslins A (2005) Abutment scour development during floods. In: *Proceedings of 17th Canadian hydrotechnical conference—hydrotechnical engineering: cornerstone of a sustainable environment*, pp 593–601

- Gjunsburgs B, Neilands R, Neilands Rj (2004) Scour development at bridge abutments on plain rivers during the flood: analysis of the method. In: Proceedings of 2nd international conference on scour and erosion, pp 199–206
- Gjunsburgs B, Neilands Rj, Govsha E (2006a) Local scour at elliptical guide banks. In Proceedings of 3rd international conference on scour and erosion, pp 235–239
- Gjunsburgs B, Rj Neilands, Govsha E (2006b) Local scour at elliptical guide banks in plain rivers. Proc Conf Fluv Hydraul River Flow 2006:1649–1655
- Grimaldi C, Gaudio R, Cardoso AH, Calomino F (2006) Local scouring at bridge piers and abutments: time evolution and equilibrium. Proc Int Conf Fluv Hydraul River Flow 2:1657–1664
- Levi II (1969) Dynamics of river flow. *Gidrometeoizdat* (in Russian)
- Melville BW, Chiew YM (1999) Time scale for local scour at bridge piers. *J Hydraul Eng* 125 (1):59–65
- Rozovskyi IL (1956) Calculation of critical velocity at the bend of wide canals. In: Proceedings of the institute of hydrology and hydrotechnics. Academy of Science of Ukraine (in Russian)
- Studenitnikov BI (1964) Flow erosion capacity and riverbed evaluation methods. *Gostroizdat* (In Russian). p 184
- Territorial Dynamics in Europe: Natural Hazards and Climate Change in European Regions (2013) Territorial Observation No. 7, p 28

# LDV Measurements of the Flow Induced by an Elongated Bridge Pier: The Fixed Bed Case

Maria M. C. L. Lima, Elsa Carvalho and Rui Aleixo

**Abstract** Elongated piers are a commonly found geometry in bridge pier design. This paper addresses the study of the flow around an elongated bridge pier, since not many studies exist concerning this geometry. To better understand the features of such pier geometry a set of measurements made upstream and downstream of an elongated bridge pier are presented. Mean and turbulent variables are presented and emphasis is given to the flow downstream of the elongated bridge pier. Results show a clockwise recirculation pattern downstream of the bridge pier and Strouhal numbers higher than those found for a circular cylinder. Along the flow axis, turbulent fluctuation clouds change in shape, when moving further downstream from the pier.

## 1 Introduction

The external turbulent flow around a circular cylinder is a well known typical fluid mechanics problem, which involves a circular wall boundary and a two-dimensional flow. Usually, an infinite cylinder is considered (e.g. Williamson 1996), with the cylinder wake characterized by the von Kármán vortex street and vortex shedding (Kasten et al. 2010; Ponta 2010). The cylinder can also be mounted on a flat bottom,

---

M. M. C. L. Lima (✉)  
Escola de Engenharia da Universidade do Minho,  
Campus de Azurém, 4800-058 Guimarães, Portugal  
e-mail: mmlima@civil.uminho.pt

E. Carvalho  
Faculdade de Engenharia da Universidade do Porto,  
Rua Dr. Roberto Frias s/n, 4200-465 Porto, Portugal  
e-mail: elsac@fe.up.pt

R. Aleixo  
Interdepartmental Centre for Industrial Research in Building  
and Construction - Fluid Dynamics Unit, University of Bologna,  
Via Del Lazzaretto 15/5, 40131 Bologna, Italy  
e-mail: rui.aleixo@unibo.it

and consequently be immersed in a plane boundary layer, case that corresponds to the flow around a bridge pier. In this case, the strong interaction between structure, flow and turbulent boundary layer originates a highly turbulent and three-dimensional flow. In case of a river alluvial bed, this interaction may result in bridge pier scour (Roulund et al. 2005), and cause the partial or total loss of bridges (Dey and Raikar 2007).

The flow around circular piers has been the subject of a large number of studies (e.g. Dargahi 1989; Graf and Yulistiyanto 1998; Roulund et al. 2005). The main features of the flow are a stagnation line in the face of the pier, which causes an elevation of the free surface and an adverse pressure gradient. In the face of the pier, a strong downflow is observed. In this flow region, the radial velocity becomes insignificant in case the flow Froude number, based on the mean longitudinal approach velocity and the water depth, is relatively low ( $Fr \approx 0.2$ ) (Roulund et al. 2005). The adverse pressure gradient is responsible for the boundary layer separation, which originates a horseshoe vortex (Roulund et al. 2005) or horseshoe vortex system (Fu and Rockwell 2005; Kirkil and Constantinescu 2009) near the bottom upstream of the pier. The size of the horseshoe vortex grows with the ratio between the boundary layer thickness,  $\delta$ , and the pier diameter,  $D$ . For a small value of this ratio,  $\delta/D \ll 0.01$ , the boundary layer may not separate and no horseshoe vortex is generated (Roulund et al. 2005). Downstream of the pier, caused by the rotation of the boundary layer over the piers' surface, lee-wake vortices are observed (Roulund et al. 2005). In this region turbulence intensities increase significantly (Graf and Yulistiyanto 1998).

Only few studies are available for non-circular piers, although a great number of bridge piers are not circular (Richardson and Davies 2001). The relatively scarce number of studies on the flow induced by an elongated bridge pier, when compared with cylindrical piers, was the motivation for this work. The first goal of this paper is to obtain insights about the flow induced by a rectangular round nosed pier over a fixed rough rigid bed, using laser Doppler velocimetry (hereafter LDV). LDV was the chosen measurement technique because it allows to do fine measurements of turbulence with good temporal and spatial resolutions (e.g. Tropea et al. 2007).

This article presents experimental results of mean velocities and turbulence intensities that cannot be found in the work of Roulund et al. (2005) and that may contribute to a deeper understanding of the flow around a bridge pier. This is the first part of a wider project on the flow induced by an elongated bridge pier, involving not only fixed bed but loose bed as well, in which case scour is expected to be observed. The flow field characterized in this paper corresponds to the instantaneous flow field around a bridge pier in the initial instant of scour, and can be used to obtain an experimental data base useful in the numerical developments of the project, namely for calibration and code validation.

The experimental set-up and measuring equipment are described in the following section. The results and their discussion are presented in Sect. 3. Section 4 is the final section, with the main conclusions.

## 2 Experimental Set-Up

### 2.1 Experimental Rig

Experiments were conducted in a 0.4 m wide ( $B$ ) and 16.7 m long water channel at the Hydraulics Laboratory of the Civil Engineering Department of the Faculty of Engineering of the University of Porto. The channel had a horizontal bottom and the test section was installed approximately 9.7 m downstream of the beginning of the flume. The flow rate was controlled by a gate valve and measured by an electromagnetic flow meter. Water depth was controlled by a sluice gate at the downstream section of the flume. The flume was operated as a closed circuit, with the water supplied by a constant head reservoir in order to absorb fluctuations originated by the elevation centrifugal pumps.

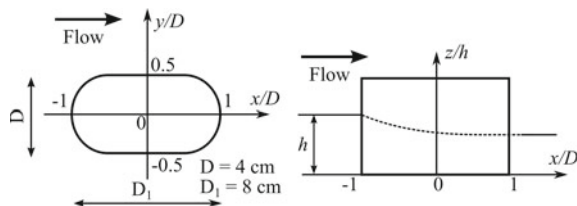
The test section consisted of a rectangular vertical pier with round nose shapes, mounted on a steady and uniform free surface flow. The pier was 4 cm wide ( $D$ ) and 8 cm long ( $D_1$ ) (Fig. 1), oriented in the longitudinal channel direction. To minimize the blockage effect of the pier (Roulund et al. 2005; Tafarojnoruz et al. 2012),  $B/D = 10$  was considered. The pier was placed in the middle of an acrylic plate 1.8 m long, where a uniform thin sand layer, with 0.376 mm mean diameter, was glued. The measurement grid is depicted in Fig. 2.

### 2.2 Flow Conditions

Two flow conditions, defined by two different flow rates,  $Q$ , are indicated in Table 1, together with the mean velocity,  $U$ , the flow depth at  $x/D = -6$ ,  $h$ , the flow Froude  $Fr = U/\sqrt{gh}$  and the flow and pier Reynolds numbers, given by  $Re_h = UR_h/\nu$  and  $Re_p = UD/\nu$ , respectively, where  $R_h$  is the hydraulic radius. The mean velocity was calculated with the water depth measured at  $x/D = -6$ .

With the considered flow parameters, namely the flow Reynolds number,  $Re_h$  and flow depth, it was estimated that the entrance length was about 3.2 m (White 1994). Since the pier model was placed 9.7 m away from the channel entrance, the flow can be considered established.

**Fig. 1** Pier scheme and coordinate scheme for the LDV measurements



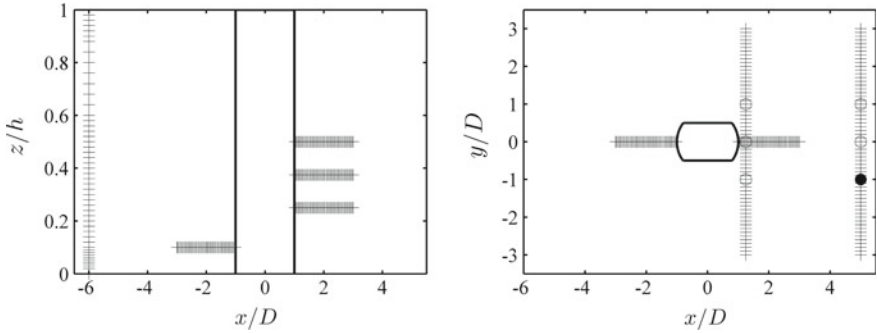


**Fig. 2** Measurement grid used for the measurements: side view and top view. Circles indicate the locations where the quadrant analysis was made. Black circle where the spectrum was determined

**Table 1** Experimental flow conditions tested defined by the flow rate,  $Q$ , the mean velocity,  $U$ , the flow depth,  $h$ , the Froude number,  $Fr$ , and the flow and pier Reynolds number  $Re_h, Re_p$  respectively. Flow height measured at  $x/D = -6$

Condition	$Q$ [ $\text{m}^3 \text{s}^{-1}$ ]	$U$ [ $\text{m s}^{-1}$ ]	$h$ [m]	$Fr$	$Re_h$	$Re_p$
C1	0.0034	0.17	0.05	0.24	5822	5822
C2	0.005	0.25	0.05	0.36	8733	8733

### 2.3 The Laser Doppler Velocimeter (LDV)

Measurements were made using a two-component laser Doppler velocimeter. The optical system included a 40 MHz frequency shifter and colour separation, combined with an 85 mm probe, beam expander and 500 mm front lens. The system was operated in forward scatter mode, with a colour separator that split the collected light into two wavelengths before reaching the corresponding photomultipliers. LDV data processing and acquisition was performed using Dantec BSA F60 Flow Analyser. Simultaneous measurements of stream wise longitudinal (horizontal) and vertical velocities were made using the overlapped coincidence method. Every point was measured with at least  $32768 (= 2^{15})$  particles with a data-rate of about 100 particles per second. It was verified that the existing particles in the water were enough for the LDV measurements. Positive horizontal velocity corresponded to the direction of flow, and positive vertical velocity corresponded to the upwards direction. No measurements of vertical velocities were possible at distances from the boundaries smaller than 5 mm, because laser beams were blocked by the flat bottom and water free surface. No measurements of horizontal velocities were possible at distances from the pier smaller than 2.5 mm, because laser beams were blocked by the pier.

To post-process the LDV data a Matlab toolbox dedicated to LDV signal processing (Aleixo et al. 2016) was used.

### 3 Experimental Results and Discussion

#### 3.1 Upstream Flow Characterization

Measurements were made to characterize the undisturbed incoming flow upstream of the bridge pier, at section  $x/D = -6$ . The non-dimensional velocity profile for the mean horizontal ( $u$ ) and vertical ( $w$ ) components are presented in Fig. 3. Figure 3 also presents the associated turbulence intensities ( $\sqrt{\overline{u'^2}}$  and  $\sqrt{\overline{w'^2}}$ ), calculated based on the mean (indicated by the overbar) of the horizontal ( $u'$ ) and vertical ( $v'$ ) velocity components' fluctuations. From the measurements it was possible to conclude that the mean vertical component was negligible, i.e.,  $w/u \approx 0$ .

The shear velocity was calculated using the logarithmic region of the law of the wall for the two flow conditions at  $x/D = -6$ . For conditions C1 and C2 the calculated shear velocity values were  $u_{*1} = 0.0096 \text{ m s}^{-1}$  and  $u_{*2} = 0.0139 \text{ m s}^{-1}$  corresponding to  $Re_{*1} = 3.58$  and  $Re_{*2} = 5.16$ . The flow is therefore turbulent smooth for both conditions. For smooth channel flows, the logarithmic method results were

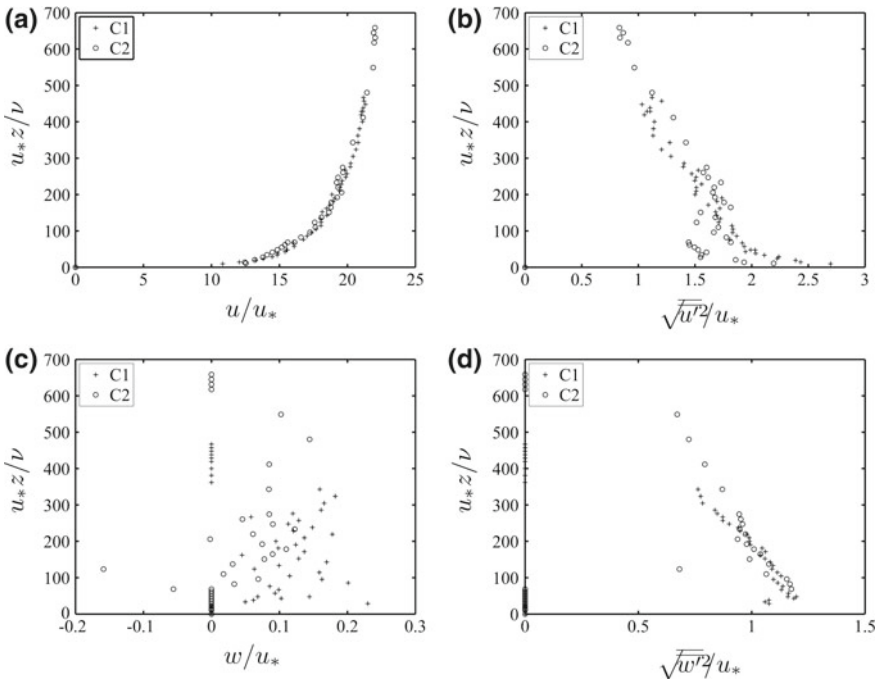


**Fig. 3** Non-dimensional vertical profiles of **a** the mean horizontal velocity component  $u/u_*$ , **b** the associated non-dimensional rms profile, **c** the mean vertical velocity component  $w/u_*$ , and **d** the associated non-dimensional rms profile, for both conditions at  $x/D = -6$

found in good agreement (mean differences less than 5%) with direct measurements using a laser Doppler shear stress probe (Carvalho et al. 2010; Carvalho 2013).

To understand how the approaching flow behaved, a longitudinal upstream profile was measured at  $z/h = 0.1$  for both conditions, C1 and C2. Figure 4 shows  $u/u_a$  and  $w/w_p$ ; the turbulent fluctuations rms and the Reynolds shear stresses,  $(\overline{u'w'})$ , are depicted in Fig. 5. To scale the horizontal mean component, the mean velocity (respectively rms) at the first measurement point,  $u_a$  (respectively  $\sqrt{\overline{u'^2}_a}$ ) was used. The mean vertical component was scaled with the mean vertical velocity (respectively rms) measured at the closest point to the pier  $w_p$  (respectively  $\sqrt{\overline{w'^2}_p}$ ).

The flow decelerates as it approaches the pier, and is deflected towards the bottom (Fig. 4). Note that the dimensionless ratio  $w/w_p$  is always positive because  $w_p$  is negative, i.e. directed towards the bottom. The pier is detected further upstream in the  $u$  component at  $x/D = -2.7$ , whereas the  $w$  component shows the pier effect only for distances smaller than  $1.8D$ . At the same distance from the bottom, Roulund et al. (2005) observed that, in their rough rigid bed case, the influence of a circular pier in the horizontal and vertical velocities components occurred at  $x/D = -2.6$  and  $-0.4$ , respectively.

The changes in the horizontal and vertical velocities fluctuations are more subtle than the ones observed in the mean flow (Fig. 5). The turbulent velocity components increase as the flow reaches the pier. Maxima in  $\sqrt{\overline{u'^2}}$  are observed at  $x/D = -1.15$  for both flow conditions. Maxima in  $\sqrt{\overline{w'^2}}$  occur immediately upstream the pier at  $x/D = -1$ . The horizontal component turbulence intensity, defined as  $\sqrt{\overline{u'^2}}/u_a$ , allows direct comparison with the results of Dargahi (1989). Based on the results of Fig. 5, it is possible to conclude that the turbulence intensity is slightly higher for condition C1. The influence of the pier manifests itself in the increase of this quantity, that occurs at  $x/D = -2.0$ , for both conditions. In the case of condition C1, a relative maximum of the  $u$  component turbulence intensity, equal to 0.2, is observed at  $x/D \approx -1.18$ . Other relative maxima, equal to 0.2, are observed both at  $x/D \approx -1.7$  and  $-1.18$ , in case of condition C2. These relative maxima are of smaller intensity, when compared with the results of Dargahi (1989), who observed values of the order of 0.8–0.9. Immediately upstream of the pier, vertical component turbulence intensity presents absolute maxima values approximately equal to 0.25, for both conditions.

Figure 5 also shows the longitudinal profile of Reynolds shear stresses. Usually, in free surface flows,  $u'$  and  $w'$  are correlated negatively, as occurs for distances from the piers' nose higher than  $1.125D$ . Closer to the pier, the Reynolds shear stresses evidence a minimum negative value at  $x/D = -1.3$  followed by two maxima in case of flow condition C2. In case of flow condition C1 the absolute maximum occurs immediately upstream the pier ( $x/D = -1$ ) and at  $x/D \approx -1.8$  a relative maximum is also observed. Near the bottom, positive Reynolds shear stresses correspond to negative bed shear stresses, which according to the work of Roulund et al. (2005) are



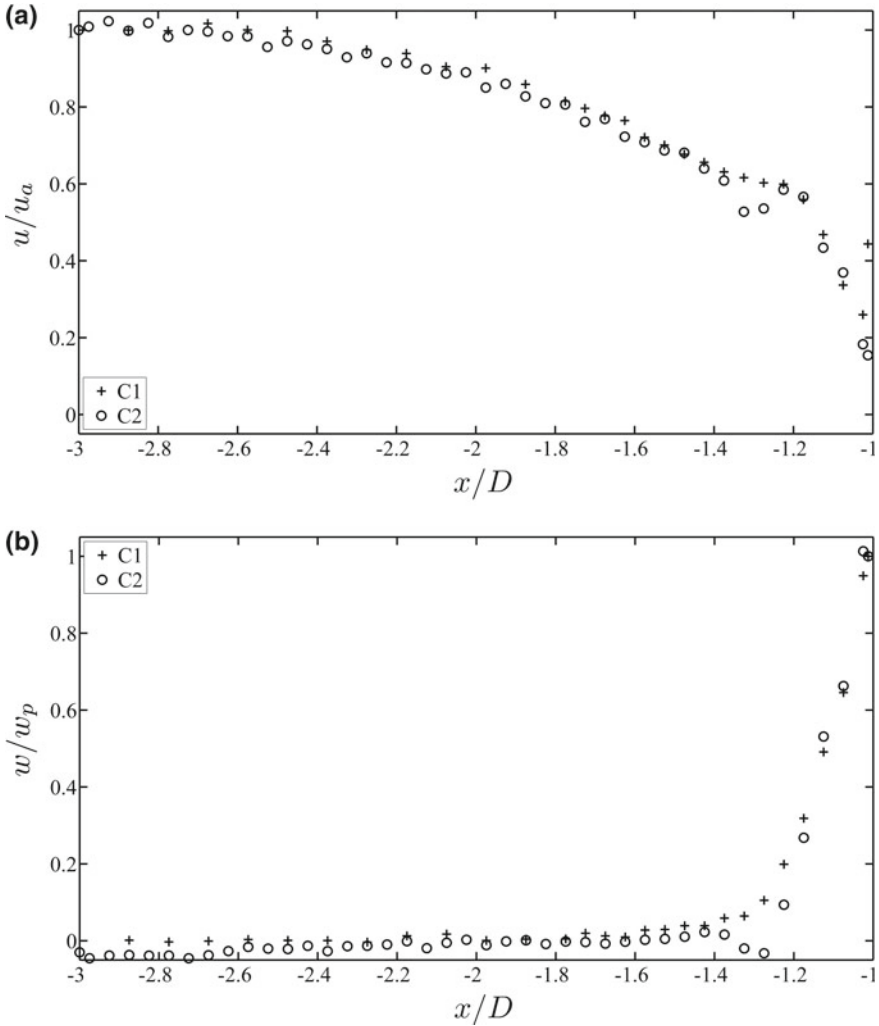


**Fig. 4** Non-dimensional longitudinal profiles of the mean velocities components,  $u$  and  $w$ , for  $z/h = 0.1$ , for both conditions. The horizontal component,  $u$ , was scaled using  $u_a$ , the velocity at the first measurement point, whereas the vertical component,  $w$ , was scaled using  $w_p$ , the velocity immediately upstream the pier

an indication of the existence of the horseshoe vortex in front of the pier. Upstream a circular pier, Graf and Yulistiyanto (1998) report a tendency of Reynolds shear stresses to become positive very close to the bed. Reynolds shear stresses are smaller in case of the round extremities pier when compared with the circular pier case. The present results provide deeper insight into the turbulence production and dissipation upstream the pier.

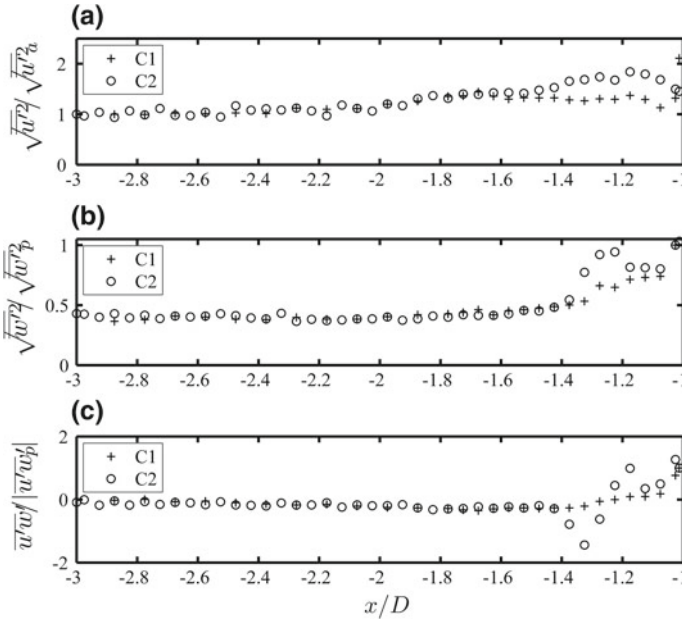


**Fig. 5** Non-dimensional longitudinal profiles for the turbulence components,  $\sqrt{u'w'}$  and  $\sqrt{w'^2}$  and  $(u'w')$  for  $z/h = 0.1$ , for both conditions. The horizontal component,  $\sqrt{u'^2}$ , was adimensionalized using the fluctuation rms measured at the first measurement point  $\sqrt{u'^2_a}$ , whereas the  $\sqrt{w'^2}$  and  $(u'w')$  variables were scaled using, respectively,  $\sqrt{w'^2_p}$  and  $(u'w')_p$  measured immediately upstream the pier

### 3.2 Downstream Flow and Wake Characterization

For a global view of the flow downstream the pier, several velocity profiles of  $u$  and  $w$  components were measured for both flow conditions, C1 and C2, at different locations. These measurements were organized in a vector plot for better clarity and depicted in Fig. 6. Despite the coarse measurement grid used it is possible to observe that: (a) immediately downstream the pier, the flow possesses a strong vertical component; (b) the recirculation zone shows a clockwise rotation sense for both conditions, also observed by Roulund et al. (2005) in the case of a rough rigid bed; (c) the recirculation zone ends at about  $x/D \approx 2.5$ .

#### 3.2.1 Longitudinal and Transverse Profiles

To further characterize the flow downstream of the pier, three longitudinal downstream profiles were measured at different heights:  $z/h = 0.25, 0.5$  and  $0.75$ . The

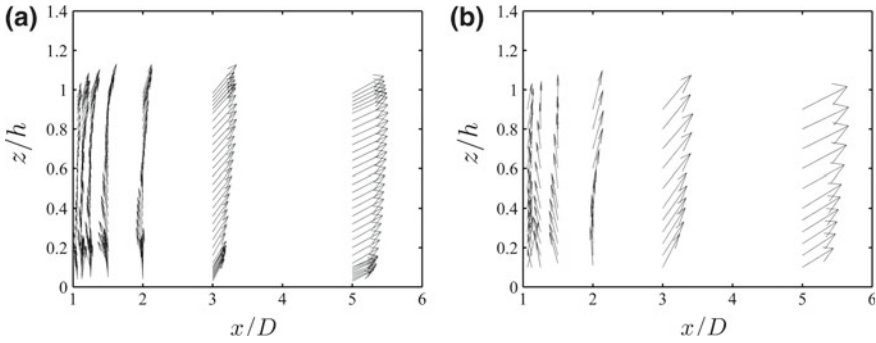


Fig. 6 Velocity vector maps for a Condition C1 and b Condition C2

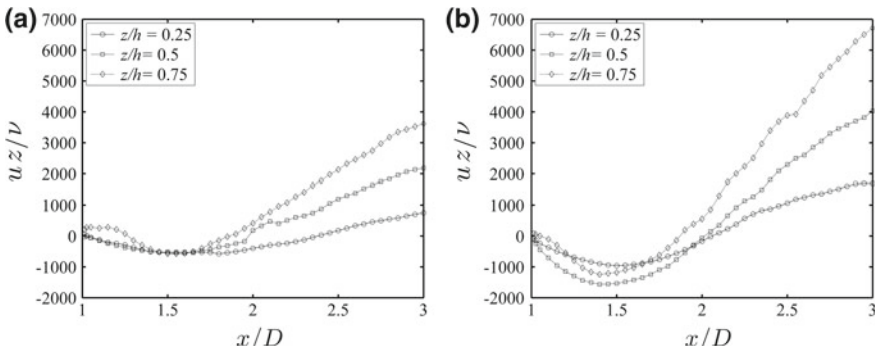
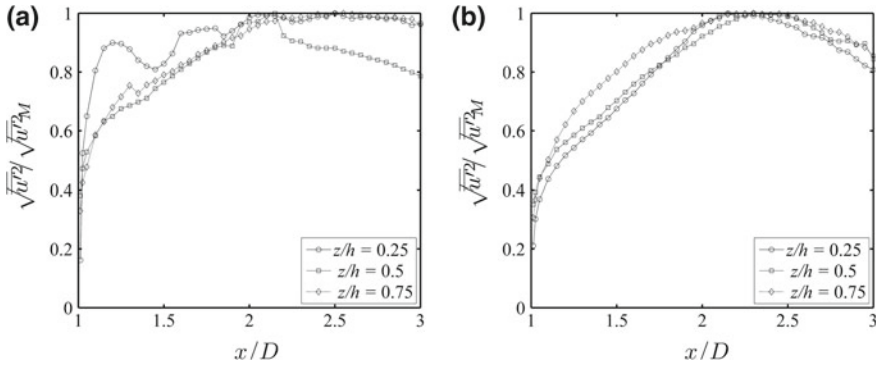


Fig. 7 Non-dimensional longitudinal profiles for the horizontal mean component,  $u$  for both conditions at three different heights

results are depicted in Figs. 7 and 8. In order to compare the different heights within the same condition, and to compare between conditions, the following scaling was adopted: mean variables  $u$  and  $w$  where scaled with  $(z/\nu)$  (Fig. 7) and turbulent quantities were scaled using the respective maximum value (Fig. 8).

From Fig. 7a, condition C1, it is possible to see that there is a narrow region where the longitudinal profiles collapse, however, the same is not observed for condition C2 (Fig. 7b). From Fig. 8, by identifying the points where  $uz/\nu = 0$ , it is possible to obtain a better estimation for the recirculation zone length along the centreline. For condition C1 one has  $x/D = 2.38$  for  $z/h = 0.25$  and for condition C2,  $x/D = 2.06$  for  $z/h = 0.25$ . A proper determination of the recirculation region requires a finer measurement grid.

The longitudinal profiles of the rms of the horizontal velocity component fluctuations are depicted in Fig. 8. Both conditions, C1 and C2, globally have the same behaviour: increasing from  $x/D = 1$  to  $x/D \approx 2.2$  and then decreasing, however the profile measured at  $z/h = 0.25$  for condition C1 seems oscillating, suggesting that there was probably a problem with the measurements of this profile. For condi-



**Fig. 8** Non-dimensional longitudinal profiles for the horizontal rms component,  $\sqrt{\overline{u'^2}}$ , for both conditions at three different heights, adimensionalized using the maximum of the fluctuation rms  $\sqrt{\overline{u'^2}_M}$

tion C2 the three measured profiles followed the same trend. For this condition the maximum of the rms values was obtained at  $x/D \approx 2.3$ .

The bridge pier effect in the flow was also investigated by means of transverse profiles measured at sections:  $x/D = 1.25$  and  $5$ . At these sections three different heights were chosen:  $z/h = 0.25, 0.50$  and  $0.75$ . As an example, the mean velocity component at  $x/D = 1.25$  and  $x/D = 5$  for  $z/h = 0.125$  is depicted in Fig. 9. To better visualize the pier effect the profiles are represented as  $1 - u/u_o$ , where the index  $o$  indicates the first measured point of the profile, corresponding to the non-disturbed flow. For  $x/D = 1.25$  it is possible to see that the pier effect is limited to a region smaller than the pier's diameter. With increasing distance downstream from the pier it is possible to observe the dissipation of the pier effect on the velocity field. Figure 9 shows that the depicted profiles have an approximate Gaussian shape. By fitting a Gaussian curve  $(1 - u/u_o) = \exp(-\alpha(y/D)^2)$  to each profile, the influence of the elongated bridge pier on the transverse velocity profile can be estimated by means of the parameter  $\alpha$ . This parameter plays the role of the standard deviation and can be seen as an attenuation factor. The evolution of  $\alpha$  as a function of  $x/D$  is depicted in Fig. 9b. The obtained expressions were:  $\alpha = 0.3896x/D, R^2 = 0.949$  and  $\alpha = 0.3072x/D, R^2 = 0.967$ , for conditions C1 and C2, respectively.

### 3.2.2 Quadrant Analysis

Quadrant analysis was employed to study the turbulence wake downstream of the bridge pier. The velocity fluctuation components  $u'$  and  $w'$  were plotted in a four quadrant Cartesian plot, according to the signal of the two components. For condition C2 the results are presented in Figs. 10 and 11, for  $x/D = 1.25$  and  $x/D = 5$ , respectively. To better interpret the results, the 95% confidence level ellipses were

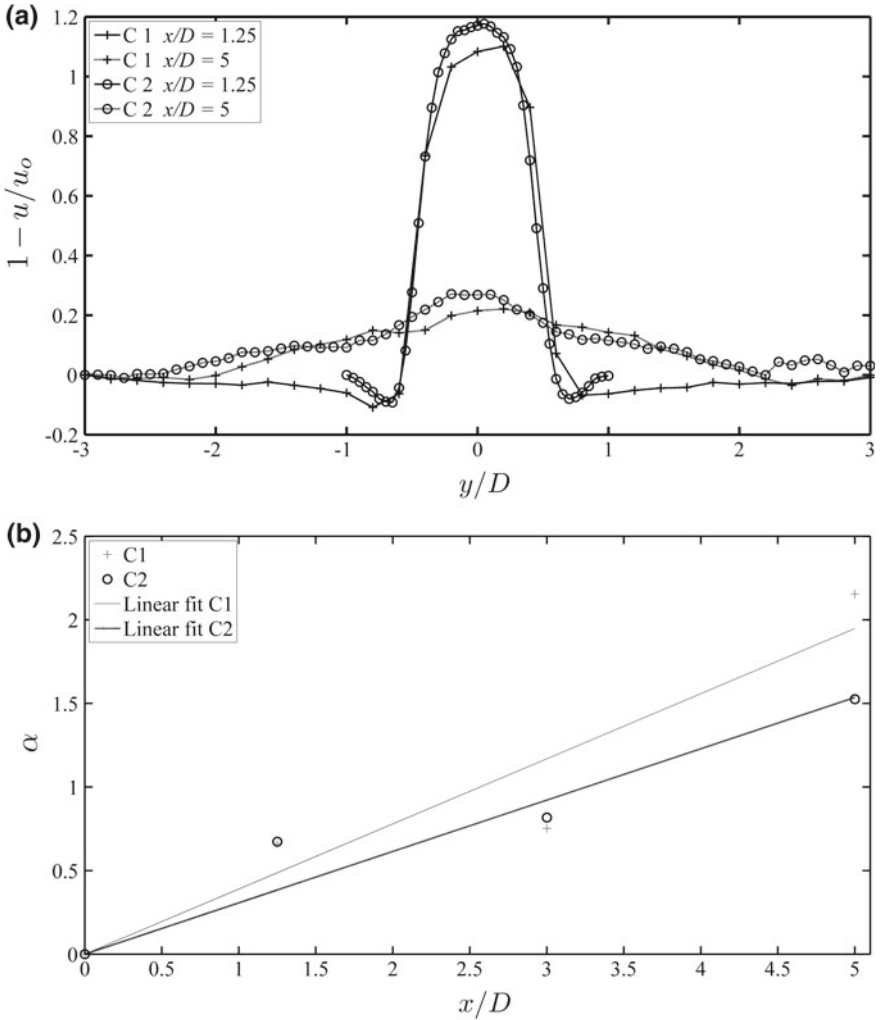


**Fig. 9** **a** Non-dimensional transverse profile of  $u$  at  $x/D = 1.25$  and  $5$  for  $z/h = 0.125$  and **b** Evolution of  $\alpha$  with  $x/D$

drawn to enclose the region of the  $u' - w'$  plane that contains 95% of all samples. For both figures it is possible to see that the cloud patterns obtained for  $y/D = \pm 1$  are quite similar for both distances from the pier, but with an increased dispersion of the  $u'$  and  $w'$  fluctuations at  $x/D = 5$ . It can also be observed that the distribution of the turbulence lies in the second and fourth quadrants with a bursting direction between  $-9^\circ$  and  $-21^\circ$  with the horizontal. Along the centreline, at  $x/D = 1.25$ , the velocity fluctuations are clustered in a circle and there is no preferential tilting towards one of the four quadrants. However, for  $x/D = 5$  the latter behaviour is not

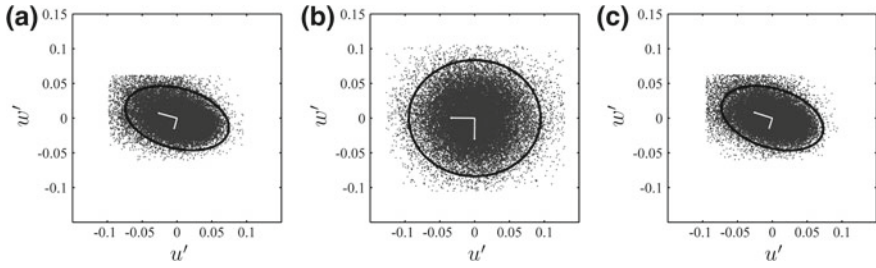


**Fig. 10** Quadrant plot  $u' - w'$  at  $x/D = 1.25$  for condition C2. **a**  $y/D = -1$ , **b**  $y/D = 0$  and **c**  $y/D = 1$ . For all cases  $z/h = 0.25$ .

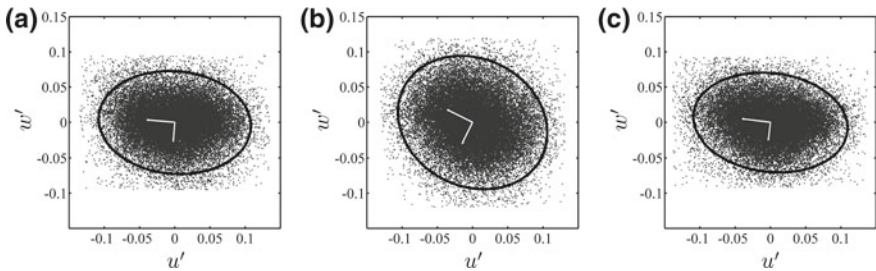


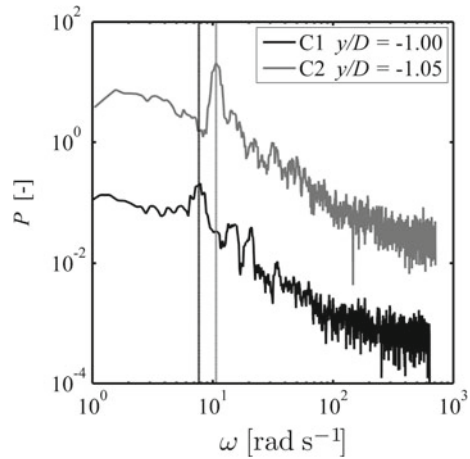
**Fig. 11** Quadrant plot  $u' - w'$  at  $x/D = 5$  for condition C2. **a**  $y/D = -1$ , **b**  $y/D = 0$  and **c**  $y/D = 1$ . For all cases  $z/h = 0.25$

observed. For this last case, the second and fourth quadrants are dominant, with a burst direction of approximately  $-30^\circ$  with the horizontal. This difference obtained for  $x/D = 1.25$  and  $x/D = 5$  may be justified by the influence of the pier. At a small distance downstream of the pier ( $x/D = 1.25$ ) its influence is significant, as it was also observed from Fig. 9. However, for  $x/D = 5$  the pier wake is almost dissipated and the fluctuations distribution tends to the typically encountered for smooth beds, with the dominance of ejections and sweep events, quadrants two and four, respectively.

### 3.2.3 Vortex Shedding

To analyze the vortex shedding, the LDV signal was reconstructed into a uniformly spaced grid using the Sample-and-Hold method, and the Fast Fourier Transform algorithm was applied to the horizontal component fluctuation,  $u'$ . For conditions C1 and C2 the spectra at ( $x/D = 5, y/D = -1, z/h = 0.375$ ) and ( $x/D = 5, y/D = -1.05, z/h = 0.375$ ), respectively, are shown in Fig. 12. For both flow conditions, several angular frequencies,  $\omega = 2\pi f$ , were observed in the spectra; however, the following analysis is focused on the frequency with maximum energy. For condition C1 a well-defined peak can be found at  $\omega = 7.901 \text{ rad s}^{-1}$ , corresponding to a

**Fig. 12** Obtained spectra at  $x/D = 5$ ,  $z/h = 0.375$  and  $y/D = -1$  (for condition C1) and  $y/D = -1.05$  (for condition C2)



frequency of 1.25 Hz. For Condition C2 a peak was identified at  $\omega = 10.93 \text{ rad s}^{-1}$ , corresponding to a frequency of 1.74 Hz. The corresponding Strouhal numbers,  $St = fD/U$ , were equal to 0.29 and 0.28 for conditions C1 and C2, respectively. The flow past a bridge pier reflects the interaction with the turbulent boundary layer and the influence of the bottom roughness (Fu and Rockwell 2005). For this reason, the present flow cannot be directly compared with the flow around a horizontal cylinder, used in several studies to determine vortex shedding frequencies. The obtained Strouhal numbers are higher than the usual values found for vortex shedding around circular cylinders (Williamson 1996). Ozgoren (2006) reports a value of 0.21 for circular cylinders. Values between 0.120 and 0.134 are reported in case of a square cylinder (Ozgoren 2006). However, Price et al. (2002) present maximum Strouhal numbers equal to 0.4, for a circular cylinder near a plane wall, when the flow Reynolds number is equal to 2000. Kirkil and Constantinescu (2009) report Strouhal numbers of 0.18 and 0.27 in case of a rectangular and circular cylinder mounted vertically in a free stream flow, respectively. The measured Strouhal numbers are in the same range of these latter values, although the present Reynolds number and the pier geometry are different. To the authors' best knowledge, no data on vortex shedding in elongated piers is found in the literature that could allow direct comparison with the present results, suggesting that this subject should be further investigated.

## 4 Conclusions

Simultaneous LDV horizontal and vertical velocity measurements were made in the vicinity of an elongated bridge pier to illustrate the main flow features. The free surface water flow was studied for a water depth equal to 5 cm and two flow conditions with mean approaching velocities equal to 0.17 and 0.25  $\text{m s}^{-1}$ .

The approaching water flow was turbulent smooth for both conditions. The pier's influence on the mean horizontal velocity is observed  $2.7D$  upstream, for both flow conditions. The decrease in mean horizontal velocity occurs simultaneously with the increase of mean vertical velocity towards the bottom of the channel, at distances from the pier's nose smaller than  $1.8D$ . For both conditions, the maxima in horizontal and vertical velocity components rms were observed at  $x/D = -1.55$  and  $-1$ , respectively. As the flow approaches the pier, Reynolds shear stresses increase and become positive. This is an indication of the presence of the horseshoe vortex.

Downstream the pier, the vertical component of the flow was dominant and a mean clockwise recirculation pattern was observed until  $x/D \approx 2.5$ . Maxima of velocity fluctuations were observed for  $z/h = 0.25$  in the axis of the flow at  $x/D = 2.2$  and  $2.3$ , for conditions C1 and C2, respectively. Mean horizontal velocity component transversal profiles show an approximate Gaussian shape, with the maximum of the velocity gradient corresponding to a double peak in the fluctuating horizontal velocity component profile.

Quadrant analysis was used to study the pier's turbulent wake. For condition C2 it was observed that the turbulent fluctuation cloud patterns obtained at  $y/D = \pm 1$  are similar, with a tilting towards the second and fourth quadrants. Along the pier centreline, at  $x/D = 1.25$ , the turbulent fluctuation cloud was practically a circle. However, for  $x/D = 5$  one observed the distortion of the cloud and the second and fourth quadrants are dominant, with a burst direction of approximately  $-30^\circ$  with the horizontal. This difference obtained for  $x/D = 1.25$  and  $x/D = 5$  may be justified by the influence of the pier.

In the wake of the pier, Strouhal numbers of the order of 0.3 were calculated. These Strouhal numbers are higher than those commonly measured for both circular and square cylinders. When compared with Strouhal numbers observed for a circular cylinder near a flat surface and in case of a vertically mounted cylinder, the present values are of the same order of magnitude.

## References

- Aleixo R, Carvalho E, Ferreira R (2016) A toolbox for laser Doppler velocimetry data post-processing. In: Constantinescu G, Garcia M, Hanes D (eds) Proceedings of the River Flow 2016 Conference
- Carvalho E (2013) Estudo experimental de escoamentos em canais com leitos de rugosidade uniforme. Caracterização do início do movimento das partículas [Experimental study of flows over uniform rugosity beds. Characterization of the beginning of sediment motion]. PhD thesis, Faculty of Engineering of University of Porto
- Carvalho E, Maia R, Proença M (2010) Shear stress measurements over smooth and rough channel beds. In: Proceedings of the River Flow 2010 Conference
- Dargahi B (1989) The turbulent flow field around a circular cylinder. *Exp Fluids* 8:1–12. <https://doi.org/10.1007/BF00203058>
- Dey S, Raikar R (2007) Characteristics of horseshoe vortex in developing scour holes at piers. *J Hydraul Eng* 133(4):399413



- Fu H, Rockwell D (2005) Shallow flow past a cylinder: transition phenomena at low Reynolds number. *J Fluid Mech* 540:75–97. <https://doi.org/10.1017/S0022112005003381>
- Graf W, Yulistiyanto B (1998) Experiments on flow around a cylinder; the velocity and vorticity fields. *J Hydraul Res* 36(4):637–654. <https://doi.org/10.1080/00221689809498613>
- Kasten J, Petz C, Hotz I, Hege HC, Noack B, Tadmor G (2010) Lagrangian feature extraction of the cylinder wake. *Phys Fluids* 10(1063/1):3483–220
- Kirkil G, Constantinescu G (2009) Nature of flow and turbulence structure around an in-stream vertical plate in a shallow channel and the implications for sediment erosion. *Water Resour Res* 45(W01):642. <https://doi.org/10.1029/2008WR007363>
- Ozgoen M (2006) Flow structure in the downstream of square and circular cylinders. *Flow Meas Instrum* 17:225–235. <https://doi.org/10.1016/j.flowmeasinst.2005.11.005>
- Ponta FL (2010) Vortex decay in the Kármán eddy street. *Phys Fluids* 10(1063/1):3481–383
- Price S, Sumer D, Smith J, Leong K, Paidoussis M (2002) Flow visualization around a circular cylinder near to a plane wall. *J Fluids Struct* 16(2):175–191. <https://doi.org/10.1006/jfls.2001.0413>
- Richardson E, Davies S (2001) Evaluating scour at bridges, vol HEC 18, FHWA-NHI-01-001, 4th edn. US Department of Transportation
- Roulund A, Sumer B, Fredsoe J, Michelsen J (2005) Numerical and experimental investigation of flow and scour around a circular pile. *J Fluid Mech* 534:351–401. <https://doi.org/10.1017/S0022112005004507>
- Tafarjnoruz A, Gaudio R, Calomino F (2012) Evaluation of flow-altering countermeasures against bridge pier scour. *J Hydraul Eng* 138(3):297–305. [https://doi.org/10.1061/\(ASCE\)HY.1943-7900.0000512](https://doi.org/10.1061/(ASCE)HY.1943-7900.0000512)
- Tropea C, Yarin A, Foss J (eds) (2007) *Handbook of experimental fluid mechanics*. Springer
- White FM (1994) *Fluid mechanics*, 3rd edn. McGraw-Hill, New Jersey, USA
- Williamson C (1996) Vortex dynamics in the cylinder wake. *Annu Rev Fluid Mech* 28:477–539. <https://doi.org/10.1146/annurev.fl.28.010196.002401>

# An Experimental Investigation on Porosity in Gravel Beds

Christy Ushanth Navaratnam, Jochen Aberle and Jana Daxnerová

**Abstract** This paper presents results from a set of laboratory measurements of the roughness geometry function and subsurface porosity at different spatial scales and with different beds using the water displacement method. For water worked gravel beds, the roughness geometry function was determined in both the interfacial sublayer and subsurface layer while for non-water worked bed configurations the vertical variation of porosity was evaluated from the manually created bed surface to the bottom, i.e. solely within the subsurface layer. The results show that the capillary action in sediment beds can have a significant influence on the porosity-values at the bed surface and the transition to a flat subsurface bottom as it was found that the capillary action over-/underestimates the porosity close to the gravel bed bottom and surface, respectively. The results are subsequently used to discuss recent findings reported in the hydraulic engineering literature in regard to the vertical variation of porosity.

## 1 Introduction

Flows in gravel bed rivers can be generally characterized as hydraulically rough-bed flows with low relative submergence and a high degree of spatial heterogeneity (Nikora et al. 2007a). The spatial flow heterogeneity can be described and taken into account using the double-averaged (time and space) momentum equations (Nikora et al. 2001; Nikora et al. 2004; Aberle 2006; Nikora et al. 2007a, b; Aberle et al. 2008), in which the spatial distribution of the roughness elements is considered through the roughness geometry function  $\varphi$ . The  $\varphi$ -function is of importance for the description of the flow in the interfacial sublayer as well as in the subsurface layer (i.e. within porous beds) and is defined as the ratio between the volume occupied by the fluid ( $V_f$ ) and the total averaging volume ( $V_0$ ) within the

---

C. U. Navaratnam (✉) · J. Aberle · J. Daxnerová  
Department of Civil and Environmental Engineering, Norwegian University of Science and Technology (NTNU), S.P. Andersens Vei 5, 7491 Trondheim, Norway  
e-mail: christy.ushanth.navaratnam@ntnu.no

averaging domain. The minimum value of the roughness geometry function corresponds typically to the porosity value of the subsurface layer, i.e.  $\varphi = 0$  for a solid subsurface layer and  $0 < \varphi < 1$  for a porous subsurface layer. The porosity of the subsurface layer is also an important parameter for exchange process (mass and momentum) between the surface and sub-surface flows, it determines the habitat conditions for aquatic organisms, and can influence colmation and depth filtration processes (or vice versa), i.e. clogging of top layer and interstices with fine particles in coarse grained beds (Brunke 1999; Boano et al. 2014).

Porosity in the subsurface layer of gravel beds can be determined using empirical predictors or direct and indirect porosity measurements. Empirical predictors have been derived based on median grain size  $d_{50}$  (e.g., Carling and Reader 1982; Wu and Wang 2006), sorting coefficient (e.g., Wooster et al. 2008), combination of different grain size characteristics (e.g., Frings et al. 2011) and combination of all these as well as the other factors, such as grain shape and depositional environment (e.g., Liang et al. 2015). There are many direct porosity measurement methods available; some of them include the water displacement/saturation method (e.g., Aberle 2007; Dey and Das 2012), gas expansion or adsorption method (e.g., Anovitz and Cole 2015) and high sophisticated techniques such as X-ray computed tomography and ultrasonic techniques (e.g., Slotwinski et al. 2014; Anovitz and Cole 2015). Despite the time consumption, the water displacement method has received more attention because it is simple, inexpensive, and considered to be more accurate than the empirical predictors, especially in the subsurface region.

Moreover, this method can be used to directly determine the roughness geometry function in the interfacial sublayer and hence to validate indirect measurements based on digital elevation models obtained from topographic data of gravel surfaces. Aberle (2007) compared  $\varphi$ -functions of a water-worked gravel bed ( $0.63 \text{ mm} < d < 64 \text{ mm}$ ) obtained by the water displacement method and laser displacement data. He concluded that the  $\varphi$ -functions determined from laser displacement data could only be used in the upper part of the interfacial sublayer (approx. 75%) as the voids formed in the lower part of the interfacial sublayer could not directly be measured using laser displacement meter or point gauges. Moreover, Aberle (2007) identified an absolute minimum value of  $\varphi \approx 6\%$  at the level of the roughness trough, i.e. at the transition from the interfacial sublayer to the subsurface layer. The absolute minimum of  $\varphi$  was believed to be the result of densely packed surface particles due to static armoring (Marion and Fraccarollo 1997) and it was speculated that the absolute minimum in natural rivers might be even smaller as the corresponding smallest grain size in fluvial environments is often smaller than the minimum grain-size used in the sand-gravel mixture investigated by Aberle (2007). However, this phenomenon has not yet been validated by independent data. In this context, Dey and Das (2012) performed porosity measurements using the water displacement method in a uniform gravel bed with  $d_{50} = 40 \text{ mm}$  and did not identify such an absolute minimum value of  $\varphi$  as their uniform gravel bed did not contain fine particles to seal the surface, as it was explained in Aberle (2007).

In this paper, we report results from a set of measurements of  $\varphi$ -functions in the interfacial sublayer and subsurface layer using the water displacement method and a

similar gravel mixture as used in Aberle (2007), as well as further bed configurations. The key objective of this study is to verify the result of the Aberle (2007) and to further investigate the occurrence of an absolute minimum of the  $\varphi$ -function at the transition from the interfacial sublayer to the subsurface layer. Section 2 describes the experimental set-up and procedure of large- and small-scale porosity measurements using the water displacement method. The results of the measurements are presented and discussed in Sects. 3 and 4 summarizes the findings.

## 2 Experimental Set-up and Procedure

### 2.1 Large Scale Porosity Measurements

Large scale porosity measurements for a manually screeded and a water worked bed, respectively, were carried out in a 12.5 m long, 1 m wide and 1 m deep tilting flume in the hydraulics laboratory of the Norwegian University of Science and Technology (NTNU), Trondheim, Norway. A well-mixed 0.2 m high gravel layer, characterized by the same grain size distribution as the one used by Aberle (2007) (see Fig. 1), was placed into the flume, screeded and surface compacted to ensure that the bed slope was parallel to the flume bottom. The length of the gravel bed section ( $L_s$ ) was 10.61 m (see Fig. 2) and the gravel was retained by a L-shaped perforated sill at the up- and downstream end to allow flow through the subsurface layer. For the porosity measurements, the flume was brought into a horizontal position ( $S = 0$ ) and a basin was created at each end the gravel bed section. The corresponding upstream sealing had a distance of 18 cm ( $L_{BU}$ ) to the beginning of the gravel section while the downstream sealing had a distance of 17 cm ( $L_{BD}$ ) to the gravel section (see Fig. 2).

After air drying the sediment bed for a period of one week, the porosity measurements were carried out. In order to determine a vertical profile of porosity, the

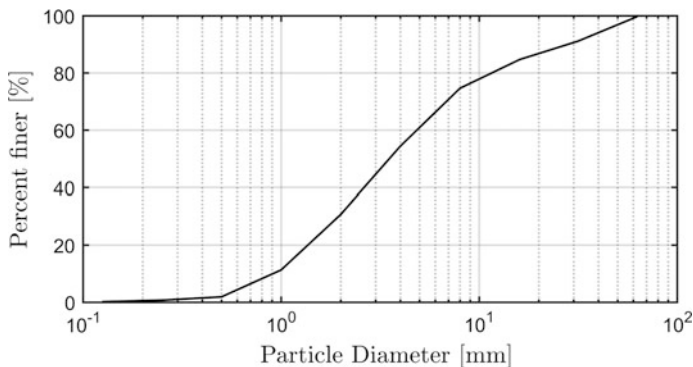


Fig. 1 Grain size distribution of the gravel mixture

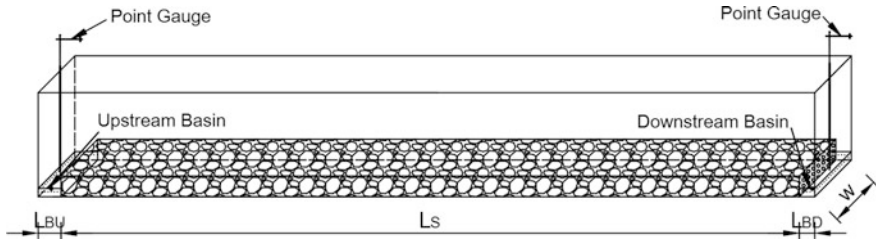


Fig. 2 Sketch of the set-up of the flume experiments

measurements were carried out in steps. First, a known volume of water (50 L) was added to the upstream basin and the corresponding water levels in the basins were measured using point gauges. These readings were also used to ensure that a stable water level was reached, i.e. that the subsurface flow was settled. Further volumes of 50 L were subsequently added until the water depth in the basins corresponded to half the bed height (10 cm). In order to increase the resolution in the upper half of the bed, the added volume was then decreased to 20 L.

Upon completion of these measurements, the basins were removed and a static armor layer was formed with an armoring discharge of  $180 \text{ l s}^{-1}$  at a flume slope of  $S = 0.27\%$  in order to reproduce a similar water-worked gravel bed as in Aberle (2007). During armoring, the upstream end of the gravel layer was 2.5 m away from the flow straighteners at the flume inlet, and the gap between flow straighteners and the gravel bed was filled with large stones to minimize the scour at the inlet during water flow. Care was taken during the armoring process that the water surface slope, which was determined from water surface elevation measurements using 4 piezometers and a point gauge attached to movable carriage, corresponded to the flume slope. This was achieved by regulating the water depth at the downstream end of the flume using a gate. The vertical profile of porosity for armored bed was determined using the same procedure as for the screeded bed.

## 2.2 Small Scale Porosity Measurements

Porosity measurements in the flume were time consuming and required a large amount of material. In order to increase the data-base of vertical porosity profiles, additional measurements were therefore carried out in a small tank (78.1 cm long, 32.9 cm wide and 43 cm deep; see Fig. 3). A first set of experiments was carried out with the same gravel mixture as in the large-scale flume experiments to cross-check the repeatability of these measurements at a different spatial scale. The porosity measurements were carried following the same strategy as in the flume measurements, with an added volume of water of 2 L during each step. The advantage of the small-scale measurements was that it was possible to carry out measurements for differently prepared gravel mixtures and hence to investigate the

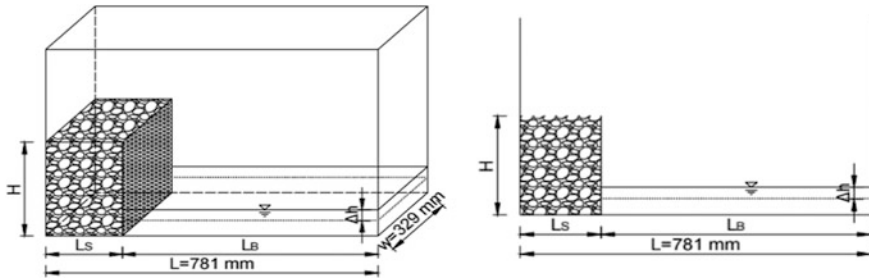


Fig. 3 Set-up of the small tank tests

effect of bed preparation on the porosity in the subsurface layer. For this purpose, the measurements were carried out for:

- *Surface-compacted gravel*: the gravel mixture was compacted only on the surface.
- *Layer-compacted gravel*: the gravel mixture gravel was compacted in approximately 4-equal-height layers.
- *Uncompacted gravel*: the gravel mixture was only poured into the tank and not compacted.
- *Manually-shaken gravel*: the gravel mixture was first poured into the tank and the tank was then shaken by two persons to compact the bed.

It is worth mentioning that due to the limited availability of gravel material, as most of the material was installed in the flume, the height of the sediment layer ranged between 0.154 and 0.2 m in these tests and that the length ( $L_S$ ) (ranged between 0.17 and 0.25 m) and was smaller compared to the basin length ( $L_B$ ).

In addition to the gravel mixture, further tests were carried out using (i) uniform gravel ( $d = 8$  mm) in order to investigate potential grain-sorting effects on the vertical distribution of porosity; (ii) uniform fine sand ( $d = 0.33$  mm) to investigate the influence of capillary action on the porosity measurement method; and (iii) using golf balls with a diameter of 42 mm to investigate the accuracy of the presented porosity measurement method. For the latter test, the golf balls were arranged as shown in Fig. 4 and the measured porosity was compared with the analytical result as will be shown later. Table 1 summarizes all the test cases with relevant parameters including bulk-porosity values determined from the measurements.

From the above measurements, the vertical porosity profile  $\varphi(z)$  was quantified using the formula:

$$\varnothing = \frac{V_f}{V_0} = \frac{V_{st} - V_B}{wL_s\Delta h} = \frac{V_{st} - wL_B\Delta h}{wL_s\Delta h} \tag{1}$$

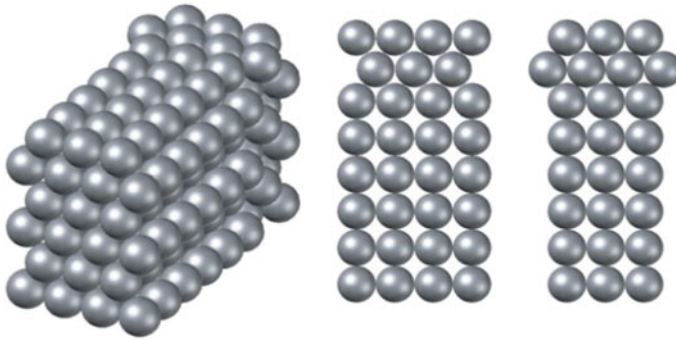


**Fig. 4** Arrangement of golf balls: Isometric view (*Left*), Plan view of layers 1, 3, 5 (*Middle*), plan view of layers 2, 4, 6 (*Right*)

**Table 1** Summary of all test cases

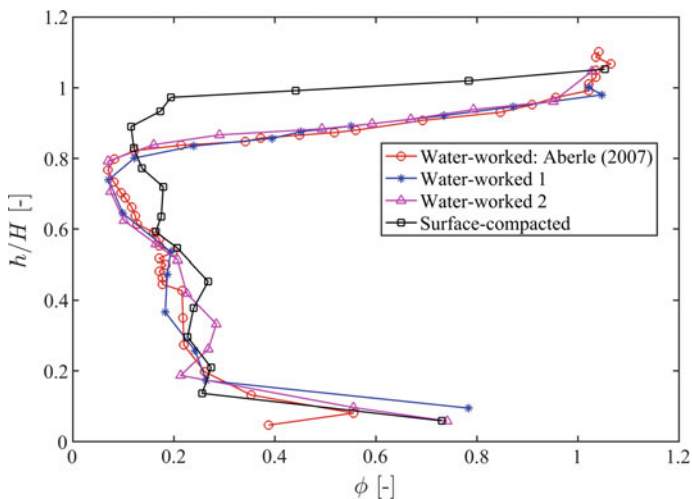
Test case	Grain size [mm]	Bed height [mm]	Bulk porosity	Minimum porosity
<i>Flume tests</i>				
Surface-compacted gravel (screeded)	0.64–64	200	0.26	0.115
Water-worked gravel	0.64–64	200	0.31	0.071
<i>Small scale tests</i>				
Surface-compacted gravel (screeded)	0.64–64	154	0.29	0.059
Layer-compacted gravel	0.64–64	184	0.25	0.055
Uncompacted gravel	0.64–64	200	0.37	0.124
Manually-shaken gravel	0.64–64	196	0.29	0.110
Uniform gravel-Run 1	8	215	0.48	0.391
Uniform gravel-Run 2	8	210	0.51	0.406
Uniform fine sand	0.33		0.37	0.001
Golf balls	42 (diameter)	232	0.51	0.249

where,  $V_f$  denotes the volume occupied by the fluid,  $V_0$  the averaging (total volume),  $V_{st}$  the water added in a step,  $V_B$  the volume of water in the basins corresponding to the water level increment  $\Delta h$ ,  $w$  the width of the flume (or tank),  $L_s$  the length of the sediment section and  $L_B$  the total length of the basins ( $L_B = L_{BU} + L_{BD}$  in the flume).

### 3 Results and Discussion

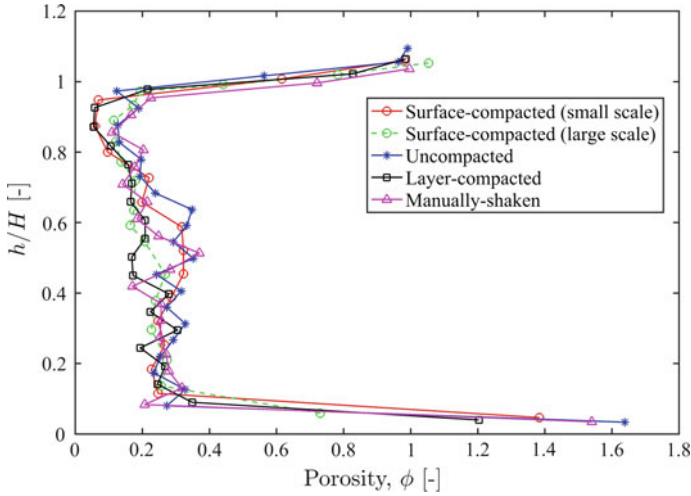
Figure 5 shows the determined vertical porosity profiles for the large-scale tests (screeded and water-worked bed) as well as the vertical porosity profile measured by Aberle (2007). In the figure, the height from the flume/tank bottom ( $h$ ) is normalized by the total bed height ( $H$ ) to directly compare the variations of  $\phi$  for the different test cases. The vertical variation of porosity in the present water-worked bed and the one of Aberle (2007) nearly collapse on a single line and both profiles show an absolute minimum of about  $\phi = 0.06$  at the roughness troughs, validating the result of the study of Aberle (2007). However, the porosity in the surface-compacted gravel bed also shows an absolute minimum ( $\phi \approx 0.11$ ) close to the surface. This indicates that the observed absolute minimum of  $\phi$  may not be solely attributed to the armoring process as was concluded by Aberle (2007), and that the surface compaction may have a certain influence. This will be elaborated in more detail below using the results from the small-scale tests. Note that the vertical shift in the porosity variation between the surface-compacted and water-worked gravel is mainly due to the change of the surface characteristics, because the water-worked gravel was coarsened and the roughness trough shifted downwards. This contributed also to a difference in bulk porosity, as shown by the values in Table 1.

Figure 6 shows the results from the small tank tests, performed with the same gravel that was used for the flume experiments, along with the observed porosity variation in the surface-compacted gravel bed in the flume tests. The direct comparison of the porosity profiles for the large- and small-scale tests with the surface



**Fig. 5** The variation of porosity in the present flume experiments and the porosity profile obtained by Aberle (2007)





**Fig. 6** The variation of porosity in small tank experiments

compacted beds shows a reasonably good agreement and the minor differences may be attributed to the different spatial scales and measurement uncertainties.

Figure 6 furthermore shows that the small-scale surface-compacted and uncompacted gravel beds are characterized by similar  $\varphi$ -values in the bottom half of the bed. The  $\varphi$ -value in this region is similar to the corresponding bulk porosity values of 0.29 and 0.37, respectively (see Table 1). On the other hand, the uncompacted gravel bed is, as expected, more porous than the surface-compacted gravel bed in the upper part of the bed. In this context, it is worth mentioning that the uncompacted gravel still has relatively low  $\varphi$  values close to the surface.

The porosity profile of the layer compacted bed has the lowest bulk porosity (Table 1) and visualizes the effect of the compaction throughout the whole sediment bed. However, similar porosity values are observed towards the surface compared to the surface-compacted bed. The effect of bed compaction is also partly visible from the porosity-values associated with the manually shaken bed, although this compaction method was not as effective in reducing porosity as the layer compaction. As for the uncompacted gravel bed, the manually-shaken gravel bed also shows a relatively low porosity values close to the surface. This is a strong indicator that a small value of  $\varphi$  close to the surface is not completely associated with compaction or armoring. Figure 6 further shows that porosity-values close to the tank bottom exceed a value of  $\varphi = 1$ , which is theoretically impossible. Values larger than  $\varphi = 1$  can be attributed to capillary action which is due to adhesion between the grains and the water as well as the surface tension of the water. In fact, the smaller the pores, the higher the capillary rise (Lohman 1972). The influence of capillarity is discussed in more detail later in this section, after the presentation of the porosity profiles of the uniform gravel beds.

Figure 7 shows the porosity variations for two experiments carried out with uncompacted uniform gravel. The slight difference in the porosity-values between the two experiments can be attributed to the experimental procedure as the gravel was taken out, dried and poured back to the tank after the first experiment. Thus, the grains were arranged differently in each experiment. As for the gravel-mixture beds, the  $\phi$ -values slightly drop close to the surface although the deviation of the absolute minimum from the bulk porosity is less compared to the gravel mixture shown in Figs. 5 and 6. Moreover, the determined porosity values also show an increase in the vicinity of the flume bed which can be used to further discuss the significance of capillary action. Based on porosity measurements with a gravel mixture, Aberle (2007) associated this increase with the poor sorting of sediments as large grains occupy the space and act as a filter layer. However, as this increase was also noted in the uniform gravel tests, poor sorting of the grains cannot be the reason for the observed increase at the tank bottom in Fig. 7. In contrast, it can be associated with capillary action as most of the added water was taken up by the pores, and the small water depth measured in the basin resulted in larger porosity-values according to Eq. 1. It is worth mentioning that the porosity measurements with the fine sand (not shown in detail here) revealed that the first 4 L of added water (two step volumes of 2 L) were completely taken up by the fine pores because of capillary action. Thus, it can be concluded that for gravel mixtures, both sorting processes as well as capillary action are of significance when determining the porosity of a layer close to a solid boundary.

Moreover, the capillary action can also influence the porosity-measurements close to the bed surface as the accumulated porewater fills the voids above the roughness trough. This in turn causes a larger rise in the water depth once the surface trough is reached and hence smaller porosity values will be obtained in this

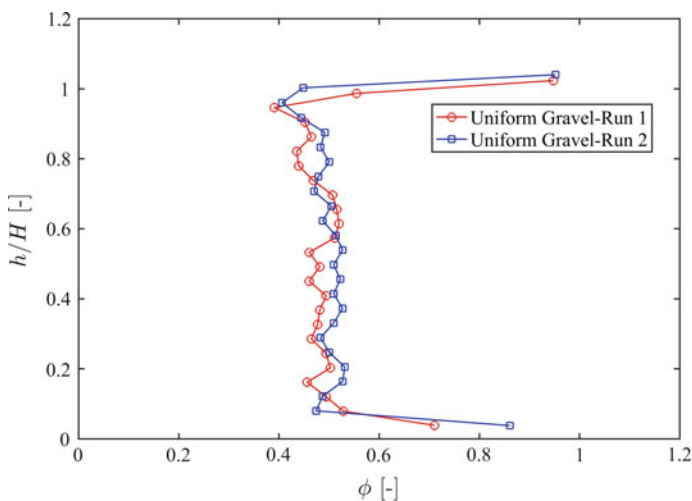
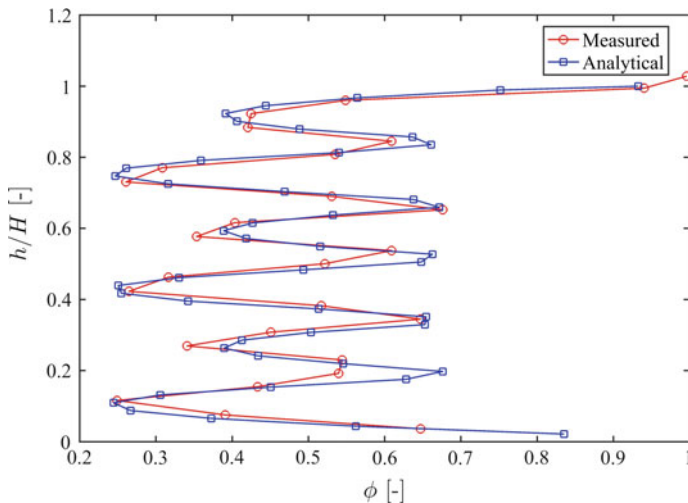


Fig. 7 The variation of porosity in the uniform gravel

region (see Eq. 1). Thus, this phenomena is inverse of what occurs close to the flume/tank bottom and it can be concluded that the stepwise water displacement method underestimates the porosity-values close to the bed surface.

The presented porosity measurement method is therefore most suitable for the determination of bulk porosities and adjustment factors for capillary action need to be incorporated when porosity is determined over depth. This conclusion can be substantiated using the porosity-measurements with the golf-ball bed for which the void space is rather large so that capillary action will almost be absent. Moreover, the known geometry of the golf-ball bed allows for the calculation of the analytical porosity profile. Figure 8 presents both the experimental and analytical result and shows a good agreement of the corresponding porosity profiles. Minor differences can be observed at heights where the analytical solution determines the maximum porosity, i.e. the overlapping region of golf ball layers. This difference may be attributed to the golf ball arrangement as well as measurement uncertainties. However, Fig. 8 clearly shows that the water displacement results in accurate porosity-measurements given that capillary action is negligible. It is also worth noting that Fig. 8 shows a significant increase in porosity towards the tank-bottom indicating that sorting effects at the transition to a flat-bed are present. A similar effect could occur in sediment beds so that both sorting and capillary effects are of importance in this region as discussed above.



**Fig. 8** The variation of porosity in multiple layers of golf balls

## 4 Summary

This paper presents results from experiments in which the vertical variation of porosity was directly measured in different gravel beds using the water displacement method. An absolute minimum value of porosity was observed at the level of the roughness troughs in armored gravel beds in accordance with results from the literature. However, it was concluded that this minimum is not exclusively due to the densely-packed layer of surface particles resulting from static armoring. Instead, it was shown that this phenomenon is also partly due to capillary action which contributes to small porosities close to the gravel surface as well as to large porosities close to the flume bottom. Generally, the porosity in soils is determined as bulk porosity, thus, the capillary action would become ineffective when using the water displacement method. Therefore, a correction factor for the influence of capillary action should be considered when porosity-profiles are measured using the water displacement method.

## References

- Aberle J (2006) Spatially averaged near-bed flow field over rough armor layers. *River Flow 2006*, Two Volume Set. Taylor & Francis
- Aberle J (2007) Measurements of armour layer roughness geometry function and porosity. *Acta Geophys* 55:23–32
- Aberle J, Koll K, Dittrich A (2008) Form induced stresses over rough gravel-beds. *Acta Geophys* 56:584–600
- Anovitz LM, Cole DR (2015) Characterization and analysis of porosity and pore structures. *Rev Miner Geochem* 80:61–164
- Boano F, Harvey JW, Marion A, Packman AI, Revelli R, Ridolfi L, Wörman A (2014) Hyporheic flow and transport processes: mechanisms, models, and biogeochemical implications. *Rev Geophys* 52:603–679
- Brunke M (1999) Colmation and depth filtration within streambeds: retention of particles in hyporheic interstices. *Int Rev Hydrobiol* 84:99–117
- Carling PA, Reader NA (1982) Structure, composition and bulk properties of upland stream gravels. *Earth Surf Proc Land* 7:349–365
- Dey S, Das R (2012) Gravel-Bed Hydrodynamics: double-averaging approach. *J Hydraul Eng* 138:707–725
- Frings RM, Schüttrumpf H, Vollmer S (2011) Verification of porosity predictors for fluvial sand-gravel deposits. *Water Resour Res* 47, n/a-n/a
- Liang R, Schriff T, Jia X, Schüttrumpf H, Frings RM (2015) Validation of a stochastic digital packing algorithm for porosity prediction in fluvial gravel deposits. *Sed Geol* 329:18–27
- Lohman SW (1972) *Ground-Water Hydraulics*. Unites States Department of the Interior, Wasgington
- Marion A, Fraccarollo L (1997) New conversion model for areal sampling of fluvial sediments. *J Hydraul Eng* 123:1148–1151
- Nikora V, Goring D, McEwan I, Griffiths G (2001) Spatially averaged open-channel flow over rough bed. *J Hydraul Eng* 127:123–133
- Nikora V, Koll K, McEwan I, McLean S, Dittrich A (2004) Velocity distribution in the roughness layer of rough-bed flows. *J Hydraul Eng* 130:1036–1042

- Nikora V, McEwan I, McLean S, Coleman S, Pokrajac D, Walters R (2007a) Double-averaging concept for rough-bed open-channel and overland flows: theoretical background. *J Hydraul Eng* 133:873–883
- Nikora V, McLean S, Coleman S, Pokrajac D, McEwan I, Campbell L, Aberle J, Clunie D, Koll K (2007b) Double-averaging concept for rough-bed open-channel and overland flows: applications. *J Hydraul Eng* 133:884–895
- Slotwinski JA, Garboczi EJ, Hebenstreit KM (2014) Porosity measurements and analysis for metal additive manufacturing process control. *J Res Nat Inst Stand Technol* 119:494–528
- Wooster JK, Dusterhoff SR, Cui Y, Sklar LS, Dietrich WE, Malko M (2008) Sediment supply and relative size distribution effects on fine sediment infiltration into immobile gravels. *Water Resour Res* 44, n/a-n/a
- Wu W, Wang SSY (2006) Formulas for sediment porosity and settling velocity. *J Hydraul Eng* 132:858–862

# Po River Morphodynamics Modelled with the Open-source Code iRIC

Michael Nones, Alessio Pugliese, Alessio Domeneghetti  
and Massimo Guerrero

**Abstract** The paper presents the numerical modelling of the hydro-morphological evolution of a 10 km reach of the Po River in Italy. The simulation is performed with the freeware code iRIC, recently developed by an international community of scientists and practitioners. Starting from a non-detailed description of the studied area and using synthetic data, the reach has been modelled adopting a 2-D solver. Based on a Digital Elevation Model of the area, the domain is discretized by an unstructured grid with triangular meshes. First results show a promising capability of the model in reproducing the behaviour of the reach, both in terms of liquid flow and morphodynamics, if compared with historical data measured along the watercourse and reported in literature. In the future, additional simulations will be performed, enlarging the studied area and using detailed input data measured with traditional and innovative techniques.

## 1 Introduction

Early river science was based on a 1-D view of river processes, emphasizing changes in discharge, sediment loads, dispersion, streamwise velocity, etc. However, the attention has shifted to a more spatially distributed and physically-based description of the river processes, considering 2-D and 3-D river forms such as point and alternate bars, but also including biology and ecology, which accounts for the importance of local variations in flow, depth, substrate and other physical variables in riverine ecosystems (Hardy 1998). The consideration of a more spatially explicit view of rivers was supercharged by the development of measurement

---

M. Nones (✉)

Interdepartmental Centre for Industrial Research in Building and Construction,  
University of Bologna, via del Lazzaretto 15/5, 40131 Bologna, Italy  
e-mail: michael.nones@unibo.it

A. Pugliese · A. Domeneghetti · M. Guerrero  
Department of Civil, Chemical, Environmental and Materials Engineering,  
University of Bologna, viale Risorgimento 2, 40136 Bologna, Italy

technology that allowed detailed realizations of flow, depth, water-surface elevation, and many other parameters. As optical and acoustic devices (ADCPs, multi-beam echo sounders, laser scanners, etc.) became readily available; modellers had to handle unprecedented datasets for testing and refining computational and conceptual models for river flow, morphodynamics, habitat, and vegetation (e.g., Guerrero et al. 2013; Baranya et al. 2014; Bufe et al. 2016; Nones and Di Silvio 2016; Nones and Varrani 2016; Ota et al. 2016). Scientists from outside the typical science fields of civil engineering and earth science began to need and use computational models for describing flow, sediment transport and morphodynamics, frequently moving from simple 1-D models to more accurate 2-D and 3-D descriptions of liquid and solid phases. Over the past years, numerical models that had been primary tools for developing simple understanding of riverine processes evolved into practical tools for a wide variety of real-world problems, including river restoration (Nabi et al. 2012; Nones and Gerstgraser 2016), prediction of channel response to natural and anthropogenic changes (Nones et al. 2013; Baranya et al. 2014; Guerrero et al. 2015), prediction of fish habitat (Kim et al. 2014) and vegetation effects (Harrison et al. 2015), or evaluation of bar and bedform sedimentology (Nelson et al. 2015). To address such changes, state-of-the-art research tools for river modelling should be available to students and other non-specialists, so they could assimilate these tools into their own suite of capabilities, both to better understand river flow and morphodynamics at a fundamental level, and to gain the ability to make meaningful assessments of various river processes using modeling tools suitable for practical river problems.

Since 2009, an open source suite of public-domain tools for computing flow and morphodynamics in geophysics was developed by the international group of scientists and engineers named International River Interface Cooperative (iRIC, [i-ric.org](http://i-ric.org)), with the aim to provide a user-friendly software system that would bridge the range of responses from simple educational case studies to more realistic assessments of flow and channel change for evaluating engineering projects in real rivers (Nelson et al. 2016).

The present work, made under the auspice on the Italian research project INFRASAFE (<https://www.infrasafe-project.com>), uses the iRIC suite to simulate the morphological evolution of a 10 km reach of the Po River, in Italy, downstream of Mantua. The research represents the first application of open source code iRIC to Italian rivers, and tries to give additional insights in the morphodynamics of the Po River, in a reach frequently subjected to floods and where sediment transport is a main driver of problems on local hydraulic structures.

After the description of the study site, the adopted model is presented, focusing on the 2-D solver MFLOW\_02 that permits to describe the riverine morphodynamics based on unstructured grid with triangular meshes. The results are presented and discussed, highlighting the capability of the iRIC code to reproduce the typical behaviour of this sandy reach, regardless of the lack of site-specific input data. Additional research is necessary to further analyze the studied domain using different numerical assumptions and more detailed field data, which are not yet implemented in this preliminary research but will be acquired in the next months.

## 2 Materials and Methods

### 2.1 Study Site

The Po River, the longest watercourse in Italy, flows eastward across northern Italy for about 660 km (Fig. 1). With a drainage area of 74,000 km<sup>2</sup>, of which 28,000 km<sup>2</sup> is in montane environments and the rest on the floodplain (i.e. 46,000 km<sup>2</sup>). The watershed can be divided into three sectors based on the lithology and on the maximum elevation: the Alpine sector of crystalline and carbonate rocks (maximum relief ~4500 m asl), the Apennine sector, mostly composed of sedimentary rocks with high clay content (maximum relief ~2000 m asl) and the central alluvial area including the Po plain and the Po River delta. The middle and lower portions of Po River are subjected to high flood-hazard and, consequently, heavily embanked (Domeneghetti et al. 2015).

The annual hydrograph shows two peaks in discharge, normally in autumn and spring, generated by rainfall and snowmelt, respectively. The mean annual

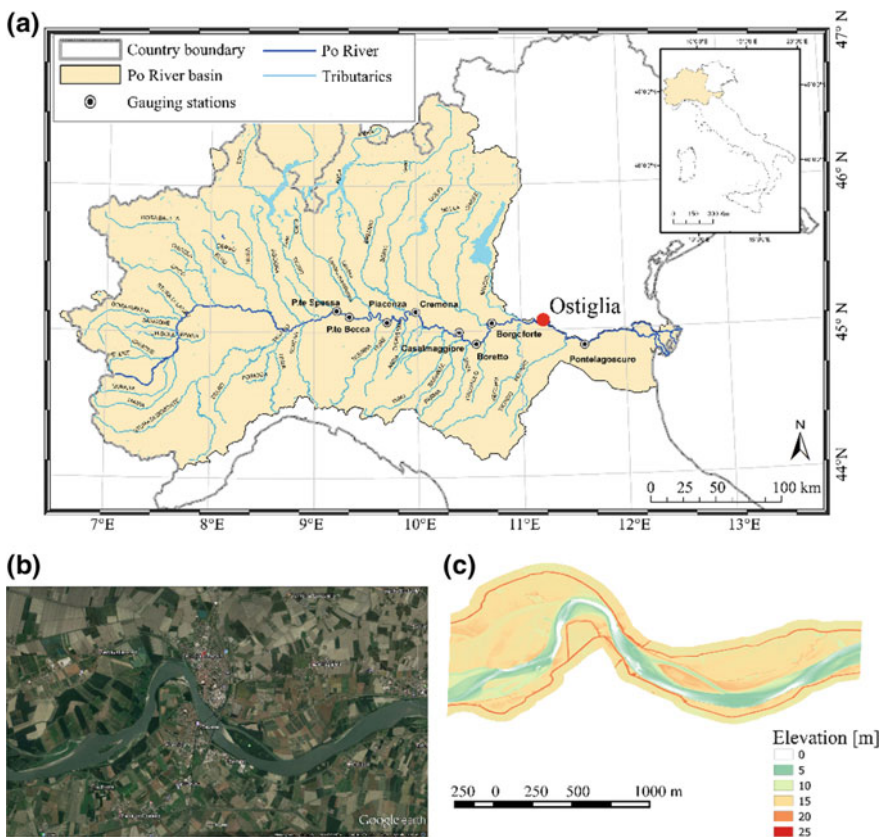


**Fig. 1** Study site: **a** Po River basin; **b** satellite image and **c** DEM of the studied reach close to Ostiglia (Mn)



discharge recorded at the Piacenza gauging station is around  $1000 \text{ m}^3 \text{ s}^{-1}$  (period 1924-2009; Montanari 2012), while the total annual sediment and freshwater discharges to the Northern Adriatic Sea are about  $13 \times 10^9 \text{ kg}$  and  $40\text{--}50 \text{ km}^3$ , respectively (Cozzi and Giani 2011; Syvitski and Kettner 2007).

The iRIC model is applied to a reach of about 10 km, located around Ostiglia, downstream of the city of Mantua (red circle, Fig. 1b). As visible from the Digital Elevation Model (DEM) acquired by the AIPO in (2005) (Fig. 1c), this reach has a mean width of 400 m and a bottom slope in the order of 0.5%.

The present river bathymetry is the result of the interaction between natural processes and anthropic activities (Lanzoni 2012). In fact, the Po River course has been deeply affected by human interventions during the last century: gravel and sand mining from the riverbed, particularly intense between 1960 and 1970, and creation of river embankments to prevent flooding of the surrounding floodplains and construction of hydropower dams in the Alpine tributaries, promoted a strong decrease in the sediment load and, consequently, an important degradation of the overall river bed (Lamberti and Schippa 1994).

## 2.2 *Input Data*

Preliminary simulations were performed using the 2-m resolution bathymetry (Fig. 1c) surveyed by AdB-Po (Po River Basin Authority) in 2005 as geometrical input, neglecting the presence of bridges and other hydraulic structures within the main current for the sake of simplicity, but also due to computational reasons. To assess the effects of such structures, site-specific simulations will be performed in the future using other solvers of the iRIC suite.

As boundary conditions (Fig. 2), the inflow data imposed at the upstream end refers to the discharges measured during the last decades at the gauging station of Piacenza, located more than 100 km upstream of the studied reach, but without important intermediate tributaries. These discharges were analyzed to create a synthetic hydrograph representing the typical behaviour of the Po River, characterized by a flow that varies between  $500$  and  $2500 \text{ m}^3 \text{ s}^{-1}$ , with a median discharge of around  $1000 \text{ m}^3 \text{ s}^{-1}$ . The downstream conditions are represented by the corresponding water elevations at the end of the reach, estimated under the hypothesis of a uniform hydrodynamic behaviour (i.e., normal depth conditions). These synthetic boundary conditions permit to reduce the computational effort required by the solver, speeding up the simulation without affecting the physics of the processes involved, thanks to the adaptation time of the river. With these conditions, the simulated period is nearly 14 h.

The river material is non-uniform and the grain-size composition has been derived from a field campaign made in the reach close to the Isola Serafini dam, not far from the study site. Assuming typical values of sandy rivers and because of the lack of detailed in situ analyses, the thickness of the active layer is assumed equal to 1 m, while the Manning's roughness coefficient changes between main channel

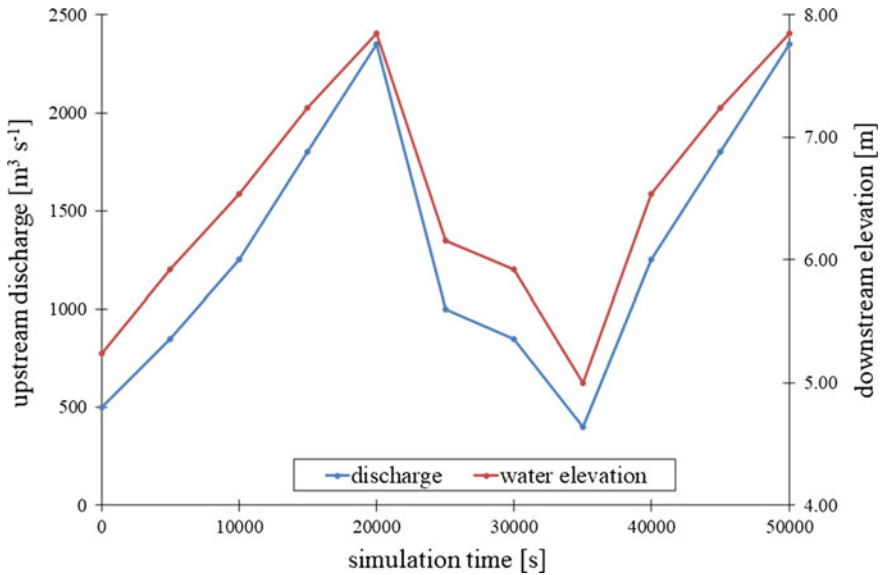


**Fig. 2** Synthetic boundary conditions for the simulation: flow discharges at upstream (blue) and water elevation at downstream (red)

( $n = 0.035$ ) and floodplains ( $n = 0.06$ ). In this preliminary analysis, neither vegetation nor wind effects are considered.

Further studies will address a more complete setup, adding local measurements that will be performed closer to the study site.

### 3 Modelling Approach: The iRIC Software

Rivers modellers have to deal with some issues, such as: (i) no single model is sufficient to completely describe river hydraulics and morphodynamics; (ii) with respect to the scale studied, models require different tools and algorithms, and build a unique interface is not feasible; (iii) models should be sufficiently feasible to deal with large datasets coming from different sources, and the outcomes should be user-specified to communicate with other software and applications; (iv) parallelization of solver codes is necessary to reduce the computational effort.

In the iRIC structure, solvers are kept separate from the interface, communicating with it through a solver definition file that instructs the interface how to configure itself for the solver to be used, and a binary data structure that exchanges information (Nelson et al. 2016). Thus, iRIC is only an interface, containing many tools to import and edit information and data, visualize inputs and output, construct orthogonal, curvilinear and non-orthogonal grids as well as triangular and quadrilateral meshes, depending on the solver chosen.

The fundamental feature of the present method is the relative simplicity of adding new solvers or modifying existing ones, aiming to investigate the same case study at different spatial and temporal scales. The interface is not recompiled; therefore, the developer can change solver definition files and add new executable solvers to the main solver folder. In addition to the solvers offered by the iRIC group, developers may freely insert their own solvers into the iRIC framework. So far, 14 solvers use the same structure, allowing for a simple comparison and to ultimately select the most appropriate one in each case study. Among the available solvers, in the present application the MFLOW\_02 is used, thanks to the capability in reproducing the 2-D riverine hydro-morphodynamics using unstructured grids.

### 3.1 *MFLOW\_02 Solver*

The applied solver adopts an unstructured grid for calculating 2-D vertically averaged unsteady flow and riverbed variation. Currently, it is the only unstructured grid model implemented in iRIC that can describe morphodynamics using the finite element method (iRIC Software 2014). By applying the characteristic of unstructured meshes, this model can calculate unsteady flow in a region including structures like piers, weirs, etc., or can model flooding events over complex areas, like floodplains connected to a river channel network with many distributaries and confluences. In addition, the solver allows for computing riverbed variations as well as the appearance, development and movement of sandbars.

Among others, main characteristics of models adopted to calculate flow field and sediment transport are:

- orthogonal coordinate system (Cartesian coordinate system);
- unstructured meshes using linear triangular elements, useful to reproduce the shape of complicate structures like landforms, piers, walls, etc.;
- Galerkin finite element method for the spatial derivatives;
- explicit model in time;
- several formulations to describe the turbulence: zero equation model, simple k- $\epsilon$  model and direct input of kinematic eddy viscosity;
- possibility to set up various boundary conditions;
- bottom friction described using the Manning roughness coefficient, spatially variable over the grid;
- consideration of additional effects due to vegetation and wind;
- two types of sediment load can be selected: only bed load, and bed load + suspended sediment;
- riverbed material can be selected from uniform or mixed grain diameter. If mixed grain diameter is selected, the variation of grain distribution can be assumed for multiple layers;
- the scour limit of riverbed can be set by scour depth and scour height.

### 3.2 Governing Equations

Flow continuity equation and momentum equation are discretized in space using the Galerkin finite element method. Such a method adopts linear triangular prisms element as shape functions for weighting the residuals (iRIC Software 2014). Turbulence is represented by the flow with large and small eddies. The present application uses the  $k$ - $\epsilon$  model, which computes the kinematic eddy viscosity as:

$$\nu = C_\mu \frac{k}{\epsilon} \quad (1)$$

where  $C_\mu$  is a constant equal to 0.09, while  $k$  indicates the turbulent energy and  $\epsilon$  the energy dissipation rate.

Adopting the empirical approach proposed by Nezu and Nakagawa (1993) to evaluate the turbulent energy as a function of the water depth, and evaluating the energy dissipation rate from the flow velocity (Lomax et al. 2013), it is possible to compute the kinematic eddy viscosity directly, without solving the transport equations of both variables.

In MFLOW\_02, the bottom friction is set up using the Manning's roughness coefficient, which can be changed spatially by each element (cell).

The application proposed here uses a mixed grain diameter to describe the riverbed material, while sediment transport is divided in suspended load and bedload, both in equilibrium with the water flow. The bedload is computed using the Meyer-Peter-Muller formula for each grain size, while the suspended load is calculated adopting the Garcia-Parker formula (1991) for the buoyancy and the Rouse approach (1937) for the reference conditions. Mixed grain size composition is handled considering the shelter effect (Ashida and Michiue 1972) and assuring the continuity for all the classes. Similarly, the sediment transport is also computed by discretizing the spatial variables through the Galerkin finite element method. To assure the stability and the convergence of the method, sensitivity analyses of used grid and time discretization were performed.

## 4 Results and Discussion

The preliminary simulation lasts 50,000 s (nearly 14 h), using a time step  $dt = 0.5$  s to guarantee the stability of the code, while the triangular cells have an area that spans from 2500 to 3000 m<sup>2</sup>, depending on the location. With these conditions, the total computational time is around 1 h for a normal laptop.

During the simulated time, the bed level varies by a few centimetres, according to past field measurements performed under normal flow conditions around 90 km upstream of the study site (Lamberti and Schippa 1994). At the end of the simulation (Fig. 3a), one can observe the formation of alternate bars at the inflection

points: the flow transports sand that deposit on the outer bank of the curves, while the inner bank is subjected to erosion.

Looking at the water velocity reported in Fig. 3b, it is visible that the main flow is located within the channel during low flow conditions, having a velocity of less than  $1 \text{ m s}^{-1}$ . The upstream part of the simulated reach reveals that flow velocities are lower than the ones in the downstream reach, due to a backwater effects frequently observed along the Po River.

The iRIC model allows the evaluation of the analysed variables on each point of the grid. As an example, Fig. 4 reports the temporal variation of bed level elevation and flow velocity in two points A and B (see Fig. 3).

As visible, point A is characterized by a slight erosion typical of the Po River. During high flow conditions, however, sand is transported and deposited in the

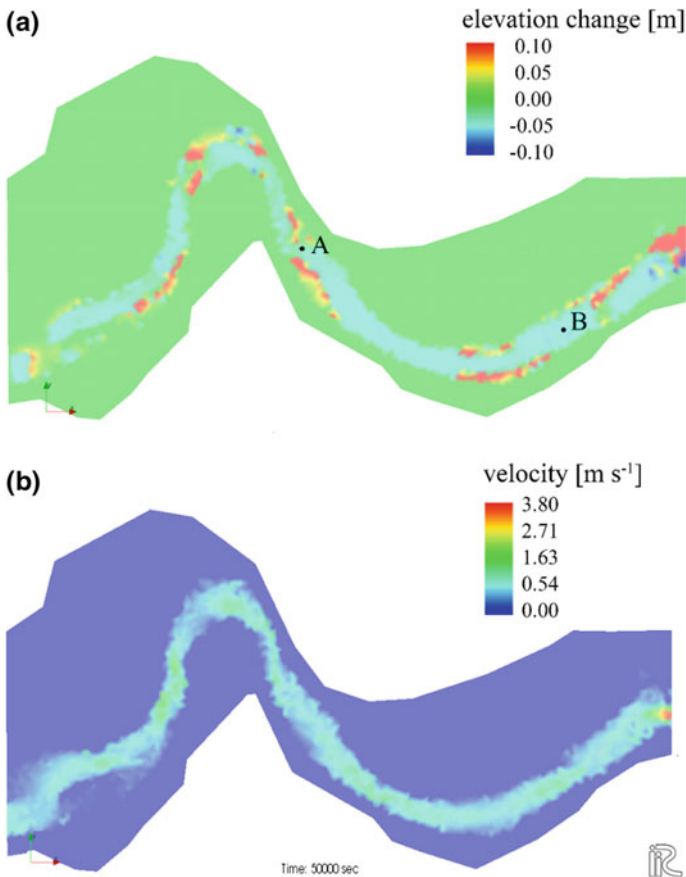


**Fig. 3** Maps of **a** bed elevation change and **b** flow velocity at the end of the simulation ( $t = 50000 \text{ s}$ ). A and B indicate the points where the temporal evolutions of bed elevation change and flow velocity are analyzed

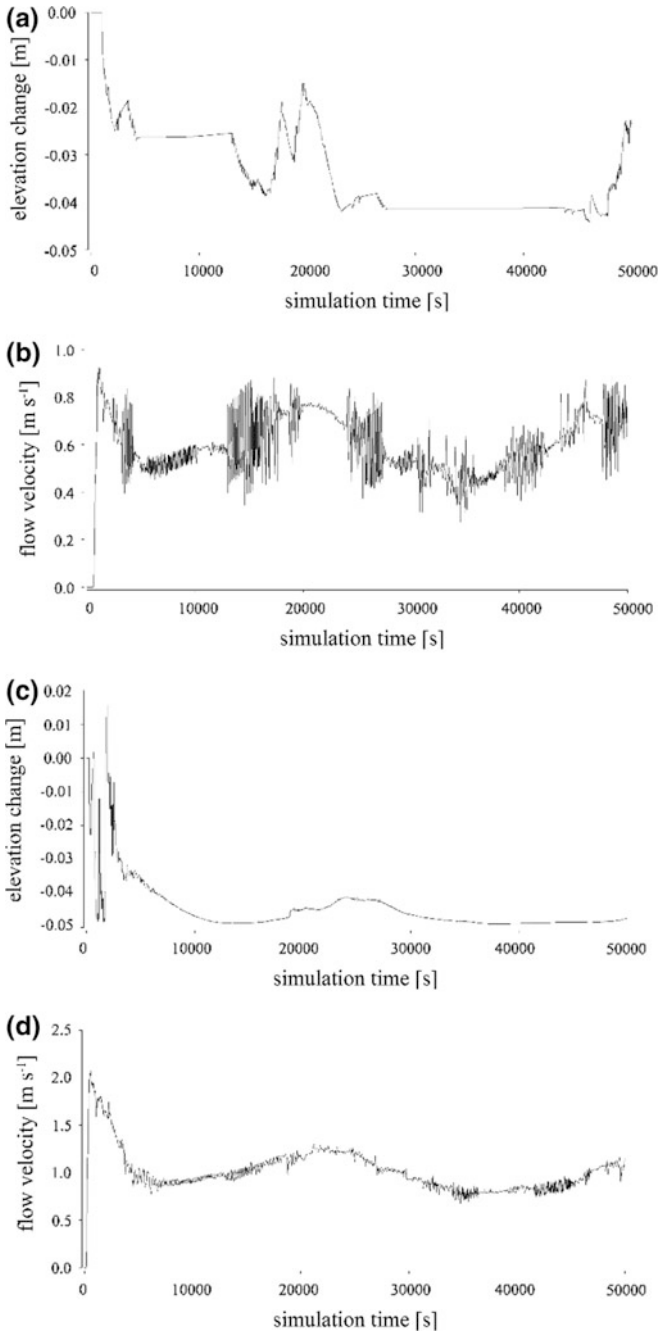


**Fig. 4** Temporal evolution of **a** bed elevation change and **b** flow velocity at the point A; **c** bed elevation change and **d** flow velocity at the point B

channel, reducing this trend. Lower velocities, associated with low discharges, do not permit any changes in the bed elevation, because the actual transport capacity results lower than the critical one. Regarding the velocity of the current, after an initial adaptation period, it spans between 0.4 and 0.8 m s<sup>-1</sup>. Overall, the flow velocity is influenced by the changing discharge (Fig. 2); nevertheless, this relationship is not as straightforward as expected. Indeed, the flow velocity resulted to be quite constant regardless of the variation of the discharge at the input cross-section.

Additional studies are necessary to address the oscillations observed on the velocity field, which are clearly non-physical and possibly consequence of the chosen time step or of the grid dimensions.

A similar behaviour is observable also for point B, but, in this case, the flow velocity profile is more stable (Fig. 4d), associated with a bed profile that seems to reach a morphological equilibrium after an initial phase of erosion (Fig. 4c).

From the previous observations, the morphodynamic evolution of the river is the main driver of such behaviour.

## 5 Conclusions

The paper presents a preliminary application of the open source code iRIC, which aims at (i) simulating the hydro-morphodynamic evolution of a reach of the Po River, in Italy; (ii) creating input data for more detailed models, necessary to evaluate the impact of a changing hydro-morphodynamics on hydraulic structures located in the channel.

Regardless of the low-precision delivered by the input data used, the performed simulation reproduces quite well the evolution of this reach, both in terms of hydraulics and morphodynamics. Indeed, as observed in past research, the variation of the bed level is usually in the order of few centimeters per year, while the flow velocity remains lower than 1 m s<sup>-1</sup>.

Because the outcomes reported here referred only to a preliminary analysis, additional studies are still necessary. On the one hand, the input data should be improved, involving local measurements of flow velocity and sediments transport to use as upstream input data, as well as water level for the downstream boundary conditions. On the other hand, the numerical description can be improved to reproduce more realistic situations, using a finer grid and a longer simulation time, or accounting for additional effects related to vegetation or spatially-variable roughness.

**Acknowledgements** This study has been developed within the INFRASAFE project, financed by the Emilia Romagna Region under the Por-Fesr Programme.

## References

- Agenzia Interregionale per il Fiume Po—AIPO (2005) Rilievo sezioni topografiche trasversali nella fascia B del Fiume Po, dalla confluenza con il Ticino al Mare in Italian
- Ashida K, Michiue M (1972) Studies on bed load transportation for nonuniform sediment and river bed variation. Disaster Prevention Research Institute Annuals 14
- Baranya S, Olsen NRB, Stoesser T, Sturm TW (2014) A nested grid based computational fluid dynamics model to predict bridge pier scour. *Proc Inst Civ Eng* 167(5):259
- Bufe A, Paola C, Burbank DW (2016) Fluvial bevelling of topography controlled by lateral channel mobility and uplift rate. *Nat Geosci* 9:706–710. <https://doi.org/10.1038/ngeo2773>
- Cozzi S, Giani M (2011) River water and nutrient discharge in the Northern Adriatic Sea: current importance and long term changes. *Cont Shelf Res* 31(18):1881–1893. <https://doi.org/10.1016/j.csr.2011.08.010>
- Domeneghetti A, Carisi F, Castellarin A, Brath A (2015) Evolution of flood risk over large areas: quantitative assessment for the Po River. *J Hydrol* 527:809–823. <https://doi.org/10.1016/j.jhydrol.2015.05.043>
- Garcia MH, Parker G (1991) Entrainment of bed sediment into suspension. *J Hydraul Eng ASCE* 117(4):414–435. [https://doi.org/10.1061/\(ASCE\)0733-9429](https://doi.org/10.1061/(ASCE)0733-9429)
- Guerrero M, Di Federico V, Lamberti A (2013) Calibration of a 2-D morphodynamic model using water-sediment flux maps derived from an ADCP recording. *J Hydroin Form* 15(3):813–828. <https://doi.org/10.2166/hydro.2012.126>
- Guerrero M, Latosinski F, Nones M, Szupiany RN, Re M, Gaeta MG (2015) A sediment fluxes investigation for 2-D modeling of large river morphodynamics. *Adv Water Resour* 81:186–198. <https://doi.org/10.1016/j.advwatres.2015.01.017>
- Hardy TB (1998) The future of habitat modeling and instream flow assessment techniques. *River Res Appl* 14(5):405–420. [https://doi.org/10.1002/\(SICI\)1099-1646\(199809\)14:5<405:AID-RRR510>3.0.CO;2-0](https://doi.org/10.1002/(SICI)1099-1646(199809)14:5<405:AID-RRR510>3.0.CO;2-0)
- Harrison LR, Dunne T, Fisher GB (2015) Hydraulic and geomorphic processes in an overbank flood along a meandering, gravel-bed river: implications for chute formation. *Earth Surf Proc Land* 40(9):1239–1253. <https://doi.org/10.1002/esp.3717>
- iRIC Software (2014) Mflow\_02 Solver Manuals, iRIC Software
- Kim HS, Nabi M, Kimura I, Shimizu Y (2014) Numerical investigation of local scour at two adjacent cylinders. *Adv Water Resour* 70:131–147. <https://doi.org/10.1016/j.advwatres.2014.04.018>
- Lamberti A, Schippa L (1994) Studio dell'abbassamento del fiume Po: Previsioni trentennali di abbassamento a Cremona. *Supplemento a Navigazione Interna, rassegna trimestrale di studi e informazioni* 3/4. Azienda Regionale per i porti di Cremona e Mantova, Cremona, Italy. in Italian
- Lanzoni S (2012) Evoluzione morfologica recente dell'asta principale del Po. *Atti dei Convegni dei Lincei, Giornata Mondiale dell'Acqua, Accademia Nazionale dei Lincei*. in Italian
- Lomax H, Pulliam TH, Zingg DW (2013). *Fundamentals of computational fluid dynamics*. Springer Science & Business Media
- Montanari A (2012) Hydrology of the Po River: Looking for changing patterns in river discharge. *Hydrol Earth Syst Sci* 16:3739–3747. <https://doi.org/10.5194/hess-16-3739-2012>
- Nabi M, de Vriend HJ, Mosselman E, Sloff CJ, Shimizu Y (2012) Detailed simulation of morphodynamics: 1. Hydrodynamic model. *Water Resour Res* 48(12). <https://doi.org/10.1029/2012WR011911>
- Nelson JM, Shimizu Y, Abe T, Asahi K, Gamou M, Inoue T, Iwasaki T, Kakinuma T, Kawamura S, Kimura I, Kyuka T, McDonald RR, Nabi M, Nakatsugawa M, Simoes FR, Takebayashi H, Watanabe Y (2016) The international river interface cooperative: Public domain flow and morphodynamics software for education and applications. *Adv Water Resour* 93:62–74. <https://doi.org/10.1016/j.advwatres.2015.09.017>



- Nelson PA, McDonald RR, Nelson JM, Dietrich WE (2015) Coevolution of bed surface patchiness and channel morphology: 1. Mechanisms of forced patch formation. *J Geophys Res: Earth Surf* 120(9):1687–1707. <https://doi.org/10.1002/2014JF003428>
- Nezu I, Nakagawa H (1993) Turbulence in open-channel flow. IAHR Monograph, Belkema, Rotterdam, The Netherlands
- Nones M, Ronco P, Di Silvio G (2013) Modelling the impact of large impoundments on the Lower Zambezi River. *Int J River Basin Manag* 11(2):221–236. <https://doi.org/10.1080/15715124.2013.794144>
- Nones M, Di Silvio G (2016) Modeling of river width variations based on hydrological, morphological and biological dynamics. *J Hydraul Eng* 142(7). [https://doi.org/10.1061/\(ASCE\)HY.1943-7900.0001135](https://doi.org/10.1061/(ASCE)HY.1943-7900.0001135)
- Nones M, Gerstgraser C (2016) Morphological changes of a restored reach: the case of the Spree River, Cottbus, Germany. in *Hydrodynamic and mass transport at freshwater aquatic interfaces. GeoPlanet earth and planetary sciences*. Springer International Publishing (eds). [https://doi.org/10.1007/978-3-319-27750-9\\_14](https://doi.org/10.1007/978-3-319-27750-9_14)
- Nones M, Varrani A (2016) Sensitivity analysis of a riparian vegetation growth model. *Environments* 3(4):30. <https://doi.org/10.3390/environments3040030>
- Ota K, Sato T, Nakagawa H, Kawaike K (2016) Three-dimensional simulation of local scour around a weir-type structure: hybrid euler-lagrange model for bed-material load. *J Hydraul Eng*. [https://doi.org/10.1061/\(ASCE\)HY.1943-7900.0001263](https://doi.org/10.1061/(ASCE)HY.1943-7900.0001263)
- Rouse H (1937) Modern conception of the mechanics of turbulence. *Trans ASCE* 102:463–543
- Syvitski JPM, Kettner AJ (2007) On the flux of water and sediment into the Northern Adriatic Sea. *Cont Shelf Res* 27(3–4):296–308. <https://doi.org/10.1016/j.csr.2005.08.029>

# Characteristics of Flow Around Aquatic Plants in Natural Conditions: Experimental Setup, Challenges and Difficulties

Łukasz Przyborowski, Anna M. Łoboda, Mikołaj Karpiński  
and Robert J. Bialik

**Abstract** Measurements of a 3D flow velocity field were conducted in lowland sandy bed river in Poland in two experiments during summer to check reliability of data gathered with the new model of Acoustic Doppler Velocimeter (Vectrino Profiler) in proximity of aquatic plants. For the purpose of this study a platform was built, on which two such velocimeters were mounted. This allowed for simultaneous measurements of flow velocity in front of and behind a single patch of submerged aquatic plants. Despite the promising readings from the first measurements, the results showed unexpected shapes in mean velocity profiles. The second experiment showed good agreement of signals from both devices, but it also revealed major differences in data quality compared with the first experiment. Further analysis showed that only few of all cells from each 35-cells section, which were simultaneously recorded by Vectrino, contained data with good characteristics of signal. The main results of this study showed that use of the Vectrino Profiler in natural conditions requires each time different setup, more densely stacked sections in each profile and constant changes of velocity range during the experiment to achieve best results.

**Keywords** Aquatic plants · Flow velocity measurements · Acoustic doppler velocimeter · Natural sandy bed river

---

Ł. Przyborowski (✉) · A. M. Łoboda · M. Karpiński · R. J. Bialik  
Institute of Geophysics, Polish Academy of Sciences, Księcia Janusza 64, 01-452 Warsaw,  
Poland  
e-mail: lprzyborowski@igf.edu.pl

R. J. Bialik  
Institute of Biochemistry and Biophysics, Polish Academy of Sciences, Pawińskiego 5a,  
02-106 Warsaw, Poland

## 1 Introduction

To understand how submerged aquatic plants affect sediment transport processes and turbulence production, one should evaluate open-channel flow in the proximity of plant patches (Siniscalchi et al. 2012). Studies on fluvial hydraulics are mostly carried out in controlled laboratory settings. Despite many advantages of that approach, the field measurements, systematic field studies and field experiments should validate laboratory studies (Sukhodolov 2015). In other words, field experiments can be treated as worthy addition and it can complement what was missing in laboratory work. Although a number of fieldwork projects have been undertaken recently using an Acoustic Doppler Velocimeter (ADV) to obtain flow profiles, the variability of water environments causes a constant lack of quantitative descriptions of what happens with flow near submerged plants. During the past two decades, this situation has changed due to the availability of new measurement techniques that can cope with the conditions of unsteady flow. The focus of previous research was especially centered on the role of interactions and system-specific studies of aquatic plants (e.g., Miler et al. 2014; Nepf 2012; Siniscalchi and Nikora 2012). Much attention has been placed on the investigation of velocity fields at the edge of plants' patches to look for patterns in flow gradients in those transition regions (e.g., Bouma et al. 2007; Folkard 2011; Zong and Nepf 2010; Souliotis and Prinos 2011; Siniscalchi et al. 2012; Sukhodolov and Sukhodolova 2012). It is important to notice that although these studies are vital for understanding river and tidal areas morphology, they are also important for biologists. For example, studies of submerged plant motions led to the discovery of *monami motions* (Okamoto and Nezu 2009).

The application of new measurement techniques, for example, in velocimetry and imaging, leads to better understanding of the water environment and complex flow-biota-sediment interactions. Although the possibilities of new studies are great, without experience, one cannot quickly adapt to and predict all the problems that often arise during fieldwork. Sharing those experiences and ideas is vital for researchers to avoid such obstacles. The idea of this study was to conduct experiments in the natural sandy bed Świder River, using two Vectrino Profilers mounted on a special platform. One of the reasons for such studies was to check the velocity profiles in front of and behind a single aquatic plant and to investigate flow characteristics and usefulness of the new measurement equipment, namely Vectrino Profilers. During the fieldwork, the important question arises: which level of confidence that water sediment density, vibrations, signal to power ratio coefficient and overall noise in received signal during measurements are acceptable. Furthermore, one has to keep in mind that collected data can be unreliable and need post-processing such as despiking, filtering and other analyzing techniques. In the result section of this study, one can see how much of the gathered data, after post-processing, have been considered as valuable. Main goal of this paper is to describe the problems in conducting measurements with use of laboratory

equipment in the field based on the experiences gathered with experiments conducted during July and September in the Świder River, Poland.

## 2 The Idea

The possibility of having velocity profiles in the vicinity of flexible aquatic plants is not a new idea, but it is still under development. The spatial resolution of the Vectrino Profiler allows one to study the velocity profile in the whole flow depth (Craig et al. 2011) in a small temporal window, when the flow conditions during the field experiment should not change. What one expects to see on the velocity profiles is that turbulence intensity should be higher at the edge of the plant (Zong and Nepf 2010) and that velocity should be lower behind the main body, but higher around the patch boundary and above the plant (Naden et al. 2006). There is also an assumption, observed in the flume with a patch of sparse of macrophytes (Siniscalchi et al. 2012), that with longitudinal velocity ( $U$ ) of about  $0.2 \text{ m s}^{-1}$ , a field of increased velocity exists near the bed and along the patch.

What has been anticipated in the current study was to check how practicable Vectrino Profilers, devices designed for very accurate laboratory measurements, are in natural conditions. There were no comparable experiments that could evaluate whether a profiling instrument is better than a single point velocimeter when used in the field. The reasons to use the Vectrino Profiler in field experiments are numerous. Recently, Craig et al. (2011), Zedel and Hay (2011) and Leng and Chanson (2016) carried out comparison measurements between single point ADV and Vectrino Profiler, which showed a good agreement of results from both devices, although those have been laboratory tests. What is more anticipated is that Vectrino Profiler allows one to gather much more data in the same time and with the same spatial resolution. The amount of fieldwork is also considerably lower. In the end, the experiment not only shows the applicability of chosen equipment and setup but later on, with simultaneous studies of sediment transport and plant biomechanics, will create an opportunity to look at the whole system of flow-biota-sediment interactions.

## 3 Methodology and Fieldwork

### 3.1 Equipment

Vectrino Profiler is a velocimeter based on a coherent Doppler processing. The internal and external structures of the device will not be described here, since it is not a goal of this paper and these descriptions are easily available via the Nortek website, <http://www.nortek-as.com>. However, to understand data gathered using

that technology, one must know how the Vectrino Profiler works. The device head emits acoustic waves into the water. Each one is called a ping. Four transducers receive the signal. The rate of emitting those pings is very high, but the acquisition rate is small, up to 100 Hz. It means that every saved value of velocity is, in fact, an average from multiple pings. The smaller the acquisition rate, the more pings are used in the calculation of the average velocity. The time between transmitting pings is called a ping interval. Bad timing leads to phase wrapping—a situation when a received signal occurs later than the next ping is started. The device allows one to use three different algorithms to calculate the optimum time between pings. These are minimum, adaptive and maximum algorithms. According to the manufacturer, the first one is best for turbulent flows, the second one is best when dealing with a moving bedform and the third one can be used when weak spots in the received signal are detected.

In the described measurements, the minimum ping algorithm has been chosen, since it is best suited for natural river conditions and therefore should provide the most accurate data having the smallest possible time between pings for given velocity range. Other parameters needed to set up are signal acquisition frequency, profile length and cell size. Cell size is responsible for setting up sampling volume of one measurement point in the profile containing normally 35 cells. Increasing cell size leads to velocity decorrelation and decreases number of cells. Acquisition frequency affects velocity averaging and is responsible for catching eddies of a certain size. Averaging velocity too much would lead to smaller eddies being missed, and certainly omits the viscous subrange level. However, boosting frequency to higher values, even if it theoretically allows to catch lower bands of the power spectrum, can be disappointing due to the Doppler noise that can effectively hide true velocities. The Nyquist criterion, on the other hand, says that the sample rate must be two times higher than the highest expected frequency of the studied signal (Nyquist 1928). With the sampling rate of 50 Hz, it can be expected that information about small scale turbulent motions above 25 Hz will be lost. According to experiments conducted by Siniscalchi et al. (2012) and Siniscalchi and Nikora (2013), an acquisition frequency of 50 Hz seems to be reasonable for the experiment purposes, although Sukhodolov and Sukhodolova (2012) have used frequency of 25 Hz.

Vectrino Profiler conducts measurement in a 3.5 cm long section, which starts 4 cm from the probe head and goes down to the point 7.5 cm from probe head. The best accuracy of received signal within that section can be found in the so-called “sweet spot” which is situated about 5 cm from the probe head. The receiver rods of Vectrino Profiler are lower than probe head, so whenever the device is submerged just below the water level, the measurement profile will start effectively about 7–8 cm below the water level to ensure that both transmitter in the head and receivers are submerged in water.

For the purpose of this study, a platform has been built. It is made from aluminum with polyethylene details. The construction is modular and consists of elements of the main frame with “legs”, two trolleys and two elevators where Vectrino Profiles are mounted. Trolleys can be mounted all the length of the frame

within 12.5 cm spaces and allow the elevators to be moved from the left to right side of the frame. The elevators allow one to change the height of the device head, while the main unit with connecting cable stays dry above the water level. The dimensions of the platform with an actual view of its deployment in the river and schemes of measured profiles within the platform range are shown in Figs. 1 and 2.

### 3.2 Carrying Out Experiment

The suitable canopies of plants, *Myriophyllum spicatum* L and *Myriophyllum alterniflorum* DC species, were found near to the river bank. *M. alterniflorum* DC is

**Fig. 1** View of the platform setup during measurement of flow behind and in front of *Myriophyllum alterniflorum* DC on July 16, 2016; arrows show platform dimensions

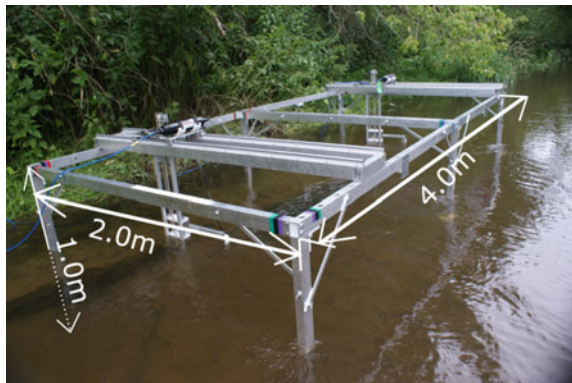


**Fig. 2** Schemes of plant patches of *Myriophyllum alterniflorum* DC and *Myriophyllum spicatum* L and the corresponding measuring points during the first experiment on July 16, 2016, and during the second experiment on September 22, 2016, on the Świder River

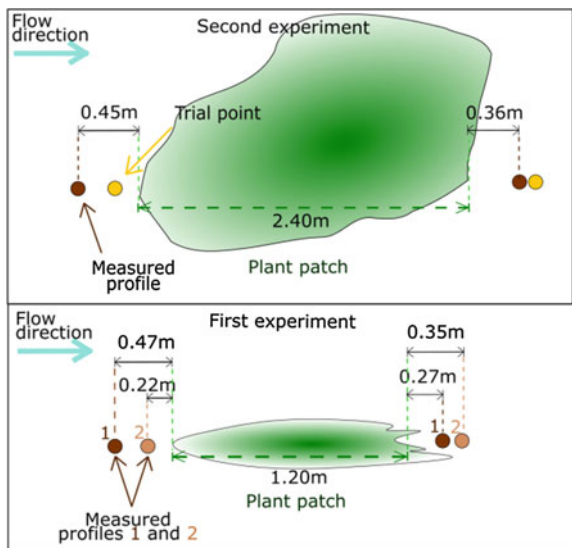
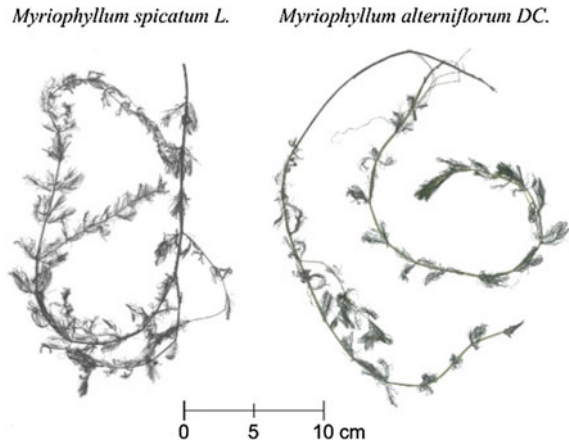


**Fig. 3** *Myriophyllum spicatum* L and *Myriophyllum alterniflorum* DC—stems of plants from the experiment on July 16, 2016



a submerged, perennial plant anchored in the bottom with a branched, delicate stem. *M. spicatum* L is also a perennial herb rooted in the bottom. The most visible difference between them is color and length of stems. *M. spicatum* L has branched, reddish stems, while the stem of second macrophyte is green. It is characteristic for them to be rather insensitive to wave motions (Kłosowski and Kłosowski 2007). Having in mind the fact that the experiment was conducted on July 16, which is in the mid-summer season, the plant patches were considered fully developed and the plants themselves were optically in good condition. At the end of the each experiment, plants were collected for biomechanical tests and it has been found that the length of some of the individual shoots exceeded 70 cm. Figure 3 shows photography of both plants taken for laboratory work after the first experiment.

The Świder River is an unregulated sandy bed lowland river. The coordinates of the location where the experiments were conducted are 52°08'24.9" N and 21°15'52.8" E. At the time of the first measurement, the discharge was  $2.46 \text{ m}^3 \text{ s}^{-1}$  and during the second measurement it was lower,  $1 \text{ m}^3 \text{ s}^{-1}$ . In the first experiment the chosen plants inhabited the right side of the river. There were two patches of plants, a smaller one was situated about 1.5 m from the bank, and a bigger one about 2 m from the bank. After assembling a platform on the shore it was carefully placed in the river with the longer axis parallel to the plant and therefore to the flow direction. The next step was to set up a horizontal alignment of the platform using a spirit level, which was needed to ensure that the probe head would not be tilted. The direction of the probe head was set up using the clamps. Then device geometry was matched with the stream direction—the fourth receiver's rod marked with the red color should be pointing in the direction in which water is flowing. Otherwise, one will have to read negative velocities as positive ones. The location of measurement points is shown in Fig. 2 After the experiment, plants were collected for biomechanical tests.

The second measurement was conducted on September 22 a few hundred metres down the Świder River than the first location. The plant species found near to the

left bank was *Myriophyllum spicatum* L, shaped in a 1 m wide and 2 m long patch, with the individual shoots not exceeding 40 cm. The setup of the platform was similar, with the measurement point 45 cm in front of a plant and 36 cm behind it. The water level was low, 21 cm in front of and 31 cm behind the plant. Lower water level allowed to conduct more than before, overlapping sections in each profile within one day. The study ended up with 11 measurements from 7 cm below the water level to the bottom in each profile. Before that, two sets of 3 min duration measurements in two points were made where profiles were composed of one 35 mm section starting 0.06 m below the water level. Swapping of both devices was made between sets to check if both devices had the same velocity profiles.

## 4 Results

### 4.1 Signal Analysis

Analysis of the quality of received signal starts in the field, with use of the visual GUI of the software used to operate the Vectrino Profilers. The Vectrino Profiler is still a rather new equipment and the knowledge of how to properly use it and read signals, although obtainable via manufacturer's web page and manuals, is limited. The following text is therefore a summary of observations with regard to the growing experience of other users and the manufacturer's guide and forum comments as well.

When the measurement begins, except for velocity profiles in x, y and z directions, one can also see the distance to the bottom, amplitude, signal to noise ratio (SNR) and correlation profiles for each of the beams. The instrument converts signal amplitude to dB values. The values are calculated for each bin and the amplitude profiles of each beam should have a curved shape with the biggest values between 5 and 15 cells, counting from the cell nearest the device head. The SNR is tied to amplitude, because it shows how much noise the device receives compared with the overall signal. A high SNR in backscatter is needed to account velocity measurements as correct (Poindexter et al. 2010) and that threshold is considered to be at a level of 20 dB. Noise is measured once at the start of measurements or when the adaptive ping algorithm is on. It is exactly the amplitude value when no signal is generated by the device head. The SNR profile shape should be slightly more curved than for the amplitude profile, with the values ranging from above 20 dB in the ends and above 30 dB in the "sweet spot".

Mean SNR values from all 4 beams, measured during the trials on the Świder River, are presented in second plot in Figs. 4 and 5 for both devices. It is visible that worse SNR values are below the "sweet spot" but the overall shape of SNR profile is not as expected and most of the values are lower than 20 dB. The SNR and amplitude are generally low when there are not enough particles in the water, which is basically not the case in the natural river, but it is very often an issue in the



laboratory flumes. Signal meeting mentioned criteria for the SNR values, the “good” signal, has been registered during the first measurements, and “bad” signal, not meeting those criteria, has been encountered during the second experiment, what is expressed as small amount of red dots in Fig. 9. Even reducing the threshold to 15 dB did not considerably raised the number of cells with “good” signal. Considering what caused that difference, one must know that the place was not the same; bed conditions were very similar although the river discharge was two times lower in the latter. The only reasonable explanation is that a ‘bad’ reading has been caused by smaller amount of particles and that the situation may happen apparently even in the natural river if the flow is low.

In order to ensure proper values and shape of the amplitude and SNR plots, one should check the correlation plot. The correlation is also calculated for each cell and it is an auto-correlation function or normalized covariance of two adjacent returning signals. Correlation values should be greater than 90%. Low correlation values occur when the SNR is low or when the velocity range is incorrectly set. In Figs. 4 and 5, the third plot represents mean correlation values. Shape of these plots reflects shape of the SNR plots. The velocity range should be adjusted to the expected velocities to prevent overlapping of the returning signal. If the velocity range is lower than real velocities, the frequency of sending signals will not be sufficient to give return from the same particles in one ping what leads to “phase wrapping”. Turbulence intensity, shear and pulse interference, as one can read in the ADV processing guide, can also alter correlation values.

Practically, the only thing that can be done in the field is to change the velocity range or the ping algorithm. Both parameters have impact on correctness of

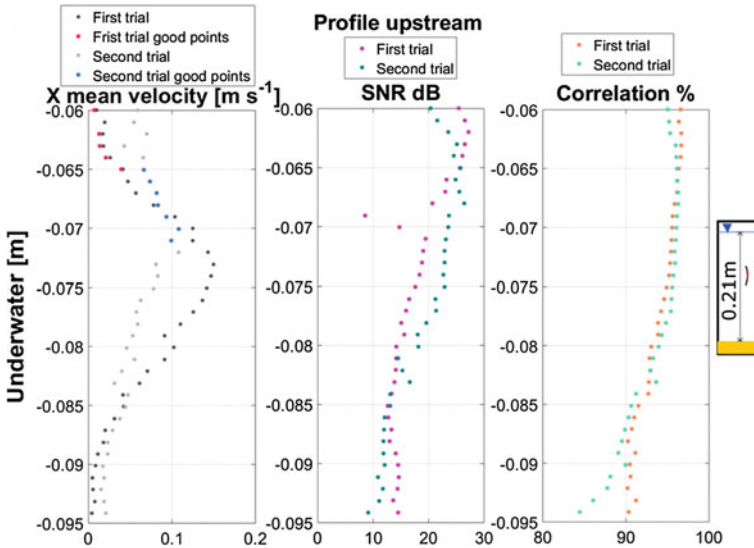


Fig. 4 Outcomes from testing Vectrino profilers by swapping devices in front of the patch

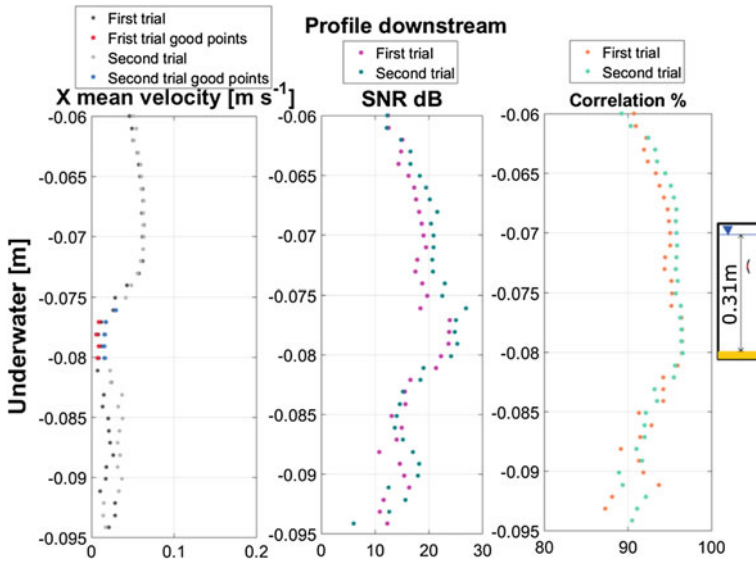


Fig. 5 Outcomes from testing Vectrino profilers by swapping devices behind the patch

measured velocities because both are changing ping frequency. Seeding water is an alternative that could bolster up SNR readings, but it depends on the currents and size of the river. In the case of the conducted experiment, seeding was considered impractical due to the possibility that seeding particles will be stuck in the plant shoots. Low SNR can give the information that there are some other sources of noise in the water, like electronic noise from another Doppler device. By default, the instrument uses high power level that should result in high SNR readings, but there is also an option to reduce transmit power to prevent induced streaming. Poindexter et al. (2010) discovered that acoustic streaming caused by the instrument can reach  $0.02 \text{ m s}^{-1}$  in the velocity component parallel to the emitter but this effect is lower in turbulent flows. In the experiment setup, the vertical velocity was parallel to the emitter but with main velocity component greater than the  $0.08 \text{ m s}^{-1}$  threshold, acoustic streaming was considered negligible.

In the investigation by Ghasemi (2016), conducted in laboratory flume, it was assumed that in order to work on good quality data, only ‘sweet spot’ data should be considered with the threshold for SNR above 15 dB and the threshold for correlation above 70% with the distance between following sections in vertical plane was 1 cm and a frequency of 50 Hz. Even with such selection, 2-D phase wrapping can effectively change true values of mean velocities. One should be aware that this situation may occur if any of the real streamwise, cross-stream or vertical velocity exceeds that velocity value which was set up in the device configuration. Phase wrapping can be detected by checking the histograms of velocity in the single cell of the profile. Analysis of data collected on the Świder River has

not revealed this 2-D phase wrapping—velocity range has been set up higher than measured velocity.

The next important factor worth considering before the results can be analyzed is data filtering. For example, the Phase-Space Thresholding Method developed by Goring and Nikora (2002) was implemented for despiking the procedure of gathered data. The results of implementing that procedure have shown a general agreement of the raw mean velocity values with the filtered ones. Some of the velocities versus time plots have occasionally shown spikes in the  $U$  velocity signal. The filtering procedure removed those spikes.

## 4.2 Velocity Profiles Around the Plant

In order to check how a plant affects the velocity field, one must conduct measurements upstream and downstream of the obstacle as was, for example, done by Siniscalchi and Nikora (2013). The point farthest from the front of a plant should not contain any disturbances from the patch but only an ambient turbulence and the velocity gradient should be the biggest in the boundary layer. Behind the patch, Kelvin-Helmholtz vortices and other turbulence driven phenomena should be visible and a mixing layer should be detected (Sukhodolov and Sukhodolova 2012). In other words, the flow downstream of the patch should be affected by a drag generated by the patch.

Results from the first patch will not be presented due to connection issues that occurred during the experiment which caused inconsistencies in data. Results from the first experiment conducted on July 16, from the second patch, are shown in Figs. 6, 7, 8 and placement of the measured profiles is shown in Fig. 2. Red dots represent cells that met certain SNR criteria—the SNR values were greater or equal to 20 dB for 80% of the measurement time if the threshold was met for all four beams. Mean values of velocity in red color dots were also corrected by the use of Phase-Space Thresholding Method to remove spikes in recorded velocities. Gray dots represent raw gathered data without any filtering. Each profile contains seven to eight profiles, called further sections, each representing single, 35 mm deep fragment where Vetrino Profiler was measuring velocities at one time. The example of division of the sections in a profile is shown in the second plot in Fig. 6.

The first experiment shows that just behind the patch mean  $U$  velocities are lowering with the depth in a slightly steep manner. Profile 1 in front of the patch shows even more steep decrease of velocities but in profile 2 mean  $U$  velocities are more scattered. Majority of the 35 mm sections in all the profiles show a non-linear shape. In most of those sections, the middle points have the highest values. Outlying points from each section—usually gray points which were not considered as having high enough SNR have lower  $U$  velocity values. Also most of the red points in each section correspond to the “sweet point” location. In Figs. 6 and 8 there are visible sharp changes in  $U$  velocity in some sections, especially in front of the patch. To consider those lower velocity values as true one should check if there are

**Fig. 6** Mean X velocity profile at the second plant patch from measurements taken on July 16, 2016. Roman numerals and dashed lines indicate separate sections

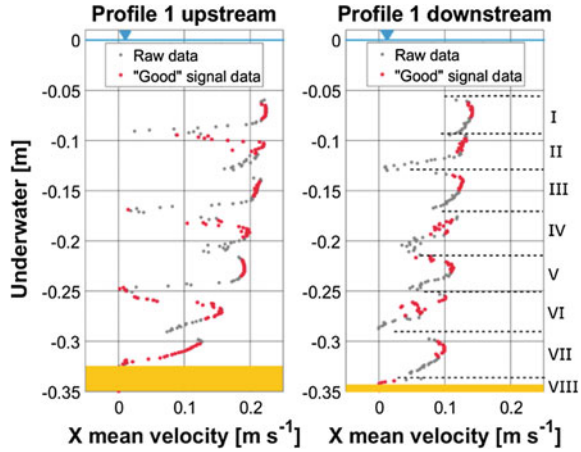
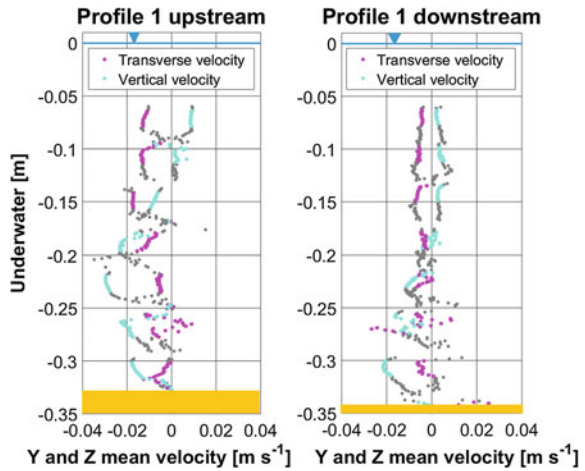
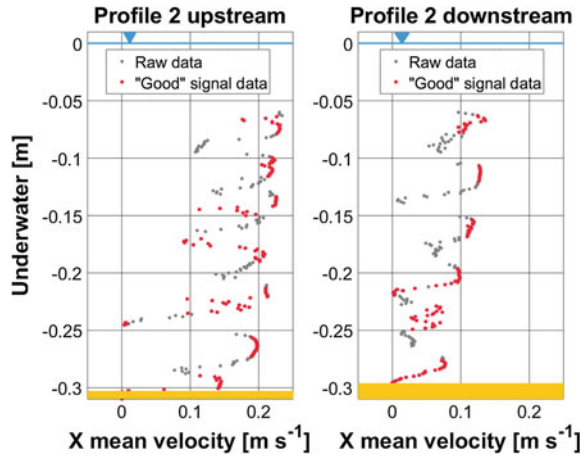


**Fig. 7** Mean transverse (purple) and vertical (cyan) velocity profiles at the second plant patch from measurements taken on July 16, 2016



higher values in vertical or transverse velocities. Those are shown in Fig. 7. Most of the sharp changes in transverse and vertical velocities can be found in the sections 5–15 cm above the bottom level. However, in the depth of 25 cm below water in front of the patch (Fig. 6) there is an abrupt drop of  $U$  velocities while vertical and transverse velocities are close to  $0 \text{ m s}^{-1}$  value, which is an unexpected result. Considering all velocities, points close to the bottom have a trend decreasing to zero as they should, even in raw data. Further,  $U$  velocities have smaller values downstream. Comparison of adjacent profiles shows few differences. On the one hand, profile 1 upstream the patch (Fig. 6) has a more smooth transition to zero velocity at the bottom level than profile 2 (Fig. 8), which was 25 cm closer to the beginning of the patch. On the other hand, in the second profile upstream the patch, the bottom level was 2 cm higher. If it had been a peak of sand wave then it could

**Fig. 8** Second X mean velocity profiles from second patch from measurements taken on July 16, 2016

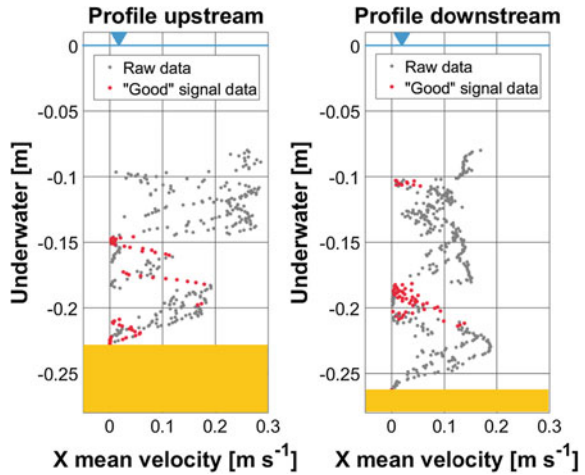


have caused a more sharp velocity decrease. Therefore, the observed change could not be an error of the instrument. Downstream of the patch, in profile 1, discontinuities in mean velocities start 17 cm below water level, while in profile 2 more adjacent points are coherent and discontinuities starts deeper, 21 cm below water level. Shoots of the patch floated up to 20 cm above bottom level. Assuming that flow disturbances induced by the plant are diminishing with the distance, those mean  $U$  velocity results are correct. However, having only two profiles behind the patch is not enough to be sure if the observed trend is true or it was just a temporal situation.

Results of dense stacked profiles, made during the second experiment, conducted on September 22, show very low SNR readings and therefore it was hard to distinguish a proper “sweet spot,” even when considering points with SNR equal or greater than 15 dB for 80% of time, which were marked as red dots in Fig. 9. One can see that the profile downstream the patch shows about 3 cm long section meeting those criteria. Mean  $U$  velocity in that section was lower than in adjacent sections and it had the exact height of the main bulk of the plant shoots, which floated no higher than 10 cm above the bottom level. Note that the profile in front of the patch also has a significant velocity decrease about 15 cm below water level and deeper points, although with low SNR, show a higher mean velocity. In the first experiment, the profile downstream does not show such clear change. Considering high correlation of signal in the second experiment and the different patch geometries in both experiments, these differences in shape of mean velocities behind patches can be treated as possible.

According to the fact that instrument setup during the first and the second experiment was the same, we have to look for possible reasons for such unclear results in the following aspects. Firstly, the velocity range in the Vectrino Profiler setup has not been decreased enough to match the slower flow observed during the second experiment; therefore, higher frequency of pings generated more noise. Next, lower water level and the plant patch which was much bigger than in the first

**Fig. 9** Mean X velocity profiles from measurements taken on September 22, 2016



experiment may have altered the specification of particles suspended in the water which also had its impact on the SNR reading. Finally, the poor results may not be necessarily bad, due to the two reasons: the correlation values were high; changes in SNR threshold during data analysis can reveal enough measured points to look for flow patterns even if velocity values are biased, considering the bias is constant for certain SNR levels. Figures 4 and 5 show that changes in SNR have its reflections in correlation, but measured velocities do not change abruptly when SNR goes down, so the bias seems to be irrelevant if a very accurate velocity reading is not necessary in the study. The same conclusion is proper for situation when there is low correlation but with good SNR reading. Velocities measured with correlation lower than 90% but higher than 60% may still be used for calculation of mean velocity, but not for calculation of turbulence statistics because they may be biased as manufacturer suggests.

## 5 Conclusions

Velocity measurements were conducted at two locations on the Świder River, with two species of aquatic plants. Data gathered during the experiment using the Vectrino Profiler show limited resemblance to a theoretical, logarithmic shape of velocity distribution in open channel flow. Velocity values from the “sweet spot” often happen to contain the same cells that meet certain SNR conditions. Mean streamwise  $U$  velocities tend to decrease toward 0 outside the “sweet spot”. What has been unexpected, is that SNR values have not always had an impact on the correlation values, which in every case have been high enough to consider velocity values as true. It is worth considering a longer time than 3 min of performing each measurement for better estimation of mean velocity values. On the other hand, a

living environment of the natural river always gives slightly different mean velocities even when performing tests one after another in the same conditions, which is shown in Figs. 4 and 5. Regarding the best placement of measurement points, the best setup is one stationary point in front of the patch and several others behind it, with increasing distance to each other with downstream direction, which should allow the investigation of the evolution of vortices behind the patch. Specific calibration of the Vectrino Profiler, e.g., adjusting velocity range, has to be performed with care to avoid loss of data quality or phase wrapping in received signal. For the purpose of further study of the turbulence characteristics, data filtering procedures, cutting “bad” signal and overall very accurate investigation of a signal at the scale of whole profiles and at the scale of individual cells will be necessary with special regard to SNR and correlation values.

Overall, further analysis of the results and continuation of the experiment in natural conditions needs to be undertaken. Velocities obtained with Vectrino Profiler cannot be treated with confidence in the whole 35 mm section; however, data from individual cells mostly in the middle part of sections seem to be valuable as they tend to have good quality. It is clear that more measurements and a different setup should be considered to obtain more valuable data.

**Acknowledgements** This work was supported by the National Science Centre, Poland, Grant No. UMO-2014/13/D/ST10/01123 ‘Field experimental investigation of hydrodynamics of water flow-vegetation-sediment interactions at the scale of individual aquatic plants’.

## References

- Bouma TJ, van Duren LA, Temmerman S, Claverie T, Blanco-Garcia A, Ysebaert T, Herman PMJ (2007) Spatial flow and sedimentation patterns within patches of epibenthic structures: combining field, flume and modelling experiments. *Cont Shelf Res* 27(8):1020–1045
- Craig RG, Loadman C, Clement B, Rusello PJ, Siegel E (2011) Characterization and testing of a new bistatic profiling acoustic doppler velocimeter: the Vectrino-II. In: *Current, waves and turbulence measurements (CWTM)*, 2011 IEEE/OES 10th. IEEE, pp 246–252
- Folkard AM (2011) Vegetated flows in their environmental context: a review. *Proc Instit Civil Eng Comput Mech* 164(EM1):3–24
- Ghasemi A (2016) Study of macroturbulence and bursting via the -1 spectral power law region of turbulent open channel flows over gravel beds. *Theses and dissertations—civil engineering, paper, vol 43*. University of Kentucky, Lexington, United States
- Goring DG, Nikora VI (2002) Despiking Acoustic Doppler Velocimeter data. *J Hydraul Eng* 128(1):117–126
- Kłosowski S, Kłosowski G (2007) *Aquatic and marsh plants* (in Polish). MULTICO Oficyna Wydawnicza, Warsaw
- Leng X, Chanson H (2016) Steady and unsteady turbulent velocity profiling in open channel flows using the ADV vectrino II profiler. In: *IAHR international symposium on hydraulic structures*. Utah State University
- Miler O, Albayrak I, Nikora V, O’Hare M (2014) Biomechanical properties and morphological characteristics of lake and river plants: implications for adaptations to flow conditions. *Aquat Sci* 76(4):465–481

- Naden P, Rameshwaran P, Mountford O, Robertson C (2006) The influence of macrophyte growth, typical of eutrophic conditions, on river flow velocities and turbulence production. *Hydrol Process* 20(18):3915–3938
- Nepf HM (2012) Hydrodynamics of vegetated channels. *J Hydraul Res* 50(3):262–279
- Nyquist H (1928) Certain topics in telegraph transmission theory. *A.I.E.E. Trans* 47:617–644
- Okamoto T, Nezu I (2009) Turbulence structure and “monami” phenomena in flexible vegetated open-channel flows. *J Hydraul Res* 47:798–810
- Poindexter CM, Rusello PJ, Variano EA (2010) Acoustic Doppler velocimeter-induced acoustic streaming and its implication for measurement. *Exp Fluids* 50(5):1429–1442
- Siniscalchi F, Nikora VI (2012) Flow-plant interactions in open-channel flows: a comparative analysis of five freshwater plant species. *Water Resour Res* 48(5):2805–2814
- Siniscalchi F, Nikora VI (2013) Dynamic reconfiguration of aquatic plants and its interrelations with upstream turbulence and drag forces. *J Hydraul Res* 51(1):46–55
- Siniscalchi F, Nikora VI, Aberle J (2012) Plant patch hydrodynamics in streams: mean flow, turbulence, and drag forces. *Water Resour Res* 48(1):273–279
- Souliotis D, Prinos P (2011) Effect of a vegetation patch on turbulent channel flow. *J Hydraul Res* 49(2):157–167
- Sukhodolov AN, Sukhodolova TA (2012) Vegetated mixing layer around a finite-size patch of submerged plants: part 2. Turbulence statistics and structures. *Water Resour Res* 48(12)
- Sukhodolov AN (2015) Field-based research in fluvial hydraulics: potential, paradigms and challenges. *J Hydraul Res* 53(1):1–19
- Zedel L, Hay A (2011) Turbulence measurements in a jet: comparing the Vectrino and Vectrino II. In: *Current, waves and turbulence measurements (CWTM), 2011 IEEE/OES 10th*. IEEE, pp 173–178
- Zong L, Nepf H (2010) Flow and deposition in and around a finite patch of vegetation. *Geomorphology* 116(3–4):363–372



# Spectral Behavior of Sand Bed Rivers at Small Wavelengths

Jie Qin and Jochen Aberle

**Abstract** The ‘-3’ scaling law of sand waves has often been verified in studies dealing with statistical properties of sand beds. Most of the data used for this verification were measured in laboratory studies in which it is possible to reach equilibrium conditions. Large scale rivers, on the other hand, are rarely characterized by steady flow conditions which means that true equilibrium conditions are special cases and a deviation from the ‘-3’ scaling law may therefore be expected. This issue is investigated in the present study by the analysis of the spectral behavior of river bed surfaces of the Elbe River in Germany. The emphasis of the study is placed on the spectral behavior at small wavelengths. The results show that the spectral behavior at small wavelengths deviates from the ‘-3’ scaling law and that this spectral region can be characterized by steeper slopes. The relationship between the spectral characteristics at small wavelengths and flow discharge is subsequently analyzed. The overall results support the hypothesis that the development of secondary dunes affects the spectral behavior at small wavelengths.

---

J. Qin (✉)

College of Harbour, Coastal and Offshore Engineering,  
Hohai University, Nanjing, China  
e-mail: qinjie@alumni.cuhk.net

J. Qin

Department of Hydraulic and Environmental Engineering, Norwegian University  
of Science and Technology, Trondheim, Norway

J. Aberle

Department of Civil and Environmental Engineering, Norwegian University  
of Science and Technology, Trondheim, Norway  
e-mail: jochen.aberle@ntnu.no; jochen.aberle@tu-braunschweig.de

J. Aberle

Leichtweiß-Institut für Wasserbau, Technische Universität Braunschweig,  
Braunschweig, Germany

© Springer International Publishing AG 2018

M. B. Kalinowska et al. (eds.), *Free Surface Flows and Transport Processes*,  
GeoPlanet: Earth and Planetary Sciences,  
[https://doi.org/10.1007/978-3-319-70914-7\\_24](https://doi.org/10.1007/978-3-319-70914-7_24)

## 1 Introduction

Sand waves form due to the interaction of flow and the motion of the bed material (e.g., Coleman and Nikora 2009, 2011). The subsequent interaction between fluid flow and sand waves affects sediment transport processes, flow resistance, and sedimentary records which is of importance for many different scientific disciplines ranging from engineering through geomorphology to ecology. In order to better understand the significance of sand waves for these processes, a thorough quantitative analysis of their morphological characteristics is desirable.

Morphological characteristics of sand waves can be described based on statistical and spectral analyses (Hino 1968; Nikora et al. 1997; Coleman et al. 2011). Based on dimensional analysis, Hino (1968) proposed the ‘-3’ scaling law for the wave spectrum of sand dunes at equilibrium stage which has since been confirmed in many different laboratory and field studies (Jain and Kennedy 1974; Nikora and Hicks 1997; Aberle et al. 2010; Coleman and Nikora 2011; Guala et al. 2014). The upper and lower boundaries of the ‘-3’ scaling region have been related to flow depth and grain size, respectively. Nikora et al. (1997) extended this scaling concept and proposed a conceptual model to describe the scaling behavior of river beds from the micro- (ripples, dunes) through the meso- (bars) to the macro-scale.

The ‘-3’ scaling law has been developed for sand waves at equilibrium conditions. For such conditions, the wave height is positively related to wavelength and the ‘-3’ law indicates self-similarity (Nikora and Hicks 1997). The requirement of equilibrium conditions is, however, difficult to be satisfied in natural conditions. In the field, the discharge is constantly varying and hysteresis effects have been reported between sand wave characteristics and flow conditions (Perumal et al. 2004; Humphries et al. 2012). Moreover, during a hydrograph the aforementioned relationship between wave height and wavelength changes. For example, following the peak of the hydrograph, the wavelength continues to increase with decreasing discharge for a certain period, while the wave height remains constant or decreases (Wilbers and Ten Brinke 2003). In this context, Baas (1994) and Venditti et al. (2005b) suggested that 2D sand waves are nonstable bedforms which may become three-dimensional given a sufficiently long flow period and a sufficient bed width for sediment transport.

The bed material has also an important effect on dune characteristics. For gravel bed rivers, Singh et al. (2012) and Qin et al. (2015) observed a scaling behavior deviating from the ‘-3’ law which was explained by the development of bed-load sheets. Tuijnder et al. (2009) investigated the morphological features of supply-limited dunes in a laboratory study and identified likewise a deviation from the ‘-3’ scaling law. These findings indicate that the ‘-3’ scaling law may only be applicable to sand wave surfaces considering the following requirements: (1) a sufficiently long steady flow period to develop an equilibrium condition; (2) well sorted sediment; and (3) an alluvial condition ensuring that an adequate amount of sand is present on a bed.

Although natural rivers rarely fulfill all these requirements (particularly the first requirement), the spectral behavior deviating from the ‘-3’ law has seldom been

addressed in the literature. In this study, we focus on the spectral behavior of sand waves surfaces collected at a straight river reach and investigate: (1) whether the spectra of the bed surfaces show a deviation from the ‘-3’ scaling law; and (2) the possible reasons causing such a deviation. Section 2 provides the background on the data used in the study and the Sect. 3 presents the results of the spectral analyses. These are discussed in detail in Sect. 4. Section 5 concludes the paper.

## 2 Data and Methods

The bed topography data analyzed in this paper are identical to the data used in the study of Aberle et al. (2010). These data were collected in a 2 km long straight reach of the Elbe River (Elbe-km 272–274) which is regulated by inclined groynes on both banks. The effective bed width for sediment transport between the groyne heads is approximately 100 m, and the bankfull flow discharge corresponds approximately to  $1000 \text{ m}^3 \text{ s}^{-1}$ . The mean diameter of bed load particles is  $d_m = 2.0 \text{ mm}$ , while the underlying bed material is slightly coarser ( $d_m = 3.3 \text{ mm}$ ). Information on flow depth and flow discharge was available from a nearby gauging station at the township of Aken. These values were used as input for a 1-D hydrodynamic model to calculate hydraulic conditions as summarized in Table 1 (for details see Aberle et al. (2010)).

Bed topography measurements were carried out between 25.02.2005 and 11.07.2006 by the Water and Shipping Authority of Dresden, Germany, on behalf of the Federal Waterways Engineering and Research Institute (BAW), Germany. The measurements were carried out with the sounding vessel Rosslau using a Leica 1200 GPS (position accuracy  $<0.5 \text{ m}$ ). A total of 37 echo sounders (200 kHz) with an accuracy of  $\pm 2 \text{ cm}$  were used to measure the bed elevations with a sampling frequency of 20 Hz. The simultaneously operated echo sounders were mounted to two 4 m long booms on either side of the vessel (12 echo sounders per boom) and on the vessel body (13 echo sounders). The separation distance between the echo sounders was 0.33 m and the covered width corresponded hence to 12 m. For a full scan of the bed, the vessel was navigating several times over the reach at different lateral positions. The echo sounders were immersed during the measurements (0.47 m below the water surface) and the cone angle was  $12^\circ$ . The bed was scanned without gaps for a distance from the echo sounder transmitters to the bed larger than 1.57 m (i.e., water depth of 2.04 m). During data acquisition, three adjacent echo sounders were considered as one unit and the only the lowest reading was recorded in order to reduce the data stream. The corresponding spatial coordinate was obtained by averaging the GPS locations of the three echo sounders. The streamwise data density corresponded to approximately 9–10 values per meter and the raw data were corrected roll, pitch, heave, and yaw. Further details in regard to the data acquisition can be found in (Aberle et al. 2010).

The available output of a measurement was a digital elevation model (DEM) in Gauss-Krueger coordinates with a grid size of  $1 \text{ m} \times 1 \text{ m}$ . The final data used by Aberle et al. (2010) were reduced elevational fields with a grid size of  $1 \text{ m} \times 1 \text{ m}$

and an area of 1664 m × 66 m which were extracted from a pre-defined rectangular area. The definition of such a subsection was required to ensure that the same bed area was investigated for the different hydraulic conditions. Moreover, Aberle et al. (2010) rotated the subsection to align the x-axis with the flow direction and this rotation made it necessary to re-grid the data.

In this paper, the analysis is based on both the data in GaussKrueger coordinates and the rotated and re-gridded data. The elevational fields were detrended by fitting a surface to the data defined by  $S_t = a + bx + cy + dx^2y$  where  $a, b, c,$  and  $d$  are coefficients, and  $x$  and  $y$  indicate longitudinal and transverse distances, respectively. Figure 1 shows exemplarily the detrended surface for the scan carried out at 2005/02/25. The spectral behavior can be investigated based on the spatial averaged longitudinal spectra:

**Table 1** Summary of flow conditions and the fitted parameters of  $R_1$  region.  $Q$  is flow discharge ( $m^3 s^{-1}$ );  $S$  is bed slope (%);  $U$  is mean flow velocity ( $m s^{-1}$ );  $H$  is flow depth (m);  $\beta_{R1}$  and  $X_I$  are spectral characteristics related to  $R_1$  regions; and  $\alpha$  is the shape parameter of a fitted gamma distribution to wavelengths

Date	$Q$	$S$	$U$	$H$	Fr	$\beta_{R1}$	$X_I$	$\alpha$
2005/02/25	779	0.02	1.22	3.66	0.15	8.59	4.67	6.9
2005/03/01	709	0.02	1.22	3.43	0.14	7.37	4.68	6.7
2005/03/23	1878	0.02	0.50	5.94	0.24	6.97	4.81	9.1
2005/03/31	1257	0.03	0.95	5.05	0.31	6.81	4.49	4.9
2005/04/06	813	0.03	1.23	3.77	0.23	7.29	4.68	5.4
2005/04/13	810	0.03	1.24	3.76	0.23	6.68	4.75	6.8
2005/04/18	619	0.03	1.17	3.10	0.19	6.22	4.91	6.8
2005/06/02	337	0.02	1.03	1.84	0.07	5.87	4.34	8.9
2005/07/19	355	0.02	1.05	1.94	0.08	6.67	5.00	9.0
2005/08/01	265	0.01	1.00	1.44	0.03	6.96	4.40	11.6
2005/09/29	277	0.01	0.96	1.51	0.03	5.28	4.24	13.6
2005/11/15	216	0.01	0.94	1.14	0.02	6.67	4.16	9.9
2006/04/24	1320	0.03	0.80	5.00	0.30	7.57	4.50	4.7
2006/04/27	1020	0.03	1.32	4.39	0.27	6.75	4.47	4.6
2006/05/02	972	0.03	1.30	4.26	0.26	7.83	4.46	4.7
2006/07/06	623	0.02	1.20	3.12	0.13	5.74	4.78	8.1
2006/07/11	397	0.01	1.06	2.15	0.04	5.04	5.80	6.6

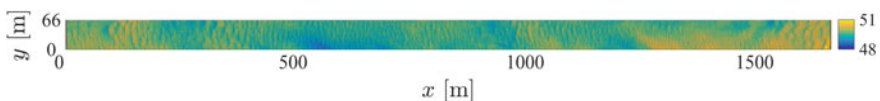


**Fig. 1** Topography of the river reach at Elbe river collected on 2005/02/25

$$E(k) = \frac{1}{M} \sum_{m=1}^M \frac{1}{N} \left| \sum_{n=0}^{N-1} z(n, m) \exp\left(\frac{-2\pi i}{N} nk\right) \right|^2 \quad (1)$$

where  $E(k)$  is power spectral density;  $k$  is wave number;  $z$  is elevation; and  $N$  and  $M$  are the dimensions of the elevation field in  $x$  and  $y$  directions, respectively.

For a further analysis of the spatial structure of the non-rotated elevation data, the second-order structure function may be used. Second-order structure functions can basically be converted to autocorrelation functions, and thus spectra, but are easier to be calculated for non-equidistant (i.e. scattered) data points (Sayles and Thomas 1977). In the calculation process, distances among data points are subdivided into a number of intervals called lags. The variance for all pairs of points whose separation distance falls within the same lag are averaged:

$$D(h) = \frac{1}{NM - h} \sum_{i=1}^{NM-h} [z(x_i + \Delta x, y_i + \Delta y) - z(x_i, y_i)]^2 \quad (2)$$

where  $D(h)$  is two-dimensional structure functions;  $h$  is spatial lag and calculated by  $h = \sqrt{\Delta x^2 + \Delta y^2}$ ;  $x_i$  and  $y_i$  are coordinate positions (Butler et al. 2001).

### 3 Results

#### 3.1 Spectral Behavior at Small Wavelengths

Figure 2 shows the power spectra for the available surfaces with the ‘-3’ law shown as reference. In the spectra it is possible to identify three different regions ( $R_1$ ,  $R_2$ , and  $R_3$ ) with  $R_2$  and  $R_3$  corresponding to the scaling regions in the conceptual model proposed by Nikora et al. (1997). Aberle et al. (2010) investigated the  $R_2$  and  $R_3$  regions and found that the upper boundary of the  $R_2$ -region may be expressed as a function of the water depth ( $H$ ) and that this boundary is close to the dune length scale,  $2\pi H$ , proposed by Yalin (1972).

The  $R_1$  region describes the morphological characteristics of bedforms at small scales, e.g. less than 6 m in this study (see next section for a more detailed discussion). Thus it can be hypothesized that the upper boundary of the  $R_1$  region corresponds to a length scale associated with secondary dunes or superimposed dunes. The spatial scale of larger dunes on which secondary dunes develop can be obtained by the method proposed by Robert and Richards (1988).

Robert and Richards (1988) calculated spatial sand wave scales by fitting the second-order structure function of a sand wave surface with a combination of exponential and periodic components. This analysis detects the wavelength of the dominant periodic bedform, i.e. the bedform that explains most of the variation of structure functions. Thus it can be hypothesized that smaller wavelengths belong

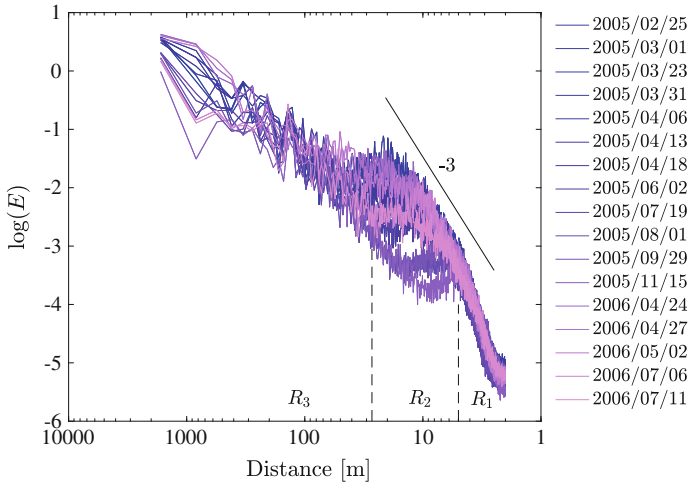
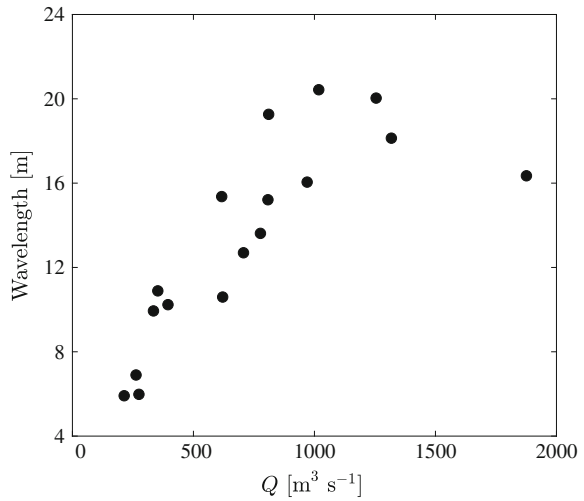


**Fig. 2** Power spectra of all measured surfaces. The ‘-3’ power law is shown for reference. The x-axis is converted into real distances

**Fig. 3** Wavelength calculated using the method proposed by Robert and Richards (1988)



to secondary dunes. Figure 3 shows the calculated dominant wavelength for each surface as a function of discharge. The minimum wavelength corresponds to 5.9 m supporting the hypothesis that the  $R_1$  regions reflect morphological characteristics of secondary dunes.

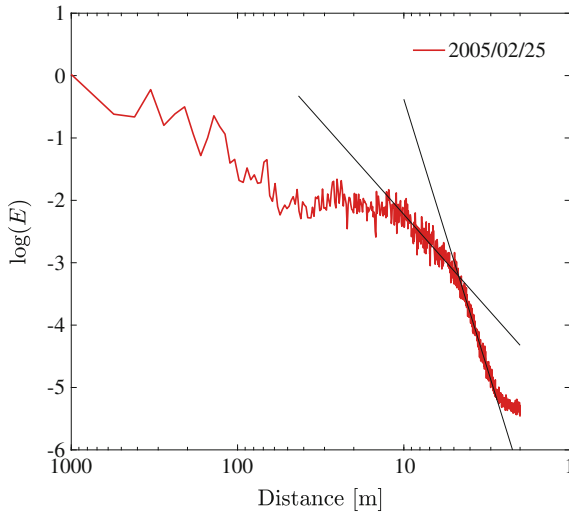


**Fig. 4** The  $R_1$  and  $R_2$  regions fitted on the spectrum. The slope of  $R_2$  regions is fixed ('-3') during the fitting process

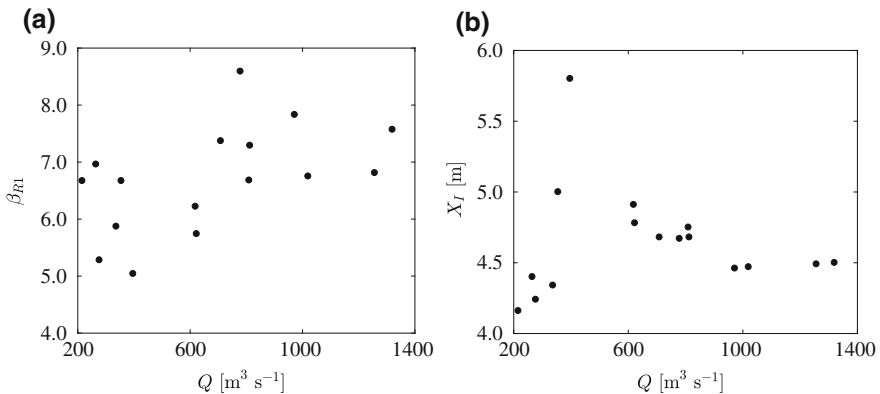


**Fig. 5** Relationships between spectral characteristics of  $R_1$  regions and flow discharge. Plot **a** shows the relationship between the fitted slope of  $R_1$  regions and flow discharge, and plot **b** shows the intersections of  $R_1$  and  $R_2$  regions and flow discharge

### 3.2 Influence of Flow Conditions on the Spectral Behavior

The characteristics of the hypothesized  $R_1$  region can be obtained by fitting a power function as shown in Fig. 4 with the slope of the  $R_1$  region ( $\beta_{R1}$ ) corresponding to the power exponent. The maximum range of the  $R_1$  region ( $X_I$ ) is the intersection between the power functions of the  $R_2$  and  $R_1$  regions, where the power exponent of the  $R_2$  region is fixed to -3 to comply with the '-3' law.

Figure 5 shows the relationships of the spectral characteristics of the  $R_1$  region ( $\beta_{R1}$  and  $X_l$ ) as a function of flow discharge ( $Q$ ). We note that the surface formed under the maximum flow discharge  $Q = 1878 \text{ m}^3 \text{ s}^{-1}$  on 2005/03/23 was not included in the analysis. This particular surface data were collected during a flood peak, whereas the remaining surfaces were measured during the falling stages of the hydrograph and during a dry season, respectively (see Aberle et al. (2010)). Thus, considering the peak value in the analysis and subsequent discussion would require the additional consideration of the hysteresis phenomenon, which would be difficult to achieve using results from a single surface scan.

The overall range of  $\beta_{R1}$  corresponds to 5.04–8.59 and Fig. 5a indicates a positive relationship of  $\beta_{R1}$  with discharge for  $200 < Q < 800 \text{ m}^3 \text{ s}^{-1}$ . However, the application of the  $t$ -test showed that the null hypothesis “the slope of the indicated relationship is zero”, i.e. that there is no significant relation between  $Q$  and  $\beta_{R1}$ , cannot be rejected (probability  $p = 0.36$ ). Consequently, the  $\beta_{R1}$  of the surfaces may be described by a mean value of 6.7 and a standard deviation of 0.9.

The relationship between the upper limit of the  $R_1$  scaling region ( $X_l$ ) and  $Q$  is shown in Fig. 5b.  $X_l$  increases with increasing  $Q$ , reaches a peak value ( $Q = 397 \text{ m}^3 \text{ s}^{-1}$ ;  $X_l = 5.8 \text{ m}$ ) before gradually decreasing. For  $Q > 800 \text{ m}^3 \text{ s}^{-1}$ ,  $X_l$  reaches approximately a stable value  $X_l \approx 4.5 \text{ m}$ . These results need to be interpreted in light of the discharge regime. In general it is expected that an increase in discharge results in an increase of bed shear stress and hence in an increase of the size and irregularity of sand waves (Coleman and Melville 1994). Thus,  $X_l$  can be expected to decrease with increasing  $Q$ , e.g. for  $Q > 400 \text{ m}^3 \text{ s}^{-1}$  in Fig. 5b. On the other hand, much smaller  $X_l$  values were obtained for  $Q < 400 \text{ m}^3 \text{ s}^{-1}$ , and this opposite trend may be associated with flow characteristics. The surface scans for these discharges were carried out for periods of rather long quasi-steady flow processes between two flood events (low-flows; see Fig. 2a in Aberle et al. (2010)), while surface data for  $Q > 400 \text{ m}^3 \text{ s}^{-1}$  were collected during the falling stages of these two flood events. Thus, surfaces measured for  $Q < 400 \text{ m}^3 \text{ s}^{-1}$  were exposed to longer quasi-steady flow conditions so that quasi-equilibrium bedforms could develop which in turn can, according to our hypothesis, result in a reduced  $X_l$ -value. Such quasi-equilibrium bedforms are expected to show a more evident ‘-3’ scaling spectral behavior than surfaces formed under unsteady flow conditions.

## 4 Discussion

The reduced slope in the power spectra at small wavelengths has been noted not only for sand waves but also for topography at the hillslope scale (e.g., Martin and Church 2004; Perron et al. 2008). The reduction has often been interpreted as an artefact resulting from the interpolation of topographic data (Gallant et al. 1994). In this paper, we argue that this is not the case for the data under investigation due to two reasons: (1) the calculated structure functions are a strong indicator for the



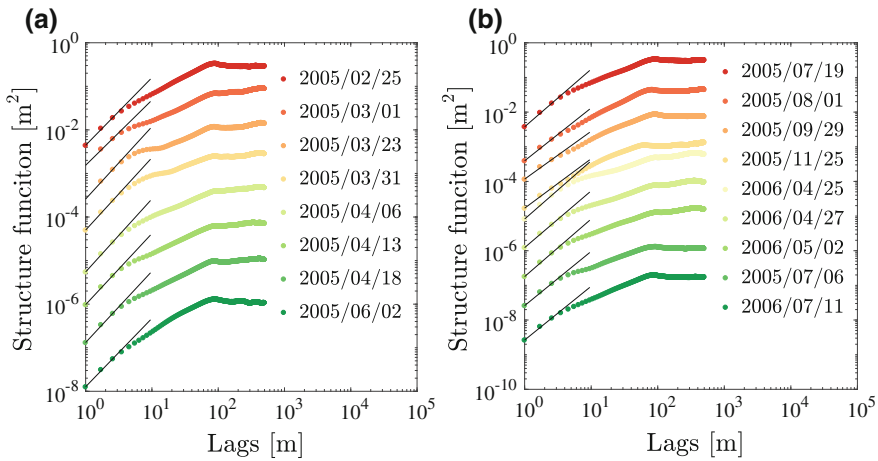


**Fig. 6** Second-order structure functions of all measured surfaces based on scattering points without interpolation. Plots **a** and **b** show the structure functions of surfaces collected from 25/02/2005 to 02/06/2005 and from 19/07/2005 to 11/07/2006, respectively

existence of such a region; and (2) the intersection between the  $R_1$  and  $R_2$  region is always greater than 4 m which is much larger than the sampling resolution.

The  $R_1$  region proposed in this paper was not analyzed in Aberle et al. (2010). Instead, it was attributed to smoothing effect introduced by the data collection procedure and re-gridding of the data. In order to clarify the mentioned smoothing effect, the second-order structure functions of the initial data (digital elevation models in Gauss-Krueger coordinates with a grid size of  $1\text{ m} \times 1\text{ m}$ ) were calculated to confirm the existence of the  $R_1$  region.

Figure 6 shows the second-order structure functions with a maximum spatial lag of 500 m. In this figure, the  $R_1$  and  $R_2$  regions can be identified for all the surfaces, and the  $R_1$  regions were fitted by a power function at small scale. The  $R_3$  region can not be observed, because of the limitation of maximum spatial lag. It is worth mentioning that the structure functions were calculated for 2D scattering points (rotated but not re-gridded data), while the spectra in Fig. 2 were obtained for gridded data (1D profiles). Consequently, the scaling exponents of these two methods cannot be unambiguously compared. Nonetheless, the existence of  $R_1$  regions in Fig. 6 suggests that the  $R_1$  regions are not introduced by the re-gridding procedure. On the other hand, an assessment of the data processing techniques from the raw-data to the DEMs in Gauss-Krueger coordinates is not possible as the raw data were not available for the analysis. In fact, these data were processed during the data collection using the software package HYMAS, developed by the Federal Institute of Hydrology (BfG), Germany (BfG 1995) and the available final data were the DEMs in Gauss-Krueger coordinates.

The ‘-3’ law is expected to be applied to sand waves at equilibrium conditions that are usually defined by statistical stable values of morphological dimensions (Baas

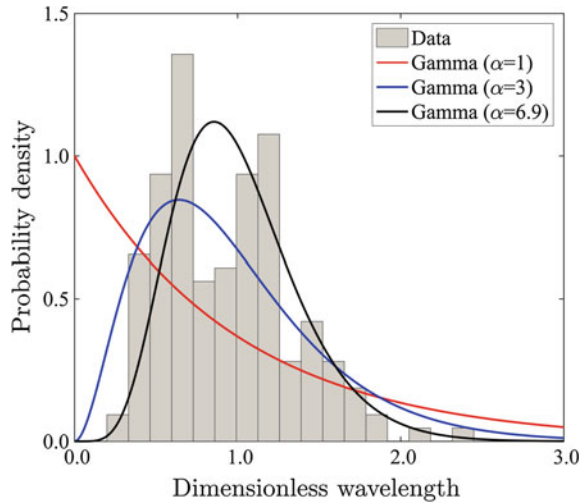
1994). Additional morphological characteristics of sand waves at equilibrium conditions include the presence of 3D pattern and small-scale superimposed sand waves. Venditti (2013) suggested that 3D bedforms are the ultimate bedform morphology in unidirectional flows that persist for long periods of time. Moreover, experimental work carried out by Venditti et al. (2005a) and Reesink and Bridge (2007) in flumes has demonstrated that bedforms of multiple scales exist in a sand wave surface in an equilibrium condition.

Shen and Cheong (1977) found that the spectra of bed profiles of sand waves in flumes were characterized by a power exponent ( $\beta$ ) varying between  $-3$  and  $-4$ . They proposed that the presence of superposed ripples on larger bedforms will decrease the exponent from  $-4$  for a ripple bed to  $-3$  for a fully developed dune surface. This can be further supported by the spectral behavior of supply-limited dunes as observed by Tuijnder et al. (2009). In these experiments, the volume of mobile sand on top of an immobile gravel layer was stepwise increased and the resulting bedforms were monitored. Adding a small amount of sand, Tuijnder et al. (2009) observed the development of ripple-like bedforms. Increasing the sand volume, straight-crested dunes developed which were characterized by a rather regular topography. A further increase in sand volume resulted in larger and more irregular bedforms, which became apparent through over-lapping dunes and the development of secondary dunes on top of larger dunes. Analyzing the spectra for their different bed-configurations, Tuijnder et al. (2009) found that the ' $-3$ ' scaling region range increased constantly with increasing sand volume. Moreover, for the ripple-like bedforms and small wavelengths, their  $\beta$  deviates from the ' $-3$ ' law and reaches a value of  $-6.5$  (we note that this value has been determined by examining the spectra obtained by Tuijnder et al. (2009)). This  $\beta$ -value is close to the mean value of  $R_1$  regions ( $-6.7$ ) in the present study. With increasing sand volume, and hence increasing bedform irregularity, the  $\beta$  at small wavelength finally reached  $-3$  for equilibrium alluvial conditions in the Tuijnder et al. (2009) study.

In Shen and Cheong (1977) and Tuijnder et al. (2009), ripple-like bedforms show a deviation from the ' $-3$ ' law. Similarly, the bedforms in this study are more close to 2D regular configurations in comparison to 3D bedforms, which can be observed from the topography shown in Fig. 1. The other surfaces show more or less similar regular bedform patterns.

Although Shen and Cheong (1977) suggested a rather limited range of  $\beta$  (from  $-3$  to  $-4$ ) in comparison to the results of Tuijnder et al. (2009) and the ones obtained in the present study, both Shen and Cheong (1977) and Tuijnder et al. (2009) found that surfaces showing the deviation behavior lack secondary dunes. Thus it may be hypothesized that the reason of the steeper slope region in the spectra is related to development of secondary bedforms. In fact, the rather limited range suggested by Shen and Cheong (1977) is debatable. Shen and Cheong (1977) explained the deviation from the ' $-3$ ' law by assuming that the dune length follows a gamma distribution with a shape parameter ( $\alpha$ ) ranging from 1 to 3. The difference between gamma distributions with  $\alpha = 1$  and 3 is that the former has a preponderance of smaller values in comparison with the latter one. With increasing  $\alpha$ , the number of smaller values in a gamma distribution decreases and the gamma distribution becomes more symmet-

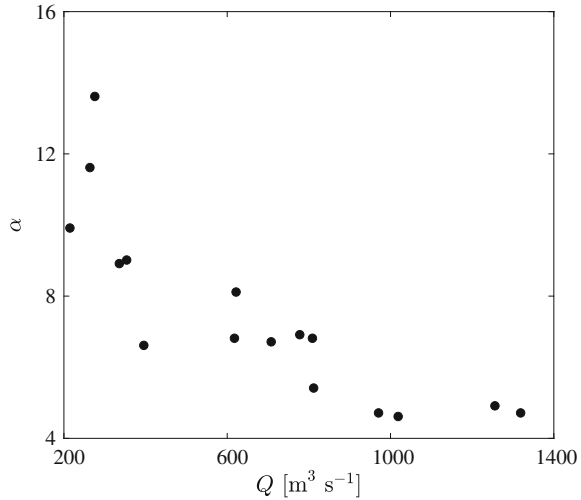
**Fig. 7** Measured and imposed probability density functions of dimensionless wavelength (wavelength divided by the mean value) for small scale sand waves of surface collected on 2005/02/25



ric. Shen and Cheong (1977) found that  $\beta$  increases from  $-4$  for  $\alpha = 3$  to approximately  $-3$  for  $\alpha = 1$ . Later research carried out by Wang and Shen (1980), however, found a much larger  $\alpha$  range than that proposed by Shen and Cheong (1977). This means that the  $\beta$  value can be much smaller than the lower boundary ( $-4$ ) as proposed by Shen and Cheong (1977).

In this study, we investigate the distribution of wavelengths for bedforms smaller than  $6H$ . For this purpose, we determined the sand wave geometry by the bedform tracking method proposed by van der Mark et al. (2008) which is a combination of different filtering processes and a zero-crossing method. After application of the method, the gamma distribution was then used to fit the wavelength data. The fitted  $\alpha$  values are listed in Table 1 and show a much larger range than the one proposed by Shen and Cheong (1977). Figure 7 shows, for the wavelengths obtained for the surface surveyed on 2005/02/25, the best-fitted gamma distribution ( $\alpha = 6.9$ ) and gamma distributions with  $\alpha = 1$  and 3. For  $\alpha = 1$ , the gamma distribution becomes an exponential distribution which is significantly different from the distributions with  $\alpha = 3$  and 6.9. The relative error is calculated to compare the goodness of distribution by  $E = \int_0^{\infty} |p_m(X) - p_i(X)| dX$ , where  $X$  is the dimensionless wavelength; and  $p_m$  and  $p_i$  denote the measured and imposed probability distributions, respectively (van der Mark et al. 2008). For the distribution with  $\alpha = 1$ , the relative error is 6.1 while the latter two distributions show rather similar values of 2.9 for  $\alpha = 6.9$  and 3.0 for  $\alpha = 3$ , respectively. Using all data from the present study, it becomes possible to highlight the dependency of  $\alpha$  from  $Q$  which is visualized in Fig. 8. The figure shows that  $\alpha$  decreases exponentially with increasing  $Q$  and this trend is in agreement with the statement that an increase in  $Q$  results in a faster process toward an equilibrium condition and more irregular sand waves, and thus smaller  $\alpha$ -values (Baas 1994). The relatively large  $\alpha$  values obtained in this study indicate that less secondary dunes

**Fig. 8** Relationship between the fitted shape parameters of gamma distributions ( $\alpha$ ) of wavelengths and flow discharge



developed in comparison to the expected number of secondary dunes for a gamma distribution with  $\alpha = 1$  so that much higher  $\beta$  values are expected.

## 5 Conclusions

In this study, the spectral behavior of river bed surfaces formed under different flow discharges has been analyzed with emphasis placed on spectral behavior at small wavelengths. The key findings of the study include:

- (1) The spectral behavior in this study at small wavelengths deviates from the ‘-3’ scaling law and shows steeper slopes.
- (2) The power exponents at small wavelengths have no significant relationship with flow discharge, while the range of the steep slope regions varies with flow discharge. Thus, this study supports the hypothesis that the insufficient development of secondary dunes makes the spectra at small wavelengths deviate from the ‘-3’ law.

**Acknowledgements** The authors are grateful to the Federal Waterways Engineering and Research Institute, Karlsruhe, Germany, for supplying the field data. The first author acknowledges supports from the National Key R&D Program of China (2016YFC0402506), the National Natural Science Foundation of China (51509074), the Natural Science Foundation of Jiangsu Province (BK20140847), and the Fundamental Research Funds for the Central Universities (2015B29114). The second author acknowledges support by the European Community’s Horizon 2020 Programme through the grant to the budget of the Integrated Infrastructure Initiative HYDRALAB+, Contract no. 654110.

## References

- Aberle J, Nikora VI, Henning M, Ettmer B, Hentschel B (2010) Statistical characterization of bed roughness due to bed forms: a field study in the Elbe River at Aken, Germany. *Water Resour Res* 46:W03521
- Baas JH (1994) A flume study on the development and equilibrium morphology of current ripples in very fine sand. *Sedimentology* 41:185–209
- Butler JB, Lane SN, Chandler JH (2001) Characterization of the structure of river-bed gravels using two-dimensional fractal analysis. *Math Geol* 33:301–330
- Coleman SE, Melville BW (1994) Bed-form development. *J Hydraul Eng ASCE* 120:544–560
- Coleman SE, Nikora VI (2009) Bed and flow dynamics leading to sediment-wave initiation. *Water Resour Res* 45:W04402
- Coleman SE, Nikora VI (2011) Fluvial dunes: initiation, characterization, flow structure. *Earth Surf Proc Land* 36:39–57
- Coleman SE, Nikora VI, Aberle J (2011) Interpretation of alluvial beds through bed-elevation distribution moments. *Water Resour Res* 47:W11505
- Federal Institute of Hydrology BfG (1995) Hydrographisches Mess und Auswerte System (HYMAS) mit satellitengestützter Ortung für den Bin- nenbereich der Bundeswasserstraßen (in German). Technical Report BfG-0902. Koblenz, Germany
- Gallant JC, Moore ID, Hutchinson MF, Gessler P (1994) Estimating fractal dimension of profiles: a comparison of methods. *Math Geol* 26:455–481
- Guala M, Singh A, BadHeartBull N, Fofoula-Georgiou E (2014) Spectral description of migrating bed forms and sediment transport. *J Geophys Res Earth* 119:123–137
- Hino M (1968) Equilibrium-range spectra of sand waves formed by flowing water. *J Fluid Mech* 34:565–573
- Humphries R, Venditti JG, Sklar LS, Wooster JK (2012) Experimental evidence for the effect of hydrographs on sediment pulse dynamics in gravel-bedded rivers. *Water Resour Res* 48:W01533
- Jain SC, Kennedy JF (1974) The spectral evolution of sedimentary bed forms. *J Fluid Mech* 63:301–314
- van der Mark CF, Blom A, Hulscher SJMH (2008) Quantification of variability in bedform geometry. *J Geophys Res Earth* 113:F03020
- Martin Y, Church M (2004) Numerical modelling of landscape evolution: geomorphological perspectives. *Prog Phys Geog* 28:317–339
- Nikora VI, Hicks DM (1997) Scaling relationships for sand wave development in unidirectional flow. *J Hydraul Eng ASCE* 123:1152–1156
- Nikora VI, Sukhodolov AN, Rowinski PM (1997) Statistical sand wave dynamics in one-directional water flows. *J Fluid Mech* 351:17–39
- Perron JT, Kirchner JW, Dietrich WE (2008) Spectral signatures of characteristic spatial scales and nonfractal structure in landscapes. *J Geophys Res Earth* 113:F04003
- Perumal M, Shrestha KB, Chaube UC (2004) Reproduction of hysteresis in rating curves. *J Hydraul Eng ASCE* 130:870–878
- Qin J, Wu T, Zhong D (2015) Spectral behavior of gravel dunes. *Geomorphology* 231:331–342
- Reesink AJH, Bridge JS (2007) Influence of superimposed bedforms and flow unsteadiness on formation of cross strata in dunes and unit bars. *Sediment Geol* 202:281–296
- Robert A, Richards KS (1988) On the modelling of sand bedforms using the semivariogram. *Earth Surf Proc Land* 13:459–473
- Sayles RS, Thomas TR (1977) The spatial representation of surface roughness by means of the structure function: a practical alternative to correlation. *Wear* 42:263–276
- Shen HW, Cheong HF (1977) Statistical properties of sediment bed profiles. *J Hydraul Eng ASCE* 103:1303–1321
- Singh A, Guala M, Lanzoni S, Fofoula-Georgiou E (2012) Bedform effect on the reorganization of surface and subsurface grain size distribution in gravel bedded channels. *Acta Geophys* 60:1607–1638

- Tuijnder AP, Ribberink JS, Hulscher SJMH (2009) An experimental study into the geometry of supply-limited dunes. *Sedimentology* 56:1713–1727
- Venditti JG (2013) Bedforms in sand-bedded rivers. *Treatise on geomorphology*. Academic Press, San Diego, pp 137–162
- Venditti JG, Church M, Bennett SJ (2005a) Morphodynamics of small-scale superimposed sand waves over migrating dune bed forms. *Water Resour Res* 41:W10423
- Venditti JG, Church M, Bennett SJ (2005b) On the transition between 2D and 3D dunes. *Sedimentology* 52:1343–1359
- Wang WC, Shen HW (1980) Statistical properties of alluvial bedforms. In: *Proceedings international symposium stochastic hydraulics*, Tokyo
- Wilbers AWE, Ten Brinke WBM (2003) The response of subaqueous dunes to floods in sand and gravel bed reaches of the Dutch Rhine. *Sedimentology* 50:1013–1034
- Yalin MS (1972) *Mechanics of sediment transport*. Pergamon Press, New York

# Spatial Distribution of Dissolved Oxygen at Rapid Hydraulic Structures as an Indicator of Local-Scale Processes

Agnieszka Rajwa-Kuligiewicz, Karol Plesiński, J. Russell Manson, Artur Radecki-Pawlik and Paweł M. Rowiński

**Abstract** This work aimed to examine the impact of rapid hydraulic structures on water temperature and dissolved oxygen concentration in the Porębianka mountain stream. This has been achieved by measurements of hydraulic characteristics and physiochemical properties of water such as water temperature and dissolved oxygen concentration. It has been shown that rapid hydraulic structures exhibit a large spatial diversity in morphology and flow paths, that manifests in the spatial heterogeneity of thermal conditions and oxygen concentrations at a single structure scale. The results have demonstrated that pools between the rapid have higher oxygen concentrations when compared to the rapid region. The highest concentrations of oxygen occurred in pools located close to the upstream edge of the rapid ramp where the flow undergoes gradual acceleration. Elevated concentrations of dissolved oxygen were also observed in the dissipation basin. The lowest concentrations were observed at stream banks. The results emphasise the relative importance of site-specific characteristics on physiochemical properties of flow, which might help to understand multi-scale processes across rivers and improve future plans of restoration practices in mountain streams.

---

A. Rajwa-Kuligiewicz (✉) · P. M. Rowiński  
Institute of Geophysics Polish Academy of Sciences, Księcia Janusza 64,  
01-452 Warsaw, Poland  
e-mail: arajwa@igf.edu.pl; arajwa@gamil.com

K. Plesiński · A. Radecki-Pawlik  
Department of Hydraulic Engineering and Geotechnics, University of Agriculture  
in Krakow, Aleja Mickiewicza 24/28, 30-059 Kraków, Poland

J. Russell Manson  
Applied Physics, Stockton University, 101 Vera King Farris Drive, Galloway, NJ, USA

A. Radecki-Pawlik  
Faculty of Civil Engineering, Institute of Structural Mechanics,  
Cracow University of Technology, Ul. Warszawska 24, 31-155 Kraków, Poland

## 1 Introduction

Hydraulic structures are important elements of water management and river restoration practices. They prevent streambanks from erosion, enable the regulation of flow, reduce channel slope and increase the oxygenation of streams (Radecki-Pawlik et al. 2013; Skalski et al. 2012; Wyżga et al. 2013, 2014; Rajwa-Kuligiewicz et al. 2015). From this point of view, rapid hydraulic structures (RHS) known also as boulder ramps play a significant role in mountain streams. Their structure resembles the natural pool-riffles sequence characteristic of high gradient mountain streams in terms of flow patterns and river bedforms (Clifford and Richards 1992; Dietrich and Whiting 1989; Carling 1992). As such, they constitute important spawning habitats for many invertebrate species, enable fish passage and natural aeration of flowing waters (Radecki-Pawlik et al. 2013).

Over the last few decades, a growing number of studies have been devoted to RHS and pool-riffle streams. Most researchers have focused on morphological properties of these structures, flow patterns (including hyporheic flows) (Tonina and Buffington 2007; Käser et al. 2009) and reaeration efficiency (Melching and Flores 1999). So far, little attention has been paid to the relative impact of site-specific interactions on the distribution of water temperature and dissolved oxygen at those structures.

Given the above, our study focused on the spatial distribution of dissolved oxygen (DO) and water temperature within a single rapid hydraulic structure, and aimed to assess the impact of rapid morphology, and flow patterns on the distribution of dissolved oxygen, and water temperature. Dissolved oxygen and water temperature were selected because they are primary indicators of water quality. Water temperature affects the rate of chemical reactions and oxygen solubility; dissolved oxygen in rivers is essential to living organisms and is frequently used in the assessment of stream water quality and stream metabolism (e.g., Odum 1956; Demars et al. 2011; Demars et al. 2015).

## 2 Study Site

For the purpose of this study, the measurements have been performed on one rapid hydraulic structure located on the Porębianka Stream (Fig. 1). The Porębianka is a typical high-gradient stream situated in the Gorce Mountains, southern Poland. The stream has a total length of 15.4 km and its catchment covers approximately 72 km<sup>2</sup> (Korpak 2007).

In the lower part the stream is regulated with a sequence of 25 RHS (Radecki-Pawlik et al. 2013). The stream bed consists of alternating coarse sand and gravel in pools with cobbles and boulders in rapids. The stream is characterised by a fast current and high variability of water levels. The highest water levels occur





**Fig. 1** Study site, the Porębianka stream. The approximate area of field measurements is marked with yellow rectangle

during spring snowmelt in April, whereas low levels often persist in February and October (Plesiński et al. 2013).

### 3 Methods

Field measurements of bathymetric and hydraulic properties (depth averaged velocity and maximum velocity) were conducted under low discharge ( $Q = 1.6 \text{ m}^3 \text{ s}^{-1}$ ). Hydraulic measurements were undertaken at 51 measurement points and the river discharge was calculated using water depth and velocity measurements taken along cross section. Instantaneous velocities were measured with an electromagnetic flow meter (model 801) manufactured by VALEPORT. This device enables the measurement of flow velocities in the range from  $0.001$  to  $10 \text{ m s}^{-1}$ , which is crucial for the estimation of water velocity in the velocity logarithmic distribution layer and consequently for the calculation of shear velocity and shear stress values. Vertical velocity profiles at particular measurement points were drawn on the basis of instantaneous velocities measured at five points above the

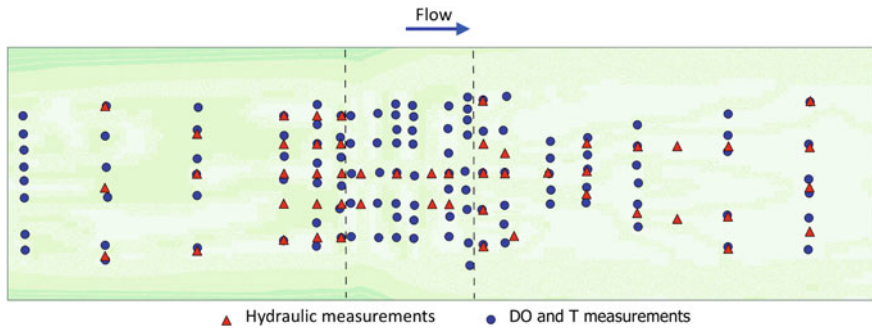


**Fig. 2** Study reach with the distribution of measurement points

streambed. In pools, instantaneous velocities were taken at 1.0, 2.0, 3.0 cm height above the streambed, mean depth and near the water surface, whereas on the rapid ramp velocities were measured at 0.5, 1.0, 1.5 cm above the bed, mean depth and near the water surface (Fig. 2). Note that the area of the rapid ramp is marked with vertical dashed lines.

Dissolved oxygen (in  $\text{mg dm}^{-3}$ ) and water temperature were measured at 118 points at mean depth using a handheld optical dissolved oxygen meter (manufactured by YSI Inc.). The sonde was equilibrated at each measurement point for about 15–30 s to obtain a stable reading. The measurement points were organised to give a representative coverage of the following positions associated with the rapid-pool sequence: (1) pool upstream of the rapid, (2) rapid, (3) scour basin behind the rapid, and (4) pool downstream of the rapid (Fig. 2). In shallow areas of the rapid ramp, the physiochemical properties were measured in the interstitial spaces between cobbles.

The data obtained from hydraulic measurements were used to calculate mean velocities, shear velocities, shear stresses, local depth averaged Reynolds and Froude numbers. Shear stress evaluations were made on the basis of vertical profiles of water velocities taken above the stream bed and analysed after semi-logarithmic transformation by means of methods described by Carling (1983) and Gordon et al. (2007). From the velocity profile, the shear velocity ( $U_*$ ) was calculated by the following formula (Gordon et al. 2007; Radecki-Pawlik 2011):

$$U_* = \frac{a}{5.75} [\text{m s}^{-1}]$$

where  $a$ —slope of a straight line taking the form of linear equation  $y = ah + b$  (where  $h$ —height above the streambed where the velocity measurement was performed;  $b$ —equation free term). Calculated values of shear velocities ( $U_*$ ) were then used to determine forces that act upon the streambed such as shear stresses ( $\tau$ ),

$$\tau = \rho U_*^2 [\text{N m}^{-2}]$$

where  $\rho$ —water density ( $1000 \text{ kg m}^{-3}$ ),  $U^*$ —shear velocity [ $\text{m s}^{-1}$ ]. Reynolds number was obtained from the formula:

$$Re = \frac{V_{av}h}{\nu} [-]$$

where  $V_{av}$ —depth averaged velocity [ $\text{m s}^{-1}$ ],  $h$ —water depth [m],  $\nu$ —kinematic viscosity [ $\text{m}^2 \text{ s}^{-1}$ ]. Finally, the mean Froude number ( $Fr$ ) was determined according to the formula:

$$Fr = \frac{V_{av}}{\sqrt{gh}} [-]$$

where  $V_{av}$ —depth averaged velocity [ $\text{m s}^{-1}$ ],  $h$ —water depth [m], and  $g$ —gravitational acceleration [ $\text{m s}^{-2}$ ].

### 4 Results

The results of bathymetric measurements are presented in Fig. 3. Under low discharge ( $Q = 1.6 \text{ m}^3 \text{ s}^{-1}$ ) water depth varied between 0.03 to 0.8 m. The highest depths were observed at the downstream edge of the rapid (in dissipation basin), whereas the lowest depths were observed at the rapid ramp. The measurements of DO concentration and water temperature are presented as blue and red dots, respectively.

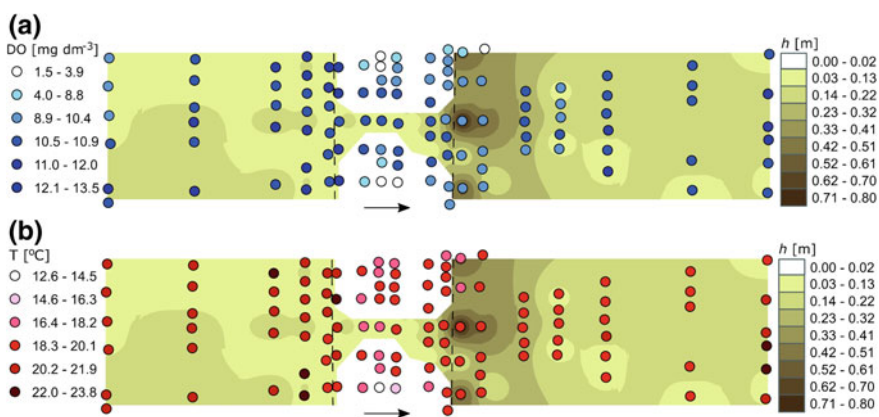


**Fig. 3** The bathymetry of hydraulic structure ( $Q = 1.6 \text{ m}^3 \text{ s}^{-1}$ ) with DO concentrations data (a) and water temperature data (b)

Considerably higher values of DO concentrations occurred in shallow areas upstream of the rapid, whereas the lowest oxygen concentrations occurred at the edges of the rapid. Despite higher water velocities in the central part of the rapid, no discernable increase in DO concentration was observed (Fig. 3a). As reported by Langbein and Durum (1967), for streams where the flow goes alternately through shallows and deeps, reaeration coefficient increases slowly with increasing stage in pools; however, it decreases sharply in the riffle. Melching and Flores (1999) argued with that statement claiming that fitted equations used for the prediction of reaeration rates are unsuitable for the pool-riffle flow regime in which the mean stream width and depth are difficult to determine and, thus, stream discharge is an indirect measure of the stream scale.

Distinct flow patterns commonly observed at rapid hydraulic structures influence not only the mixing processes, but also determine the extent and amount of vertical and horizontal penetration of solutes into the streambed. Figure 4 presents contour maps of dissolved oxygen concentrations (Fig. 4a) and water temperature (Fig. 4b), respectively, with corresponding vectors of depth averaged velocities. As visible, the flow at the rapid is concentrated in the central part of the channel. In the remaining part of the rapid, the flow goes beneath the cobble surface. This scheme enables fish migration even at low discharges. A strong acceleration of flow is visible toward and over the central part of the rapid (up to  $2.18 \text{ m s}^{-1}$ ) and deceleration can be observed as the flow plunges into pools (Fig. 4). Several measurements made within the upper and lower pool yielded velocities between  $0.01\text{--}1.31 \text{ m s}^{-1}$ .

Elevated velocities in the dissipation basin usually intensify oxygen transfer from the air. However, during low flow conditions, little aeration occurs because most of the flow goes around pore spaces between cobbles that protrude above the free surface. The submergence of cobbles and its spatial distribution substantially

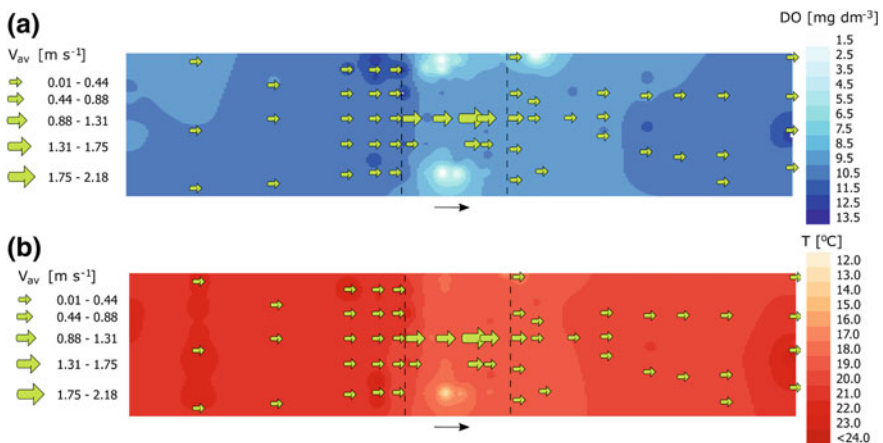


**Fig. 4** Contour maps of dissolved oxygen concentration (a) and water temperature (b). Arrows represent the depth averaged velocity at individual measurement points

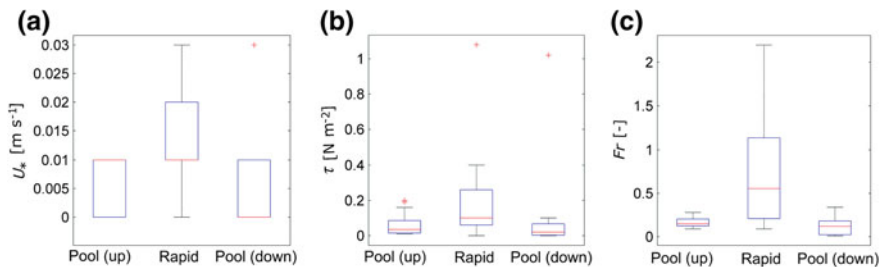


**Fig. 5** Hydraulic characteristics along the structure: (a) shear velocity, (b) shear stress, (c) local Froude number

affects the velocity distribution and Froude numbers, which are the key factors responsible for the kinetic energy and the formation of hydraulic jump downstream of the structure (Ślizowski and Radecki-Pawlik 2000).

The detailed hydraulic characteristics along the rapid hydraulic structure are presented in Fig. 5. As visible, the complex topography of the structure results in a high degree of spatial variability in shear velocity (Fig. 5a), shear stress (Fig. 5b) and Froude number (Fig. 5c). It is visible that the maxima of shear stress, shear velocity and Froude number occur at the rapid ramp, and are concentrated along the centreline of the stream channel (Figs. 6, 7, 8). Pools are characterised by sub-critical flow ( $Fr < 1$ ), whereas rapids exhibit all three types of regimes, namely: subcritical ( $Fr < 1$ ), critical ( $Fr = 1$ ) and supercritical ( $Fr > 1$ ). The supercritical flow occurred especially on the rapid ramp and in the central part of the dissipation basin (Fig. 8). As noted by earlier studies (e.g., Jowett 1993), both Froude number and the velocity/depth ratio are two frequently used criteria for discriminating

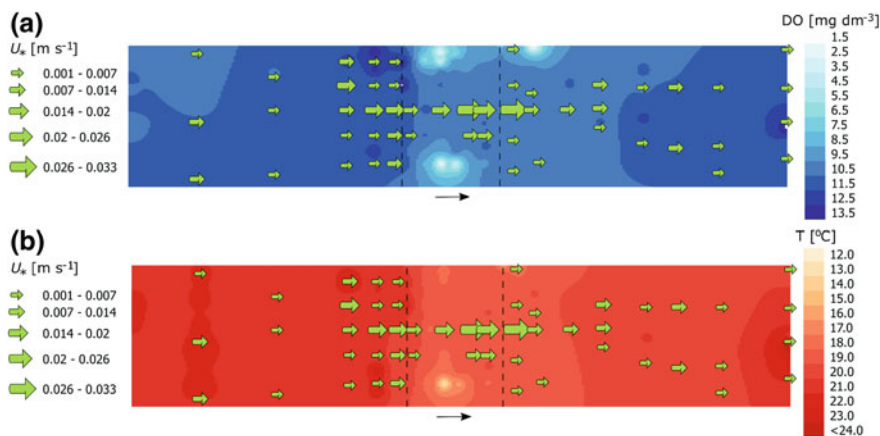


**Fig. 6** Contour maps of dissolved oxygen concentration (a) and water temperature (b). Arrows represent the shear velocity at individual measurement points

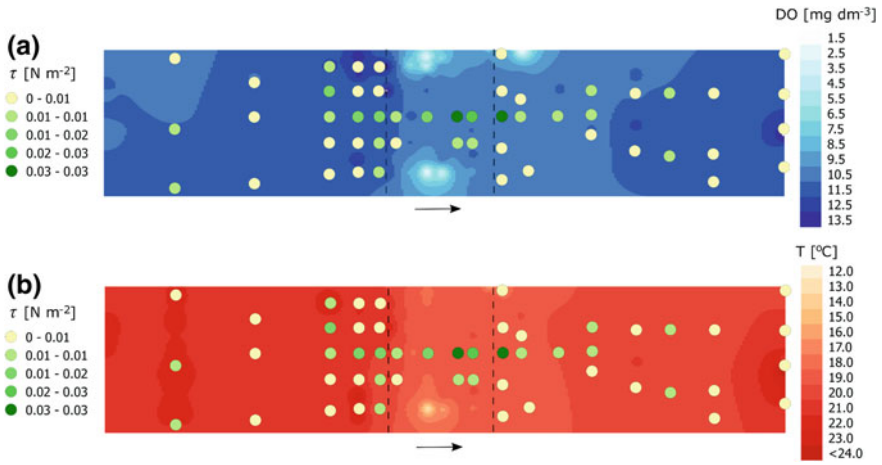


**Fig. 7** Contour maps of dissolved oxygen concentration (a) and water temperature (b). Dots represent the shear stress at individual measurement points

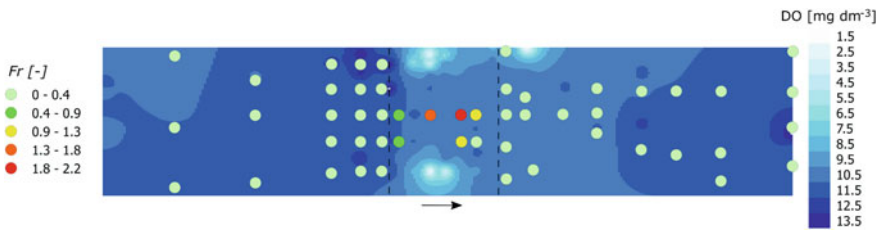


**Fig. 8** Contour map of dissolved oxygen concentration. Dots represent Froude number at individual measurement points

between pool and riffle forms and corresponding types of aquatic habitats. The flow along the structure was turbulent. The mean value of Reynolds number was similar at all three locations along the structure (Fig. 9).

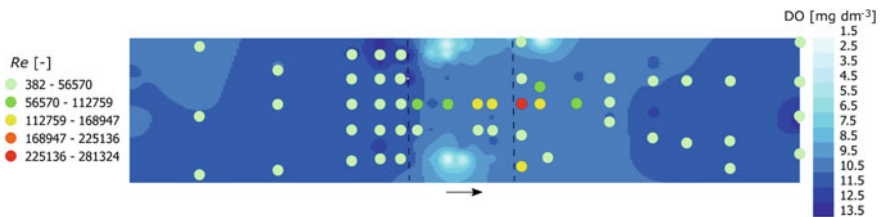


**Fig. 9** Contour map of dissolved oxygen concentration. Dots represent Reynolds number at individual measurement points

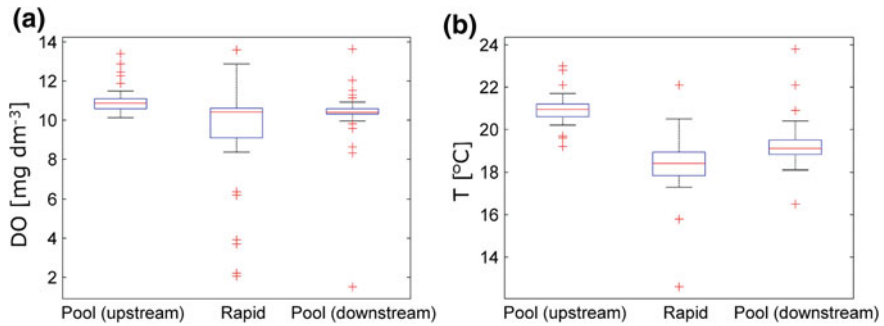


**Fig. 10** Boxplots: (a) dissolved oxygen concentration, (b) water temperature

The results indicated that during summer season the rapid itself is characterised by steep gradients in water temperature and DO concentration. For the investigated structure, water temperature varied from 12.6 to 23.8  $^{\circ}\text{C}$ , which yields more than 11  $^{\circ}\text{C}$  difference. Pools are characterised by higher water temperature than rapids. It is visible that water temperature drops below 13.0  $^{\circ}\text{C}$  in pore spaces at the rapid ramp. Subsequent measurements of DO concentration have shown that the selected structure is characterised by relatively high differences in DO concentration ranging from 1.5 to 13.6  $\text{mg dm}^{-3}$ . Notably, the highest water temperature overlaps with the areas of higher oxygen concentration. DO concentration in pools upstream and downstream of the structure has remained at a similar level (Fig. 10a). Surprisingly, maximum oxygen concentration has not occurred at the rapid. Instead, the highest oxygen contents were observed in shallow areas located close to the upstream edge of the rapid. Sharp drops in DO concentrations occurred in interstitial spaces at the edges of the rapid ramp parallel to stream banks. Low water temperature and reduced oxygen content in these spaces may potentially be attributed to upwelling fluxes of hyporheic waters. In contrast, potholes—small cylindrical holes formed by vertical erosion of turbulent flow, exhibited higher DO concentrations, despite unfavourable elevated water temperature.

Our results demonstrated that the flow within the rapid region chiefly controls the DO concentration distribution in pore spaces. It has been shown that pore spaces at the rapid ramp act either as the sinks of dissolved oxygen or thermal niches providing ideal spots for lush growth of benthic organisms and algal biofilm on the sediment surface. As noted by Malard et al. (2002), the distribution of benthic organisms is governed by oxygenation of particular areas of streambed and in this sense corresponds to the morphological units such as bar, pool, and bar fringe.

Similar observations have been made from the natural pool-riffle streams. According to Ingendahl et al. (2009), riffle sections exhibit higher vertical exchange, which is related to permeable sediment and strong head variations along the streambed of the channel. As a consequence, the greater intensity of turbulence in these places enhances the upwelling and downwelling fluxes responsible for the oxygen transfer.

## 5 Conclusions

Our results have revealed a great spatial heterogeneity of oxygen and thermal conditions at rapid hydraulic structures. It has been demonstrated that the distribution of dissolved oxygen and water temperature is strongly associated with flow patterns and morphological features of the structure. These observations provide a valuable insight into the spatial variability of dissolved oxygen and water temperature at rapid hydraulic structures, and their impact on water reaeration. In this regard, our findings demonstrate the importance of considering the hydraulic properties when studying dissolved oxygen distribution and stream metabolism within this type of hydraulic structures.

## References

- Carling PA (1983) Threshold of coarse sediment transport in broad and narrow natural streams. *Earth Surf Process Land* 8(1):355–367
- Carling PA (1992) In-stream hydraulics and sediment transport. In: Carlow P, Petts GE (eds) *The rivers handbook*. Blackwell, Malden, Mass, pp 101–125
- Clifford NJ, Richards KS (1992) The reversal hypothesis and the maintenance of riffle–pool sequences: a review and field appraisal. In: Carling PA, Petts GE (eds), *Lowland floodplain rivers: geomorphological perspectives*, Wiley, Chichester, U.K., pp 43–70, ISBN: 0-471-93119-5
- Demars BOL, Manson JR, Ólafsson JS, Gislason GM, Gudmundsdottir R, Woodward G, Reiss J, Pichler DE, Rasmussen JJ, Friberg N (2011) Temperature and the metabolic balance of streams. *Freshw Biol* 56(6):1106–1121
- Demars BOL, Thompson J, Manson JR (2015) Stream metabolism and the open diel oxygen method: principles, practice, and perspectives. *Limnol Oceanogr Method* 13(7):356–374
- Dietrich WD, Whiting PJ (1989) Boundary shear stress and sediment transport in river meanders of sand and gravel. In: Ikeda S, Parker G (eds) *River meandering. geophysical monograph series, vol 12*, AGU, Washington D.C pp 1–50
- Gordon ND, McMahon TA, Finlayson BL, Gippel CJ, Nathan RJ (2007) *Stream hydrology—an introduction for ecologists*. Wiley, London
- Ingendahl D, Borchardt D, Saenger N, Reichert P (2009) Vertical hydraulic exchange and the contribution of hyporheic community respiration to whole ecosystem respiration in the River Lahn (Germany). *Aquat Sci* 71(4):399–410
- Jowett IG (1993) A method for objectively identifying pool, run, and riffle habitats from physical measurements. *New Zealand J Mar Freshw Res* 27(2):241–248
- Käser DH, Binley A, Heathwaite AL, Krause S (2009) Spatio-temporal variations of hyporheic flow in a riffle-step-pool sequence. *Hydrol Process* 23(15):2138–2149
- Korpak J (2007) The influence of river training on mountain channel changes (Polish Carpathian Mountains). *Geomorphology* 92:166–181
- Langbein WB, Durum WH (1967) The aeration capacity of streams. U.S. Geological Survey Circular 542
- Malard F, Tockner K, Dole-Olivier MJ, Ward JV (2002) A landscape perspective of surface-subsurface hydrological exchanges in river corridors. *Freshw Biol* 47(4):621–640
- Melching CS, Flores HE (1999) Reaeration equations derived from U.S. geological survey database. *J Environ Eng* 125(5):407–414
- Odum HT (1956) Primary production in flowing waters. *Limnol Oceanogr* 1(2):102–117



- Plesiński K, Janas M, Radecki-Pawlik A (2013) Analysis of hydraulic parameters in the region of rapid hydraulic structure in the porębianka stream in the gorce mountains. *Acta Scientiarum Polonorum: Formatio Circumiectus* 12(1): 101–114, ISSN: 1644–0765 (in Polish)
- Rajwa-Kuligiewicz A, Bialik RJ, Rowiński PM (2015) Experimental investigations on the oxygen transfer efficiency at low-head hydraulic structures. In: Rowiński PM, Marion A (eds), *Geoplanet: earth and planetary sciences, hydrodynamic and mass transport at freshwater interfaces*, Springer, pp 115–127
- Radecki-Pawlik A (2011) *Hydromorphology of rivers and mountain streams*. Wydawnictwo Uniwersytetu Rolniczego, ISBN: 978-83-60633-40-3 (in Polish)
- Radecki-Pawlik A, Plesiński K, Wyzga B (2013) Analysis of Chosen Hydraulic Parameters of a Rapid Hydraulic Structure (RHS) in the porębianka river in the gorce mountains, polish carpathians. In: Bung DB, Pagliara S (eds), *IWLHS—The International Workshop on Hydraulic Design of Low-Head Structures*, Bundesanstalt fur Wasserbau, Aachen, pp 121–128, ISBN: 978-3-939230-04-5
- Skalski T, Kędzior R, Radecki-Pawlik A (2012) Riverine ground beetles as indicators of inundation frequency of mountain stream: a case study of the Ochotnica Stream. South Poland. *Baltic J Coleopterol* 12(2):117–126
- Ślizowski R, Radecki-Pawlik A (2000) Distribution of maximum velocities and Froude number on a rapid hydraulic structure apron. *Electron J Pol Agric Univ* 3(1),#01
- Tonina D, Buffington JM (2007) Hyporheic exchange in gravel bed rivers with pool-riffle morphology: Laboratory experiments and three-dimensional modeling. *Water Resour Res* 43: W01421
- Wyzga B, Oglęcki P, Hajdukiewicz H, Zawiejska J, Radecki-Pawlik A, Skalski T, Mikuś P (2013) Interpretation of the invertebrate-based BMWP-PL index in a gravel-bed river: insight from the Polish Carpathians. *Hydrobiologia* 712(1):71–88
- Wyzga B, Amirowicz A, Oglęcki P, Hajdukiewicz H, Radecki-Pawlik A, Zawiejska J, Mikuś P (2014) Response of fish and benthic invertebrate communities to constrained channel conditions in a mountain river: Case study of the Biała, Polish Carpathians. *Limnologica* 46:58–69

# Characterizing Retention Processes in Streams Using Retention Metrics

Jevgenijs Savickis, Mattia Zaramella, Andrea Bottacin-Busolin, Matteo Tregnaghi and Andrea Marion

**Abstract** The temporal retention in storage zones (SZs) has a strong influence on mass transport processes in natural streams. It has been shown that solute retention affects solute breakthrough curves (BTCs) by producing longer tails and thereby increasing their skewness. In terms of ecological effects, this retention increases the contact time of solute with aquatic interfaces and living species, which can lead to degradation of eco-systems when the transported substances are pollutants. An important question that arises is whether the currently available metrics can adequately represent complex retention processes. In this study, we examine the performance of two existing metrics: the hydrological retention factor ( $R_H$ ) and the fraction of median travel time due to transient storage ( $F_{med}$ ). The results presented are based on two conservative tracer tests. The tracer tests were performed in streams with distinct morphological, sediment composition, vegetation and hydraulic characteristics. The recorded concentration-time series were used to derive storage zone parameters such as storage zone area, exchange coefficient and mean residence time. The storage zone parameters were computed using a multiple storage zone model STIR with two separate exponential residence time models for

---

J. Savickis (✉) · M. Zaramella

Water and Environmental Technologies (WET) Srl, VialeBrigata  
C. Battisti 32, 31033 Castelfranco Veneto, Italy  
e-mail: jevgenijs.savickis@inbox.com

M. Zaramella

e-mail: mattia.zaramella@gmail.com

A. Bottacin-Busolin

School of Mechanical, Aerospace and Civil Engineering, University of Manchester,  
Manchester M13 9PL, UK  
e-mail: andrea.bottacinbusolin@manchester.ac.uk

M. Tregnaghi · A. Marion

Department of Industrial Engineering, University of Padua, Via F. Marzolo 9,  
35131 Padua, Italy  
e-mail: matteo.tregnaghi@unipd.it

A. Marion

e-mail: andrea.marion@unipd.it

© Springer International Publishing AG 2018

M. B. Kalinowska et al. (eds.), *Free Surface Flows and Transport Processes*,  
GeoPlanet: Earth and Planetary Sciences,  
[https://doi.org/10.1007/978-3-319-70914-7\\_26](https://doi.org/10.1007/978-3-319-70914-7_26)

transient storage, representing short timescale (STS) and long timescale storage (LTS) processes. The retention metrics were estimated separately for short and long timescale retention, and for the combined retention. The cross-correlation between the retention metrics and the storage parameters was analyzed using Pearson's  $R$ - and significance  $p$ -values. In general, the results reveal a poor correlation between retention metrics and storage zone parameters, except for the exchange rate associated with long timescale storage,  $\alpha_2$ . A strong cross-correlation is instead found between the retention metrics.

## 1 Introduction

Mass transport and mixing processes in open channel flows occur due to advection and dispersion mechanisms. Solutes are advected downstream in the main channel by the bulk flow and dispersed longitudinally by velocity gradients, and vertically and transversally by turbulent fluctuations. Solutes are also subjected to trapping in storage zones such as vegetated side pockets and the sediment bed, where solutes are temporarily retained and released back to the main channel after some time (Marion et al. 2014). Storage zones are generally distinguished based on their retention capacity and can be divided into short and long timescale storage zones. Short timescale processes are typically associated with surface storage zones (STS), which include recirculation zones, vegetation, side pockets and localized changes in channel geometry. Long timescale storage (LTS) processes are associated with the hyporheic zone.

A widely accepted mathematical formulation of storage processes was given by Bencala and Walters (1983) who proposed the Transient Storage Zone (TSZ) model as an extension of the one-dimensional (1D) advection-dispersion equation (ADE) presented by Taylor (1954). In the TSZ model, the exchange between the main channel and the storage domain is represented as a first-order mass transfer. However, previous studies have demonstrated that the TSM is not able to capture long timescale pumping processes (Marion et al. 2003). Since Bencala and Walters presented transient storage (TS) model, researchers have attempted to develop a more comprehensive formulation of retention processes in transient storage zones (Haggerty et al. 2000; Kim and Kavvas 2006; Murphy et al. 2007). In this work, storage processes are parameterized using the one-dimensional model Solute Transport In Rivers (STIR) presented by Marion et al. (2008). The STIR model is a quantitative separation of short-term and long-term retention processes. Under the assumption of Fickian transport, the STIR model reduces to an advection-dispersion mass-transfer model presented by Haggerty et al. (2000). The storage zone parameters, including the exchange rate  $\alpha$  and residence time  $T$ , can be derived by applying the STIR code to field recorded concentration-time series. Then we used the STIR model calibrated parameters for the calculation of different retention metrics.

This study analyzes the correlation between different retention metrics and the transient storage parameters of a two-storage zone solute transport model. The retention metrics considered include the fraction of median travel time due to storage

(Runkel 2002),  $F_{med}$ , and the hydrological retention factor,  $R_H$  (Morrice et al. 1997). By looking at the correlation between these metrics and storage parameters, the study aims to improve the physical interpretation of such metrics. The STIR (Solute Transport In Rivers) model is applied assuming two distinct exponential residence time distributions for short timescale storage (STS) and long timescale storage (LTS). The fraction of median travel time due to storage (Runkel 2002),  $F_{med}$ , and the hydrological retention factor,  $R_H$  (Morrice et al. 1997) are calculated separately, also combining the processes in STS and LTS storage zones. The metric  $F_{med}$  was evaluated for the aggregated effect of the TS zones and for the separate STS and LTS zones. This was calculated at a standard distance of 200 meters using the TS parameters of the STIR model, including the mean particle residence time  $T$  and the exchange rate between the main channel and transient storage zone  $\alpha$ . The  $R_H$  metrics were also estimated for aggregated and separate STS and LTS processes. The cross-correlation between retention metrics and transient storage parameters was then evaluated using Pearson's  $R$  coefficient and significance  $p$ -values.

## 2 Study Site and Methods

### 2.1 Study Site

#### *The Erpe River, Germany (lowland spring river)*

The Erpe River is a small, 31 km lowland spring river flowing northwards through Brandenburg and Berlin federal states. The Erpe River is a tributary of the Müggelspree River and is strongly affected by anthropogenic actions, such as agriculture and wastewater treatment.

The analyzed river stretch is located upstream from the municipal wastewater treatment plant (Klärwerk Münchehofe) effluent and has a total length of 521 m, nearly uniform width and several bends. Due to the mild slope,  $S = 0.00007$ , the stream is not subjected to high sediment transport and banks erosion. The upper layer of streambed consists of fine sand and organic material. During the test period, thick riparian and submerged vegetation (*Stuckenia pectinata* and *Sparganium emersum*) were present along the study reach (Fig. 1). Reach length, flow discharge and bed slope for the study reaches are reported in Table 1.

#### *The Serrières-de-Briord canal, France (lowland drainage canal)*

The Serrières-de-Briord canal is a drainage channel of the Upper Rhône River (France), which is fed by Rhône River seepage and hillslope aquifers. This canal is mainly used to drain agricultural land, collect seepage from Rhône River and participate to piezometric equilibrium of groundwater.

The canal stretch of 500 m with a uniform cross section, flood plains and natural banks has been studied. At the period of the fieldwork, the canal was characterized by natural submerged aquatic vegetation (*Callitriche platycarpa* Kütz., *Groenlandia densa* (L.) Fourr., *Berula erecta* (Huds.) Coville). Coverage by aquatic vegetation

**Fig. 1** Part of the Erpe river study reach



**Table 1** Characteristics of the study reaches: length  $L$  [m], average width  $W$  [m], main cross-sectional area  $A$  [m<sup>2</sup>], estimated flow rate  $Q$  [m<sup>3</sup> s<sup>-1</sup>] and slope  $S$

Reach	Erpe		Serrières-de-Briord	
	0–1	0–2	0–1	0–2
$L$ [m]	325	521	300	500
$W$ [m]	4.52		6.50	
$A_{\text{measured}}$ [m <sup>2</sup> ]	1.88		3.54	
$Q$ [m <sup>3</sup> s <sup>-1</sup> ]	0.19		1.10	
$S$ ( $\times 10^{-3}$ )	0.07		0.06	

**Fig. 2** Picture of a study reach of the Serrières-de-Briord canal



**Table 2** The STIR calibrated TS zone parameters considering an exponential residence time distribution in STS and LTS zones

Reach	Erpe		Serrières-de-Briord	
	0-1	0-2	0-1	0-2
$U$ [ $m\ s^{-1}$ ] <sup>a</sup>	0.14	0.14	0.25	0.25
$A$ [ $m^2$ ]	1.39	1.35	4.44	4.34
$D$ [ $m^2\ s^{-1}$ ]	0.14	0.10	0.25	0.27
$\alpha_1$ [ $\times 10^{-4}\ s^{-1}$ ]	10.22	9.12	10.15	10.01
$\alpha_2$ [ $\times 10^{-4}\ s^{-1}$ ]	0.12	0.17	0.04	0.05
$T_1$ [s]	144	160	153	144
$T_2$ [s]	1402	1294	3959	1841

<sup>a</sup> $U$  is the mean velocity in main channel flow estimated from the flow rate  $Q$  (Table 1) and the calibrated cross-sectional area of the main channel  $A$  (Table 2)

ranges from 30% to 40% depending on canal section, as shown in Fig. 2. The sediment bed is composed by a mixture of coarse gravel and fine sand. The average slope  $S$  is very mild, equal to 0.00006 (Table 1).

## 2.2 Methods

All tracer tests were performed using a conservative fluorescent dye, rhodamine WT (RWT). During the experiments, the dye solution was continuously (step) injected using a constant flow rate peristaltic pump. The RWT was injected for 55 to 90 min in the Erpe River and the Serrières-de-Briord canal, respectively. The breakthrough curves (BTC) were recorded by sampling the stream water at downstream stations with a time interval of 10 s using portable field fluorometers. All fluorometers were installed in the middle of the channel, with the detection optics at a depth of 10 cm from the water surface. The fluorometers used in the Erpe River are the SCUFA and YSI 6920 fluorometers, whereas in the Serrières-de-Briord canal the GGUN-FL fluorometers were used. The recording stations were located at two locations downstream, allowing the analysis of short (0-1) and long (0-2) reaches. For better data control, all fluorometers were equipped with turbidity probes, which allowed simultaneous measurement of turbidity and concentration. No correction due to changes in turbidity was necessary for the concentration data.

The main channel flow rate  $Q$  was estimated using an electromagnetic current meter (B07-FlowSens, SEBA) at Serrières-de-Briord canal and propeller-type current meter at Erpe River. The velocity readings were taken at various depths with a vertical distance of 10 to 20 cm, and across the channel with a horizontal distance of 40 to 60 cm. The values of the flow rates are reported in Table 1.

### 3 STIR Model

The STIR model is a general residence time distribution model that allows parameterization of multiple storage zones.

Under the assumption of Fickian dispersion in the main channel, and that the exchange between the main channel and the storage zone is a Poisson process, the in-stream concentration  $C_W(x, t)$  at a given time and space can be described by the following equation:

$$\frac{\partial C_W(x, t)}{\partial t} + U \frac{\partial C_W(x, t)}{\partial x} = D_W \frac{\partial^2 C_W(x, t)}{\partial x^2} - \alpha \left( C_W(x, t) - \int_0^t C_W(x, t - \tau) \varphi(\tau) d\tau \right), \quad (1)$$

where  $C_W(x, t)$  is the solute concentration in the main channel water [ $\text{M L}^{-3}$ ],  $U$  is the mean cross-sectional velocity [ $\text{L T}^{-1}$ ],  $D_W$  is the longitudinal dispersion coefficient [ $\text{M}^2 \text{T}^{-1}$ ],  $\alpha$  is the exchange rate between the main channel and storage zone [ $\text{T}^{-1}$ ], and  $\varphi(t)$  is the probability density function (PDF) of the residence time in the storage zone [ $\text{T}^{-1}$ ]. Equation (1) is a special case of the STIR model. In this study, the residence time distribution in the storage zones for a single trapping event is parameterized as follows:

$$\alpha_i = \frac{q_{i,b}}{d} \quad (2a)$$

$$\alpha = \alpha_1 + \alpha_2 \quad (2b)$$

$$\varphi_i = \frac{1}{T_i} e^{-\frac{t}{T_i}} \quad (3a)$$

$$\varphi(t) = \frac{1}{\alpha} (\alpha_1 \varphi_1(t) + \alpha_2 \varphi_2(t)), \quad (3b)$$

where  $q_{i,b}$  ( $i = 1, 2$ ) is the average flow rate into the LT or ST storage zone per unit surficial cross-section area [ $\text{L T}^{-1}$ ] and  $d$  is the flow depth [ $\text{L}$ ];  $\alpha_i$ ,  $\varphi_i(t)$  and  $T_i$  ( $i = 1, 2$ ) correspond to the exchange rate [ $\text{L}^{-1}$ ], PDF of the residence time distribution [ $\text{T}^{-1}$ ] and retention timescale of the storage zone [ $\text{T}$ ] of the LTS and STS. In this study, the PDFs of the residence time in STS and LTS zones are assumed to be exponential (Eq. 3a). Calibration of the longitudinal dispersion coefficient  $D_W$ , the mean particle residence time  $T$ , the exchange rate  $\alpha$  and the main channel cross-sectional area  $A$  is accomplished by minimizing the root mean square error (Bottacin-Busolin et al. 2011; Zaramella et al. 2016). For the fitting procedure optimization, a linear scale is used to fit the bulk data of the BTC and a log-scale is used to fit the tail. The STIR coding calibration results are reported in Table 2.

## 4 The Storage Metrics

The retention metrics were estimated for the individual and the combined STS and LTS zones. In all cases, excluding the general form of  $F_{med}$ , the retention metrics were calculated using the STIR code derived TS zone parameters.

The storage zone cross sectional areas,  $A_S$ , are defined for both transient storage zones using the following expression (Thackston and Schnelle 1970):

$$A_{S,i} = AT_i\alpha_i, \tag{4}$$

where  $A$  is the stream cross sectional area [ $L^2$ ],  $T_i$  ( $i = 1, 2$ ) is the mean particle residence time in storage zone [T] and  $\alpha_i$  ( $i = 1, 2$ ) is the exchange rate between the main channel and storage zone [ $T^{-1}$ ]. The total area of the storage zones was estimated by summing the  $A_S$  of STS and LTS zones.

The temporal retention of tracer was examined by estimating the hydrological retention metric  $R_{H,i}$  (Morrice et al. 1997) for both transient storage zones as

$$R_{H,i} = \frac{A_{S,i}}{Q}, \tag{5}$$

where  $Q$  is the main channel flow rate [ $L^3 T^{-1}$ ]. To evaluate the combined effect of the TS zones on the  $R_H$  index, the total cross-sectional area of TS zones  $A_S$  was used.

Another retention metric considered in this work is the fraction of median travel time due transient storage zones  $F_{med}$  (Runkel 2002). The general form of this metric allows assessment of the retention processes in all storage compartments. The general form of  $F_{med}$  proposed by Runkel (2002) is defined as follows:

$$F_{med} = \frac{t_{med} - t_{M,med}}{t_{med}}, \tag{6}$$

where  $t_{med}$  is the total median travel time (including effects of the TS zones) [T] and  $t_{M,med}$  is the median travel time due to the main channel only. These times are numerically interpolated from the BTCs and equal the time at which 50% of total mass passes the observation station located at a distance  $L = x$  downstream:

$$\frac{\int_0^{t_{med}} QC_W(L=x, t) dt}{\int_0^t QC_W(L=x, t) dt} = 0.5 \tag{7}$$

The time  $t_{M,med}$  is defined similarly to the  $t_{med}$  but from the STIR code simulated breakthrough curves excluding the transient storage zones. This can be reached by setting the STS and LTS zones exchange rates  $\alpha = 0$ . Therefore, under this



**Fig. 3** Interpolated  $t_{med}$  and  $t_{M,med}$  times for the Erpe Stream according to Eq. 7. These time values were used to calculate the  $F_{med}$  metrics (Eq. 6) for reaches 0–1 and 0–2

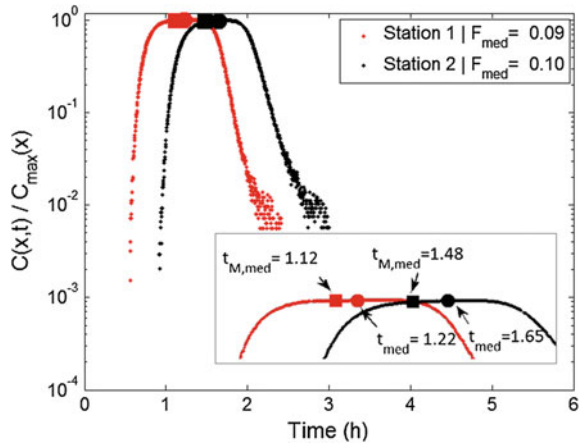
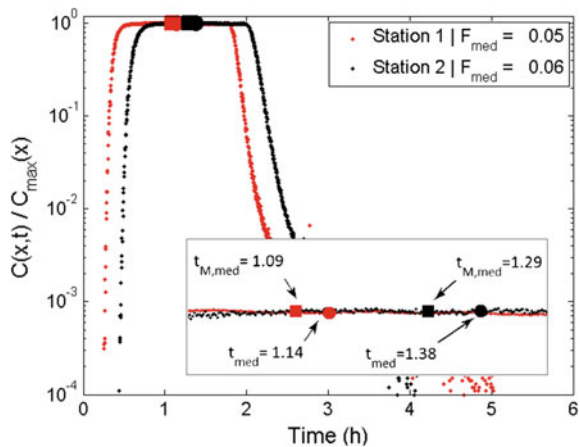


**Fig. 4** The Serrières-de-Briord canal interpolated  $t_{med}$  and  $t_{M,med}$  times for the  $F_{med}$  metrics calculation (Eq. 7)



condition the STIR model reduces to the 1-D advection dispersion equation (ADE). The positions of interpolated values of  $t_{M,med}$  and  $t_{med}$  are presented in Figs. 3 and 4.

The relevance of individual TS zones on the retention processes was analyzed with the fraction of median travel time due to storage zone at a standard distance  $L = 200$  m:

$$F_{med,i} = \left(1 - e^{-L \frac{a_i}{U}}\right) \frac{A_{S,i}}{A + A_{S,i}} \tag{8}$$

where  $U$  is the mean flow velocity in the main channel [ $LT^{-1}$ ] (Table 2). The following expression was developed by Runkel (2002) for assessment of retention

using the calibrated TS zone parameters of the OTIS model. In this study, the  $F_{med,1}$  and  $F_{med,2}$  were evaluated using the STIR model derived parameters of the STS and LTS zones.

## 5 Results and Discussion

The comparison of the retention metrics and correlation of these with the TS zone parameters is based on the Pearson’s  $R$  parameter and the significance  $p$ -values. The calculated fraction of median travel time  $F_{med}$  and the hydrological retention metrics  $R_H$  are shown in Table 3.

The flow rate in the Erpe Stream is 5.8 times smaller comparing to the Serrières-de-Briord canal. Therefore, higher values of retention metrics were expected. This trend is clearly seen for all  $R_H$  metrics,  $F_{med}$  and  $F_{med,2}$  metrics. However, the  $F_{med,1}$  metrics showed smaller dependence on the flow rate magnitude, where the difference between the streams  $F_{med,1}$  is 24.5% for the reach 0–1 and 25.3% for the reach 0–2.

The results confirm previous finding that the general form of the estimated retention metric  $F_{med}$  (Eq. 6) is almost the same as for a standard distance  $F_{med,1}$  (Eq. 8). It should be stressed that both formulations have limitations such as: the fraction of median travel time estimated at a standard distance  $F_{med,1}$  was developed on a single storage zone concept and the general form of this metric  $F_{med}$  is based on the first arriving 50% of mass. Thus, the calculated long timescale storage zone retention metric  $F_{med,2}$  (Eq. 8) is negligible in terms of retention process. This is because of the formulation concept and missing information about the LTS zone retention processes that is contained in the tail of breakthrough curve (BTC). Due to the formulation of the  $R_H$  metric, the values of  $R_{H,1}$  are greater than those of  $R_{H,2}$  as a result of bigger STS zone areas  $A_{S,1}$ . According to the  $R_{H,1}$  results, the temporal solute retention per unit reach length is longer for the short timescale storage

**Table 3** Retention metrics estimated with the STIR model for the Erpe river and the Serrières-de-Briord canal

Reach	Erpe		Serrières-de-Briord	
	0–1	0–2	0–1	0–2
$R_H$ [s m <sup>-1</sup> ]	1.21	1.19	0.68	0.60
$R_{H,1}$ [s m <sup>-1</sup> ]	1.08	1.03	0.63	0.57
$R_{H,2}$ [s m <sup>-1</sup> ]	0.13	0.15	0.06	0.03
$F_{med}$	0.09	0.10	0.05	0.06
$F_{med,1}$	0.10	0.09	0.08	0.07
$F_{med,2}$ ( $\times 10^{-4}$ )	3.02	5.01	0.39	0.30

$F_{med}$  and  $R_H$  are the retention metrics with the combined TS zone properties

**Table 4** Correlation of retention metrics between each other and TS zone parameters.<sup>a</sup>

	$R_H$	$R_{H,1}$	$R_{H,2}$	$F_{med}$	$F_{med,1}$	$F_{med,2}$
$F_{med}$	0.91(0.09)	0.90(0.10)	0.93(0.07)	–	–	–
$F_{med,1}$	0.98(0.02)	0.99(0.01)	0.92(0.08)	–	–	–
$F_{med,2}$	0.92(0.08)	0.90(0.10)	0.98(0.08)	–	–	–
$T_1$	0.27(0.73)	0.23(0.77)	0.49(0.51)	0.34(0.66)	0.14(0.86)	0.54(0.46)
$T_2$	0.64(0.36)	0.65(0.35)	0.58(0.42)	0.84(0.16)	0.56(0.44)	0.67(0.33)
$\alpha_1$	0.43(0.57)	0.39(0.61)	0.61(0.39)	0.68(0.32)	0.24(0.76)	0.75(0.25)
$\alpha_2$	0.94(0.06)	0.92(0.08)	0.97(0.03)	0.99(0.01)	0.84(0.16)	0.99(0.01)

<sup>a</sup>Values in parentheses are the significance  $p$ -values with significance threshold of 0.05

(STS) zones than for the long timescale storage (LTS) zones by an average of 86.7 to 92.6% for the Erpe Stream and the Serrières-de-Briord canal, respectively.

The correlation results, based on the Pearson's  $R$  coefficient and significance  $p$ -values, reveal a strong relationship between the combined TS zone  $R_H$  metric and  $F_{med,1}$  with  $p$ -value of 0.02 (Table 4). Similarly, the  $R_{H,1}$  metric is well correlated to the  $F_{med,1}$  metric. The significance  $p$ - and Pearson's  $R$ -values suggest that both these metrics are dependent on the LTS zone exchange rate  $\alpha_2$ , as shown in Table 4.

The retention metrics  $F_{med}$  and  $F_{med,2}$  can be predicted by the  $\alpha_2$  parameters which is confirmed by a high  $R = 0.99$  and low significance  $p = 0.01$  values. The worst retention metrics predictors are the residence time  $T_1$  and the exchange rate  $\alpha_1$ , because, depending on the case, the  $p$ -values are in range of 0.25 to 0.86 and  $R$  values are between 0.14 to 0.75. The study results also demonstrated negligible correlation of the residence time  $T_2$  and retention metrics.

## 6 Conclusions

The aim of this work was to demonstrate the possibility of using a single metric for characterizing temporal retention processes in multiple transient storage domains. The experimental results confirm previous findings of quasi-equality of the general form of the median travel time due to storage  $F_{med}$  and  $F_{med,i}$  estimated at a standard distance using the STIR calibrated transient storage parameters. In general, the combined TS zone retention metrics  $R_H$  and  $F_{med}$  are very close to the metrics calculated for the short timescale storage (STS) zones.

The results show a clear dependence of  $R_H$  and  $F_{med}$  on the flow rate  $Q$ , as increases in flow rate are associated with decreases in the values of the retention metrics. However, this trend was not observed for  $F_{med,2}$ , as an increase of  $Q$  by 5.8 times led to a decrease of around 25%.

The cross-correlation analysis of retention metrics revealed a strong correlation between  $F_{med,1}$  and  $R_H$  with  $R_{H,1}$ . The rest of metrics also demonstrated some correlation, but with  $p$ -values slightly above the threshold of 0.05. Since most

retention metrics, except for  $F_{med}$ , were derived from the TS zone parameters, a good correlation was expected with these parameters. The results presented clearly show that the long timescale exchange rate  $\alpha_2$  is the only TS zone parameter that can be used as a predictor of retention metrics. The results of this study suggest that the rest of TS parameters,  $T_1$ ,  $T_2$  and  $\alpha_1$ , are poorly correlated to the retention metrics considered.

In this paper, it was shown that the hydrological retention metric  $R_H$  and the fraction of median travel time  $F_{med}$  and  $F_{med, (1,2)}$  can be highly correlated. Both retention metrics have some limitations, which future studies should aim to overcome. This can be achieved either by a new retention metric or by an improved formulation of existing metrics. The analysis conducted is based on two tracer tests with two recording stations at each test. Further investigation is needed to confirm the findings of this work.

**Acknowledgements** This work was supported by the Research Executive Agency through the 7th Framework Programme of the European Union, Support for Training and Career Development of Researchers (Marie Curie-FP7-PEOPLE-2012-ITN), as part of the Initial Training Network (ITN) HYTECH 'Hydrodynamic Transport in Ecologically Critical Heterogeneous Interfaces', N. 316546.

## References

- Bencala KE, Walters RA (1983) Simulation of solute transport in a mountain pool-and-riffle stream: a transient storage model. *Water Resour Res* 19(3):718–724
- Bottacin-Busolin A, Marion A, Musner T, Tregnaghi M, Zaramella M (2011) Evidence of distinct contaminant transport patterns in rivers using tracer test and a multiple domain retention model. *Adv Water Resour* 34(6):737–746
- Haggerty R, McKenna SA, Meigs LC (2000) On the late-time behavior of tracer test breakthrough curve. *Water Resour Res* 36(12):3467–3479
- Kim S, Kavvas ML (2006) Generalized Fick's law and fractional ADE for pollution transport in a river: detailed derivation. *J Hydrol Eng* 11(1):80–83
- Marion A, Nikora V, Puijalon S, Bouma T, Koll K, Ballio F, Tait S, Zaramella M, Sukhodolov A, O'Hare M, Wharton G, Aberle J, Tregnaghi M, Davies P, Nepf H, Parker G, Statzner B (2014) Aquatic interfaces: a hydrodynamic and ecological perspective. *J Hydraul Res* 52(6):744–758. <https://doi.org/10.1080/00221686.2014.968887>
- Marion A, Zaramella M, Bottacin-Busolin A (2008) Solute transport in rivers with multiple storage zones: The STIR model. *Water Resour Res* 44(10):W10406
- Marion A, Zaramella M, Packman AI (2003) Parameter estimation of the transient storage model for stream-subsurface exchange. *J Environ Eng* 129(5):456–463
- Morrice JA, Valett H, Dahm CN, Campana ME (1997) Alluvial characteristics groundwater-surface water exchange and hydrological retention in headwater streams. *Hydrol Process* 11(3):253–267
- Murphy E, Ghisalberti M, Nepf H (2007) Model and laboratory study of dispersion in flows with submerged vegetation. *Water Resour Res* 43(5):W05438
- Runkel RL (2002) A new metric for determining the importance of transient storage. *J North Am Benthol Soc* 21(4):529–543

- Taylor GI (1954) The dispersion of matter in turbulent flow through a pipe. Proc. Roy. Soc. London Ser. A 223:446–468
- Thackston EL, Schnelle KB (1970) Predicting effects of dead zones on stream mixing. J Sanit Eng Div Am Soc Civ Eng 96:319–331
- Zaramella M, Marion A, Lewandowski J, Nützmann G (2016) Assessment of transient storage exchange and advection–dispersion mechanisms from concentration signatures along break-through curves. J Hydrol 538(2016):794–801. <https://doi.org/10.1016/j.jhydrol.2016.05.004>

# Higher Order Statistics of Reynolds Shear Stress in Nonuniform Sand Bed Channel

Anurag Sharma and Bimlesh Kumar

**Abstract** Experimental investigation was carried out to investigate the flow turbulent structure, including the Reynolds stresses distribution in non-uniform sand bed channels with and without seepage. Steady flows over non-uniform sand bed channel were simulated experimentally with downward seepage applied through the boundary. Measured time average velocity and Reynolds stresses increase with the presence of seepage. The quadrant analysis suggests that the relative contributions of bursting events increased throughout the flow layer and the thickness of the zone of dominance of sweep event increases with seepage which is responsible for increment in bed material transport. The mean time of occurrence of ejections and sweeps in downward seepage are more persistent than those in no seepage.

## 1 Introduction

Flow over a sand bed occurs frequently in nature. Riverbeds are usually composed of non-uniform sediment mixtures and the respective particle size distribution of sediment in transport is generally finer than the distribution of bed material because of selective transport (Wu et al. 2004). Most of the early experiments on sediment transport were confined to the homogeneous sediment mixture (Wilcock 1993; Zyserman and Fredsøe 1994). Recent years experimental studies have attempted to understand the basic grain-sorting process during sediment transport in heterogeneous sediment mixtures (Kleinhans 2005; Curran 2007). Most of the studies on the non-uniform sediment transport are based on introducing correction factors to understand the hiding and exposure effect and use these factors to modify the existing formula for uniform sediment transport (Parker et al. 1982; Andrews 1983). Fractional sediment transport was calculated for non-uniform sediment based on correction factors related to bed material sizes (Fang and Yu 1998; Karim 1998). On transport of sediments mixture, the effect of sand and gravel contents on

---

A. Sharma (✉) · B. Kumar  
IIT, Guwahati, India  
e-mail: anurag.sharma@iitg.ernet.in

overall transport rate was studied in the laboratory flume (Wilcock and Crowe 2003; Curran and Wilcock 2005). Previous researchers (Mittal et al. 1990; Patel and Range Raju 1996) assumed that the motion of fine particles is led by the lift force while the motion of coarse particles is by the drag force, and introduced a semi-theoretical hiding-exposure correction factor. Flume experiments were conducted for non-uniform sediment to find the sediment transport rate of individual fraction of sediment mixture (Misri et al. 1984; Samaga et al. 1986). Ghoshal et al. (2010) investigated the bed layer concentration of each size fraction that is transported as bedload over a mixture of sand/sand-gravel beds.

The important hydraulic nature of sand bed in natural channels is that it provokes downward flow as seepage. Depending on the difference in water level in the channel and the surrounding groundwater table, seepage can occur either as flow from the channel (suction) or flow into the channel (injection). The important features is that the seepage influences the main stream flow characteristics in the wall shear layer as well as the outer-flow layer (Devi et al. 2016). Devi et al. (2016) observed that downward seepage increased stream-wise velocity near the bed, resulting in the formation of a more uniform velocity distribution. Increment of bed shear stress with downward seepage causes increased sediment transport (Sreenivasulu et al. 2011). Franca et al. (2014) investigated quadrant analysis of coherent structures in open channel flows over mobile and immobile hydraulically rough beds. They observed that sweeps are dominant in the turbulence production in the near bed region of the flow.

Although many studies have investigated flow hydrodynamics or turbulent characteristics with seepage in case of uniform sand, the flow characteristics over non-uniform sand bed channel with downward seepage remain unexplored. Since riverbeds are usually composed of non-uniform sand, the present study therefore focuses on the influence of downward seepage flow on the turbulent flow characteristics over a mobile rough boundary (made of non-uniform sand of 0.5 mm size). The experimental result will deliver important information related to the turbulence characteristics, such as velocity, Reynolds shear stress and conditional Reynolds shear stresses.

## 2 Experimentation

In the present work, experiment was conducted in a large tilting flume with dimensions of 17.24 m in length, 1 m in width, and 0.72 m in depth (Fig. 1). A tank of 2.8 m length, 1.5 m width and 1.5 m depth is provided at the upstream of the flume which straightens the flow before its introduction into the flume. A control valve was located at the overhead tank and was used to regulate the flow in the main channel. A couple of wooden baffle was installed at the upstream tank to prevent turbulences in the water coming from the overhead tank to enter the main channel. A tail gate was provided at the downstream end of the main channel to control the flow depth.

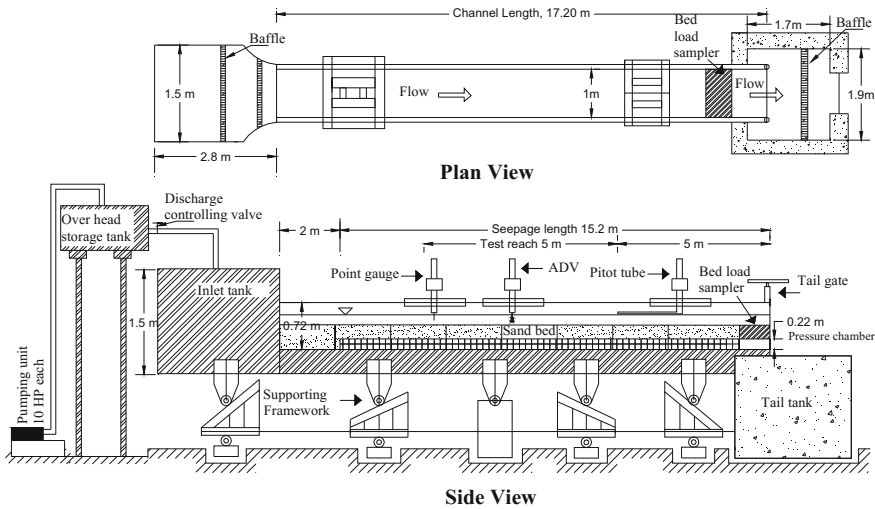


Fig. 1 Schematic diagram of tilting flume

The flume is having a seepage chamber of 15.2 m length, 1 m width and 0.22 m depth located at 2 m from the upstream end of the flume that collects water and allows free passage of water through the sand bed. Non-uniform river sand of particle sizes  $d_{50} = 0.5$  mm was used as bed material in the experiments that was kept on the fine mesh in order to prevent the entrance into the bottom chamber. A bottom pressure chamber was formed between the bottom of the mesh and the channel. The bottom pressure chamber was used to absorb water from the channel through the sand bed in a perpendicular direction in the form of downward seepage. The seepage flow rate that was measured by an electromagnetic flow meter (accuracy of  $\pm 0.5\%$ ) could be controlled by a valve which is installed at the downstream end of the flume. The flow depth in the channel was measured with digital point gauge attached to a moving trolley. Main flow discharge in the channel was measured by using the flow depth over the rectangular notch at the downstream collection tank.

Non-uniformity in the particle size distribution for the sand was confirmed with the value of geometric standard deviation ( $\sigma_g$ ) greater than 1.4 (Marsh et al. 2004). The characteristics of sediment mixture and flow parameters used in the study are shown in Table 1. In the no-seepage (NS) run, water is introduced to the channel by gradually opening a valve located at the overhead tank, till the required discharge

Table 1 Summary of flow measurement

Median grain size, $d_{50}$ [mm]	Discharge, $Q$ [ $\text{m}^3 \text{s}^{-1}$ ]	Depth of flow, $y$ [m]	Kramers coefficient, $M$	Bed slope, $S_0$
0.50	0.0402	0.112	0.16	0.001



$Q$  and corresponding flow depth  $y$  are registered. Consequently, after conducting the experiment with no-seepage, different downward seepage discharge of 10 and 15% of the main flow discharge were applied by controlling the electromagnetic flow meters installed at the downstream section of the flume.

Instantaneous velocity measurements were captured with the help of acoustic Doppler probe manufactured by Nortek. The ADV worked with an acoustic frequency of 10 MHz. The instrument allowed data collection at a higher sampling rate, up to 200 Hz. The instrument collects data in a cylindrical remote sampling volume of user adjustable height located 5 cm below the central transmitter.

To minimize the effects of flow entrance and exit conditions in the main channel, the test section in the experiments was considered as 5–10 m length from the downstream end of the flume. Data was collected at the center line of the channel cross-section at a distance of 8 m from the downstream end of the flume. In all the experiments, signal to noise ratio was kept at 15 or above and the signal correlation between received and transmitted signals of 70% was recommended as cut-off value. The data measured from the vectrino contained spikes, so spike removal algorithm based on the acceleration threshold method is used to filter the data (Goring and Nikora 2002). The acceleration threshold value was maintained in between 1 and 1.5 based on trial and error basis so that velocity power spectra should acceptably fit with Kolmogorov “ $-5/3$  scaling law” in the inertial sub range (Lacey and Roy 2008). Figure 2 shows the velocity power spectra before and after spike removal at flow depth  $z = 10$  mm for no-seepage and seepage runs.

### 3 Results and Discussion

Time averaged stream-wise ( $\bar{U}$ ) and vertical ( $\bar{W}$ ) velocities were calculated as:

$$\begin{aligned}\bar{U} &= \frac{1}{n} \sum_{i=1}^n U_i \\ \bar{W} &= \frac{1}{n} \sum_{i=1}^n W_i\end{aligned}\tag{1}$$

where  $U_i$  and  $W_i$  are the instantaneous velocities in the stream-wise and vertical directions, respectively, and  $n$  is the number of samples. Reynolds shear stress ( $\tau_{uw}$ ) was calculated as:

$$\begin{aligned}\tau_{uw} &= -\rho_w \overline{u'w'} \\ \overline{u'w'} &= \frac{1}{n} \sum_{i=1}^n (U_i - \bar{U})(W_i - \bar{W})\end{aligned}\tag{2}$$

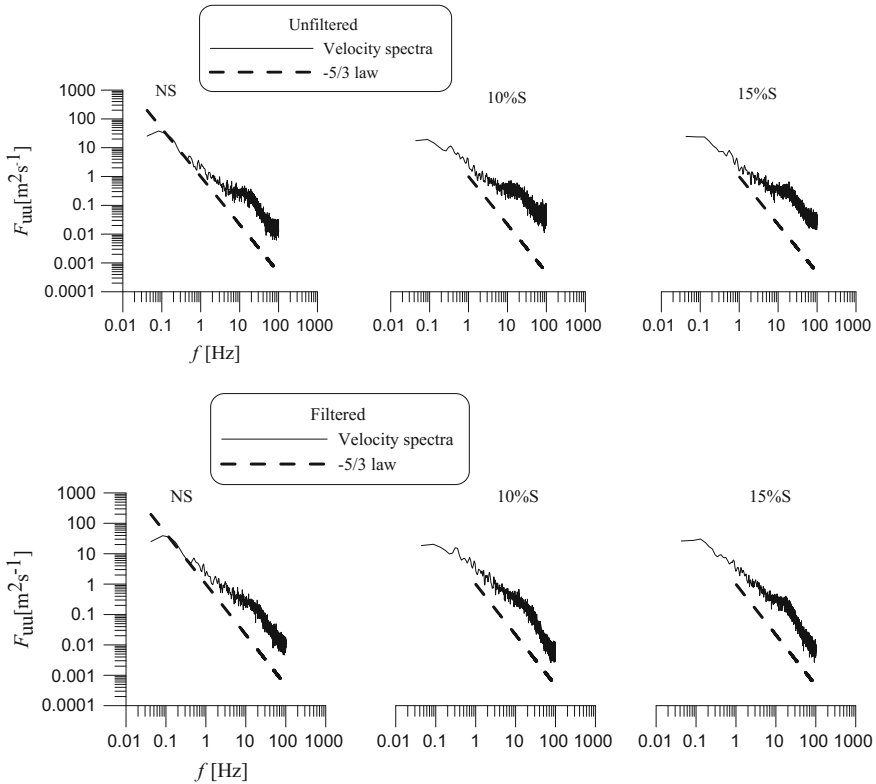
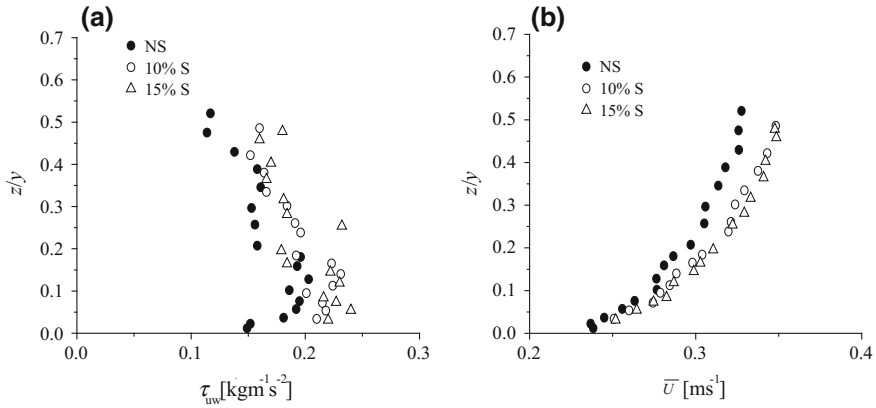


Fig. 2 Velocity power spectra

where  $\rho_w$  is the density of water,  $u'$  and  $w'$  are the fluctuating components of velocities in the stream-wise and vertical directions respectively and  $n$  is the number of samples. Figure 3a show the vertical variations of Reynolds shear stress (RSS) in flows subjected to no-seepage and seepage runs where the vertical ordinate ( $z$ ) has been made non-dimensional with the flow depth ( $y$ ). Figure 3a shows that RSS increases along the channel bed are associated with the provided momentum from the main flow to maintain sediment particle motion overcoming the bed resistance and attain a maximum value in between  $0.05 < z/y < 0.2$  and then again decrease towards the boundary because of the presence of a roughness sub layer in the near bed region. In the present experiments, the profiles of Reynolds shear stress distribution were found to be similar for both no-seepage and seepage runs but the magnitude is higher in both inner and outer layer with the application of seepage. The maximum value of  $\tau_{uw}$  is about 13.80% greater with 10% S and about 14.30% greater with 15% S, as compared to that with no-seepage. Figure 3b shows the variations of time averaged stream wise velocity  $\bar{U}$  with normalised vertical distance ( $= z/y$ ) in flows subjected to no-seepage and seepage. The velocity increased with downward seepage as compared to no-seepage for a particular discharge.



**Fig. 3** Vertical profiles of **a** Reynolds shear stress **b** Mean stream wise velocity

Further, quantitative analysis suggests that very near to the bed ( $z/y = 0.03$ ) the velocity increases on an average value of 2.36% with 10% seepage. It is also observed that in the lower flow region ( $z/y = 0.03$ ), the velocity for 15% seepage case is slightly higher with an average increasing value of 0.40%, than the velocity for 10% seepage.

### 3.1 Quadrant Analysis

The Reynolds shear stress at any given point is the summation of different types of bursting events. To quantify the bursting events, it is necessary to plot velocity fluctuation,  $u'$  and  $w'$  on  $u'w'$  plane (Lu and Willmarth 1973). The hyperbolic hole region  $H$  is introduced to differentiate the larger contributions to  $-\overline{u'w'}$  from each quadrant leaving the smaller  $u'$  and  $w'$  corresponding to more quiescent periods. Hence, depending upon the relative sign of velocity fluctuations  $u'$  and  $w'$ , the bursting events are defined by four quadrants such as outward interactions ( $i = 1, u' > 0, w' > 0$ ), ejections ( $i = 2, u' < 0, w' > 0$ ), inward interactions ( $i = 3, u' < 0, w' < 0$ ) and sweeps ( $i = 4, u' > 0, w' < 0$ ). At any point, the contribution to the total Reynolds stress through the different forms of momentum transfer can be calculated as:

$$\langle u'w' \rangle_{i,H} = \lim_{T \rightarrow \infty} \frac{1}{T} \int_0^T u'(t)w'(t)I_{i,H}[u'(t)w'(t)]dt \tag{3}$$

where  $t$  is time,  $T$  is the sampling duration, and  $I_{i,H}$  is the indicator function defined as

$$I_{i,H}(t) = \begin{cases} 1 & \text{when } |u'w'| \geq H\sqrt{\overline{u'u'}}\sqrt{\overline{w'w'}} \\ 0 & \text{otherwise} \end{cases} \quad (4)$$

The quadrant analysis provides the estimation of stress fraction transported by the contribution

$$S_{i,H} = \frac{\langle u'w' \rangle_{i,H}}{u'w'} \quad (5)$$

Here,  $S_{i,H}$  is positive for  $i = 2$  and  $4$  (Q2 and Q4) and  $S_{i,H}$  is negative for  $I = 1$  and  $3$  (Q1 and Q3). Hence, sum of contributions from bursting events is unity. Figure 4 shows the variation of fraction contribution  $S_{i,H}$  with hole size  $H$  for each of the four quadrants at  $z/y = 0.036$  (near the boundary) for no-seepage and seepage experiment. Governing events are Q2 and Q4 for no-seepage flow, while Q1 and Q3 rarely contribute towards the production of RSS.

Figure 4 show that the fractional contribution from Q1 and Q3 events vanishes for  $H > 7$  and  $H > 4$ , respectively. On the other hand, contribution from the Q2

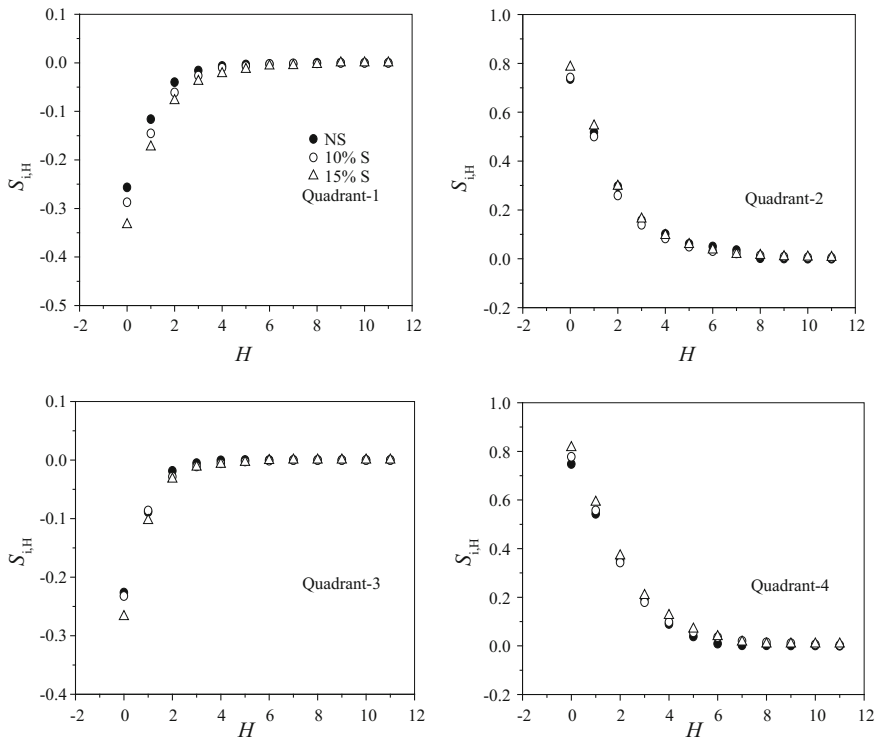
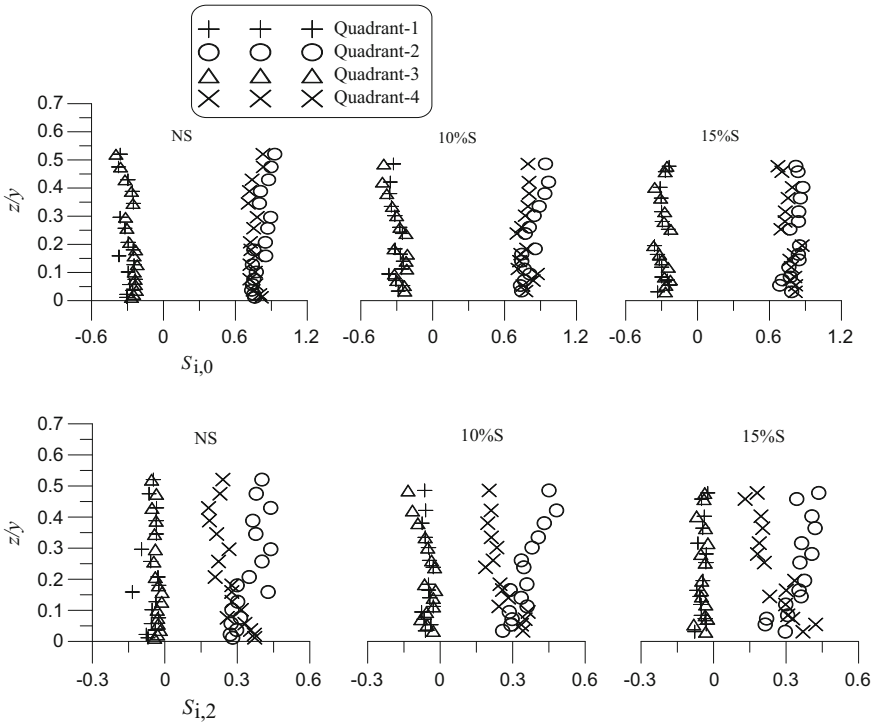


Fig. 4 Variations of  $S_{i,H}$  with  $H$

and Q4 events vanishes for  $H > 9$  and  $H > 10$ , respectively. However,  $S_{i,H}$  is slightly affected with seepage in such a way that variations of  $S_{i,H}$  with  $H$  concludes that Q2 (Q4) events with seepage are decreased (increased) respectively as compared to that with no-seepage, which results in arrival of a high speed fluid parcel due to acceleration of fluid in stream-wise direction. In the flow associated with seepage, the feebly contributions from both Q1 and Q3 events cease for  $H > 8$  (10% S case) and  $H > 6$  (15% S case) while Q2 and Q4 events dominate even for  $H > 11$  with sweeps still being the largest contributor towards the production of RSS.

The vertical distributions of  $S_{i,H}$  in flows for no-seepage and seepage are examined. The most frequent events,  $H = 0$  and  $H = 2$ , are considered associated with the use of  $u'$  and  $w'$  in flows subjected to no-seepage and seepage cases (Fig. 5). For  $H = 0$ , primary contribution is from Q2 and Q4 events and feebly contribution from Q1 and Q3 towards the RSS production. The divergence in between Q2 and Q4 events is accomplished with the large scale of eddies. These results are in agreement with previous study (Franca et al. 2014). In Fig. 5 (NS case) with  $H = 0$ , Q2 and Q4 events in near bed ( $z/y \sim 0.03$ ) contribute about 73.5% and 74.7%, respectively, towards the production of RSS, while Q1 and Q3 events contribute minimally, as 25.6% and 22.6%, respectively. The dominance of



**Fig. 5** Variations of  $S_{i,0}$  for  $H = 0$  and  $S_{i,2}$  for  $H = 2$

sweep events over ejection extends nearly up to  $z/y \sim 0.057$ , while away from the bed ( $z/y > 0.057$ ), ejection events dominate in contributing to the Reynolds shear stress production. At this junction point of flow layer ( $z/y \sim 0.057$ ), average contributions from ejections and sweeps are 74% and 77%, respectively. For 10% S, within the near bed surface ( $z/y \sim 0.03$ ), Q2 and Q4 events contribute about 74.2% and 77.7%, respectively, while Q1 and Q3 events contribute minimally as 28.7% and 23.2%, respectively. With the increase of seepage to 15% near the bed ( $z/y \sim 0.03$ ), contribution from Q4 and Q2 events becomes 78.4% and 81.55%, respectively, while feeble contribution from Q1 and Q3 becomes 33.3% and 26.7%, respectively. The result predicts that the contribution from all bursting events to RSS production in the near bed flow zone increases with the increase of percentage of seepage as compared to that with no-seepage run. Further, the present result suggests that dominants of sweep events over the ejection events at near the bed increase progressively with the further increase of downward seepage.

The thickness of the zone of sweep dominance increases from  $z/y \sim 0.057$  with no-seepage to  $z/h \sim 0.09$  and  $z/h \sim 0.12$  in the seepage run of 10% S and 15% S. These increased contributions from sweep events and thickening of the zone of sweep dominance in the seepage run increase the momentum exchange from the flow to bed particles due to which sediment transport is increased with the application of downward seepage as compared to no-seepage. Hence, for downward seepage, sweep is the major event in the near bed flow zone. With the application of downward seepage, the high speed fluid parcel becomes more persistently preserving near to the bed as compare to that with no-seepage. Compared to the RSS contributions from more extreme events occurring for hole size  $H = 2$  for both no-seepage and seepage run (Fig. 5), the most energetic events, Q2 and Q4, have distinct behaviours throughout the flow depth, since the divergence between Q2 and Q4 events gets stronger with  $z/y$ . However, there remains a consensus that there is a similar predominating feature of Q2 and Q4 events within the wall shear layer while contributions from Q1 and Q3 events remain insignificant.

The probability  $P_{i,H}$  of occurrence of the bursting events is expressed as (Cellin and Lemmin 2004)

$$P_{i,H} = \frac{\int_{t=0}^{t=T} I_{i,H} dt}{\int_{t=0}^{t=T} [I_{1,H} + I_{2,H} + I_{3,H} + I_{4,H}] dt} \quad (6)$$

where  $I_{i,H}$  is an indicator function given by Eq. (4). The vertical variations of  $P_{i,H}$  in flows for no-seepage, 10% S and 15% S, are plotted in Fig. 6. The probabilities are calculated for hole region,  $H = 0$  and  $H = 2$ . However for  $H = 0$  and  $H = 2$  subjected to no-seepage case, values of  $P_{1,H}$  and  $P_{3,H}$  for Q1 and Q3 events overlap, bearing small probabilities. Considering  $H = 0$ ,  $P_{2,0}$  and  $P_{4,0}$  for Q2 and Q4 events are dominant events in the near bed surface for no-seepage runs. However, the

dominance of  $P_{2,H}$  changes to  $P_{4,H}$  with an increase in hole size ( $H = 2$ ). Therefore, the strongest bursting events are  $P_{4,2}$  (Q4 events) while the most frequent ones are  $P_{2,0}$  (Q2 events). Interestingly,  $P_{i,H}$  ( $i = 1, 3$ ) and  $P_{4,0}$  remain almost invariant of  $z/y$ , whereas  $P_{2,0}$  and  $P_{4,2}$  decrease with  $z/y$ . Although there is no significant difference observed in the profiles of  $P_{i,H}$  for no-seepage and seepage, the values of  $P_{4,H}$  ( $H = 0, 2$ ) and  $P_{2,H}$  ( $H = 0, 2$ ), near the bed are higher and lower respectively with seepage than that with no-seepage.

In order to study the time scales of Q2 and Q4 events, the occurrences of bursting events Q2 and Q4 in a sample were counted by keeping a hole size  $H$  and calculating the number of changes over of the series of  $(u'w')$  in the applicable quadrant. The mean time of occurrence of Q2 and Q4 events,  $t_E$  and  $t_S$ , respectively, were thus obtained. Figure 7 show the vertical profiles of normalised time scales,  $T_E (= t_E u_* / y)$  and  $T_S (= t_S u_* / y)$ , in flows subjected to no-seepage and seepage for  $H = 0$  and 2. Generally for  $H = 0$ ,  $T_E$  increases with  $z/y$  while  $T_S$  decreases with  $z/y$ . But the phenomenon has changed for  $H = 2$  in case of no-seepage and seepage runs. It suggests that the time of occurrence of stronger Q4 events is less than that of stronger Q2 events. It is evident from Fig. 7 that both,  $T_E$  and  $T_S$ , in seepage are more persistent than those in no-seepage.

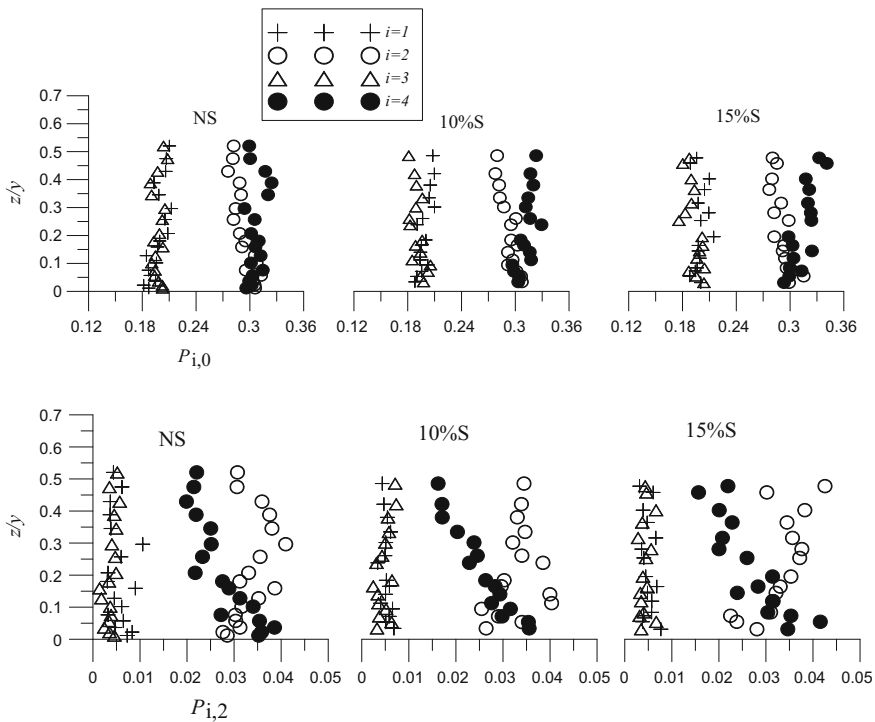


Fig. 6 Vertical profiles of  $P_{i,H}$  for  $H = 0$  and  $H = 2$

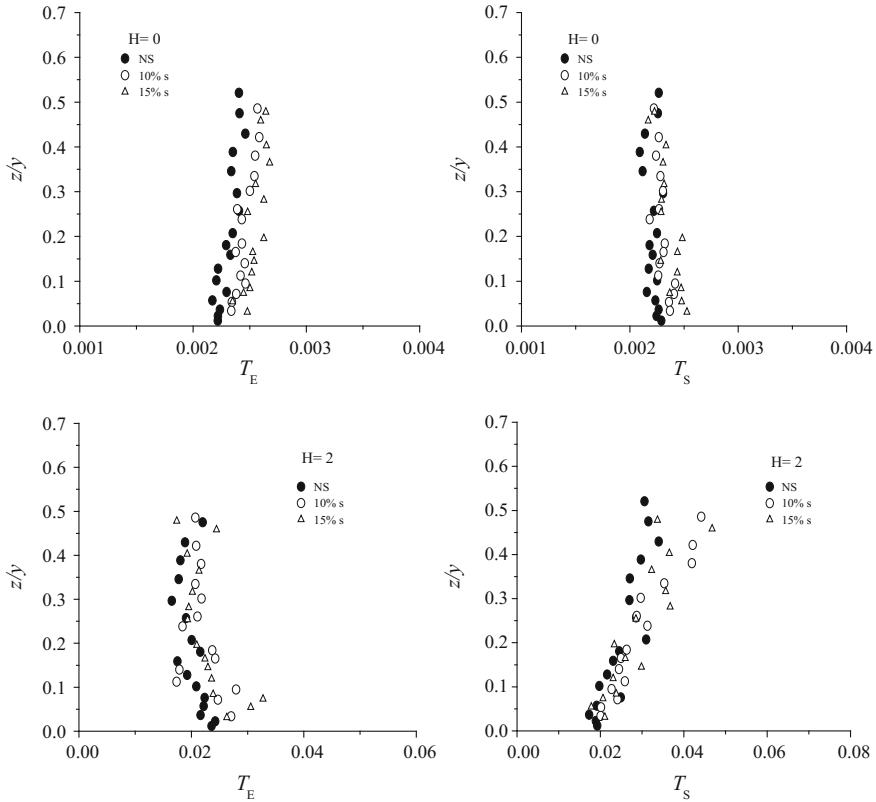


Fig. 7  $T_E$  and  $T_S$  as a function of flow depth for  $H = 0$  and  $H = 2$

### 4 Conclusions

An experimental study has been carried out to observe changes in the higher order statistics of flow when downward seepage was applied to an alluvial channel composed of non-uniform sediment mixture. The present study addresses on the flow zone in the vicinity of the bed surface. The variations of stream-wise velocity with vertical distance in flows with downward seepage in the near bed region are higher as compared to no-seepage flow. This increase in stream-wise velocities was sufficient for increased rate of sediment transport with seepage. The profiles of Reynolds shear stress are slightly scattered in general and increased with seepage, which signifies the greater momentum transfer towards the boundary. The distribution of Reynolds shear stress undergoes a damping due to a decreasing level of turbulence fluctuation within the wall shear layer. In quadrant analysis, the contribution of sweep events towards Reynolds shear stress production near the boundary is increased with increased zone of sweep dominance. This increase in high speed fluid parcel towards the boundary in seepage runs is responsible for



higher rate of sediment transport. The mean time of occurrence of ejections and that of sweeps in seepage are longer than those in no-seepage.

In the framework of river engineering, the present study contributes to the knowledge on the link between the turbulent flow and sediment transport with non-uniform flow, which is a governing process on the river morphodynamics.

## References

- Andrews ED (1983) Entrainment of gravel from naturally sorted riverbed material. *Geol Soc Am Bull* 94:1225–1231
- Cellino M, Lemmin U (2004) Influence of coherent flow structures on the dynamics of suspended sediment transport in open channel flow. *J Hydraul Eng* 130(11):1077–1088
- Curran JC (2007) The decrease in shear stress and increase in transport rates subsequent to an increase in sand supply to a gravel-bed channel. *Sed Geol* 202:572–580
- Curran JC, Wilcock PR (2005) Effect of sand supply on transport rates in a gravel-bed channel. *J Hydraul Eng* 131(11):961–967
- Devi TB, Sharma A, Kumar B (2016) Turbulence characteristics of vegetated channel with downward seepage. *J Fluids Eng* 138(12):121102
- Fang D, Yu GL (1998) Bedload transport in cobble-bed rivers. In: *Proceedings of international water resources engineering conference*, Memphis, USA
- Franca MJ, Santos BO, Antico F, Ferreira RML (2014) Quadrant analysis of shear events in open channel flows over mobile and immobile hydraulically rough beds. *ERCOFTAC Bulletin* 100:29–36
- Ghoshal K, Mazumder BS, Purkait B (2010) Grain-size distributions of bed load: inferences from flume experiments using heterogeneous sediment beds. *Sed Geol* 223(1–2):1–14
- Goring DG, Nikora VI (2002) Despiking acoustic Doppler velocimeter data. *J Hydraul Eng* 128(1):117–126
- Karim F (1998) Bed material discharge prediction for nonuniform bed sediments. *J Hydraul Eng* 124(6):597–604
- Kleinmans MG (2005) Autogenic cyclicity of foreset sorting in experimental Gilbert-type deltas. *Sed Geol* 181(3):215–224
- Lacey RW, Roy AG (2008) Fine-scale characterization of the turbulent shear layer of an in-stream pebble cluster. *J Hydraul Eng* 134(7):925–936
- Lu SS, Willmarth WW (1973) Measurements of the structure of the Reynolds stress in a turbulent boundary layer. *J Fluid Mech* 60(03):481–511
- Marsh NA, Western AW, Grayson RB (2004) Comparison of methods for predicting incipient motion for sand beds. *J Hydraul Eng* 130(7):616–621
- Misri RL, Garde RJ, Ranga Raju KG (1984) Bed load transport of coarse nonuniform sediment. *J Hydraul Eng* 110(3):312–328
- Mittal MK, Porey PD, Raju KGR (1990) Bed load transport of nonuniform sediments. In: *Proceedings of the Euromech 262-colloquium on sand transport in rivers, estuaries and the sea*, Wallingford, UK
- Parker G, Kilington PC, Mclean DG (1982) Bed load and size distribution in paved gravel-bed streams. *J Hydraul Div ASCE* 108(4):544–571
- Patel PL, Ranga Raju KG (1996) Fraction wise calculation of bed load transport. *J Hydraul Res* 34(3):363–379
- Samaga BR, Raju KGR, Garde RJ (1986) Bed load transport of sediment mixtures. *J Hydraul Eng* 112(11):1003–1017
- Sreenivasulu G, Kumar B, Ramakrishna Rao A (2011) Variation of stream power with seepage in sand bed channels. *Water SA* 37(1):115–119

- Wilcock PR (1993) Critical shear stress of natural sediments. *J Hydraul Eng* 119(4):491–505
- Wilcock PR, Crowe JC (2003) Surface-based transport model for mixed-size sediment. *J Hydraul Eng* 129(2):120–128
- Wu B, Molinas A, Julien PY (2004) Bed-material load computations for non-uniform sediments. *J Hydraul Eng* 130(10):1002–1012
- Zyserman JA, Fredsøe J (1994) Data analysis of bed concentration of suspended sediment. *J Hydraul Eng* 120(9):1021–1042

# Analysis of Yellow River Delta Evolution with Flux Variations of Runoff and Sediment

Hongling Shi, Qin Lu and Zuwen Ji

**Abstract** Due to the abundant runoff and sediment flux from the Yellow River, the Yellow River Delta (YRD) is one of the quickest continent-building areas worldwide. The YRD land area growth rate was controlled mainly by the amount of provided runoff and sediment. In this paper, the runoff and sediment load of Lijin hydro gauge station, located at the entrance of the YRD, are selected as the representatives, and the relationship between the supplements of the water/sediment and the land area is analyzed by correlation methods; besides, the variation trends of the incoming runoff and sediment load are illustrated based on the Mann–Kendal statistics test. The results indicate that, in the period of record, the annual land area is in perfect linear correlation with the accumulated annual runoff, as well with the accumulated annual sediment load; both the annual runoff and annual sediment load fluxes from Lijin station are in significantly decreasing trends. At last, considering the crisis the YRD faced, rational allocation of the water and sediment resources is put forward.

## 1 Introduction

The normal coastal areas are formed and developed by the co-action of neo-tectonic movement, sediment siltation, local precipitation, runoff and tidal currents. Most of them are in alternations of extending by river sediment siltation and retrograding by erosion of tidal current, which also concerns the Yellow River Delta.

The Yellow River is well-known as a highly sediment-laden river in the world; it carries lots of fine sediment flowing northeast to the Bohai Sea, depositing most of fine particles of sediment on the estuarine area annually, and builds and rebuilds new land permanently.

---

H. Shi (✉) · Q. Lu · Z. Ji

State Key Laboratory of Simulation and Regulation of Water Cycle in River Basin, China Institute of Water Resources and Hydropower Research (IWHR), 20 Chegongzhuang West Road, Beijing 100048, China  
e-mail: shihl@iwhr.com

Based on long time aggradations of the Yellow River sediment, the YRD land is extending to the sea year by year. However, with the lesser amount of incoming runoff and sediment load, some coast has been retrograded. The amounts and areas of eroded coast calculated from satellite photography, as shown in Fig. 1, illustrated that, besides the Chahe river, the flowing waterway of the Yellow River mouth, which was continually in aggradation, other coast shores were also eroded in the 20 years before 2009. Notably, the estuary of Qingshuigou River area, the Yellow River old channel at the east-south corner, was eroded fastest. In the past, owing to lots of incoming sediments from the Yellow River, the total alluviation area was larger than the erosion area, while with the lesser amount of incoming sediments of the Yellow River, extreme drying-up, and, in addition to the rising sea level, the coast would be eroded quickly, and even the net erosion would take place.

Many researchers have analysed the variations of the fluxes of water and sediment from the Yellow River, and indicated the effect of the fluxes to the YRD area evolution. Walling and Fang (2003), Walling (2006), Peng and Chen (2009) and Shi et al. (2016) assessed that the human activities were the main cause for the reduction of water and sediments into the sea; Ding and Pan (2007) and Ren et al. (2015) considered the abrupt points of water flux in the year 1985; Liu et al. (2011) divided the sediment flux sequences into 4 phases by the abrupt points of 1955, 1962, and 1968; Xu (2002) and Xu and Sun (2003) estimated the changes in water

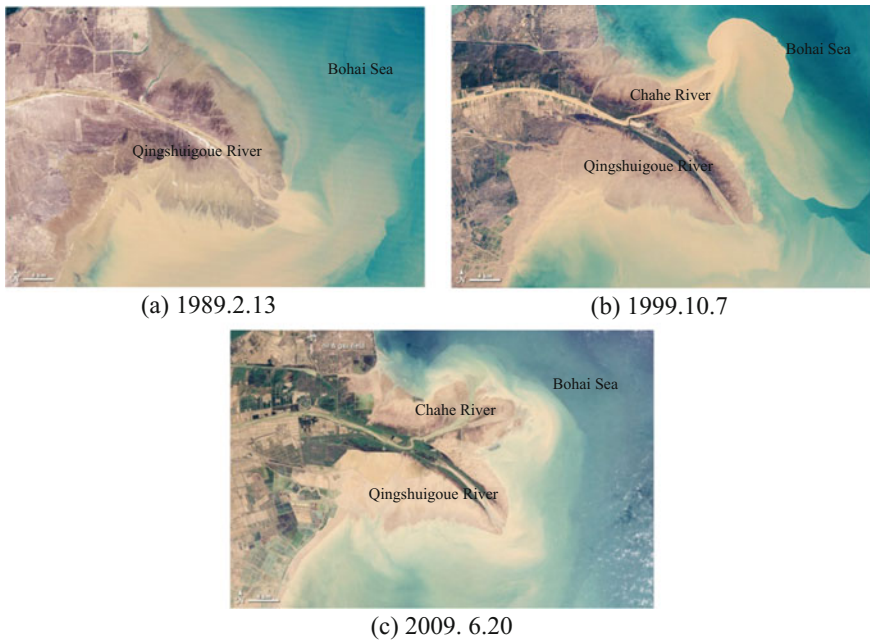


**Fig. 1** Satellite image of the Yellow River mouth in different time ([http://earthobservatory.nasa.gov/Features/WorldOfChange/yellow\\_river.php](http://earthobservatory.nasa.gov/Features/WorldOfChange/yellow_river.php))

and sediment fluxes into the sea with established multiple regression equations. Peng and Chen (2009) and Liu et al. (2011) illustrated that there was a positive relationship between the progradation rate of estuarine coastline and riverine sediment input, and, furthermore, the coastline near river mouth stretched and the delta area increased when the ratio of accumulative sediment load and accumulative water discharge into the sea was 25.4–26.0 kg m<sup>-3</sup>. Ren (2015) collected the data since 150 ka BP, and drew the conclusion that the effect of human activity on sediment discharge of the Yellow River is especially strong; and in response to global warming and increase of water diversion, the sediment flux of the Yellow River to the sea will most likely remain small in the next two to three decades.

Owing to the close reliance of the evolution of the YRD to the incoming runoff and sediment load, under the condition of global climate change, the variation trends of runoff and sediment are of concern. Therefore, the purpose of the paper is to (1) examine the variations of the fluxes of water and sediment of the Yellow River with recent sequences from 1950 to 2014; (2) confirm the relationship between the YRD land area evolution and the incoming runoff and sediment load tendency; (3) make it clear that there are crises from the shortage of water and sediment, and put forward strategies to protect the YRD from new land building, and protect the wetlands, the local ecosystem and local economy.

## 2 Research Method

### 2.1 Trend Analysis Method—M-K Rank Correlation Test

For a long series of researches on hydrologic and sediment trends, common methods include moving-average test, linear regression trend test, Spearman Rank correlation test, Mann-Kendall rank correlation test, the cumulative average method, etc. (Xu and He 2005).

The Mann-Kendall (M-K) rank correlation test is a non-parametric statistical method, applicable to evaluating the time-series trends of climate variables. This approach releases the sample from compliance with a certain distribution, but also itself from interference of a few outliers, which is more suitable for the type variables and ordinal variables (Yue et al. 2002 and Zhang et al. 2007). Also, it is well-known for extensive applications, less artificialities and a high degree of quantification (Qin et al. 2005).

Given a time-series sample ( $x_1, x_2, \dots, x_n$ ), the principle of the M-K statistics is to construct a rank sequence  $S_k$ :

$$S_k = \sum_{i=2}^k \sum_{j=1}^{i-1} \text{sign}(x_i - x_j) \quad (k=2, 3, 4, \dots, n). \quad (1)$$

In the above formula,

$$\text{sign}(x_i - x_j) = \begin{cases} +1 & \text{when } x_i > x_j \\ 0 & \text{else} \end{cases} \quad (j = 1, 2, 3, \dots, i - 1).$$

Assuming the time series stochastic independence, definite the statistics:

$$UF_k = \frac{[S_k - E(S_k)]}{[Var(S_k)]^{1/2}} \quad (k = 2, 3, 4, \dots, n). \quad (2)$$

In the above formula (2),  $UF_1 = 0$ ;  $E(S_k)$  and  $Var(S_k)$  are mathematical expectation and variance of the accumulating sequence  $S_k$ , when  $x_1, x_2, \dots, x_n$  are independent of each other, and have the same continuous distribution; they can be calculated by the following formulas:

$$E(S_k) = \frac{n(n-1)}{4}, \quad (3)$$

$$Var(S_k) = \frac{n(n-1)(2n+5)}{72}. \quad (4)$$

As  $n$  increases,  $UF_k$  quickly converges to the standardized normal distribution. If the  $UF_k$  value is greater than 0, it indicates that the sequence is in ascendant trend; if the  $UF_k$  value is less than 0, it indicates that the series declined. Given significance level  $\alpha$ , check the normal distribution table; if  $|UF_k| > U_\alpha$ , it indicates that there is an obvious trend in the analyzed sequence.

## 2.2 Abrupt Changes Analysis Method—Rank Sum Test

For the research of hydrologic sequence trend, a possible leap (abrupt change) during the trend variation shall also be explored. The leap (abrupt change) refers to the abrupt changes of hydrologic sequence when it transforms from one status into another; the turning point at which the time sequence changes abruptly is the abrupt change point. The abrupt change refers to the parallel rise or drop of the statistical characteristics of hydrologic sequence (often refers to the average of the sequence) before and after the abrupt change point. The abrupt changes of hydrologic sequence are caused by human or natural factors.

For the determination of abrupt changes, first find the abrupt change point and then conduct an abrupt change significance test to the hydrologic sequence before and after the abrupt change point. In the article, a simple and intuitive correlation curve of cumulative time sequence is selected to determine the abrupt change point and the rank sum test is used to test the abrupt changes.

The research sequence is  $x_1, x_2, \dots, x_n$  and the reference sequence is  $y_1, y_2, \dots, y_n$ . Compute their cumulative time sequences, respectively.

$$\left. \begin{aligned} g_j &= \sum_{i=1}^j x_i \\ m_j &= \sum_{i=1}^j y_i \end{aligned} \right\} (j = 1, 2, \dots, n). \tag{5}$$

Draw the relationship diagram between sink points  $m_j$  and  $g_j$ . If the leap of research sequence  $X_t$  is not obvious,  $m_j$  and  $g_j$  are a beeline through the origin, or a fold line with turning point at the abrupt change point.

After the abrupt change point is determined, it should be checked whether there is an obvious difference between the first and the second part. If yes, there is a leap, or the leap is not obvious.

Assume a hydrologic sequence  $x_1, x_2, \dots, x_\tau, x_{\tau+1}, x_{\tau+2}, \dots, x_n$ , of which the abrupt change point is  $\tau$ , and there are  $n_1$  and  $n_2$  values before and after  $\tau$ . Rank the sequence from low to high or from high to low and number it uniformly (from 1); the corresponding number of each value is defined as its “rank”. The rank sum of samples with small capacity is denoted by  $W$ . When  $n_1, n_2 > 10$ ,  $W$  approaches normal distribution. Define statistical variable

$$U = \frac{W - \left( \frac{n_1(n_1 + n_2 + 1)}{2} \right)}{\sqrt{\frac{n_1 n_2 (n_1 + n_2 + 1)}{12}}}. \tag{6}$$

For a given significance level  $\alpha$ , compute  $U_{\alpha/2}$ . When  $|U|$  is greater than  $U_{\alpha/2}$ , a leap occurs before and after the abrupt change point, or the leap is not obvious.

### 3 Variation of the Land Area and Fluxes of Runoff and Sediment

#### 3.1 Variation of the Land Area

The continent-building area was 2500 km<sup>2</sup> in the years after 1855, equivalent to an annual increasing rate of 22.5 km<sup>2</sup> a<sup>-1</sup>. As shown in Table 1, the annual increasing rates of continent-building area were different in various year spans: they amounted to 23.6 km<sup>2</sup> a<sup>-1</sup> during 64 years (1855–1953.6); then dropped to 9.6 km<sup>2</sup> a<sup>-1</sup> during 12.1 years (1996.7–2000); after which there was even an erosion by -9.4 km<sup>2</sup> a<sup>-1</sup> during 2000–2007 (Peng and Chen 2009).

It should be noticed from Table 1 that, with decreasing annual net silting rate, both the incoming annual runoff and sediment load in the different period were reduced.

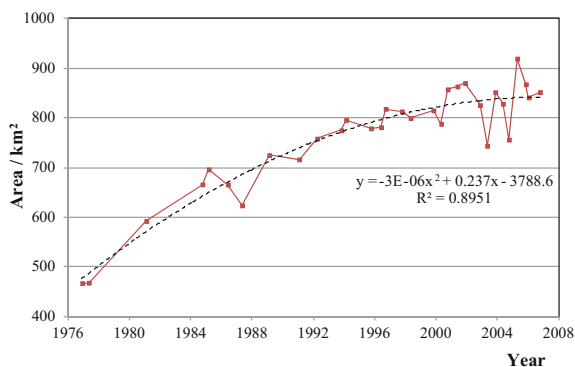
**Table 1** Continent-building after 1855 in YRD (Peng and Chen 2009)

Period	Interval [years]	Total runoff [ $10^9 \text{ m}^3$ ]	Total sediment [ $10^9 \text{ t}$ ]	Reclamation area [ $\text{km}^2 \text{ a}^{-1}$ ]	Costal line extension rate [ $\text{km a}^{-1}$ ]
1855–1953.6	64			23.6	2.00
1953.7–63.12	10.5	505	13.03	39.2	2.57
1964.1–76.5	12.4	563	14.28	40.8	2.66
1976.6–96.6	4.25	485	12.42	22.1	1.90
1996.7–2000	12.1	39.7	1.03	9.6	2.82
2001–2007	8	108	1.19	−9.4	

The Lijin hydrological station, located at the entrance of the Yellow River Delta, can be considered as the control station. And the gauged runoff and sediment load of Lijin station can be considered as the incoming water and sediment of the Delta.

According to the researches of Lu et al. (2007) by remote sensing technique, as shown in Fig. 2, the land area of the Yellow River mouth from 1976 to 2006 was continuing to grow. The variation of land area could be divided into three stages, according to the growth rate. The first stage is a fast growing period from the year 1976–1986, with the mean annual area variation rate of  $+19.86 \text{ km}^2$ ; the second stage is a slightly growing period during 1986–2000, with the mean annual area variation rate of  $+9.95 \text{ km}^2$ ; and the last stage is the leveled off growing period after 2000, with the mean annual area variation rate of  $+5.96 \text{ km}^2$ . Besides, it should be noticed that the data points in Fig. 2 changed in a wide amplitude around the periods 1985–1989 and 2000–2006.

Based on regression test, the land area growing tendency fits the quadric curve very well. And the regression equation (as shown in Fig. 2) could be used to calculate the approximate values of land area at a given time. The fitted annual land area calculated by the regression equation will be used in the following analyses.

**Fig. 2** Variation of the land area of the Yellow River Delta during 1976–2006



### 3.2 Variation of Fluxes of Runoff and Sediment

Based on M-K statistics test, the last M-K statistics on 2009 of annual runoff and annual sediment load of Lijin station are  $-6.20$  and  $-6.29$ , respectively, as illustrated in Table 2. Both of the test values are negative and significantly lower than the critical value of  $-1.96$  ( $U_{0.05/2} = 1.96$ ) in M-K test when significance level  $\alpha = 0.05$  on 1986, and are even lower than the critical value of  $-2.58$  ( $U_{0.01/2} = 2.58$ ) when the significance  $\alpha = 0.01$ . This manifested abnormally sharp declining trends on both the normal runoff and sediment load of the Lijing station for the analyzed data.

The cumulative time sequence and rank sum test were adopted for annual runoff and annual sediment load leap test. The cumulative annual runoff curve and the cumulative annual sediment load at Lijin station with time were plotted in Figs. 3 and 4. Based on the curve of cumulative time sequence, it can be seen from the accumulated sequence during 1952–2009 that both the annual runoff and sediment

**Table 2** M-K tests for annual runoff and annual sediment load of Lijin station

M-K test	Test for runoff	Test for sediment load
Values	$-6.20$	$-6.29$
Tendency	Sharp drop	Sharp drop

**Fig. 3** Identification of abrupt change points at Lijin station by accumulated annual runoff

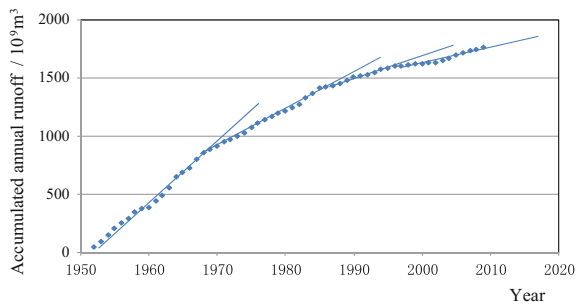
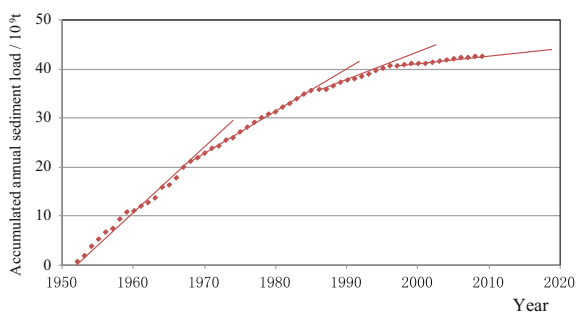


**Fig. 4** Identification of abrupt change points at Lijin station by accumulated annual sediment load



load changed abruptly with an obvious turning point in the years 1968, 1986 and 1997.

Regarding the result of rank sum test (see Table 3), the above-mentioned years both pass the leap test (the absolute value of test value is over the critical value 1.96 when the significance  $\alpha = 0.05$ ) and show an obvious leap.

### 4 Relationship Between the Land Area and Incoming Runoff/Sediment of the YRD

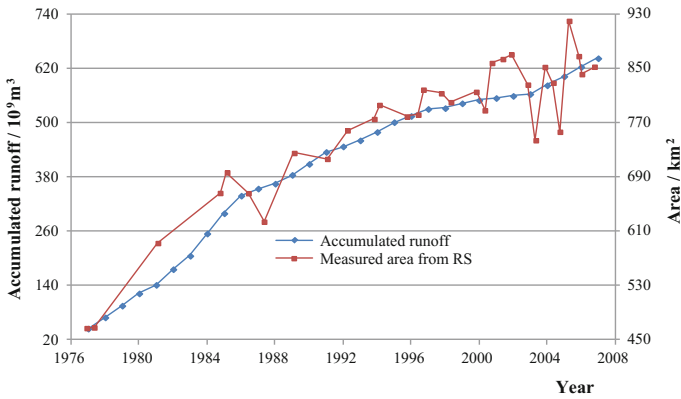
In reference to the period of the above-mentioned remote sensing measured land area of the Yellow River mouth, the same period of annual incoming runoff and sediment load of Lijin station has been selected and analyzed. It is not difficult to see that the yearly accumulated runoff or sediment load is well consistent with the annual land area, as shown in Fig. 5.

For further analysis of the relationship between annual land area and the hydrological data, the yearly accumulated runoff and the fitted land area are combined and the correspondence curve is drawn, as shown in Fig. 6a. The perfect linear correlation of the above-mentioned two factors is obvious, and their coefficient of coherence is up to 0.9922. Also, analyzing the relationship between the yearly accumulated sediment load and the fitted land area (as shown in Fig. 6b), the same result is clearly seen, with the coherence coefficient reaching 0.9968.

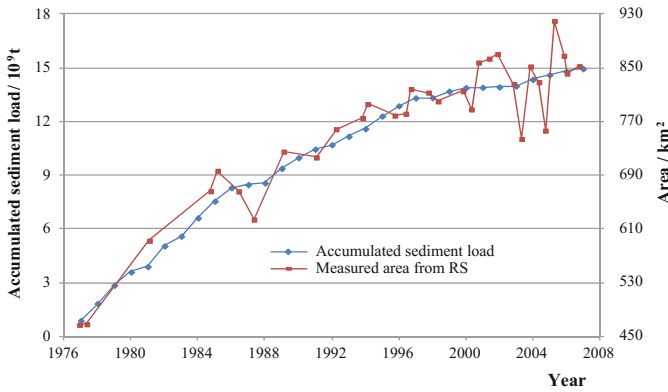
It should be noted that, after 2000, both data points of Fig. 6 deviate from the linear correlation lines and drop to flat. They manifest that, based on the reduced incoming runoff and sediment after 2000, the land area growth rate is less than for the whole sequences. It is significant to note a clear variation trend of the incoming runoff and sediment load, which control the new land area evolution.

**Table 3** Leap test for Lijin station (significance standard  $U_{0.05/2} = 1.96$ )

Period		1952–1967	1968–1985	1986–1996	1997–2009
Number of samples		16	42		
Statistical test value	Runoff	4.54			
	Sediment load	3.90			
Number of samples		24		34	
Statistical test value	Runoff	−5.90			
	Sediment load	−5.59			
Number of samples		45			13
Statistical test value	Runoff	−4.39			
	Sediment load	−5.08			



(a) land area and runoff



(b) land area and sediment load

**Fig. 5** Land area coherent with the hydrological data of the Yellow River mouth

Based on the above analysis of the 31-year sequence of the gauged field data, a conclusion can be drawn that the incoming runoff and sediment load are of great relevance to the estuarine land area of the Yellow River Delta. The greater the incoming runoff or sediment load, the faster the land area growth.

## 5 Potential Crisis and Coping Strategy of the YRD

The bay of Bohai Sea is dominated by long-term settlement in neo-tectonic motion; the average depth of the bay is 18 m. At Bohai shore, most of areas covered by silt settling from the Yellow River are at an altitude lower than 3–5 m (UNDP report, 1997). Relative rising of sea level will inundate the coastal area directly, then contribute to more storm surges and floods, and hence deteriorate the coast eco-environment.

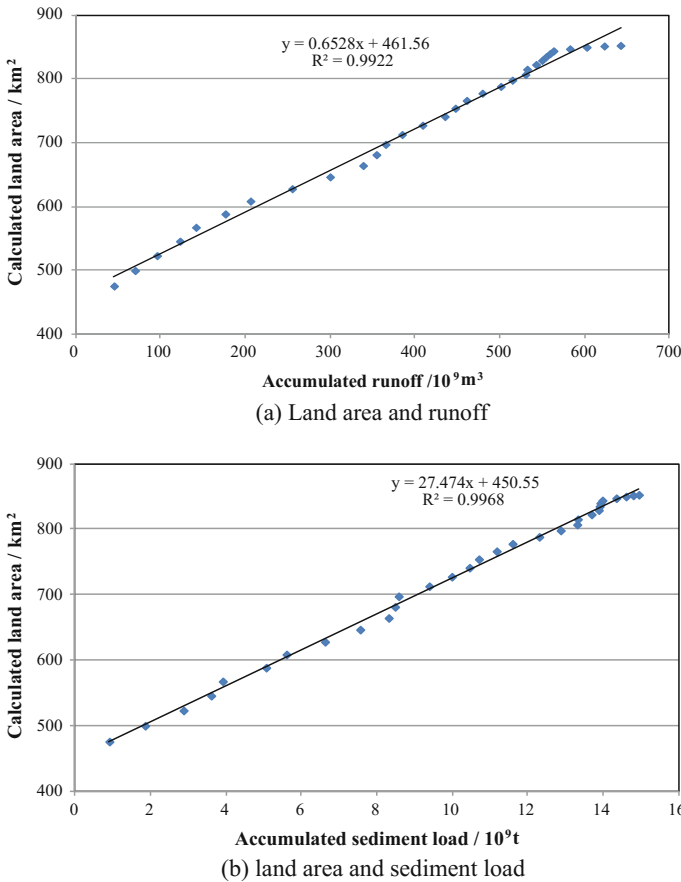


Fig. 6 Relationship between land area and the hydrological data of Yellow River mouth

### 5.1 Crisis Brought by Less Runoff and Sediment

The local YRD yields little water resources. The direct surface runoff by precipitation is 0.4485 billion m<sup>3</sup>; as for underground water, except brine, salt water or brackish water which are more than 90% of the total, the underground water useful for agriculture or domestic consumption is only 58.472 million m<sup>3</sup>. Among the sediment load transported by the Yellow River, nearly 20% of the incoming sediment load is deposited in the river channel and the Delta, 50% in the estuary, and the rest (30%) is carried by tidal waves to the sea area deeper than 15 m.

The Yellow River flows through the Delta, and supplies a lot of foreign water. However, due to the effects of precipitation decreasing in water original area and water diversion increasing along the River, the incoming water of Delta was in a reduced trend. Moreover, even though the water volume from the Yellow River is

abundant in an annual average, there is a serious problem of seasonal shortage. A smaller Yellow River incoming runoff will decrease the replenishment of fresh water for wetlands, and bring a lot of ecological problems, such as soil salinization, phytocommunity inverse to salt-proof, vegetation cover decrease and original eco-system degradation, etc., owing to the destroyed balance of fresh water and salinity. Moreover, the lesser amount of fresh water will reduce the wetlands' clarification capacity, aggravate water pollution, and enlarge red tide probability. At present, the area of saline-alkaline soil accounts for 3/4 of the whole YRD area. Among that, high and moderate grades of saline-alkaline soil are nearly  $440 \times 10^3 \text{ hm}^2$ , accounting for 56.2% of the total (Mao et al. 2003).

## **5.2 Rational Allocation of the Water and Sediment Resources**

The Yellow River incoming water and sediment are of dominance for forming and keeping YRD original land area, and local ecosystem. The runoff coming from the Yellow River as the main fresh water resources of the Delta will keep the balance of local ecosystem. Besides, it is an economic way to take advantage of sedimentation to fill offshore oil field and change the offshore operation to land extraction.

The reduced incoming water and sediment of Yellow River inevitably will make the wetland degradation, the coastal line retreat, and ultimately will affect sustainable development. Therefore, rational allocation of the water resources and sediment resources will be the basic strategy for dealing with the crisis of resources shortage. Taking into account the fact that the greater the amount of incoming water, the greater the sediment load, the regulation of water flow along the Yellow River is very important. Firstly, the reservation measures of water source region should be strengthened by legislation; the schemes of water allocation and diversion in each district of the Yellow River basin should be scientifically planned. Secondly, the water-saving society should be gradually constructed and implemented both in ordinary life of citizens and agriculture irrigation, notably the abolishment of the surface flooding irrigation. Thirdly, the structure of property should be modified, including some planned constructive items with large water consumption should be prudently considered.

## **6 Conclusion**

Based on the analysis of the 31-year sequences of the gauged incoming runoff coupled with sediment load, and the RS calculated land area of the Yellow River Delta, it is obvious that the former are of great relevance to the latter. The greater the incoming runoff or sediment, the faster the land area grows; the lesser the amount of incoming runoff or sediment, the slower the new area builds.

The annual incoming runoff and sediment load of the Yellow River estuary have obviously decreasing trends, which is a great challenge for keeping the local ecological environment balance and sustainable development.

To deal with the shortage of incoming water and sediment of the Yellow River Delta, the rational allocation of the water and sediment resources is one of the principal measures.

**Acknowledgements** This study has been financed by National Key Research and Development Program of China (2016YFC0402407), the National Natural Science Foundation of China (Grant No. 51309255), the Foundation of State Key Laboratory of Simulation and Regulation of Water Cycle in River Basin (2016TS07), the Technology Demonstration Projects of Ministry of Water Resources (SF2016-10), and Research and Development Projects on Application Technology of Heilongjiang Province (GZ16B011).

## References

- Ding YF, Pan SM (2007) Evolutionary characteristics of runoff into the sea of the Yellow River and their causes in recent 50 years. *Quat Sci* 27(5):709–717 (in Chinese)
- Liu F, Chen SL, Peng J, Chen GQ (2011) Temporal variability of water discharge and sediment load of the Yellow River into the sea during 1950–2008. *J Geog Sci* 21(6):1047–1061
- Lu JX et al (2007) Remote sensing analysis of evolution of Yellow River estuary coast. Research report, Remote Sensing Technology Application Center, pp 32–36 (in Chinese)
- Mao H, Zhao Q, Gao Q (2003) Consider the modes of resources exploitation under the limit of eco-environment sustainable development in the Yellow River Delta. *J Nat Resour* 18(4) (in Chinese)
- Peng J, Chen SL (2009) The variation process of water and sediment and its effect on the Yellow River Delta over the six decades. *Acta Geogr Sin* 64(11):1353–1362
- Qin N, Jiang T, Xu C (2005) trend change and analysis on abrupt changes in the runoff of Yangtze River. In: Resources and environment along the Yangtze River Basin, vol 5, pp 589–594 (in Chinese)
- Ren H, Li GS, Cui LL, He L (2015) Multi-scale variability of water discharge and sediment load into the Bohai Sea from 1950 to 2011. *J Geog Sci* 25(1):85–100
- Ren M (2015) Sediment discharge of the Yellow River, China: past, present and future—A synthesis. *Acta Oceanol Sin* 34(2):1–8
- Shi HL, Hu CH, Wang YG, Liu C, Li HM (2016) Analyses of trends and causes for variations in runoff and sediment load of the Yellow River. *Int J Sed Res* 32(2):171–179
- UNDP (1997) Support for sustainable development of the Yellow River Delta general report. Dongying, Shandong, China
- Walling DE, Fang D (2003) Recent trends in the suspended sediment loads of the world's rivers. *Glob Planet Change* 39(2003):111–126
- Walling DE (2006) Human impact on land–ocean sediment transfer by the world's rivers. *Geomorphology* 79(2006):192–216
- Xu JX (2002) Sediment flux into the sea as influenced by different source areas in the drainage basin: example of the Yellow River, China. *J Hydrol Sci* 47(2):187–202
- Xu JX, Sun J (2003) Influence of precipitation and human activities on water fluxes from the Yellow River into the sea in the past 50 years. *Adv Water Sci* 14(6):690–695
- Xu Z, He W (2005) Trend analysis of evaporation pan and volume in the Yellow River for nearly 40 years. *J Hydrol* 6:6–11

- Yue S, Pilon P, Cavadias G (2002) Power of the Mann-Kendall and Spearman's rho testes for detecting monotonic trends in hydrological series. *J Hydrol* 2002(259):254–271
- Zhang J, Zhang J, Wang J, Li Y (2007) Trend Research on the annual runoff of China's six major River Basins in the past 50 years. *J Water Sci Adv* 2:230–234 (in Chinese)

# Mathematical Modelling of Sand-Gravel Bed Evolution in One Dimension

Kseniia Snigur and Igor Potapov

**Abstract** In the paper a one-dimensional riverbed model is proposed. In the model the bed load sediment transport is described by an analytical formula. This formula doesn't contain phenomenological parameters and takes into account the influence of the bed shear stress, the local bed slope, granulometrical and physical-mechanical parameters of the bed material. Three types of riverbed problems are solved by using the proposed model: the problem of bed degradation under the influence of the purified water flow, the problem of bed aggregation and the problem of the trench evolution under the influence of the transit flow. The comparison analysis of the predicted data with the established experimental data and the data obtained by the other models was carried out. It was shown that the proposed model adequately describes the bed evolution; in all three problems, the accuracy of the predicted data is sufficient for practice.

## 1 Introduction

At present there are a lot of mathematical models to describe the bed evolution (van Rijn 1986; Wu 2001; Singh 2002; Wu and Vieira 2002; Sanchez and Wu 2011). However, most of such models contain empirical parameters and semi-analytical dependencies which makes the model complicated and requires an additional adaptation for a specific object modelling. By using such models, the researcher can estimate only the qualitative nature of riverbed processes. In the paper, a one-dimensional riverbed model based on the models (Petrov 1991; Potapov and Snigur 2011, 2014) is proposed. The model takes into account a suspended and bed-load sediment transport. The hydrodynamic part of the model consists of the shallow water equations. A bed-load transport part of the model is described by the original formula derived analytically from the equation of thin bed layer motion with the Coulomb rheology

---

K. Snigur (✉) · I. Potapov  
Computer center FEB RAS, Kim U Chena 65, Khabarovsk, Russia  
e-mail: snigur.ks@ccfebras.ru

I. Potapov  
e-mail: potapov2i@gmail.com



for granular medium and the Prandtl rheology for liquid medium. The formula takes into account the influence of the bed shear stress, the local bed slope, granulometric and physical-mechanical parameters of the bed material on the bed-load transport. In order to verify the proposed model a number of test problems are solved. The comparison analysis of the predicted data, established experimental data (Newton 1951; van Rijn 1986; Seal et al. 1995) and data obtained by the other authors was made (van Rijn 1986; Wu 2001; Singh 2002; Wu and Vieira 2002; Sanchez and Wu 2011).

## 2 Mathematical Formulation

The problem of describing sandy bed long-wave deformations in a plain river or channel with a quiet flow and constant water rate  $Q$  is considered.

Assume that the bed elevation changes much more slowly than the flow velocity does; then the hydrodynamic flow can be considered as quasi-stationary at every time step  $\Delta t$  and can be described by the stationary hydrodynamic equations in shallow water approach (Kartvelishvili 1973; Grishanin 1974)

$$\frac{\partial}{\partial x} \left( \frac{U^2}{2g} + \eta \right) + \frac{\tau}{gH\rho_w} = 0, \quad Q = UH, \quad (1)$$

where  $g$ —the acceleration of gravity,  $\tau$ —the bed shear stress,  $\rho_w$ —the water density,  $H$ —the flow depth,  $x$  axis is directed along the flow velocity  $U$ ,  $y$  axis is perpendicular to  $x$  axis,  $y = \zeta(t, x)$ —the bed elevation and  $y = \eta(t, x) = H + \zeta(t, x)$ —the free surface elevation.

The bed elevation  $\zeta$  is determined from Exner equation (Exner 1925; Belolipetcky and Genova 2004)

$$(1 - \varepsilon)\rho_s \frac{\partial \zeta}{\partial t} + \frac{\partial G}{\partial x} = -\alpha \frac{W}{H} (S_* - S), \quad (2)$$

where  $t$ —the time coordinate,  $\varepsilon$ —the bed material porosity,  $\rho_s$ —the bed material density,  $G$ —the bed load transport rate,  $\alpha \in (0; 1)$ —the adaptation coefficient determined from matching with the experiment (Karaushev 1977; Belolipetcky and Genova 2004),  $W$ —the particle fall velocity,  $S$ —the depth averaged mass concentration of suspended load and  $S_*$ —the suspended transport capacity.

The bed load transport rate  $G$  depends on the bed shear stress, local bed slopes, granulometrical and physical-mechanical parameters of the bed material (Petrov 1991):

$$G = G_0 \tau^{3/2} \left[ (1 - \chi) - \frac{1}{\tan \varphi \cos \gamma} \left( 1 - \frac{\chi}{2} \right) \frac{\partial \zeta}{\partial x} \right], \quad (3)$$

$$G_0 = \frac{4}{3} \frac{\rho_s m}{\kappa \sqrt{\rho_w} (\rho_s - \rho_w) g \tan \varphi \cos \gamma}, \quad m = \begin{cases} 1, & \chi < 1 \\ 0, & \chi \geq 1 \end{cases},$$

$$\chi = \sqrt{\frac{\tau_*}{\tau}}, \quad \tau_* = \frac{3}{8} \frac{\kappa^2 d (\rho_s - \rho_w) g \tan \varphi \cos \gamma}{c_x}, \quad (4)$$

where  $\tau_*$ —the critical bed shear stress,  $\varphi$ —the internal friction angle of particles,  $c_x$ —the frontal particle drag coefficient,  $d$ —the mean particle diameter,  $\gamma$ —the acute angle between the normal to bed and the vertical line and  $\kappa$ —the Karmans constant.

To determine the depth averaged mass concentration of suspended load in Eq. (2) the following transport equation (Karushev 1977; Belolipetcky and Genova 2004; Singh 2002) is used

$$\frac{\partial S}{\partial t} + \frac{\partial SU}{\partial x} = \alpha \frac{W}{H} (S_* - S). \quad (5)$$

The suspended transport capacity  $S_*$  is determined from the following formula (Karushev 1977)

$$S_* = \begin{cases} \beta \frac{U^3}{WH}, & W < u_* \\ 0, & W \geq u_* \end{cases}, \quad u_* = \sqrt{\frac{\tau}{\rho_w}}, \quad \beta = 0.2. \quad (6)$$

Chezy-Manning formula is used to determine the bed shear stress  $\tau$  (Grishanin 1974)

$$\tau = \rho_w g \frac{U^2}{C^2}, \quad C = \frac{1}{n_s} H^{\frac{1}{6}}, \quad (7)$$

where  $n_s$ —the Manning's roughness coefficient.

When the value of the water rate  $Q$  is given, Eqs. (1)–(7) are closed by the following initial conditions

$$\zeta(x, 0) = \zeta_0(x), \quad S(x, 0) = S_b(x) \quad (8)$$

and boundary conditions

$$S(0, t) = S_0, \quad G(0, t) = G_0, \quad \frac{\partial \zeta(L, t)}{\partial x} = J, \quad H(L, t) = H_0, \quad (9)$$

where  $\zeta_0$ —the initial bed elevation,  $H_0$ —the flow depth at the output of the calculation area,  $G_0$ —the bed load transport rate incoming to the computational area,  $S_b$ —the initial averaged mass concentration of suspended load,  $S_0$ —the averaged mass concentration of suspended load incoming to the computational area,  $J$ —the mean bed slope and  $L$ —the computational area length.

### 3 Numerical Method

The reverse calculation method (Tanagoz 1964) is used to solve the stationary hydrodynamic Eq. (1); the method has the first order of accuracy. The Patankar's method (Patankar 1980) and explicit approximation scheme of time are used to solve Exner Eq. (2), which provides the second order of accuracy in space and the first order of accuracy in time. A regular space and time mesh is used for the calculation, where the space step is  $\Delta x$  and the time step is  $\Delta t$ . To obtain a stable solution of Eq. (2), the following condition is fulfilled (Fletcher 1988)

$$Cu = \frac{U\Delta t}{\Delta x} < 1, \quad (10)$$

where  $Cu$ —the Courant number.

The implicit running-count scheme (Belolipetcky and Genova 2004) is used to obtain the solution of the suspended transport Eq. (5); it has the first order of accuracy in space and time.

The problem solution is sequentially carried out on the mesh twice fined than the previous mesh until the following condition is fulfilled (Fletcher 1988)

$$\max_{i=0..N, n=0..T} \frac{[\zeta_i^n]_{old} - [\zeta_{2i}^n]_{new}}{[\zeta_i^n]_{old}} \leq 0.0001, \quad (11)$$

where  $[\zeta_i^n]_{old}$ —the value of  $\zeta$  at  $i$  node and  $n$  time layer of the mesh without fining (previous),  $[\zeta_{2i}^n]_{new}$ —the value of  $\zeta$  at  $2i$  node and  $n$  time layer of the mesh with fining (current).

Step by step algorithm of the problem (1)–(9) solving is performed in the paper (Potapov and Snigur 2014).

### 4 Application

In order to verify the model outlined above a number of model riverbed problems were solved:

1. The problem of bed degradation under the influence of the purified hydrodynamic flow (Newton 1951).
2. The problem of bed aggregation (Seal et al. 1995).
3. The problem of the trench evolution under the influence of the transit hydrodynamic flow (van Rijn 1986).

These test problems solving allows estimating the ability of the model to describe the bed degradation and aggregation processes adequately. Before solving each prob-

lem, it is necessary to estimate the contribution of suspended load to the bed forming process.

In accordance with the gravitational theory of suspended sediment transportation (Velikanov 1954), the distribution of suspended sediment concentration in flow depth  $H$  is

$$S = S_0 \left( \frac{a}{y} \right)^K, \quad K = \frac{W}{\kappa u_*} = \frac{1.4 \sqrt{(\rho_s - \rho_w)gd}}{\kappa \sqrt{\rho_w g H J}}, \quad (12)$$

where  $a \approx 2d$ —the depth of the bed active layer,  $u_*$ —the dynamic velocity,  $\kappa = 0.4$ ,  $a < y < H$ .

If the power coefficient  $K$  belongs to the range from 3 to 12 it indicates the fast decreasing of suspended sediment concentration in flow depth (Petrov and Petrov 2000). In this case the influence of suspended sediment may be neglected suggesting that when  $H \leq x < a$  the suspended sediment concentration  $S$  quickly reaches the value  $S_*$  due to its smallness. Hence, there is no need to solve the Eq. (5) containing the phenomenological parameters  $\alpha$  and  $\beta$ .

The power coefficient  $K$  varies within 7.9–9 for the problems of bed degradation under the influence of the purified hydrodynamic flow and it is equal to 10.19 and 10.81 for the bed aggregation problems. All the above-mentioned values of  $K \in (3, 12)$ , hence the suspended sediment transport may be neglected in these problems. However, the power coefficient  $K$  is equal to 0.01 for the trench evolution problem, so it is necessary to take into account the suspended sediment transport in this problem.

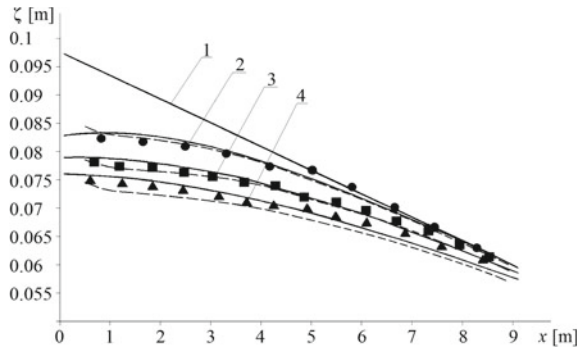
#### 4.1 The Problem of Bed Degradation Under the Influence of a Purified Hydrodynamic Flow

The solving of this kind of problems allows to estimate the ability of the model to describe the bed evolution when the bed degradation process is primary. The following parameters agreed with the parameters from the experimental paper (Newton 1951) are used for solving the problems of bed degradation under the influence of the purified hydrodynamic flow:  $d = 0.00069$  m,  $\varphi = 32^\circ$ ,  $c_x = 0.45$ ,  $\varepsilon = 0.375$ ,  $n_s = 0.015$ ,  $\rho_w = 1000$  kg m<sup>-3</sup>,  $\rho_s = 2650$  kg m<sup>-3</sup>,  $g = 9.8$  m s<sup>-2</sup>,  $\kappa = 0.4$ ,  $L = 9.14$  m,  $\zeta_0 = \zeta_b - Jx$ ,  $\zeta_b = 0.1$  m,  $S_b = 0$  kg m<sup>-2</sup>,  $G_0 = 0$  kg m<sup>-1</sup> s<sup>-1</sup>,  $S_0 = 0$  kg m<sup>-2</sup>. The values of  $U$ ,  $H_0$  and  $J$  for different problems are shown in Table 1. The space step of the calculation mesh is  $\Delta x = 0.11$  m, the time step of the calculation mesh  $\Delta t = 0.2$  s.

In Fig. 1 the predicted bed elevations (solid lines), measured bed elevations (Newton 1951) (point sets) and the bed elevations obtained by the model Singh (2002) (dotted lines) are shown. In Fig. 1 the line 1 indicates the initial bed elevation, the groups of lines 2, 3 and 4 indicate the bed elevations at time point 1, 2 and 3 h, respectively. The bed elevations obtained by the model Singh (2002) deviates from the measured bed elevations at the inlet of the computation area; here the relative

**Table 1** The parameters for the problem of bed degradation

Problem #/Parameter	$H_0$ (m)	$U$ ( $\text{m s}^{-1}$ )	$J$
Problem 1	0.0411	0.45	0.00416
Problem 2	0.0411	0.45	0.00416
Problem 3	0.0365	0.5	0.0061

**Fig. 1** The comparison between the measured and predicted bed elevations. Bed degradation problem 1

error in comparison with the measured bed elevations reaches 12%. The bed elevations predicted by the proposed model have a better agreement with the measured bed elevations; the maximum relative error does not exceed 9% in the whole calculation area.

In Figs. 2 and 3 the predicted bed elevations (solid lines), measured bed elevations (Newton 1951) (point sets) and the bed elevations obtained by the model CCHE1D Wu and Vieira (2002) (dotted lines) are shown. In Fig. 2 the line 1 indicates the initial bed elevation, the lines groups 2, 3 and 4 indicate the bed elevations at time point 1, 4 and 24 h, respectively. In Fig. 3 the line 1 indicates the initial bed elevation, the lines groups 2, 3, 4, 5 and 6 indicate the bed elevations at time point 1, 2.17, 4, 12 and 27 h, respectively. In Figs. 2 and 3 it can be seen that the maximum deviation of the obtained bed elevations from the measured ones at time point 1, 2.17 and 4 h does not exceed 5%. The model Wu and Vieira (2002) at the same observation times describes the bed elevations with less accuracy; its relative error reaches 18%. However, at longer observation time (12, 24 and 27 h) the predicted bed elevations deviate from the measured bed elevations larger than the bed elevations obtained by the model Wu and Vieira (2002). The slope of the predicted bed elevations is greater than the slope of the measured ones.

It should be noted that in the experiment (Newton 1951) the roughness varies from 0.016 at the inlet of the calculation area to 0.012 at the outlet of the calculation area, which indirectly indicates the formation of shortwave bed forms. In the proposed model the roughness assumes a constant value and is equal to 0.015 in all three problems. It can be the reason of the deviation of the predicted bed elevations from the measured bed elevations at long degradation.

**Fig. 2** The comparison between the measured and predicted bed elevations. Bed degradation problem 2

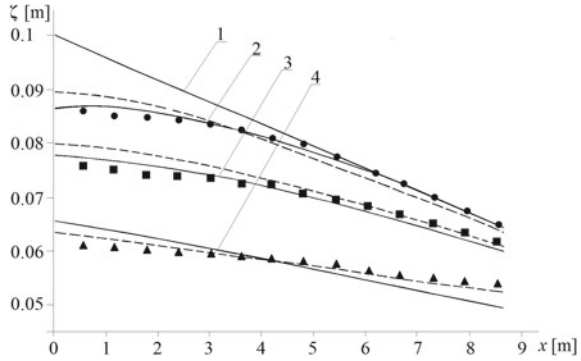
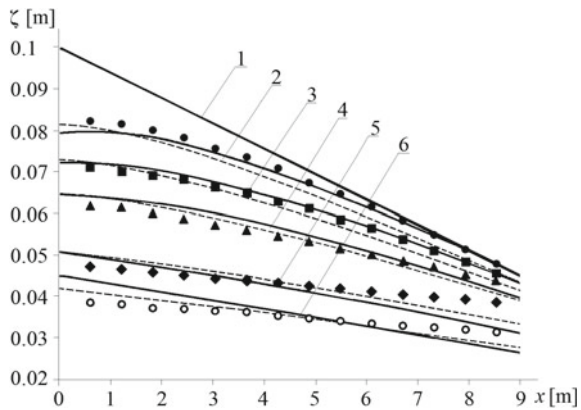


**Fig. 3** The comparison between the measured and predicted bed elevations. Bed degradation problem 3



In the model CCHE1D Wu and Vieira (2002) the roughness distribution is defined using the regression function. But the bed elevations obtained by the proposed model and the model Wu and Vieira (2002) are qualitatively the same and have the mean slope greater than the measured mean slope.

Nevertheless, in general the proposed model qualitatively and quantitatively describes the bed degradation process under the influence of the purified hydrodynamic flow. The predicted bed elevations have a good agreement with the measured ones; the mean relative error of the predicted data does not exceed 22% in all three problems.

**4.1.1 The Problem of Bed Aggregation**

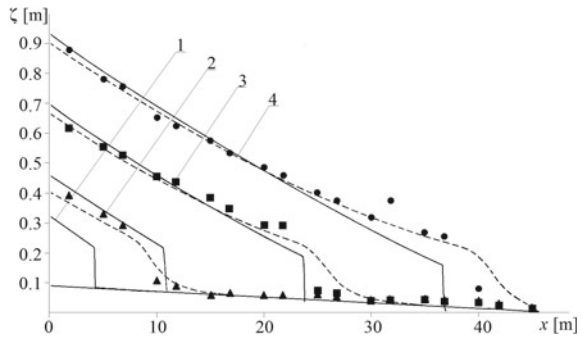
The solving of this kind of problems allows to estimate the ability of the model to describe the bed evolution when the bed aggregation process is primary.

The following parameters agreed with the parameters from the experimental paper (Seal et al. 1995) are used for solving the problems of the bed aggrega-

**Table 2** The parameters for the problem of bed aggregation

Problem # /Parameter	$H_0$ (m)	$U$ (m s <sup>-1</sup> )	$G_0$ (kg m <sup>-1</sup> s <sup>-1</sup> )
Problem 1	0.4	0.4	0.62
Problem 2	0.45	0.357	0.31

**Fig. 4** The comparison between the measured and predicted bed elevations. Bed aggregation problem 1



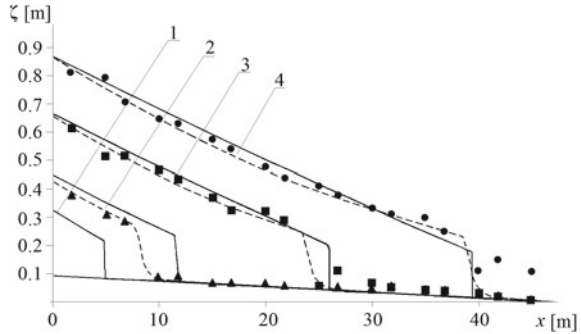
tion:  $\varphi = 47[^\circ]$ ,  $c_x = 0.15$ ,  $\varepsilon = 0.23$  (Wu and Vieira 2002),  $\rho_w = 1000 \text{ kg m}^{-3}$ ,  $\rho_s = 2650 \text{ kg m}^{-3}$ ,  $g = 9.8 \text{ m s}^{-2}$ ,  $\kappa = 0.4$ ,  $L = 45 \text{ m}$ ,  $S_b = 0 \text{ kg m}^{-2}$ ,  $S_0 = 0 \text{ kg m}^{-2}$ ;  $\zeta_0 = \zeta_k - J_k x$ ;  $\zeta_k = 0.33 \text{ m}$ ,  $J_k = 0.02$  when  $x \leq 5 \text{ m}$ ;  $\zeta_k = 5.58 \text{ m}$ ,  $J_k = 1.07$  when  $5 < x \leq 5.13 \text{ m}$ ;  $\zeta_k = 0.1 \text{ m}$ ,  $J_k = 0.002$  when  $x > 5.13 \text{ m}$ . In the experiment, the particle size varies from 0.125 to 64 mm. In the computations, the particle size is constant and equal to  $d = 4.63 \text{ mm}$  in both considered problems. The values of  $H_0$ ,  $U$  and  $G_0$  for problem 1 and 2 are shown in Table 2.

The space step of the calculation mesh is  $\Delta x = 0.12 \text{ m}$ , the time step of the calculation mesh is  $\Delta t = 0.2 \text{ s}$ .

In Fig. 4 the predicted bed elevations (solid lines), the measured bed elevations (Seal et al. 1995) (point sets) and the bed elevations obtained by the model Wu (2001) (dotted lines) are shown. In Fig. 4 the line 1 indicates the initial bed elevation, the groups of lines 2, 3 and 4 indicate the bed elevations at time point 2, 8 and 16.8 h, respectively. In Fig. 5 the predicted bed elevations (solid lines), measured bed elevations (Seal et al. 1995) (point sets) and the bed elevations obtained by the model Wu and Vieira (2002) (dotted lines) are shown. In Fig. 5 the line 1 indicates the initial bed elevation, the groups of lines 2, 3 and 4 indicate the bed elevations at time point 4, 16 and 32.4 h, respectively.

One can see in Figs. 4 and 5 that the predicted bed elevations have a good agreement with the measured bed elevations in spite of the assumption about constant particle size. The proposed mathematical model describes heights and celerities of the gravel deposit front well. The maximum deviation of the predicted bed elevations from the measured bed elevations is observed at the vertical front of the gravel deposit. At this area the measured gravel deposit profiles are smooth because the flow depth strongly increases here, which causes fine particles sedimentation. The proposed mathematical model assumes that gravel particles have the same size, hence

**Fig. 5** The comparison between the measured and predicted bed elevations. Bed aggregation problem 2



the predicted gravel deposit profiles are not smooth. The mean relative error of the data predicted by the proposed model is equal to 3% and 5% for the first and second problems, respectively.

The bed elevations obtained by the model CCHE1D Wu and Vieira (2002) and CCHE2D Wu (2001) are more smooth and describe better the locations, heights and celerities of the gravel deposit front. It should be noted that the mean relative error of the data obtained by the models Wu (2001); Wu and Vieira (2002) is equal to 2.3% and 2% for the problem 1 and 2, respectively; it is insignificantly less than the mean relative errors of the data predicted by the proposed model. Thus the proposed model and the models (Wu 2001; Wu and Vieira 2002) reproduce qualitatively the same results.

### 4.2 The Problem of the Trench Evolution Under the Influence of the Transit Hydrodynamic Flow

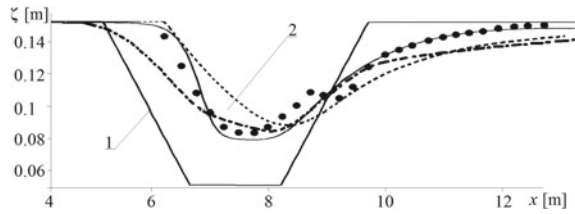
The solving of this kind of problems allows to estimate the ability of the model to describe the bed evolution when the bed degradation and bed aggregation processes are equivalent.

The problem of the trench evolution is solved by using the following parameters agreed with the parameters of the experimental paper (van Rijn 1986):  $d = 0.0001$  m,  $c_x = 0.4$ ,  $\varphi = 26[^\circ]$ ,  $\alpha = 0.25$ ,  $\varepsilon = 0.4$ ,  $\rho_w = 1000$  kg m<sup>-3</sup>,  $\rho_s = 2650$  kg m<sup>-3</sup>,  $g = 9.8$  m s<sup>-2</sup>,  $\kappa = 0.4$ ,  $L = 17$  m,  $J = 0.0002$ ,  $U = 0.18$  m s<sup>-1</sup>,  $H_0 = 0.255$  m,  $h = 0.125$  m—the trench depth,  $L_m = 4.5$  m—the trench length,  $L_c = 1.5$  m—the length of trench bottom part,  $W = 0.005$  m s<sup>-1</sup>,  $S_b = S_*$  kg m<sup>-2</sup>,  $G_0 = 0.0063$  kg m<sup>-1</sup> s<sup>-1</sup>,  $S_0 = 0.9213$  kg m<sup>-2</sup>. The space step of the calculation mesh is  $\Delta x = 0.57$  m, the time step of the calculation mesh is  $\Delta t = 2$  s.

In Fig. 6 the predicted bed elevations (solid line), the measured bed elevations (point set) (van Rijn 1986), the bed elevations obtained by the model Sanchez and Wu (2011) (dotted line) and model van Rijn (1986) (dashed-dotted line) are shown. In Fig. 6 the line 1 indicates the initial bed elevation, the lines group 2 indicates



**Fig. 6** The comparison between the measured and predicted bed elevations. Trench evolution problem



the bed elevations at 10 h. The comparison of the bed elevations in Fig. 6 shows that the models (Sanchez and Wu 2011; van Rijn 1986) underestimate the upstream bank migration and overestimate the downstream bank erosion; the relative error in these areas varies up to 15–30%. The predicted bed elevation has a good agreement with the measured one, the proposed model correctly describes the upstream bank migration, downstream bank erosion and trench depth and does not overestimate the erosion at the channel outlet area. The mean relative error of the obtained data does not exceed 5%, that is close to the systematic error of separate experimental measurements (van Rijn 1986).

## 5 Conclusion

At present there is a lot of riverbed models aimed at real riverbed computation. Such models explicitly or implicitly use different methods of averaging bed microforms influence in the sediment rate evaluation. These models are successfully used for engineer computations but are not right for the research of local-scale bed evolution, such as dunes development, local bed degradation behind the dam, siltation of water reservoir, ship channel evolution etc.

In the paper, a one-dimensional riverbed model for sand or sand-gravel plain rivers or channels is proposed. The model includes the analytical bed-load transport equation, suspended transport equation, Exner equation, hydrodynamic equations in shallow water approach.

The main benefit of the proposed model is the bed-load rate formula which is derived analytically from the equation of thin bed layer motion with the Coulomb's rheology for granular medium and the Prandtl's rheology for liquid medium (Petrov 1991). This formula does not contain the phenomenological parameters except the parameters of Coulomb-Prandtl model. It takes into account the influence of the bed shear stress, the local bed slope, granulometrical and physical-mechanical parameters of the bed material (particle porosity, diameter, internal friction angle etc.) on the bed-load transport. These features of bed-load rate formula make it unique for riverbed processes research.

A number of model riverbed problems were solved by using the proposed model to estimate the ability of the model to describe the local bed degradation and bed deposition processes adequately. The comparison of the predicted bed elevations

with the experimentally measured bed elevations was carried out. In spite of the relative simplicity of the proposed model, the predicted bed elevations have a good agreement with the measured ones in all considered problems. It was shown that the data obtained by the proposed model and by the models of other authors Sanchez and Wu (2011); Singh (2002); van Rijn (1986); Wu (2001); Wu and Vieira (2002) have almost the same accuracy; in problem of the trench evolution the proposed model provides a better accuracy. It can be concluded that the proposed model is applicable for describing local bed evolution during pipe building on the river bed, for bed degradation prediction behind the water drain of hydro-electrical power station and for prediction of water reservoirs siltation.

## References

- Belolipetcky VM, Genova CN (2004) The computational algorithm for the suspended and bed load dynamics determination in river channel. *Comput Technol* 2:9–25
- Exner FM (1925) *Über die Wechselwirkung zwischen Wasser und Geschiebe in Flüssen*. Sitzungsber. Akad. Wiss. Wien, Math.–Naturwiss. Kl. Abt. 2A. 134, 165–180
- Fletcher CAJ (1988) *Computational techniques for fluid dynamics 2*. Springer, Berlin
- Grishanin KV (1974) *River channels stability*. Gidrometeoizdat, Leningrad
- Karashev AV (1977) *Theory and calculation methods of river sediment*. Gidrometeoizdat, Leningrad
- Kartvelishvili NA (1973) *Streams in non-deformable beds*. Gidrometeoizdat, Leningrad
- Newton CT (1951) *An experimental investigation of bed degradation in an open channel*. *Transc Boston Soc Civ Eng*, 28–60
- Patankar SV (1980) *Numerical heat transfer and fluid flow*. Hemisphere Publishing Corporation, New York
- Petrov AG, Petrov PG (2000) Sediment-discharge vector in a turbulent flow above an eroded bottom. *J Appl Mech Tech Phys*. <https://doi.org/10.1007/BF02465272>
- Petrov PG (1991) Motion of a bed load. *J Appl Mech Tech Phys*. <https://doi.org/10.1007/BF00851941>
- Potapov II, Snigur KS (2011) The ground deformations analysis of the inoherent bottom of the channel in lower hydrosite bief. *Comput Technol* 4:114–119
- Potapov II, Snigur KS (2014) The evolution of a cross-channel trench under the influence of the transit hydrodynamic flow. *The Bulletin of Udmurt University. Math Mech Comput Sci* 2:146–152
- Sanchez A, Wu W (2011) A non-equilibrium sediment transport model for coastal inlets and navigation channels. In: Roberts TM, Rosati JD, Wang P (eds) *Proceedings, Symposium to Honor Dr. Kraus NC*, pp 39–48. West Palm Beach, FL. Coastal Education and Research Foundation
- Seal R, Parker G, Paola C, Mullenbach B (1995) *Laboratory experiments on downstream fining of gravel, narrow channels runs 1 through 3: supplemental methods and data*. In: External memorandum M-239, St. Anthony Falls Hydraulic Lab, University of Minnesota
- Singh V (2022) *Two dimensional sediment transport model using parallel computers*. In: *Civil and environmental engineering (2002)* Available via DIALOG. [http://etd.lsu.edu/docs/available/etd-03312005-193516/unrestricted/Singh\\_thesis.pdf](http://etd.lsu.edu/docs/available/etd-03312005-193516/unrestricted/Singh_thesis.pdf). Cited 01 Nov 2016
- Tanagoz IS (1964) *Analitical method of nonsteady water motion calculation in hydroelectric power station downstream*. In: *Leningradproject proceedings*. Leningrad, 1964, pp 23–27
- van Rijn LC (1986) *Sedimentation of dredged channels by currents and waves*. *J. Waterw Port Coast Ocean Eng* 112:541–559

- Velikanov MA (1954) Gravitational theory of sediment transport. *J Sci Sov Union Geophys* 4:349–359
- Wu W (2001) CCHE2D sediment transport model—technical report # NCCHE-TR-2001-3. In: National center for computational hydroscience and engineering. The University of Mississippi, p 45
- Wu W, Vieira DA (2002) One-dimensional channel network model CCHE1D 3.0—technical report # NCCHE-TR-2002-1. In: National center for computational hydroscience and engineering. The university of Mississippi, p 122

# Numerical Modeling of Flow Dynamics on a Gravel Bar During High Discharge in a Mountain River

Andrzej Strużyński, Dorota Gariat, Ludivine Bouchet,  
Maciej Wyřębek and Krzysztof Kulesza

**Abstract** Numerical modeling of changing parameters on a gravel bar during different discharges in a small mountain river is presented here. The study bar is one of the best developed bars of the upper Wisłoka. Within its reach, the river may erode its banks and transport bed material. Flowing out from the Magurski National Park, the Wisłoka may be assumed as being close to a natural river. As fluvial processes are very dynamic there, the bar and channel transformations occur every year. Granulometry measurements demonstrated high variation of bed material composition in different parts of the bar and the channel. The bed material was classified as fine gravel, coarse gravel, cobbles, and coarse sand. This simulation was performed based on a 2015 measurement campaign; however, in situ measurements were started in 2008. From among a wide spectrum of parameters yielded by numerical simulations, the study focused on average vertical velocity and bed shear stresses. They were compared to critical parameters of the bed material movement. The simulations were performed for different flows, from low

---

A. Strużyński (✉) · M. Wyřębek  
Department of Hydraulic Engineering and Geotechnics,  
University of Agriculture in Kraków, Mickiewicza Ave. 24/28,  
30-059 Kraków, Poland  
e-mail: rmstruzy@cyf-kr.edu.pl

M. Wyřębek  
e-mail: m.wyrebek@gmail.com

D. Gariat  
Department of Geomorphology, Faculty of Geography and Regional Studies,  
University of Warsaw, Krakowskie Przedmieřcie 30, 00-927 Warsaw, Poland  
e-mail: dagariat@uw.edu.pl

L. Bouchet  
University of Strassbourg, Strassbourg, France  
e-mail: ludivine.bouchet@live.fr

K. Kulesza  
Board of Water-Management Systems, Institute of Meteorology and Water,  
Management - National Research Institute, PiotraBorowego 14, 30-215 Kraków, Poland  
e-mail: Krzysztof.Kulesza@imgw.pl

discharges to bankfull ones, and they indicated potential dynamic changes in the bed activity.

## 1 Introduction

Gravel-bed rivers have several features that differentiate them from sand-bed rivers. Their channel bed and banks are composed usually of non-cohesive material. The width/depth ratio is higher because gravel-bed channels are wider and shallower than the sand-bed ones, and bedload transport is responsible for channel changes (Leopold 1992). Gravel bars (mid-channel, transverse or side-bar, with or without vegetation and of different particle size) are common and important feature of this type of rivers (Rice et al. 2009). A structure and formation of the bars may provide information on sediment discharge activity at the reach scale (Parker and Klingeman 1982; Buffington 2012). The sediment transport is usually not measured directly in the gravel-bed rivers as it may be a dangerous, complicated and expensive task. Instead, indirect or morphological strategies are used (e.g. Gray et al. 2010; Mathias Kondolf and Lisle 2016). An alternative for assessing sediment dynamics in a gravel-bed river is the use of numerical models. There are three types of models available: one-dimensional for the analysis of water depth, longitudinal flow velocities and shear stresses over tens of kilometers; two-dimensional for the analysis of specific morphological units; and three-dimensional for the analysis of specific sites, such as bridges or embankments. These models are based on the Saint-Venant equations or the Reynold's equation. Recently, thanks to the development of data acquisition technology, numerical terrain modeling and GIS software, modeling of channel evolution and sediment transport have been the focus of many studies (Kaless et al. 2015; Mrokowska et al. 2016; Strużyński et al. 2013; Zhiwei et al. 2014). Computer simulations of river flow conditions are widely used in engineering and restoration programs to assess a potential impact of different river management strategies (Habersack and Piégay 2006; Formann et al. 2007). However, accumulation features such as gravel-bars, are still modeling challenges (Nagata et al. 2000; Jang and Shimizu 2005; Garcia-Martinez et al. 2006; Li and Millar 2007; Strużyński et al. 2011; Tritthart and Gutknecht 2007a, b; Tritthart et al. 2009; Tritthart et al. 2011a, b).

This paper focuses on a simulation of flow conditions over a typical gravel bar located in the upper Wisłoka, in the Polish Carpathians (Low Beskids). Over the last few years, major changes in the channel and increased bar accretion were observed in many sites along the upper Wisłoka course. A possible cause of these changes is a combination of intense afforestation (an increase in forest cover by about 40%) started in 1947 as a result of the region depopulation, an increase in flood frequency (from 0.7 to 2.2 per year), and episodic inputs of sediment generated by bank erosion, landslides, river regulation and gravel-bed mining. Since 2005, intensity of these processes has increased. Locally, significant channel bar accretion was noticed following the floods in May and June 2005, March 2007, June 2009, July 2010 and 2011, and May 2015.

The aim of this study was to use a 2D model to simulate water flow velocity and shear stresses over the surface of a diagonal, side gravel bar, so as to interpret current channel changes and to outline hydrodynamic reference condition. A specific research objective was to determine when the gravel bed was active, and therefore when the channel reorganization may occur. Flow variables were related to channel-shaping processes based on the magnitude of shear stresses acting on the bed at different flows (Dietrich et al. 1989; Buffington and Montgomery 1999; Monteith and Pender 2005; Hassan et al. 2006). Therefore, identification of flow thresholds by computing the range of discharges at which certain channel features are likely to be mobile could be a key issue in a description of the gravel bed reference conditions.

The simulation was performed for specific flow conditions, ranging from 3 to 149 m<sup>3</sup> s<sup>-1</sup>, as per the data provided by the Institute of Meteorology and Water Management—National Research Institute for Krempana-Kotań gauge station. The model presented in this paper was developed with CCHE2D pack software, created and designed by NCCHE (National Center for Computational Hydroscience and Engineering) of the University of Mississippi School in Engineering (Zhang 2006).

## 2 Study Site

The study area is located in the upper Wisłoka river valley, in the Low Beskids, south-eastern part of Poland (Fig. 1). The relief of the area is dominated by flattened and dome-shaped ridges elevated at 700–850 m a.s.l., separated by river valleys located at about 400 m a.s.l. This landscape is typical for the Low Beskids.

The upper Wisłoka channel is diversified and strongly depends on the valley lithology. In the ravine sections, the channel is straight, while in the valleys the

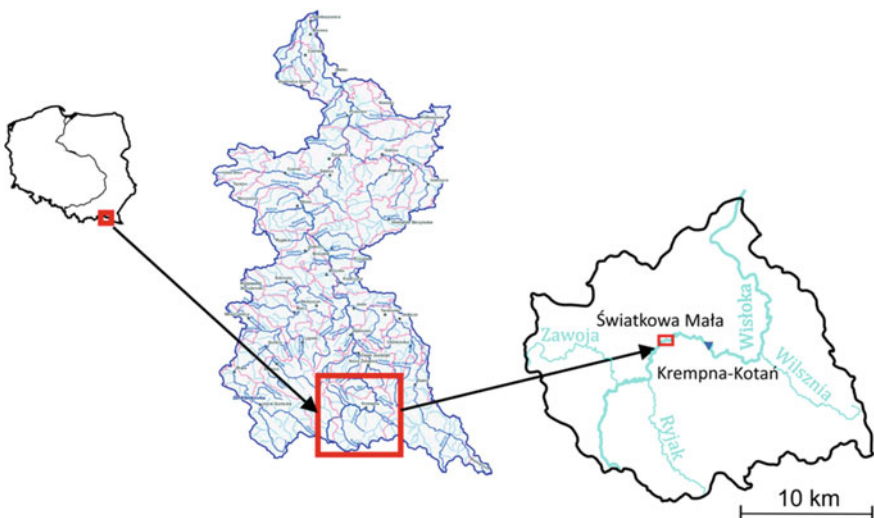
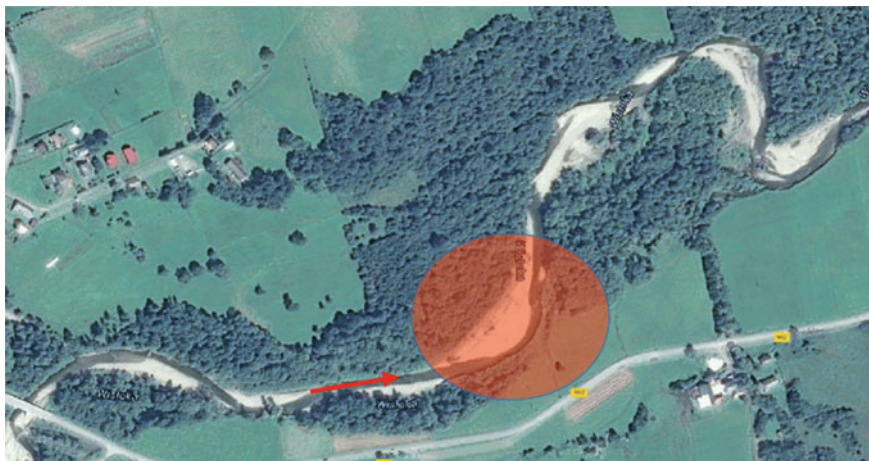


Fig. 1 Location of the study site in the Wisłoka basin, Poland



**Fig. 2** The study area (the arrow shows water flow direction)

river is winding or meandering, and in some reaches braided. The gauging station Krempana is located 5 km downstream of the study reach. The last flood occurred on 14 May 2014 and it considerably changed the channel morphology.

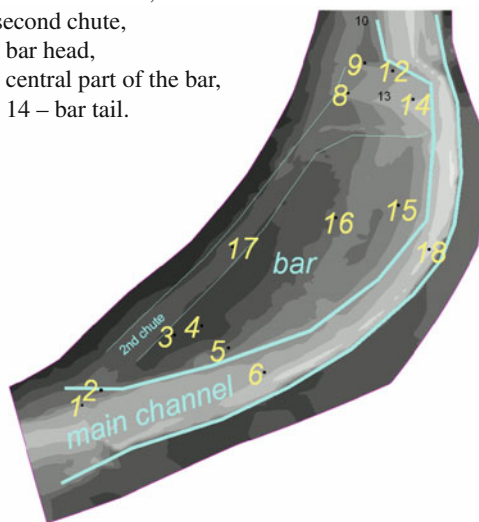
The investigated gravel bar is located in ŚwiątkowaMała village, about 15.5 km from the river spring (Fig. 2). The measured channel section spans between two right tributaries of the Wisłoka, Świerzówka and Rzeszówka. The subbasin area of 139 km<sup>2</sup> is in almost 70% covered by forest. ŚwiątkowaMała is located on the border of the Magurski National Park. The main channel of the Wisłoka is cut into an alluvial terrace (up to about 350–400 m wide). The study was conducted within a 400 m long section of the channel. The channel gradient in this reach equals 3.7%. Water depth during the measurements was from 0.15 to 1 m at different locations.

Field measurements were performed on the surface of the left bank-attached compound gravel bar. The bar is one of the largest side-bars in this river reach. It is 170 m long and almost 50 m wide. In its highest point, the bar is elevated about 1.6 m over the low-flow channel. During low flow conditions, the depositional morphology of the studied gravel bar is complex. Proximal part of the bar is connected with the riffle. There are several secondary forms on the bar surface: gravel sheets, local scours behind large woody debris, and chutes.

Particle size distribution ranges from the finest grains near the channel to the largest ones on the top of the bar. Some areas behind obstacles, particularly downstream of the fallen trees but also in the bar tail are covered by sand. The bar has two characteristic parts, the one near the low-flow channel that is frequently flooded and the higher part flooded only during bank-full flows. The bar is partly covered by plants, mostly annual flower weeds with a few young trees. The bar surface harbors some woody debris accumulated during recent floods. During in-channel water rise events, the bar surface is usually emerged and water flows through the chutes. Only bank-full and overbank flows may completely cover the

**Fig. 3** Localization of measured samples of bed material and numerical modeling monitoring points

- 1, 6, 18 – main channel,
- 2, 17 – second chute,
- 3, 4, 5 – bar head,
- 15, 16 – central part of the bar,
- 8, 9, 12, 14 – bar tail.



bar and model the entire macroform. The analyzed points (Fig. 3) were classified into the following groups.

### 3 Materials and Methods

#### 3.1 Topographic Data

Elevation measurements with a GPS-RTK receiver were performed in the spring of 2015 (Fig. 4). Bathymetry data were collected in cross-sections every 6–10 m. Cross-section step was about 40 cm. About 2000 points were measured within the entire study area (low-flow channel, bar and the river banks). Vertical and horizontal accuracy of the measurements ranged from 1.3 to 3.0 cm. Other measurement errors due to improper holding of the gauge were negligible when compared with the size of the bed material and measured slopes.

#### 3.2 Granulometry Data

The bar granulometry was determined by aerial photographs of  $0.5 \times 0.5$  m sample and direct measurements of the same area. The photographs were taken at random at 16 locations and then five samples were collected by hand (direct measurements) by measuring a, b, and c axes of 100 particles from the surface layer



**Fig. 4** Visualization of cross-sections surveyed in June 2015



of the river bed (Fig. 3). These axes were measured manually with a millimeter precise ruler and the weight of each particle was recorded. The particles immeasurable by hand were weighted in a laboratory. Each sample was localized with a GPS receiver.

Bed surface granulometry was assessed at 16 locations of the gravel bar alone (Table 1). The locations were then used during modeling as monitoring points.

Shear stresses  $\tau_0$  were calculated from the equation presented below (Shields 1936):

$$\tau^* = \frac{\tau_0}{(\rho_s - \rho)gd} \quad (1)$$

where:  $\tau^* = \tau_{cr}$ —applied Shields stresses,  $\rho$ —water density,  $\rho_s$ —sediment density,  $g$ —specific gravity and  $d$ —grain diameter.

Presented Shields stresses values were calculated using formulas proposed by Bartnik and Michalik on the basis of radio tracer measurements of incipient motion performed in Polish Carpathian rivers (Bartnik 1992). Location 10 (low-flow channel downstream of the bar, below location 9) was covered with coarse sand ( $\tau_{cr} = 16.2 \text{ N m}^{-2}$ ) (Fig. 3), and locations 8 and 12 with fine gravel ( $\tau_{cr}$  from 19.4 to 20.2  $\text{N m}^{-2}$ ). Locations 4, 6, 9, and 14 were covered with coarse gravel ( $\tau_{cr}$  from 26.1 to 29.9  $\text{N m}^{-2}$ ) and sites 1, 2, 3, 5, 11, 13, 15, 16, and 17 featured cobbles ( $\tau_{cr}$  from 32.0 to 36.5  $\text{N m}^{-2}$ ).

**Table 1** Bedload median diameter ( $d_{50}$ ) for selected samples

Sample N°	$d_{50}$ [m]
1	0.086
2	0.071
3	0.083
4	0.019
5	0.092
6	0.041
8	0.003
9	0.036
12	0.005
14	0.041
15	0.099
16	0.108
17	0.085
18	0.070

### 3.3 Model Methodology

Modeling was performed using CCHE software designed by National Center for Computational Hydroscience and Engineering (NCCHE), University of Mississippi, School of Engineering (Zhang and Jia 2009). A MESH file was created using CCHE-MESH software in which the DTM (.geo file) was generated. I and J line numbers were 70 and 200, respectively, and resulted in a cell size of average dimensions  $0.7 \times 0.85$  m. Then, the data such as initial water level, roughness and boundary conditions were determined and put into the model. Bank roughness was determined by reading the Manning table (Chow 1959), bed roughness was calculated from Cowan’s formula (Arcement and Schneider 1989), and Manning’s values used were 0.045 and 0.032, respectively. Inlet boundary condition was chosen as total water discharge without sediment discharge. Outlet boundary condition (water level) was calculated for all discharges with “Konsum” software (including the Chezy-Manning formula). Simulations were run for six different discharges (semi-steady flow conditions): 3, 30, 45, 79, 110 and  $149 \text{ m}^3 \text{ s}^{-1}$  during one hour with time step of 0.2 s.

## 4 Results

Modeling results were analyzed in two stages. The first stage concerned flow velocity and the second involved energy spread analysis. For the smallest discharges ( $3$  and  $30 \text{ m}^3 \text{ s}^{-1}$ ), water flowed only through the main channel. From a discharge of  $45 \text{ m}^3 \text{ s}^{-1}$ , water started flowing also on the left side of the bar (Fig. 5). The bar itself was submerged from  $79 \text{ m}^3 \text{ s}^{-1}$  flow. Unexpected results are

presented in Fig. 6. Maximum velocity and bed shear stresses were not directly related to water depth. Two-dimensional modeling indicated a prevailing influence of the shape of the Wisłoka cross-sections as well as the channel curvature on the spatial pattern of these parameters.

Flow direction in the main channel and over the bar was concurrent with the main flow direction, with exceptions only in the shallow-water flow zones on the bar. A rise in the discharge was accompanied by growing velocity at all monitoring points and the same was observed for bed shear stresses with the exception of points 6, 9 and 18. Dynamics of these parameters differed among particular locations, so the main erosion and transportation zones varied with changing discharges. For the maximum modeled discharge, flow velocity reached a maximum value of  $3.29 \text{ m s}^{-1}$  in location 5. Bed shear stresses achieved its maximum of  $107.2 \text{ N m}^{-2}$  within the same region. The highest values of the modeled parameters achieved at different discharges are indicated in Table 2.

For the smallest flows, the highest velocity and bed shear stresses values occurred in the main channel (points 18 and 6), but at higher discharges the biggest scour was observed in the upstream-right part of the bar (point 5).

When new parts of the bar were submerged at a higher discharge, new flow conditions appeared. The parameters shown in Fig. 7 indicated different trends for different monitoring points. In points 1, 2, 3 and 8 the parameters grew steadily. Shear stresses in points 13, 12, 14, 17 grew as well but with variable dynamics.

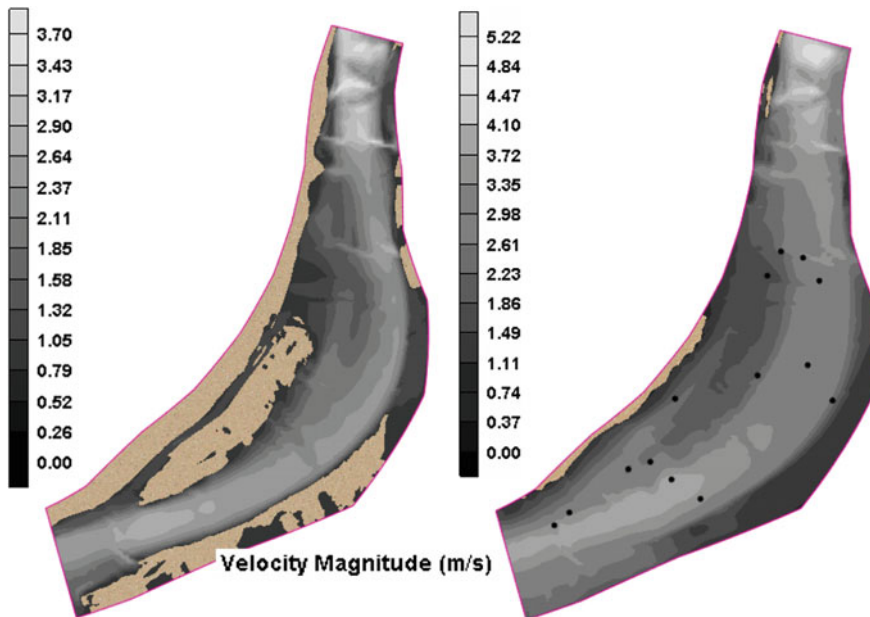


**Fig. 5** Exemplary model of a spatial pattern of flow velocity at water discharge of  $45 \text{ m}^3 \text{ s}^{-1}$  (left) and  $145 \text{ m}^3 \text{ s}^{-1}$  (right)

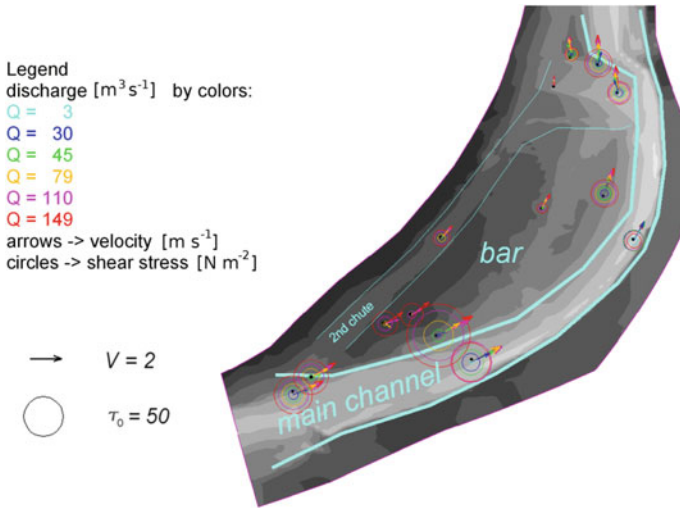


**Fig. 6** Visualization of modeling results—velocity and bed shear stresses (velocities are represented by vectors and bed shear stresses by circles)

**Table 2** Maximum values of flow velocity and bed shear stresses with their locations

Discharge [ $\text{m}^3 \text{s}^{-1}$ ]	Point/Value					
	3	30	45	79	110	149
max $V$ [ $\text{m s}^{-1}$ ]	18/0.95	18/1.81	6/2.16	6/2.73	6/2.88	5/3.29
max $\tau_0$ [ $\text{N m}^{-2}$ ]	18/13.5	6/30.3	6/43.6	6/65.3	5/85.2	5/107.2

In points 6 and 18 (main channel), it reached its maximum for the discharge of  $110 \text{ m}^3 \text{ s}^{-1}$ . The dynamics of shear stresses in points 6, 18, 16, and 9 was even more complex.

## 5 Discussion

Although a vast amount of research has been aimed at understanding gravel bed-related processes, the relationship between controlling variables (such as changes in flow dynamics) and gravel bed river morphology is not well recognized yet. The main scope of this study was to interpret contemporary channel changes and to outline hydrodynamic reference conditions in the river gravel bed with the use of a 2D model.

Whereas previous studies focused on gravel beds with sparse data sets, often with a nearly uniform channel form and limited topography data (i.e. Legleiter et al. 2011),

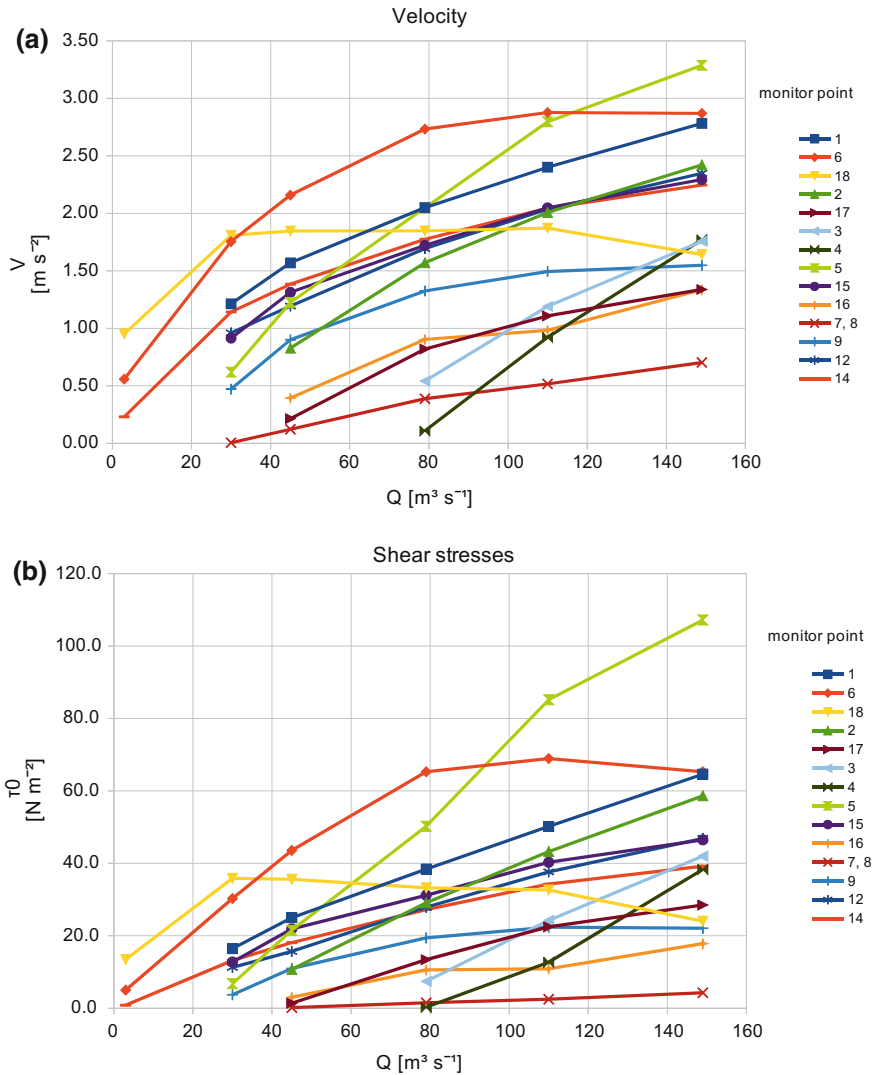


Fig. 7 Values yielded by 2D-modeling; a velocity, b shear stresses

we used high-resolution LIDAR data, and surface material analysis to model the flow conditions.

The modeled velocity and shear stresses indicated a strong influence of the bar shape on the distribution of flow in the Wisłoka during floods. Currently, due to considerable widening of the channel during floods, the main channel is shifted to the left, towards the bar (the area around points 5–15). This area is ended near point 14 and could be responsible for a strong increase of bed shear stresses and velocity

in point 5. This indicated that flood-induced erosion could be the most intensive near point 5. Transport ability in the main channel was stabilized after the discharge of  $79 \text{ m}^3 \text{ s}^{-1}$  was attained (values below  $70 \text{ N m}^{-2}$ ). The coarse material measured in points 5, 15 and 16 indicated that intensive erosion appeared quickly but also rapidly disappeared so fine particles did not cover the bar surface in this region.

The finest bed material was found in the bar tail, mostly downstream of smaller overflow channels. Relatively fine material was also found in the upper part of the bar and in the main channel. Coarse material was found mostly in the upper part of the investigated area in the channel but also in the upper part of the bar. The biggest cobbles were located in point 5 but also in the central part of the bar (locations 15 and 16). Exceptionally fine grained material accumulated in point 4 settled behind tree branches disturbing the flow.

The most suitable conditions for bed material transport occurred in the main channel up to the discharge of  $79 \text{ m}^3 \text{ s}^{-1}$ . At higher discharges, the overflow channel between points 5 and 14 was activated and had a steeper slope than the main channel. These conditions affected the highest values of bed shear stresses there. In the main overflow channel (extending from point 2 to 17 and to 8) average values of bed shear stresses were perceived. This overflow channel was located too high to participate in the transport of significant amount of the flow. Relatively high values of shear stresses were reported for the downstream part of the bar (points 12 and 14) where right bank has been stabilized by tree. Local intensive fluvial processes in the bar tail created elongated erosion regions filled with fine material in the last phase of the wave pass (points 8 and 12).

Fluvial processes in the right bank regions (main channel during low flows) seemed stable. The forces appearing during bank-full flows spread over the bar, so the most intensive fluvial processes focused on the bar itself and not on the opposite bank. It may be concluded that the process of developing a meander or river wandering were slowed down or even completely stopped in this region.

These results are consistent with previous research findings that topography has the greatest influence on flow characteristics and that high resolution DEM surfaces are required for predicting flow properties accurately with 2D hydraulic modeling (Horritt and Bates 2001; Pasternack et al. 2006). The research has pointed out the relation between flood magnitude and channel changes (especially bed material re-mobilization, accumulation), and stressed the role of possible static armor layer, and pebble clusters in channel bar development. In general, a higher magnitude of flooding corresponds to a more intense active channel modification (Surian and Cisotto 2007); nevertheless, at a certain discharge, the flow conditions are stabilized.

## 6 Conclusions

The modeling results were consistent with field observations. The proximal part of the bar underwent the most intensive transformations. The largest simulated flow velocity achieved in this bar section was  $3.29 \text{ m s}^{-1}$  and the shear stresses reached

107.2 N m<sup>-2</sup>. In the main channel, during the discharge of 79 m<sup>3</sup> s<sup>-1</sup>, the sediment transport was fixed (shear stresses value below 70 N m<sup>-2</sup>). In the central part of the gravel bar, shear stresses and velocity values were lower; however, in the distal part of the bar, the values of the analyzed hydraulic parameters slightly increased.

Erosion of the right concave bank decreased during bank-full flows due to rapidly increasing width of the river channel and the backwater generated within the region of points 12 and 14. During floods, the main current shifts towards the bar. The flowing water sculpts the shape of the downstream section of the bar and improves the capacity of its profile.

The discussed modeling confirmed a tendency to frequent and significant morphodynamic changes in this section of the upper Wisłoka. The use of CCHE2D software provided new possibilities for the spatial data analysis, and enabled recognition of the relationships between the morphology of the gravel bar, its grain size characteristics, and water flow conditions.

**Acknowledgements** The research was funded by Polish National Science Centre, Project No. NN 306 402738. Measurements performed in 2015 were financed by the Department of Water Engineering and Geotechnics, University of Agriculture in Kraków. Grant No. DS 3322/2015.

## References

- Arcement GJ, Schneider VR (1989) Guide for selecting Manning's roughness coefficients for natural channels and flood plains. US Geological Survey Water-Supply Paper, 2339 pp
- Bartnik W (1992) *Hydraulika potoków i rzek górskich z dnem ruchomym-Początek ruchu rumowiska wlezonego* [Fluvial hydraulics of streams and mountain rivers within mobile bed beginning of bed load motion] Zeszyty Naukowe Akademii Rolniczej w Krakowie Kraków, 122 pp
- Buffington JM, Montgomery DR (1999) Effects of hydraulic roughness on surface textures of gravel-bed rivers. *Water Resour Res* 35(11):3523–3530. <https://doi.org/10.1029/1999WR900138>
- Buffington JM (2012) Changes in channel morphology over human time scales. In Church M, Biron PM, Roy AG (eds) *Gravel-Bed Rivers: processes, tools, environments* John Wiley & Sons, Ltd, Chichester, UK. <https://doi.org/10.1002/9781119952497.ch32>
- Chang-Lae J, Yasuyuki S (2005) Numerical simulation of relatively wide, shallow channels with erodible banks. *J Hydraul Eng* 131(7):565–575. [https://doi.org/10.1061/\(ASCE\)0733-9429](https://doi.org/10.1061/(ASCE)0733-9429)
- Chow VT (1959) *Open-channel hydraulics*. McGraw-Hill, New York, p 680. <http://heidarpour.iut.ac.ir/sites/heidarpour.iut.ac.ir/files/u32/open-chow.pdf>
- Dietrich WE, Kirchner JW, Ikeda H, Iseya F (1989) Sediment supply and the development of the coarse surface layer in gravelbedded rivers. *Nature* 340:215–217
- Formann E, Habersack HM, Schober ST (2007) Morphodynamic river processes and techniques for assessment of channel evolution in Alpine gravel bed rivers. *Geomorphology* 90:340–355. <https://doi.org/10.1016/j.geomorph.2006.10.029>
- Garcia-Martinez R, Espinoza R, Valera E, Gonzalez G (2006) An explicit two-dimensional finite element model to simulate short- and long-term bed evolution in alluvial rivers. *J Hydraul Res* 44:755–766. <https://doi.org/10.1080/00221686.2006.9521726>
- Gray JR, Laronne JB, Marr JDG (2010) *Bedload-surrogate monitoring technologies*. US Geological Survey Scientific Investigations Report 2010–5091, 37 pp
- Habersack H, Piégay H (2006) River restoration in the Alps and their surroundings: past experience and future challenges. In: Habersack H, Piégay H, Rinaldi M (eds) *Gravel-bed*

- rivers VI: From processes understanding to river restoration. Elsevier, Amsterdam, London. [https://doi.org/10.1016/S0928-2025\(07\)11161-5](https://doi.org/10.1016/S0928-2025(07)11161-5)
- Hassan MA, Egozi R, Parker G (2006) Experiments on the effects of hydrograph characteristics on vertical grain sorting in gravel bed rivers. *Water Resour Res* 42(9):W09408. <https://doi.org/10.1029/2005WR004707>
- Horritt MS, Bates PD (2001) Effects of spatial resolution on a raster based model of flood flow. *J Hydrol* 253:239–249. [https://doi.org/10.1016/S0022-1694\(01\)00490-5](https://doi.org/10.1016/S0022-1694(01)00490-5)
- Kaless G, Mao L, Moretto J, Picco L, Lenzi MA (2015) The response of a gravel-bed river planform configuration to flow variations and bed reworking: a modelling study. *Hydrol Process* 29:3812–3828. <https://doi.org/10.1002/hyp.10504>
- Legleiter CJ, Kyriakidis PC, McDonald RR, Nelson JM (2011) Effects of uncertain topographic input data on two-dimensional flow modeling in a gravel-bed river. *Water Resour Res* 47:n/a–n/a. <https://doi.org/10.1029/2010WR009618>
- Leopold LB (1992) Sediment size that determines channel morphology. In: Billi P, Hey RD, Thorne CR, Tacconi P (eds) *Dynamics of gravel-bed rivers*. Wiley, Chichester, pp 297–311
- Li SS, Millar RG (2007) Simulating bed-load transport in a complex gravel-bed river. *J Hydraul Eng* 133:323–328. [https://doi.org/10.1061/\(ASCE\)0733-9429\(2007\)133:3\(323\)](https://doi.org/10.1061/(ASCE)0733-9429(2007)133:3(323))
- Mathias Kondolf G, Lisle TE (2016) Measuring bed sediment. In: *Tools in fluvial geomorphology*. Wiley Ltd, Chichester, UK, pp 278–305. <https://doi.org/10.1002/9781118648551.ch13>
- Monteith H, Pender G (2005) Flume investigations into the influence of shear stress history on a graded sediment bed. *Water Resour Res* 41:W12401. <https://doi.org/10.1029/2005WR004297>
- Mrokowska M, Rowiński P, Książek L, Strużyński A, Wyrębek M, Radecki-Pawlik A (2016) Flume experiments on gravel bed load transport in unsteady flow—preliminary results. In: Rowiński P, Marion A (eds) *Hydrodynamic and mass transport at freshwater aquatic interfaces*. GeoPlanet, earth and planetary sciences. 34th international school of hydraulics. Springer, Heidelberg, pp 221–233. <https://doi.org/10.1007/978-3-319-27750-9>
- Nagata N, Hosoda T, Muramoto Y (2000) Numerical analysis of river channel processes with bank erosion. *J Hydraul Eng* 126:243–252. [https://doi.org/10.1061/\(ASCE\)0733-9429\(2000\)126:4\(243\)](https://doi.org/10.1061/(ASCE)0733-9429(2000)126:4(243))
- Parker G, Klingeman PC (1982) On why gravel bed rivers are paved. *Water Resour Res* 18(5):1409–1423. <https://doi.org/10.1029/WR018i005p01409>
- Pasternack GB, Gilbert AT, Wheaton JM, Buckland EM (2006) Error propagation for velocity and shear stress prediction using 2D models for environmental management. *J Hydrol* 328:227–241. <https://doi.org/10.1016/j.jhydrol.2005.12.003>
- Rice SP, Church M, Wooldridge CL, Hickin EJ (2009) Morphology and evolution of bars in a wandering gravel-bed river; lower Fraser river, British Columbia, Canada. *Sedimentology* 56:709–736. <https://doi.org/10.1111/j.1365-3091.2008.00994.x>
- Shields A (1936) Anwendung der Aehnlichkeitsmechanik und der Turbulenzforschung auf die Geschiebe-bewegung, Mitteilungen der Preussischen Versuchsanstalt für Nassexbau und Schiffbau, Berlin
- Surian N, Cisotto A (2007) Channel adjustments, bedload transport and sediment sources in a gravel-bed river, Brenta River, Italy. *Earth Surf Process Landforms* 32:1641–1656. <https://doi.org/10.1002/esp.1591>
- Strużyński A, Kulesza K, Strutyński M (2013) Bed stability as a parameter describing the hydromorphological balance of a mountain river. In: Rowinski R (ed) *Experimental and computational solutions of hydraulic problems*. GeoPlanet: earth and planetary sciences. Springer, Heidelberg, pp 249–251. [https://doi.org/10.1007/978-3-642-30209-1\\_17](https://doi.org/10.1007/978-3-642-30209-1_17)
- Strużyński A, Wyrębek M, Strutyński M, Kulesza K (2011) Cross-section changes in the lower part of a mountain river after the flood in spring 2010, as presented by means of CCHE2D program. In: *Experimental methods in hydraulic research*, GeoPlanet: Earth and Planetary Sciences, vol 1, pp 287–297. [https://doi.org/10.1007/978-3-642-17475-9\\_21](https://doi.org/10.1007/978-3-642-17475-9_21)
- Trithart M, Gutknecht D (2007a) Three-dimensional simulation of free-surface flows using polyhedral finite volumes. *Eng Appl Comput Fluid Mech* 1:1–14. <https://doi.org/10.1080/19942060.2007.11015177>



- Tritthart M, Gutknecht D (2007b) 3D computation of flood processes in sharp river bends. *Water Manag* 160:233–247. <https://doi.org/10.1680/wama.2007.160.4.233>
- Tritthart M, Liedermann M, Habersack H (2009) Modelling spatiotemporal flow characteristics in groyne fields. *River Res Appl* 25:62–81. <https://doi.org/10.1002/rra.1169>
- Tritthart M, Liedermann M, Schober B, Habersack H (2011a) Nonuniformity and layering in sediment transport modelling 2: river application. *J Hydraul Res* 49(3):335–344. <https://doi.org/10.1080/00221686.2011.583528>
- Tritthart M, Schober B, Habersack H (2011b) Non-uniformity and layering in sediment transport modelling 1: flume simulations. *J Hydraul Res* 49(3):325–334. <https://doi.org/10.1080/00221686.2011.583528>
- Zhang Y (2006) CCHE-GUI—graphical users interface for NCCHE model user’s manual—Version 3.0. National Center for Computational Hydroscience and Engineering Technical report no NCCHE-TR-2006-2, October
- Zhang YX, Jia YF (2009) CCHE-MESH: 2D structured mesh generator user’s manual – Verion 3.X. Technical Report No. NCCHE-TR-2009-01. National Center for Computational Hydroscience and Engineering. The University of Mississippi, University. U.S.A.
- Zhiwei Li, Zhaoyin Wang, Baozhu Pan, Haili Zhu, Wenzhe Li (2014) The development mechanism of gravel bars in rivers. *Quat Int* 336:73–79. <https://doi.org/10.1016/j.quaint.2013.12.039>

# The Impact of Deflectors on Sediment Transport Processes on the Basis of Modelling and Simulations

Ewelina Szalkiewicz, Tomasz Dysarz, Tomasz Kałuza,  
Albert Malingier and Artur Radecki-Pawlik

**Abstract** The presented research analyses the impact of deflectors on sediment transport processes. The basis for analysis is a hydrodynamic model of downstream part of the Flinta river. The geometry reproduction was performed using spatial data: digital elevation model (DEM) and cross-sections of considered reach. The computations were calculated in HEC-RAS 5.0.1, a common software used to calculate water surface profiles and sediment transport. In the research, two calculation variants were analysed: (1) with initial geometry of channel, and (2) with geometry after introducing deflectors. In order to take into account uncertainty, five scenarios of 10-year flow hydrographs were tested. To calculate the intensity of sediment transport, the Engelund-Hansen formula was used. The results suggest a possible initiation of local scours near the structures.

## 1 Introduction

The strongest human impact on aquatic ecosystems was probably recorded at the end of the 19th and in the 20th century. Then the industrialization of society, intensification of agriculture, regulation of rivers, construction of dams and drainage of wetlands occurred. An excessive exploitation of water resources contributed to significant deterioration of water state and loss of valuable aquatic ecosystems. As a result of decrease in the number of fish, the first steps related to

---

E. Szalkiewicz (✉) · T. Dysarz · T. Kałuza  
Department of Hydraulic and Sanitary Engineering, Poznan University of Life Sciences,  
ul. Piątkowska 94A, 60-649 Poznań, Poland  
e-mail: sonnenbergewelina@gmail.com

A. Malingier  
Flood and Drought Modeling Center, Institute of Meteorology and Water Management,  
ul. Dąbrowskiego 174/176, 60-594 Poznań, Poland

A. Radecki-Pawlik  
Faculty of Civil Engineering, Institute of Structural Mechanics, Cracow University  
of Technology, ul. Warszawska 24, 31-155 Kraków, Poland

the restoration of rivers were taken in the United States in the late 19th century (Roni and Beechie 2013).

Since then, the restoration actions have spread significantly. Currently many examples of river restoration projects, based on “eco-friendly” technical solutions can be found (Byczkowski and Okruszko 1996; Jędryka 2003; Obolewski et al. 2009; Hammond et al. 2011; Crammer 2012; Puczko and Jekatierynczuk-Rudczyk 2014). However, there is no recommended methodology of proceedings and assessment of the impact of individual technical solutions on hydraulic or hydro-morphological parameters. This problem is related to the frequent abandonment of monitoring the completed restoration projects.

One of the structures used for the river restoration needs are deflectors. They can be built from materials such as stones, wicker or wood. The main deflector’s role is to change the longitudinal profile of the river, because these encourage watercourse to meander. As an effect of changes in velocity of water flow, processes related to sediment transport are also altered (Żelazo and Popek 2014). Deflectors are very popular structures but just in few cases more precise analysis about their impact has been done (Zhou and Endreny 2011; Seidel and Brunke 2015).

The main goal of the presented study is to evaluate the deflectors impact on sediment transport processes: (1) amount of sediment and (2) erosion—accumulation processes. For simulations, the HEC-RAS software is used and calculations are performed on the basis of Engelund-Hansen formula. Two calculation variants are analysed: (1) channel without structures and (2) after introducing deflectors.

## 2 Study Area

The case study in the research is a downstream reach of the Flinta river of the length of 1.8 km. The Flinta river is a small lowland stream, which disembogues to the Wełna river in Rożnowo-Młyn village (the municipality Rogoźno). The source of the watercourse is located in the Nature Reserve “Źródlika Flinty.” The total river length is about 27 km and its catchment area equals 345.47 km<sup>2</sup>. The catchment of the Flinta river is a controlled watershed—the cross-section with water gauge is located in km 14 + 800 in the Ryczywół village (watershed area in this cross-section equals 251.00 km<sup>2</sup>). According to topology (on the basis of the Water Framework Directive) the Flinta river is a sandy lowland stream. In the area adjacent to the Flinta river, grassy vegetation, coniferous and mixed forests and arable lands dominate (GIOŚ 2016). The outlet of the analyzed reach is located in the Flinta river estuary.

The Flinta River is a representative example of the majority of Polish lowland rivers, which from the end of the 20th century have undergone significant modifications. Both the technical regulation and the ongoing maintenance treatments have resulted in making the selected reach an object requiring restoration. It is locally straight, deep and show little variety (Fig. 1).

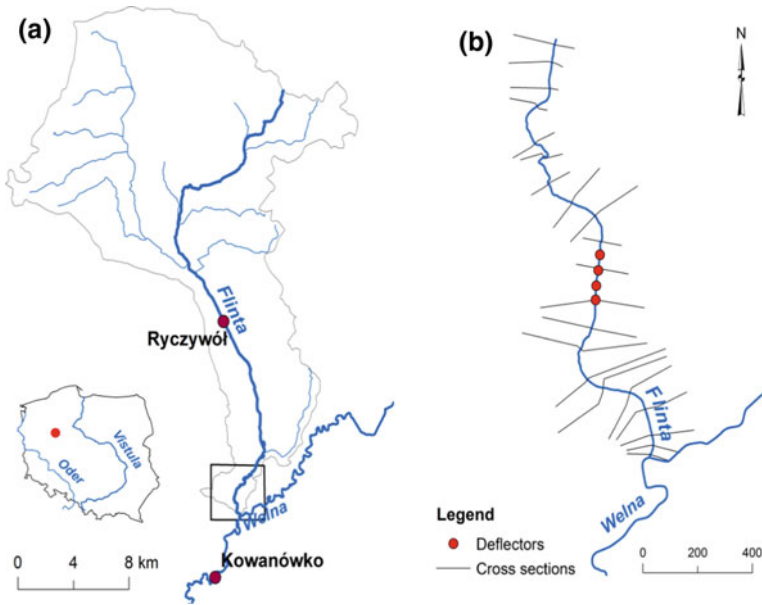


**Fig. 1** Location of the Flinta river: **a** watershed and **b** the analysed reach

### 3 Materials and Methods

#### 3.1 Materials

To develop a model of the analyzed reach of the Flinta river, various types of data were used. The basis was the digital elevation model, which was obtained from the Geodesic and Cartographic Documentation Centre (CODGiK). The resolution of the DEM is  $1 \times 1$  m and its vertical accuracy is 0.15 m. To complement information about channel ordinates below the water surface, the field measurements of channel ordinates made by BIPROWODMEL company were applied (Fig. 2).

The hydrologic data were obtained from the Institute of Meteorology and Water Management (IMGW) on the basis of the agreement between Poznan University of Life Sciences (PULS) and IMGW. For calculations, daily flow hydrographs for water gauge Ryczywół from the period 1951–2014 were used. The highest flow of the multiyear period amounted to  $7.28 \text{ m}^3 \text{ s}^{-1}$ , average flow being  $0.66 \text{ m}^3 \text{ s}^{-1}$  and the lowest flow  $0.01 \text{ m}^3 \text{ s}^{-1}$  (Fig. 3).

For simulations of sediment transport, the sediment granulation is required. The sample was collected during field measurements and then analyzed on the basis of sieve analysis rules. The largest fraction in the sample is sand (Fig. 4).

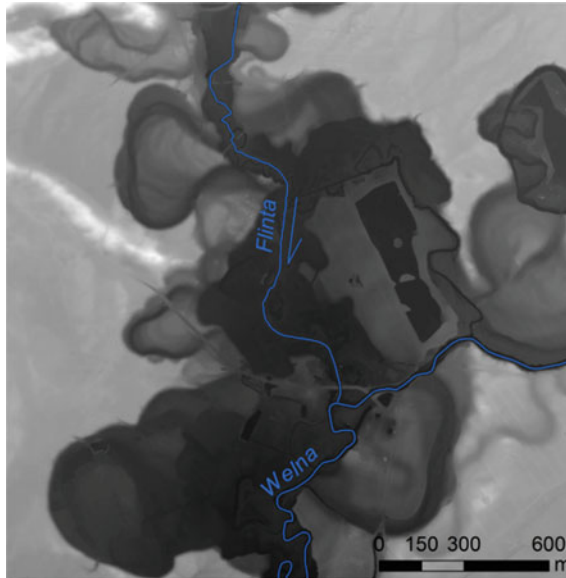


**Fig. 2** The digital elevation model of area adjacent to the Flinta river

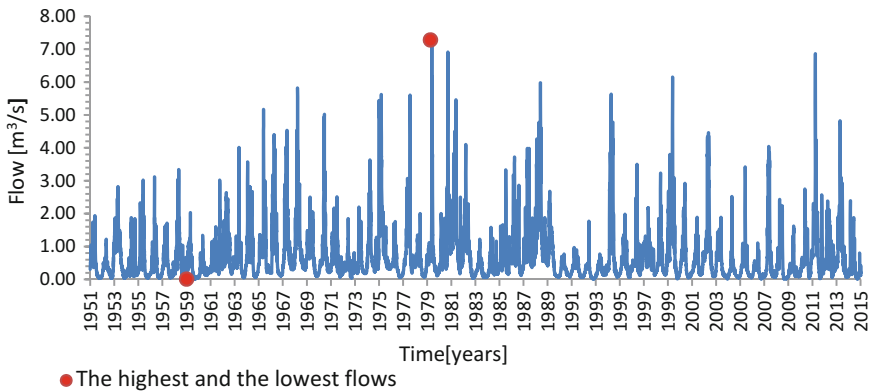


**Fig. 3** The flow hydrograph for the period 1951–2014 for water gauge Ryczywół

### 3.2 Methods

The methodology used in the research can be divided into two parts: (1) methods used for preparation of the geometry and (2) methods used for preparation of simulation models. Most of the elements were prepared in the HEC-RAS 5.0.3, using specific features of this software (Brunner 2010).

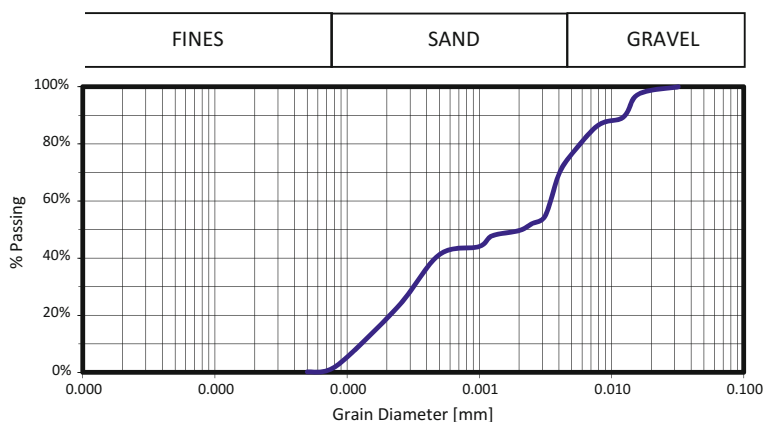


**Fig. 4** Sieve curve of the sediment samples collected in the Flinta river

The HEC-RAS 5.0.0 package consists of four basic computational modules: (1) steady and (2) unsteady flow in compound channels, (3) water quality assessment with heat distribution and (4) sediment transport in quasi-unsteady or fully unsteady flow conditions. In addition, the HEC-RAS contains many features supporting preparation of geometry and analysis of the results. The very important convenience is a possibility to exchange data between HEC-RAS 5.0.0. and GIS tools, such as ArcGIS (Booth and Mitchell 2016) and QGIS (QGIS Project 2016). This is caused by application of plug-ins such as HEC-GeoRAS (Cameron and Ackerman 2012) or RiverGIS (Pasiok et al. 2015).

In the research, the most important module of HEC-RAS 5.0.0 was sediment routing. Taking into account purposes of the presented research, the quasi-unsteady flow model is a sufficient basis for the simulation of long-term bed changes. The idea behind this algorithm is based on the assumption that time scales of the two processes, flow and sediment transport, are different (Cao et al. 2007, 2011). Hence, the description of flow may be simplified to fit the scale of sediment routing in long-term computations. The sediment transport simulation is based on the numerical solution of the well-known Exner's equation (Parker 2004; Wu 2007; Brunner 2010). The equation describes the mass balance of sediment, taking into account changes in the river bed elevations and sediment net inflow. The concept of Exner's equation has to be completed with empirical formula for the calculation of sediment transport intensity. The Engelund-Hansen (EH) formula (Engelund and Hansen 1966, 1972; Yang 1996; Parker 2004; Radecki-Pawlik 2014) is tested in the presented paper. This formula, marked as EH, was derived for and tested on rivers with sandy beds similar to those met in the Greater Poland (Wielkopolska) region.

To run the simulations, the model geometry has to be defined. Two geometries were tested, namely (1) the existing geometry without deflectors, (2) designed geometry with deflectors. The first geometry was prepared on the basis of DEM model obtained from CODGiK (2016) and measurements of river cross-sections

made accessible by BIPROWODMEL company. The DEM was used to generate the cross-sections for the computational model. The HEC-GeoRAS plug-in for ArcGIS 10.3 was used in the process of geometry generation for computational purposes. The number of generated cross-sections, including channel and floodplains, was 51. The average distance between cross-sections was about 35 m. The location of cross-sections was the same as for the measurements made by BIPROWODMEL company. Then the information about cross-sections was inserted in the geometry module of HEC-RAS 5.0.0. In this way, the all geometry data were implemented. Taking into account the features of the sediment routing model in HEC-RAS 5.0.0, the basic hydraulic structures such as bridges, weirs, etc. were reconstructed by proper modification of river cross-sections. This modification was made directly in the geometry module of HEC-RAS 5.0.0. In order to properly reconstruct such elements in the channel, cross-sections were located at shorter distances.

The second geometry was created by modifications of the first one in the places of location of deflectors. The modifications were introduced according to the same concept which had been tested for typical hydraulic structures. The first step was interpolation of additional cross-sections around location of deflectors. In the next step, these cross-sections were modified so as to imitate the constricted cross-section caused by the deflector. Four structures were introduced in the reach from 714.45 to 860.92 m along the channel and they were inserted in a maximum distance of 50 m. Deflectors were located on opposite sides—two on the right bank and the other two on the left one. The dimensions (length and width) of each structure were 2 m.

The biggest problem in flow modelling is a proper choice of the roughness coefficients. These coefficients are used to calibration of model which should correspond to the observed conditions of the river. The most popular method is a calibration model on the basis of historical flood hydrographs and that method is usually recommended. The other approach is assessing sensitivity of the model for various values of the unknown roughness coefficient. For many reasons and to avoid inconvenience, the second approach was used in this study. The reference roughness coefficients were estimated on the basis of field observations and table of roughness coefficients to Manning's formula (Chow 1959). For the main channel it was  $0.040 \text{ s m}^{-1/3}$  and for floodplain  $0.050 \text{ s m}^{-1/3}$ . The reference values of the coefficients were applied in the analysed reach of the Flinta river because the channel sediment and vegetation cover in the floodplains were relatively uniformly distributed in the case study area. To assess sensitivity of the model, two additional variants of roughness coefficients were tested: (1)  $0.037 \text{ s m}^{-1/3}$  for main channel and  $0.047 \text{ s m}^{-1/3}$  for floodplains and (2)  $0.042 \text{ s m}^{-1/3}$  for main channel and  $0.055 \text{ s m}^{-1/3}$  for floodplains.

The main sources of uncertainty were inflows. The calculations of sediment transport were performed for 5 scenarios of 10-year duration. The hydrographs for the scenarios were taken randomly from daily flow hydrograph for water gauge located in the Ryczywół village. Before calculations, flow hydrographs were recomputed on the basis of watershed area in the inflow cross-section of the

analysed reach and in the cross-section of water gauge. In the simulations, two bed variants were compared: (1) the one without structures and (2) that with deflectors. It gives total number of calculations equal to  $5 \times 2 = 10$ . The result of each simulation is bed profile, shape of particular cross-sections and amount of transported sediment.

### 4 Results

In the research, uncertainties associated with roughness coefficients were considered. Flow calculations for initial geometry and three scenarios of Manning’s values were performed. Water surface elevations for cross-sections with the biggest differences between variants are listed in Table 1. Maximum differences between variants occurred in cross-section 41.01 m along the channel (0.17 m for variants I-II and 0.11 m for variants II-III). For remaining cross-sections, differences amounted to a few centimetres. The obtained results of water surface elevations shows that the impact of uncertainty related to roughness coefficients is not significant.

Predicted changes are presented as profiles of water surface and bottom elevations of the analysed reach (Fig. 5). The longitudinal profile shows initial stage of the river and ordinates of bottom and water surface profile after calculations. To assess the impact of deflectors on sediment transport processes, the results for the cases without and with deflectors were compared.

It is well seen that, regardless of the case, sediments are accumulated just in the middle part of the analyzed reach from 860 to 1300 m along the channel. The erosion processes prevail in the downstream part of the river, from 860 m along the channel. The changes of water surface follow the variability of bed changes. In the upper reach, the water surface is significantly increased. In the downstream reach, the water surface decreased.

For part of the reach, from 714.45 to 860.92 m along the channel (location of deflectors), there occurred significant differences in results obtained for geometry with deflectors and without structures. Less erosion has occurred in the case of geometry with deflectors. The maximum change is 0.93 m observed at 713.95 m along the channel.

The average amount of transported sediment shows Fig. 6. The positive numbers mean the amount of bed material in places with accumulation and negative numbers

**Table 1** Water surface elevation after calculations performed for three variants of Manning’s values

Manning’s variant	Cross-section along the channel (m)			
	935.92	759.92	712.45	41.01
I	56.36	56.00	55.95	54.12
II	56.34	55.96	55.92	53.95
III	56.30	55.93	55.88	54.01



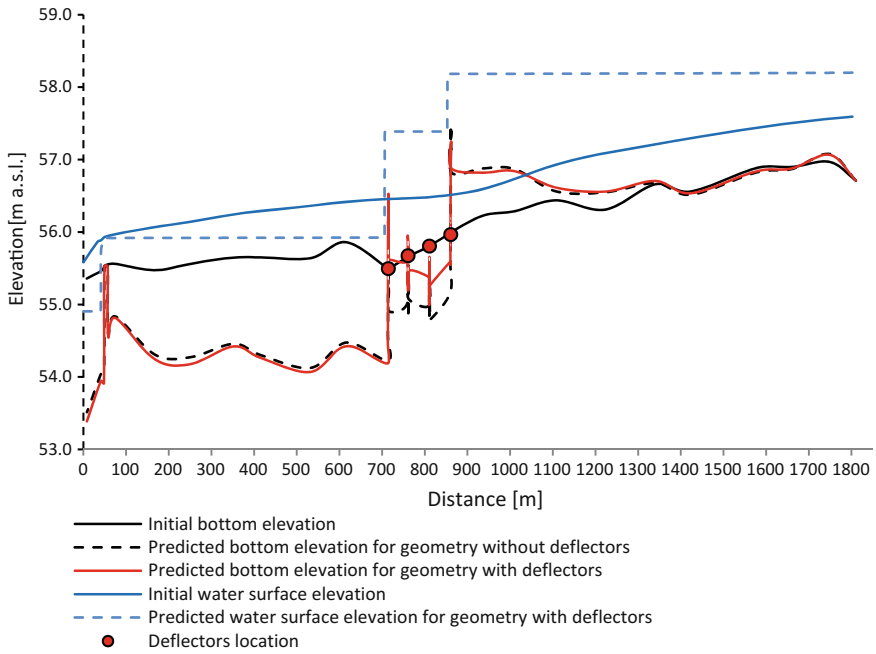


**Fig. 5** Changes in bottom elevation after simulations for geometry with and without deflectors calculated adopting the Engelund-Hansen formula

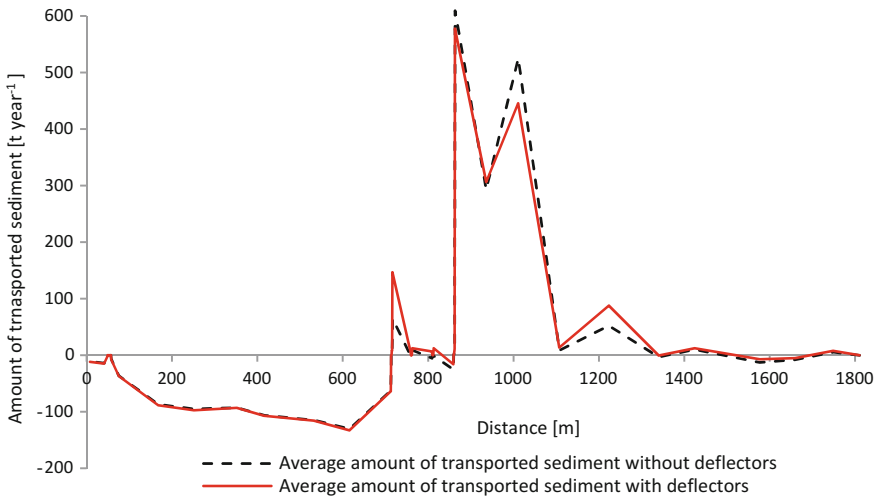


**Fig. 6** Average amounts of transported sediments for variants without deflectors and with deflectors

occur in location of erosion. The highest values of transported bed material occurred in the in the middle part of the analyzed reach, from 860 to 1100 m along the channel ( $577.56 \text{ t year}^{-1}$  for variant with deflectors and  $609.21 \text{ t year}^{-1}$  without structures in cross-section 862.92 m along the channel). In locations with erosion the highest values was  $-132.74 \text{ t/year}$  for variant with deflectors and  $-130.62 \text{ t year}^{-1}$  without structures in cross-section 615.97 m along the channel Differences in amounts of transported sediment between analysed cases were not significant. Maximum variance occurred in cross-section 716.45 m along the channel and equalled  $81.56 \text{ t year}^{-1}$ .

## 5 Conclusions

Choosing deflectors for tests, we expected development of changes in fluvial processes. Channel narrowing caused by deflectors results in increasing water levels and decreasing the channel capacity. Although contraction of flow area should increase the flow velocity in the local cross-section, the average velocities in the cross-sections upstream of the deflectors should be smaller due to greater depths present there. Smaller velocities lead to good conditions for sediment transport deposition. But as in case of other hydraulic structures (weirs, culvert or bridges) deflectors may cause local erosions.

The results obtained for geometry without deflectors show the occurrence of accumulation and strong erosion in the middle part of the analysed reach. This is probably caused by locally great depth and slope. In the variant “with deflectors”, the results are similar (erosion and accumulation in the same locations). Just in the location of deflectors, the erosion is smaller—bottom ordinates are higher in comparison with variants without deflectors. It may be concluded that deflectors cause accumulation rather than erosion.

To get more information about deflector’s impact, the presented research should be tested with other formulas for intensity of sediment transport and confronted with observations in nature.

## References

- Booth B, Mitchell A. Getting started with ArcGIS. [http://webfacstaff.sas.upenn.edu/~dromano/classes/gis/files/Getting\\_Started\\_with\\_ArcGIS.pdf](http://webfacstaff.sas.upenn.edu/~dromano/classes/gis/files/Getting_Started_with_ArcGIS.pdf). Accessed 24 Oct 2016
- Brunner GW (2010) HEC-RAS river analysis system hydraulic references manual, US Army Corps of Engineers, Hydrologic Engineering Center (HEC), Report No. CPD-69
- Byczkowski A, Okruszko H (1996) The scope of research directed on the restoration of drained areas in the Middle Biebrza Basin. *Probl Issues Agric Sci Prog* 432:183–192 (In Polish)
- Cameron T, Ackerman PE (2012) HEC-GeoRAS GIS tools for support of HEC-RAS using ArcGIS user’s manual; Report No. CPD-83; 2012, US Army Corps of Engineers, Hydrologic Engineering Center (HEC): Davis, CA, USA

- Cao Z, Hu P, Pender G (2011) Multiple time scales of fluvial processes with bed load sediment and implications for mathematical modelling. *J Hydraul Eng* 137:267–277
- Cao Z, Li Y, Yue Z (2007) Multiple time scales of alluvial rivers carrying suspended sediment and their implications for mathematical modelling. *Adv Water Resour* 30:715–729
- CODGiK. Geodesic and cartographic documentation center. <http://www.codgik.gov.pl/>. Accessed 8 Nov 2018
- Chow VT (1959) *Open—channel hydraulics*. McGraw-Hill, New York
- Cramer ML (managing editor) (2012) *Stream habitat restoration guidelines*. Co-published by the Washington Departments of Fish and Wildlife, Natural Resources, Transportation and Ecology, Washington State Recreation and Conservation Office, Puget Sound Partnership, and the U.S. Fish and Wildlife Service. Olympia, Washington
- Engelund F, Hansen E (1972) *A monograph on sediment transport in alluvial streams*. Teknisk Forlag, Technical Press, Copenhagen
- Engelund F, Hansen E (1966) Hydraulic resistance in alluvial streams. *J Hydraul Divis, ASCE* 92 (2):315–326
- GIOS (2016) General inspectorate of environmental protection. <http://www.gios.gov.pl>. Accessed Dec 2016
- Hammond D, Mant J, Holloway J, Elbourne N, Janes M (2011) *Participial river restoration appraisal guidance for monitoring options (PRAGMO)*. The River Restoration Centre. Bedfordshire
- Jędryka E (2003) *Restoration of river valleys on drainage areas which are excluded from agriculture production on example of Radunia, Małynka and Tyniewiczze*, Publishing of IMUZ, Falenty (In Polish)
- Obolewski K, Osadowski Z, Miller M (2009) Renaturation methods for small river basins in the example of the Kwacza river (Ślupia river basin). *Sci Nat Technol* 3:3 (In Polish)
- Parker G (2004) *1D Sediment Transport Morphodynamics with Applications to Rivers and Turbidity Currents*. E-book available at Gary Parker's Morphodynamics Web Page, 2004, last update April 13, 2006. <http://hydrolab.illinois.edu/people/parkerg/>
- Pasiok R, Dębek Ł, Parda R, Zieliński K (2015) RiverGIS—QGIS plugin. <http://rivergis.com/>. Accessed 8 Nov 2018
- Puczko K, Jekatierynczuk-Rudczyk E (2014) Dlaczego warto renaturyzować miejskie rzeki? *Water Manag* 5:180–188 (In Polish)
- QGIS Project 2016, QGIS User Guide Release 2.14. [http://docs.qgis.org/2.14/pl/docs/user\\_manual/](http://docs.qgis.org/2.14/pl/docs/user_manual/). Accessed 8 Nov 2018
- Radecki-Pawlik A (2014) *Hydromorphology of mountain rivers and streams. Selected topics*, Publishing of Cracow University of Agriculture, Cracow
- Roni P, Beechie T (2013) Introduction to restoration: key steps for designing effective programs and projects. In: Roni P, Beechie T (eds) *Stream and watershed restoration, a guide to restoring riverine processes and habitats*. Wiley, pp 1–11
- Seidel M, Brunke M (2015) Flow deflectors as instream restoration measures in lowland streams of schleswig-holstein—effects and recommendations for a more natural design. *Wasserwirtschaft* 105(12):55–61
- Wu W (2007) *Computational river dynamics*. Taylor & Francis Group, London
- Yang CT (1996) *Sediment transport: theory and practice*. McGraw-Hill Companies Inc, New York
- Żelazo J, Popek Z (2014) *Fundamentals of river restoration*. SGGW Publishing, Warsaw (In Polish)
- Zhou T, Endreny T (2011) Meander hydrodynamics initiated by river restoration deflectors. *Hydrol Process* 26(22):3378–3392

# Numerical Modeling of Water and Ice Dynamics for Analysis of Flow Around the Kiezmark Bridge Piers

Michał Szydłowski and Tomasz Kolerski

**Abstract** This paper presents the results of a numerical model study on the effect of ice on the proposed bridge piers in the Vistula River outlet and its effect on flow conditions in the river. The model DynaRICE is used in this study, which is a two-dimensional hydro-ice dynamic numerical model developed for dynamic ice transport and jamming in rivers. To simulate river hydrodynamics in the vicinity of the bridge piers, two-dimensional numerical model basing on finite volume technique was also used. Simulation results indicated notable effect of new structure on water and ice flow pattern. Ice forces on structures were also determined, but the load was not considerably high.

## 1 Introduction

The hydraulic analysis of the water flow near the bridge river cross-section and in the vicinity of piers is required and regulated by Polish law. Unfortunately, while looking at engineering structures built recently in Poland, this part of the bridge design process has been often omitted. Numerical modeling of the river hydrodynamics affected by proposed bridge structure is included only in small extent, and laboratory modeling is mostly neglected. Therefore, the estimation of the bridge influence on environment as well as the definition of the interaction between the bridge structure and the river is not possible. Experiences gained from bridge utilization have shown its remarkable input on river bathymetry in a relatively short period of time. As a notable example, the highway bridge in Korzeniewo could be used (Szydłowski and Zima 2013). This bridge caused 6 m deep scour in the river

---

M. Szydłowski · T. Kolerski (✉)  
Faculty of Civil and Environmental Engineering, Gdańsk University  
of Technology, G. Narutowicza 11/12, 80-233 Gdańsk, Poland  
e-mail: tomkoler@pg.gda.pl

M. Szydłowski  
e-mail: mszyd@pg.gda.pl

bed which was eroded in a period of one year only. Bed scour of this size, if not properly managed, may cause structure stability problems.

The paper also aims at determining the possibilities of applying a mathematical model in the context of aspects that are important for management of water areas in winter. Due to the lack of an adequate tool, a significant part of this information is usually obtained through approximation or on the basis of subjective expertise. By referring to the example of the bridge on the Vistula River, it was shown how the results obtained from a mathematical model can support decision-making when designing hydrotechnical objects.

The designed bridge, as part of the S7 express road from Gdansk to Warsaw, is planned in km 930 + 010 of the Vistula River. The new object is in the direct vicinity of the existing bridge on DK7 road and will be located about 26 m downstream. The bridge consists of 12 spans supported on piers which overlap with existing pillars. The main span over the Vistula River has a length of 130 m and is located over the waterway. Low chord of the bridge's deck has variable elevation, but its minimum elevation at the waterway gauge is 10.98 m Kr, which allows 8.2 m vertical clearance for normal and high flow condition. Even though the vessel traffic on the Vistula River is insignificant nowadays, the sufficient air draught is critical for icebreakers operation in the river outlet. The number of dangerous situations recorded on the Odra River has shown that low bridge clearance may hamper or even stop the icebreaking operation (Kreft 2011).

Due to the upper, weak layers of topsoil all the bridge piers have been designed with deep foundation. Two types of foundations have been considered: footing on reinforced concrete, prefabricated piles driven into the ground (Franki type) and Micropiles technique which may lower the total cost of the structure. Piers located in the river bed are 3 m wide and 9.5 m long gravity walls on 2 m plinths (Fig. 1a). Larsen sheet piling has been considered as a structural stay-in-place formwork for piers plinths. In one case, the Larsen retaining wall should reach over the water

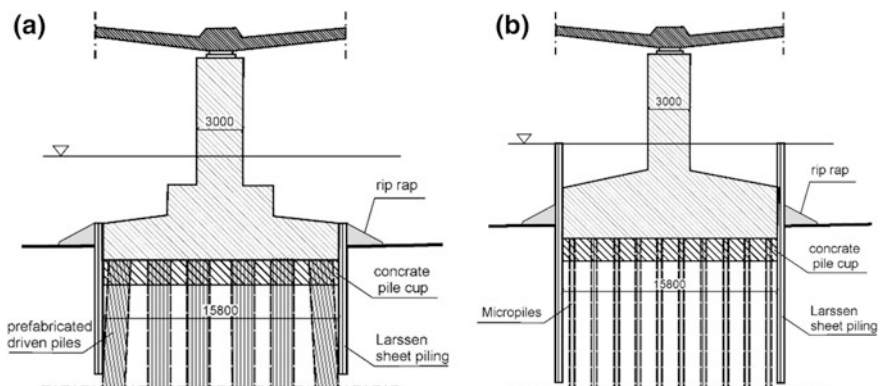


**Fig. 1** Cross-sectional view of the bridge pier on prefabricated piles (a), and pier on Micropiles with sheet piling exceed over the water surface (b)

surface to increase piers resistance for bending (Fig. 1b). However the final width of the single pier increases to 16 m, significantly reducing river conveyance. For average flow condition, the main river channel width in a bridge cross-section is about 300 m (312 m between abutments). Reduction of the cross-section area by 10% may be a reason for severe bed erosion as well as may lead to more frequent ice accumulation and jamming.

## 2 Modeling of Flow Dynamics

Free surface water flow dynamics at the Kiezmark bridge river cross-section was simulated using two-dimensional shallow water equations (SWE) model. It can be derived from the Navier–Stokes model using a depth averaging procedure, assuming hydrostatic pressure and uniform velocity distribution along water depth (Tan 1992). The SWE model can be presented in following conservative form (Szymkiewicz 2010):

$$\frac{\partial \mathbf{U}}{\partial t} + \frac{\partial \mathbf{E}}{\partial x} + \frac{\partial \mathbf{G}}{\partial y} + \mathbf{S} = 0, \tag{1}$$

where:

$$\mathbf{U} = \begin{pmatrix} h \\ uh \\ vh \end{pmatrix}, \quad \mathbf{S} = \begin{pmatrix} 0 \\ -gh(S_{ox} - S_{fx}) \\ -gh(S_{oy} - S_{fy}) \end{pmatrix} \tag{2a, b}$$

and

$$\mathbf{E} = \begin{pmatrix} uh \\ u^2h + 0.5gh^2 \\ uvh \end{pmatrix}, \quad \mathbf{G} = \begin{pmatrix} vh \\ uvh \\ v^2h + 0.5gh^2 \end{pmatrix}. \tag{3a, b}$$

In the system (1)–(3),  $h$  represents water depth,  $u$  and  $v$  are the horizontal components of the velocity,  $S_{ox}$  and  $S_{oy}$  denote the bed slope terms,  $S_{fx}$  and  $S_{fy}$  are the hydraulic slopes defined using Manning formula and  $g$  is the acceleration due to gravity. In order to integrate the SWE in space, the finite volume method (LeVeque 2002) was used. The SWE integration in time was conducted using explicit two-step finite-difference scheme.

The model was built to simulate an unsteady, gradually and rapidly varied flow (Szydłowski 2007). It was calibrated and used to analyze a number of real problems as inundations in natural river valleys (Szydłowski and Magnuszewski 2007) and catastrophic floods (Szydłowski et al. 2013). It was also used with satisfactory results to simulate the rapidly varied flow in open channel with bridge piers section (Szydłowski 2011; Szydłowski and Zima 2013).

### 3 Modeling of River Ice Dynamics

River ice dynamics and ice load on the bridge piers have been calculated by mathematical model DynaRICE which is a two dimensional, coupled ice and hydrodynamic tool (Shen et al. 2000). The model allows unsteady ice and water simulation driven by dynamic balance of all internal and external forces and was calibrated and validated to a number of real case scenarios (i.e. Shen et al. 1997; Kolarski et al. 2013; Kolarski and Shen 2015). Hydrodynamic module is a solution of two-dimensional shallow water equation including mutual interaction between ice and water flow. Dynamic transport of river ice is mathematically described as a movement of the number of particles carrying all ice properties and being subjected to force balance. The governing equation for ice dynamics can be presented in the following form (Shen et al. 2000):

$$M_L \frac{d\mathbf{V}_L}{dt} = \mathbf{R} + \mathbf{F}_a + \mathbf{F}_w + \mathbf{G}, \quad (4)$$

where:  $M_L$  is unity mass (per area) of ice particle,  $\mathbf{V}_L$  is ice velocity vector,  $\mathbf{R}$  is ice internal resistance force,  $\mathbf{F}_a$  and  $\mathbf{F}_w$  are wind and water drag, and  $\mathbf{G}$  is a gravity force. Solution to the ice dynamic equation was carried out by using the SPH method with method of images implemented to the land boundaries (Shen et al. 2000).

If the ice is stopped by any obstacles in the river, mechanical thickening occurs and the ice load builds up. The total ice force acting on the structure could be presented in the following form (Liu and Shen 2000):

$$\begin{aligned} \sum F_x = & -\sigma_{xx}N\eta dy - \sigma_{yx}N\eta dx + XN\eta dl + \frac{1}{2}\tau_{wx}N dx dy + \frac{1}{2}\tau_{ax}N dx dy \\ & + \frac{1}{2}\rho N \frac{dh}{dx} dx dy = 0 \end{aligned} \quad (5)$$

$$\begin{aligned} \sum F_y = & -\sigma_{yy}N\eta dx - \sigma_{xy}N\eta dy + YN\eta dl + \frac{1}{2}\tau_{wy}N dx dy + \frac{1}{2}\tau_{ay}N dx dy \\ & + \frac{1}{2}\rho N \frac{dh}{dy} dx dy = 0 \end{aligned} \quad (6)$$

in which  $\eta$  is a thickness of ice,  $X$  and  $Y$  are the  $x$  and  $y$  components of the ice load on the boom,  $N$  is the ice concentration;  $\tau_{ax}$ ,  $\tau_{ay}$  are components of wind drag in  $x$ - and  $y$ -directions, respectively;  $\tau_{wx}$ ,  $\tau_{wy}$  are components of water drag in  $x$ - and  $y$ -directions, respectively,  $\sigma_{xx}$ ,  $\sigma_{yy}$  and  $\sigma_{xy} = \sigma_{yx}$  are internal ice stresses. Assuming that the ice rubble in a front of the structure is stationary and neglecting higher order terms in above equations lead to the following formulas on ice loads in normal and tangential directions:



**Fig. 2** Ice rubble in the Vistula Outlet acting on the west jetty (January 2003)

$$\sigma_n = \sigma_{xx} \left( \frac{dy}{dl} \right)^2 + \sigma_{yy} \left( \frac{dx}{dl} \right)^2 + \sigma_{yx} \frac{dx}{dl} \frac{dy}{dl}, \quad (7)$$

$$\sigma_t = (\sigma_{xx} - \sigma_{yy}) \frac{dx}{dl} \frac{dy}{dl} + \sigma_{yx} \left[ \left( \frac{dy}{dl} \right)^2 + \left( \frac{dx}{dl} \right)^2 \right]. \quad (8)$$

The loads are determined on the vertical wall of length  $dl$ . Finally, normal and tangential force from ice can be determined by multiplying the loads by ice thickness and concentration:

$$F_n = \sigma_n N \eta, \quad (9)$$

$$F_t = \sigma_t N \eta. \quad (10)$$

As shown above, the direct relation between ice load and the thickness of the ice rubble exists. There is no systematic observations of ice thickness in the Vistula River outlet, therefore in simulation initial ice thickness of 0.2 and 0.3 m was used. Ice floes of this thickness were observed during January 2003 ice breakup in the Vistula outlet (Fig. 2).

## 4 Input Data

Model domain covers 300 m reach of the Vistula River in both downstream and upstream direction from the new bridge cross-section. River bathymetry within the model domain was measured with high accuracy for the study. On basis of the bed bathymetry, finite element meshes have been prepared for each model setup, which was always considered to be a fixed bed and no scour was included (Fig. 3).



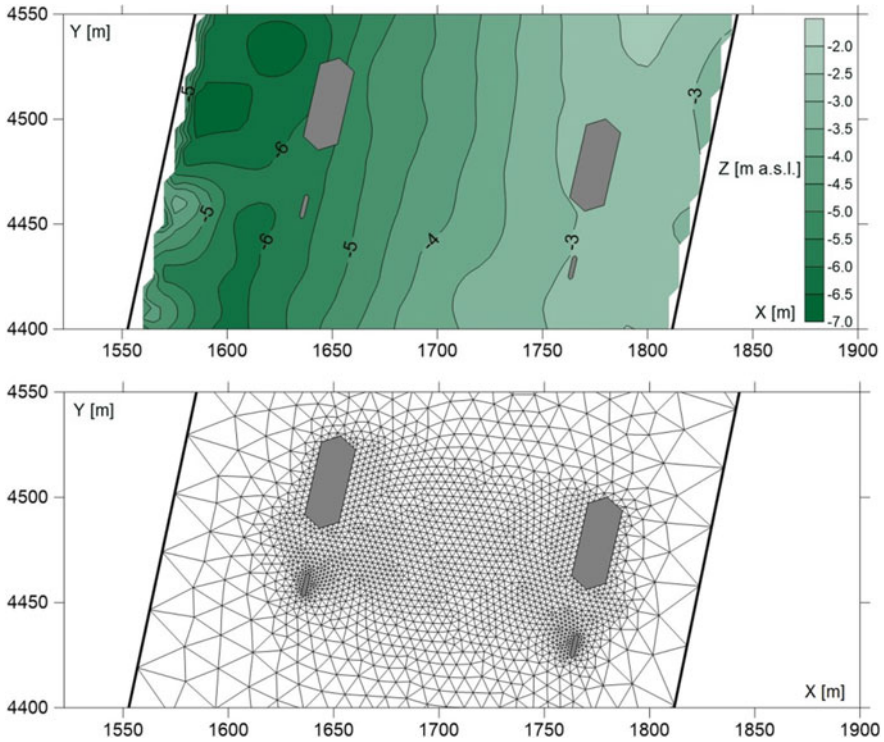


**Fig. 3** River bathymetry and finite element mesh around the piers in case 2

Full numerical analysis was conducted for three cases: existing condition (case 0); proposed bridge with two double piers (case 1) and proposed bridge with two large piers (case 2). In addition, simulations with cofferdams were included in order to check river bank stability during the bridge construction. For each case, the 500 year flow  $Q_{0.2\%} = 9450 \text{ m}^3 \text{ s}^{-1}$ , together with 100 year flow  $Q_{1\%} = 7744 \text{ m}^3 \text{ s}^{-1}$ , was used as the high flow conditions. Ice dynamics was only simulated for average (SSQ =  $1046 \text{ m}^3 \text{ s}^{-1}$ ) and low (SNQ =  $411 \text{ m}^3 \text{ s}^{-1}$ ) flow conditions, because with high flow the ice will pass the bridge without jamming. It is confirmed by historical observations which have shown more frequent ice jamming on the Lower Vistula River during average and low discharge. The only exception was 1982 ice jam flood which was the combination of unfavorable hydrological and meteorological condition (Kolerski 2011). During this event, water discharge of  $3900 \text{ m}^3 \text{ s}^{-1}$  was observed, but it didn't cause any flood risk on the Vistula outlet. In last century, only two flood risk events happened and both with water discharge below average (Kolerski 2014). For low and average flow conditions, the water remains in the main channel only; however, for high flow condition, part of the river discharge was on the floodplains.

For river ice simulations, no thermal effects were included, which is consistent with conditions observed during ice breakup. Possible melting could occur, although in a short period of time (simulations were conducted for 24 h), and the reduction of ice mass would be neglectable.

In the current study, the effect of wind on ice transport wasn't taken into consideration. Wind blowing from opposite direction may significantly reduce the ice velocity or even lead to complete stoppage of ice transport in downstream direction. As shown in Kolarski (2014), the most critical condition in the Vistula outlet will occur during a storm with northern wind. However, the wind effect is dominant on rivers with low flow velocity, reservoirs or lakes. Therefore, because the study was focused on local, small scale phenomena, this impact was omitted.

## 5 Simulation Results of Water Flow Through the Bridge Section

The SWE model was used to assess the effects the construction of new piers will have on a structure of water flow. In the first part of numerical simulations, the actual and new piers configurations in final form were investigated. In this paper, we present only the 100 year flow case with cofferdams, which are temporary structures built within the river to protect the new piers during bridge construction. These 40 m long sheet piling walls are placed between new and existing piers, about 5 m upstream from the new bridge, as shown in Fig. 3. The layout of the cofferdams was set to consist of two sections connected at 4° angle.

In order to simulate the two-dimensional water flow in the Vistula River through the cross-section constricted by the bridge piers using the FVM, the geometry of the river channel had to be transformed into numerical mesh. The flow domain was covered by unstructured triangular mesh composed of almost 4000 computational cells. The length of the side of standard triangle was equal to 30 m except the area near the bridge. In order to ensure the high resolution of simulation results, the mesh was locally refined in the direct vicinity of bridge section, as can be seen in Fig. 3. The cells edges adjacent to the bridge piers and cofferdams were 3 m long. The areas inside the piers' contours were excluded from the computational domain as a consequence of the closed boundaries imposed around the bridge piers.

The other boundary conditions were also imposed in accordance with the simulated case study. The Vistula riverbanks were treated as closed boundaries and the free slip condition was used there. It means that inundation of floodplains was not investigated in the simulation. At the inflow and outflow river cross-sections, the open boundaries were located. At the inlet to the river channel, the appropriate part of  $Q_{1\%}$  flow rate was imposed as an upstream boundary condition. At the outlet, the water stage was forced. The river hydrodynamics was simulated starting from the steady flow initial condition, which was computed for the channel devoid of bridge piers. Then, if the obstructions were present in the channel, the flow became unsteady for a while due to formation of backwater profile upstream of the bridge

and surface depression downstream from the piers. After the setup period, because constant boundary conditions were simulated, flow approached a steady state. The calculations were carried out with the time step  $\Delta t = 0.01$  s.

Results of the numerical simulations of cofferdams case study have been shown in Figs. 4a, 4b and 4c. The figures present contour plot of water level distribution over the flow domain as well as vectors and module of flow velocity.

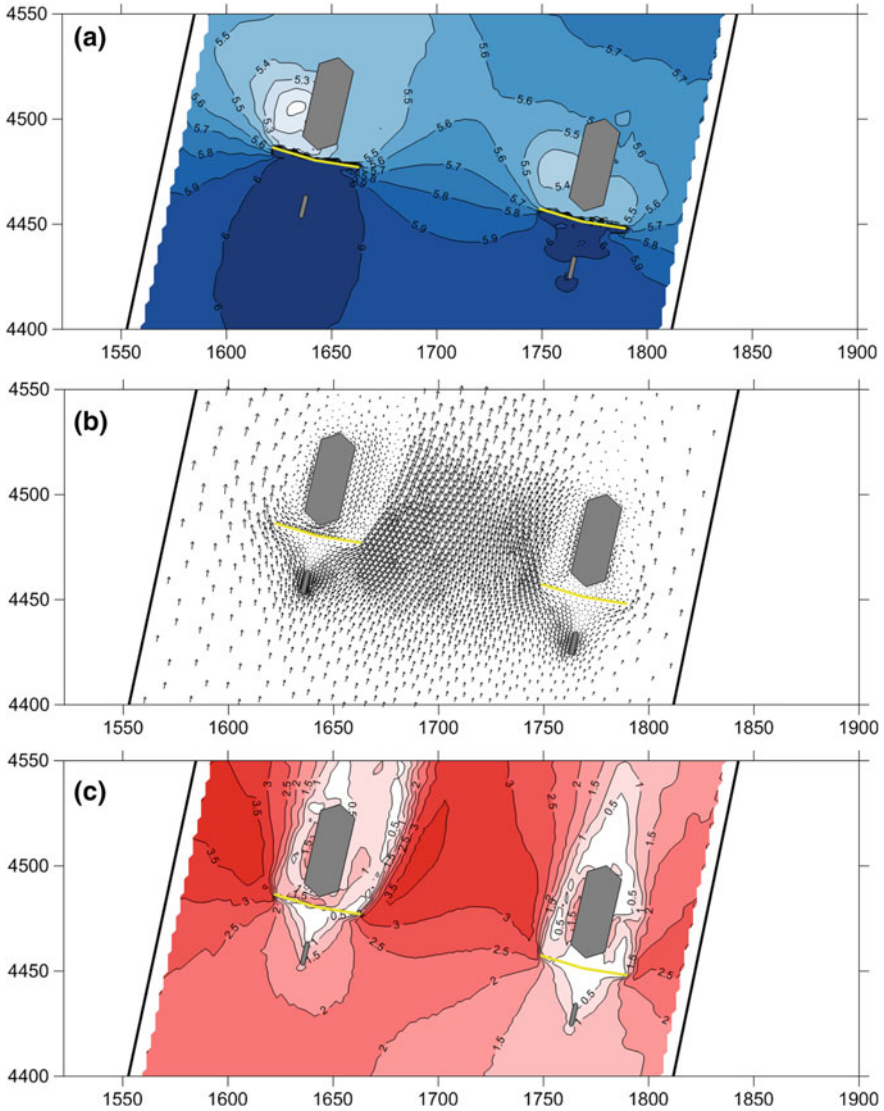


**Fig. 4** Water surface level [m ASL] (a) and flow velocity [m s<sup>-1</sup>] (b, c) around the piers for the case 2 with cofferdams (horizontal dimensions in m)

Analyzing the simulated flow parameters it can be found that the water flow is subcritical along the river channel and in the vicinity of structures. In front of the old piers, the water surface is increasing but the backwater upstream the cofferdams is overtopping this effect. As can be seen in Fig. 4a, the cofferdams cause a water damming in front of the bridge section. This phenomenon is accompanied by a change of flow velocity, which is decreased in the backwater area and increased between the two piers and between piers and riverbanks.

Behind the cofferdams and upstream from the new piers, as well as around them, the strong reduction of water level can be observed. In the area behind the new piers, local depressions can be seen. In the simulation for the  $Q_{1\%}$  flow rate, the water head between upstream and downstream side of the cofferdams is about 1.0 m. It means that the temporary cofferdams will be affected to an increased strength of pressure force. In this area the flow circulations can be also observed. Downstream from the bridge section, the water surface is increasing up to normal depth in the river.

Moreover, the existence of cofferdams and pillars splits the water flow and directs it to the riverbanks. The  $Q_{1\%}$  flow partition can cause streams directed towards the left bank at a velocity exceeding  $3.5 \text{ m s}^{-1}$  and towards the right bank at velocity exceeding  $2.5 \text{ m s}^{-1}$ . Such high velocities along the riverbanks can result with the destruction of the banks, wing dams and other regulation works. In the area between the bridge piers, the water velocity can be higher than  $3.0 \text{ m/s}$ , which can be a reason of intensive debris flow, deformation of the riverbed and local scour near the piers, which should be investigated in details to avoid the bridge destruction.

## 6 Simulation Results of Ice Dynamics

In this study, the calibrated DynaRICE model was used to determine the effects of ice on the proposed bridge piers and to assess the effects the construction of new piers will have on ice transport in the Vistula River outlet. From all simulated cases, the highest impact on bridge piers was for the ice run with initial ice thickness of 0.3 m. Also the maximum force on bridge piers was recorded for the case with two 15 m piers; therefore, the results from this case only will be presented below. The results of numerical simulations have been shown in Figs. 5 and 6. Both figures presents contour plot of ice thickness distribution over the model domain. Calculated ice force acting on both existing and proposed piers in normal and tangential direction is also presented in the figures. The ice force is presented in  $[\text{kN m}^{-1}]$  i.e. per meter of the structure perimeter.

In case 2, simulations were performed with two 15 m width piers which caused significant reduction of channel conveyance. From the point of view of ice transport, 10% decrease of channel cross-section area will hump the ice movement and may affect possible ice jam. The larger the incoming ice concentration, the larger the effect.

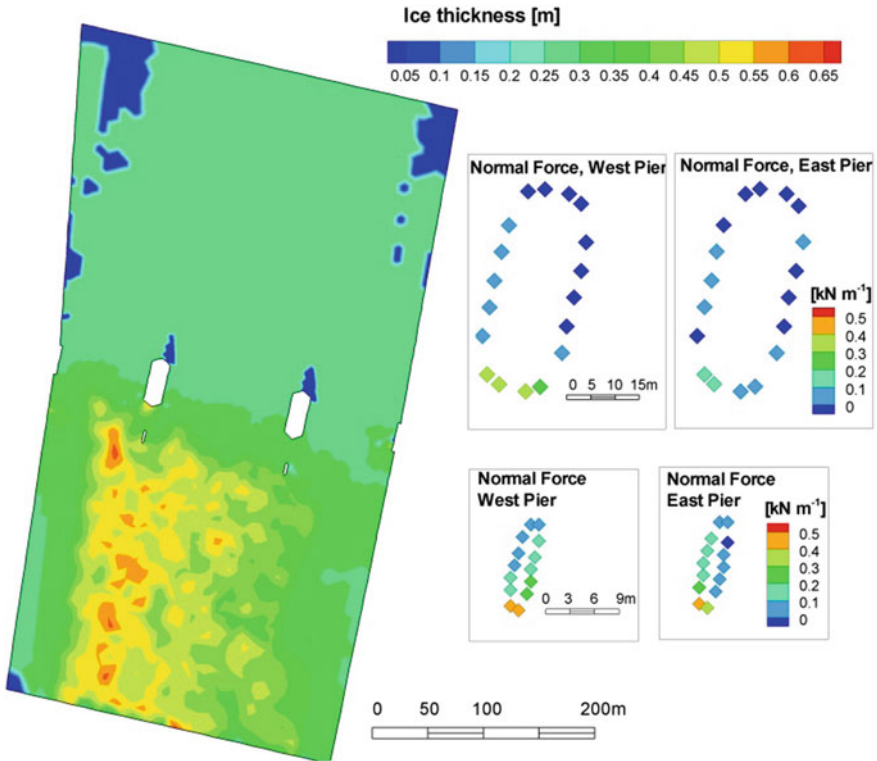


**Fig. 5** Ice thickness distribution and maximum normal ice force on the bridge piers for low flow condition ( $Q = 411 \text{ m}^3 \text{ s}^{-1}$ ); thickness of single ice floe  $\eta = 0.3 \text{ m}$

Simulation results have shown that the maximum load was observed for the case with average water discharge. These conditions lead to ice accumulation in front of all piers. However, the formation at proposed piers is more stable and, once formed, it stays until the end of simulation run. Ice rubble piled up forming 0.7 m thick accumulation. The condition is still not severe, because simulated maximum ice force did not exceed  $1.1 \text{ kNm}^{-1}$ . However, if the ice accumulation occurs during the mid-winter breakup, it will possibly freeze solid to the piers. Later, while spring breakup will cause ice movement, the formation will be difficult to remove and may affect an additional jamming upstream of the bridge.

Location of the new bridge piers directly downstream of the existing piers will cause most favorable condition for ice transport. Notwithstanding, wide bridge piers will impede ice movement and increase the chance of ice stoppage and jamming. To reduce ice related risk, icebreaking should proceed in further seasons with particular focus on bridge cross-section. The other possibility of bridge setup, namely new piers in a form of two double piers, 3 m width each, will reduce ice jam hazard significantly.

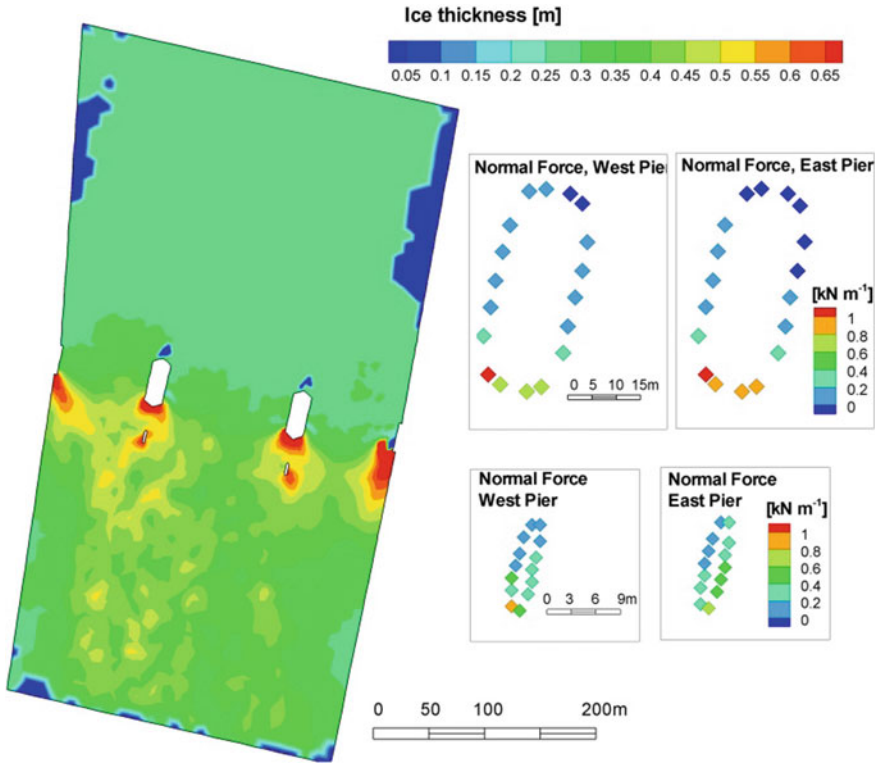


**Fig. 6** Ice thickness distribution and maximum normal ice force on the bridge piers for average flow condition ( $Q = 1046 \text{ m}^3 \text{ s}^{-1}$ ); thickness of single ice floe  $\eta = 0.3 \text{ m}$

Regardless of the final bridge setup, the new piers of the proposed bridge will interact with ice. The mouth of the Vistula River is currently maintained by ice-breakers during the breakup and the ice run which prevents ice from stopping and jamming. Ice monitoring and ice jam prevent operation have to be continued over next winter seasons to reduce the flood hazard caused by ice jams in the river mouth.

## 7 Conclusions

Mathematical models are precise tools to predict possible conditions that may occur in a future structure operation. As shown in the paper, in a bridge case results of numerical modeling was used to assess the effect of bridge piers on hydrodynamic and ice transport. The ice load on the piers was also determined. Even though numerical modeling is generally accepted and defined as a best practice in bridge

design, there is shortage of such activity in Poland. Insufficient structure to environment interaction analysis may lead to a variety of dangerous situations, including stability problems, river degradation, increased flood risk and other environmental issues.

**Acknowledgements** Authors express gratitude to Metrostav a.s. for providing the data which made it possible to carry out the calculations presented in the article.

## References

- Kolerski T (2011) Numerical modeling of ice jam formation in the wrocławek reservoir. *TASK Q* 15(3–4):283–295
- Kolerski T, Shen HT, Kioka S (2013) A numerical model study on ice boom in a coastal lake. *J Coastal Res* 29(6a):177–186
- Kolerski T (2014) Modeling of ice phenomena in the mouth of the Vistula River. *Acta Geophys* 62 (1):11–22
- Kolerski T, Shen HT (2015) Possible effects of the 1984 St. Clair River ice jam on bed changes. *Can J Civ Eng* 42(9):696–703
- Kreft A (2011) Ice-breaking action course on lower and border stretch of the Odra River-winter season 2010/2011. *Logistyka* 6
- LeVeque RJ (2002) Finite volume method for hyperbolic problems. Cambridge University Press, NY
- Liu L, Shen HT (2000) Numerical simulation of river ice control with booms (No. ERDC/CRREL-TR-00–10). Engineer Research and Development Center Hanover NH Cold Regions Research and Engineering Lab
- Shen HT, Lu S, Crissman RD (1997) Numerical simulation of ice transport over the Lake Erie-Niagara River ice boom. *Cold Reg Sci Technol* 26(1):17–33
- Shen HT, Su J, Liu L (2000) SPH simulation of river ice dynamics. *J Comput Phys* 165(2):752–770
- Szydłowski M (2007) Mathematical modeling of flood waves in urban areas, Monographs of Gdańsk University of Technology, 86, Gdańsk
- Szydłowski M, Magnuszewski A (2007) Free surface flow modeling in numerical estimation of flood risk zones: a case study. *TASK Q* 11(4):301–313
- Szydłowski M (2011) Numerical simulation of open channel flow between bridge piers. *TASK Q* 15(3–4):271–282
- Szydłowski M, Zima P (2013) Numeryczna analiza wpływu budowy podpory mostu na rzece Wiśle na przepływ i rozmycie dna koryta rzeki (Numerical analysis of the influence of Vistula river bridge pier on the water flow and local scour). *Inżynieria i Budownictwo*, 10, Wydawnictwo PZITB Warszawa, 553–558
- Szydłowski M, Szpakowski W, Zima P (2013) Numerical simulation of catastrophic flood: the case study of hypothetical failure of the Bielkowo hydro-power plant reservoir. *Acta Geophys* 61(5):1229–1245
- Szymkiewicz R (2010) Numerical modeling in open channel hydraulics. Springer, London
- Tan W (1992) Shallow water hydrodynamics. Elsevier, Amsterdam

# Flow Dependence of the Parameters of the Transient Storage Model

Stephen G. Wallis and J. Russell Manson

**Abstract** Using 25 tracer experiments, parameters of the transient storage model (TSM) were evaluated for a reach of the river Brock in north-west England with the primary aim of investigating their dependence on flow rate. Since only a very few previous studies have considered this issue, these new results aid our understanding on how the TSM could be applied to a reach at flow rates beyond the range of flow rates for which observations of solute transport exist. Velocity increased with increasing flow rate in a manner consistent with current knowledge. In contrast, and unexpectedly, the dispersion coefficient reduced (weakly) with increasing flow rate and the values were rather scattered. The transient storage exchange rate increased with increasing flow rate, which corroborates some of the sparse existing knowledge of this parameter's behaviour. The ratio of transient storage area to main channel area was essentially constant over the range of flow rates examined, which is consistent with some studies on single reaches.

## 1 Introduction

The transport of solutes along rivers has been studied for about 50 years and has been motivated by a need to predict the environmental consequences of pollution incidents. The earliest work was primarily concerned with understanding the bulk movement of polluted water following short-term pollutant releases and identified the Advection Dispersion Model (ADM) as a suitable basis for making predictions about solute concentrations (Fischer 1967). In this, a solute cloud stretches longitudinally as it is carried downstream through the interaction of differential advection and cross-sectional mixing (the so-called advection-dispersion or shear-flow mechanism). As observations from controlled tracer experiments increased in

---

S. G. Wallis (✉)  
Heriot-Watt University, Edinburgh, UK  
e-mail: s.g.wallis@hw.ac.uk

J. R. Manson  
Stockton University, Galloway Township, NJ, USA



number and the range of river characteristics covered expanded, it began to be recognised that although this model was quite successful in describing most of the key features of solute transport, there were some deficiencies. These mainly concerned the tendency of the passage of solute to be delayed in so-called dead-zones, occurring around the periphery of the main river channel, and/or in recirculating flow structures (such as those found in pool-riffle and meander sequences), resulting in longer and more elevated tails of observed tracer concentration profiles compared to those from model outputs (Nordin and Sabol 1974; Day 1975). Thus were born the Transient Storage Model (TSM), which extended the ADM to cater for such solute trapping (Bencala and Walters 1983), and the Aggregated Dead Zone Model, which postulated rather radically that the mechanics of transient solute trapping rather than those of shear-flow could form the basis of a modelling approach for the whole channel (Beer and Young 1983).

By the 2000s, many authors had identified the importance of the hyporheic zone (HZ) for solute transport and stream ecology, i.e. the area of saturated material that surrounds river channels (Elliott and Brooks 1997). It was found that the TSM could describe the effects of the HZ as well as being able to cater for the more direct interactions with dead zones and recirculating flow structures. However, there were rather different time- and space-scales associated with the various processes, such that the TSM could not simultaneously cater for them all. Clearly, a logical development of the TSM was to create models containing both short and long time-scale transient storage interactions (Choi et al. 2000; Briggs et al. 2009), but with the (unavoidable) penalty of introducing more parameters. A more radical innovation characterised the solute exchange between the main channel and the storage zones using a general residence time distribution approach for single (Gooseff et al. 2003b) or multiple storage zones (Bottacin-Busolin et al. 2011), whilst Deng et al. (2010) advocated a variable residence time approach and Liao and Cirpka (2011) employed a hyporheic travel-time distribution.

When applying these models to practical problems it is necessary to cater for the full range of hydrological conditions likely to be encountered. In this the dependence of model parameters on river flow rate is a key concept because pollution incidents may occur during periods of high, medium or low flow rate. Thus an ability to predict parameter values that quantify shear flow dispersion and (multi-scale) transient storage at significantly different flow rates is required. Despite the innumerable tracer experiments undertaken throughout the world, however, only a very few studies contain multiple experiments executed over a wide range of flow rates in a single reach. Furthermore, whilst these single reach studies generally suggest a positive correlation between ADM velocity and flow rate and between ADM dispersion coefficient and flow rate (Wallis and Manson 2005; Romanowicz et al. 2013) they yield less consistent information regarding the behaviour of the TSM parameters (Hart et al. 1999; Gooseff et al. 2003a; Jin and Ward 2005; Camacho and Gonzalez 2008). Even fewer attempts have been made to predict transient storage parameters using correlations with familiar hydraulic and mass transport terms or dimensionless groups (Cheong et al. 2007; O'Connor et al. 2010).

Herein, we address this particular issue with the primary objective of the work being to identify the flow rate dependency of the original single time-scale TSM parameters over a flow rate range of 300–2000 L s<sup>-1</sup> in a single reach of the river Brock in north-west England. To help assess the robustness of the results and to aid their interpretation, the parameters of the ADM are also considered.

## 2 Solute Transport Models

This section provides brief background information on the two models used in this research, namely the Advection-Dispersion Model (ADM) and the Transient Storage Model (TSM). Some further details are given in Manson et al. (2016).

Once a solute cloud has been evolving for long enough in a steady, longitudinally uniform, turbulent shear flow, Taylor (1954) showed (1) that the ADM describes the evolution of the cross-sectional average concentration of a conservative solute and (2) that the magnitude of the dispersion coefficient is controlled by the longitudinal velocity and cross-sectional mixing fields. His model is given by:

$$\frac{\partial c(x, t)}{\partial t} + U_{AD} \frac{\partial c(x, t)}{\partial x} = D_{AD} \frac{\partial^2 c(x, t)}{\partial x^2} \quad (1)$$

where  $c$  is the cross-sectional average solute concentration,  $U_{AD}$  is the cross-sectional average longitudinal flow velocity,  $D_{AD}$  is the dispersion coefficient,  $t$  is time and  $x$  is the longitudinal co-ordinate direction.

The TSM extends the ADM by including terms that describe the exchange of solute between the main channel (in which shear flow causes dispersion) and storage zones which temporarily trap solute. Several workers contributed to the development of the model (e.g. Thackston and Krenkel 1967; Bencala and Walters 1983). The TSM is described by the following two equations assuming steady and longitudinally uniform flow and a conservative solute:

$$\frac{\partial c(x, t)}{\partial t} + U_{TS} \frac{\partial c(x, t)}{\partial x} = D_{TS} \frac{\partial^2 c(x, t)}{\partial x^2} + k_1(s(x, t) - c(x, t)) \quad (2)$$

$$\frac{\partial s(x, t)}{\partial t} = -k_2(s(x, t) - c(x, t)) \quad (3)$$

where  $U_{TS}$  is the cross-sectional average flow velocity in the main channel,  $D_{TS}$  is the dispersion coefficient in the main channel,  $k_1$  and  $k_2$  are model parameters (see below),  $s$  is the solute concentration in the storage zones, and the other symbols are as previously defined. Equation (2) represents solute transport in the main river channel, including advection, dispersion and the effect of transient storage, whilst Eq. (3) represents a dynamic mass balance of solute in the storage zones

themselves. In these equations a first-order exchange mechanism is used to describe the transport of solute between the main channel and the storage zones (and back again). Note that the velocity and dispersion appearing in Eq. (2) are not the same as the corresponding parameters appearing in Eq. (1).

The transient storage parameters introduced above are defined as:

$$k_1 = \alpha \quad (4)$$

$$k_2 = k_1 \frac{A}{A_S} \quad (5)$$

where  $\alpha$  is the exchange rate between the main channel and the storage zones,  $A$  is the cross-sectional area of the main channel and  $A_S$  is the cross-sectional area of the storage zones.

### 3 Tracer Data

The data used in this study were collected in the mid-1980s as part of a NERC funded project undertaken by Lancaster University, UK. About 35 experiments were undertaken in a short reach of the River Brock, which is located between Lancaster and Preston in north-west England. Briefly, each experiment consisted of the approximately instantaneous release of a known mass of Rhodamine WT followed by the measurement of temporal tracer concentration profiles at two longitudinal sites using microcomputer controlled data acquisition systems, see Wallis et al. (1987) for full details. The study reach consisted of a straight channel containing one major pool-riffle structure and with bed material of medium cobbles. It had the following characteristics: length 128 m; mean width 8.5 m; slope 0.006 (Wallis et al. 1989). The experiments covered a flow rate range of 300–2000 L s<sup>-1</sup>. The flow rates were evaluated using dilution gauging and agreed closely with observations from a nearby water authority operated flow gauging weir (Wallis et al. 1987). Data were recorded at a fixed sampling interval of 15 s. Consequently, the tracer profiles were described by between 50 and 150 data points with the lowest resolution occurring at the upstream site at the highest flow rate and the highest resolution occurring at the downstream site at the lowest flow rate.

The data were available as original logged files from the data acquisition systems that had been archived on 5.25 in. floppy discs during the 1980s, so some IT assistance was required to access the data. Although most of the extracted data appeared to be sound, there were some inconsistencies in the data from a few of the experiments. Clearly, only data that were considered to be robust were used in the current study. Apart from obvious timing errors that ruled out some concentration profiles, the reliability of the remaining data was checked by comparing the reach travel times with those obtained in the 1980s. Minor differences could be attributed

to differences in the numerical integration methods used to calculate temporal moments of the concentration profiles in the 1980s and currently (see Haas (1996) for an interesting comparison of two popular approaches). A total of 25 experiments were considered satisfactory and were used in the subsequent analysis.

Prior to use the upstream data of each experiment was scaled (by the ratio of upstream to downstream concentration profile areas) to remove any effect from lateral inflow, non-conservative behaviour of tracer or calibration errors. Generally, this was not a major issue with the mean downstream to upstream concentration profile area ratio being 0.985 ( $\pm 0.052$ ).

## 4 Application of Models

The ADM and TSM model equations were solved using a semi-Lagrangian finite volume approach, as summarized in Manson et al. (2016). This method has a proven track record of robust applications since its inception in the late 1990s. The model parameters were optimized by fitting the model downstream concentration profile to the corresponding observed concentration profile. In this the sum of squared residuals was minimised by a modified Levenberg-Marquardt algorithm (Press et al. 1992). The TSM parameters  $\alpha$  and  $A_s/A$  were evaluated from the optimized values of  $k_1$  and  $k_2$  using Eqs. (4) and (5).

## 5 Results and Discussion

### 5.1 Parameter Optimisation Results from the ADM and the TSM

Figures 1 and 2 show, respectively, velocity ( $U_{AD}$ ) and dispersion coefficient ( $D_{AD}$ ), obtained by fitting the ADM to the tracer data, plotted against flow rate. The velocity results show a well-defined increasing trend that is consistent with open

**Fig. 1** Variation of velocity with flow rate for ADM

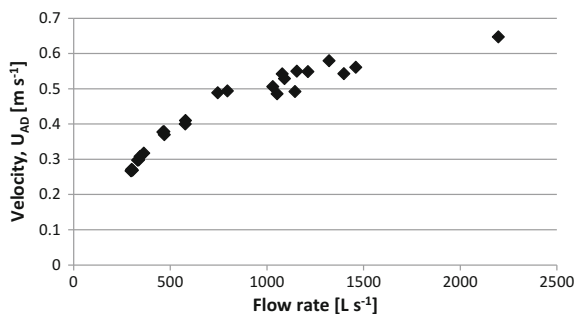


**Fig. 2** Variation of dispersion coefficient with flow rate for ADM

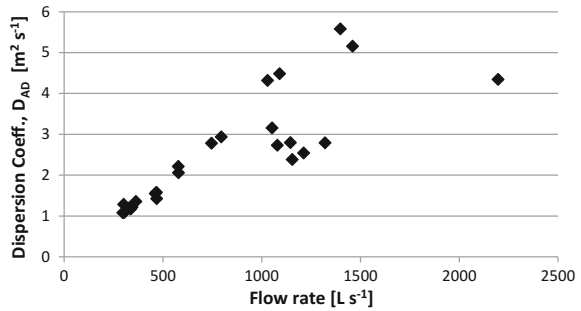
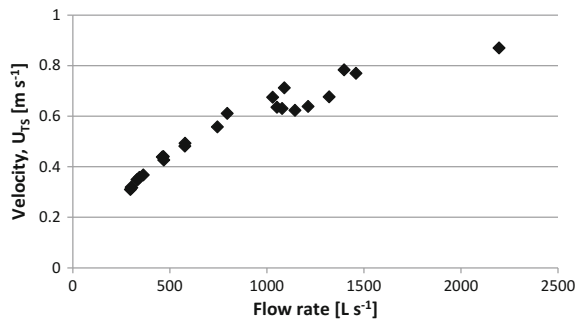


**Fig. 3** Variation of velocity with flow rate for TSM



channel flow hydraulics and with trends published in similar previous studies (Wallis and Manson 2005; Romanowicz et al. 2013). The dispersion coefficients are in the range 1–6 m<sup>2</sup> s<sup>-1</sup> and also show an increasing trend, but it is less well-defined than the velocities, particularly at flow rates >1000 L s<sup>-1</sup>. Both the trend and the values are consistent with previously published results from tracer studies in rivers of similar sizes (Rutherford 1994; Heron 2015).

Figures 3, 4, 5 and 6 show results, respectively, for  $U_{TS}$ ,  $D_{TS}$ ,  $k_1$  and  $k_2$  obtained by fitting the TSM to the tracer data. The  $U_{TS}$  results show the same trend as the  $U_{AD}$  results, but all the  $U_{TS}$  values are larger than the corresponding  $U_{AD}$  values, with percentage differences being between 12.5 and 30.7%. This reflects the fact that in the ADM the velocities are retarded by the interaction of the tracer with the transient storage zones. In general, the smaller percentage differences are associated with the lower flow rates and vice versa. Clearly, the retardation appears to increase with increasing flow rate. The  $D_{TS}$  results are rather different to the  $D_{AD}$  results. Not only are the values much smaller, being in the range 0–0.6 m<sup>2</sup> s<sup>-1</sup>, there is a lot of scatter and there is a weak decreasing trend with increasing flow rate. The smaller values of  $D_{TS}$  compared to  $D_{AD}$  reflect the fact that in the ADM all dispersive processes are catered for by  $D_{AD}$  whilst in the TSM  $D_{TS}$  only accounts for shear dispersion in the main channel (dispersion due to transient storage being accounted for separately). Similar values have been reported by Hart et al. (1999), Gooseff et al. (2003a), Jin and Ward (2005) and Camacho and Gonzalez (2008) in single

**Fig. 4** Variation of dispersion coefficient with flow rate for TSM

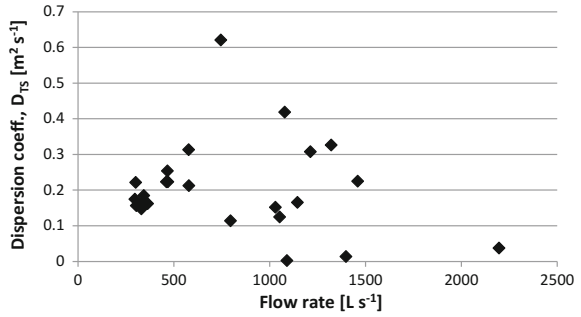
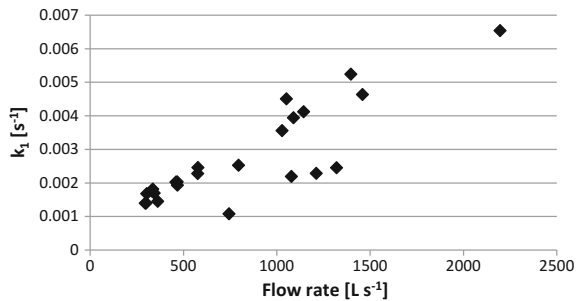


**Fig. 5** Variation of TSM parameter,  $k_1$ , with flow rate



reach studies on similar sized or smaller rivers to the Brock. In contrast to the Brock results, however, all four of these studies reported that  $D_{TS}$  was positively correlated with flow rate.

The  $k_1$  results lie in the range 0.001–0.007 s<sup>-1</sup> and show an increasing trend with flow rate. These values are at the high end of those published in Hart et al. (1999), Gooseff et al. (2003a), Jin and Ward (2005) and Camacho and Gonzalez (2008), which probably suggests that transient storage in the Brock is caused by dead zones and/or recirculating flow structures rather than by interaction with the hyporheic zone. An increasing trend was also found by Hart et al. (1999), Gooseff et al. (2003a) and Camacho and Gonzalez (2008), but there is little or no evidence for this in the results of Jin and Ward (2005). A plausible explanation for the increasing trend is that there is an increasingly more turbulent and thinner boundary layer between the main channel and the transient storage zones as flow rate increases. Thus at higher flow rates there is a more effective exchange of solute between the two domains than at lower flow rates. This is consistent with the increasing velocity retardation discussed above. The  $k_2$  results lie in the range 0.005–0.02 s<sup>-1</sup> and show an increasing trend with flow rate, which is not surprising because  $k_2$  is highly correlated with  $k_1$ , see Eq. (5). It is more useful to consider the ratio  $k_1/k_2$ , which describes the size of the transient storage zones in comparison to the size of the main channel ( $A_s/A$ ). These results are shown in Fig. 7 and reveal values between 0.2 and 0.4 with no clear trend with flow rate. Similar or smaller values were found by Hart et al. (1999), Gooseff et al. (2003a) and Jin and Ward

**Fig. 6** Variation of TSM parameter,  $k_2$ , with flow rate

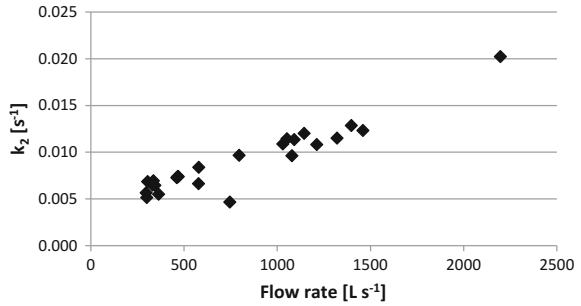
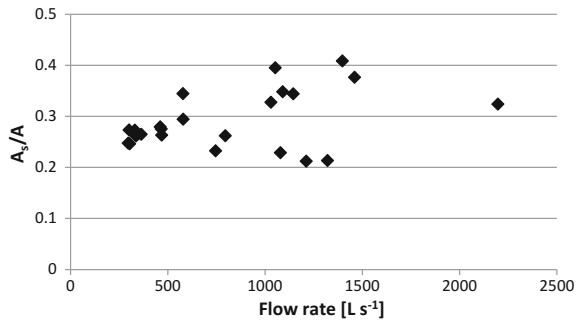


**Fig. 7** Variation of derived TSM parameter,  $A_3/A$ , with flow rate



(2005); Camacho and Gonzalez (2008) found similar values in one river but some larger values in another river. Whilst Hart et al. (1999) and Jin and Ward (2005) found no correlation with flow rate, the other two studies found a weak reducing trend.

## 5.2 Performance of the ADM and the TSM

A visual impression of the ability of the two models to fit the tracer data is given in Fig. 8, which shows typical observed and modelled temporal concentration profiles, this example being for a medium flow rate case. Clearly the ADM has difficulty in fitting the peak and the tail. In contrast, the TSM profile represents the observations faithfully throughout the entire profile. Several objective ways of comparing the performance of the two models are considered next. Firstly, the residuals of the parameter optimisation were expressed as normalised root-mean-square error (NRMSE) values, i.e. for each tracer experiment the root-mean-square residual was divided by the peak concentration of the downstream profile. These results are shown in Fig. 9 for the both models. Clearly, the NRMSE values for the ADM are greater than those for the TSM (values averaged over all the tracer experiments are 0.034 and 0.009, respectively). Whereas the NRMSE values tend to decrease

**Fig. 8** Comparison of ADM and TSM modelled concentration profiles, flow rate 579 L s<sup>-1</sup>

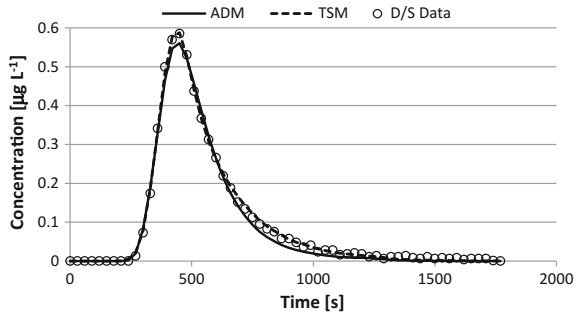
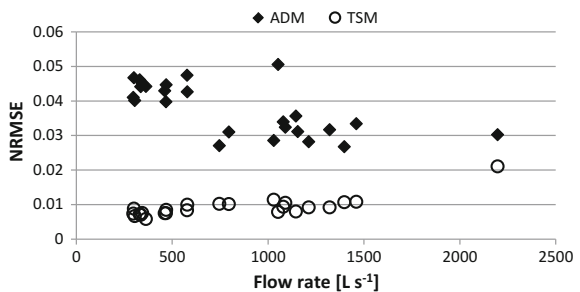


**Fig. 9** Variation of NRMSE with flow rate for ADM and TSM



with increasing flow rate for the ADM they tend to increase with increasing flow rate for the TSM. Amongst several things, this might suggest that the two models have different sensitivities to the temporal resolution of the tracer profiles (as noted in Sect. 3, the tracer profiles are less well temporally resolved at high flow rates than they are at low flow rates). The lower NRMSE values for the TSM reflect, unsurprisingly, that a four-parameter model is better able to fit the data than a two-parameter model. However, it is important to also consider the possibility that the TSM is over-parameterised (containing more parameters than can be justified). This was assessed by examining values of the Akaike Information Criteria (AIC) for both model optimisations (Burnham and Anderson 2002). In all cases the AIC for the TSM was smaller than the AIC for the ADM, which suggests that the extra two parameters are indeed justified.

Another check on the reliability of the results from the two models was undertaken using the centroid velocity ( $U_c$ ) following Manson et al. (2016). For each experiment the observed  $U_c$  was calculated from the temporal moments of the two concentration profiles. For the ADM the optimised  $U_{AD}$  should be directly equivalent to the observed  $U_c$ , whilst for the TSM the optimised  $U_{TS}$  should be modified to allow for the presence of transient storage before being compared with the observed  $U_c$ . The modification encapsulates the velocity retardation issue discussed earlier. Figures 10 and 11 show the results of this analysis for the ADM and TSM, respectively. Clearly, in both cases there is a good agreement between the observed  $U_c$  and the corresponding estimate obtained from the model optimisations.



**Fig. 10** Comparison of ADM velocity and centroid velocity

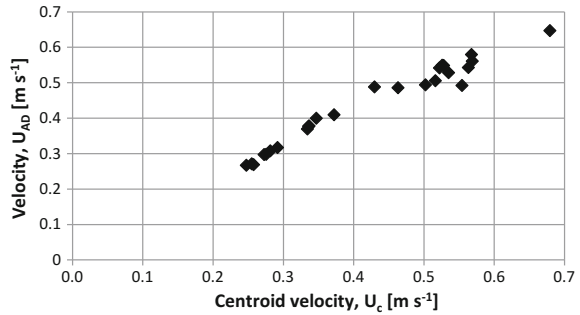
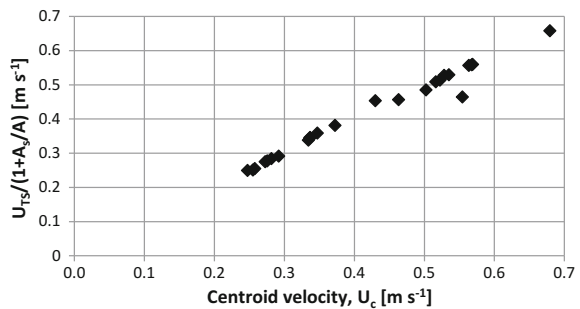


**Fig. 11** Comparison of modified TSM velocity and centroid velocity



Finally, several authors recommend using the Damkohler number to assess the reliability of TSM optimisations (e.g. Wagner and Harvey 1997; Worman and Wachniew 2007). This compares the residence timescales of main channel storage to transient storage. It has been argued that only when the timescales are of a similar order of magnitude is it possible to extract reliable TSM parameters from tracer data. For the river Brock optimisations the Damkohler number was in the range 1–4 for all the experiments, which satisfies the recommended criterion.

## 6 Conclusions

Based on several criteria, e.g. comparison with the corresponding ADM parameter values, use of the centroid velocity and referral to Damkohler numbers, the TSM parameter values obtained appear to be reliable. The increasing trend of  $U_{TS}$  and  $k_1$  with increasing flow rate is consistent with previous work in single reaches. Values of  $D_{TS}$  seem to be less robust, displaying more scatter than the other parameters and the weak reduction with increasing flow rate is at odds with previous work in single reaches. The ratio  $A_s/A$  was essentially constant over the flow rate range examined, which is consistent with some previous work in single reaches.

## References

- Beer T, Young PC (1983) Longitudinal dispersion in natural streams. *J Env Eng Am Soc Civ Eng* 109:1049–1067
- Bencala KE, Walters RA (1983) Simulation of solute transport in a mountain pool-and-riffle stream: a transient storage model. *Water Resour Res* 19:718–724
- Bottacin-Busolin A, Marion A, Musner T, Tregnaghi M, Zaramella M (2011) Evidence of distinct contaminant transport patterns in rivers using tracer tests and a multiple domain retention model. *Adv Water Resour* 34:737–746
- Briggs MA, Gooseff MN, Arp CD, Baker MA (2009) A method for estimating surface transient storage parameters for streams with concurrent hyporheic storage. *Water Resour Res* 45: W00D27. <https://doi.org/10.1029/2008WR006959>
- Burnham KP, Anderson DR (2002) Model selection and multimodel inference: a practical information-theoretic approach, 2nd edn. Springer
- Camacho LA, Gonzalez RA (2008) Calibration and predictive ability of longitudinal solute transport models in mountain streams. *Environ Fluid Mech* 8:597–604
- Cheong TS, Younis BA, Seo IW (2007) Estimation of key parameters in model for solute transport in rivers and streams. *Water Resour Manag* 21:1165–1186
- Choi J, Harvey JW, Conklin MH (2000) Characterizing multiple timescales of stream and storage zone interaction that affect solute fate and transport in streams. *Water Resour Res* 36:1511–1518
- Day TJ (1975) Longitudinal dispersion in natural channels. *Water Resour Res* 11:909–918
- Deng Z-Q, Jung H-S, Ghimire B (2010) Effect of channel size on solute residence time distributions in rivers. *Adv Water Resour* 33:1118–1127
- Elliott AH, Brooks NH (1997) Transfer of nonsorbing solutes to a streambed with bedforms: theory. *Water Resour Res* 33:123–136
- Fischer HB (1967) The mechanics of dispersion in natural streams. *J Hydraul Div Proc Am Soc Civ Eng* 93:187–216
- Gooseff MN, McGlynn BL, McGlynn RS (2003a) Transient storage processes and stream discharge recession in a headwater stream, Maimai, New Zealand. Proc N Am Benthol Soc Annual Meeting, May, 2003 (Poster)
- Gooseff MN, Wondzell SM, Haggerty R, Anderson J (2003b) Comparing transient storage modeling and residence time distribution (RTD) analysis in geomorphically varied reaches in the Lookout Creek basin, Oregon, USA. *Adv Water Resour* 26:925–937
- Haas CN (1996) Moment analysis of tracer experiments. *J Env Eng Am Soc Civ Eng* 122:1121–1123
- Hart DR, Mulholland PJ, Marzolf ER, DeAngelis DL, Hendricks SP (1999) Relationships between hydraulic parameters in a small stream under varying flow and seasonal conditions. *Hydrol Process* 13:1497–1510
- Heron AJ (2015) Pollutant transport in rivers: estimating dispersion coefficients from tracer experiments. MPhil Thesis, Heriot-Watt University
- Jin H-S, Ward GM (2005) Hydraulic characteristics of a small coastal plain stream of the southeastern United States: effects of hydrology and season. *Hydrol Process* 19:4147–4160
- Liao Z, Cirpka OA (2011) Shape-free inference of hyporheic traveltime distributions from synthetic conservative and “smart” tracer tests in streams. *Water Resour Res* 47:W07510. <https://doi.org/10.1029/2010WR009927>
- Manson JR, Wallis SG, Demars BOL, Mick JD, Gislason GM, Olafsson JS, Friberg N (2016) A comparison of three solute transport models using mountain stream tracer experiments. In: Rowinski PM, Marion A (eds) *Hydrodynamic and mass transport at freshwater aquatic interfaces*. Springer, pp 77–90
- Nordin CF, Sabol GV (1974) Empirical data on longitudinal dispersion in rivers. USGS, *Water Resour Investig* 20–74

- O'Connor BL, Miki H, Harvey JW (2010) Predictive modelling of transient storage and nutrient uptake: implications for stream restoration. *J Hyd Eng Am Soc Civ Eng* 136:1018–1032
- Press WH, Teukolsky SA, Vetterling WT, Flannery, BP (1992) *Numerical recipes in C: the art of scientific computing*, 2nd edn. Cambridge University Press
- Romanowicz RJ, Osuch M, Wallis S (2013) Modelling of solute transport in rivers under different flow rates: a case without transient storage. *Acta Geophys* 61:98–125
- Rutherford JC (1994) *River mixing*. Wiley
- Taylor GI (1954) The dispersion of matter in turbulent flow through a pipe. *Proc R Soc Lond A* 233:446–468
- Thackston EL, Krenkel PA (1967) Longitudinal mixing in natural streams. *J Sanit Eng Div Proc Am Soc Civ Eng* 93:67–90
- Wagner BJ, Harvey JW (1997) Experimental design for estimating parameters of rate-limited mass transfer: analysis of stream tracer studies. *Water Resour Res* 33:1731–1741
- Wallis SG, Manson JR (2005) Modelling solute transport in a small stream using Discus. *Acta Geophys Pol* 53:501–515
- Wallis SG, Blakeley C, Young PC (1987) A microcomputer based fluorometric data logging and analysis system. *J Inst Water Eng Sci* 41:122–134
- Wallis SG, Young PC, Beven KJ (1989) Experimental investigation of the aggregated dead zone model for longitudinal solute transport in stream channels. *Proc Inst Civ Eng Part 2*, 87:1–22
- Worman A, Wachniew P (2007) Reach scale and evaluation methods as limitations for transient storage properties in streams and rivers. *Water Resour Res* 43:W10405. <https://doi.org/10.1029/2006WR005808>

# Mathematical Modeling of the Impact Range of Sewage Discharge on the Vistula Water Quality in the Region of Włocławek

Piotr Zima

**Abstract** The paper presents results of analysis of the industrial sewage discharge influence at km 688 + 250 of the Vistula River on water quality. During the analysis, two-dimensional models of flow, impurities and temperature transport were used. Hydrological conditions of the analyzed section of the river, characteristic flows and bathymetry of the riverbed in the first instance were defined. Calculations of velocity distribution at steady flow conditions were carried out for the mean of the observed low discharges  $MLQ = 293 \text{ m}^3 \text{ s}^{-1}$ . For this purpose, a simplified two-dimensional kinematic model for variable depth of flow was used. The analysis of the impact of the discharge of impurities in steady flow conditions was performed by solving an equation of unsteady transport of pollution. Numerical simulations were carried out for pollution in the form of a non-degradable substance (tracer) and water temperature higher than measured in summer and winter conditions. The analysis included distribution of concentration of contaminants at the discharge site, as well as its range along the river bank.

## 1 Introduction

In practical applications, we often need to determine the extent of the impact of sewage discharge on river water. This applies both to the final value of the polluting indicator (concentration or temperature), as well as its spatial extent. These two are influenced by location and method of sewage discharge into the river, construction of the discharge itself and (perhaps principally) the conditions prevailing in the river at the point of discharge. It is especially important for wide rivers, where the shore location of discharge can result in exposure of river banks to contaminants introduced with sewage discharges. In case of existing discharge installations, the range of their impact can be determined on the basis of measurements. However, they can

---

P. Zima (✉)

Faculty of Civil and Environmental Engineering, Gdansk University  
of Technology, G. Narutowicza 11/12, 80-233 Gdańsk, Poland  
e-mail: piotr.zima@pg.gda.pl

only verify the concentration of individual pollution indicators in the measurement location—usually a few points located along the shore, whereas for offshore locations this is difficult or impossible. In case of planned investments, the situation is similar. The only method is to perform mathematical modeling using the solution of equations describing transport of pollutants in water (e.g. Wielgat and Zima 2016). In Poland, data on flows and water levels can be obtained from the Institute of Meteorology and Water Management (IMWM).

In the literature, we can find many ways to carry out the mathematical modeling of the impact range of sewage discharge on the river (e.g. Kalinowska et al. 2012; Wielgat and Zima 2016). The first step is to create a mathematical model that will best reflect the real object and create a mathematical model of the calculation area. For wide rivers, the most commonly used models are flat two-dimensional models, in which the actual flow area is defined on a two-dimensional  $x$ - $y$  plane.

Construction of a comprehensive model describing the process of pollution transport requires linking together into one functional unit at least two important elements: the model of water flow in the river and the model of pollution transport (Szymkiewicz 2010). Pollution concept applies in this case to every factor which is introduced into the river in excess, meaning both: an increase in water temperature and substances dissolved in water. The adoption of such assumptions requires the solution of two main issues:

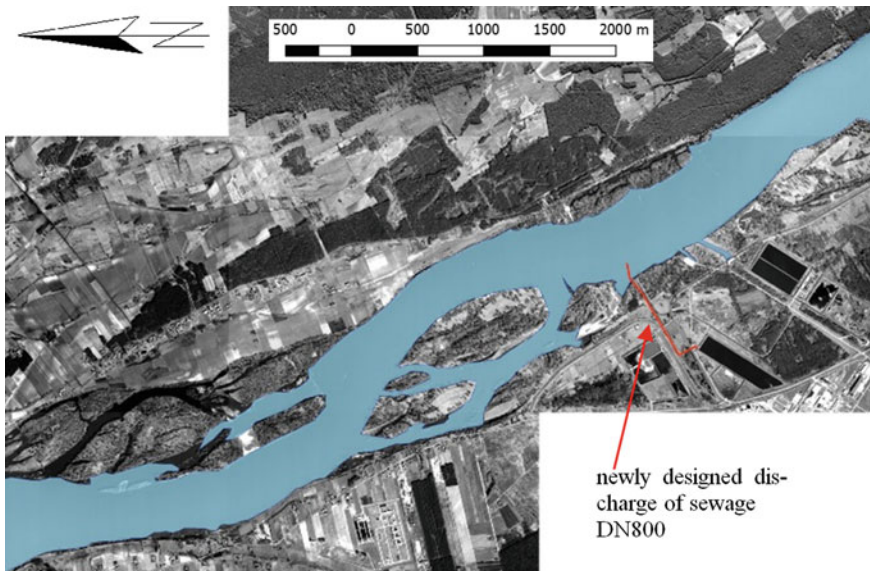


**Fig. 1** Topographic map with the location of the planned sewage discharge at km 688 + 250 of the Vistula River with indication of the reach of water during the mean of the observed low discharges  $MLQ = 293 \text{ m}^3 \text{ s}^{-1}$

- determination of parameters describing the hydrodynamics of flow in the river,
- and description of unsteady advection-dispersion transport of the solute or heat.

This paper shows how to determine the extent and influence of the discharges of industrial sewage at km 688 + 250 of the Vistula River. It is planned to replace the existing left bank discharge of industrial sewage (by Ośła Struga channel) with a newly designed pipeline DN800 (Fig. 1). At this point the coastline of the Vistula is varied and there are several islands. The pipe outlet will be away from the coast by approx. 150 m in the direction of the river current. This is to prevent the deposition of impurities in the areas where the water flow is less intensive.

## 2 Model Development

### 2.1 Description of the Velocity Field in the River

To describe the process of transport of pollutants in the river, the knowledge of the velocity field is required. The equations describing motion of water in the river are mathematical expression of the laws of conservation of mass and momentum, complemented by the constitutive equation defining the relationship between tangential stress and viscosity (Szymkiewicz 2010). Simplified models are often used in practical applications (Zima 2014; Wielgat and Zima 2016; Zima 2017). One of them is the kinematic model (Glowinski and Pironneau 1977) which assumes the kinematic condition for the rotation of the fluid element. A commonly applied approach assumes variability of the rotation of the fluid element. For a two-dimensional velocity vector,  $\mathbf{u} = [u_x, u_y]$ , this condition can be written as follows:

$$\text{rot } \mathbf{u} = \Omega(x, y), \quad (1)$$

where  $\Omega(x, y)$  is the assumed function of vorticity distribution. If we introduce the Stokes assumption (omission of inertia forces) for steady conditions of flow and take into account relation (1), we obtain:

$$\Delta \Omega = 0. \quad (2)$$

This is the equation for the harmonic function of  $\Omega$ , called the Helmholtz equation. If we define the stream function  $\psi(x, y)$  as:

$$\frac{\partial \psi}{\partial y} = hu_x, \quad - \frac{\partial \psi}{\partial x} = hu_y, \quad (3)$$

where  $h$  is the depth; we can write Eq. (2) (the biharmonic equation) in the following form (Wielgat and Zima 2016):

$$\Delta\Omega = \Delta\Delta\psi = \Delta\left(\frac{1}{h}\Delta\psi - \frac{1}{h^2}\nabla\psi\nabla h\right) = 0. \tag{4}$$

Equation (4) can be interpreted as a generalization of kinematic models in which the rotation of velocity is a harmonic function described by the Laplace equation. In general case, we consider the Dirichlet problem for the biharmonic operator (Glowinski and Pironneau 1977). Solution of this problem in a two-dimensional space  $(x, y)$  is a stream function  $\psi(x, y)$ . Finally, using relation (3) we can calculate the components of the velocity vector in the whole domain.

### 2.2 The Equation of the Dissolved Matter Transport

Transport of a non-degradable solute in a two-dimensional space can be written by the following equation (Crank 1975; Sawicki and Zima 1997):

$$\begin{aligned} \frac{\partial hc}{\partial t} + \frac{\partial(hu_x c)}{\partial x} + \frac{\partial(hu_y c)}{\partial y} = & \frac{1}{h} \frac{\partial}{\partial x} \left( hD_{xx} \frac{\partial c}{\partial x} + hD_{xy} \frac{\partial c}{\partial y} \right) \\ & + \frac{1}{h} \frac{\partial}{\partial y} \left( hD_{yx} \frac{\partial c}{\partial x} + hD_{yy} \frac{\partial c}{\partial y} \right), \end{aligned} \tag{5}$$

where:  $t$ —time, and  $c$ —concentration of dissolved matter. The coordinates of the dispersion tensor  $\mathbf{D}$  are defined as follows:

$$\begin{aligned} D_{xx} &= D_L n_x^2 + D_T n_y^2 \\ D_{xy} &= D_{yx} = (D_L - D_T) n_x n_y, \\ D_{yy} &= D_L n_y^2 + D_T n_x^2 \end{aligned} \tag{6}$$

where  $\mathbf{n} = [n_x, n_y]$  is the directional velocity vector:  $n_x = \frac{u_x}{|\mathbf{u}|}$ ,  $n_y = \frac{u_y}{|\mathbf{u}|}$ .

Longitudinal  $D_L$  and transverse  $D_T$  coordinates of the dispersion tensor (6) are described by the Elder formulas (Elder 1959; Czernuszenko 1990):

$$\begin{aligned} D_L &= \alpha h v^* \quad 30 < \alpha < 3000, \\ D_T &= \beta h v^* \quad 0.15 < \beta < 0.30, \end{aligned} \tag{7}$$

where  $v^*$  is the dynamic velocity. In this paper, values of coefficients  $\alpha$  and  $\beta$  were estimated basing on available studies (e.g. Rutherford 1994). The finally adopted values are  $\alpha = 300$  and  $\beta = 0.23$ .

### 2.3 The Equation of Heat Transport

Temperature changes are described by the equation of unsteady heat transfer (with no external sources) (Rutherford 1994):

$$\frac{\partial hT}{\partial t} + \frac{\partial(hu_x T)}{\partial x} + \frac{\partial(hu_y T)}{\partial y} = \frac{1}{h} \frac{\partial}{\partial x} \left( hD_{xx} \frac{\partial T}{\partial x} + hD_{xy} \frac{\partial T}{\partial y} \right) + \frac{\partial}{\partial y} \left( hD_{yx} \frac{\partial T}{\partial x} + hD_{yy} \frac{\partial T}{\partial y} \right), \tag{8}$$

where  $T$  is the temperature of water. Equations (5) and (8) are partial differential equations that require determination of the boundary conditions (among other things, the initial values of concentration  $c(x, y)$  and temperature  $T(x, y)$  in the river).

### 2.4 Numerical Methods

In general, Eqs. (5) and (8) are solved only by means of numerical methods (Szymkiewicz 2010). In this study, the finite difference method (FDM) for the biharmonic equation (Potter 1980) and the finite volume method (FVM) for the unsteady transport equations (LeVeque 2002) were used. In order to apply these methods, we divided the domain into square elements (cells) with  $x = y = \Delta$  (Fig. 2). In case of the biharmonic equation, as a result of the applied approximation of the difference quotients, an equation is obtained in each computational node. Figure 2a shows a 13-points scheme (Potter 1980) with nodes  $(i, j)$ , resulting from the adopted approximation of Eq. (4), and patterns of the central differential schemes. In case of boundary nodes, the above scheme has been changed according to the specified boundary condition.

Applied to solve the unsteady transport equation, FVM refers to the physical conservation laws on the control volumes level. This can be described by homogeneous hyperbolic equation as (LeVeque 2002):

$$\frac{\partial(h\varphi)}{\partial t} + \frac{\partial(hF_x)}{\partial x} + \frac{\partial(hF_y)}{\partial y} = 0. \tag{9}$$

Therefore, streams on the edges in Eq. (9) will also be in line with directions of the coordinate system ( $x$  and  $y$ ). The form of the flux vector components ( $\mathbf{F} = [F_x, F_y]$ ) on the edges  $x$  and  $y$  will be as follows:



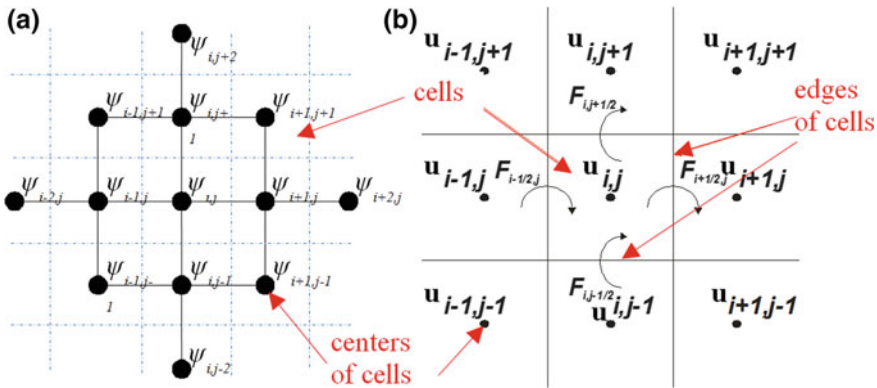


**Fig. 2** Division of the domain into two-dimensional cells and adoption of parameters of the models used in the solution of the equation: **a** biharmonic, **b** unsteady solute and heat transport

$$\begin{aligned}
 F_x &= u_x \varphi - \frac{1}{h} D_{xx} \frac{\partial \varphi}{\partial x} - \frac{1}{h} D_{xy} \frac{\partial \varphi}{\partial y} \\
 F_y &= u_y \varphi - \frac{1}{h} D_{yy} \frac{\partial \varphi}{\partial y} - \frac{1}{h} D_{yx} \frac{\partial \varphi}{\partial x},
 \end{aligned}
 \tag{10}$$

where  $\varphi$  is concentration  $c$  or temperature  $T$ . In order to determine the numerical fluxes by the cell edges in advection equation, the Lax-Wendroff scheme was used (Potter 1980). In case of the dispersion equation, the central differential schemes were used. In the method of integrating Eq. (10), it was assumed that the control area is an equivalent of a grid cell. This approach causes that values of components of the velocity vector  $\mathbf{u}$  are given in grid points and functions located in the central points of cells are unknown (Fig. 2b). Determination of intermediate values positioned between grid nodes (which are needed in determining the value of fluxes by individual cell edges) were calculated by averaging the neighboring values. This approach was applied to the function of concentration, temperature and velocity vector components.

### 3 Numerical Simulations

#### 3.1 Mathematical Model and Domain Definition

Execution of numerical simulations of pollutant transport requires defining the solution area. It is a mathematical interpretation (model) of the actual conditions in which the flow takes place in the river. This model is a result of the bathymetry of the river and the water level in identified flow conditions. The result of the

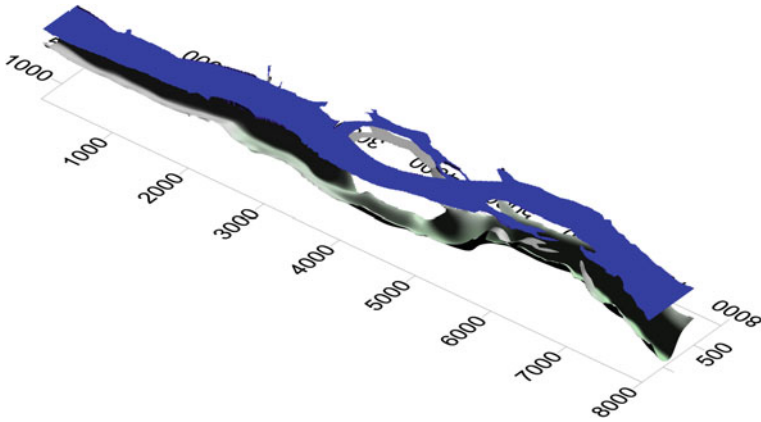


**Fig. 3** The numerical model of the bottom and the water level in the analyzed section of the Vistula River in the area of the proposed waste discharge

calculations of the area for the analyzed case (from km 685 + 300 to km 693 + 300 of the Vistula River) is shown in Fig. 3.

Bathymetry was adopted on the basis of IMWM data and measurements in the field (in designated sections). The location of cross-sections was calibrated with a topographical map. The bottom areas between the measured cross-sections were obtained by geometric interpolation in the Surfer program from Golden Software Inc. The kriging method as a gridding method was used. Areas of the bottom above water level (for the mean of the low water level for the analyzed region of the Vistula River) have been determined. In this way, a specific flow area and coastline for the position of the water table have been designated (this is especially important in case of island areas). Then, for given data, numerical calculations of the velocity field were performed. Helmholtz Eq. (4) as a simplified model was used. Calculations were made for the multi-year mean of the observed low discharges  $MLQ = 293 \text{ m}^3 \text{ s}^{-1}$ . Finite difference method to solve Eq. (4) was applied. For this purpose, the continuous domain with a length of 8 km (Fig. 3) was discretized using a square grid with step  $\Delta x = \Delta y = 5 \text{ m}$ . Two types of boundary conditions were adopted in place of the mathematical edge of the domain: the value of the stream function and the value of the normal derivative of the stream function to the edge. The boundary has the form of a curve that gives a value for the normal derivative and the variable itself. Thus, it is the Cauchy boundary condition.

### 3.2 Velocity Distribution

The boundary conditions were defined on the basis of IMWM data for the MLQ flow. Discharge of wastewater was assumed as the maximum flow rate  $Q_{max} =$

$0.686 \text{ m}^3 \text{ s}^{-1}$  with maximum velocity  $v_{max} = 1.36 \text{ m s}^{-1}$ . The calculations performed yielded an image of the velocity distribution in the relevant section of the Vistula River (shown in Fig. 4). The maximum value of the velocity vector in the current was about  $0.98 \text{ m s}^{-1}$ , average velocity in a cross-section was  $0.67 \text{ m s}^{-1}$ , and they were similar to IMWM data. The velocity distribution in the vicinity of the dump (from km 2 + 200 to 7 + 200 of the adopted model) is shown in Fig. 7. The velocity vector is drawn every hundredth value of the computing grid  $5 \text{ m} \times 5 \text{ m}$ . The location of the discharge is indicated schematically on the drawings by a green line.

### 3.3 Solution of the Advection-Dispersion Equation

In order to solve the transport Eq. (5) or (8), the same area as in case of the velocity distribution was adopted, except that the distribution of solute concentration and temperature was calculated relative to the center of the cell area (finite volume)—Fig. 2. Thus, a natural shift of grid was obtained which has a beneficial effect on the used numerical scheme (Potter 1980). The transport equation was supplemented by the boundary conditions: initial condition (at all points of the calculation area) and the boundary conditions at the points that are the physical and the mathematical banks of the calculation area. The initial condition was the concentration or temperature measured in the water of the Vistula River in the vicinity of the designed dump (so called “background”). The boundary condition was adopted in two ways: the condition on the physically impermeable edge (the Neumann condition) and conditions on the mathematical edge (at the inlet with known values of the background concentration or temperature—the Dirichlet condition, and at the outlet—the Neumann condition). The sewage discharge point to the river requires an additional comment. In the conducted study it was assumed that from the moment of sewage introduction into the water body, the process of mixing takes place. This is described by a simple equation of the balance of streams:

$$Q\phi = Q_z\phi_z + Q_w\phi_w \quad (11)$$

where:  $\phi$ ,  $Q$ —concentration or temperature and flow rate at the discharge point in the river after mixing,  $\phi_z$ ,  $Q_z$ —concentration or temperature and flow rate of the discharged sewage in the pipeline,  $\phi_w$ ,  $Q_w$ —concentration or temperature and flow rate in the river before mixing (Kalinowska et al. 2012):

$$Q_w = h_z u \Delta \quad (12)$$

where:  $h_z$ ,  $u$ —depth and velocity of water at the discharge point in the river, and  $\Delta$ —step of the grid.

Calculations were carried out for pollution in the form of a non-degradable substance (tracer) and temperature higher than in the river. In all cases, no

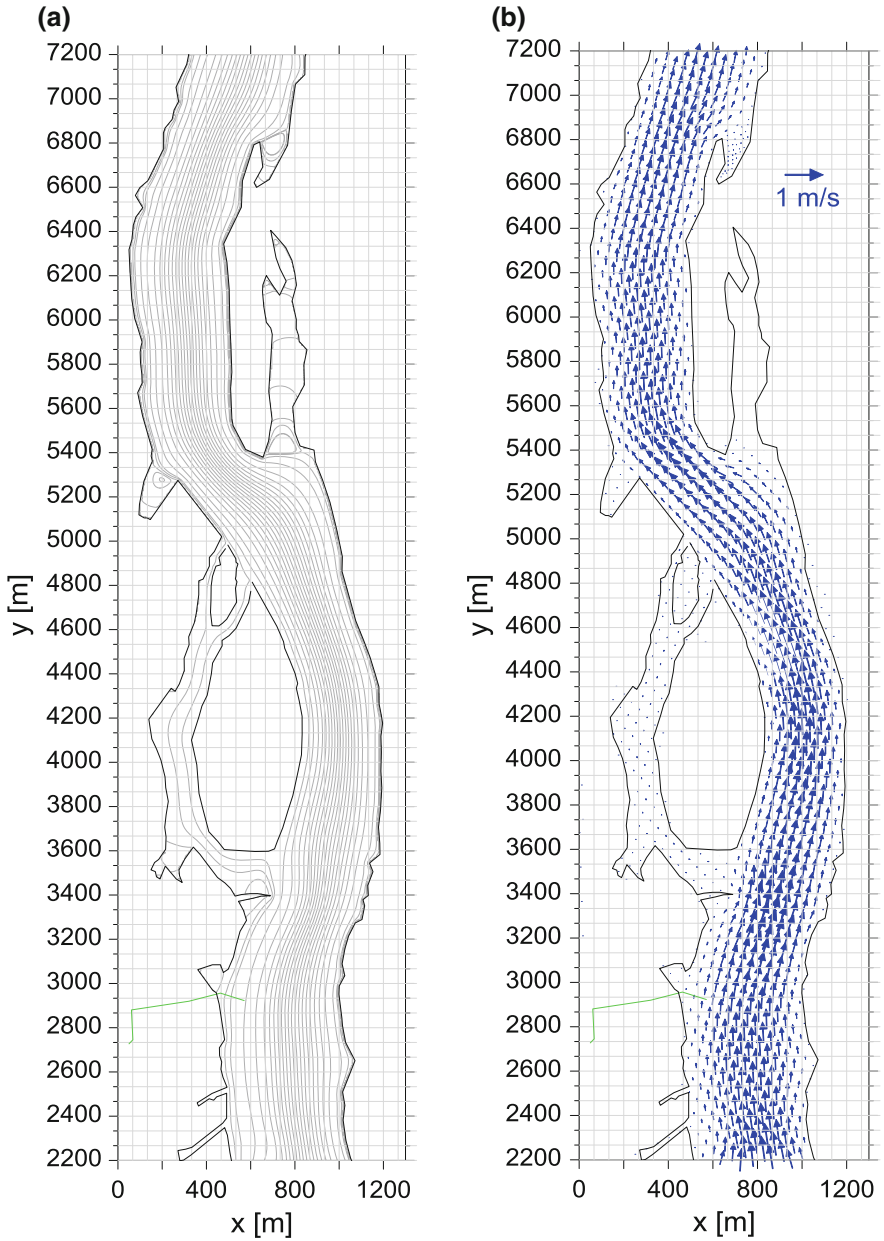


**Fig. 4** Distribution of the stream function  $\psi(x, y)$  (a) and the velocity vector  $\mathbf{u}$  (b) on the section from km 2 + 200 to km 7 + 200 of the calculation area (the velocity vector drawn every hundredth value of the computing grid  $5\text{ m} \times 5\text{ m}$ ). Location of the discharge is indicated schematically by a green line

additional external factors affecting the change in concentration or temperature were introduced. Simulations were performed assuming constant discharge of wastewater with a maximum concentration or temperature during the whole simulation time—until concentration or temperature distribution was established.

The finite volume method to solve Eqs. (5) and (8) (LeVeque 2002), and the Lax-Wendroff scheme (Potter 1980) to determine the numerical fluxes by the edges of cells were used.

The results are shown in a graphic form in Figs. 5, 6 and 7 in two ways. The range of influence of a particular pollutant discharged in the adopted calculation area is shown in panel (a) and against the background of a topographic map in panel (b). The results of computer simulation of the non-degradable dissolved matter (tracer) are shown in Fig. 5a. It was assumed that the concentration of the substance at the outlet of the pipeline at the point of discharge was  $C = 100\%$ , and

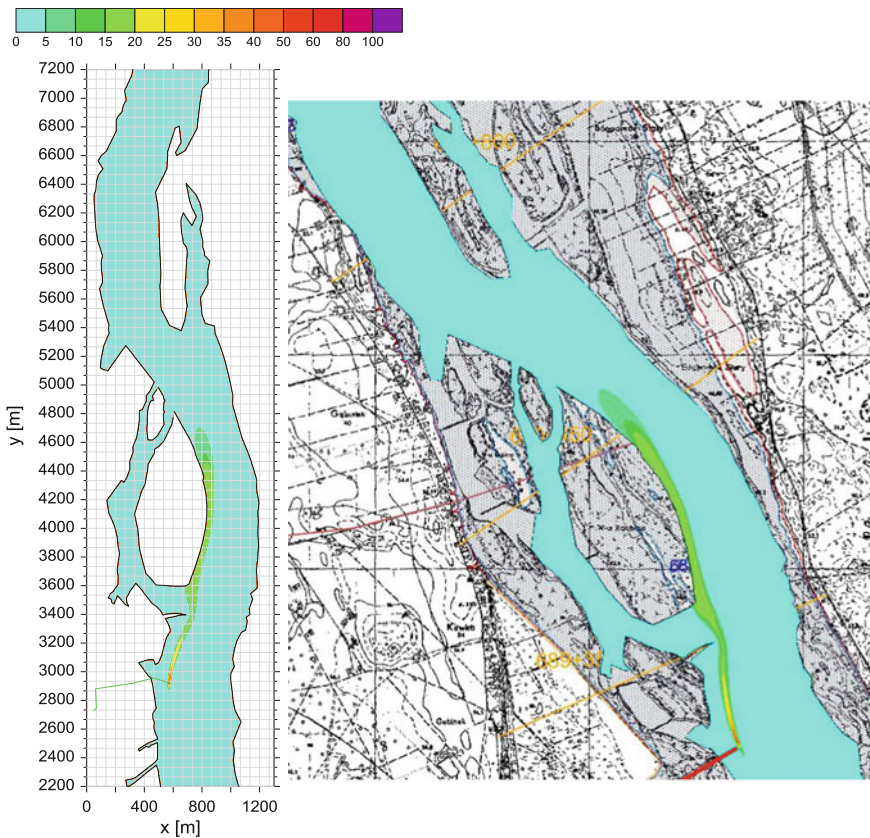


**Fig. 5** Distribution of concentration of the non-degradable dissolved matter (tracer) in the area of the dump. The results obtained from the mathematical model (left) were transferred to the topographic map (right)

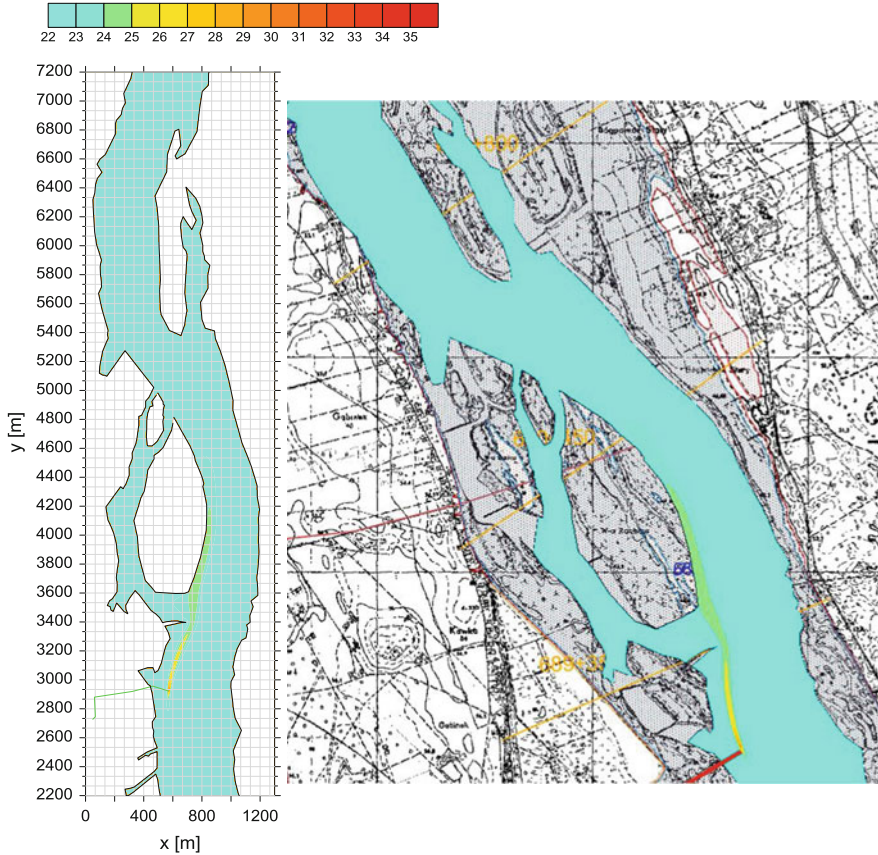


**Fig. 6** Distribution of water temperature in the area of the dump in summer conditions, temperature of sewage 35 °C, after taking into account mixing in the river at the point of discharge: 26.6 °C, temperature of river water 22.9 °C. The results obtained from the mathematical model (left) were transferred to the topographic map (right)

concentration in the river  $C_0 = 0\%$ . The concentration after mixing with water in the river (11) falls to approx. 50.1%. The distribution in space against a topographical map is shown in Fig. 5b.

The results of computer simulation of temperature changes at the point of discharge are shown in Fig. 6 (in summer conditions) and Fig. 7 (in winter conditions). It was assumed that the sewage temperature at the outlet of the pipeline at the point of discharge is  $T = 35\text{ }^\circ\text{C}$ , and the water temperature in summer conditions  $T_0 = 22.9\text{ }^\circ\text{C}$ , while in winter conditions  $T_0 = 0.29\text{ }^\circ\text{C}$ . After taking into account the process of mixing in the river at the point of discharge, temperature fell to approx. 26.6 °C in summer conditions (Fig. 6a) and increased up to approx. 10.8

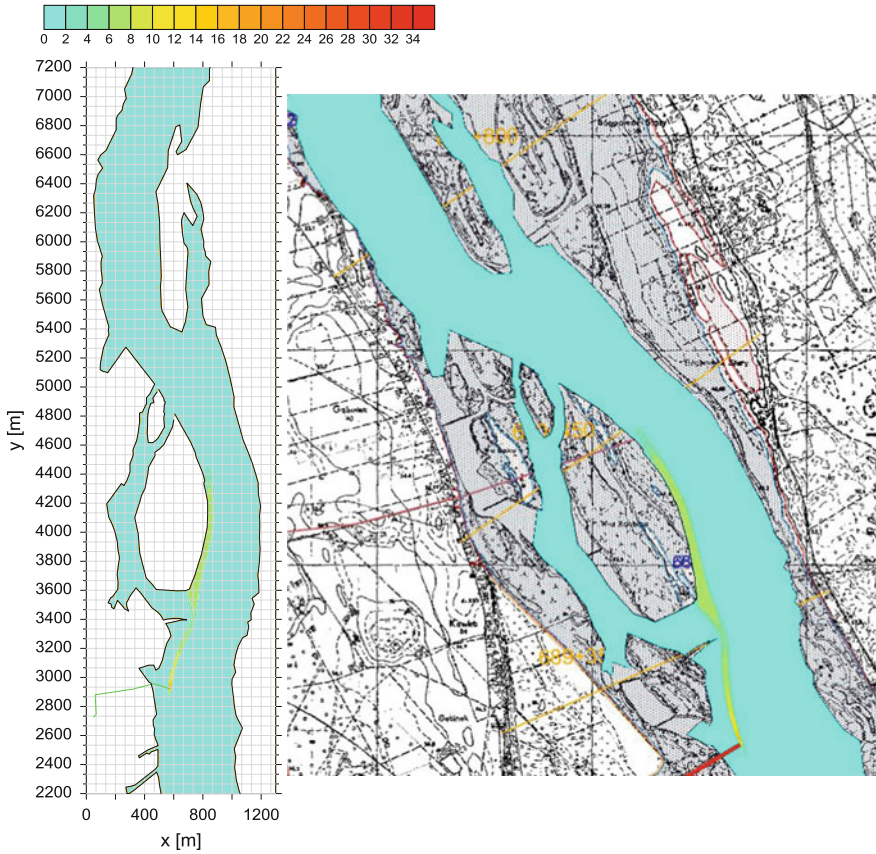


**Fig. 7** Distribution of water temperature in the area of the dump in winter conditions, temperature of sewage 35 °C, after taking into account mixing in the river at the point of discharge: 15.6 °C, temperature of river water 0.29 °C. The results obtained from the mathematical model (left) were transferred to the topographic map (right)

°C in winter conditions (Fig. 7a). The distribution in space against a topographic map is shown, respectively, in Fig. 6b in summer conditions and Fig. 7b in winter conditions.

### 4 Conclusions

In order to obtain the results of numerical simulations of pollutant transport in the section of the Vistula River (from km 685 + 300 to km 693 + 300), as described above, a mathematical model had to be created. One of the basic assumptions for simplification was the adoption of the steady conditions on the hydrodynamics of

flow. In case of the model used, data on characteristic flow  $MLQ = 293 \text{ m}^3 \text{ s}^{-1}$  (flow rate and water level) were designated by hydrological methods, based on the information for the gauging cross-section Włocławek. Data of the geometry of the calculation area were adopted from IMWM information and measurements. The coastline was determined on a topographic map on the basis of information concerning water level in the cross-sections located along the adopted calculation area. Information on the bottom of the river between the two cross-sections was generated by geometric interpolation. The distance between the cross-sections on this extent of the river (IMWM data) was from 1.1 to 3.35 km. Additional measurements were performed in designated places (in the areas near the islands).

Next, computer simulations of the velocity distribution and transport of contaminants in the examined part of the river were carried out. The results of velocity distribution under steady flow conditions were compared with IMWM data. Maximum velocity in the current ( $0.98 \text{ m s}^{-1}$ ) and average velocity in a cross-section ( $0.67 \text{ m s}^{-1}$ ) were similar to those data. Calculations of pollution transport were carried out in unsteady conditions (for the steady velocity distribution) for pollution in the form of a non-degradable substance (tracer) and temperature higher than in the river. Discharge of sewage into the river was adopted in accordance with the project at approx. 150 m from the shore. The estimated range of dissolved matter was about 2 km from the dump (the area where the concentration was higher by at least 10% than the concentration in the river). Maximum concentration amounted to 50.1% of the initial concentration in the effluent (100%) at the point of discharge after mixing in the river. Contamination moved along the right shore of the island and did not spread into the branch, where due to low velocity the exchange of water is impeded. In case of temperature distribution, its values increased due to discharge of heated sewage. Calculations were carried out in conditions of summer and winter. Temperature at the outlet of the pipeline at the point of discharge was  $35 \text{ }^\circ\text{C}$ , and water temperature in summer conditions was  $22.9 \text{ }^\circ\text{C}$ , while in winter conditions it was  $0.29 \text{ }^\circ\text{C}$ . After taking into account mixing in the river at the point of discharge, temperature has fallen to approx.  $26.6 \text{ }^\circ\text{C}$  in summer conditions and increased up to approx.  $10.8 \text{ }^\circ\text{C}$  in winter conditions. The range of change in space in summer conditions is on the approx. 1.5 km and in winter conditions approx. 2 km.

## References

- Crank J (1975) *The mathematics of diffusion*. Clarendon Press, Oxford
- Czernuszenko W (1990) Dispersion of pollutants in flowing surface waters. In: Cheremisinoff NP (ed) *Encyclopedia of fluid mechanics*, vol 10. Surface and groundwater flow phenomena. Gulf Publishing, Houston, pp 119–168
- Elder JW (1959) The dispersion of marked fluid in turbulent shear flow. *J Fluid Mech* 5(4):544–560



- Glowinski R, Pironneau O (1977) Numerical methods for the first biharmonic equation and for the two-dimensional stokes problem, Raport STAN-CS-77-615, May 1977, Computer Science Department, School of Humanities and Sciences, Stanford University
- Kalinowska MB, Rowiński PM, Kubrak J, Mirosław-Świątek D (2012) Scenarios of the spread of a waste heat discharge in a river—Vistula river case study. *Acta Geophys* 60(1):214–231
- LeVeque RJ (2002) Finite volume method for hyperbolic problems. Cambridge University Press, New York
- Potter D (1980) Computational physics. Wiley, New York
- Rutherford JC (1994) River mixing. Wiley, Chichester
- Sawicki JM, Zima P (1997) The influence of mixed derivatives on the mathematical simulation of pollutants transfer. In: 4th international conference on water pollution, Bled, Slovenia, pp 627–635
- Szymkiewicz R (2010) Numerical modeling in open channel hydraulics. *Book Ser: Water Sci Technol Libr* 83:1–419
- Wielgat P, Zima P (2016) Analysis of the impact of the planned sewage discharge from the ‘North’ power plant on the Vistula water quality. In: 16th international multidisciplinary scientific GeoConference SGEM 2016, Vienna, Book 3 vol 3, pp 19–26
- Zima P (2014) Numerical simulations and tracer studies as a tool to support water circulation modeling in breeding reservoirs. *Arch Hydro-Eng Environ Mech* 61(3–4):113–123
- Zima P (2017) Investigations on water circulation in animal sea-water basins—on the example of seals’ breeding pools. *Polish Maritime Res* 24, No S1(93):224–229